

UNIVERSITY OF BIRMINGHAM

TOOLS TO DETECT AND CHARACTERISE CIRCUMBINARY EXOPLANETS

by

THOMAS BAYCROFT

A thesis submitted to the University of Birmingham for the degree of

DOCTOR OF PHILOSOPHY

Sun, Stars, and Exoplanets research group

School of Physics and Astronomy

College of Engineering and Physical Sciences

University of Birmingham

April 2025

UNIVERSITY OF
BIRMINGHAM

University of Birmingham Research Archive

e-theses repository

This unpublished thesis/dissertation is copyright of the author and/or third parties. The intellectual property rights of the author or third parties in respect of this work are as defined by The Copyright Designs and Patents Act 1988 or as modified by any successor legislation.

Any use made of information contained in this thesis/dissertation must be in accordance with that legislation and must be properly acknowledged. Further distribution or reproduction in any format is prohibited without the permission of the copyright holder.

© Copyright by THOMAS BAYCROFT, 2025

All Rights Reserved

Abstract

Circumbinary exoplanets, those planets orbiting around a binary star, are a fascinating class of exoplanet which, while prevalent in science fiction (e.g. LucasFilm et al. 1977), were only confirmed to exist in 2011. Circumbinary planets are particularly useful as a *controlled experiment* for planet formation since certain theorised planet formation mechanisms around single stars are not available to planets orbiting binaries. In this thesis I develop tools better to detect and understand circumbinary planets, and then deploy these across different stages of binary evolution and to various types of data. Chapter 1 provides an introduction to the field of exoplanet research and to circumbinary planets specifically.

Chapter 2 contains an introduction to Bayesian statistics and its use in model comparison for exoplanet detection. The various code contributions that I have made, in particular to `kima` are also described in Chapter 2. One contribution is the BINARIESmodel, tailored to analysis of radial velocity data of binaries and circumbinary planets. This model includes general relativistic and tidal corrections for close binaries; the apsidal precession of the binary as a free parameter; and the ability to analyse double-lined binaries which have two simultaneous radial velocity timeseries. Other contributions to `kima` are models to fit eclipse timing variations and *Gaia* astrometry.

Chapter 3 and Chapter 4 present results on main-sequence binaries. Chapter 3 is focused on double-lined binaries, which includes radial velocities confirming the detection of a circumbinary planet around TIC 172900988 and an analysis of a sample of double-lined binaries showing that new spectral disentangling methods allow us to obtain more precise and more accurate radial velocities than previously. A discussion of future circumbinary planet detections with *Gaia* data

is also included. Chapter 4 divulges results from the BEBOP survey for circumbinary planets. Results include individual systems with planet detections and candidates, the BEBOP-3 system is highlighted. Other results from BEBOP are included, presenting the growing population of circumbinary planets. This population is compared to previous results from samples of transiting circumbinary planets.

Circumbinary planets have been claimed orbiting post main-sequence binaries, I revisit a famous example of a post common-envelope binary *HW Virginis*, which has claimed planets from eclipse timing variations, in Chapter 5. The eclipse timing variations are studied to test whether there are credible planetary signals in the data, and *Gaia-Hipparcos* astrometry is used to find marginal evidence for the existence of a planet in the system. Predictions are also made in Chapter 5 for how future *Gaia* data releases will allow for confirmation or refutation of many of the claimed eclipse timing variation systems like HW Vir.

Chapter 6 describes the use of apsidal precession measurements of binaries in greater detail and how such a measurement can be used to predict the presence of a circumbinary planet and glean information about its orbital configuration. I present the analysis of a rare binary brown dwarf which is found to have a retrograde apsidal precession, and show that ruling out all other possibilities it must be due to a circumbinary planet on an orbit inclined at 90° to the orbital plane of the binary.

Concluding remarks are made in Chapter 7.

To Berlioz, he was a good boy.

Acknowledgements

I would first like to thank my supervisor Amaury Triaud, your enthusiasm for science has been inspiring. I have appreciated your advice, support, and willingness to be distracted whenever I think I've found something cool. I would also like to thank my secondary supervisor Guy Davies for your help with my regular worries about statistics, as well as the other faculty in SSE who have always been available whenever I need help or advice. I would like to thank Lou, you are always quick to help with any issues I have with university systems. I would like to thank my examiners, Nicolás Cuello and Annelies Mortier, for taking the time to read the ramblings that follow.

I want to thank the friends and colleagues at the university of Birmingham across SSE and ASR and across many years: Alex Gill, Aysha, Cress, Dan, Emily and Owen, as well as Alex, Alice, Alix, Amalie, Andres, Daisy, Daniel, Daria, Eliot, Emma, Evan, George, Joscha, Lalitha, Maddy, Martin, Matt, Natalie, Paige, Simona, Yaz, among more that I do not have space to name. You have made my day-to-day fun and bright, my time in Birmingham will always be remembered as some of the best years of my life. I thank my family: Tim, Christine, Emily and Victor for your love and support.

I finally thank Lucy, you are always there for me if I need it. You have helped me countless times with scientific discussions, cooked unhinged dinners with me, and listened to me babble about my work, my interests, and any random thought that pops into my head.

Contents

Abstract i

Acknowledgements v

Contents vii

List of Figures xi

List of Tables xxv

1 Introduction 1

1.1 Overview of exoplanets . . . 1

1.1.1 Exoplanet definition . . . 1

1.1.2 Stellar and exoplanet naming conventions . . . 3

1.2 Orbits and the Celestial sphere . . . 4

1.3 Exoplanet detection methods . . . 7

1.3.1 Radial velocities . . . 8

1.3.2 Transits . . . 13

1.3.3 Direct Imaging . . . 17

1.3.4 Gravitational microlensing . . . 19

1.3.5 Astrometry . . . 21

1.3.6 Timing variations . . . 22

1.4 Exoplanet population demographics . . . 25

1.4.1 Classes of exoplanet . . . 25

1.4.2 The radius valley . . . 26

1.4.3 Other population trends . . . 28

1.5 Exoplanet formation and evolution . . . 31

1.5.1 Exoplanet formation models . . . 31

1.5.2 Exoplanet evolution and migration . . . 32

1.6 Circumbinary planets . . . 33

1.6.1 Circumbinary orbits and stability . . . 34
1.6.2 Circumbinary planet detection . . . 36
1.6.3 Circumbinary planet demographics . . . 45

2 Methods **53**
2.1 Bayesian Statistics and the use of `kima` . . . 53
2.1.1 The Bayesian way . . . 53
2.1.2 Bayesian model comparison and Occam's razor . . . 54
2.1.3 Choice of priors . . . 58
2.1.4 Nested sampling . . . 59
2.1.5 `kima` . . . 62
2.1.6 GJ 9404 b: a confirmed eccentric planet, and not a candidate . . . 64
2.1.7 Bayesian detection limits with `kima` . . . 69
2.2 `kima` BINARIESmodel . . . 70
2.2.1 Contributions to the paper. . . . 70
2.2.2 Improving circumbinary planet detections by fitting their binary's apsidal precession . . . 72
2.2.3 A binary update to `kima` . . . 73
2.2.4 Performances of `kima-binaries` . . . 74
2.2.5 Application of `kima-binaries` to Kepler-16 . . . 77
2.2.6 Conclusions . . . 78
2.2.7 Appendix A: Derivation of the planetary induced precession rate . . . 79
2.2.8 Appendix B: Tables of parameters . . . 80
2.2.9 Fitting double-lined binary data . . . 81
2.2.10 Inclination of the binary orbit . . . 83
2.3 `kima` ETVmodel . . . 84
2.4 `kima` GAIAmodel and RVGAIAmodel . . . 88
2.4.1 Model for *Gaia* epoch astrometry . . . 88
2.4.2 Testing the GAIAmodel and RVGAIAmodel . . . 89

3 Planets orbiting main-sequence binary stars: double-lined binaries **95**
3.1 New methods for radial-velocity measurements of double-lined binaries, and detection of a circumbinary planet orbiting TIC 172900988 . . . 96
3.1.1 Introduction . . . 98
3.1.2 GP-based radial velocity extraction . . . 99
3.1.3 Application to TIC 172900988 . . . 102
3.1.4 Results . . . 103
3.1.5 Conclusions . . . 108

3.1.6 Appendix: Some extra material . . . 110
3.2 A geometric advantage for circumbinary planet transits . . . 116
3.2.1 The one-two punch . . . 116
3.2.2 Using the one-two punch in kima . . . 116
3.2.3 The one-punch . . . 117
3.3 BEBOP VI. Enabling the detection of circumbinary planets orbiting double-lined binaries with the DOLBY method of radial–velocity extraction . . . 121
3.3.1 Introduction . . . 123
3.3.2 A summary of our double-lined binary observations . . . 124
3.3.3 A summary of the DOLBY method of radial velocity extraction . . . 126
3.3.4 Results from fitting the radial velocities . . . 126
3.3.5 Conclusions . . . 130
3.3.6 Appendix A: Observed and modelled radial velocities . . . 132
3.3.7 Appendix B: Uncertainties and RMS values . . . 134
3.3.8 Appendix C: Detection limits . . . 134
3.3.9 Appendix D: Radial velocities . . . 136
3.4 Predicting *Gaia*'s yield . . . 142
3.4.1 A synthetic population of binaries and circumbinary planets . . . 143
3.4.2 Testing *Gaia* sensitivity to circumbinary populations . . . 146

4 Planets orbiting main-sequence binary stars: single-lined binaries/BEBOP 153
4.1 The BEBOP survey . . . 153
4.2 BEBOP VII: Discovery of BEBOP-3b with SOPHIE, a circumbinary giant planet on an eccentric orbit . . . 154
4.2.1 Introduction . . . 156
4.2.2 Radial velocity data . . . 157
4.2.3 Analysis and Methods . . . 157
4.2.4 Results . . . 159
4.2.5 Disucssion . . . 162
4.2.6 Conclusion . . . 164
4.2.7 Appendix . . . 166
4.3 Detections and candidates from BEBOP . . . 170
4.3.1 BEBOP detections . . . 170
4.3.2 BEBOP tentative detections . . . 181
4.3.3 BEBOP candidates . . . 185
4.3.4 BEBOP long-period planetary-mass signals . . . 197
4.3.5 Overview of BEBOP results . . . 197
4.4 Circumbinary planet population results . . . 202

5 Planets orbiting evolved binaries **207**

5.1 New evidence about HW Vir's circumbinary planets from *Hipparcos-Gaia* astrometry and a reanalysis of the eclipse timing variations using nested sampling 207

5.1.1 Introduction . . . 209

5.1.2 Astrometry using the proper-motion anomaly method . . . 210

5.1.3 Fitting eclipse timing variations with `kima` . . . 213

5.1.4 Fitting eclipse times . . . 213

5.1.5 Discussion and conclusions . . . 217

5.2 Post common-envelope binaries with *Gaia* . . . 219

5.2.1 Previously claimed planets . . . 219

5.2.2 Sensitivity to a population . . . 221

6 Apsidal precession: a powerful predictive tool **225**

6.1 Evidence for a polar circumbinary exoplanet orbiting a pair of eclipsing brown dwarfs . . . 225

6.1.1 Introduction . . . 230

6.1.2 Results . . . 232

6.1.3 Discussion . . . 234

6.1.4 Materials and Methods . . . 238

6.2 Detecting circumbinary planets using apsidal precession . . . 260

6.2.1 Apsidal precession from radial velocities . . . 260

6.2.2 Apsidal precession from eclipse timing variations . . . 265

7 Concluding remarks **271**

References **273**

List of Figures

1.1 Diagram of orbit and orbital angles *Credit:* Lasunncty. 6
1.2 Cumulative histogram of exoplanet detections seperated by technique. Data taken from the NASA exoplanet archive 7
1.3 The known exoplanets shown in the $M \sin i$ - Period space. This only shows those with 1σ measurements of period and mass. Data taken from the NASA exoplanet archive 8
1.4 Depiction of the cross-correlation function and radial velocity curve. Top: cross-correlation functions for a series of radial velocity measurements. Bottom: the corresponding radial velocity measurements. The time is shown by the colour. This example is for a 10 day orbit with $e = 0.1$ and $K = 75$ km/s. Twice the semi-amplitude K and the time at which the pericentre passage occurs are indicated on the bottom panel. 9
1.5 Right: Conditions for a solar eclipse. From *The Fountain of Knowledge* by John of Damascus (Arab, about 675-749 CE) from the Rare Book & Manuscript Library, Columbia University Libraries, New York. 14
1.6 *TESS* data for eclipsing binary TIC 139721086. Demonstration of some of the transit/eclipse parameters discussed in the text from which orbital and physical parameters can be derived. 15
1.7 From Marois et al. (2010). Directly imaged planets around HR 8799. 18
1.8 From Gaudi (2010). Left: schematic of the microlensing event. Right: microlensing magnification againt time with the perturbation from a planet shown. 20
1.9 The astrometric motion of DE0823-49, paralactic motion at the bottom, with a zoom in of the orbit above. Figure taken from Sahlmann et al., 2013. 21
1.10 Occurence of exoplanets by their radius demonstrating the radius valley between super-Earths an mini-Neptunes. Figure adapted from Fulton et al. (2017). . . . 27
1.11 The hot-Neptune desert. Left: planet radius vs orbital period. Right: planet radius vs planet instellation. Planets are taken from the NASA exoplanet archive, only those with 3σ measurements of radius and period are included. 29
1.12 Configurations of planets in binary systems. 33

1.13 Configurations of circumbinary orbits precessing about the binary angular momentum vector (left) and precessing about the binary eccentricity vector (right). These are referred to as *Circulating* and *Librating* configurations respectively. . 37

1.14 Circumbinary planet transits across the primary star at different orbital phases. Binary orbit shown on the left with four binary phases shown and labelled A-D, location of planet shown on right transiting the primary star at each of those phases. E: Equivalent single star system which would lead to stricly periodic transits all of the same duration. A: Star is moving along the line of sight, transit is near normal duration and is late. B: Near primary eclipse star and planet are moving in opposite directions, transit is very short and close to on time. C: near secondary eclipse star and planet are moving in the same direction, transit is very long and nearly on time. D: star is moving along the line-of sight, transit is near normal duration and is early. 38

1.15 From Orosz et al., 2012a, paper on the discovery of two planets in the Kepler-47 system. The durations of the transits for the inner planet (filled circles) and the outer planet (filled squares) as a function of the orbital phase of the binary. The solid curves are the predicted durations assuming a circular, edge-on orbit for the planet. At phases near the primary eclipse, the planet and the primary star are moving in opposite directions, resulting in a narrower transit. At phases near the secondary eclipse, the planet and the primary star are moving in the same direction, resulting in a longer transit. The outer planet is moving slower than the inner planet, resulting in longer transits at the same binary phase. 39

1.16 Dynamical eclipse timing variations for a circular planet orbiting an eccentric binary. Left: system integrated for 500 days, top is the system configuration; middle are the residuals of a linear ephemeris; bottom are the residuals phase folded on the orbital phase of the planet. Right: system integrated for 180 days, top is the system configuration with location of the planet at each eclipse shown; bottom are the phase folded residuals. In all cases (except top left) the colouring is scaled by the time of the eclipse. 43

1.17 The Kepler circumbinary planets in various parameter configurations. Top: Proximity to stability limit with increasing binary orbital period anti-clockwise. Middle left: planet mass vs total binary mass. Middle right: planet mass vs proximity to stability limit. Bottom left: eccentricity vs proximity to stability limit, stable orbits should be below the red envelope. Bottom right: binary orbital period vs planet orbital period, blue region shows unexpected dearth of planets implying pile-up. 48

2.1 Prior and posterior distributions for 8 analyses of Kepler-16 radial velocity data, showing the dependency of the Bayes Factor on prior width. 57

2.2 Relationship between prior width and Bayes Factor showing the predicted reciprocal dependency. 58

2.3 Difference in likelihood-level exploration between classic nested sampling and diffusive nested sampling. Figure from Brewer et al. (2011). 61

2.4 Top row: left, a Lombe-Scargle periodogram of the simulated radial velocity data of a 50-day period signal shown on right, the true model is shown as well. Second row: left, histogram of periods with from `kima`; right, FIP periodogram from the same `kima` run. Bottom: phase-folded radial velocity data on six different periods (specified above each panel). 68

2.5 Detection limits for additional Keplerian signals using SIM1. 76

2.6 Detection limits for additional signals around KOI-126. 77

2.7 Kepler-16: histogram of the density of posterior samples for fitted value and theoretically calculated value of $\dot{\omega}$ 77

2.8 Detection limits for Kepler-16 with and without accounting for precession. . . . 78

2.9 Posterior and prior distributions on the inclination of the binary orbit of HD 13974. 84

2.10 Corner plot showing the posteriors from the analysis of the synthetic eclipse timing data with the ETVmodel of `kima`, the injected values are shown in blue. The parameters are Jitter, T_0, P_0, $\left(\frac{dP}{dt}\right)_0$, $\left(\frac{d^2P}{dt^2}\right)_0$, $P_{\rm pl}$, $K_{\rm pl}$, $T_{\rm peri,pl}$, $e_{\rm pl}$, $\omega_{\rm pl}$. . . 87

2.11 Corner plot showing the posteriors from the analysis of the synthetic *Gaia* data with the GAIAmodel of `kima`, the injected values are shown overtop. The paramters are $\Delta\alpha^\star$, $\Delta\delta$, $\mu_{\alpha^\star}$, μ_δ, ϖ, $P_{\rm pl}$, ϕ_0, $e_{\rm pl}$, $a_{0,\rm pl}$, $\cos i_{\rm pl}$, $\Omega_{\rm pl}$, $\omega_{\rm pl}$. The *Gaia* data and orbit model are shown in the top right, with the colours representing the time of the observations. 92

2.12 Corner plot showing the posteriors from the analysis of the synthetic *Gaia* and radial velocity data with the RVGAIAmodel of `kima`, the injected values are shown overtop. The paramters are $\Delta\alpha^\star$, $\Delta\delta$, $\mu_{\alpha^\star}$, μ_δ, ϖ, $P_{\rm pl}$, ϕ_0, $e_{\rm pl}$, $M_{\rm pl}\cos i_{\rm pl}$, $\Omega_{\rm pl}$, $\omega_{\rm pl}$.The radial velocity and *Gaia* data and orbit models are shown in the top right, with the colours representing the time of the observations for the *Gaia* data. 93

3.1 A time-series of CCF for HD 189733 and the residual map of time-series on removal of stellar profile showing the *wiggles* 100

3.2 Schematic diagram showing the double-line binary problem and our solution to the problem using method 2 (CCF-GP) 100

3.3 Multivariate realization vector from prior distribution draw for GP hyperparameters of the primary and the secondary stars and the mean prediction from the posterior predictive distribution of GP drawn by conditioning on the observed data from a single-epoch observation 101
3.4 A time-series of cross-correlation for double-line binary star showing the strong signals for each component and the *wiggles* as modelled by method 2 (CCF-GP) 103
3.5 Comparison of the radial velocities extracted using method 1 versus the radial velocities from method 2 104
3.6 Violin plot of the radial velocity residuals from each of the four reduction methods: TODCOR, TODMOR, SD-GP, CCF-GP 105
3.7 Lomb–Scargle periodogram of TIC172900988 radial velocities for CCF-GP and SD-GP after having removed the binary motion 105
3.8 Best-fitting Keplerian circumbinary models for each of CCF-GP data and SD-GP data 106
3.9 Orbital configuration of TIC 172900988 showing the orbits of the binary and the planet drawn from the posterior distribution 106
3.10 Detection sensitivity to planets plotted as semi-amplitude as a function of orbital period of planets plotted for each of the four reduction methods: TODCOR, TODMOR, SD-GP, CCF-GP 107
3.11 Corner plot showing the distributions and correlations of the planetary parameters from the simultaneous fit of the radial velocity data and the 1–2 punch transit times 108
3.12 Seven epochs of composite spectra for two chunks between 5379–5384 Åand 5437–5443 Å 111
3.13 SOPHIE radial velocities as a function of time and the corresponding residuals for SD-GP, CCF-GP, TODCOR, and TODMOR 112
3.14 The residual periodgram after removing the signals of both the binary and the planet 113
3.15 Scatter plot showing the planets consistent with the posterior distribution on the apsidal precession rate along with the true planet parameters, detection limit, and stability limit 113
3.16 Detection limits on further signals after removing the planet's signal 113
3.17 Orbital configuration of TIC 172900988 showing the orbits of the binary and the planet drawn from the posterior distribution of the analysis including the 1-2 punch into the fit 114
3.18 Corner plot for the orbital parameters of TIC 172900988b showing the radial velocity data alone being fit (red) and the one-two punch being included (black). 118

3.19 Configuration and angles used in the one-punch method. The black point is the centre-of-mass of the binary. The purple and salmon circles show the two stars at primary eclipse, the red is the primary star at time T_i. The observer is on the right. Angles shown are ω the argument of pericentre of the primary orbit, $\nu_{\rm ecl}$ the true anomaly of the primary when it is eclipsed, ν_i the true anomaly of the primary at time T_i, and $\theta_i = \nu_i - \nu_{\rm ecl}$. 120
3.20 Three tests showing recovered orbital period using the one-punch on a transit of TIC 172900988b. Left: neither impact parameter not eccentricity of planet accounted for. Middle: impact parameter accounted for but not the planet's eccentricity. Right: both impact parameter and eccentricity of planet accounted for. In each case the dashed green line is the true value from the radial velocity detection. 120
3.21 Periodograms of SB2s before and after removing the binary signal 127
3.22 Comparison of the detecion limits for the SB2 systems computed using `DOLBY` and the literature results 129
3.23 Planet mass versus period plot showcasing the detection limits of the SB2 systems and the known circumbinary planets 130
3.24 Observed and modelled radial velocities for the SB2s showing the binary radial velocity curve and the residuals 132
3.25 Observed and modelled radial velocities for the SB2s showing the binary radial velocity curve and the residuals continued 133
3.26 Uncertainties presented for three measurement methods 134
3.27 Detection limits comparing literature results and `kima` analysis of the literature data 135
3.28 Detection limit comparison with literature with scaling to ensure fair comparison between number of datapoints 135
3.29 Distributions of parameters for the synthetic population of binary stars which will be used for simulation fo *Gaia* yield of circumbinary planets. 144
3.30 Planet mass and scaled orbital period distributions used in circumbinary planet injections to test *Gaia* yield. There are three different mass distributions used (left), and four different scaled period distributions used (right). The middle distribution (in black) in each case is our fiducial one, it is kept the same when varying the other parameter. 146
3.31 Distributions of the binary orbital periods around which circumbinary planets are expected to be detected in setup 1.1 (the default setup see Table 3.12). Left for DR4 and right for DR5, the coloured distributions are the sample divided into the different methods by which the binaries would be detected. 148

3.32 Distributions of detected planet masses of *Gaia* circumbinary planets in the setups 1.1, 1.2, and 1.3 (top-left,top-right,bottom). The coloured distributions are the sample divided into the different methods by which the binaries would be detected. 149
3.33 Distributions of planet's scaled orbital period for predicted *Gaia* circumbinary planet detections in the setups 1.1, 2.1, 2.2, and 2.3 (top-left,top-right,bottom-left,bottom-right). The coloured distributions are the sample divided into the different methods by which the binaries would be detected. 150
3.34 Distributions of the primary star mass for the systems in which circumbinary planets are detected in the normal setup 1.1 (left) and in the setup where the planet mass scales with mass of the binary star (right). The coloured distributions are the sample divided into the different methods by which the binaries would be detected. 151

4.1 HRCCS 5.5-σ detection of the secondary. Upper panel: Cross-correlation map and `Saltire` model for SOPHIE data. White dotted lines show the positions of slices (a,b). Lower panel: Slices a & b through CCF map at maximum significance. Red line: best-fitting `Saltire` model, red shaded area: 1σ Uncertainties from the MCMC. Errorbars represent the MCMC jitter term ($\sigma_{\rm jit}$) from the two dimensional fit. 159
4.2 False Inclusion Probability (FIP) periodogram. The two colours are based on calculations using the raw samples from `kima` as well as the derived posterior samples, the dashed purple line is at a 1% false inclusion probability. 160
4.3 Phased RV plot of BEBOP-3 b, with the residuals below. The parameters for the planet shown are the maximum-likelihood solution. The binned RV data are shown to guide the eye. 160
4.4 Orbital configuration of BEBOP-3 showing the orbits of each star and the planet for 600 posterior draws. The stability limit is shown as a dashed line, this was calculated given the binary orbital parameters from the maximum-likelihood solution. 161
4.5 Detection limit for BEBOP-3. In blue, the posterior density of the `kima` run forced to fit a signal, with planet b removed. The posterior distribution for planet-b is shown in green and that for the candidate outer signal is shown in red. Dashed lines show expected signals of solar-system mass planets. 161
4.6 Periodograms of the activity indicators H-alpha and NaD are presented in orange and green, respectively. 162
4.7 Stability analysis of an inner planet in the BEBOP-3 system assuming $m_{\rm inner} \sim 10\ {\rm M}_\oplus$ and coplanar orbits. 163

4.8 Eccentricity distribution of the population of currently known Circumbinary exoplanets. The x-axis is the semi-major axis of the planets scaled by the Holman-Wiegert stability radius for each binary. The green point represents BEBOP-3 b. The red curve is an indicative stability envelope above which orbits are expected to be unstable. 164

4.9 Distributions of potential transitability of BEBOP-3 b from the radial velocity fit. The TESS sectors in which BEBOP-3 was observed are shown, along with the range of time over which the radial velocities were taken. 165

4.10 Left panels: Phase folded primary eclipses for the binary and the residuals for the best fit model. Right panels: Phase folded secondary eclipses for the binary and the residuals for the best fit model. 167

4.11 Corner plot showing posterior distributions and correlations for the 1-planet model. 167

4.12 Corner plot showing posterior distributions and correlations for planet 1 in the 2-planet model. 167

4.13 Corner plot showing posterior distributions and correlations for planet 2 in the 2-planet model. 168

4.14 J0110-44b. Top-left: N_p histogram showing Bayes Factors comparing models $N_p = n$ to $N_p = n - 1$. Bottom-left: phased radial velocity curve and residuals for planet model. Top-right: corner plot of planet parameters P, K, e, ω, ϕ_0. Bottom-right: Orbital configuration of binary (secondary orbiting primary) and planet, points show the radial velocity measurements coloured by time, the dashed grey line is the stability limit. 172

4.15 J0503-25b. Top-left: N_p histogram showing Bayes Factors comparing models $N_p = n$ to $N_p = n - 1$. Bottom-left: phased radial velocity curve and residuals for planet model. Top-right: corner plot of planet parameters P, K, e, ω, ϕ_0. Bottom-right: Orbital configuration of binary (secondary orbiting primary) and planet, points show the radial velocity measurements coloured by time, the dashed grey line is the stability limit. 173

4.16 J0503-25b/c. Top-left: FIP periodogram. Bottom-left: phased radial velocity curve of the outer planet and residuals for the 2-planet model. Top-right: corner plot of planet parameters P, K, e, ω, ϕ_0 of the outer planet. Bottom-right: Orbital configuration of binary (secondary orbiting primary) and the two planets, points show the radial velocity measurements coloured by time, the dashed grey line is the stability limit. 175

4.17 J1250+26b. Top-left: N_p histogram showing Bayes Factors comparing models $N_p = n$ to $N_p = n - 1$. Bottom-left: phased radial velocity curve and residuals for planet model. Top-right: corner plot of planet parameters P, K, e, ω, ϕ_0. Bottom-right: Orbital configuration of binary (secondary orbiting primary) and planet, points show the radial velocity measurements coloured by time, the dashed grey line is the stability limit. 176

4.18 J1525-36b. Top-left: N_p histogram showing Bayes Factors comparing models $N_p = n$ to $N_p = n - 1$. Bottom-left: phased radial velocity curve and residuals for planet model. Top-right: corner plot of planet parameters P, K, e, ω, ϕ_0. Bottom-right: Orbital configuration of binary (secondary orbiting primary) and planet, points show the radial velocity measurements coloured by time, the dashed grey line is the stability limit. 178

4.19 J1540-09 longer period circular model. Top-left: N_p histogram showing Bayes Factors comparing models $N_p = n$ to $N_p = n - 1$. Bottom-left: phased radial velocity curve and residuals for planet model. Top-right: corner plot of planet parameters P, K, e, ω, ϕ_0. Bottom-right: Orbital configuration of binary (secondary orbiting primary) and planet, points show the radial velocity measurements coloured by time, the dashed grey line is the stability limit. . . . 179

4.20 J1540-09b shorter period eccentric model. Top-left: False Inclusion Probability periodogram. Bottom-left: phased radial velocity curve and residuals for planet model. Top-right: corner plot of planet parameters P, K, e, ω, ϕ_0. Bottom-right: Orbital configuration of binary (secondary orbiting primary) and planet, points show the radial velocity measurements coloured by time, the dashed grey line is the stability limit. 180

4.21 Radial velocity curves for 100 random draws from the competing models for J1540-09b. The points where the data has been taken is shown by the points. The vertical dashed lines show the range of time over which more data is going to be taken. 181

4.22 J0310-31b. Top-left: N_p histogram showing Bayes Factors comparing models $N_p = n$ to $N_p = n - 1$. Bottom-left: phased radial velocity curve and residuals for planet model. Top-right: corner plot of planet parameters P, K, e, ω, ϕ_0. Bottom-right: Orbital configuration of binary (secondary orbiting primary) and planet, points show the radial velocity measurements coloured by time, the dashed grey line is the stability limit. 183

4.23 J0418-53b. Top-left: N_p histogram showing Bayes Factors comparing models $N_p = n$ to $N_p = n - 1$. Bottom-left: phased radial velocity curve and residuals for planet model. Top-right: corner plot of planet parameters P, K, e, ω, ϕ_0. Bottom-right: Orbital configuration of binary (secondary orbiting primary) and planet, points show the radial velocity measurements coloured by time, the dashed grey line is the stability limit. 184

4.24 J0708-68b. Top-left: N_p histogram showing Bayes Factors comparing models $N_p = n$ to $N_p = n - 1$. Bottom-left: phased radial velocity curve and residuals for planet model. Top-right: corner plot of planet parameters P, K, e, ω, ϕ_0. Bottom-right: Orbital configuration of binary (secondary orbiting primary) and planet, points show the radial velocity measurements coloured by time, the dashed grey line is the stability limit. 186

4.25 J1305-31b. Top-left: N_p histogram showing Bayes Factors comparing models $N_p = n$ to $N_p = n - 1$. Bottom-left: phased radial velocity curve and residuals for planet model. Top-right: corner plot of planet parameters P, K, e, ω, ϕ_0. Bottom-right: Orbital configuration of binary (secondary orbiting primary) and planet, points show the radial velocity measurements coloured by time, the dashed grey line is the stability limit. 187

4.26 J0353-16b. Top-left: N_p histogram showing Bayes Factors comparing models $N_p = n$ to $N_p = n - 1$. Bottom-left: phased radial velocity curve and residuals for planet model. Top-right: corner plot of planet parameters P, K, e, ω, ϕ_0. Bottom-right: Orbital configuration of binary (secondary orbiting primary) and planet, points show the radial velocity measurements coloured by time, the dashed grey line is the stability limit. 189

4.27 J1200+42b. Left: circular short-period solution, top is phased radial velocity curve, and bottom is the orbital configuration of binary (secondary orbiting primary) and planet, points show the radial velocity measurements coloured by time, the dashed grey line is the stability limit. Right: same as left but for long-period eccentric model, this is the favoured model. 191

4.28 J1204-47b. Top-left: N_p histogram showing Bayes Factors comparing models $N_p = n$ to $N_p = n - 1$. Bottom-left: phased radial velocity curve and residuals for planet model. Top-right: corner plot of planet parameters P, K, e, ω, ϕ_0. Bottom-right: Orbital configuration of binary (secondary orbiting primary) and planet, points show the radial velocity measurements coloured by time, the dashed grey line is the stability limit. 192

4.29 J1329+48b. Top-left: N_p histogram showing Bayes Factors comparing models $N_p = n$ to $N_p = n - 1$. Bottom-left: phased radial velocity curve and residuals for planet model. Top-right: corner plot of planet parameters P, K, e, ω, ϕ_0. Bottom-right: Orbital configuration of binary (secondary orbiting primary) and planet, points show the radial velocity measurements coloured by time, the dashed grey line is the stability limit. 193

4.30 J1403-32b. Top-left: N_p histogram showing Bayes Factors comparing models $N_p = n$ to $N_p = n - 1$. Bottom-left: phased radial velocity curve and residuals for planet model. Top-right: corner plot of planet parameters P, K, e, ω, ϕ_0. Bottom-right: Orbital configuration of binary (secondary orbiting primary) and planet, points show the radial velocity measurements coloured by time, the dashed grey line is the stability limit. 195

4.31 J2046+06b. Top-left: N_p histogram showing Bayes Factors comparing models $N_p = n$ to $N_p = n - 1$. Bottom-left: phased radial velocity curve and residuals for planet model. Red is the HARPS data and blue the SOPHIE data. Top-right: corner plot of planet parameters P, K, e, ω, ϕ_0. Bottom-right: Orbital configuration of binary (secondary orbiting primary) and planet, points show the radial velocity measurements coloured by time, the dashed grey line is the stability limit. 196

4.32 J2233+43b. Top-left: N_p histogram showing Bayes Factors comparing models $N_p = n$ to $N_p = n - 1$. Bottom-left: phased radial velocity curve and residuals for planet model. Top-right: corner plot of planet parameters P, K, e, ω, ϕ_0. Bottom-right: Orbital configuration of binary (secondary orbiting primary) and planet, points show the radial velocity measurements coloured by time, the dashed grey line is the stability limit. 198

4.33 Long-period signals consistent with a planetary-mass companion orbiting BEBOP targets. When two sources of data are present they are shown in different colours. 199

4.34 The circumbinary planets (Transiting, Transiting+RVs, BEBOP detections, and BEBOP Candidates) in various parameter configurations. Top: Proximity to stability limit with increasing binary orbital period anti-clockwise, radially is a_{sc} where the uncertainties include the potential eccentricity of the planet. The radial direction is log-scaled. Middle left: planet mass vs total binary mass. Middle right: planet mass vs proximity to stability limit. Bottom left: eccentricity vs proximity to stability limit, stable orbits should be below the red envelope. Bottom right: binary orbital period vs planet orbital period, blue region shows unexpected dearth of planets from *Kepler* implying pile-up. 203

4.35 Left: same as bottom right of Figure 4.34 binary period against planet period. Right: Semi-major axis of the stability limit against pericentre distance of planet orbit. Purple and magenta lines here are $1.2 \times a_{\rm stab}$ and the approximate location of the formation limit. Coloured points represent the various circumbinary planets(Transiting, Transiting+RVs, BEBOP detections, and BEBOP Candidates). 205

5.1 Diagram of the proper motion anomaly method 210

5.2 Sensitivity curve for proper motion anomaly applied to V471 Tau 211

5.3 Sensitivity curve for proper motion anomaly applied to HW Vir and posterior density histogram of the periods of planets from the analysis of the full eclipse timing dataset 212

5.4 Fit showing lack of interpolation in eclipse timing data and posterior density smoothed corner plots showing inconsistencies in the period and semi-amplitude of signals found 214

5.5 Orbital configuration and keplerian fit to the data of the best-fitting model . . . 216

5.6 *Gaia* signal-to-noise ratio vs distance for the claimed planets orbiting post common-envelope binaries shown in Table 5.6. Each has two markers showing the signal-to-noise ratio for *Gaia* DR4 and DR5, with the size and darkness of the marker showing how much of the orbit of the claimed planet would have been covered. Dashed lines show the strong and weak detection thresholds of 20 and 10. . . . 221

5.7 The *Gaia* signal-to-noise ratio that would be acheived by a 6.5 $M_{\rm Jup}$ planet on a 3000 day orbit for each system in the post common-envelope binary catalogue. Horizontal dashed line shows the detection sensitivity threshold of SNR = 20. . 222

5.8 *Gaia* DR5 sensitivity to planets of varying mass and orbital period for the catalogue of post common-envelop binaries. Left: range of masses for 4 different periods. Right: range of periods for 4 different masses. 223

6.1 Apsidal precession rate induced by a polar companion with $m = 17.7\ M_{\rm Jup}$ for a range of eccentricities and apocentre distances. Line at 4 AU is the separation at which the companion was observed by Calissendorff et al. (2019). 227

6.2 Comparison of N-body residuals and static-Keplerian residuals. The division into different groups used to see the evolution of $\dot{\omega}$ is shown. The RMS of the resiudals for each dataset is also listed 252

6.3 Indepedent analysis of primary and secondary radial velocity data. Panel A (left) shows the lack of correlation between the residuals of the primary and secondary. Panel B (right) shows the posterior distribution of $\dot{\omega}$ for the analyses of the primary, the secondary, and the full dataset compared to the prior distribution 253

6.4 Planet masses and periods. Corner plot of Periods and masses consistent with the induced precession rate from an N-body fit. Regions of sensitivity are shown for: 1) a three year astrometric campaign with the VLT in blue and 2) two years of eclipse timing monitoring with 1 minute timing precision (as was achieved with SPECULOOS) in red 254

6.5 Level curves of the Hamiltonian for 2M1510 with the colours denoting the regions of libration and circulation. These are trajectories of test particles orbiting the binary. The red trajectories show the regions of libration and orange trajectories the regions of circulation. The 584 stable orbits of 600 randomly drawn simulations from the posterior of the N-body fit are integrated and the trajectories overplotted in blue. Note that since the simulations shown in blue are drawn from the N-body fit they are for massive objbects not test particles. Two different projections are shown 255

6.6 Configuration of 2M1510 and naming convention for the various bodies. Brown dwarfs are in red and the planet is in blue. Direction to the earth relative to the binary is shown 255

6.7 Comparison of radial velocity reduction methods. Figure showing residuals relative to the first epoch in m/s for the two stars, primary (circles) and secondary (squares). The blue points represent the RVs measured using the DOLBY-SD method (this work) and the red circles represent literature values from (27). Panel B (bottom) is a zoom-in of panel A (top) so the the uncertainties on the DOLBY-SD data can be seen 256

6.8 Top: apsidal precession's effect on the offset between primary and secondary eclipse. Bottom left: apsidal precession's effect on the orbit, the arrow points to the observer. Bottom right: apsidal precession's effect on the shape of the radial velocity curve. Colours in all panels correspond to the value of ω. 261

6.9 Planet masses and orbital periods consistent with apsidal precession rate relative to instability limit and radial velocity sensitivity threshold. Left: AI Hya. Right: TIC 172900988 (figure similar to Figure 3.15). 262

6.10 J1250+26. Left: planet masses and periods consistent with $\dot{\omega}$ measurement, posterior distribution from the planet detection is also shown as well as the instability zone. Right: Histograms of measured $\dot{\omega}$ and the calculated 3^{rd} body induced $\dot{\omega}$. 263

6.11 J0310-31. Left: Histograms of measured $\dot{\omega}$ and the calculated general relativity induced $\dot{\omega}$. Right: planet masses and periods consistent with residual $\dot{\omega}$ values, posterior distribution of all planets up to Np=3 are shown as well as the instability zone. 264

6.12 J0759-69. Planet masses and periods consistent with $\dot{\omega}$ values, posterior distribution of all planets up to Np=3 are shown as well as the instability zone. . . . 264
6.13 Distribution of the significance of the $\dot{\omega}$ measurements from the BEBOP sample shown alongside a Gaussian with $\mu = 0$, $\sigma = 1$. Left: all binaries. Right: restricted to binaries with $e > 0.05$. 265
6.14 Estimated yields of circumbinary planets inducing a significant apsidal precession, for a potential study of a eclipse timing variations. Vertical dashed lines show the cutoffs in sensitivity to $\dot{\omega}$. Left: Gas giant planets $0.1M_{\rm Jup} \leq M \leq 2M_{\rm Jup}$. Right: sub-neptune planets $1M_{\oplus} \leq M \leq 0.1M_{\rm Jup}$. For visual clarity, all binaries with no planets (and hence $\dot{\omega} = 0$) have been removed. 268

List of Tables

1.1 Planets from the exoplanets.eu circumbinary planet catalogue. Ordered by increasing binary separation. The *Other* detection method is as listed in the catalogue and refers to all methods except transit or radial velocity. There is only one entry per system with the planet parameters being those of the innermost planet. The detection method is that of the first planet detected in the system (i.e. TOI-1338c was detected by the radial velocity method but since TOI-1338b was detected in transit the system as a whole is listed as detected using the Transit method). Systems in **bold** are also included in the NASA exoplanet archive. . . 46

1.2 Planets from the NASA exoplanet archive which have the circumbinary flag. Ordered by discovery year and discovery method. Planets in **bold** are also included in the exoplanets.eu circumbinary catalogue. Values of primary star mass, and planet period, mass, and radius are shown if included in the archive. Secondary masses are not included in the information. 47

2.1 Bayes Factor confidence thresholds as interpreted by previous publications . . . 56

2.2 Standard priors I use in `kima` analysis for exoplanet detection. $\mathcal{U}$ is a Uniform distribution, $\mathcal{LU}$ a LogUniform distribution (Uniform in $\log_{10}$ of the parameter), $\mathcal{MLU}(A, B)$ a ModifiedLogUniform distribution which is Uniform between 0 and A and the LogUniform between A and B each half with equal weight. . . . 60

2.3 For SIM1 we show the parameters from `rebound` alongside the fitted parameters both with precession (`kima-binaries`) and without (`kima`). 76

2.4 The Bayes Factors for SIM2 (containing two circumbinary planets) comparing models with increasing numbers of planets both for the standard version of `kima` and the new `kima-binaries` version. 77

2.5 Comparison of binary periods for Kepler-16AB. 78

2.6 The fitted and derived and assumed parameters for KOI-126 for the orbit of the binary B + C around star A. 80

2.7 The fitted and derived and assumed parameters for Kepler-16. 80

2.8 Table of parameters used in the injection of a planet into an eclipse timing variation dataset. . . . 86
2.9 Table of parameters used in the injection of a planet into *Gaia* and radial velocity data. . . . 91

3.1 Best-fitting parameters for each methods both including and not including the 1–2 punch into the fit, solutions that cross the instability limit are excluded here 104
3.2 Best-fitting parameters for each methods both including and not including the 1–2 punch into the fit, solutions that cross the instability limit are not excluded here . . . 114
3.3 Table of radial velocities for TIC 172900988 from SD-GP . . . 115
3.4 Properties and parameters for SB2 systems . . . 125
3.5 Radial velocity data for HD210027 . . . 136
3.6 Radial velocity data for HD13974 . . . 137
3.7 Radial velocity data for HD78418 . . . 138
3.8 Radial velocity data for HD9939 . . . 139
3.9 Radial velocity data for HD195987 . . . 140
3.10 Radial velocity data for HD282975 . . . 141
3.11 Fraction of stars in the synthetic sample to which a binary companion is assigned, divided by spectral type. Distribution based on Raghavan et al. (2010). . . . 143
3.12 The 6 setups and yields of circumbinary planets from *Gaia*. The input planet mass and scaled semi-major axis distributions are shown along with the planet yield from DR4 and DR5. . . . 147
3.13 Circumbinary planet yields in *Gaia* DR5 separated by the method by which the binary would be detected. . . . 148

4.1 Stellar and binary parameters from three different analysis methods. . . . 158
4.2 Orbital parameters for the BEBOP-3 binary and general fit parameters. Parameters are taken from the `kima` analysis of RVs only unless otherwise specified. . 160
4.3 Orbital parameters of BEBOP-3 b. . . . 161
4.4 Radial velocity observations taken with SOPHIE between 2018-11-13 and 2024-11-18. . . . 166
4.5 Prior distributions used in the `kima` analysis. . . . 166
4.6 The BEBOP catalogue of circumbinary planets with radial velocity measurements. 1σ uncertainties on parameters are provided at the level of the last two significant digits. . . . 169

4.7 Binary and planet parameters for BEBOP detections, tentative detections and candidates presented in this thesis. 1σ uncertainties are shown at the significance of last digits of the value. The uncertainty values in a_{sc} are the closest and furthest that the orbit moves relative to stability limit based on both the 84% confidence upper limit on eccentricity and the uncertainty in orbital parmaters. 201

5.1 Tangential velocities from the proper motion anomaly method for V471 Tau and HW Vir 211
5.2 Division of the eclipse time data into *chunks* 214
5.3 Prior distributions for the nested sampling analysis 215
5.4 Bayes Factors produced by KIMA when analysing the entire eclipsing timing data set of HW vir 215
5.5 Parameters from the analysis of the full data set with a quadratic ephemeris . . 217
5.6 Table of post common-envelope binaries with planetary-mass companions claimed from eclipse timing variations. Those in bold are the 12 that meet the relaxed criteria for detection with *Gaia*. [(1)] There is evidence against its existence from Hardy et al. (2015) and Section 5.1. 220

6.1 Table of parameters for the binary brown dwarf. Parameters from both the Keplerian (+precession) fit and from the n-body fit. 1σ uncertainties are reported in brackets precise to the last two significant digits 257
6.2 Radial velocity data. Radial velocity observations taken with UVES between August 2017 - April 2019. RV extraction performed with `DOLBY-SD` 258
6.3 Radial velocity data continued. Radial velocity observations taken with UVES between May 2019 - August 2023. RV extraction performed with `DOLBY-SD` . . 258
6.4 Parameters used in yield estimate of detectable apsidal precession rates. Binaries are generated based on the distributions shown, planets are drawn from the NASA exoplanet archive based on the constraints shown, with caveats for those that would be inside the unstable region. Unstable gas giants are replaced with a random other planet until stable. *Sub-neptunes that are unstable are with 50% chance either placed at 1.2× the stability limit or removed, this assumes that in their migration, half of the sub-neptunes are ejected and half park outside the disc cavity (Martin and Triaud, 2014). This leads to a true injected occurrence of sub-neptunes of $\sim$ 26% 267

Chapter 1

Introduction

1.1 Overview of exoplanets

1.1.1 Exoplanet definition

An exoplanet is a celestial body which acts as an exoplanet. This silly definition, a reference to a frustrating definition that mathematicians often give for a tensor, holds a grain of truth. There is no universally accepted and obvious definition for an exoplanet.

A typical definition (which side-steps the point) is that *an exoplanet is a planet that orbits a star other than the Sun.* This bypasses a key issue and assumes the definition of a planet. The definition of a planet, as decided by the International Astronomical Union (IAU) General Assembly in 2006[1] is as follows: *A "planet" is a celestial body that (a) is in orbit around the Sun, (b) has sufficient mass for its self-gravity to overcome rigid body forces so that it assumes a hydrostatic equilibrium (nearly round) shape, and (c) has cleared the neighbourhood around its orbit.* This makes planets well defined for the solar system and is careful to differentiate low-mass objects such that Pluto fails at c), and the Moon fails at a). However this definition fails quickly when extending it to extra-solar systems.

Clearly a) is to be ignored for exoplanets and replaced with the central star of that system (or

[1] https://www.iau.org/news/pressreleases/detail/iau0603/

perhaps any star in the system). b) and c) can generally be extended as a lower-limit on mass such that very small objects are not classed as exoplanets.

Beyond this, there are still multiple issues with simply applying the IAU definition. The most obvious being that a secondary stellar companion would class as a planet. Hence, adding an upper mass limit is needed as well, but where this limit should be is not obvious. The limit between planets and stars is not clear cut. Brown dwarfs are objects that have enough mass to fuse deuterium in their cores but not hydrogen. The typical cutoff for deuterium fusion is at $\sim 13\,M_{\rm J}$ and this is sometimes taken as the upper limit of exoplanet masses, with the upper limit on brown dwarf masses being $\sim 80\,M_{\rm J}$. However, the mass-distribution of brown dwarfs orbiting stars is bimodal with many at low-mass, many at high-mass, and few in the middle (Grether and Lineweaver, 2006; Ma and Ge, 2014; Triaud et al., 2017). Hence, sometimes the upper- limit on an exoplanet's mass is extended up to $\sim 25\,M_{\rm J}$ (Sahlmann et al., 2011b; Schneider et al., 2011) to include objects that are thought to form in the same way as planets in a disc around a star (see Section 1.5). Other issues with extending the definition include: a very young planet embedded in a protoplanetary disc could warrant being called a planet without having fully cleared its orbit; some planets do not have a host star at all and are referred to as free-floating or rogue exoplanets (Mróz et al., 2019); the contents of the celestial body matters and in principle a planet-mass primordial black hole could act like a planet since most of the discussion of what a planet/exoplanet is depends only on its mass (though potentially it could fall at hurdle b); planets can in principle cross each other's orbits, this is seen for minor bodies in the solar system but might eventually be found for extra-solar bodies which are undoubtedly planets.

This discussion leads to a workable definition of an exoplanet, that I will use in this thesis: *a rocky, icy, or gaseous body outside the solar system whose mass is in the order-of-magnitude range* $0.1\,M_{\oplus} \lesssim M \lesssim 10\,M_{\rm J}$.

1.1.2 Stellar and exoplanet naming conventions

The naming of exoplanets is typically among the first things an exoplanet scientist is asked: "Do you get to name exoplanets after yourself?". The answer being almost certainly not.

Exoplanet naming conventions are linked to stellar naming conventions, so that should be discussed first. Stars have many names, the brightest stars may have names dating back to antiquity (eg: Altair). Stars can also be named by the constellation they are in and an identifier (usually to indicate brightness). This could be greek letters followed by the name of the constellation (as in Bayeri, 1603) such as Alpha Centauri, or a numerical identifier followed by the constellation (as in Flamsteed, 1725) such as 51 Pegasi. Stars were also given identifiers/names by various catalogues such as the *Bonner Durchmusterung* catalogue (BD) or the *Henry Draper* catalogue (HD). Currently, many telescopes or surveys create a catalogue of stars either as an input catalogue of stars that will be analysd (e.g. the *TESS* Input Catalogue TIC) or as an output of the survey (e.g. the *Gaia* catalogues), these are all therefore acceptable names for the star (though referring to the star by the full *Gaia* ID is unwieldy).

Lone stars are given these names with an implicit A, labelling them as the primary star of a system. Binaries and higher order multiples typically all have the same system name with a letter identifying them within the system A being the primary star, B a secondary companion, etc. The capital letters were sometimes use to refer to resolved companions, with unresolved stellar companions using lowercase letters, for example: a wide binary system could be called HD 65498 A and HD 65498 B, but star A could turn out to be an eclipsing binary with two components named HD 65498 Aa and HD65498 Ab (Tokovinin, 2018). Exoplanets typically follow the same naming convention as unresolved stellar companions using lowercase letters and named alphabetically starting with b in the order they are discovered within a particular system. Directly imaged exoplanets, despite being resolved, are still usually named with a lowercase letter (e.g. Marois et al., 2010). Exoplanet surveys are also creating catalogues of stars (i.e. catalogues of stars with exoplanets), they can therefore also give names to the planets they find by giving the star that is hosting the planet a name in their catalogue, e.g. the planets

from the *Kepler* telescope. A planet orbiting the primary star of Kepler-61 would be designated Kepler-61 Ab, if it was orbiting the secondary star it would be Kepler-61 Bb. A circumbinary planet orbiting around both stars of the Kepler-16 system would be called Kepler-16 (AB)b though sometimes the AB is omitted and it would be called Kepler-16 b.

In this way a planet can have many names, here are a few of the different names of 51 Peg b, the first known exoplanet orbiting a Sun-like star: 51 Peg b, GJ 882 b, HD 217014 b, BD+19 5036 b, TIC 139298196 b, *Gaia* DR3 2835207319109249920 b. The star has 46 accepted identifiers.

1.2 Orbits and the Celestial sphere

The majority of the work in this thesis involves orbits, most often Keplerian orbits (though some deviations from this will be discussed at times). Kepler's laws of motion state that an orbit is an ellipse with the centre-of-mass at a focus (Kepler, 1609; Murray and Dermott, 1999), this is derivable from Newton's law of gravitation as in Murray and Correia (2010). Equating the forces acting on both bodies gives

$$\ddot{\mathbf{r}} + \frac{G(m_1 + m_2)\mathbf{r}}{r^3} = 0, \tag{1.1}$$

where $\mathbf{r}$ is the vector between the bodies, r its magnitude, and m_1 and m_2 the masses. Taking a cross product of this with $\mathbf{r}$ and integrating leads to the angular momentum $\mathbf{h} = \mathbf{r} \times \dot{\mathbf{r}}$. Now in a polar coordinate system (r, θ, z)

$$\begin{aligned} \mathbf{r} &= r\hat{\mathbf{r}}, \\ \dot{\mathbf{r}} &= \dot{r}\hat{\mathbf{r}} + r\dot{\theta}\hat{\theta}, \\ \ddot{\mathbf{r}} &= (\ddot{r} - r\dot{\theta}^2)\hat{\mathbf{r}} + \left[\frac{1}{r}\frac{d}{dt}\left(r^2\dot{\theta}\right)\right]\hat{\theta}. \end{aligned} \tag{1.2}$$

Therefore $\mathbf{h} = r^2\dot{\theta}\hat{\mathbf{z}}$, and since the area swept out dA in the elliptical orbit over a small angle $d\theta$ is

$$dA = \int_0^r r dr d\theta = \frac{1}{2}r^2 d\theta, \tag{1.3}$$

then $2\dot{A} = r^2\dot{\theta} = h$ is constant, which is Kepler's second law. Substituting Equation 1.2 into Equation 1.1 and taking the $\hat{\mathbf{r}}$ component gives

$$\ddot{r} - r\dot{\theta}^2 = -\frac{G(m_1 + m_2)}{r^2}. \tag{1.4}$$

Using the conservation of angular momentum and solving the differential equation with a $r = 1/u$ substitution results in

$$r = \frac{h^2/G(m_1 + m_2)}{1 + e\cos(\theta - \varpi)}, \tag{1.5}$$

where e is the eccentricity (or ellipticity) of the orbit and ϖ the longitude of pericentre. To relate to Figure 1.1, $\varpi = \omega + \Omega$. If at the pericentre, $r = \frac{h^2}{G(m_1+m_2)}/(1+e)$ and from the geometry of an ellipse $r = a(1-e)$ where a is the semi-major axis of the ellipse. Combining these makes

$$h = \sqrt{G(m_1 + m_2)a(1 - e^2)}, \tag{1.6}$$

which together with Equation 1.5 finally gives the equation associated with Kepler's first law:

$$r = a\frac{1 - e^2}{1 + e\cos\nu}, \tag{1.7}$$

where ν is the true anomaly which is $\theta - \varpi$. The angle ν can be seen in Figure 1.1 along with the other angles defining a generic orbit in 3D space.

The true anomaly, ν, is the angle between the position of the body and the pericentre which is the point of closest approach to the focus of the ellipse. Given the reference plane (usually the plane of the sky for exoplanetary orbits) the line of intersection between the plane and the orbit is called the *line of nodes* and the angle between the planes, i, is the inclination, the point at which the orbit rises from below the reference plane to above it is the *ascending node*. There is

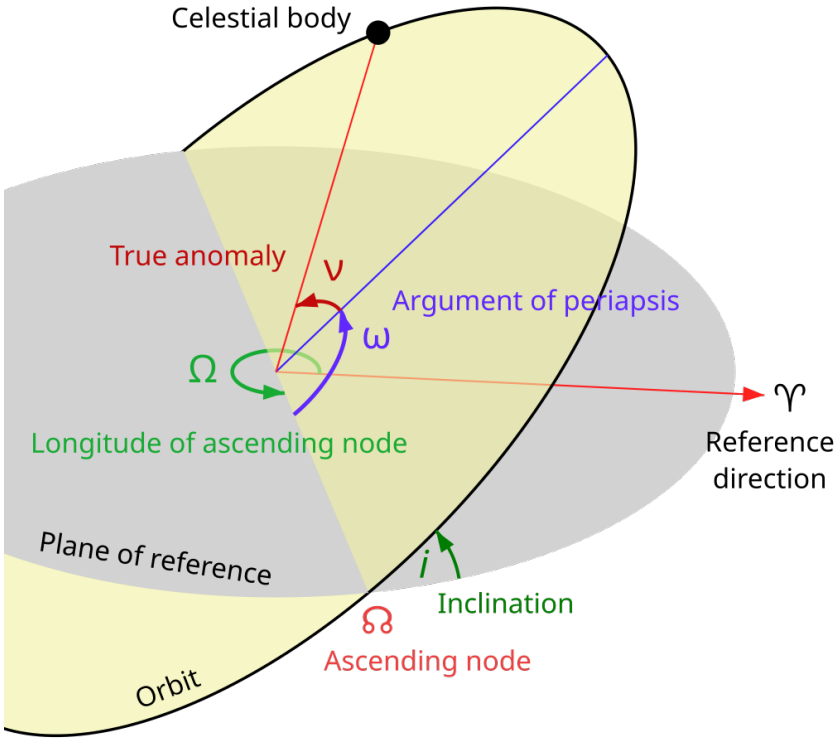


Figure 1.1: Diagram of orbit and orbital angles *Credit:* Lasunncty.

no consensus on how to define the position of the observer so I will take the observer to be below the plane, hence in an observed system the ascending node is the point at which the body passes through the plane of the sky away from the observer. Ω is the *longitude of ascending node* the angle between the ascending node and the reference direction. ω is the argument of pericentre the angle between the ascending node and the pericentre position.

Note that these elements are for a body orbiting the centre of mass of a system; in a two-body system each body orbits the centre of mass and will have mostly similar but not identical orbital elements. In fact, the two bodies will have identical motion except that $\omega_2 = \omega_1 - \pi/2$ and $a_2 = a_1 \frac{M_1}{M_2} = a_{\rm tot} \frac{M_1}{M_1+M_2}$.

Kepler's third law can be derived from Kepler's second law $\frac{dA}{dt} = \text{const} = h/2$ and that the whole area of the ellipse (πab) is swept out during one period, hence $P = \pi a(a\sqrt{1-e^2})/(h/2)$. Combining this with Equation 1.6 results in Kepler's third law

$$P^2 = \frac{4\pi^2}{G(m_1+m_2)} a^3. \tag{1.8}$$

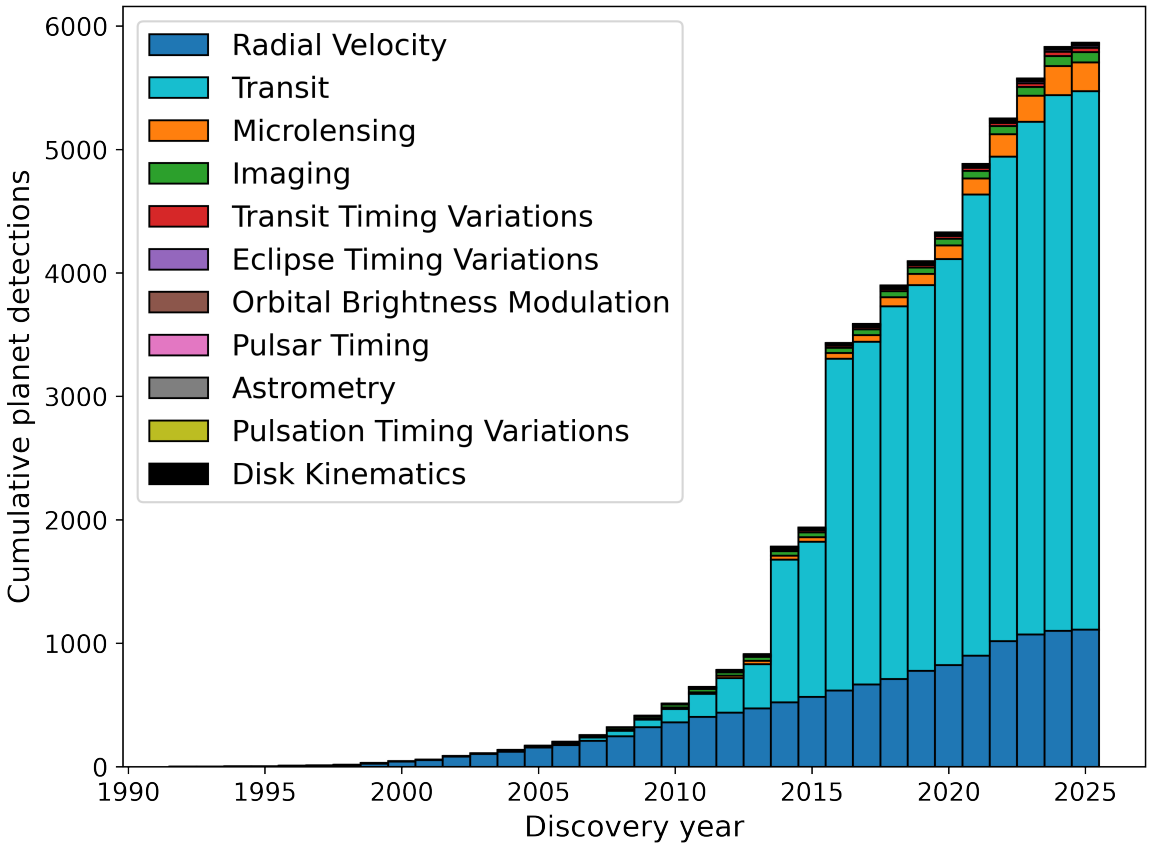


Figure 1.2: Cumulative histogram of exoplanet detections seperated by technique. Data taken from the NASA exoplanet archive

1.3 Exoplanet detection methods

The first exoplanets were detected in the early 1990s, some orbiting a pulsar from the timing of the pulses in 1992 (Wolszczan and Frail, 1992), and another orbiting a main-sequence star using radial velocities in 1995 (Mayor and Queloz, 1995). Since then, many exoplanets have been detected using multiple detection techniques. Figure 1.2 shows a cumulative histogram of the prevalence of various techniques in the detected exoplanet population over time, and Figure 1.3 the various detected planets in the Mass-Period space, with colour and shape distinguishing the different detection methods[2]. The masses are either the true mass if known or the mass modulated by $\sin i$ when the inclination i is unknown (e.g. radial velocity only planets). The

[2]note that this only shows those planets with Mass and Period both constrained to at least 1σ away from 0

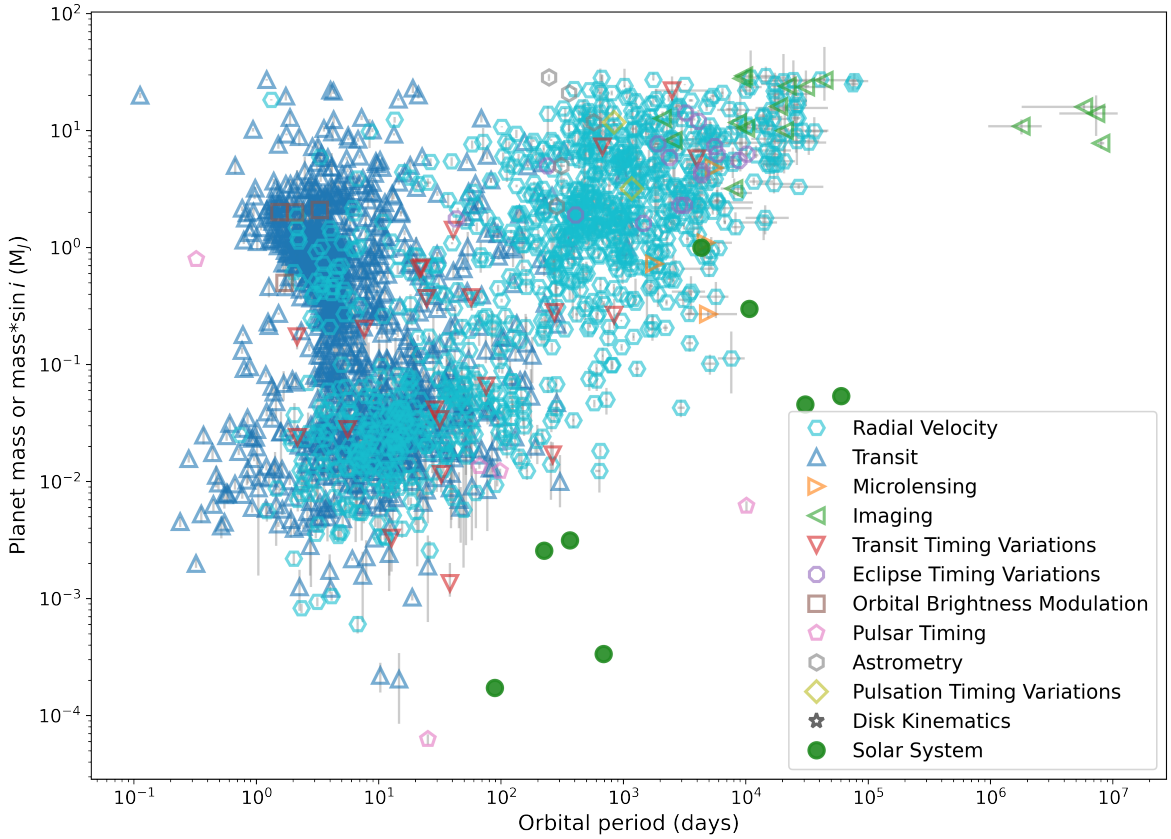


Figure 1.3: The known exoplanets shown in the $M \sin i$ - Period space. This only shows those with 1σ measurements of period and mass. Data taken from the NASA exoplanet archive

following sections will discuss some of the main detection methods that have been used.

1.3.1 Radial velocities

The orbit of a body such as a planet around a star is in fact an orbit of both bodies around the centre-of-mass. Therefore, over an exoplanet's orbit, the velocity of the star along the line-of-sight will oscillate[3]. This variation in velocity can be measured using the radial velocity technique, which at a given instant measures the velocity of a star by calculating the Doppler shift induced on the absorption lines in the star's spectrum (Lovis and Fischer, 2010).

The typical method used for radial velocity extraction from a stellar spectrum is the cross-correlation technique. A template mask is compared to the measured spectrum, and performing the comparison for a range of different potential Doppler shifts will show a clear peak at the

[3]except in the case where the orbit is exactly face-on and no motion along the line-of-sight occurs

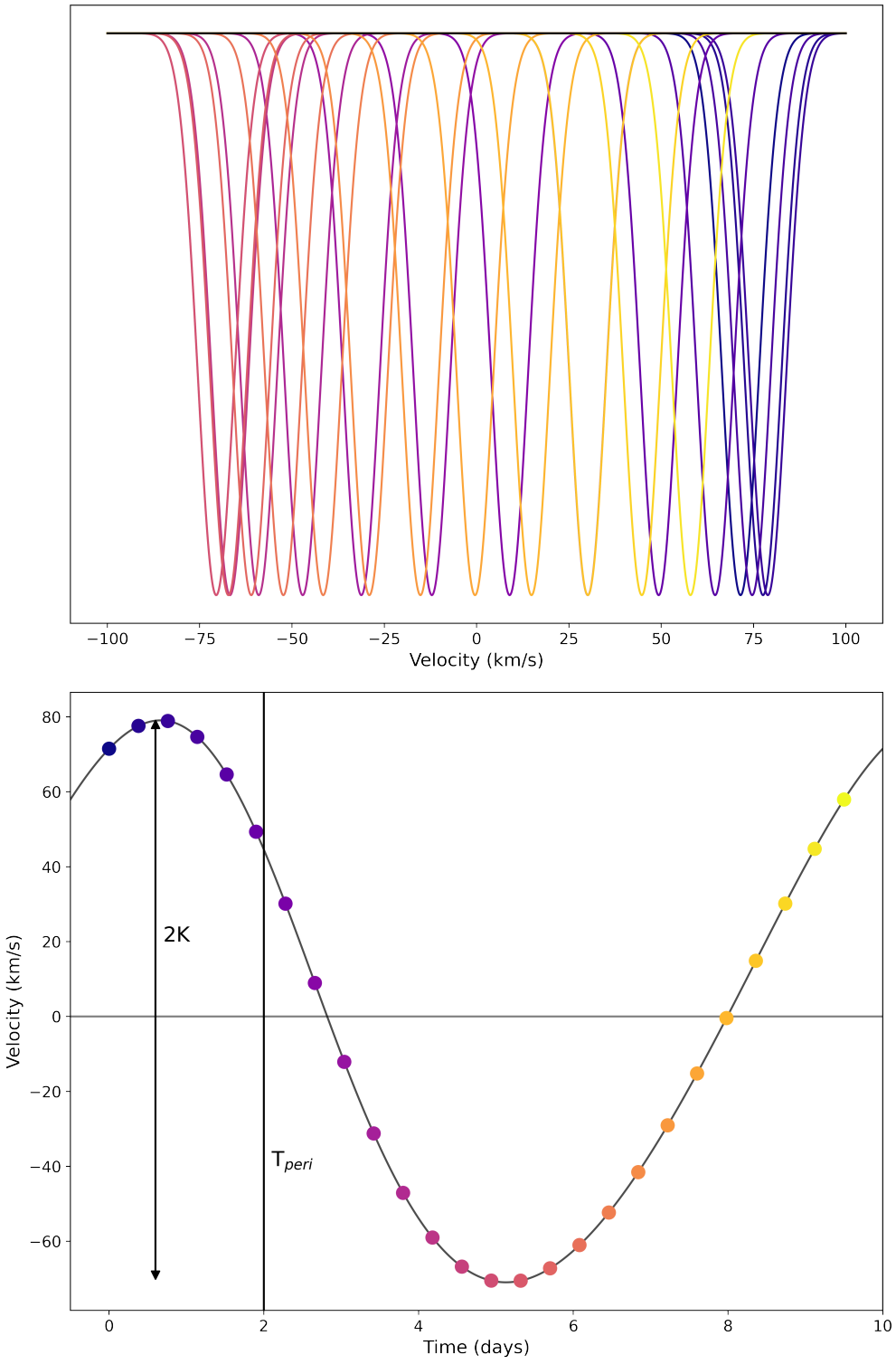


Figure 1.4: Depiction of the cross-correlation function and radial velocity curve. Top: cross-correlation functions for a series of radial velocity measurements. Bottom: the corresponding radial velocity measurements. The time is shown by the colour. This example is for a 10 day orbit with $e = 0.1$ and $K = 75$ km/s. Twice the semi-amplitude K and the time at which the pericentre passage occurs are indicated on the bottom panel.

point where the two match. The peak in the cross-correlation function allows the measurement of the star's velocity at the time the spectrum was obtained (Baranne et al., 1996). A depiction of cross-correlation functions and corresponding radial velocities for a binary star with amplitude 75 km/s is shown in Figure 1.4.

With the advance of detector technology, the realm of extremely precise radial velocity (EPRV) measurements is being attained (Pepe et al., 2021). The field has reached an astrophysical limit where stellar activity signals are present and detectable in the spectra we measure (Bouchy et al., 2001; Gray, 2009; Meunier et al., 2010). Stellar activity obfuscates planet detection, therefore modelling or removing this activity is an important task that needs to be addressed in order to be able to detect lower-mass planets. Two main ways of dealing with stellar activity exist. Firstly modelling it, typically using one or more independent measures of activity to model the effect on the radial velocities, which often uses Gaussian processes (Aigrain et al., 2012; Haywood et al., 2014). Gaussian processes are used to model the red noise (in this case from stellar activity) using a covariance matrix (e.g. Barragán et al., 2022) often a quasi-periodic covariance matrix (Roberts et al., 2013). Secondly removing it, making use of the fact that a planet's orbit will cause a shift in the spectral lines whereas activity will typically cause a deformation and in principle the two effects are separable (Collier Cameron et al., 2021; de-Beurs et al., 2022; Cretignier et al., 2022).

The radial velocity of an object can be derived from the Keplerian motion (Murray and Correia, 2010). The conversion from the orbital plane (x,y,z) to the reference frame (X,Y,Z) takes three parameters around which rotations occur, these are (ω, i, Ω) defined as in Equation 1.2 such that

$$\begin{pmatrix} X \\ Y \\ Z \end{pmatrix} = \begin{pmatrix} \cos\Omega & -\sin\Omega & 0 \\ \sin\Omega & \cos\Omega & 0 \\ 0 & 0 & 1 \end{pmatrix} \begin{pmatrix} 1 & 0 & 0 \\ 0 & \cos i & -\sin i \\ 0 & \sin i & \cos i \end{pmatrix} \begin{pmatrix} \cos\omega & -\sin\omega & 0 \\ \sin\omega & \cos\omega & 0 \\ 0 & 0 & 1 \end{pmatrix} \begin{pmatrix} x \\ y \\ z \end{pmatrix}. \tag{1.9}$$

Now an orbit can be defined with polar coordinates (r, ν) such that $x = r\cos\nu$, $y = r\sin\nu$, and

$z = 0$. This gives

$$X = r(\cos\Omega\cos(\omega+\nu) - \sin\Omega\sin(\omega+\nu)\cos i), \tag{1.10}$$

$$Y = r(\sin\Omega\cos(\omega+\nu) - \cos\Omega\sin(\omega+\nu)\cos i), \tag{1.11}$$

$$Z = r\sin(\omega+\nu)\sin i. \tag{1.12}$$

The usual convention is that (X, Y) is the plane of the sky such that the radial velocity is along the Z axis,

$$RV = V_z + \frac{m_2}{m_1+m_2}\left[\dot{r}\sin(\omega+\nu)\sin i + r\dot{\nu}\cos(\omega+\nu)\sin i\right]. \tag{1.13}$$

V_z is the velocity that the system as a whole has, referred to as the *systemic velocity*. The mass fraction term comes from the fact that since both orbiting bodies have mass, the semi-major axis of the ellipse that each body traces around the centre-of-mass is proportional to the fraction of the total mass that is in the other body. Here the velocity is that of body 1. Differentiating Equation 1.7 and then using Equation 1.5 and $h = r^2\dot{\nu} = \text{const}$ gives

$$\dot{r} = \frac{na}{\sqrt{1-e^2}}e\sin\nu, \tag{1.14}$$

$$r\dot{\nu} = \frac{na}{\sqrt{1-e^2}}(1+e\cos\nu), \tag{1.15}$$

where the mean motion $n = \frac{2\pi}{P}$. Therefore

$$RV = V_z + K(\cos(\omega+\nu) + e\cos\omega), \tag{1.16}$$

where the semi-amplitude

$$K = \frac{m_2}{m_1+m_2}\frac{na\sin i}{\sqrt{1-e^2}}. \tag{1.17}$$

A series of radial velocity measurements will therefore be able to constrain V_z, K, e, and ω based on Equation 1.16. The true anomaly ν is calculated based on the position in the orbit, and therefore constrains the orbital period P and also some other parameter to give a starting point (Orbital phase/mean anomaly at a reference time ϕ_0, or time of pericentre passage T_{peri}, ...). Since

parameter estimation based on radial velocities is generally performed as an inverse problem, with iteratively suggested parameters being compared to the data until a good agreement is reached (see Chapter 2), it requires solving Kepler's equation. Given an orbital period P and a time of pericentre passage T_{peri}, the mean anomaly M at a time T is

$$M = \frac{2\pi}{P}\left(T - T_{\text{peri}}\right). \tag{1.18}$$

M is the angle through which the orbit would have moved if it was a circular orbit. Given an eccentricity e, the eccentric anomaly E is defined by

$$E - e\sin E = M. \tag{1.19}$$

E is the angle through which the orbit would have moved on an elliptical orbit around the centre of the ellipse. To get the true anomaly ν, this is shifted to be an elliptical orbit around the focus of the ellipse.

$$\tan\frac{\nu}{2} = \left(\frac{1+e}{1-e}\right)^{\frac{1}{2}}\tan\frac{E}{2}. \tag{1.20}$$

Equation 1.19 is referred to as *Kepler's equation* which is not analytically solvable for E. Solving Kepler's equation numerically is generally the limiting factor for the computational efficiency of parameter estimation of Keplerian orbits.

A total of 5 orbital parameters can therefore be directly constrained by the radial velocity method: P, K, e, T_{peri}, and ω. From Equation 1.17 it is possible to extract information about the mass of the orbiting planet up to some assumptions. Re-arranging Equation 1.17 gives the radial velocity mass function

$$f(m_2) = \frac{m_2^3\sin^3 i}{(m_1+m_2)^2} = \frac{PK^3(1-e^2)^{3/2}}{2\pi G}. \tag{1.21}$$

With the assumption that the planet is much less massive than the star ($m_2 \ll m_1$), and knowing the mass of the star (m_1), $m_2 \sin i$ can be calculated.

The semi-amplitude $K \propto P^{-1/3}$. The radial velocity technique thus has a slight bias towards

short period planets, and of course also towards more massive planets (although the radial velocity technique on its own will only measure $m \sin i$ of a planet). To detect a planet, the orbit of the planet should also be well-sampled and ideally covered more than twice to be confident of the period measurement.

The first exoplanet around a main-sequence star was detected using the radial velocity method (Mayor and Queloz, 1995). Since then $\sim$ 1000 planets have been detected using this method. In Figure 1.2 the number can bee seen to slowly and steadily increase over time. The slow increase is because detecting planets using the radial velocity method takes a large amount of ground-based observing time over a long baseline, and the stars need to be observed one-by-one.

1.3.2 Transits

When a body passes in front of a luminous body, such as a star, relative to the Earth, a decrease in brightness is observed. This is what occurs during solar eclipses when the Moon passes in front of the Sun, a phenomenon known about for 1000s of years (see Figure 1.5[4]).

The Moon is not the only solar system body that passes in front of the Sun. The transit of Venus was observed first in 1639, where Venus passed in front of the Sun, but unlike the Moon it did not completely cover the solar disc. The solar system hence gives rise to different words for a body passing in front of another: eclipse or occultation when the body is fully obscured (Solar eclipse or Lunar eclipse) and transit when only partially obscured (transit of Venus). This distinction is partially extended to extrasolar systems. When an exoplanet passes in front of its host star it is called a transit or sometimes a primary eclipse, though very rarely would the star be fully eclipsed. When the exoplanet passes behind the star this is called the eclipse, secondary eclipse, or occultation. In the case of an eclipsing binary star the word transit is not used even when only partial coverage is achieved; primary eclipse is used for when the secondary star eclipses the primary and secondary eclipse for the converse. Sometimes the word conjunction (inferior or superior) is also used for an alignment of two bodies along the line-of-sight. In a circumbinary planet's case a conjunction refers to the passage of the planet in between the

[4]Picture taken by Dr. Lucy Thomas during special exhibition *Lumen* at the Getty museum, Los Angeles, California.



Figure 1.5: Right: Conditions for a solar eclipse. From *The Fountain of Knowledge* by John of Damascus (Arab, about 675-749 CE) from the Rare Book & Manuscript Library, Columbia University Libraries, New York.

binary as a whole and Earth rather than either of the individual transit events.

Exoplanets are typically detected in transit across single stars by relying on the fact that the transit will appear repeatedly at the same interval and with the same duration and depth. Many algorithms exist to detect such signatures, even when each individual transit does not have enough signal to be detected on its own (e.g. Box Least Squares; Kovács et al., 2002). The transit signature allows for inferences about multiple exoplanetary parameters (Winn, 2010), some of the key parameters which are discussed below are shown in Figure 1.6 in the case of an eclipsing binary. The time between each transit gives the orbital period P of the planet. The shape of the individual transits also provide information. The depth of a transit indicates the

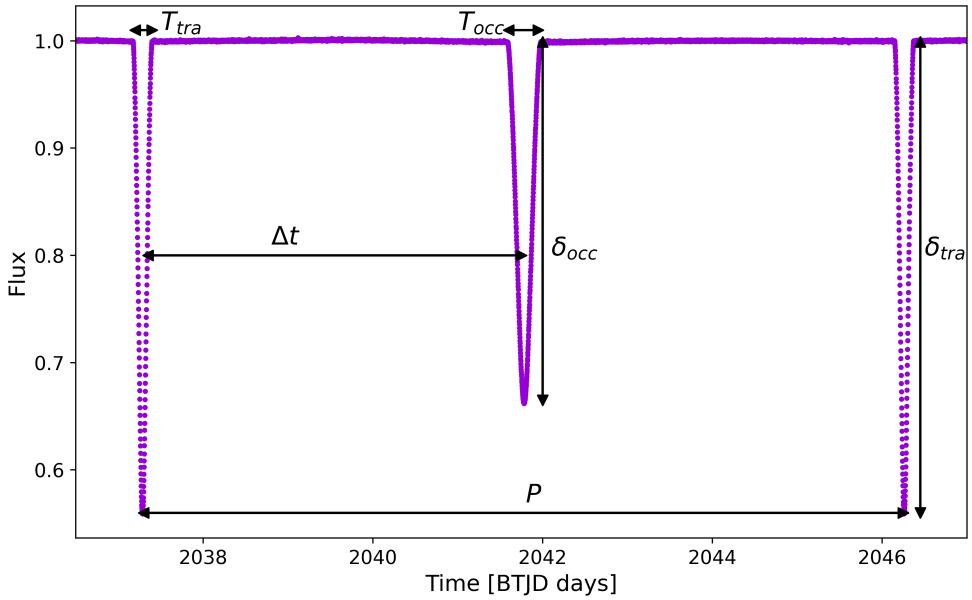


Figure 1.6: *TESS* data for eclipsing binary TIC 139721086. Demonstration of some of the transit/eclipse parameters discussed in the text from which orbital and physical parameters can be derived.

size of the planet (relative to the size of the star)

$$\delta_{\rm tra} \approx \left(\frac{R_p}{R_\star}\right)^2 \left[1 - \frac{I_p}{I_\star}\right], \tag{1.22}$$

where R_p and $R_\star$ are the radii of the planet and star respectively, similarly I_p and $I_\star$ the disc-averaged intensities of radiation from the planet and star. With the approximation that $I_p \ll I_\star$, then $\delta_{\rm tra} \approx R_p^2/R_\star^2$. For a secondary eclipse or occultation $\delta_{\rm occ} \approx R_p^2/R_\star^2 \times I_p/I_\star$. The duration of the transit has a few definitions depending on whether the start or end of ingress and egress are used. For a thorough discussion of what can be inferred from each of the different time differences see Winn (2010). With both transit and occultation, the eccentricity and argument of pericentre can be constrained.

$$\Delta t \approx \frac{P}{2}\left[1 + \frac{4}{\pi} e \cos\omega\right], \tag{1.23}$$

$$\frac{T_{\rm occ}}{T_{\rm tra}} \approx \frac{1 + e\sin\omega}{1 - e\sin\omega}, \tag{1.24}$$

where Δt is the offset between primary and secondary eclipse (transit and occultation), and $T_{\rm tra}$ and $T_{\rm occ}$ are the durations of transit/primary eclipse and occultation/secondary eclipse. With only the transit, it is potentially possible to obtain some information about the eccentricity of the orbit from the *photoeccentric effect* (Dawson and Johnson, 2012; MacDougall et al., 2023). This uses the principle that an eccentric planet may (depending on ω) cause a particularly long or short transit since its orbital velocity at the time of transit may be much higher or lower than that of a planet on a circular orbit at the same orbital period.

The transit signature is also affected by the fact that the stellar disc is not uniformly bright; *limb-darkening* causes the centre of the stellar disc to be brightest (e.g. Mandel and Agol, 2002). This smooths out the transit shape which would otherwise be trapesoidal, rounding off the corners. Additionally, the planet may not transit through the centre of the stellar disc, but only across the limb. This is quantified by the impact parameter b, a measure of how far the transit midpoint is from the centre. $b = 0$ for a transit that passes through the centre of the stellar disc and $b = 1$ if the centre of the planet kisses the edge of the stellar disc. In some cases not all of the planet will pass in front of the star. An impact parameter near 1 (or even above) can mean a grazing transit. The impact parameter can also therefore affect the duration of the transit, meaning that care is needed when measuring eccentricity from transit duration. b can be derived from the shape of the transit but degeneracies exist, especially for small planets (Dawson and Johnson, 2012).

The transit method is biased towards planets with large radii (easier to detect) and planets close to their host stars (more likely to transit). The shadow of a planet orbiting a star will sweep out a ring on the celestial sphere. For humanity to be able to detect the planet in transit, the Earth must happen to lie in that ring. The probabilities of a transit or eclipse/occultation are (Winn, 2010)

$$P_{\rm tra} = \frac{R_\star \pm R_p}{a}\left(\frac{1 + e\sin\omega}{1 - e^2}\right), \tag{1.25}$$

$$P_{\rm occ} = \frac{R_\star \pm R_p}{a}\left(\frac{1 - e\sin\omega}{1 - e^2}\right). \tag{1.26}$$

Here, the two options of ± refer to the probability of a total transit/eclipse vs a partial (i.e. grazing) transit/eclipse. Integrating over possible values of ω this gives

$$P_{\rm tra} = P_{\rm occ} = \frac{R_\star \pm R_p}{a}\left(\frac{1}{1-e^2}\right). \tag{1.27}$$

In the simplified case of a circular orbit and $R_p \ll R_\star$, then $P_{\rm tra} = P_{\rm occ} \approx R_\star/a$.

Transiting planets now account for the majority of discovered exoplanets, numbering ≈ 4000. Early transiting planets came from ground-based surveys such as OGLE (Udalski et al., 2002), HAT (Bakos et al., 2009), and SuperWASP (Pollacco et al., 2006), but the biggest hauls of transiting exoplanets have been from space based surveys, in particular *Kepler* (Borucki et al., 2003) and *TESS* (Ricker et al., 2015).

1.3.3 Direct Imaging

The planets of the solar system can be observed simply by looking at them directly. In many cases this does not even require a telescope. The light of the Sun needs to be blocked out, and then the planets are detectable. On Earth, within the solar system, one needs only to wait for the night to fulfill this condition. Exoplanets can also be detected by directly seeing them, but "blocking out" the light of the host star is more difficult (Traub and Oppenheimer, 2010). Typically direct imaging is performed either with a *coronagraph*. An *interferometer* can also be used to isolate the light from a planet, and while similar this is not typically considered direct imaging.

Different setups exist for direct imaging, but they all share the same general biases that it is easiest to measure a bright planet that is far from its star. This brightness can be a mixture of reflected light from the host star and intrinsic brightness from the planet. This probes a different class of exoplanets than the other methods, often much further from the star. Direct imaging also has a bias towards young systems with planets that are still hot from their formation (Marley et al., 2007), especially if that formation comes from gravitational instability (see Section 1.5), sometimes called a hot-start scenario (Spiegel and Burrows, 2012). An advantage direct imaging

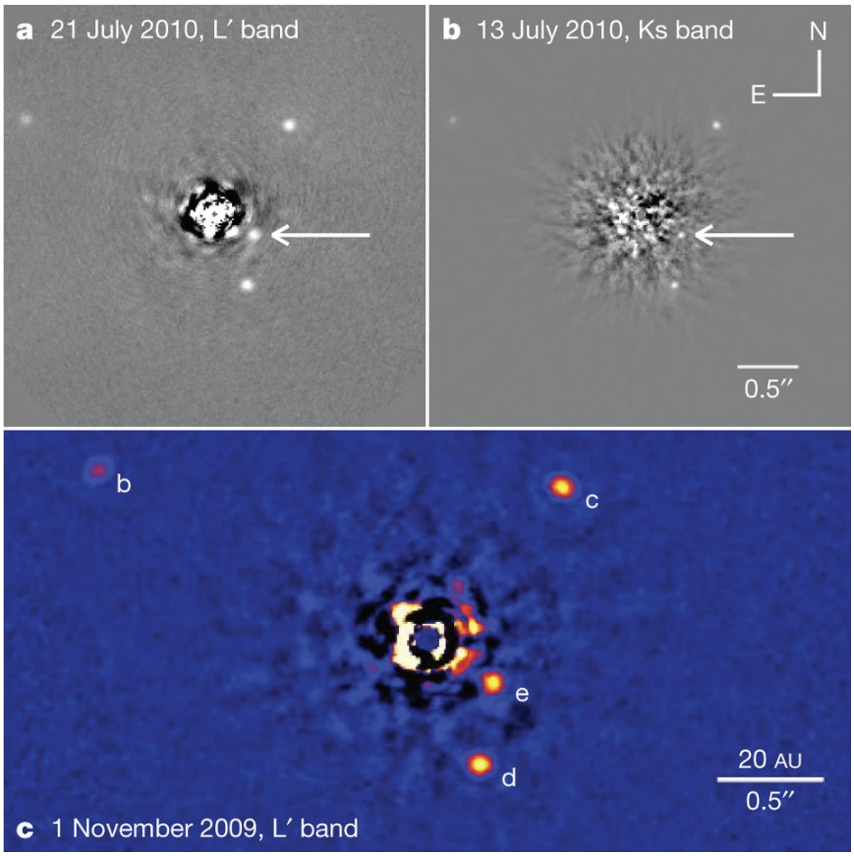


Figure 1.7: From Marois et al. (2010). Directly imaged planets around HR 8799.

has is that only 2 epochs seperated by just a few months are needed to confirm a planet (Lagrange, 2014), unlike the radial velocity method which would require monitoring for the whole orbit multiple times which makes ultra long-period planets inaccessible.

There are now $\sim$ 100 directly imaged planets. From Figure 1.3 it is apparent that some of the direct imaging planets overlap with the outermost population of radial velocity detections, but there are also some that are orders of magnitude further from their star. A famous example of a directly imaged system with four planets is HR 8799 shown in Figure 1.7 taken from Marois et al. (2010).

1.3.4 Gravitational microlensing

Light being deflected by a massive object (and by how much) was one of the first tested predictions of general relativity (Einstein, 1911) where the Sun deflecting the light of a background star was measured (Dyson et al., 1920). In the case of microlensing for exoplanet detection, the lensing event is usually a foreground star passing in front of a background star. With close (but not exact) alignment of the source and lens, the light of the background source get split into two images and therefore there is a magnification (Mao and Paczynski, 1991; Gaudi, 2010). The right panel of Figure 1.8 shows the magnification curve, and the left shows the configuration with the two images. If the alignment of lens and source is exact, the light of the source is spread around the *Einstein ring* (shown in green in the left hand panel of Figure 1.8). If a planet orbiting the star happens to pass in front of one of the images an extra perturbation will occur (also shown on the right hand panel of Figure 1.8).

The mass of the planet is related to the timescale of this extra event relative to the timescale of the whole microlensing event.

$$t_{E,p} = q^{\frac{1}{2}} t_E, \tag{1.28}$$

where q is the mass ratio $m_P/M_\star$. This is because that is the relation between the size of the Einstein rings of the star and the planet.

Microlensing requires the planet to pass in front of one of the images, which are close to the

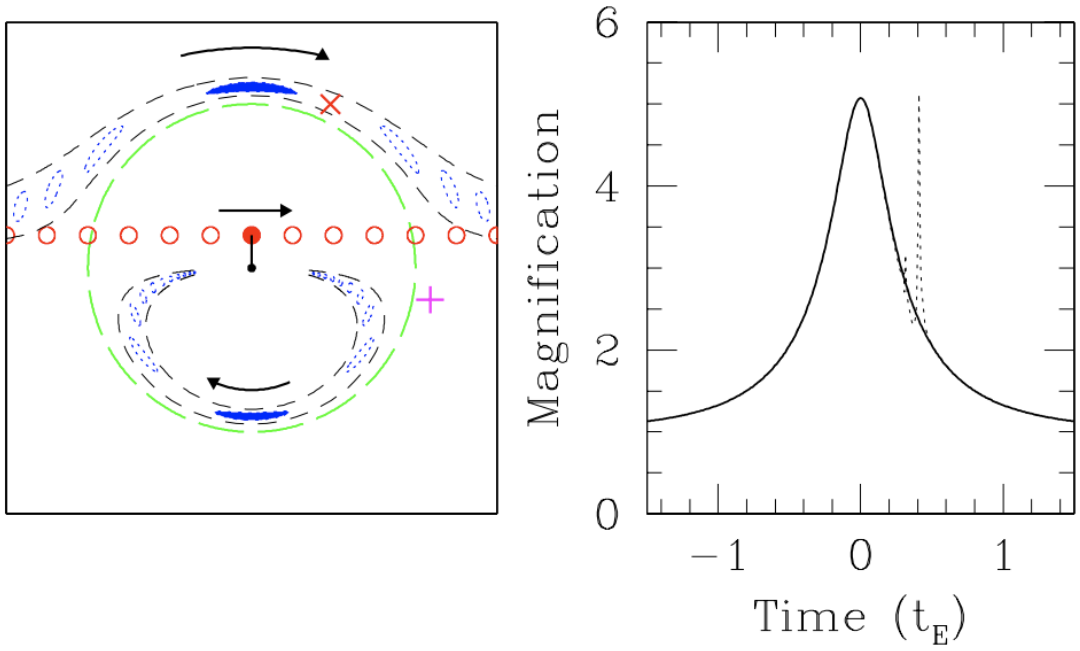


Figure 1.8: From Gaudi (2010). Left: schematic of the microlensing event. Right: microlensing magnification againt time with the perturbation from a planet shown.

Einstein ring, which has a radius (Gaudi, 2010)

$$\theta_E = \sqrt{\frac{4GM}{c^2(D_L^{-1} - D_S^{-1})}}, \tag{1.29}$$

with M the mass of the lens, and D_L and D_S the distances to the lens and the source. Microlensing will therefore only detect planets with a projected separation $\approx \theta_E$. Planets with an orbital radius less than this will not be detectable. They are most easily detectable at a distance of θ_E and remain detectable at larger distances though become less likely as a chance configuration (inclination, orbital phase, ...) is needed.

There is therefore a strong bias towards long-period (though not too long) planets. Substituting typical values of a solar mass star and a few kiloparsec distances gives a radius of ≈ 4 AU. Since the mass of the planet mainly affects the duration but not the presence of the signal, microlensing can find even very low mass planets. A total of ~ 200 microlensing planets have been detected so far.

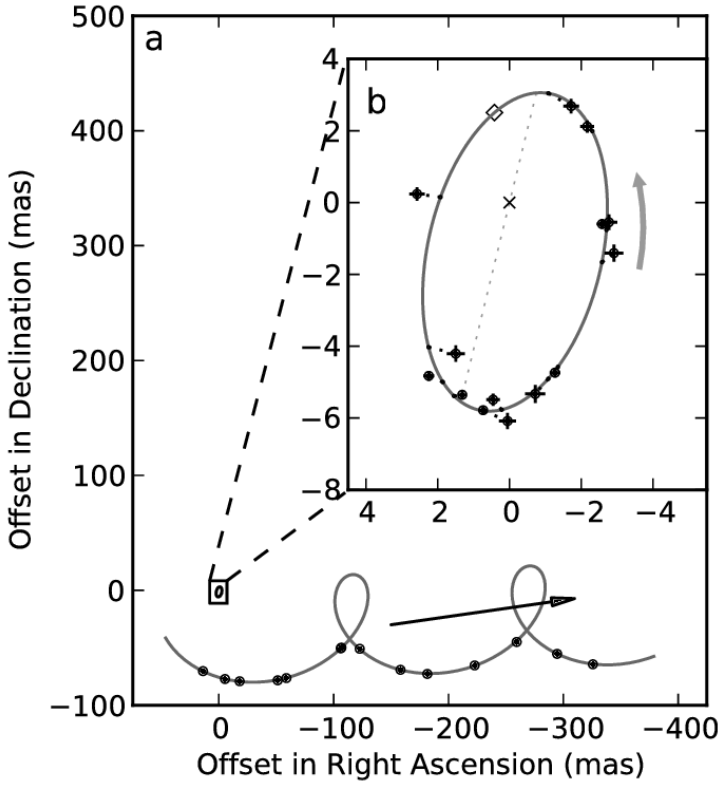


Figure 1.9: The astrometric motion of DE0823-49, paralactic motion at the bottom, with a zoom in of the orbit above. Figure taken from Sahlmann et al., 2013.

1.3.5 Astrometry

While the radial velocity method measures the motion of a star along the line-of-sight to detect an orbiting companion, astrometry measures the motion of a star in the sky-plane. By localising the star very precisely on the sky, the orbit of the star around the centre-of-mass can be observed.

The motion of a star in the sky-plane (as visible from Earth) due to a companion is a second order effect; the first order effect is the parallactic motion. To measure the motion of a star in the sky, the reference points used are other stars nearby, in particular stars that are very distant and therefore have approximately fixed positions. When observing a star nearer to Earth, the change in viewing angle as the Earth orbits the Sun has a clear effect. The star will trace an ellipse in the sky which takes 1 year to complete and the size of which depends on how close the star is to Earth. Astrometry is therefore used to measure the distance to a star based on the parallax. The star will also be moving within the galaxy relative to Earth, leading to what is called the *proper-motion*.

Once the parallactic motion and proper-motion have been accounted for, a planet's orbital signature can be detected. The parallactic and orbital signatures for DE0823-49 are shown in Figure 1.9 (Sahlmann et al., 2013). The wider the orbit, the further the star is from the centre-of-mass, and so the larger the signal (unlike with the radial velocity method). There is still however the need for a whole orbit or the majority of an orbit to be covered for the parameters of the orbit to be well constrained. The semi-major axis of the orbit in angular units is (Perryman, 2018)

$$\alpha = \frac{M_p a}{M_\star d}, \tag{1.30}$$

where M_p and $M_\star$ are the masses of the star and planet, a is the semi-major axis of the planet's orbit in distance units, and d the distance to the star. This means that astrometry is biased towards massive planets on long-period (but not too long-period) orbits around nearby stars. One of the big advantages is that astrometry maintains sensitivity at all orbital inclinations and will in fact measure the inclination of the orbit (Perryman, 2018).

There are currently 5 planets discovered using astrometry. The upcoming *Gaia* data releases are expected to astrometrically discover $\sim$ 10000 exoplanets (Perryman et al., 2014). In the past, *Hipparcos* detected brown dwarfs with astrometry (Sahlmann et al., 2011a) and *Gaia*, with much better sensitivity and observing many orders of magnitude more stars, is expected to surpass this by far.

Gaia and *Hipparcos* were scanning astrometric missions. These obtain one-dimensional measurements by rotation and measuring the positions of start as they cross a row of CCDs. The rotational axis of the satellite precesses such that the same stars are revisited many times from a different angle and build up two-dimensional information (Gaia Collaboration et al., 2016).

1.3.6 Timing variations

Variation in the timing of an otherwise strictly periodic signal can be used to infer the presence of a planet. The periodic signal can be many things; this section will mention Pulsar timing and Transit timing, for a discussion of Eclipse timing see Section 1.6.2.

Pulsar timing

The very first exoplanets found were detected around PSR B1257 + 12 using pulsar timing variations (Wolszczan and Frail, 1992). This relies on the pulsar's orbit around the centre-of-mass of the system being detectable due to the variation in arrival time of the pulses over the orbit, this is a Light Travel-Time Effect (LTTE) analogous to that used for planets claimed from Eclipse timing variations (see Section 1.6.2).

A pulsar is a type of neutron star that, due to a rapid rotation and misaligned magnetic and rotational axes, emits a stream of radio waves which pass into our line-of-sight periodically (Gold, 1968). These can be slow pulsars with pulses repeating on the timescale of $\sim$ 1 s, down to millisecond pulsars with pulses repeating apporixmately every $\sim$ 1 ms (Kramer et al., 1998). Planets have been found only around millisecond pulsars.

PSR B1257 + 12 hosts 3 terrestrial mass planets[5] ($\approx 0.02, 4.3, 3.9\, M_{\oplus}$), of which at least the outer two are coplanar and it is reasonable to assume the third is as well (Wolszczan, 1994; Konacki and Wolszczan, 2003). The coplanarity is a strong indication that the planets formed in a disc.

Despite planets orbiting pulsars being the first detected, they are rare: $< 0.5\%$ of pulsars host planets comparable to PSR B1257 + 12 (Niţu et al., 2022). This low occurence rate is likely due to rare formation channels requiring a second generation disc which would be formed due to an extreme mass ratio pulsar binary (Martin et al., 2016). A total of 8 planets have been discovered using pulsar timing variations.

Transit timing

Transit timing variations (TTVs) come in various forms, all sharing the basic premise that a single planet orbiting a star should follow a Keplerian orbit and thus have strictly periodic transits, but that the presence of another planet can alter this and cause the transits to not occur quite so strictly periodic.

[5]Contradictory to the discussion in Section 1.1.2, these were initially referred to as planets A,B and C. Inconsistency in naming planets appears to be the rule.

Any multi-planet transiting system will have TTVs but they are most detectable for systems close to mean-motion resonances (Agol et al., 2005). These are multi-planet systems where the ratio of the orbital periods is close to the ratio of two (typically small) integers, for example Kepler-36 has two planets with orbital periods $P_b = 13.84$ days: $P_c = 16.23$ days, which is close to a ratio of 7:6 (Carter et al., 2012).

The TTVs from a near-resonant system contain both a long-term signal and a short term signal (Holman et al., 2010). The long term signal is related to the timescale over which the resonant interactions cause a full libration cycle of the planet semi-major axes (Agol et al., 2005). If both planets are transiting, their long-term TTVs are anti-corellated (Fabrycky et al., 2012). The period of this long-term TTV signal is called the *super-period*, and for a $P_2 : P_1 \approx j : j-1$ first order resonance this period is

$$P_{\rm sup} = \frac{1}{\left|\frac{j-1}{P_1} - \frac{j}{P_2}\right|} \tag{1.31}$$

(Agol et al., 2005; Lithwick et al., 2012).

The shorter term TTV signals, referred to as *chopping*, occur on the timescale at which the planets return to the same configuration (Deck and Agol, 2015). For Kepler-36 in an 7:6 resonance this would happen at ≈ 100 days $\approx 6 \times P_c \approx 7 \times P_b$.

For a given planet's TTVs, the long-term signal constrains the orbital period of the perturbing planet (as seen above), the amplitude of the long-term signal depends on the mass and eccentricity of the perturber. The *chopping* signal also depends on the masses and periods. With both types present, TTVs can constrain the masses and periods and eccentricities of the planets (Deck and Agol, 2015).

TTVs have been used to detect perturbing companions to transiting planets (Ballard et al., 2011; Nesvorný et al., 2012; Leleu et al., 2021a) and to confirm that transiting signals are real and from multiple planets orbiting the same star (Holman et al., 2010; Fabrycky et al., 2012). They have also been used to obtain mass measurements of the planets involved (Nesvorný et al., 2013). Comparing the masses and radii of the TTV planets to those with radial velocity mass

measurements has shown that TTV planets seem to be less dense (Hadden and Lithwick, 2017; Leleu et al., 2023). It is possible this is due to implicit biases in the mass calculations with each method or observing biases for the kind of planet that would be detected, but there is likely a true underlying reason that TTV planets (and hence those near resonances) are more inflated (Leleu et al., 2024). A total of 35 planets have been discovered using transit timing variations.

1.4 Exoplanet population demographics

With 1000s of exoplanets now detected, various population trends have come to light. Many of these are under active investigation, attempting to understand their cause and to what extent they are impacted by various known and unknown biases. There are two clear trends visible from Figure 1.3. The first is that barely any planets have been found of comparable mass and orbital period to any of the solar system planets apart from Jupiter. This is generally accepted to be because of the inability to reliably detect such planets with the tools and methods available, rather than their non-existence. The second trend is that within the space where planets have been detected they are not uniformly spaced, the planets form three distinct groups.

1.4.1 Classes of exoplanet

Cold gas giants, comparable to Jupiter, abound in the population. These have mostly been detected using the radial velocity method, but also some from timing variations, direct imaging or microlensing. Their occurence rate has a range of values in the literature, which may depend on unknown biases of samples used but also on the definitions of cold gas giant used in each study. With a definition of $m \sin i > 50\,M_\oplus$, $P < 10$ years, an occurence rate of $\approx 14\%$ was found by Mayor et al. (2011). With constraints of $30\,M_\oplus < M < 6000\,M_\oplus$ Fulton et al. (2021) measure occurence rates of $\approx 14\%$ for the semi-major axis range $2 - 8$ AU, and an occurence of $\approx 9\%$ for $8 - 32$ AU. For planets with masses in the range $1 - 20\,M_{\rm Jup}$ and semi-major axes $5 - 20$ AU, Bryan et al. (2016) calculate an occurence rate of $\approx 50\%$. Wittenmyer et al. (2020) estimate an occurence rate of cool gas giants of $\approx 7\%$ (with no clear criteria on the definition).

The first two studies were done on the larger samples and so the typically quoted occurence rate is in the $10 - 15\%$ range.

Hot Jupiters, gas giants of mass greater than that of Saturn orbiting very close to their star, were a unpredicted discovery, the first one found being the first exoplanet found orbiting a main-sequence star (Mayor and Queloz, 1995). In Figure 1.3, hot-Jupiters appear to be very numerous because they are easier to detect than any other kind of planet. Comparative studies always agree that they are less common than cold gas giants (Wittenmyer et al., 2020). There are various measurements that put the occurence rate in the range $0.2 - 1.2\%$ (Boley et al., 2021).

A large population of **sub-Neptunes** also exists. These are planets generally between the sizes of Earth and Neptune, sometimes defined in terms of mass and sometimes in terms of radius. Howard et al. (2010) find that $\approx 23\%$ of stars host a planet in the mass range $0.5\,M_\oplus < M < 2\,M_\oplus$, and Mayor et al. (2011) calculate that $\approx 50\%$ of stars host a planet with $M < 30\,M_\oplus$. Bryson et al. (2021) estimate that there are $0.4 - 0.6$ planets per star in the radius range $0.5\,R_\oplus < R < 1.5\,R_\oplus$. Sub-Neptunes are sometimes divided into two categories: super-Earths and mini-Neptunes. This division is because of the observed bimodality in radius of sub-Neptunes sometimes called the *radius valley*.

1.4.2 The radius valley

The radius valley is an observed phenomenon in the population of small exoplanets. At around $R = 1.6\,R_\oplus$ there is a dearth of exoplanets compared to peaks in the occurence at around $1.3\,R_\oplus$ and $2.4\,R_\oplus$ (see Figure 1.10, adapted from Fulton et al., 2017). This has been found to be the case for planets with orbital periods < 100 days.

Many explanations have been proposed for the existence of the radius valley. Generally the different explanations all result in those planets below the valley being effectively bare rocks, and those above it having either retained some amount of a hydrogen atmosphere or having a very high water content (Venturini et al., 2024). These explanations have different mechanisms for causing the dichotomy in composition. The different mechanisms include: mass loss from photoevaporation (Lopez and Fortney, 2013; Owen and Wu, 2013) where extreme ultra-violet

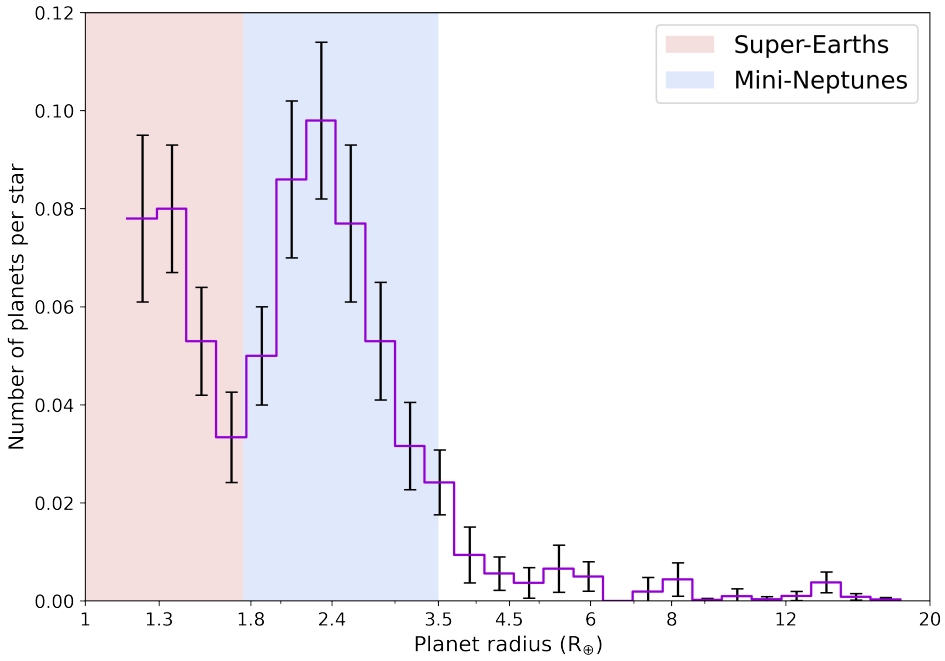


Figure 1.10: Occurence of exoplanets by their radius demonstrating the radius valley between super-Earths an mini-Neptunes. Figure adapted from Fulton et al. (2017).

radiation from the star strips the atmosphere; core-powered mass loss (Ginzburg et al., 2018) where heat from the inner layers of the planet's atmosphere can expel the outer atmosphere as the planet cools following its initial formation and as energy absorbed from the host star is re-radiated; and location of planet formation in the disc (Venturini et al., 2020) where planets forming beyond ice lines have a higher amount of volatiles and can end up retaining more of their atmosphere compared to rocky cores that form inside the ice line. In reality it is likely that all these effects come into play, and a better understanding of the radius distribution of planets across the parameter space will help uncover which mechanisms are dominant in which scenarios. In the study of circumbinary planets the different conditions around a binary star can help elucidate which conditions cause the radius valley.

The radius valley gets shallower as the host star's mass decreases, but a density valley persists. This has been seen both observationally (Luque and Pallé, 2022; Ho et al., 2024) and in theoretical simulations (Venturini et al., 2024). This is a consequence of migration where around low-mass stars, even low-mass planets can migrate inwards, meaning that small (less

dense) icy planets can reach the inner regions of the planetary system and smooth out the valley. Around higher mass stars this is more difficult and the small icy planets remain further out in the disc (Venturini et al., 2024).

1.4.3 Other population trends

A few other trends have been found in the population of exoplanets. Many of these trends are relevant to the study of circumbinary planets, as the dynamics of a circumbinary environment will affect each trend in a specific way and help us understand the origins of such trends.

Mass distribution

The mass distribution of exoplanets is sensitive to a few different parameters. One key way it can be quantified is in the occurence rate of gas giant planets. The occurence rate of giant planets has been found to have a slight peak at $\approx$ 3 days (hot-Jupiters) decreasing after this peak and then a rising occurence rate with longer orbital period (Santerne et al., 2016). Gas giant occurence rate has also been found to have a strong dependence on the metallicity of the star (i.e. the abundance of metals[6] in the envelope of the star) where the higher the metallicity the more common gas giants are (Johnson et al., 2010; Mortier et al., 2013; Reffert et al., 2015). It was also found that even taking metallicity into account, there is a dependence of gas giant occurence on stellar mass (Reffert et al., 2015). Johnson et al. (2010) found fewer planets around M dwarfs (3%) and more around A stars (14%). Reffert et al. (2015) found that gas giant occurence rate peaks for stars of 2 $M_\odot$, and that past $M > 3.5 M_\odot$ the occurence rate is very poorly constrained. The study of circumbinary planets provide a chance to study this mass correlation further, as it can extend the total "stellar" mass range higher. For example the frequency of planets orbiting binaries with both stars at 2 $M_\odot$ can be a proxy for the frequency of planets orbiting single 4 $M_\odot$ stars, around which planets are difficult to find due to their rarity, activity levels, and their quick evolution through the main-sequence.

[6]For astronomers, a metal is any element that is not hydrogen or helium

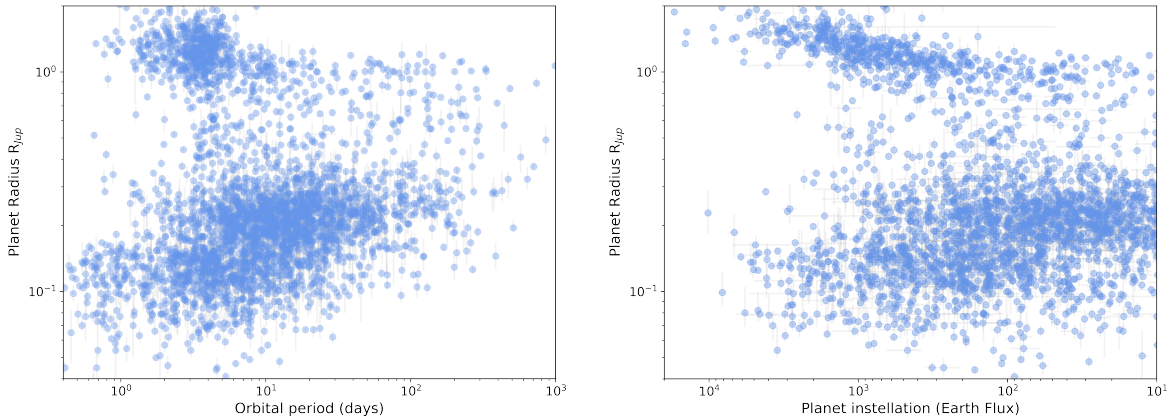


Figure 1.11: The hot-Neptune desert. Left: planet radius vs orbital period. Right: planet radius vs planet instellation. Planets are taken from the NASA exoplanet archive, only those with 3σ measurements of radius and period are included.

The hot-Neptune desert

There exists an underdensity of planets around the size of Neptune at very short orbital periods, in comparison with both more massive and less massive planets at the same period (Szabó and Kiss, 2011; Mazeh et al., 2016). This area can be seen in Figure 1.3, and is sometimes known as the hot-Neptune desert. The hot-Neptune desert is better shown with the radius on the y-axis rather than the mass. This is seen in Figure 1.11, on the left is radius vs orbital period, and on the right is radius vs instellation. There are a few differences between the two versions. The centre of the desert is more empty when plotting the instellation, which is a signature of the likely role of photoevaporation in the formation of the desert (Lopez and Fortney, 2014). When plotting with orbital period the super-Earths are closer to the star, but when plotting with instellation the hot Jupiters are more irradiated. This disparity is possibly a signature of giant planets forming more readily around more massive stars (which are hotter). When using orbital period, there is an overdensity at the edge of the desert (around 4 days, 0.5 $M_{\rm Jup}$), this disappears when using instellation.

Eccentricity distribution

The distribution of exoplanetary eccentricities from radial velocity surveys was studied by Kipping (2013) who found that the best parametrisation for the eccentricity distribution is a Beta

distribution $\beta(a, b)$ where the shape parameters should take the values $a = 0.867 \pm 0.044$ and $b = 3.03^{+0.17}_{-0.16}$. Kipping (2013) also found that dividing the planets into short period and long period (split at 382.3 days) led to a significant difference, where the short period planets were more circular and long-period planets more eccentric. With a larger sample size, Stevenson et al. (2025) find results in broad agreement with Kipping (2013), they also find a difference in the eccentricity distribution of high-mass and low-mass planets and that the presence of an outer companion (giant planet or secondary star) did not affect the eccentricity distribution of inner planets. Another similar study was performed by Van Eylen et al. (2019) investigating small planets from *Kepler*. They found a difference in the eccentricity distribution of single-planets vs planets in multi-planet systems, with multi-planet systems being more often closer to circular and single-planets more eccentric. The distributions of eccentricities of known planets is often used as a prior distribution for Bayesian parameter estimation of a new planet's properties, typically the distribution used is the Beta distribution from Kipping (2013) (see Section 2.1.3).

Obliquity distribution

Obliquity is the measure of misalignment between two angular momenta. In the typical exoplanet case, these are the orbital angular momentum of the planet and the rotational angular momentum of the star. The typical view of planet formation is that planets form in a disc around a star such that all the planets are coplanar to each other and in the same plane as the rotation of the star. This has, however, not been the case for all the observed exoplanets (Triaud et al., 2010; Triaud, 2018; Albrecht et al., 2022). Many planets exist on misaligned orbits to their host-star's rotation, but the distribution of obliquities is not uniform. The majority of planets are aligned or close to aligned with the rotation axis of the star, with obliquities $\psi < 40°$, and the majority of the remaining planets have obliquities $80 < \psi < 125°$ (Albrecht et al., 2021). These polar orbits aligned at close to 90° are seen for many classes of planets, even hot-Jupiters. There is a link here to circumbinary planets as well, but rather than the spin axis of the central star, a binary has an orbital plane relative to which the orbit of a planet can be computed, and unlike the rotation axis of a single star this is typically easier to measure.

1.5 Exoplanet formation and evolution

1.5.1 Exoplanet formation models

Planets are generally believed to form in a protoplanetary disc around a star. This was hypothesised long ago based on the knowledge that the planets in the solar system are almost entirely coplanar (Kant, 1755).

There are two main proposed pathways for exoplanet formation. The first is direct instability of the disc (Kratter and Lodato, 2016), which will only form gas giants, far from the star, and will make the young planet hot (Ormel, 2024). The second is that planets can form in a bottom-up way (often referred to as core-accretion; Armitage, 2024; Clement et al., 2024; Ormel, 2024), this can form all/most types of observed planets, and the young planet will be cooler than if formed by gravitational instability.

Core accretion has many possible versions, but all share the basic premise of starting with small building blocks and assembling them into larger and larger objects. Many of these require collisions of two objects to cause them to stick together which depends on the material the objects are made of as well as the relative velocity at the point of impact. Core accretion can typically be divided up into mechanisms that utilise or form: dust (μm in size) pebbles (mm-m in size), planetesimals (100m-100km in size), embryos (>100km) and planets (see Section 1.1.1). It is not clear which if any of the various mechanism is dominant, and there are outstanding problems to solve. Planetesimals are unlikely to form simply from subsequent collisions of smaller bodies as retaining bodies that have reached a stokes number of 1 is difficult, they typically drift inwards towards the star on a quick timescale (Weidenschilling, 1977). This is often referred to as the *metre-size barrier* (Clement et al., 2024), although depending on the local disc conditions (e.g. gas surface density) the location of this barrier can vary, ranging from sizes of $\sim$ 1 mm to $\sim$ 10 m (Weidenschilling, 1977; Laibe et al., 2012). Instead of the *metre-size barrier* it can also be called the *radial-drift barrier* (Laibe et al., 2012). This barrier may also manifest differently for discs in multi-stellar systems, meaning that circumbinary planet formation may encounter a

radial-drift barrier differently to planets around single stars, which could result in a difference in the circumbinary planet population.

A popular theory for forming planetesimals from pebbles is by the streaming instability (Youdin and Goodman, 2005). Once a planet has formed, it can accrete gas to become a giant planet or stay a rocky core to remain a rocky planet. Small rocky planets can grow from collisions with each other, sometimes referred to as giant impacts. It is thought that the last giant impact in the solar system was the Moon's formation event (Canup, 2004; Palme, 2004). For more details on the various parts of core accretion planet formation theory see Armitage (2024), Clement et al. (2024), and Ormel (2024) and references therein.

1.5.2 Exoplanet evolution and migration

Planetary systems are not expected to stay static once formed. While the planet is embedded in a gas disc, instabilities will often be damped. Once the disc has dissipated (typically on a timescale of $\sim$ 5 Myr; Bitsch et al., 2015), gravitational interactions will take hold and excite the eccentricities of planets often leading to crossing orbits and instability (Ogihara and Ida, 2009; Izidoro et al., 2017). This can be one of the ways the giant impacts (mentioned above) can be induced (Clement et al., 2024).

Even before the disc has dissipated, the planetary system may evolve. In particular, planets can migrate from their original location (Kley and Nelson, 2012). Disc-driven migration is typically divided into two types. Type I is where the planet excites a spiral density wave in the disc with slightly different inner and outer torques resulting in migration through the disc (Lubow and Ida, 2010; Ormel et al., 2012). Type II is where the planet is massive enough to open a gap in the disc, and then the gap and planet migrate with the disc as a whole as it slowly accretes onto the star (Lin and Papaloizou, 1986). Type II is generally slower than Type I. It is often thought that migration can lead multi-planet systems to form into a resonant chain. The expected pathway is that a pair of planets will migrate independently until they reach a mean-motion resonance and will then migrate together staying locked in the resonance, subsequently picking up other planets into a resonant chain (Delisle et al., 2015; Tamayo et al., 2017). When

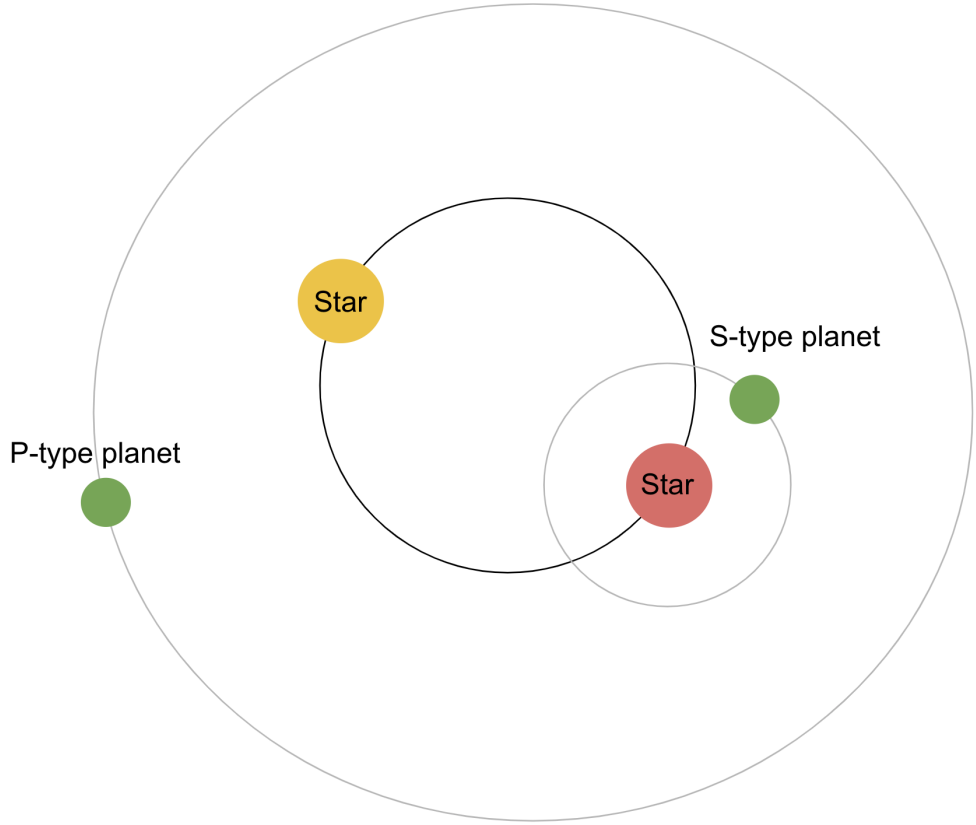


Figure 1.12: Configurations of planets in binary systems.

the disc eventually dissipates these resonant chains might then disperse as described above, or they could persist in a metastable equilibrium. Several systems with resonant chains of up to 7 planets have been found (e.g. Trappist-1: Gillon et al. (2017), and TOI-178: Leleu et al. (2021b)).

1.6 Circumbinary planets

There are two types of planets in binary systems[7]. These are S-type (satellite-type) planets which orbit one of the two stars, and P-type (planetary-type) planets which have a wide orbit around the centre-of-mass of the system (Dvorak, 1982). The configurations are shown in Figure 1.12. *Circumbinary* is another word for P-type and is the kind of system primarily considered in this thesis.

[7]Occasionally a third type (L-type) is mentioned which would orbit in a Trojan configuration at one of two Lagrangian points (L4 or L5) of the binary system

Circumbinary planets are generally thought to only be able to form at a large distance from the binary, planet formation in the inner regions of the circumbinary protoplanetary disc being inhibited (Moriwaki and Nakagawa, 2004; Meschiari, 2012; Paardekooper et al., 2012). Typically the point at which the transition from formation being inhibited to formation being possible occurs at $\sim 50 \times P_{\rm bin}$ (Moriwaki and Nakagawa, 2004). This means that any planet that is found closer to the binary than this, most likely must have migrated to that position (e.g. Nelson, 2003; Kley and Haghighipour, 2014; Penzlin et al., 2021). On top of being interesting in their own right, circumbinary planets near their host binaries are therefore a somewhat *controlled experiment* in planet formation. While it is not possible to truly control variables in astronomy, circumbinary planets are likely selecting only a population that form far out in a protoplanetary disc and then migrate inwards. Comparing the population of circumbinary planets to planets orbiting single stars and to S-type planets in wide binaries can help narrow down which aspects of planet formation models are dominant in various regimes.

1.6.1 Circumbinary orbits and stability

The dynamics and orbital stability of circumbinary exoplanets has been studied long before they were confirmed to exist (Dvorak et al., 1989; Holman and Wiegert, 1999). It is a form of the 3-body problem, for which there is no generalised analytical formulation. Many works have studied circumbinary dynamics and stability with semi-analytic or numerical methods, varying different combinations of physical and orbital parameters (Doolin and Blundell, 2011; Correia et al., 2016; Georgakarakos et al., 2024). The main effect is that if the orbit of a planet is too close to that of the binary it will likely be ejected.

The boundary between unstable and stable orbits (in period or semi-major axis) is often referred to as the stability limit, or stability criterion. Sometimes two limits are used, an inner one inside of which all orbits are expected to be unstable and an outer limit beyond which all orbits are expected to be stable (Dvorak et al., 1989). The region between these is sometimes stable and depends on the specific configuration. For individual circumbinary planets a specific stability analysis is often performed (e.g. Standing et al., 2023), and the use of an analytic

stability criterion is reserved for comparing different circumbinary systems or for giving prior expectations of what orbital periods are possible. In these cases a single criterion (closer to the inner limit) is preferable for simplicity.

The most commonly used stability criterion for a coplanar circumbinary system is that from Holman and Wiegert (1999), which was based on numerical simulations with the planet represented by a test particle. They varied the mass ratio and eccentricity of the binary and derived an empirical critical semi-major axis

$$\begin{aligned} a_c =&(1.60 \pm 0.04) + (5.10 \pm 0.05)e + (-2.22 \pm 0.11)e^2 + (4.12 \pm 0.09)\mu \\ &+ (-4.27 \pm 0.17)e\mu + (-5.09 \pm 0.11)\mu^2 + (4.61 \pm 0.36)e^2\mu^2, \end{aligned} \tag{1.32}$$

where e is the binary eccentricity, and μ the binary mass ratio. This relation was defined over the ranges $0 \leq e \leq 0.7$ and $0.1 \leq \mu \leq 0.9$. When using this stability criterion in the rest of this thesis I use the value of

$$a_c = 1.60 + 5.10e - 2.22e^2 + 4.12\mu - 4.27e\mu - 5.09\mu^2 + 4.61e^2\mu^2. \tag{1.33}$$

This defines a circular region as the boundary of stability and instability. I typically consider an orbit that is inside this limit (or crosses inside it due to an eccentric orbit) to be unstable. The stability of an individual circumbinary planet is (again) rarely based on this, instead having an individual numerical stability analysis (e.g. Section 4.2). This formula is useful however for comparing the circumbinary planet semi-major axis to the radius of the stability region across a population, as is done in Section 1.6.3.

The stability of circumbinary systems is not restricted to coplanar orbits. The distance from the binary at which stable orbits are possible varies for different mutual inclinations, and varies differently for different binary parameters (Doolin and Blundell, 2011; Chen et al., 2019).

For low binary eccentricities, a mutual inclination of π leads to the most stable orbit (and is usually more stable than a mutual inclination of 0) (Farago and Laskar, 2010; Doolin and Blundell, 2011). This corresponds to a retrograde orbit with the planet orbiting in the opposite

direction to the binary. If the binary is eccentric, there are stable solutions near the binary with a mutual inclination of $\pi/2$ (Farago and Laskar, 2010; Doolin and Blundell, 2011). This is a polar orbit analogous to those discussed in Section 1.4.3. For binaries with high eccentricity polar planets are stable closer-in than coplanar planets (Chen et al., 2020).

The difference between planets being in the *coplanar* regime and the *polar* regime has a clear distinction, even for orbits that are inclined somewhere between 0 and $\pi/2$. This distinction is based on the properties of the orbit and which dynamical state it is in. The orbital plane is defined by the direction the angular momentum vector is pointed in. Shown in Figure 1.13, the two states are defined by whether the angular momentum of the circumbinary planet is precessing about the binary's angular momentum vector, or about the binary's eccentricity vector. These are referred to as *circulating* and *librating* orbits based on how Ω is varying. The critical mutual inclination at which the transition from circulating to librating occurs depends on the binary parameters, in particular the eccentricity ($e_{\rm bin}$) (Doolin and Blundell, 2011). The value of the critical inclination, $i_{\rm crit}$, (assuming a planet at a separation of $\approx 25a_{\rm bin}$[8]; Farago and Laskar, 2010) is

$$i_{\rm crit} = \arcsin\sqrt{\frac{1-e_{\rm bin}^2}{1+4e_{\rm bin}^2}}. \tag{1.34}$$

Numerical integrations by Doolin and Blundell (2011) show that this criterion is a good approximation even at smaller orbital distances. This criterion also depends on Ω of the planet's orbit and ω of the binary orbit, the critical angle being minimised and Equation 1.34 holding if $\omega_{\rm bin} - \Omega_{\rm pl} = \pi/2$ (Cuello and Giuppone, 2019).

1.6.2 Circumbinary planet detection

Transits

Circumbinary planets can and have been detected in transit when the planet transits the disc of one or both of the two stars (Borucki and Summers, 1984; Schneider, 1994; Doyle et al., 2011). Section 1.3.2 describes how detecting planets in transit generally relies on the transit events

[8]This is required for the secular quadrupole approximation, from which this equation was derived, to hold.

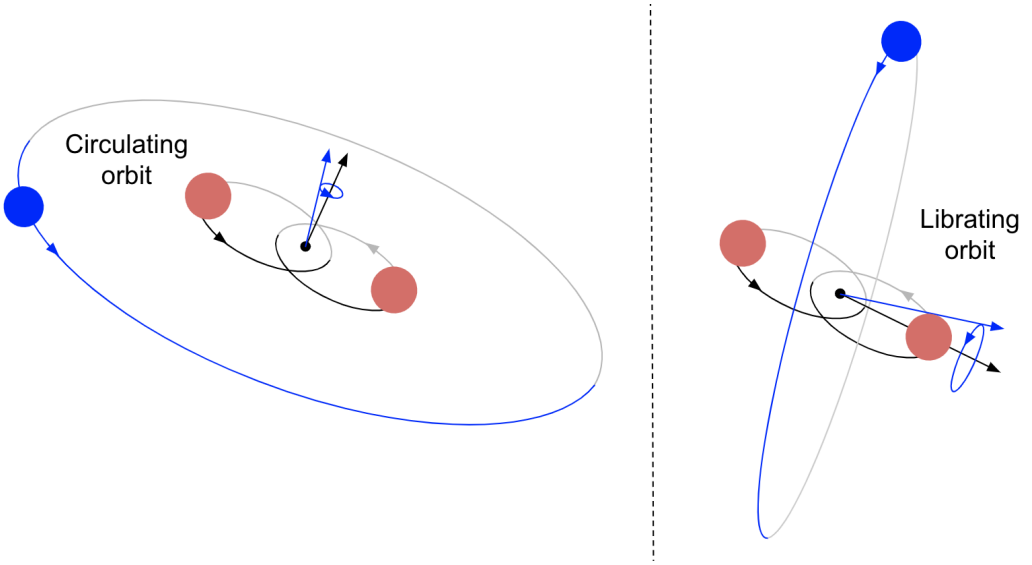


Figure 1.13: Configurations of circumbinary orbits precessing about the binary angular momentum vector (left) and precessing about the binary eccentricity vector (right). These are referred to as *Circulating* and *Librating* configurations respectively.

occuring strictly periodically, and always having the same depth and duration. Multi-planet dynamics do sometimes cause small deviations from this (see Section 1.3.6). In a circumbinary system multi-body dynamics do have an effect, but additionally there are geometrical effects which mean that transits are far from strictly periodic and have extreme changes in transit duration and depth (Martin and Fabrycky, 2021).

Consider the transit of a circumbinary planet across the primary star. From one transit of the primary to the next, the orbital phase of the primary star (within the binary orbit) will be different. Thus, the difference in time between two consecutive transits will be the planet's orbital period modulated by the time it takes for the planet to travel the increased or reduced distance. This is exemplified in Figure 1.14. With a very slight mutual inclination, transiting the same star at different orbital phases would lead to different impact parameters, and hence different transit depths. The relative velocities of the planet and star at the point of transit will also vary as the star changes velocity dramatically across its orbit leading to variations in duration that can span hours to days. The duration varying at different binary phases is described in Figure 1.14, and seen in Figure 1.15. These effects conspire to make circumbinary planet transit detection difficult. This difficulty is especially strong for automatic algorithms; all of the currently known

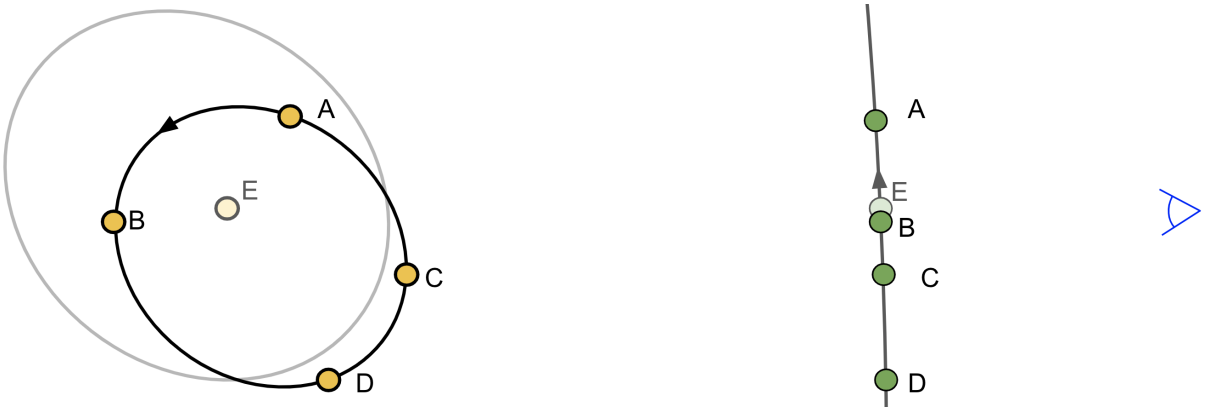


Figure 1.14: Circumbinary planet transits across the primary star at different orbital phases. Binary orbit shown on the left with four binary phases shown and labelled A-D, location of planet shown on right transiting the primary star at each of those phases. E: Equivalent single star system which would lead to stricly periodic transits all of the same duration. A: Star is moving along the line of sight, transit is near normal duration and is late. B: Near primary eclipse star and planet are moving in opposite directions, transit is very short and close to on time. C: near secondary eclipse star and planet are moving in the same direction, transit is very long and nearly on time. D: star is moving along the line-of sight, transit is near normal duration and is early.

transiting circumbinary planets were first identified by eye (Martin and Fabrycky, 2021).

Circumbinary planets in near coplanar orbits will undergo nodal precession. This is the same as the circulation described in Section 1.6.1 and shown in Figure 1.13. In many cases there will therefore be a long stretch of time where a circumbinary planet will not be able to transit followed by a stretch where it will (Martin and Triaud, 2014). The configuration where a circumbinary planet is able to transit is referred to a *transitable* configuration (Martin and Triaud, 2015).

The nodal precession and transitability is a double-edged sword. On one hand, a planet that is transiting may eventually stop, and follow-up transit observations become impossible. This is already the case for many of the *Kepler* circumbinary systems such as Kepler-16b (Doyle et al., 2011) (Kepler-16b stopped transiting the secondary in 2014 and the primary in 2018 and is expected to begin transiting again in 2042; Doyle, 2019). On the other hand, this means that a wider range of inclinations will eventually transit; approximately 90% of circumbinary planets orbiting eclipsing binaries will eventually transit regardless of the orbital period of the planet (Martin and Triaud, 2015). Thus the strong geometric observation bias of the transit method

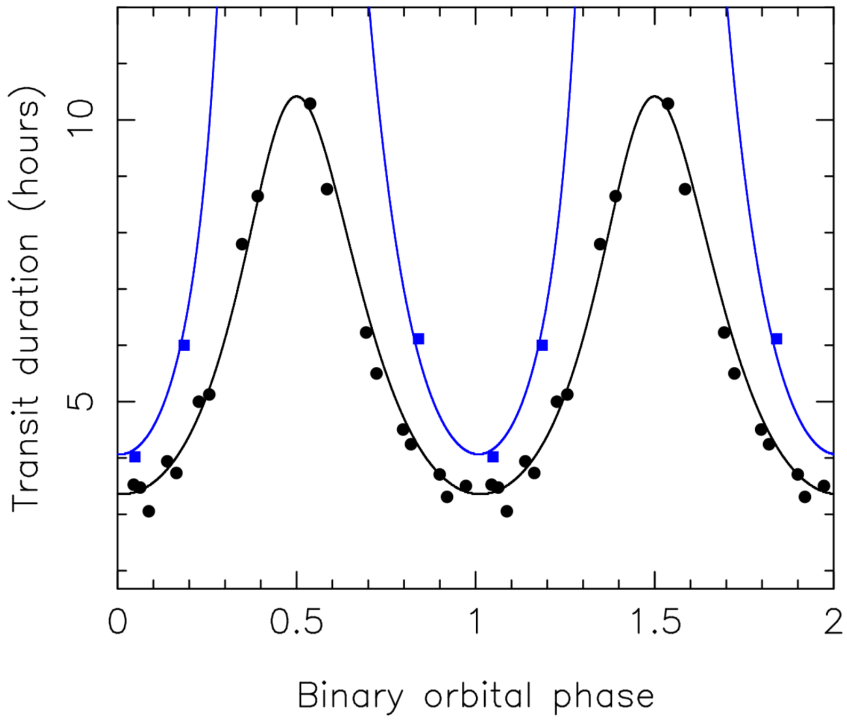


Figure 1.15: From Orosz et al., 2012a, paper on the discovery of two planets in the Kepler-47 system. The durations of the transits for the inner planet (filled circles) and the outer planet (filled squares) as a function of the orbital phase of the binary. The solid curves are the predicted durations assuming a circular, edge-on orbit for the planet. At phases near the primary eclipse, the planet and the primary star are moving in opposite directions, resulting in a narrower transit. At phases near the secondary eclipse, the planet and the primary star are moving in the same direction, resulting in a longer transit. The outer planet is moving slower than the inner planet, resulting in longer transits at the same binary phase.

around single stars is lessened around binary stars.

There is another geometric advantage to circumbinary transits. During a single orbit, the circumbinary planet can transit both stars one after the other. This is referred to as the *one-two punch* (Kostov et al., 2020a). This particularly unique signature of circumbinary planets, which is hard to mimic, means that a circumbinary planet can be identified from a single inferior conjuntion. The orbital period can be estimated based on the calculated distance travelled and time taken between transits. Knowing the distance travelled and the time taken gives the instantaneous velocity v at which the planet is travelling. The period estimate is therefore (Kostov et al., 2020a)

$$P_{\rm pl} = \frac{2\pi G M_{\rm bin}}{v^3} \left(\frac{e \sin\omega + \sin(\nu + \omega)}{\sqrt{1 - e^2}} \right)^3 , \tag{1.35}$$

where $P_{\rm pl}$ is the derived orbital period of the planet, G the gravitational constant, $M_{\rm bin}$ the total mass of the binary, e and ω the eccentricity and argument of periastron of the planet's orbit, and ν the true anomaly of the planet during the one-two punch.

The *Kepler* space mission detected 12 circumbinary planets in 10 binary systems: Kepler-16b (Doyle et al., 2011), Kepler-34b and Kepler-35b (Welsh et al., 2012), Kepler-38b (Orosz et al., 2012b), Kepler-47b, c, and d (Orosz et al., 2012a, 2019), Kepler-64b (Schwamb et al., 2013), Kepler-413b (Kostov et al., 2014), Kepler-453b (Welsh et al., 2015), Kepler-1647b (Kostov et al., 2016), Kepler-1661b (Socia et al., 2020). Some of the *Kepler* systems have planet mass measurements based on eclipse timing variations of the binary (e.g. Kostov et al., 2016) or transit timings of other planets in the system (e.g. Orosz et al., 2012a, 2019). These mass measurements are sometimes still imprecise. Others only have an upper limit on the mass from the lack of eclipse timing variations (e.g. Orosz et al., 2012b).

So far, *TESS* has detected two transiting circumbinary planets: TOI-1338b (Kostov et al., 2020b) and TIC 172900988b (Kostov et al., 2021). TIC 172900988b was discovered based on a single one-two punch event.

Radial velocities

The radial velocity method has detected three/four circumbinary planets so far. The first detection, HD202206, is slightly controversial. It was proposed by Correia et al. (2005) that the system could be a two-planet system with the inner *planet* being on the planet-brown dwarf boundary. The inclination of the system is uncertain so the masses of both bodies could be higher. It was subsequently proposed, based on Hubble astrometry, that the system is in fact a circumbinary brown dwarf (Benedict and Harrison, 2017). However there is doubt as to whether the astrometry is reliable, since that solution had previously been excluded due to stability arguments (Couetdic et al., 2010).

Spectroscopic binaries are divided into two classes, single-lined and double-lined. Double-lined binaries are those where the two sets of spectral lines are seen/resolved in the individual spectra. In single-lined binaries only the primary star is resolved spectroscopically; the binarity is inferred from the high amplitude ($>$ 1 km/s) radial velocity orbit. For two main sequence stars, the boundary for binaries to be single/double lined is typically at a mass ratio $q \approx 0.3$ (Triaud et al., 2017).

The TATOOINE (The Attempt To Observe Outer-planets In Non-singlestellar Environments) survey was a project that aimed to detect circumbinary planets orbiting non-eclipsing double-lined binaries (Konacki et al., 2009, 2010). Of the 13 published systems they studied, none had planet detections. Despite big improvements in the data reduction method, they found a typical scatter in the radial velocity data on the order of 10s of m/s (Konacki et al., 2009). This is due to what is sometimes called the *double-lined binary problem*.

The double-lined binary problem arises from the imperfect disentangling of the two component spectra. This means that subsequent individual radial velocity measurements are inaccurate. Methods to counter/solve the double-lined binary problem are used in Chapter 3. Double-lined binaries have advantages that make them useful to study. The two sets of spectral lines mean that (up to a potential unknown inclination) the absolute dynamical mass of the stars can be measured with high precision ($\approx 0.03\%$ in the case of TIC 172900988, see Section 3.1). Additionally, the two sets of radial velocities can be treated as independent so up-to twice the amount

of information is in any given spectrum. Detecting the planet in both of the radial velocity timeseries independently is a powerful diagnostic that the planet is real and not stellar activity.

The double-lined binary problem can be sidestepped by sacrificing the advantages of double-lined systems and only observing single-lined binaries. This is what has been done in the BEBOP (Binaries Escorted By Orbiting Planets) project so far. Initiated using the *CORALIE* spectrograph (Martin et al., 2019) and moved to the *HARPS* and *SOPHIE* spectrographs (Baycroft et al., 2024), BEBOP is a survey of eclipsing single-lined binaries searching for circumbinary planets. Within BEBOP there has also been a reconnaissance sub-survey on double-lined binaries selecting some systems from TATOOINE among others (see Section 3.3).

BEBOP has published three circumbinary planets so far: a confirmation of Kepler-16b (Triaud et al., 2022); the detection of BEBOP-1c in a system with a known transiting planet TOI-1338b from *TESS* (Standing et al., 2023); and a detection of TIC 172900988b, finding that the planet period that had been obtained from the one-two punch was an overestimate (see Section 3.1). Other results from the BEBOP survey, including currently un-published planets and candidates, will be discussed in Chapter 4.

One particular interesting result from Standing et al. (2023) is the detection of the outer planet BEBOP-1c, along with the non-detection of the inner planet TOI-1338b. This puts an upper mass limit on the inner planet of $\approx 22\,M_\oplus$ and therefore constraining it to a low density $\rho < 0.36\,(\mathrm{g\,cm^{-3}})$.

Eclipse timing variations

Third bodies orbiting eclipsing binaries can cause variations in the timings of the eclipses, thus allowing for circumbinary planet detection. The eclipse timing variations come in two flavours: dynamical and light travel-time.

The dynamical eclipse timing variations arise from interactions between the three bodies. They occur on the timescale of the outer body's orbital period, with a characteristic frequency approximately half of that. This is exemplified in Figure 1.16. These are analogous to the *chopping* signals in transit timing variations discussed in Section 1.3.6. The dynamical eclipse

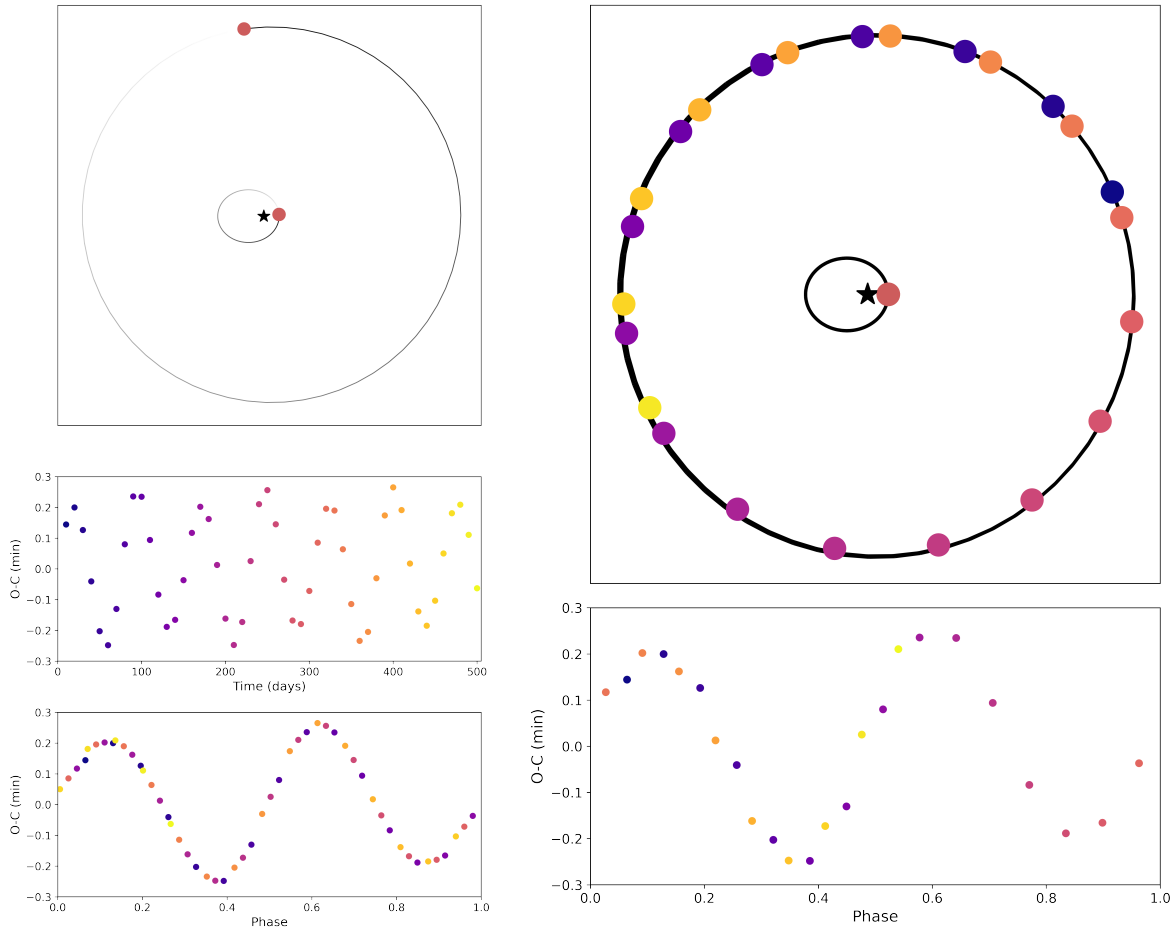


Figure 1.16: Dynamical eclipse timing variations for a circular planet orbiting an eccentric binary. Left: system integrated for 500 days, top is the system configuration; middle are the residuals of a linear ephemeris; bottom are the residuals phase folded on the orbital phase of the planet. Right: system integrated for 180 days, top is the system configuration with location of the planet at each eclipse shown; bottom are the phase folded residuals. In all cases (except top left) the colouring is scaled by the time of the eclipse.

timing variations are maximised for circumbinary planets on orbits close to the binary.

The light travel-time eclipse timings occur from the orbit of the binary around the centre-of-mass of the system and the ensuing variation in the distance the light travels. Eclipse timing variations based on light travel-time variations are maximised for planets far from the binary, they are analogous to the pulsar timing variations described in Section 1.3.6.

Planetary orbits have been detected using both methods. A handful have been proposed based on dynamical eclipse timing variations. Only one of these, Kepler-1660 (AB)b, is typically classed as confirmed, since the binary orbit has been studied using radial velocities

(Goldberg et al., 2023). Other candidates include KIC 3853259, KIC 177553, and KIC 7821010 (Borkovits et al., 2016).

Many circumbinary planets have been claimed based on light travel-time variations, mostly orbting post common-envelope binaries. These are binaries consisting of an evolved star (white dwarf or sdB) usually orbited by an M-dwarf star. They have short orbital periods $\sim$ 1 hr, having spiralled towards each other during a common-envelope phase (Ivanova et al., 2013). A catalogue of claimed planets orbiting post common-envelope binaries based on eclipse timing variations is shown in Section 5.2.1. This catalogue contains 33 planet candidates orbiting 25 binaries. These would likely be planets that survived the evolution of the binary (e.g. Columba et al., 2023). There are issues with these planetary solutions (Pulley et al., 2022), many of which are very poor at predicting future eclipses. The planet models are constantly being updated, often needing multiple planets in an unstable configuration to explain the data. Alternative explanations for the signals, such as magnetic interactions between the stars, have been proposed (Applegate, 1992; Lanza, 2020). More details on these types of systems can be found in Chapter 5.

Other detection methods

Microlensing, described in Section 1.3.4, has detected a handful of circumbinary planets (e.g. Bennett et al., 2016; Kuang et al., 2022). Typically the planet is detected as in Section 1.3.4, and the binarity is inferred from a slight asymmetry or residual signal which is attributed to a non-point-source lens (Bennett et al., 2016).

Astrometry has yet to detect a fully confirmed circumbinary planet in its own right. It contributed to HD202206 as discussed above. Additionally the *Gaia-Hipparcos* proper-motion anomaly was detected for HD155555 (Gratton et al., 2023) implying a tertiary companion. More details of the proper-motion anomaly method can be found in Section 5.1. See Sections 3.4 and 5.2.1 for discussions of the potential of *Gaia* astrometry to detect circumbinary planets in the future.

Direct imaging has also detected circumbinary planetary-mass objects (typically low mass

brown dwarfs). Examples are b Cen (AB)b (Janson et al., 2021) orbiting a binary of very high mass stars (total binary mass $\sim 10\,M_{\odot}$); and Delorme-1 (AB)b (Delorme et al., 2013) and VHS 1246 (AB)b (Dupuy et al., 2023) which are both very low mass binaries (total binary mass $\sim 0.1\,M_{\odot}$). The VHS 1246 (AB)b has a measured mutual inclination between binary and planet orbits of $115 \pm 14^{\circ}$ (Dupuy et al., 2023).

Pulsar timing variations (as discussed in Section 1.3.6) combined with imaging to get the inclination and mass of the binary system were used to detect an outer planetary-mass object and an inner white dwarf orbiting the pulsar PSR1620-26 (Sigurdsson et al., 2003).

1.6.3 Circumbinary planet demographics

At the point of writing this thesis, there are 39 circumbinary planets in 31 systems included in the exoplanets.eu catalogue of circumbinary planets[9], these are shown in Table 1.1. The NASA exoplanet archive[10] lists 48 circumbinary planets in 40 systems, shown in Table 1.2. Only 33 circumbinary planets are common to both lists, shown in Table 1.1 and Table 1.2 in bold. The tables include the layout, names, and parameters[11] that are included in the respective catalogues, therefore there are some inconsistencies between them (e.g. Kepler-64 is referred to as PH1 in the NASA archive).

The best sample of un-controversial circumbinary planet detections is the transiting sample from *Kepler*. The eclipse timing variation sample has many controversial entries. The microlensing, pulsar timing and radial velocity[12] planets have a smaller number of entries. The imaging planets, while more numerous have less well constrained paramteres (e.g. Period) and the masses of the planets and stars both range into the brown dwarf domain. On top of these, *Kepler* provides a more homogeneous sample with better understood completeness and statistics. These have been studied as a population and preliminary conclusions can be achieved even from a population of only 12 planets in 10 systems.

Based on the *Kepler* population, an occurence rate of circumbinary gas giants was found to

[9] https://exoplanet.eu/
[10] https://exoplanetarchive.ipac.caltech.edu/
[11] in the case of the exoplanets.eu
[12] for now...

Table 1.1: Planets from the exoplanets.eu circumbinary planet catalogue. Ordered by increasing binary separation. The *Other* detection method is as listed in the catalogue and refers to all methods except transit or radial velocity. There is only one entry per system with the planet parameters being those of the innermost planet. The detection method is that of the first planet detected in the system (i.e. TOI-1338c was detected by the radial velocity method but since TOI-1338b was detected in transit the system as a whole is listed as detected using the Transit method). Systems in **bold** are also included in the NASA exoplanet archive.

Name	Detection method	$M_{\rm pri}$ $[M_\odot]$	$M_{\rm sec}$ $[M_\odot]$	# planets	Planet semi-major axis [AU]	Planet mass $[M_{\rm Jup}]$
DPLeo	Other	0.69	0.09	1	8.19	6.05
NNSer	Other	0.535	0.111	3	3.39	2.28
Kepler451	Other	0.48	0.12	3	0.2	1.76
NYVir	Other	0.46	0.14	2	3.39	2.78
BXTri	Other	0.51	0.21	1	4.5	7.5
RRCae	Other	0.44	0.182	1	5.2	3.
KIC3853259	Other	0.736	0.736	1	1.06	10.
HD155555	Other	1.156	1.08	1	7.28	3.8
OGLE2007BLG349L	Other	0.41	0.3	1	2.59	0.25
Kepler47	Transit	1.043	0.362	3	0.2956	0.006
Kepler413	Transit	0.82	0.542	1	0.3553	0.211
Kepler1647	Transit	1.22	0.97	1	2.7205	1.52
TOI1338	Transit	1.098	0.307	2	0.4607	0.0686
Kepler38	Transit	0.949	0.249	1	0.4644	0.38
Kepler35	Transit	0.888	0.809	1	0.603	0.1268
Kepler64	Transit	1.384	0.336	1	0.634	0.53
Kepler453	Transit	0.944	0.194	1	0.7903	0.03
Kepler1661	Transit	0.841	0.262	1	0.633	0.053
KIC7177553	Other	1.043	0.986	1	1.61	5.
TIC172900988	Transit	1.238	1.202	1	0.7433	1.84
PSRB1620-26	Other	1.35	0.34	1	23.	2.5
Kepler1660	Other	1.136	1.082	1	1.12	4.89
Kepler16	Transit	0.654	0.196	1	0.7048	0.333
Kepler34	Transit	1.048	1.021	1	1.0896	0.22
KIC7821010	Other	1.309	1.21	1	2.65	2.6
OGLE2018BLG1700	Other	0.42	0.12	1	2.8	4.4
bCen	Other	5.16	3.45	1	556.	10.9
OGLE2019BLG1470	Other	0.51	0.18	1	3.1	2.2
OGLE2023BLG0836	Other	0.71	0.56	1	3.7	4.36
Ross458	Other	0.6	0.09	1	1168.	7.
2MASSJ0103-5515	Other	0.2	0.2	1	84.	13.

Table 1.2: Planets from the NASA exoplanet archive which have the circumbinary flag. Ordered by discovery year and discovery method. Planets in **bold** are also included in the exoplanets.eu circumbinary catalogue. Values of primary star mass, and planet period, mass, and radius are shown if included in the archive. Secondary masses are not included in the information.

Planet Name	Discovery [year]	Discovery Method	$M_{\rm pri}$ [$M_\odot$]	$M_{\rm pl}$ [$M_{\rm Jup}$]	$R_{\rm pl}$ [$R_{\rm Jup}$]	$P_{\rm pl}$ [days]
DP Leo b	2009	ETVs	0.69	6.28	1.14	10220
NN Ser c	2010	ETVs	0.54	7.33	1.13	5573.55
NN Ser d	2010	ETVs	0.54	2.3	1.19	2883.5
HU Aqr AB b	2011	ETVs	0.88	5.9	1.14	2390
HU Aqr AB c	2011	ETVs	0.88	4.5	1.15	4368
NY Vir b	2011	ETVs	0.46	2.3	1.19	3160
UZ For b	2011	ETVs	0.7	6.3	0	5840
UZ For c	2011	ETVs	0.7	7.7	0	1916.25
RR Cae b	2012	ETVs	0.44	4.2	1.16	4343.5
2MASS J19383260+4603591 b	2015	ETVs	0.48	1.9	1.2	406
MXB 1658-298 b	2017	ETVs	1.98	23.7	1.07	760
DE CVn b	2018	ETVs	0.51	12	1.1	4098.1
NSVS 14256825 b	2019	ETVs	0.42	14.15	1.1	3225
NY Vir c	2019	ETVs	0.46	5.54	1.14	8799
Kepler-451 c	2022	ETVs	0.48	1.61	1.21	1460
Kepler-451 d	2022	ETVs	0.48	1.76	1.2	43
Kepler-1660 AB b	2023	ETVs	1.14	4.992	1.15	239.5044
Ross 458 c	2010	Imaging	0.56	6	1.25	—
SR 12 AB c	2010	Imaging	—	13	1.1	—
2MASS J01033563-5515561 AB b	2013	Imaging	0.19	13	1.1	—
ROXs 42 B b	2013	Imaging	1	9	1.12	—
VHS J125601.92-125723.9 b	2015	Imaging	0.07	16	1.22	5800000
HD 284149 AB b	2017	Imaging	1.13	26.28	1.07	—
2MASS J0249-0557 c	2018	Imaging	0.05	11.6	1.11	—
HIP 79098 AB b	2019	Imaging	3.75	20.5	1.08	—
b Cen AB b	2021	Imaging	5.5	10.9	1.11	1790000
OGLE-2007-BLG-349L AB c	2016	Microlensing	0.41	0.251708	0.952	2557
OGLE-2016-BLG-0613L AB b	2017	Microlensing	0.72	4.18	1.16	—
OGLE-2018-BLG-1700L b	2020	Microlensing	0.42	4.4	1.15	—
OGLE-2019-BLG-1470L AB c	2022	Microlensing	0.57	2.2	1.19	—
OGLE-2023-BLG-0836L b	2024	Microlensing	0.71	4.36	1.15	—
PSR B1620-26 b	2003	Pulsar Timing	1.35	2.5	1.18	—
HD 202206 c	2004	Radial Velocity	1.07	17.9	1.08	1260
TOI-1338 c	2023	Radial Velocity	1.09	0.237235	0.92	215.79
Kepler-16 b	2011	Transit	0.69	0.333	0.754	228.776
Kepler-34 b	2011	Transit	1.05	0.22	0.764	288.822
Kepler-35 b	2011	Transit	0.89	0.127	0.728	131.458
Kepler-38 b	2012	Transit	0.94	0.384	0.384	105.599
Kepler-47 b	2012	Transit	0.96	0.006513	0.272	49.4643
Kepler-47 c	2012	Transit	0.96	0.009974	0.415	303.227
Kepler-47 d	2019	Transit	0.96	0.059843	0.628	187.366
PH1 b	2012	Transit	1.53	0.531	0.551	138.317
Kepler-413 b	2014	Transit	0.82	0.211	0.388	66.262
Kepler-453 b	2015	Transit	0.94	0.050341	0.553	240.503
Kepler-1647 b	2016	Transit	1.22	1.51968	1.059	1107.5923
Kepler-1661 b	2020	Transit	0.84	0.053488	0.345	175.06
TOI-1338 b	2020	Transit	1.09	0.0355	0.683	95.4001
TIC 172900988 b	2021	Transit	1.24	2.963863	1.004	200.452

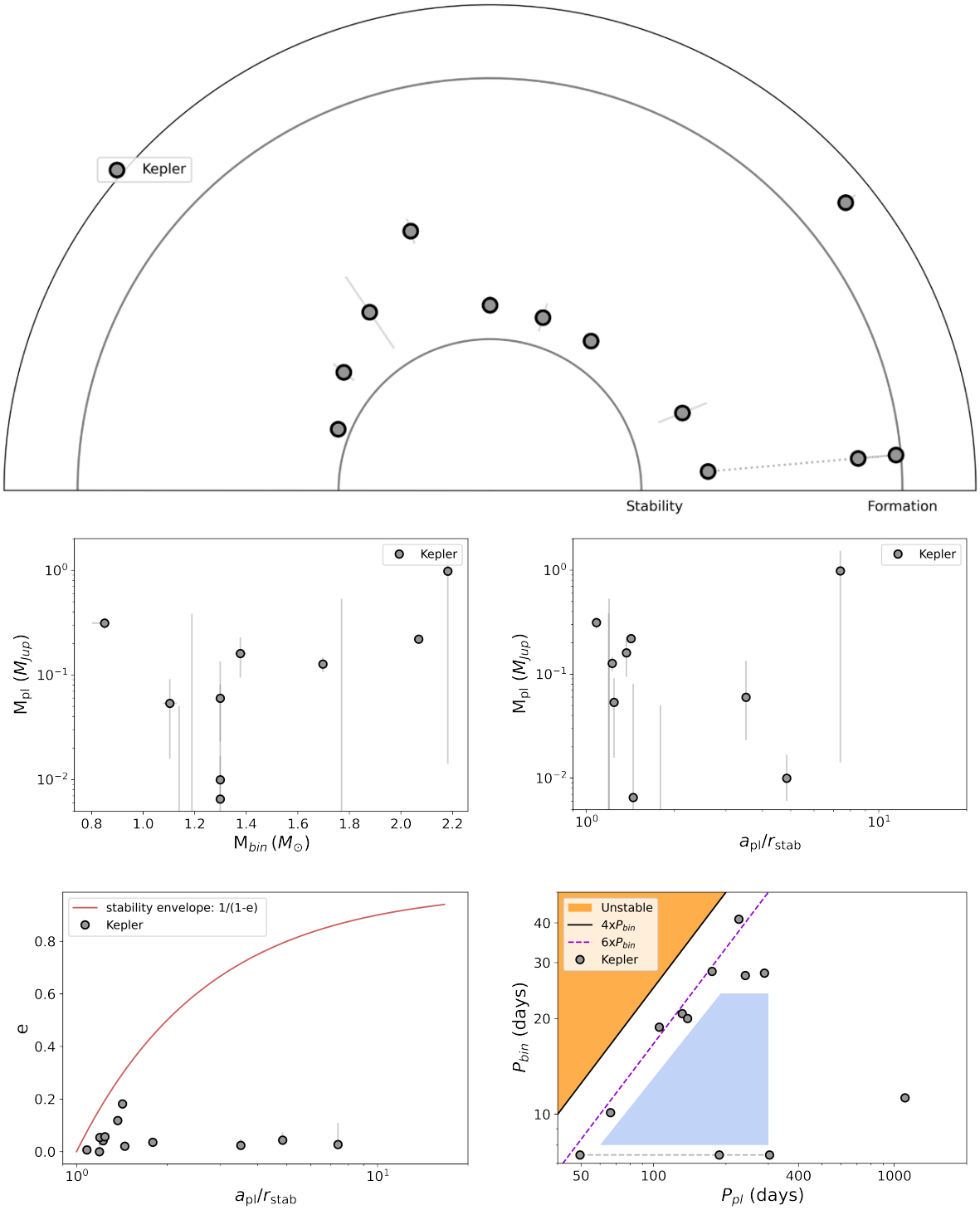


Figure 1.17: The Kepler circumbinary planets in various parameter configurations. Top: Proximity to stability limit with increasing binary orbital period anti-clockwise. Middle left: planet mass vs total binary mass. Middle right: planet mass vs proximity to stability limit. Bottom left: eccentricity vs proximity to stability limit, stable orbits should be below the red envelope. Bottom right: binary orbital period vs planet orbital period, blue region shows unexpected dearth of planets implying pile-up.

be $\sim$ 10% (Armstrong et al., 2014; Martin and Triaud, 2014). While this might seem a high occurence rate based on 12 planets, it is due mainly to two reasons. First, the nodal precession-induced times of transitability means that for each transiting circumbinary planet there will be multiple others that are not transiting at the moment. Second, the number of eclipsing binaries in *Kepler* is small ($\sim$ 4000) to begin with, and no planets were found to transit non-eclipsing binaries (Martin and Triaud, 2014).

This number of $\sim$ 10% is dependent on the population probed being almost coplanar, with a spread of inclinations not exceeding $\sim 5^\circ$ (Armstrong et al., 2014). A larger spread of inclinations would lead to more undetected planets and therefore a higher occurence rate. If the mutual inclination of circumbinary planets relative to their host binaries were isotropically distributed, the occurence rate would be close to 100% (Armstrong et al., 2014) which is unfeasibly high in comparison to the single-star population (see Section 1.4).

As discussed above, the masses of many of the *Kepler* transiting circumbinary planets are not well constrained. This is highlighted in the middle panels of Figure 1.17, where the planet mass is shown plotted against binary mass on the left and planet semi-major axis scaled by the radius of the stability limit on the right. Many of the planets have large uncertainties on the mass or even only upper bounds (the empty lines with no datapoint). These panels do not show any strong trends other than perhaps a correlation between planet mass and binary mass.

The scaled semi-major axis $a_{\rm sc} = a_{\rm pl}/r_{\rm stab}$ is a useful dimensionless parameter for a circumbinary planet's orbit. The radius of the instability zone ($r_{\rm stab}$) is calculated using equation Equation 1.33 (Holman and Wiegert, 1999), this takes the mass ratio and eccentricity of the binary into account. $a_{\rm pl}/r_{\rm stab}$ allows to compare the proximity of the planet to the stability limit for circumbinary systems with different properties.

The bottom left panel of Figure 1.17 shows the eccentricity distribution of circumbinary planets with scaled semi-major axis. The red curve shows the envelope where, if a planet were above it, the eccentricity of the planet would bring it inside the unstable region during its orbit. A potential alternative dimensionless parameter to $a_{\rm sc}$ would be the scaled pericentre distance which would take the planetary eccentricity into account as well.

The top panel of Figure 1.17 shows a_{sc} in the radial direction and has the *Kepler* circumbinary systems ordered anticlockwise with increasing binary orbital period (evenly spaced). The inner circle is the stability limit and the outer circle labelled *formation* is a $50 \times P_{bin}$ orbit, equivalent to the approximate point beyond which it would be expected that a planet could form (Moriwaki and Nakagawa, 2004). The radial uncertainties are a combination of the uncertainty in a_{sc}, and the eccentricity meaning the orbital distance varies over the orbit. This diagram showcases the *pile-up* of circumbinary planets near the stability limit.

This pile up is a phenomenon that was noticed early on from the *Kepler* systems (Welsh et al., 2014). Of the 10 systems, 9 of them (excluding Kepler-1647b) have the innermost planet close to the stability limit. This has been claimed to be a real phenomenon and not due to the observing bias of the transit method towards shorter orbital periods (Martin and Triaud, 2014; Li et al., 2016). Other analyses find no strong evidence of a pile-up (Armstrong et al., 2014; Quarles et al., 2018). This is partly due to definition of pile-up: Quarles et al. (2018) conclude that there is no pile-up since many of the *Kepler* systems have space for a dynamically stable planet closer to the binary; whereas Martin and Triaud (2014) conclude that an injected population of circumbinary planets must be preferentially close to the stability limit to recover the detected rates.

The argument for the pile-up not being solely an observing bias is illustrated in the bottom right panel of Figure 1.17. The binary and planet orbital periods are shown, the orange shaded area is where $P_{pl} < 4 \times P_{bin}$ and therefore the orbit is likely unstable. As discussed above, the circumbinary planets are preferentially found near the stability limit, clustered around $6 \times P_{bin}$. The argument against it being a transit detection bias is that there are no detections in the region highlighted in blue. A strict transit detection bias should actually slightly favour the blue area over the regions above the blue area, i.e. planets at the same orbital period should be preferentially found orbiting shorter period binaries since these are more common in the *Kepler* sample (Martin, 2018).

There is a natural (and predicted) explanation for such a pile-up. Circumbinary protoplanetary discs are truncated near where the stability limit is, and planets migrating inwards can

park near this inner edge (Pierens and Nelson, 2008; Penzlin et al., 2021). Saturn-mass planets are expected to park in this way, more massive (Jovian) planets are more likely to migrate too far inwards and a close encounter with the binary would then lead to ejection or scattering to large orbital distances (Pierens and Nelson, 2008). Jovian circumbinary planets can exist but would either not have migrated so close to the binary or would have been scattered, and therefore should not preferentially exist near the stability limit. This is in accordance with the results from *Kepler* (see the middle row of Figure 1.17). Only one potentially Jovian planet (Kepler-1647b) is found and it is at the largest orbital distance.

Two final results from the *Kepler* circumbinary planets are the lack of detections transiting very short period binaries < 7 days, and the lack of very small planets $< 3\,R_\oplus$. Shorter period binaries are more common in the *Kepler* eclipsing binary sample (Martin, 2018) and yet no planets were found there. This is thought to be linked to the formation mechanisms of very tight binaries likely requiring a third star (Martin et al., 2015). The presence of a third star would mean that a planet is simultaneously S-type and P-type. Planet formation in such a circumbinary disc with a nearby tertiary would likely be difficult, or might manifest differently, and subsequent orbital evolution could perturb the planet's orbit, giving rise to longer periods and misalignments with the inner binary (Martin et al., 2015; Alaguero et al., 2024).

The circumbinary planets from *Kepler* all have radii $> 3R_\oplus$. While initially thought to likely be an observational bias, it may in fact be a real effect[13]. One potential cause of this is interactions between multiple circumbinary planets destabilising the smaller less massive planets (Fitzmaurice et al., 2022). Another possible explanation is that close-in low-mass circumbinary planets have inflated radii. TOI-1338b is potentially a very low-mass circumbinary planet that happens to have a large radius[14] this may mean that there are no small-radius circumbinary planets due to an unknown mechanism that inflates their radii (for more discussion of this based on the radial velocity surveys see Chapter 4).

[13]Results presented at a conference claimed a real dearth of circumbinary planets with $R < 3R_\oplus$ https://indico.ict.inaf.it/event/3003/overview

[14]Based on results presented at https://indico.ict.inaf.it/event/3003/overview, and on Standing et al. (2023).

Chapter 2

Methods

2.1 Bayesian Statistics and the use of `kima`

2.1.1 The Bayesian way

Statistics can, broadly speaking, be divided into two schools of thought: Frequentist and Bayesian. These have historically been at odds (no pun intended), the issue being a philosphical one of what is meant by a *probability*. Traditional or frequentist statistics expresses the probability of an event A as the fraction of times event A occurs out of a large sample of identical experiments (Gregory, 2005). Modern science (astronomy in particular) is not always suited to the practicality of repeating an experiment many times (Jefferys and Berger, 1992), nor is this always a good way of thinking about probability. Bayesian statistics frames a probability as the degree of confidence in a given statement or hypothesis. The Bayesian way also lends itself to updating the degree of confidence in a statement (the probability) as more data is acquired, this is formulated through Bayes' Theorem (Gregory, 2005):

$$P(M|D,I) = \frac{P(M|I)P(D|M,I)}{P(D|I)}, \tag{2.1}$$

where P refers to the *probability of some proposition*, $'|'$ represents a *conditional probability* and $','$ represents *and*. In this case, M is some model, D some data, and I is the prior information[1], so $P(M|D,I)$ is the *probability of the model given the data and the prior information*, this is called the *posterior probability*. $P(M|I)$ is the *prior probability*, i.e. with no knowledge of the data how does the prior information alone constrain the probability of M. $P(D|M,I)$ is called the *likelihood*. $P(D|I)$ is a normalising factor referred to as the *evidence*, note that the model in question does not figure in the evidence. $P(D|I)$ can be rewritten as the marginal sum over all possible models M_i

$$P(D|I) = \sum_i P(M_i|I)P(D|M_i,I). \tag{2.2}$$

2.1.2 Bayesian model comparison and Occam's razor

Model comparison refers to using data (and prior information) to attempt to distinguish between two competing hypotheses or models. Bayesian statistical analysis lends itself well to this through the use of Bayes' Theorem, and the fact that it has an in-built *Occam's razor*.

Occam's Razor is a well known philosophical principle that has been stated in various ways over the centuries (sometimes in Latin) (Jefferys and Berger, 1992). My interpretation of it is: *A simple explanation is more likely than a complex one*. In general a model with more free parameters is more complex and a model with fewer parameters or which makes precise predictions is simpler. The way Occam's razor occurs in Bayesian model comparison is not, as one might first think, through giving a prior bias towards a simpler model.

One can compare two models by taking the ratio of their posterior probabilities, this is called the *odds ratio* (Gregory, 2005).

$$O_{i,j} = \frac{P(M_i|D,I)}{P(M_j|D,I)} = \frac{P(M_i|I)}{P(M_j|I)}\frac{P(D|M_i,I)}{P(D|M_j,I)} = \frac{P(M_i|I)}{P(M_j|I)}B_{i,j}. \tag{2.3}$$

The odds ratio is the ratio of the chosen prior probabilities for each model multiplied by the *Bayes Factor* $B_{i,j}$. Notice that the normalisation constant from equation Equation 2.1 is not present in

[1]This could be constraints from previous experiments, or the general prior expectation for the results of an experiment.

this expression. In practical uses of Bayes Factors, the models being compared will have free parameters. In these cases the Bayes Factor is the ratio of the likelihoods, each marginalised over their parameters. This can be thought of as being marginalised of all the possible sub-models within the model. Therefore the Bayes Factor $B_{i,j}$ is the ratio of the fraction of the evidence that is in model i compared to model j. This makes nested sampling a useful tool for calculating Bayes Factors (see Section 2.1.4).

In many cases scientists choose not to a priori prefer one model over another, and allow the priors equal weight. With equally weighted priors, the Bayes Factor is the metric that matters, and it is in the Bayes Factor that Occam's razor appears.

The likelihood can be expressed as the maximum value of the likelihood of a model with a parameter θ, multiplied by some term that is dubbed the *Occam factor* (Ω_θ) (Gregory, 2005)

$$P(D|M_i, I) = \mathcal{L}_{\max,i}\Omega_\theta. \tag{2.4}$$

Now for the parameter θ, under the simplifications of a uniform prior of width $\Delta\theta$ and a Gaussian likelihood of width $\delta\theta$, then (Gregory, 2005)

$$\Omega_\theta \approx \frac{\delta\theta}{\Delta\theta}. \tag{2.5}$$

The Occam factor thus penalises a very large prior volume relative to the posterior volume, this means a *simpler* model is one that has a smaller prior volume. This can be the case if it has fewer free parameters, or if the prior ranges are smaller. Consider an example of this using the circumbinary planet Kepler-16b.

Kepler-16 is an eclipsing binary, with a circumbinary planet detected in transit (Doyle et al., 2011), which is detectable in radial velocities (Triaud et al., 2022), the planet has an orbital period of 228 days. I perform radial velocity analysis on the first 60 datapoints using the BINARIESmodel of `kima` (see Section 2.2). All the input parameters and prior distributions are kept the same across 8 distinct analyses, except that the prior on the orbital period of the planet is varied. The priors for the orbital period take a `Uniform` distribution bounded between: (200,

Table 2.1: Bayes Factor confidence thresholds as interpreted by previous publications, effectievely various versions of the Jeffreys' scale.

Jeffreys (1961)	Kass and Raftery (1995)	Trotta (2008)
$BF \leq 3.2$ -Not worth more than a bare mention	$BF \leq 3$ -Not worth more than a bare mention	$BF \lesssim 3$ -Inconclusive
$3.2 \leq BF \leq 10$ -Substantial	$3 \leq BF \leq 20$ -Positive	$BF \sim 3$ -Weak evidence
$10 \leq BF \leq 100$ -Strong	$20 \leq BF \leq 150$ -Strong	$BF \sim 12$ -Moderate evidence
$100 \leq BF$ -Decisive	$150 \leq BF$ -Very strong	$BF \sim 150$ -Strong evidence

300), (100, 300), (100, 400), (100, 500), (100, 600), (100, 700), (100, 800), and (100, 900). These lead to Bayes Factors of approximately: 22000, 12000, 7900, 6100, 4800, 4100, 3400, 3100 in favour of the 1-planet model relative to the 0-planet model. The prior and posterior distributions are shown in Figure 2.1 along with the respective Bayes Factors for the planet for each analysis. As expected the Bayes Factors are more heavily penalising the more complex models. i.e. the models with more flexibility in the parameter space. The results can be tested to confirm that the approximation of Equation 2.5 holds. Figure 2.2 shows the Bayes Factors and the prior widths as points, the line of $1/\Delta\theta$ is also shown scaled vertically such that at $\Delta\theta = 100$ the Bayes Factor is the mean value of $BF \times \Delta\theta/100$ (*note that this is not a fit*). The Bayes Factors follow the expected relation, albeit the point at $\Delta\theta = 100$ is a tad too low.

Bayesian model comparison with no a priori preference, other than Occam's razor favouring simpler models, between two competing models can thus be performed by calculating the Bayes Factor. If the Bayes Factor overwhelms Occam's razor and still favours the more complex model, then we can accept that model with a certain degree of confidence. The usual metric for favouring a model over another based on a Bayes Factor uses the Jeffreys' scale, versions of which are shown in Table 2.1 (Jeffreys, 1961; Kass and Raftery, 1995; Trotta, 2008). In this thesis, Bayesian model comparison is used to compare models with n planets to models with n-1 planets. I take a Bayes Factor of 150 as the threshold for a confident detection.

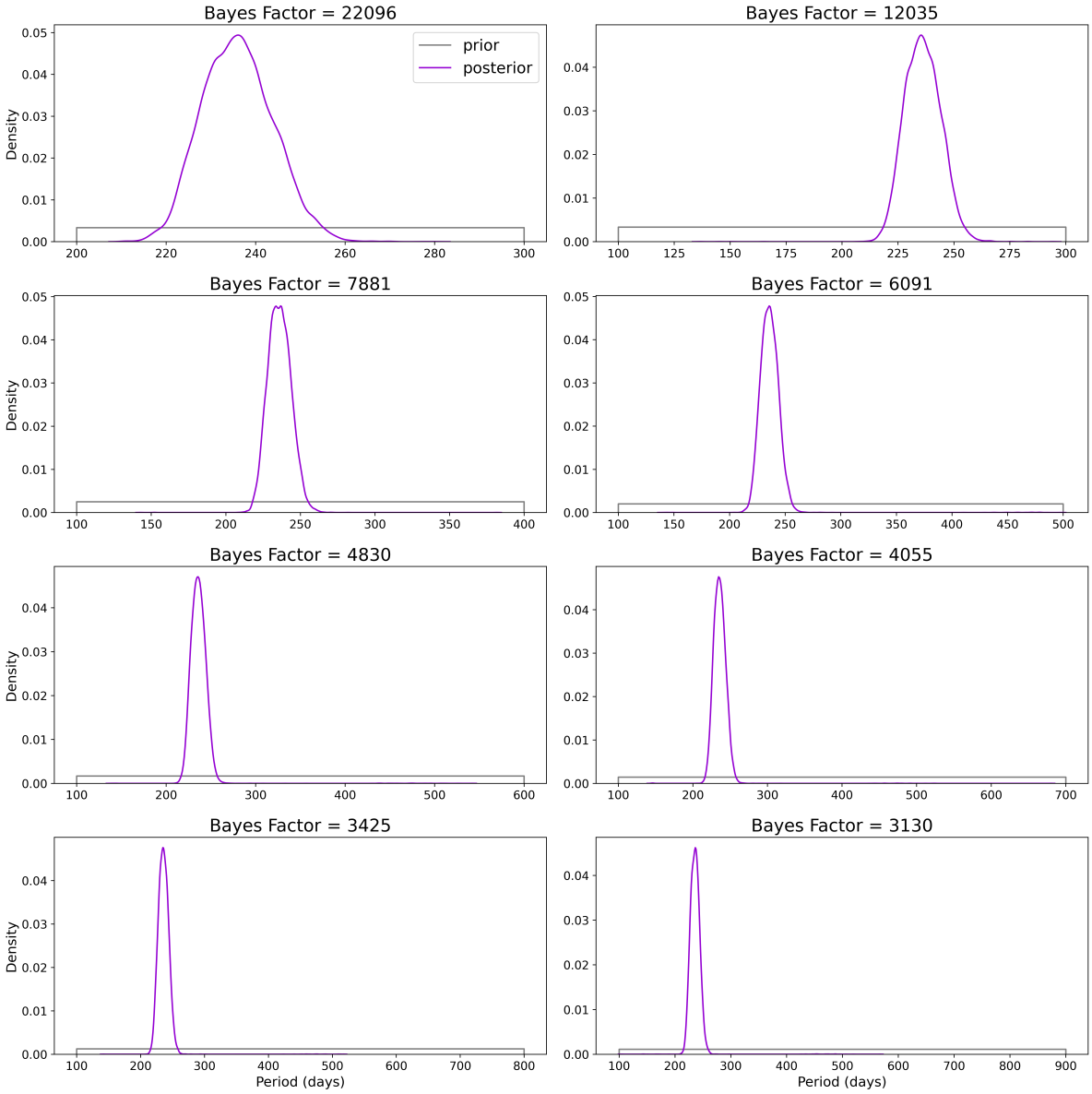


Figure 2.1: Prior and posterior distributions for 8 analyses of Kepler-16 radial velocity data, showing the dependency of the Bayes Factor on prior width.

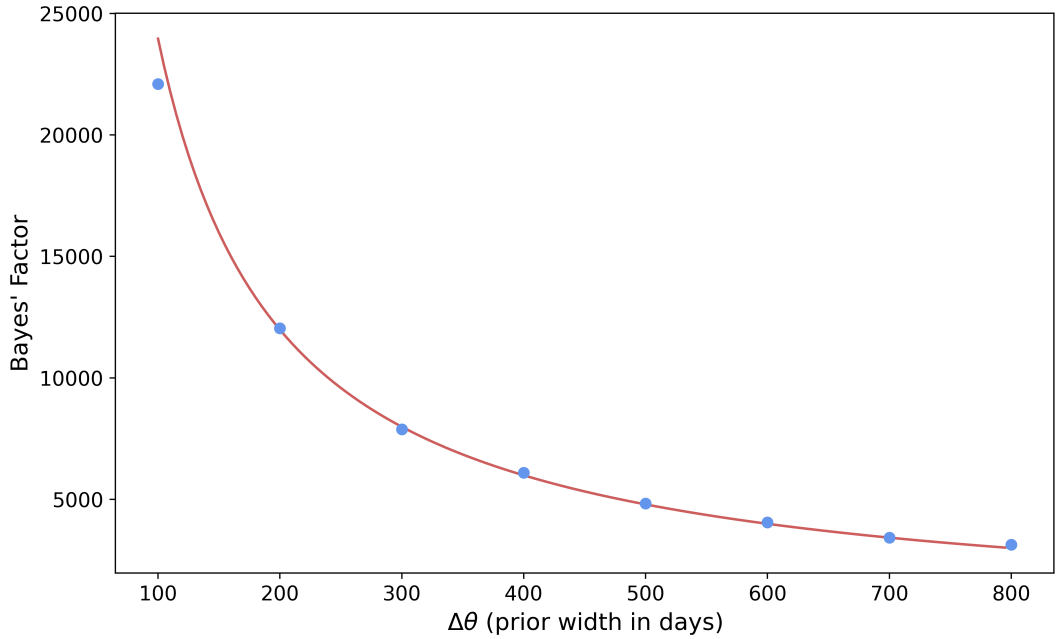


Figure 2.2: Relationship between prior width and Bayes Factor showing the predicted reciprocal dependency.

2.1.3 Choice of priors

Having seen that prior choice impacts the Occam's razor inbuilt into Bayesian model comparison, if one chooses priors that are too wide, it will artificially inflate the Occam penalty, but too restrictive and the results may be biased towards a more complex model.

The fact that a choice of prior must be made, and that this can be subjective has been an argument against Bayesian statistics (Jefferys and Berger, 1992). The Bayesian reply to this criticism is that subjectivity is not inherently a problem and is always the case even in frequentist statistics (Berger and Berry, 1988). If a conclusion depends on the subjectivity of a particular scientist, it is perhaps simply not a strong conclusion. This can be reframed as: *if the posterior is strongly dependent on the chosen prior, then better data is required, and if better data is not possible, one should be extremely judicious in the choice of prior used.*

The choice of a prior can in some sense be about belief. Strictly speaking it should mathematically represent what all of the prior data and information has revealed, for example the prior distribution I use for eccentricity of a planetary orbit is $e \sim \beta(0.867, 3.03)$, which

was the distribution of eccentricities in the planet population found by Kipping (2013). It is not always so simple to incorporate prior information into a simple prior distribution. The next best thing is to choose a prior which represents one's belief or expectation of what distribution is reasonable, this effectively incorporates all of the prior data and information through the nebulous entity which is *scientific intuition*. One example is the distribution of orbital periods in radial velocity planet search pipelines. The distribution of orbital periods of planets is known to some extent, but it varies for different masses and our understanding is not complete (especially with observational biases in play). Instead, a simple choice of prior is to consider the range of periods to which the data is sensitive (i.e. not exceeding the span of the data by too much) and use a `LogUniform` distribution for the prior. This distribution allows the prior to span multiple orders of magnitude in orbital period, that are all as plausible as each other to contain a planet, without biasing towards long periods as a `Uniform` prior would. Table 2.2 shows the standard priors that I use for various types of parameters when using `kima` to search for an unknown planet.

2.1.4 Nested sampling

Nested sampling is a relatively new ($\lesssim$ 20 years) technique for Bayesian computation, compared to Markov Chain Monte Carlo (MCMC) methods. The nested sampling method is described in detail in Skilling (2006). It works by constraining the prior mass, systematically creating level contours in likelihood as it hones in on the high-likelihood areas of parameter space (see the top of Figure 2.3). The main output of nested sampling is the calculation of the evidence (denominator of equation Equation 2.1). Nested sampling effectively performs an integral/sum to calculate this. Posterior samples can also be obtained as a by-product of the computation. That it naturally calculates the evidence makes it particularly useful for Bayesian model comparison, where the Bayes Factor comparing two models is the ratio of the marginal likelihoods for each of those models, i.e. the ratio of the total evidence for each model.

Various different nested sampling algorithms exist which perform the evidence integral slightly differently. These algorithms can be optimised for computation speed, thoroughness, or

Table 2.2: Standard priors I use in `kima` analysis for exoplanet detection. $\mathcal{U}$ is a Uniform distribution, $\mathcal{LU}$ a LogUniform distribution (Uniform in $\log_{10}$ of the parameter), $\mathcal{MLU}(A, B)$ a ModifiedLogUniform distribution which is Uniform between 0 and A and the LogUniform between A and B each half with equal weight.

Parameter	Prior	Reasoning
Orbital period	$\mathcal{LU}$(P0,2.5×T)	A LogUniform distribution allows all orders of magnitude to be sampled equally without biasing towards high values as a Uniform distribution would. The inner period bound can be related to the shortest expected signal, e.g. for a binary system there is a stability limit. Above 2.5× the dataspan the sensitivity to a planet decreases with most methods that I use.
Eccentricity	$\beta(3.03, 0.687)$	A Beta distribution favouring eccentricities close to 0 but allowing for larger ones. Parameters based on an emirical fit to eccentricity distributions by Kipping (2013).
Angles	$\mathcal{U}(0, 2\pi)$	Uniform distributions are typically used for unknown angles (except inclination).
Inclination	$\cos i \sim \mathcal{U}(0, \pi/2)$	Cosine of the inclination is Uniformly distributed, this is the result of assuming an isotropic distribution of inclinations.
Mass-related	$\mathcal{MLU}(K_0, K_{\max})$	The ModifiedLogUniform prior gives equal weight to different orders of magnitude while also allowing for arbitrarily small numbers, this is suited to mass-related parameters where an extremely low-mass planet can exist.
Extra jitters	$\mathcal{MLU}(\sigma_0, \sigma_{\max})$	Similarly to above this allows the extra uncertainty added to be arbitrarily small but also to reach significant values without biasing towards high values.

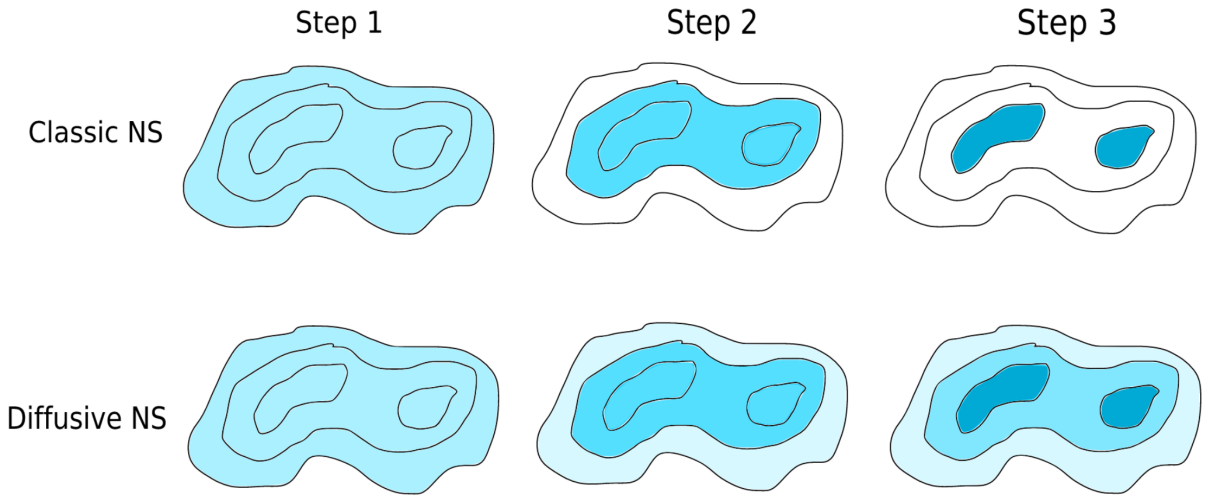


Figure 2.3: Difference in likelihood-level exploration between classic nested sampling and diffusive nested sampling. Figure from Brewer et al. (2011).

parallelisation, among other factors.

Diffusive nested sampling (Brewer et al., 2011) is one such algorithm, the basic way in which it differs from classic nested sampling is illustrated in Figure 2.3. Once a certain amount of exploration has happened and a new likelihood level has been defined, where classic nested sampling would explore only inside the new level, diffusive nested sampling instead explores a mixture (weighted sum) of the previous levels. In other words, during the building of levels, particles can go back and explore lower levels. The target distribution is no longer the posterior but a weighted mixture of the prior and the constrained prior distributions (Brewer, 2015). This setup deals well with multimodality, parameter degeneracies, and phase transitions[2] (Skilling, 2006). Additionally, once the levels are created, there is a period of sampling uniformly across all levels which runs as long as specified (similar to classic MCMC methods; Gamerman and Lopes, 2006), this allows more posterior samples to be obtained and to refine the estimate of the evidence (Brewer et al., 2011).

The diffusive nested sampling implementations allow for trans-dimensional sampling through the reversible jump object `RJObject` class (based on Green, 1995). This allows a parameter space with multiple optional subspaces of different dimensionalities. A typical version of this

[2]Named after a thermodynamic concept, these occur when part of the log-likelihood function is a convex function of the prior volume.

is a parameter space where you can have any number of a certain component included in the model (e.g. the number of planets in your model). In this case, the free parameters include the number of components included and the set of parameters within each component. The different components are independent and share the same priors/hyperpriors. This allows for Metropolis-Hastings proposals that change the number of components using what are often called *birth and death* proposals which add or remove components (Brewer, 2015). The trans-dimensional MCMC is then used inside the diffusive nested sampling process to generate new proposals, the MCMC allowing for easy moves through multiple dimensions and the nested sampling the thorough exploration of the parameter space, dealing with multimodalities and phase transitions. This multidimensionality has been used for applications in astrophysics such as the number of galaxies detected in an image (Brewer, 2015) or the number of exoplanets detected in a set of radial velocity measurements (Brewer and Donovan, 2015).

2.1.5 `kima`

`kima` is a package which, while intially conceived for radial velocity analysis (Faria et al., 2018), is now being extended to the analysis of a variety of time-domain datasets. `kima` uses an implementation (`DNest4`; Brewer and Foreman-Mackey, 2018) of diffusive nested sampling which is described above. `kima` fits *Keplerians* to the radial velocity data, these are manifestations of a closed elliptical orbit, that follow the functional form of Equation 1.16 in the case of a radial velocity timeseries.

Within `kima`, using the trans-dimensionality of `DNest4`, the number of Keplerian orbits included in the fit is a free parameter with a `Uniform` prior between the different numbers of planets up to the maximum number $N_{p,\max}$ specified. Very few other similar codes have trans-dimensionalty built-in and require the number of Keplerians to be fixed.

Up to $N_{p,\max}$ Keplerians are fit simultaneously, sharing the same prior distributions. Additionally, Keplerians can be added on top of this (with different priors) that are not included in the number of planets freely searched for, this is called the *known object* mode and is particularly useful if there are any planets/Keplerians with well constrained parameters based on a different

dataset (e.g. an eclipsing binary).

The number of Keplerians being a free parameter means that Bayesian model comparison can be used as a detection metric. The procedure involves calculating a Bayes Factor for the 1-Keplerian model vs 0-Keplerian model and if this exceeds the detection threshold, it can be claimed that there is a Keplerian present within the data. In a similar way, Bayes Factors for 2-Keplerians vs 1-Keplerian, 3-Keplerians vs 2-Keplerians and so on can be used to test whether more signals are present.

A few caveats should be noted. A Keplerian does not necesarily mean a planet, other effects such as stellar activity/stellar rotation could induce a sufficiently Keplerian signal to be detected in this way. The Bayes Factor is purely comparing all models with n signals to all models with $n-1$ signals, with no knowledge of what the signals are. The Bayes Factor can therefore also favour a 1-planet model without it being clear what that planet's parameters, such as orbital period, are. An example of this is shown by simulating radial velocity data with clear aliases.

A Keplerian radial velocity signal is generated with amplitude $K = 24$ m/s, period $P = 50$ days, $e = 0.3$, and $\omega = 1.26$. It is then sampled on three upwards slopes every three orbits as shown on the top right-hand panel of Figure 2.4. The top left-hand panel shows the Lomb-Scargle periodogram (Lomb, 1976; Scargle, 1982), and two panels in the second row show a posterior histogram of the orbital periods (for posteriors with $N_p = 1$) and the False Inclusion Probability periodogram (FIP; Hara et al., 2022). These three periodograms display the various aliases that are present. `kima` doesn't care about the aliases and tries to fit them all, giving a Bayes Factor for 1 Keplerian vs 0 Keplerians of 365 (clear detection) but this in itself does not tell us which of the possible solutions is the real one. The second row of Figure 2.4, showing the periodograms from the `kima` analysis, would be difficult to interpret and identify which solution is correct. The bottom 6 panels of Figure 2.4 show the data phase-folded on the 6 solutions corresponding to the truth and 5 aliases. Finding the true solution would require more data to be obtained to rule out the various aliases. Aliases are often imprinted into radial velocity data due to earthly constraints (Dawson and Fabrycky, 2010) for example: Earth's rotation and observing being performed at night; the orbit of Earth around the sun meaning that stars are not observable

for the whole year; the lunar cycle meaning that some observations may have gaps when the moon is near full; or telescope time being awarded in uneven groupings with large gaps.

A `kima` run simultaneously performs a signal search and parameter estimation. The detection of signals is different to standard periodogram methods, a main advantage being that `kima` uses Keplerians, so eccentricity and phase information is included. This is exemplified in Section 2.1.6 where using `kima`, a previously overlooked eccentric signal is detected around the M-dwarf star GJ 9404. The main disadvantage compared to a periodogram search is that `kima` is much more computationally intensive taking on the order of hours-days rather than on the order of seconds.

`kima` has many different model classes with the ethos that each can be a bespoke model aiming to deal with a specific kind of problem. These can be different types of data, dealing with stellar activity in different ways, etc. I am an active devloper of `kima` and am responsible for the models which will be described in later sections: BINARIESmodel Section 2.2, ETVmodel Section 2.3, GAIAmodel Section 2.4, and RVGAIAmodel Section 2.4.

2.1.6 GJ 9404 b: a confirmed eccentric planet, and not a candidate

This section is a short research note which I first-authored (Baycroft et al., 2023b). The other authors are Amaury Triaud, and two master's students Harry Badnell and Samuel Blacker. In their project which I co-supervised HB and SB analysed radial velocities from a sample of M-dwarfs observed with HARPS-N (Pinamonti et al., 2022), they detected the planetary signal published here, which I confirmed with an independent analysis and on which I ran a FIP analysis (Hara et al., 2022). HB and SB wrote the introduction, I wrote the analysis & results section, and AT wrote the conclusion.

Draft version April 14, 2025
Typeset using LaTeX default style in AASTeX631

GJ 9404 b: a confirmed eccentric planet, and not a candidate

Thomas A. Baycroft [1], Harry Badnell,[1] Samuel Blacker,[1] and Amaury H.M.J. Triaud [1]

[1] School of Physics & Astronomy, University of Birmingham, Edgbaston, Birmingham B15 2TT, United Kingdom

ABSTRACT

Eccentric orbits can be decomposed into a series of sine curves which affects how the false alarm probability is computed when using traditional periodograms on radial-velocity data. Here we show that a candidate exoplanet orbiting the M dwarf GJ 9404, identified by the HADES survey using data from the HARPS-N spectrograph, is in fact a bona-fide planet on a highly eccentric orbit. Far from a candidate, GJ 9404 b is detected with a high confidence. We reach our conclusion using two methods that assume Keplerian functions rather than sines to compute a detection probability, a Bayes Factor, and the FIP periodogram. We compute these using nested sampling with `kima`.

Keywords: Exoplanets — Radial velocity method — Nested sampling — Keplerian orbit

1. INTRODUCTION

Recently, Pinamonti et al. (2022) reported partial results of the HADES survey, where they analyse the radial-velocity monitoring of 56 nearby M dwarfs stars obtained using the HARPS-N spectrograph at TNG (La Palma). The stars range from spectral types M0 to M3, and mass 0.3 $M_\odot < M_\star < 0.71$ $M_\odot$. Radial-velocities were extracted using the `TERRA` template matching algorithm (Anglada-Escudé & Butler 2012). Planets are identified if they exceed a standard False Alarm Probability (FAP) of 0.1%, calculated from a generalized Lomb-Scargle periodogram. Pinamonti et al. (2022) list 11 planets detected by the HADES survey in several publications.

In order to compute occurrence rates, Pinamonti et al. (2022) additionally identify five more systems which they call 'candidates' mentioning they need additional, more in-depth analysis. To find these, they perform a periodogram analysis along with, in some cases, a Gaussian process (GP) regression in order to model the effects of stellar rotational periods, which are prominent in M dwarfs. Stellar noise correction from activity indexes (as in Gomes da Silva et al. 2011) are also used to remove observations affected by flares, and to detrend radial-velocity time series from magnetic cycles. One of these candidates is GJ 9404 b, with an orbital period $P = 13.46^{+0.01}_{-0.51}$ day and mass of $m_p sin(i) = 10.3^{+1.8}_{-1.8}$ $M_\oplus$. The star has a mass of $M_\star = 0.62 \pm 0.07\,M_\odot$. Calculating a FAP requires a periodogram, which is a Fourier decomposition. As such Pinamonti et al. (2022) assume sinusoidal (circular) radial-velocity modulations to assess a planet's detection, however GJ 9404 b is eccentric.

In order to test a new method to compute detection limits (as in Standing et al. 2022) to be used to estimate occurrence rates, we reanalysed the entire HADES sample with the `kima` nested sampling algorithm (Faria et al. 2018). As part of that re-analysis we find that GJ 9404 b is not just a candidate, but can be confirmed as a planet.

2. KIMA ANALYSIS & RESULTS

For the radial velocity analysis we use the package `kima` (Faria et al. 2018). The model includes Keplerian orbits for planets, a systemic velocity, and a jitter added in quadrature to account for any unmodelled variability. A Student's t-distribution is used for the likelihood evaluations. Compared to a Gaussian distribution, this naturally accounts for any outliers present in the data. The `kima` package uses diffusive nested sampling (Brewer & Foreman-Mackey 2018) to explore parameter space and the number of Keplerian orbits is a free parameter. This allows for a Bayesian model comparison between models with different numbers of planets using a Bayes Factor. We take a Bayes Factor, BF > 150 as very strong evidence in favour of the more complex model (as in Kass & Raftery 1995). We also use the samples obtained by the nested sampling to compute a False-Inclusion Probability (FIP) periodogram (as described in Hara et al. 2022). We take a FIP < 0.01 as a detection threshold. Given a series of detections with FIP < 0.01 we would expect $< 1\%$ of them to be false detections (Hara et al. 2022). At first sight this threshold might appear more

Parameters	Units	Values
$M_\star$	$M_\odot$	0.62 ± 0.07
P	days	$13.4586^{+0.0044}_{-0.0067}$
$K_\star$	$m\,s^{-1}$	$5.13^{+1.04}_{-0.85}$
e		$0.49^{+0.11}_{-0.13}$
T_{per}	BJD	$2\,457\,095.30^{+0.59}_{-0.38}$
ω	rad	1.90 ± 0.33
$m_p \sin i_p$	$M_\oplus$	11.9 ± 1.9
a_p	AU	0.0943 ± 0.0036
σ_{jit}	$m\,s^{-1}$	$2.27^{+0.40}_{-0.42}$

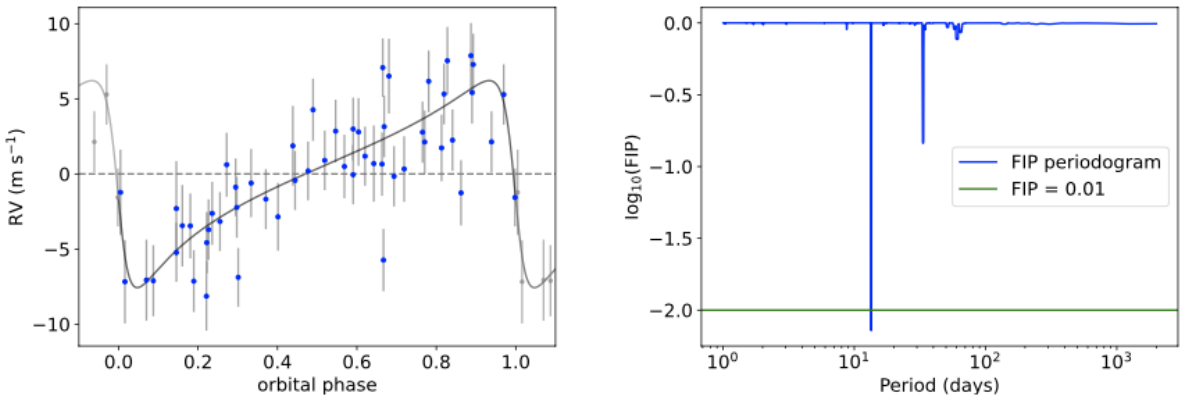


Figure 1. Top: Median values and 1σ uncertainties for the parameters of GJ9404b from `kima`. Bottom left: phase plot of best-fitting planetary solution. Bottom right: in blue the false-inclusion probability (FIP) periodogram, in green the threshold at which the false-incusion probability is 0.01.

permitting than the FAP, but FAPs are sensitive to false positives, whereas the FIP is a more reliable metric (Hara et al. 2022).

We reanalyse with `kima` the radial velocity data for GJ 9404 which we obtained from Pinamonti et al. (2022). This analysis results in BF = 782 for a 1-planet model vs a 0-planet model, and BF = 7 in favour of a 2-planet model vs a 1-planet model. This means that there is conclusive evidence for one Keplerian signal and moderate evidence for a second. The best-fitting solution is shown on the bottom left of Figure 1. In contrast to the analysis used in the Pinamonti et al. (2022), the use of Keplerian orbits within `kima` allows for eccentric orbits.

The false-inclusion probability periodogram is shown on the bottom right of Figure 1. This shows two periodicities, one of which passes the detection threshold. The more prominent signal in the FIP periodogram corresponds to the best-fitting solution and the posterior distributions for the parameters are shown in the table in Figure 1. We note that this planet was claimed as a candidate in Pinamonti et al. (2022) and that our period and mass values are compatible to the parameters presented in that publication. The rotation period of the star is 23.2 ± 0.1 days (Pinamonti et al. 2022), so the signal we confirm is likely not stellar activity, and thus of planetary origin.

3. CONCLUSION

The example of GJ 9404 highlights the limitations of traditional periodograms to identify exoplanetary signals in radial-velocity data and measure the robustness of their detections. Our re-analysis of the HADES data (Pinamonti et al. 2022) using `kima` (Faria et al. 2018; Baycroft et al. 2023) reveals that GJ 9404 hosts at least one exoplanet with a very high degree of confidence from the Bayes Factor. We confirm this by performing a FIP periodogram (Hara et al. 2022), which assume Keplerian functions rather than sines. Fig. 1 shows the FIP periodogram confirming the Bayes

Factor estimated by `kima`. This research note should be seen a reminder of the limitation of traditional periodograms to assess detection confidence, and a reminder that more powerful and accurate statistical tools now exist.

This research received funding from the European Research Council (ERC) under the European Union's Horizon 2020 research and innovation programme (grant agreement n° 803193/BEBOP).

Facilities: TNG(HARPS-N)

Software: kima (Faria et al. 2018), DNEST4 (Brewer & Foreman-Mackey 2018)

REFERENCES

Anglada-Escudé, G., & Butler, R. P. 2012, The Astrophysical Journal Supplement Series, 200, 15, doi: 10.1088/0067-0049/200/2/15

Baycroft, T. A., Triaud, A. H. M. J., Faria, J., Correia, A. C. M., & Standing, M. R. 2023, MNRAS, 521, 1871, doi: 10.1093/mnras/stad607

Brewer, B. J., & Foreman-Mackey, D. 2018, Journal of Statistical Software, 86, 1, doi: 10.18637/jss.v086.i07

Faria, J. P., Santos, N. C., Figueira, P., & Brewer, B. J. 2018, The Journal of Open Source Software, 3, 487, doi: 10.21105/joss.00487

Gomes da Silva, J., Santos, N. C., Bonfils, X., et al. 2011, A&A, 534, A30, doi: 10.1051/0004-6361/201116971

Hara, N. C., Unger, N., Delisle, J.-B., Díaz, R. F., & Ségransan, D. 2022, A&A, 663, A14, doi: 10.1051/0004-6361/202140543

Kass, R. E., & Raftery, A. E. 1995, Journal of the American Statistical Association, 90, 773, doi: 10.1080/01621459.1995.10476572

Pinamonti, M., Sozzetti, A., Maldonado, J., et al. 2022, A&A, 664, A65, doi: 10.1051/0004-6361/202142828

Standing, M. R., Triaud, A. H. M. J., Faria, J. P., et al. 2022, MNRAS, 511, 3571, doi: 10.1093/mnras/stac113

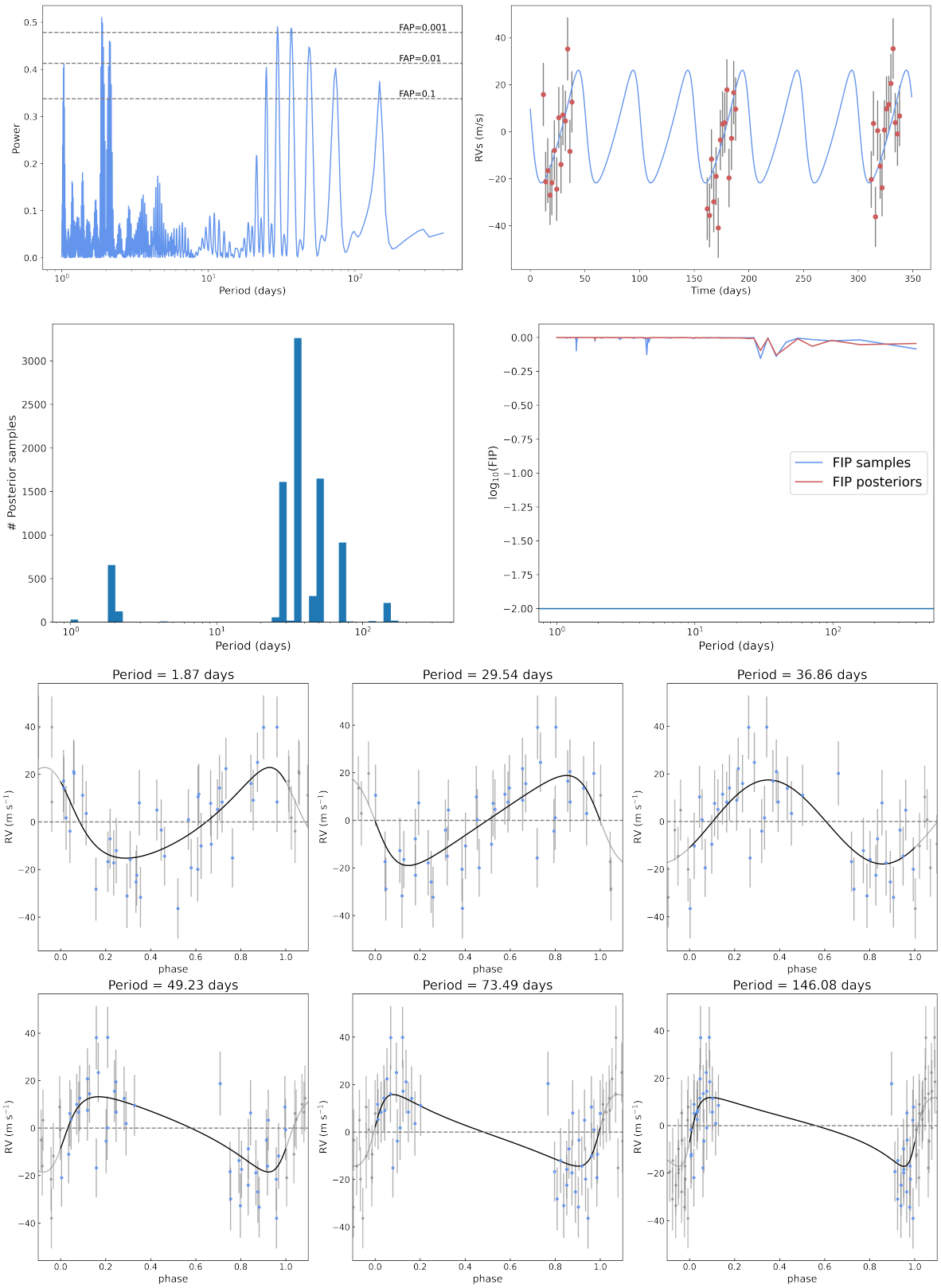


Figure 2.4: Top row: left, a Lombe-Scargle periodogram of the simulated radial velocity data of a 50-day period signal shown on right, the true model is shown as well. Second row: left, histogram of periods with from `kima`; right, FIP periodogram from the same `kima` run. Bottom: phase-folded radial velocity data on six different periods (specified above each panel).

2.1.7 Bayesian detection limits with kima

Understanding the populations and demographics of exoplanets is an important goal of the field (see Section 1.4), this includes understanding the occurrence rate of all kinds of planets across different stellar types and configurations. Obtaining occurrence rates from a radial velocity campaign requires a thorough understanding of each system, what planetary signals can be ruled out so that the completeness of the survey can be understood. This typically requires the use of detection/sensitivity limits on each system such that, given a certain number/distribution of detections, the underlying population of planets can be estimated.

Traditionally, detection limits are calculated with a suite of injection-recovery tests (e.g. Cumming et al., 2008; Bonfils et al., 2013; Rosenthal et al., 2021; Sabotta et al., 2021). In these tests, a grid of planet parameters is injected into the data and each element is put through the detection pipeline to see if that planet is detected. A detection limit can be calculated as the threshold where 90% (or whatever confidence is chosen) of the planets are recovered (e.g. Rosenthal et al., 2021). Since the use of kima as a detection metric is computationally intensive we cannot perform an injection-recovery test in the same way, however another avenue is available to perform a different kind of detection limit.

Consider a system with no detected planets. If kima is forced to fit a planet (which is an option, since the number of Keplerians can be fixed to 1 or any other value) this will result in all of the posterior samples corresponding to Keplerians that are consistent with the data. These naturally lead to a threshold above which signals are incompatible with, and below which signals are compatible with the data. This is the kind of detection limit that I use in this thesis.

This kind of detection limit is asking a different question than the traditional kind. A subtle but important distinction, we ask *what signals are compatible with the data?* rather than *what signals are recoverable when injected in the data?* These are both reasonable questions to ask, however the method I use has the same advantage that kima has as a detection metric. kima fits freely for Keplerians and all eccentricities and phases are considered, whereas injection recovery tests usually only inject sinusoids varying the period and amplitude only. Some also use a small

discrete set of orbital phases (e.g. Mignon et al., 2025, use 12), but much more than this and the grid of injections becomes too large. A lengthier discussion of this kind of detection limit and the relative merits can be found in Standing et al. (2022).

The procedure for this type of detection limit when there is a detected Keplerian is more complicated. A few options exist: 1) Remove the best-fitting signal and run the detection limit as above. 2) Force `kima` to fit 2 (or n+1) Keplerians meaning the 1 (or n) known signal(s) will be fit and the additional free Keplerian will create the detection limit. 3) Use the known object mode to fit known signals separately.

The different options were investigated and issues were found with 2) and 3) (Standing et al., 2023). In these cases, aliases of the known signal would appear in the detection limits. This included the 1× alias, where the algorithm would return the known planet with a slightly smaller amplitude plus an additional signal at the same period such that the signals would constructively interfere. Method 1) gets around these and is more similar to what is done traditionally, this is the method I have used in this thesis, however it still has the issue that only a single realisation of the planet parameters is used which may bias the results.

Removing the signal becomes even less reliable when the signal is a candidate, in which case I have generally opted for method 2) (e.g. in some of the systems in Section 3.3).

2.2 `kima` BINARIESmodel

2.2.1 Contributions to the paper.

The following is a published paper (Baycroft et al., 2023c) that I first-authored describing the BINARIESmodel (as it is now called) of `kima` that is tailored to the analysis of binary stars and to detecting circumbinary planets.

The impetus for this paper was based on Standing et al. (2022) where the binary apsidal precession was identified as a potential source of extra noise in BEBOP radial velocity timeseries. That, along with referee reports on BEBOP papers recommending that relativistic and tidal effects should be included in our analysis prompted the writing of the BINARIESmodel tailored

to studying binary stars and circumbinary planets. I developed the model and performed tests which led to combining it all into this publication.

`kima` was initially developed by João Faria, he assisted in the implementation of the BINARIESmodel, Alexandre Correia assisted in the derivations of the equations in Appendix A. I wrote the model into `kima`, performed the analysis presented, and wrote the manuscript.

Monthly Notices of the ROYAL ASTRONOMICAL SOCIETY

MNRAS **521,** 1871–1879 (2023) https://doi.org/10.1093/mnras/stad607
Advance Access publication 2023 February 27

Improving circumbinary planet detections by fitting their binary's apsidal precession

Thomas A. Baycroft [1]★ Amaury H. M. J. Triaud [1] João Faria [2,3] Alexandre C. M. Correia [4,5] and Matthew R. Standing [6]

[1]*School of Physics and Astronomy, University of Birmingham, Edgbaston, Birmingham B15 2TT, UK*
[2]*Instituto de Astrofísica e Ciências do Espaço, Universidade do Porto, CAUP, Rua das Estrelas, 4150-762 Porto, Portugal*
[3]*Departamento de Física e Astronomia, Faculdade de Ciências, Universidade do Porto, Rua do Campo Alegre, 4169-007 Porto, Portugal*
[4]*CFisUC, Departamento de Física, Universidade de Coimbra, 3004-516 Coimbra, Portugal*
[5]*IMCCE, UMR8028 CNRS, Observatoire de Paris, PSL Université, 77 avenue Denfert-Rochereau, 75014 Paris, France*
[6]*School of Physical Sciences, The Open University, Milton Keynes, MK7 6AA, UK*

Accepted 2023 February 22. Received 2023 January 26; in original form 2022 November 21

ABSTRACT

Apsidal precession in stellar binaries is the main non-Keplerian dynamical effect impacting the radial-velocities of a binary star system. Its presence can notably hide the presence of orbiting circumbinary planets because many fitting algorithms assume perfectly Keplerian motion. To first order, apsidal precession ($\dot{\omega}$) can be accounted for by adding a linear term to the usual Keplerian model. We include apsidal precession in the `kima` package, an orbital fitter designed to detect and characterize planets from radial velocity data. In this paper, we detail this and other additions to `kima` that improve fitting for stellar binaries and circumbinary planets including corrections from general relativity. We then demonstrate that fitting for $\dot{\omega}$ can improve the detection sensitivity to circumbinary exoplanets by up to an order of magnitude in some circumstances, particularly in the case of multiplanetary systems. In addition, we apply the algorithm to several real systems, producing a new measurement of aspidal precession in KOI-126 (a tight triple system), and a detection of $\dot{\omega}$ in the Kepler-16 circumbinary system. Although apsidal precession is detected for Kepler-16, it does not have a large effect on the detection limit or the planetary parameters. We also derive an expression for the precession an outer planet would induce on the inner binary and compare the value this predicts with the one we detect.

Key words: binaries: general – planets and satellites: dynamical evolution and stability – techniques: radial velocities – methods: data analysis.

1 INTRODUCTION

Exoplanets exhibit a range of configurations much vaster than is present within the Solar system. Nearly three decades of discoveries have revealed that most known exoplanets are not analogous to any Solar system planets (e.g. Winn & Fabrycky 2015). This applies to individual planets being different such as hot Jupiters (e.g. Dawson & Johnson 2018) or planets with extreme eccentricities (e.g. Angelo et al. 2022), but this can also apply to entire planetary systems having more exotic configurations, such as TRAPPIST-1 a multiplanetary resonant chain orbiting a late M-dwarf (Gillon et al. 2016, 2017). One such type of exotic planetary systems are the circumbinary exoplanets that orbit about both stars of a tight stellar binary (Schneider 1994; Doyle et al. 2011).

To date there have been only 15 fully confirmed circumbinary planets.[1] All but one have transited at least one of the two stars, and were first detected from space with *Kepler* (e.g. Doyle et al. 2011; Orosz et al. 2012; Kostov et al. 2016) and with *TESS* (Kostov et al. 2020, 2021). The pace of detections is slow, since the two most common exoplanet detection techniques (transit and radial velocity) have so far both been hamstrung, each with their own issues. Circumbinary planets will generally have longer periods than planets around single stars because they need to orbit outside of an instability region produced by the binary stars' motion (Dvorak, Froeschle & Froeschle 1989; Holman & Wiegert 1999; Doolin & Blundell 2011). Because of this extra distance, circumbinary planets are geometrically less likely to produce transits than planets orbiting single stars. However, for similarly distant planets, nodal precession makes circumbinary planets more likely to create transits (Martin & Triaud 2015), even if transits do not happen at every planetary orbit (e.g. Schneider 1994; Martin & Triaud 2014).

For the radial velocity method, interference between the spectra of both components of the binary star makes it harder to obtain precise radial velocity measurements (e.g. Konacki et al. 2009). The latter issue can be circumvented by observing single-lined binaries (Konacki et al. 2010; Martin et al. 2019). This is the observing strategy employed by the Binaries Escorted By Orbiting Planets

★ E-mail: txb187@bham.ac.uk

[1]Circumbinary planets orbiting stellar remnants are claimed using eclipse timings, however, there are doubts about their existence and as such we do not consider them as fully confirmed.

© 2023 The Author(s).
Published by Oxford University Press on behalf of Royal Astronomical Society. This is an Open Access article distributed under the terms of the Creative Commons Attribution License (https://creativecommons.org/licenses/by/4.0/), which permits unrestricted reuse, distribution, and reproduction in any medium, provided the original work is properly cited.

Downloaded from https://academic.oup.com/mnras/article/521/2/1871/7059214 by University of Birmingham user on 08 October 2024

(BEBOP) survey. BEBOP has been collecting radial velocities on eclipsing single-lined binaries for over four years and has demonstrated that it can detect circumbinary planets, notably by having independently detected Kepler-16b (Triaud et al. 2022). There is also the first circumbinary planet discovered in radial velocities BEBOP-1c (Standing et al. submitted).

One significant advantage of the radial velocity method over the transit method is that radial velocities probe the full orbit, instead of just the inferior conjunction. This leads to good precision on the eccentricity e (sometimes down to 10^{-4}; Triaud et al. 2017) and the argument of periastron ω of the binary orbit. An issue this raises is that variation in e and ω will cause problems when fitting a static Keplerian orbit, a point raised in Konacki et al. (2010); Sybilski et al. (2013). One such variation is apsidal precession of the binary: an evolution of ω with time, denoted by $\dot{\omega}$. This can be caused by relativistic effects, tidal effects, or – most excitingly to exoplanet hunters – planetary perturbations (Correia et al. 2013). Because the BEBOP survey has collected data over several years, the scatter caused by this precession is slowly starting to exceed the rms scatter of the residuals on some systems (Standing et al. 2022). Accounting for this effect would improve the accuracy of the fits for the binary orbit, and in turn improve our ability to detect planets, and the precision on their physical and orbital parameters. As explored in Standing et al. (2022), in most cases the radial-velocity signal of a single planet would be detected well before a non-zero $\dot{\omega}$ is significantly detected. In this paper we show that, in some multiplanetary configurations, low-amplitude planetary signals can be hidden by the precession induced by another, heavier planet.

In addition, measuring the apsidal precession rate adds new information to our knowledge of the system. Usually, it is not possible to measure orbital inclinations from radial velocities alone. However, the binary's precession rate due to an external perturber is dependent on the mutual inclination between the binary's orbital plane and the perturber's (e.g. Correia et al. 2013; Correia, Boué & Laskar 2016). In this work, we derive an equation to calculate the apsidal precession that a third body induces on an inner binary pair which can be used to calculate the mutual inclination, this can be found in Appendix (A). In the case of BEBOP, where all binaries are known to eclipse, an upper bound on the mutual inclination directly translates into an upper bound on the orbital inclination of the planet, meaning those radial velocity data can be used to obtain not just a minimum mass $m_{\rm p}\sin i_{\rm p}$, but also a maximum mass. Finally, for close binaries, measuring the precession rate also provides information on the stars' internal structure (Claret & Giménez 2010).

In this paper, we first we describe a binaries-specific radial velocity model applied in the `kima` package in Section 2. This new model (which we will occasionally refer to as `kima-binaries` when comparing it with the old model) moves beyond fitting pure Keplerian orbits (as done in Faria et al. 2018), by including an apsidal precession parameter to the fitted model. The section details those changes and describes the inclusion of other tidal and relativistic effects that are known to affect orbital solutions. In Section 3, the new model is used on both simulated and observed data. The ability to accurately recover the apsidal precession rate is demonstrated, and we show how fitting for apsidal precession can improve a survey's sensitivity to circumbinary planets by producing Bayesian detection limits. Finally, in Section 4 we present a detection of the precession rate for Kepler-16, and conclude in Section 5.

2 A BINARY UPDATE TO KIMA

In this section we present an update to `kima`, developing a binary-specific radial velocity model. This model accounts for various factors that are generally ignored when looking at radial velocities for a single star, but recommended when seeking to detect circumbinary planet signals (Konacki et al. 2009; Sybilski et al. 2013). The new model includes tidal and relativistic effects as well as, most notably, apsidal precession of the binary's orbit. The new model is also given the capability to fit double-lined binary data.

`kima` is an orbital fitting algorithm which makes use of diffusive nested sampling (DNest; Brewer, Pártay & Csányi 2011) to sample the posterior distribution for the model parameters. It allows for the number of Keplerian signals being fit to vary freely which is advantageous for Bayesian model comparison. There is a so called 'known-object' mode where separate priors can be defined for certain already known signals while allowing to search for further signals freely; this model is ideal to apply to circumbinary systems. As will be discussed further, this method of sampling allows for an efficient method of calculating detection limits.

2.1 Adding precession to `kima`

2.1.1 A linear approximation

As a first order approximation, we add a linear precession parameter, $\dot{\omega}$ to `kima`. This parameter is free during a fit and its posterior is estimated. We take the usual equation for the radial velocity of a Keplerian orbit (e.g Murray & Correia 2010):

$$V = K(\cos(f+\omega) + e\cos(\omega)) + \gamma, \tag{1}$$

with ω now being time dependent:[2]

$$\omega(t) = \omega_0 + \dot{\omega}(t - t_0). \tag{2}$$

K is the semi-amplitude of the radial velocity signal, f the true anomaly, e and ω the eccentricity and argument of pericentre for the orbit, t_0 is some reference time, and γ is the mean velocity of the system (which can be affected by the zero-point calibration of an instrument, but does not impact other parameters). In our case, we use the mean of the times of observation for t_0.

2.1.2 Period correction

The period of an orbit as a single value is, in any realistic scenario, not completely well defined. Various angles associated with an orbit will vary in time, such as the argument of pericentre ω or the mean anomaly M. Different combinations of these variations could all be called periods. We consider two of these defined as in the equations (3) and (4). We denote these as *observational period*, $P_{\rm obs}$ which is the time taken peak-to-peak in radial velocity, and the *anomalistic period*,[3] $P_{\rm ano}$, which is the time between consecutive pericentre passages.

$$\frac{2\pi}{P_{\rm obs}} \approx \dot{\omega} + \dot{M}, \tag{3}$$

$$\frac{2\pi}{P_{\rm ano}} \approx \dot{M}. \tag{4}$$

$P_{\rm obs}$ is the period that is usually referred to by observational astronomers and can be precisely measured from time between transits or eclipses. In this work, we set priors on the binary period based on eclipses so want to use $P_{\rm obs}$ for this. When including $\dot{\omega}$ into

[2] We neglect terms that are order $\mathcal{O}(t-t_0)^2$

[3] This nomenclature is often used to refer to the time between two consecutive pericentre passages in precessing systems (e.g. Rosu et al. 2020; Borkovits et al. 2021).

Downloaded from https://academic.oup.com/mnras/article/521/2/1871/7059214 by University of Birmingham user on 08 October 2024

radial velocity fits we want to use $P_{\rm ano}$ as the period parameter to avoid the expected correlation between $P_{\rm obs}$ and $\dot{\omega}$. Hence we need to be able to convert from one to the other. To do this we combine the two equations to get

$$\frac{2\pi}{P_{\rm obs}} = \dot{\omega} + \frac{2\pi}{P_{\rm ano}}, \tag{5}$$

and hence, neglecting terms of order $\mathcal{O}(\dot{\omega}P)^2$,

$$P_{\rm ano} = \frac{P_{\rm obs}}{\left(1 - \frac{\dot{\omega}P_{\rm obs}}{2\pi}\right)} \approx P_{\rm obs}\left(1 + \frac{\dot{\omega}P_{\rm obs}}{2\pi}\right), \tag{6}$$

$$P_{\rm obs} = \frac{P_{\rm ano}}{\left(1 + \frac{\dot{\omega}P_{\rm ano}}{2\pi}\right)} \approx P_{\rm ano}\left(1 - \frac{\dot{\omega}P_{\rm ano}}{2\pi}\right). \tag{7}$$

Our model fits for $P_{\rm obs}$ as a parameter (i.e. the period prior is for $P_{\rm obs}$ as is the output posterior distribution), but the model internally converts this to $P_{\rm ano}$.

2.2 Other additions to the binaries model

Here, we describe the other additions made to the binary model on top of the apsidal precession described earlier, namely, we add relativistic and tidal corrections, and give the ability to fit the radial velocities for a double-lined binary.

2.2.1 Relativistic and tidal corrections

We include relativistic corrections for binary orbits, the main ones being light-travel time and transverse doppler (LT, TD; Sybilski et al. 2013) and gravitational redshift (GR; Zucker & Alexander 2007):[4]

$$\Delta V_{\rm LT} = \frac{K_1^2}{c}\sin^2(f+\omega)(1+e\cos f), \tag{8}$$

$$\Delta V_{\rm TD} = \frac{K_1^2}{c\sin^2 i}\left(1 + e\cos f - \frac{1-e^2}{2}\right), \tag{9}$$

$$\Delta V_{\rm GR} = \frac{K_1(K_1+K_2)}{c\sin^2 i}(1+e\cos f), \tag{10}$$

where e, f, ω, and i are respectively the eccentricity, true anomaly, argument of pericentre, and inclination of the binary orbit relative to the plane of the sky; K_1 and K_2 are the semi-amplitudes of the primary and secondary, respectively, and c is the speed of light.

The tidal effect is calculated as in Arras et al. (2012), assuming a circular orbit. The equation for the tidally induced radial velocity signal is as follows:

$$v_{\rm tide} = 1184\,\frac{M_2 R_1^4}{M_1(M_1+M_2)}P^{-3}\sin^2 i\,\sin[2(f-\phi_0)]\,{\rm m\,s^{-1}}, \tag{11}$$

where M_1, M_2, and R_1 are the mass and radius of the primary and secondary (in solar units), P the orbital period (in days) (we use $P_{\rm ano}$), f the true anomaly, and $\phi_0 = \pi/2 - \omega$ is the observer's reference position.

These equations are incorporated as an optional feature into the model such that when a binary model is fit, these contributions to the radial velocities can be naturally accounted for. We do not include these effects for the general planet search objects as their effects will be much smaller (by orders of magnitude since these corrections scale with M^2) and so does not warrant the increase in computation time.

[4]Sybilski et al. (2013) also have an equation for the gravitational redshift, but it contains errors, hence we use the equation from Zucker & Alexander (2007)

2.2.2 Adding in a double-lined binary model

The vast majority of spectroscopic binaries are double-lined (e.g. Kovaleva et al. 2016), and although the detection of circumbinary planets in double-lined system is problematic (as in Konacki et al. 2009, 2010), new methods to disentangle both spectral components accurately enough to detect circumbinary planets are being developed (e.g. Lalitha et al. in prep). To prepare for the time when circumbinary planets can be searched for, and be detected in double-lined binaries, we add a feature to `kima` to model such a configuration. As an input, the software requires files containing radial-velocities for each component of the binary. The sets of data are fit simultaneously, each with an independent γ parameter to account for differing zero-point calibrations.[5] In addition, each set has its own *jitter* term, added in quadrature to the RV uncertainties to account for any additional sources of white noise. Only one extra common parameter is fit, the mass ratio q.

Any given solution consists of a binary orbit, some number of planetary orbits, and polynomial trends up to cubic order. The binary orbit is fit to each data set with the secondary having the semi-amplitude K scaled by q, and its argument of periastron reversed $\omega_2 = \omega_1 - \pi$. The planetary orbits are then fit in the same way to each data set just as `kima` usually does.

2.3 Using the model

The additions in the new binary model can be used in various combinations. The tidal correction and relativistic correction can each be turned on or off, they will then apply to any known objects included. *A priori* on $\dot{\omega}$ will need to be given for each known object as well as for general signals.

One important thing to note is that equation (11) assumes a circular orbit. We therefore recommend not using the tidal correction for eccentric binaries. We currently assume an inclination of 90°, and therefore we only consider eclipsing systems in this paper. A future update may include the inclination as a free parameter to either attempt to constrain or at the very least marginalize over.

The use of double lined binaries is also included in the options. This requires a data set (or multiple) with five columns: date; RV of primary; uncertainty on primary RV; RV of secondary; and uncertainty on secondary RV. The primary will therefore automatically be the signal placed in the second column. The mass ratio q can be larger than 1 (at which point the 'secondary' is actually the more massive star), so for example in an almost equal mass case *a priori* can straddle $q = 1$.

3 PERFORMANCES OF `KIMA-BINAIREs`

We now show tests and applications of the binaries model using data from simulations as well as from real systems. We first show that the model is able to recover consistent values of apsidal precession, and demonstrate the improvement in the fit that ensues. We illustrate this improvement by computing detection limits.

The standard way to perform detection limits is to inject a fine grid of simulated Keplerian signals (often assuming $e = 0$) into the data where any planetary signal has been removed, and to measure which signals are recovered by the algorithm (e.g. Konacki et al. 2009, 2010; Mayor et al. 2011; Bonfils et al. 2013; Rosenthal et al. 2021). Here,

[5]Even though one would expect the same γ for components observed with the same instrument, this may not be the case (Southworth 2013).

Downloaded from https://academic.oup.com/mnras/article/521/2/1871/7059214 by University of Birmingham user on 08 October 2024

instead, we use the posterior distribution of the undetected Keplerian signals to measure the amplitudes which can still be present in the data, as described in Standing et al. (2022).

Briefly, if the analysis indicates there are no planets in a system (circumstellar or circumbinary), we then apply a strict prior on the number of planets by fixing $N_p = 1$. One Keplerian signal is assumed to be present and the algorithm is thus forced to return all solutions that are compatible with the data, but not formally detected. We then analyse the posterior samples and compute a limit of K as a function of P that envelops the lower 99 per cent of the samples. Practically speaking, the limit is produced by creating log-linear bins along the P axis. It is best to ensure there are at least at least 1000 samples in each bin. Should a system have a formally detected planet (Bayes factor exceeding 150), that planet is subtracted from the data (the maximum likelihood parameters are used for this), and the detection limit is then computed as given earlier using the residual radial velocities.

The advantage of using such a method over traditional methods is the ability to sample over all orbital parameters as finely as the algorithm allows (indeed also, all γ variables and *jitters*, as well as e, ω, $\dot{\omega}$, and ϕ_0 which are sometimes avoided by the traditional methods). While a traditional insertion/recovery asks the question *can these exact signals be recovered?* our method instead asks *what is compatible with the data?* A planet below the detection threshold is consistent with the data, and thus, is not formally detected, whereas a planet above the line is inconsistent with the data and would therefore have been detected had it been there.

3.1 Analytic equation for precession

In Appendix A we derive an analytic equation for the expected precession rate due to an outer perturber (equation (A11)), and due to rotational and relativistic effects (equation A17). This is done in a similar way to in Correia et al. (2013) but where that was done in the invariant plane, we do the calculation in the sky plane, which is directly applicable to observations results.

The precession due to a perturber (equation A11) is under the assumption of both an eclipsing and transiting system, such as Kepler-16. If applying this to a system that does not conform to these assumptions, then equation (A5) should be used.

3.2 Testing `kima-binaries` with simulated data

We begin by testing our ability to recover the apsidal precession using simulated data, showing that we can recover a good measurement of the apsidal precession rate $\dot{\omega}$, and that including it can greatly improve the fit.

We perform two simulations, both with a primary star of mass $M = 1\,\mathrm{M}_\odot$, a secondary with $M = 0.37\mathrm{M}_\odot$, $P = 21.08$ d, and $e = 0.16$ and a (roughly Jupiter mass) planet with $M = 0.001\,\mathrm{M}_\odot$, $P = 134.5$ d, and $e = 0.01$. The first simulation, SIM1, has just these 3 bodies, whereas the second simulation, SIM2, has an additional planet with $M_{\rm pl} = 0.00015\mathrm{M}_\odot$, $P = 911.2$ d, and $e = 0$, corresponding to about 3 times the mass of Neptune. We chose these parameters to emulate a typical circumbinary planet: the binary is similar to Kepler-16 in mass-ratio and eccentricity, with a shorter period to increase the amount of precession that will have happened across the time that we 'observe'. Planet 1 was placed between the 6:1 and 7:1 mean-motion resonances with the binary and Planet 2 at a similar period ratio again. Three different masses of Planet 2 were tried and we report here the one that had the right mass to be missed without using precession but detected when including it. The decimal places for the periods were chosen randomly to try and avoid integer numbers of days and potential accidental resonances.

Simulations are made using the `rebound` package (Rein & Liu 2012), the integrations used the `IAS15` integrator (Rein & Spiegel 2015). Radial velocity simulations are taken as the velocity along the line of sight within the simulation. The simulation uses the same observational cadence as for Kepler-16 (Triaud et al. 2022), thus producing a simulated data set including all Newtonian perturbations. Both simulated data sets are given a Gaussian white noise.

3.2.1 *Improving scatter and derived parameters*

First, we consider SIM1. From the values of ω at each point in the `rebound` simulation, we obtain $\dot{\omega} = 308.4 \pm 3.7$ arcsec yr^{-1} for the binary. Using equation (A11) we get a theoretical value of $\dot{\omega} = 301.1^{+0.8}_{-1.5}$ arcsec yr^{-1} A fit using the binaries model results in *a posteriori* estimate of $\dot{\omega} = 304 \pm 16$ arcsec/yr, which is in agreement with both the simulated and theoretical values. This run is done with the apsidal precession of the binary fit for, but without the relativistic or tidal corrections. The uncertainty in the `rebound` value comes from 'sampling' ω at various times, calculating $\dot{\omega}$ from these and then taking its mean and variance. The uncertainty on the theoretical value is propagated in a Monte Carlo way from the posterior uncertainty on the binary and planetary parameters. The `kima-binaries` value's uncertainty is defined from 16 to 84 per cent of the posterior distribution.

Table 1 lists the parameters of the binary and planet taken from `rebound` and fit with precession (`kima-binaries`) and without precession (`kima`). The 1σ uncertainty in each measurement is shown in brackets as the last few significant figures, to make comparison easier these are all scaled so that each value on a row is shown to the same number of decimal places. The parameters for `rebound` are read out as the osculating parameters at the times of each data point and then the mean and standard deviation of the values are calculated.

We note that in many cases the fitted values are inconsistent with the `rebound` values, and give a word of warning for using the Keplerian parameters from an N-body fitter such as this. When taking the Keplerian orbital parameters of a body from a `rebound` simulation at a given time, these are taken from the osculating Keplerian orbit which may not be representative of the average orbit. Consider the planet's orbital period, `rebound` effectively gives us an anomalistic period as defined in Section 2.1.2. Because of the perturbed motion this is not the time it will take to actually complete one orbit and we get an observed period a few days shorter. This effect cannot be fit as an apsidal precession of the planet as the orbit is not detectably eccentric.

So a Keplerian (or quasi-Keplerian) fit does not reproduce the osculating Keplerian parameters from a N-body simulation, but it does (to a reasonable accuracy) reproduce the mass. We see in Table 1 that the mass of the binary is accurate to 3 decimal places (which is more than the precision we usually get on the mass of the primary star anyway) and the mass of the planet is accurately characterized (more so when apsidal precession is take into account).

We can also compare the precision of the two fits, in the sense of how tight *a posteriori* distribution we get for each parameter. In most cases we can see an improvement in precision by about a factor of two.

The reduction in residual scatter can be seen in Fig. 1 where the rms improves from rms $= 6.61\,\mathrm{m\,s^{-1}}$ to $3.15\,\mathrm{m\,s^{-1}}$. When apsidal precession is not accounted for, if we move further from the reference

Downloaded from https://academic.oup.com/mnras/article/521/2/1871/7059214 by University of Birmingham user on 08 October 2024

Table 1. For SIM1 we show the parameters from `rebound` (Rein & Liu 2012) (note these are keplerian parameters taken from a Newtonian simulation) alongside the fitted parameters both with precession (`kima-binaries`) and without (`kima`). For the planet we state the upper bound on the eccentricity and omit the angle parameters as these are not resolved (close to circular orbit). The 1σ uncertainties are shown as the last few significant digits, all of which are on the same scale as the smallest uncertainty to allow for easy comparison. Goodness-of-fit parameters are also shown to compare the two fits.

	`rebound`	`kima`	`kima-binaries`	Units
$P_{\rm B}$	21.0805330(8492)	21.0810474(52)	21.0810395(21)	days
$M_{\rm B}$	0.37	0.3700886(153)	0.3700981(57)	$M_\odot$
$K_{\rm B}$	23415.30(45)	23419.67(80)	23420.11(31)	ms^{-1}
$e_{\rm B}$	0.160106(53)	0.160114(34)	0.160096(15)	
$\omega_{\rm B}$	4.50018(236)	4.50061(24)	4.50016(20)	rad
$\phi_{0,\rm B}$	6.27400(23628)	6.28256(24)	6.28288(26)	rad
$\dot{\omega}_{\rm B}$	308.4(3.7)	0	304.0(15.8)	arcsec yr^{-1}
$P_{\rm pl}$	135.084(1.147)	131.373(120)	131.392(57)	days
$M_{\rm pl}$	1.0476	1.076(27)	1.046(14)	M_J
$K_{\rm pl}$	33.62(09)	34.81(90)	33.82(43)	ms^{-1}
$e_{\rm pl}$	0.0161(79)	<0.050	<0.033	
rms		6.61	3.15	ms^{-1}
Jitter		6.27	2.04	ms^{-1}
χ^2_ν		12.35	3.15	

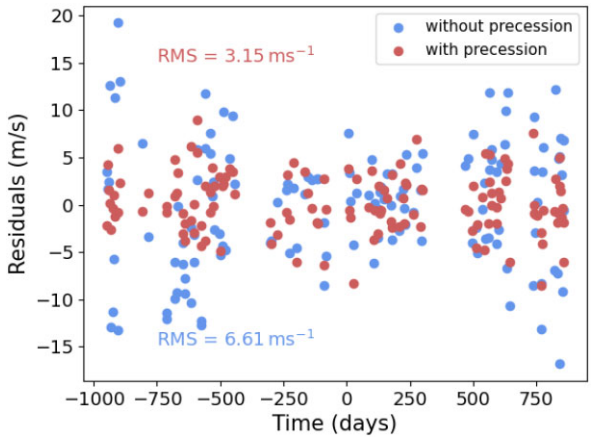


Figure 1. A comparison of radial velocity residuals, after removing the binary's orbital solution, for SIM1 where apsidal precession is included in the `kima-binaries` model (in red) and not included in `kima` (in blue).

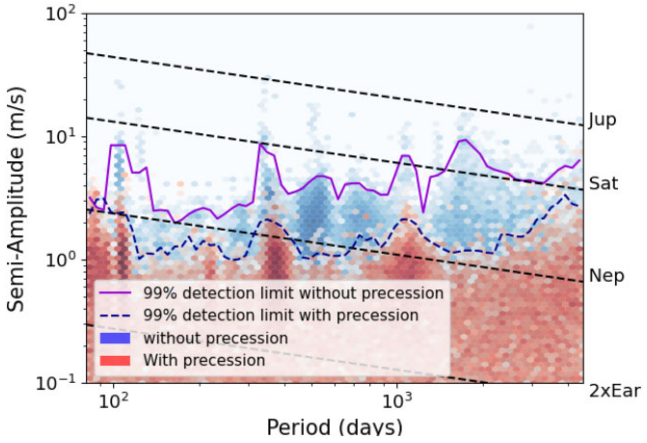


Figure 2. Detection limits for additional Keplerian signals using SIM1. The hexbins represent the density of posterior samples in each run. The purple-dashed line and solid-blue line are the 99 per cent detection limits. The black-dashed lines show where bodies of various masses would sit on this plot.

time T_0 (near the centre of the figure), the fit worsens, giving a characteristic *bow-tie* shape, but if precession is accounted for, the spread in the residuals is reduced.

The detection limits both with and without precession can be seen in Fig. 2. The improvement in detection limit is slightly larger at high periods where the radial-velocity signature of apsidal precession can be confused for a long-term trend. This improvement means the data would allow the detection of another planet signal within this system, almost an order of magnitude lower in mass at orbital periods between 1000 and 2, 000d. Whilst this sounds impressive, this simulation only had a very small amount of extra white noise added to maximize the effect of apsidal precision in order to reveal its importance. In other systems we may expect more marginal improvements (see Section 4).

3.2.2 *Detecting a hidden planet*

Here, we consider SIM2 and test how many planets are formally detected. To register as an n-planet detection, the Bayes Factor for the n-planet solution compared to the $(n-1)$-planet solution needs to be greater than 150. The sampling in `kima` is trans-dimensional, meaning that solutions with different numbers of planets are all searched simultaneously. Therefore, the Bayes Factor $BF_{i+1,i}$ comparing the model with $i+1$ planets to that with i planets, is the ratio of the number of posterior samples with $i+1$ planets N_{i+1} to the number with i planets N_i

$$BF_{i+1,i} = \frac{N_{i+1}}{N_i} \tag{12}$$

where $N_i = 0$, the Bayes Factor in equation (12) becomes infinite. This can happen if the BF is larger than the number of effective posterior samples, and would be solved eventually had the sampling continued. In this case we therefore choose to report $BF_{i+1,i} = N_{i+1}$, effectively setting $N_i = 1$. More information can be found in Faria et al. (2018); Standing et al. (2022); Triaud et al. (2022).

Running `kima` on the data from SIM2 without including precession, the outer planet is not formally detected but visible within the posterior as an over-density. With $BF_{2,1} = 12.5 < 150$, it would be

Downloaded from https://academic.oup.com/mnras/article/521/2/1871/7059214 by University of Birmingham user on 08 October 2024

Table 2. The Bayes Factors for SIM2 (containing two circumbinary planets) comparing models with increasing numbers of planets both for the standard version of `kima` and the new `kima-binaries` version, which includes apsidal precession.

	`kima`	`kima-binaries`
$BF_{1,0}$	538	0
$BF_{2,1}$	12.5	6086
$BF_{3,2}$	0.9	0.8

classified as a candidate planet. We can attribute this non-detection to the apsidal precession since when we do fit for the precession, the planet is formally detected with $BF_{2,1} > 6086 > 150$. The Bayes Factors for each attempted fit are found in Table 2.

3.3 Testing `kima-binaries` on data from the KOI-126 system

In this section, we test the ability to recover a value for the precession rate consistent with a previous solution from literature, as well as show the improvement in sensitivity to planets that accounting for precession could bring in a highly precessing system.

KOI-126 is a compact triply-eclipsing hierarchical triple star system. It contains a roughly circular, low-mass, and tight binary which is in an eccentric orbit about a more massive tertiary star. The system was first reported in Carter et al. (2011). There are radial velocity data as well as photometry during multiple eclipses. As such, the apsidal precession rate of the tertiary orbit is well measured with a period of 21 850 d (Yenawine et al. 2022) which corresponds to $\dot{\omega} = 21\,650$ arcsec yr^{-1}. We used 29 radial velocity data from Yenawine et al. (2022). Our fit with the new binaries model recovers a consistent value for the apsidal precession, with $\dot{\omega} = 21\,800 \pm 600$ arcsec yr^{-1}. Equivalently this is $\dot{\omega} = 0.56 \pm 0.009^{\circ}$ per cycle.

We run the analysis with apsidal precession fit for, as described in Section 2, but do not include either the general relativity or the tidal corrections. A more complete analysis would be to use a Newtonian model, rather than Keplerian with added precession, as in Yenawine et al. (2022), however including the precession improves the χ^2_ν from 640.9 to 1.5. This amply justifies adding an extra parameter, $\dot{\omega}$, to the fit and suggests that a full dynamical model is not necessary with the current precision of the data, hence illustrating the importance of $\dot{\omega}$, since even in this dynamically complex triple system, the linear apsidal precession removes the majority of the excess noise. The detection limits are shown in Fig. 3 for reference. Here too, including precession improves the detection limit by an order of magnitude in semi-amplitude and removes much of the long-period noise where, as with the simulated data, the precession may be being mildly confused for a long term trend.

We do not use the analytic equation derived in Appendix (A) as KOI-126 is in a different orbital configuration where the precessing orbit is the outer (rather than inner) one.

As an interesting note, the orbital periods shown in Fig. 3 would be for putative *circumtertiary planets*, of which none are known in Nature. We can nonetheless state there are no stellar or brown dwarf mass companions within $\sim 10^4$d of the inner tertiary.

We show the parameters from our fit of KOI-126 in Table B1

4 APPLICATION OF `KIMA-BINARIES` TO KEPLER-16

The announcement of Kepler-16b marked the first unambiguous detection of a circumbinary planet (Doyle et al. 2011), made thanks

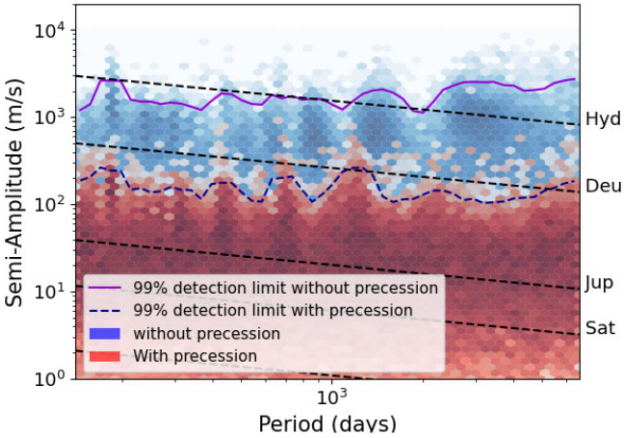


Figure 3. Detection limits for additional signals around KOI-126. The hexbins show the density of posterior samples with the red being those when precession is included in the fit, blue when it is not included. The dashed-purple line and solid-blue line show the 99 per cent confidence detection limits. The dashed lines show where bodies of various masses, and where the Deuterium and Hydrogen fusing limits would sit on this plot.

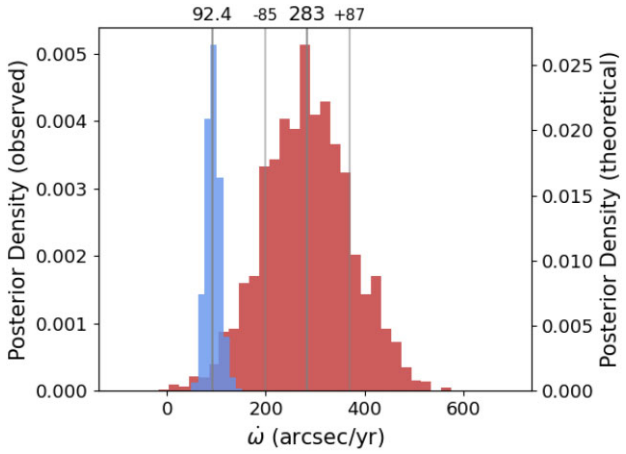


Figure 4. Kepler-16: red: histogram of the density of posterior samples for fitted value of $\dot{\omega}$ with the median and 1σ values shown in grey. Blue: histogram of the density of posterior samples for the theoretically calculated value of $\dot{\omega}$ with the median value shown in grey. (Note that $\dot{\omega}$ is not cut at zero, there are in fact posteriors below zero.).

to the *Kepler* spacecraft (Borucki et al. 2010). This system is unique in also being the only circumbinary planet independently detected with radial velocity (Triaud et al. 2022). We re-analyse these radial-velocity data with with our new model, and successfully detect an apsidal precession rate of $\dot{\omega}_1 = 283^{+87}_{-85}$arcsec yr^{-1}, which is 3.3σ from 0. Using equations (A11) and (A17) we obtain a value of $\dot{\omega}_1 = 92.4^{+14.3}_{-13.8}$arcsec yr^{-1}, which is 2.2σ away from the observed value. This theoretical value takes into account the planetary-induced and relativistic precessions (we do not include the rotational and tidal contributions as they would be very small in comparison and parameters like the Love numbers are not very well known). The posterior distributions for both the measured and theoretical precession rates are shown in Fig. 4.

The theoretical $\dot{\omega}$ is lower than the value that we measure; more data are required to determine how significant this discrepancy is. The difference is likely too important to be accounted for entirely by mutual inclination. An alternative (or additional) explanation could be further undetected planets contributing to the precession rate.

Downloaded from https://academic.oup.com/mnras/article/521/2/1871/7059214 by University of Birmingham user on 08 October 2024

Table 3. Various binary periods for Kepler-16AB. The first two values denoted by asterisk (∗) are taken from Triaud et al. (2022) using their two different algorithms, the other two are obtained using `kima-binaries` 1σ uncertainties are shown in brackets as the last 2 significant figures (3 in the last case for easy comparison with the others).

Type of period and algorithm used	Value
P (`yorbit`)∗	41.077779(54)
P (`kima`)∗	41.077772(51)
$P_{\rm obs}$ (`kima-binaries`)	41.077716(55)
$P_{\rm ano}$ (`kima-binaries`)	41.078737(305)

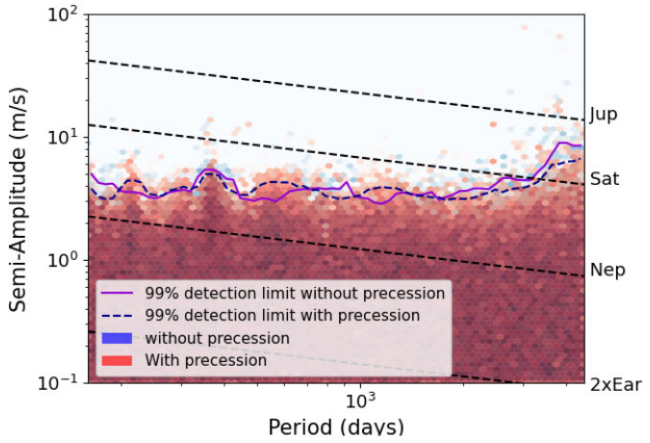


Figure 5. Detection limits for Kepler-16 with and without accounting for precession. The posterior sample for each of these are plotted in the hexbins with the version including precession plotted in red and in front. Since there is no improvement the density plot for the model without precession is hard to see. The dashed-purple and solid-blue lines show the 99 per cent confidence detection limits with and without including precession.

We explore the difference between $P_{\rm obs}$ and $P_{\rm ano}$. These values for Kepler-16 are presented in Table 3 alongside values published in Triaud et al. (2022). The value we get for $P_{\rm obs}$ is in statistical agreement with the previous publication, however $P_{\rm ano}$ is 3.3σ above this. $P_{\rm ano}$ is the time between consecutive pericentre passages, the period that should in theory be used to compute physical parameters such as semimajor axis and planet mass, in a Keplerian context. In practice the difference is negligible due to there being a small difference between $P_{\rm ano}$ and $P_{\rm obs}$, as well as the uncertainty in the mass of the primary often being dominant. For Kepler-16 the difference in mass using the two periods is $\approx 2 \times 10^{-6}\,{\rm M}_{\odot}$. It would take a case with very precise mass and a very high precession rate for this difference to be significant, even for KOI-126 (B + C), the difference is $\approx 2 \times 10^{-4}\,{\rm M}_{\odot}$ which is about a fifth of the currently measured uncertainty.

In addition, we produce a detection limit for Kepler-16, comparing the results with and without including $\dot{\omega}$. The detection limits, plotted in the same way as the previous ones, are shown in Fig. 5. In this case, as we only get a marginal detection of apsidal precession there is no real improvement in the detection limits.

We show the parameters from our fit of Kepler-16 in Table B2.

5 CONCLUSIONS

We have shown that fitting for the apsidal precession of a binary's orbital parameters improves the radial velocity sensitivity to circumbinary planets. Our conclusions are in line with previous work such as Konacki et al. (2010) and Sybilski et al. (2013), but extend theirs to a fully Bayesian framework. The improvement in the detection limits can be of up to an order of magnitude in some configurations, but in most cases, improvements are expected to be marginal as in the case of Kepler-16. Accounting for precession can also give improvements in the precision of the parameters recovered from a fit, as well as the potential to uncover planets that were hidden by precession (or instead require less data to detect the same planet).

We have derived a formula for calculating the theoretical precession induced in a binary (equation A11) and have discussed the potential use of a measurement of the apsidal precession rate as a way to constrain the mutual inclination of the planetary and binary orbital planes using this formula.

The theoretical and observed values of precession for Kepler-16 are in slight tension, this may be because of undetected planets or some other unknown mechanism.

The longer the baseline of radial velocity observations, the more important it is to account for apsidal precession. As the field progresses, and the number of data from surveys like BEBOP increases, fitting the apsidal precession of the binaries will become vital. To prepare for that time, we have presented an updated version of the `kima` package which is more adapted to fitting radial velocities for single and double-lined binaries. The code is made public on github.

ACKNOWLEDGEMENTS

The authors thank the anonymous reviewer as well as Darin Ragozzine for their useful comments. This research is in part funded by the European Union's Horizon 2020 research and innovation programme (grants agreements number 803193/BEBOP). AC acknowledges support from CFisUC (UIDB/04564/2020 and UIDP/04564/2020), GRAVITY (PTDC/FIS-AST/7002/2020), and ENGAGE SKA (POCI-01-0145-FEDER-022217), funded by COMPETE 2020 and FCT, Portugal. MRS acknowledges support from the UK Science and Technology Facilities Council (ST/T000295/1).

6 DATA AVAILABILITY

The radial velocity data for Kepler-16 can be found in Triaud et al. (2022).The radial velocity data for KOI-126 can be found in Yenawine et al. (2022).

The code used for the analysis in this paper can be obtained at https://github.com/j-faria/kima

REFERENCES

Angelo I., Naoz S., Petigura E., MacDougall M., Stephan A. P., Isaacson H., Howard A. W., 2022, AJ, 163, 227
Arras P., Burkart J., Quataert E., Weinberg N. N., 2012, MNRAS, 422, 1761
Bonfils X., et al., 2013, A&A, 549, 109
Borkovits T., et al., 2021, MNRAS, 510, 1352
Borucki W. J., et al., 2010, Science, 327, 977
Brewer B. J., Pártay L. B., Csányi G., 2011, Stat. Comput., 21, 649
Carter J. A., et al., 2011, Science, 331, 562
Claret A., Giménez A., 2010, A&A, 519, 57
Correia A. C. M., Boué G., Laskar J., Morais M. H. M., 2013, A&A, 553, 39
Correia A. C. M., Boué G., Laskar J., 2016, Cel. Mech. Dyn. Astron., 126, 189
Dawson R. I., Johnson J. A., 2018, ARA&A, 56, 175
Doolin S., Blundell K. M., 2011, MNRAS, 418, 2656
Doyle L. R., et al., 2011, Science, 333, 1602
Dvorak R., Froeschle C., Froeschle C., 1989, A&A, 226, 335

Downloaded from https://academic.oup.com/mnras/article/521/2/1871/7059214 by University of Birmingham user on 08 October 2024

Farago F., Laskar J., 2010, MNRAS, 401, 1189
Faria J. P., Santos N. C., Figueira P., Brewer B. J., 2018, J. Open Source Softw., 3, 487
Gillon M., et al., 2016, Nature, 533, 221
Gillon M., et al., 2017, Nature, 542, 456
Holman M. J., Wiegert P. A., 1999, AJ, 117, 621
Konacki M., Muterspaugh M. W., Kulkarni S. R., Hełminiak K. G., 2009, ApJ, 704, L513
Konacki M., Muterspaugh M. W., Kulkarni S. R., Hełminiak K. G., 2010, ApJ, 719, L1293
Kostov V. B., et al., 2016, ApJ, 827, L86
Kostov V. B., et al., 2020, AJ, 159, 253
Kostov V. B., et al., 2021, AJ, 162, 234
Kovaleva D., Malkov O., Yungelson L., Chulkov D., 2016, Baltic Astron., 25, 419
Martin D. V., Triaud A. H. M. J., 2014, A&A, 570, 91
Martin D. V., Triaud A. H. M. J., 2015, MNRAS, 449, 781
Martin D. V., et al., 2019, A&A, 624, 68
Mayor M., et al., 2011, preprint (arXiv.1109.2497)
Morais M. H. M., Correia A. C. M., 2012, MNRAS, 419, 3447
Murray C. D., Correia A. C. M., 2010, Exoplanets. Keplerian Orbits and Dynamics of Exoplanets, University of Arizona Press, p. 15
Murray C. D., Dermott S. F., 1999, Solar system dynamics. Cambridge Univ. Press, Cambridge
Orosz J. A., et al., 2012, Science, 337, 1511
Rein H., Liu S.-F., 2012, A&A, 537, 128
Rein H., Spiegel D. S., 2015, MNRAS, 446, 1424
Rosenthal L. J., et al., 2021, ApJS, 255, 8
Rosu S., Rauw G., Conroy K. E., Gosset E., Manfroid J., Royer P., 2020, A&A, 635, 145
Schneider J., 1994, Planet. Space Sci., 42, 539
Southworth J., 2013, A&A, 557, 119
Standing M. R., et al., 2022, MNRAS, 511, 3571
Sybilski P., Konacki M., Kozłowski S. K., Hełminiak K. G., 2013, MNRAS, 431, 2024
Triaud A. H. M. J., et al., 2017, A&A, 608, 129
Triaud A. H. M. J., et al., 2022, MNRAS, 511, 3561
Winn J. N., Fabrycky D. C., 2015, ARA&A, 53, 409
Yenawine M. E., et al., 2022, ApJ, 924, L66
Zucker S., Alexander T., 2007, ApJ, 654, L83

APPENDIX A: DERIVATION OF THE PLANETARY INDUCED PRECESSION RATE

In this section, we derive the equation for the apsidal precession of an inner orbit (Binary or planet) due to an outer perturber.

The dominating term for the apsidal precession is the planet–binary gravitational interactions. We take the secular quadrupole Hamiltonian after averaging over the mean anomaly of both orbits is given by (e.g. Farago & Laskar 2010; Morais & Correia 2012)

$$\mathcal{H} = C_2 \left[2 - 12e_1^2 - 6(1-e_1^2)\cos^2 i + 30e_1^2\cos^2\alpha\right], \tag{A1}$$

where

$$C_2 = \frac{\mathcal{G}}{16}\frac{m_0 m_1}{m_0+m_1}\frac{m_2}{(1-e_2^2)^{3/2}}\frac{a_1^2}{a_2^3}, \tag{A2}$$

and

$$\cos i = \sin I_1 \sin I_2 \cos(\Omega_1 - \Omega_2) + \cos I_1 \cos I_2, \tag{A3}$$

$$\begin{aligned}\cos\alpha = {} & \sin I_1 \sin\omega_1 \cos I_2 - \sin I_2 \cos\omega_1 \sin(\Omega_1 - \Omega_2) \\ & - \sin I_2 \cos I_1 \sin\omega_1 \cos(\Omega_1 - \Omega_2).\end{aligned} \tag{A4}$$

In these equations, a, e, I, ω, and Ω refer to the semimajor axis, eccentricity, orbital inclination, argument of pericentre, and longitude of ascending node of an orbit, with subscripts 1 and 2 referring to the inner and outer orbits, respectively. $\mathcal{G}$ refers to the gravitational constant, while m_0, m_1 and m_2 are the masses of the star A, B, and planet, respectively. Cos i and cos α are direction cosines, where the angle i corresponds to the true mutual inclination between the two orbital planes.

Then, we can compute the precession of the pericentre of the inner orbit using the Lagrange Planetary Equations (e.g. Murray & Dermott 1999) as

$$\frac{d\omega_1}{dt} = -\frac{(1-e_1^2)}{e_1 G_1}\frac{\partial\mathcal{H}}{\partial e_1} + \frac{\cot I_1}{G_1}\frac{\partial\mathcal{H}}{\partial I_1}, \tag{A5}$$

where G_1 is the norm of the orbital angular momentum

$$G_1 = \frac{m_0 m_1}{m_0+m_1}\sqrt{\mathcal{G}(m_0+m_1)a_1(1-e_1^2)}, \tag{A6}$$

$$\frac{\partial\mathcal{H}}{\partial e_1} = C_2\left[-24e_1 + 12e_1\cos^2 i + 60e_1\cos^2\alpha\right], \tag{A7}$$

$$\frac{\partial\mathcal{H}}{\partial I_1} = C_2\left[-12(1-e1^2)\cos i\frac{\partial\cos i}{\partial I_1} + 60e_1^2\cos\alpha\frac{\partial\cos\alpha}{\partial I_1}\right], \tag{A8}$$

and

$$\frac{\partial\cos i}{\partial I_1} = \cos I_1 \sin I_2 \cos(\Omega_1 - \Omega_2) - \sin I_1 \cos I_2, \tag{A9}$$

$$\frac{\partial\cos\alpha}{\partial I_1} = \cos I_1 \sin\omega_1 \cos I_2 + \sin I_2 \sin I_1 \sin\omega_1 \cos(\Omega_1 - \Omega_2). \tag{A10}$$

In the case of an eclipsing binary and a transiting planet, such as Kepler-16 we can take $I_1 \approx I_2 \approx 90°$, which allow us to simplify expression (A5) as

$$\begin{aligned}\frac{d\omega_1}{dt} &\approx \frac{12C_2}{G_1}(1-e_1^2)\left[2 - \cos^2 i - 5\cos^2\alpha\right] \\ &\approx \frac{12C_2}{G_1}(1-e_1^2)\left[1 + (1 - 5\cos^2\omega_1)\sin^2 i\right].\end{aligned} \tag{A11}$$

Therefore, for an eclipsing and transiting system, a constraint on the precession rate can be used to measure the mutual inclination.

For close-in binaries, additional sources of apsidal precession may become relevant, such as general relativity, rotational flattening, and tidal deformation. These effects, can also be modelled using a Hamiltonian formalism as[6] (e.g. Correia et al. 2013; Correia et al. 2016)

$$\begin{aligned}\mathcal{H}' = {} & -\frac{C_g}{(1-e_1^2)^{1/2}} - \frac{C_{r,0}+C_{r,1}}{(1-e_1^2)^{3/2}} \\ & - \frac{C_{t,0}+C_{t,1}}{(1-e_1^2)^{9/2}}\left(1 + 3e_1^2 + \tfrac{3}{8}e_1^4\right),\end{aligned} \tag{A12}$$

where

$$C_g = \frac{3\mathcal{G}^2 m_0 m_1 (m_0+m_1)}{a_1^2 c^2} \tag{A13}$$

corresponds to the general relativity correction (c is the speed-of-light),

$$C_{r,i} = \frac{\mathcal{G}m_0 m_1 J_{2,i} R_i^2}{2a_1^3} \tag{A14}$$

accounts for the rotational flattening, and

$$C_{t,i} = k_{2,i}\frac{\mathcal{G}m_{1-i}^2 R_i^5}{2a_1^6} \tag{A15}$$

[6]We assume that the spin axes of both stars are normal to the orbit.

Downloaded from https://academic.oup.com/mnras/article/521/2/1871/7059214 by University of Birmingham user on 08 October 2024

for the tidal contribution.

$$J_{2,i} = k_{2,i} \frac{\Omega_i^2 R_i^3}{3\mathcal{G}m_i} \,, \tag{A16}$$

$k_{2,\,i}$ is the second Love number for potential, Ω_i is the rotation rate, and R_i is the radius of the star with mass m_i.

Then, according to expression (A5), the correction in the apsidal precession is given by

$$\frac{d\omega_1}{dt} = \frac{C_g}{G_1(1-e_1^2)^{1/2}} + \frac{3(C_{r,0}+C_{r,1})}{G_1(1-e_1^2)^{3/2}} + \frac{15(C_{t,0}+C_{t,1})}{G_1(1-e_1^2)^{9/2}} \left(1 + \tfrac{3}{2}e^2 + \tfrac{1}{8}e^4\right). \tag{A17}$$

The first term is the relativistic contribution, the middle one is the rotational contribution, and the last term is the tidal contribution. These can be taken separately as we do in Section (4)

APPENDIX B: TABLES OF PARAMETERS

Table B1. The fitted and derived and assumed parameters for KOI-126 for the orbit of the binary B + C around star A. ∗ since we only fit a single orbit in the radial velocity data the mass here is the combined masses of stars B and C. The quality of fit indicators (rms, Jitter, and χ^2_ν) are taken for the best fitting model. The mass M_A is obtained from Yenawine et al. (2022). Excepting parameters with highly asymmetric distributions, the 1σ uncertainties are shown as the last few significant digits.

	`kima-binaries`	Units
Assumed parameters		
M_A	1.2713(47)	$\mathrm{M}_\odot$
Fitted parameters		
P_obs	33.77943(33)	days
P_ano	33.83207(69)	days
K	21 395(25)	$\mathrm{m\,s^{-1}}$
e	0.3113(13)	
ω	1.1794(50)	rad
ϕ_0	1.0210(40)	rad
$\dot{\omega}$	21 800(370)	$\mathrm{arcsec\,yr^{-1}}$
γ	-27852^{+193}_{-76}	$\mathrm{m\,s^{-1}}$
Derived parameters		
$M^*_\mathrm{B+C}$	0.4424(11)	$\mathrm{M}_\odot$
T_0	51047.4547(27)	BJD – 2 400 000
Fit indicators		
$\mathrm{rms_{Tull}}$	207	$\mathrm{m\,s^{-1}}$
$\mathrm{rms_{Tres}}$	84.2	$\mathrm{m\,s^{-1}}$
$\mathrm{Jitter_{Tull}}$	0.36	$\mathrm{m\,s^{-1}}$
$\mathrm{Jitter_{Tres}}$	49.3	$\mathrm{m\,s^{-1}}$
χ^2_ν	3.07	

Here, we show the parameters for KOI-126 in Table B1 and for Kepler-16 in Table B2 from the fits using the binaries model. The parameters for KOI-16 are of the outer orbit of the triple, modelling the short period binary as a single massive body.

Table B2. The fitted and derived and assumed parameters for Kepler-16 subscripts B refer to the binary orbit and b to the planetary orbit. The quality of fit indicators (rms, Jitter, and χ^2_ν) are taken for the best fitting model. Excepting parameters with highly asymmetric distributions, the 1σ uncertainties are shown as the last few significant digits.

	`kima-binaries`	Units
Assumed parameters		
M_A	0.654(20)	$\mathrm{M}_\odot$
Fitted parameters		
$P_\mathrm{B,\,obs}$	41.077716(55)	days
$P_\mathrm{B,\,ano}$	41.07874(31)	days
K_B	13678.9(1.4)	$\mathrm{m\,s^{-1}}$
e_B	0.159925(88)	
ω_B	4.60203(79)	rad
$\phi_{0,\,\mathrm{B}}$	1.63340(76)	rad
$\dot{\omega}_\mathrm{B}$	284(86)	$\mathrm{arcsec\,yr^{-1}}$
P_b	225.8(1.7)	days
K_b	11.7(1.6)	$\mathrm{m\,s^{-1}}$
e_b	<0.29	
ω_b	3.90(92)	rad
$\phi_{0,\,\mathrm{b}}$	2.32(87)	rad
γ	$-33811.5^{+3.1}_{-0.2}$	$\mathrm{m\,s^{-1}}$
Derived parameters		
M_B	0.1965(32)	$\mathrm{M}_\odot$
$T_{0,\,\mathrm{B}}$	58498.4796(52)	BJD – 2 400 000
M_b	0.308(42)	$\mathrm{M_{Jup}}$
$T_{0,\,\mathrm{b}}$	58 388(33)	BJD – 2 400 000
Fit indicators		
rms	11.01	$\mathrm{m\,s^{-1}}$
Jitter	0.91	$\mathrm{m\,s^{-1}}$
χ^2_ν	0.92	

This paper has been typeset from a TEX/LATEX file prepared by the author.

Downloaded from https://academic.oup.com/mnras/article/521/2/1871/7059214 by University of Birmingham user on 08 October 2024

2.2.9 Fitting double-lined binary data

Many binary stars are double-lined, these binaries contain two stars with comparable luminosities such that there are visible spectral lines from both stars. This is typically the case for main sequence binaries with a mass ratio $q = M_2/M_1 \gtrsim 0.3$ (Triaud et al., 2017). The two sets of spectral lines mean that, in principle, one can obtain two independent radial velocity timeseries, one for each star.

A planet orbiting a close double-lined binary causes a reflex motion on the centre-of-mass of the binary. This means that both stars feel the effect of the planet in the same way, and therefore the planet induces the same Keplerian signal in both radial velocity timeseries.

As is mentioned in Section 2.2.3 (section 2 in the paper), within the BINARIESmodel of `kima` I have included an option to analyse data from double-lined binaries. This requires a `double_lined = True` flag to be given both to the RVdata class and to the BINARIESmodel. The analysis proceeds on data which has a single set of times, each of which has a radial velocity measurement and uncertainty for each of the primary and secondary star.

There is only one additional orbital parameter needed to fit the secondary star's radial velocities in addition to the primary's: q the mass ratio. The radial velocity curve for the secondary can then be calculated, it is the same as for the primary (Equation 1.16) but with $K_2 = K_1/q$ and[3] $\omega_2 = \omega_1 - \pi$. There is additionally both a separate $V_{\rm sys}$ and a separate jitter term for the secondary star, for a total of three additional parameters.

Any planets orbiting around both components would therefore have the same signature in both stars, and two independent radial velocity measurements are obtained from each individual spectrum. Since for a given epoch the two are measured at the same time, this only takes one iteration of solving Kepler's equation, there is therefore little difference in computation time for a double-lined system vs a single-lined system.

Analysis of double lined binaries can be found in Chapter 3, with a planet detected around the double-lined binary TIC 172900988 in Section 3.1, and an analysis of a set of double-lined binaries in Section 3.3.

[3] subscript 1 refers to the radial velocity analysis of the primary star and 2 that of the secondary

Eclipsing double-lined binaries allow us to measure stellar masses precisely and accurately. For the majority of exoplanetary systems, the mass of the host star is calculated based on the spectral type which gives a $\sim$ 10% precision (Soderblom, 2010), for some cases asteroseismology allows to improve upon this getting up to a 4% precision (Silva Aguirre et al., 2017). Double-lined binaries allow for much more precise mass measurements ($\approx$ 0.03% in the case of TIC 172900988, see Section 3.1) and not only that but they are model-independent (or at least the only assumed model is Newtonian gravity).

The mass function for the secondary star (Equation 1.21) can generally be determined from the observables of the radial velocity analysis (see Section 1.3.1). Writing it again with capital M's to represent both bodies being stars gives

$$f(M_2) = \frac{M_2^3 \sin^3 i}{(M_1 + M_2)^2} = \frac{P K_1^3 (1 - e^2)^{3/2}}{2\pi G}. \tag{2.6}$$

The mass function for the primary star is similarly

$$f(M_1) = \frac{M_1^3 \sin^3 i}{(M_1 + M_2)^2} = \frac{P K_2^3 (1 - e^2)^{3/2}}{2\pi G}. \tag{2.7}$$

Analysing radial velocities from a double-lined binary constrains the mass ratio q as well. Since $\frac{M_2}{M_1} = q$, $M_1 + M_2 = M_1(1 + q)$. Substituting this into Equation 2.7 gives:

$$\frac{M_1^3 \sin^3 i}{M_1^2 (1 + q)^2} = \frac{P K_2^3 (1 - e^2)^{3/2}}{2\pi G} \tag{2.8}$$

$$M_1 \sin^3 i = \frac{P K_2^3 (1 - e^2)^{3/2} (1 + q)^2}{2\pi G}. \tag{2.9}$$

Thus, $M_1 \sin^3 i$ can be constrained directly and $M_2 \sin^3 i = q M_1 \sin^3 i$. Both masses can be known up to $\sin^3 i$ and if the binary is eclipsing, then the inclination is known and the absolute dynamical masses of both stars can be calculated. Alternatively if the binary is not eclipsing, this method will not give the dynamical masses but can instead be used to calculate the inclination by measuring the masses in a second way (e.g. spectroscopy or asteroseismology) and substituting

that in.

Since within `kima` we constrain K_1 and q, masses for both stars are calculated at each step of the sampling process. These masses are then used in the relativistic corrections described in Section 2.2.3 (section 2 in the paper) making the corrections more precise and accurate, and also faster than for the single-lined binaries. For single-lined binaries M_2 needs to either be assumed intially before the analysis is performed, or be calculated at each step using a Newton-Raphson method which takes longer.

2.2.10 Inclination of the binary orbit

The relativistic and tidal corrections from Section 2.2.3 (section 2 in the paper) and the equations for the masses derived from the radial velocity method (Equation 2.9) all rely on some assumption or knowledge about the inclination of the binary orbit. For eclipsing binaries, it is usually sufficient for the radial velocity corrections to assume that the inclination is 90°. However in the case of a non-eclipsing binary the inclination should be accounted for. Within the BINARIESmodel I have also included the binary inclination as a parameter, the flag `eclipsing = True` will fix the inclination to 90°, alternatively it can be set to `False` and a prior distribution given for the inclination if it is known from some other source. If no prior is given and `eclipsing = False`, the default prior is $\cos i \sim \mathcal{U}(0, \pi/2)$.

In principle, with precise enough data, the inclination of a non-eclipsing binary could be constrained in this way by the tidal and relativistic effects on the binary. Using general relativity was suggested by Zucker and Alexander (2007) but has yet to be tested thoroughly. I do test the ability of the tidal correction to give rise to a measurement of the inclination of a system, I use the BINARIESmodel on the data from double-lined binary HD 13974 (see Section 3.3), I include the tidal correction and set the radii of each star to be 1 $R_\odot$, this is of course not accurate but the approximation is suitable for the purpose of testing whether the tides can constrain the inclination in principle. The resulting posterior distribution on the inclination is shown in Figure 2.9, the inclination is indeed constrained by the tidal correction, however converting this to a stellar mass gives very large uncertainties ($\gtrsim 1\ M_\odot$) so this is not a practical way to get precise

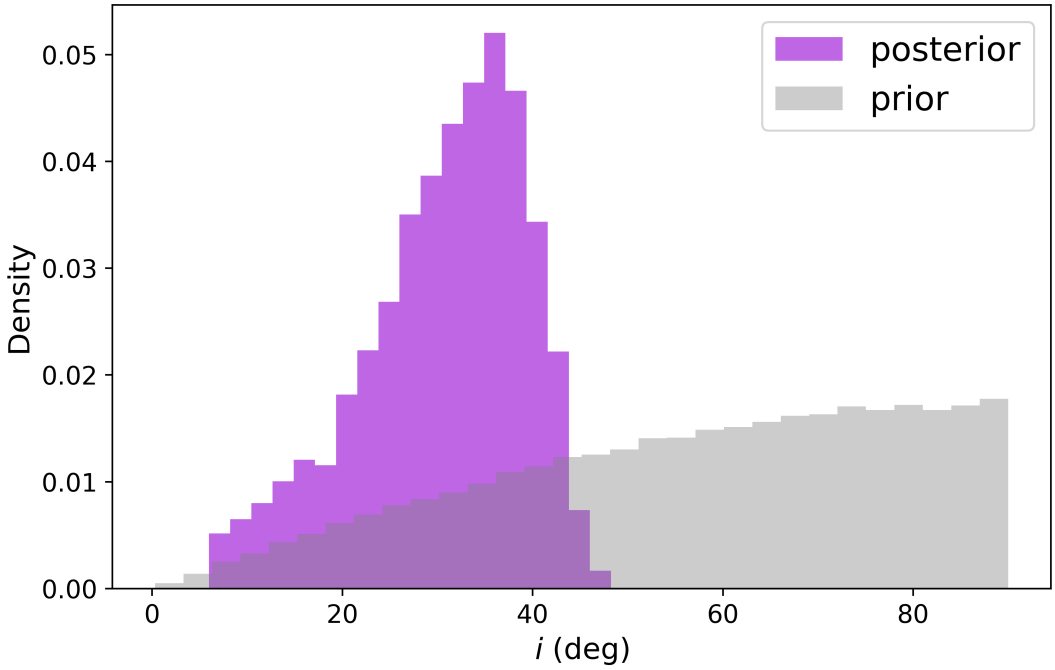


Figure 2.9: Posterior and prior distributions on the inclination of the binary orbit of HD 13974.

mass constraints on non-eclipsing double-lined binaries.

2.3 `kima` ETVmodel

Another model within `kima` is the ETVmodel which I developed to analyse Eclipse Timing Variations (ETVs) of binaries with precise mid-eclipse timings. Of the different kinds of eclipse timing variations (see Section 1.6.2) this model specifically fits for light travel-time effect. This is when the orbit of the eclipsing binary about the centre-of-mass of the system causes periodic variations in the measured time of mid-eclipse as distance to the binary modulates.

Similarly to the radial velocity method the shape of the eclipse timing curve will be a Keplerian, but since the measurements are due to the projected distance rather than velocity, the shape is not quite the same. Another slight peculiarity of modelling eclipse timing variations, is that both the dependent and independent variables are time, but that measurements cannot happen at any time. The true dependent variable is the Epoch (E), this is the number of the

eclipse, with the first eclipse measured usually being $E = 0$[4] the second $E = 1$ and so on. The model for the times of eclipses is then

$$T(E) = T_0 + P_0 E + \frac{1}{2}\left(\frac{dP}{dt}\right)_0 P_0 E^2 + \frac{1}{6}\left(\frac{d^2P}{dt^2}\right)_0 P_0^2 E^3 + \sum_i \tau_i(E), \tag{2.10}$$

where T_0 is the time at which eclipse 0 occurs, P_0, $\left(\frac{dP}{dt}\right)_0$, and $\left(\frac{d^2P}{dt^2}\right)_0$ the orbital period of the eclipsing binary and its first and second derivatives measured at the reference time T_0. Excluding the final term, this is a Taylor expansion to third order, it would be possible to keep going to higher order but polynomials past cubic can be fit with a Keplerian. The τ's are Keplerians and can be expressed as (Irwin, 1959)

$$\tau = \frac{K}{\sqrt{1 - e^2\cos^2\omega}}\left[\frac{1 - e^2}{1 + e\cos\nu}\sin(\nu + \omega) + e\sin\omega\right], \tag{2.11}$$

where the orbital parameters are defined as in Section 1.2, and the semi-amplitude of the signal K depends on the mass of the planet/third body.

$$K = \frac{1}{c}\frac{M_2\sin i}{M_1 + M_2}\left(\frac{G(M_1 + M_2)}{4\pi^2}\right)^{1/3} P^{2/3}, \tag{2.12}$$

where M_1 is the total mass of the eclipsing binary, M_2 the mass of the third body, P and i the orbital period and inclination of the third body, and c and G are the speed of light and the gravitational constant.

τ depends on the true anomaly ν, which is a function of time, however as mentioned above, the true dependent variable is the Epoch. I use an approximation for the time $t \approx T_0 + P_0 E$. It would be possible to instead use the third order polynomial. Ideally $T(E)$ as derived above would be used, but that depends on τ and would therefore require a recursive algorithm. In most circumbinary cases the orbital period of the companion is significantly longer than the time difference it induces, such that this approximation is acceptable.

Another caveat worth noting is how to deal with the reference time T_0. It cannot just be any

[4]Using the convention $\mathbb{N} = \{0, 1, \ldots\}$

Table 2.8: Table of parameters used in the injection of a planet into an eclipse timing variation dataset.

Parameter	Injected value	Unit
Binary parameters		
$P_{\rm bin}$	2.823	days
$\dot{P}_{\rm bin}$	1×10^{-7}	
$\ddot{P}_{\rm bin}$	-1×10^{-10}	days^{-1}
Keplerian orbit parameters		
$P_{\rm pl}$	54.3	days
$K_{\rm pl}$	30.9	s
$e_{\rm pl}$	0.32	
$\omega_{\rm pl}$	2.88	rad
$T_{\rm peri,pl}$	5624.54	days
Other parameters		
$T_{\rm ref}$	5601.23	days
$\sigma_{\rm ETV}$	5	s

reference time since, based on Equation 2.10, T_0 must be the time at which the first eclipse (with epoch $E = 0$) occurs. In the ETVmodel I allow T_0 to be a free parameter on which a prior can be imposed. It should not be fixed to the measured time of the first eclipse as this could lead to biases.

I test the model on some synthetic data produced using Equation 2.10. The parameters of the injection are in Table 2.8. White noise is added to the data, and it is analysed with the ETVmodel. The results can be seen in Figure 2.10. The corner plot shows the posterior distributions from `kima` along with the injected values in blue. The phased ETV curve is also shown. The injected values are consistently recovered within the posterior distributions. There are a few correlations between parameters, ω and $T_{\rm peri}$ are postively correlated as is expected, and the various ephemeris parameters (T_0, P_0, $\dot{P}_0$, and $\ddot{P}_0$) are correlated as well. The sampler deals well with these correlations.

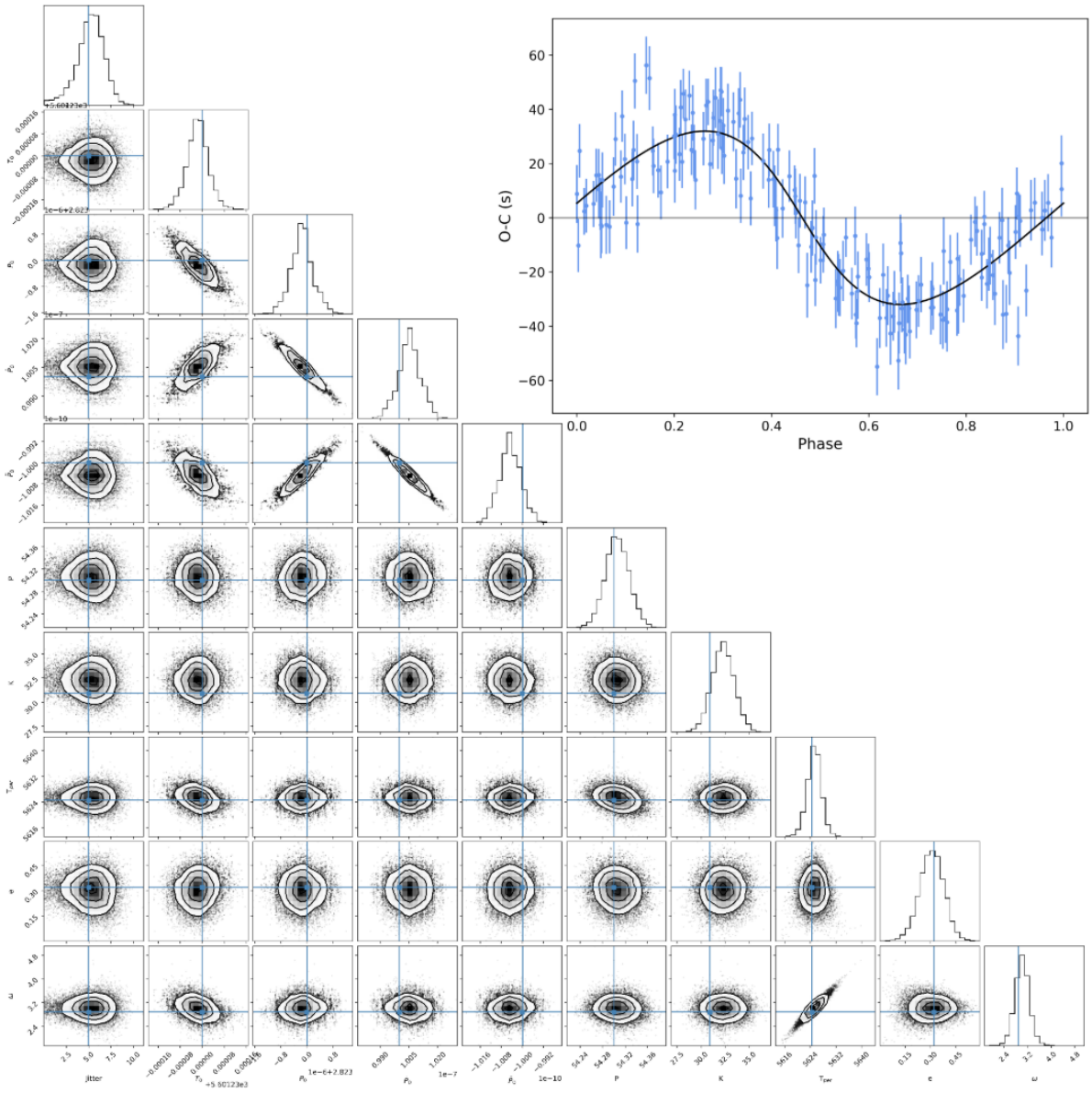


Figure 2.10: Corner plot showing the posteriors from the analysis of the synthetic eclipse timing data with the ETVmodel of `kima`, the injected values are shown in blue. The parameters are Jitter, T_0, P_0, $\left(\frac{dP}{dt}\right)_0$, $\left(\frac{d^2P}{dt^2}\right)_0$, $P_{\rm pl}$, $K_{\rm pl}$, $T_{\rm peri,pl}$, $e_{\rm pl}$, $\omega_{\rm pl}$.

2.4 `kima` GAIAmodel and RVGAIAmodel

2.4.1 Model for *Gaia* epoch astrometry

Gaia data release 4 (DR4) is planned for "no later than mid-2026", it will include the release for the first time of the individual epoch astrometric measurements for every source for the first 5.5 years of the *Gaia* mission. I have included a model in `kima` to fit the individual epoch astrometry from *Gaia* as well as one to simultaneously fit *Gaia* and radial velocity data. These are named GAIAmodel and RVGAIAmodel. *Gaia* is a scanning astrometric telescope as described in Section 1.3.5, this means that each measurement is only sensitive along the scan direction which changes all the time as the spacecraft precesses. The scan angle, ψ, is part of the known values at all times for the spacecraft, as well as the parallax factor, f_ϖ, based on where it is pointing in the sky. Given these and the times the measurements are taken t the model for the along-scan astrometry of a single-star with no companions is (Holl et al., 2023)

$$\omega_{ss} = \left(\Delta\alpha^\star + \mu_{\alpha^\star} t\right) \sin\psi + \left(\Delta\delta + \mu_\delta t\right) \cos\psi + \varpi f_\varpi, \tag{2.13}$$

where $\alpha^\star$ and δ are the source's coordinates at the reference time in right ascension and declination, $\mu_{\alpha^\star}$ and μ_δ the proper motions in the coordinate directions, and ϖ is the parallax. These five free parameters make of the *5-parameter astrometric solution* as referred to in the *Gaia* documentation. Accelerations have been included in the *Gaia* DR3 solutions to account for orbits that don't need to be fit with a full Keplerian, however I implemented the astrometric Keplerian such that the full model is (Holl et al., 2023)

$$\omega = \omega_{ss} + \sum_i \omega_{k,i}, \tag{2.14}$$

where for a given Keplerian

$$w_k = (BX + GY) \sin\psi + (AX + FY) \cos\psi. \tag{2.15}$$

In this equation, we use the Thiele-Innes parameters (Perryman, 2018), defined as

$$A = a_0 \left(\cos\omega\cos\Omega - \sin\omega\sin\Omega\cos i\right), \tag{2.16}$$

$$B = a_0 \left(\cos\omega\sin\Omega + \sin\omega\cos\Omega\cos i\right), \tag{2.17}$$

$$F = -a_0 \left(\sin\omega\cos\Omega + \cos\omega\sin\Omega\cos i\right), \tag{2.18}$$

$$G = -a_0 \left(\sin\omega\sin\Omega - \cos\omega\cos\Omega\cos i\right), \tag{2.19}$$

where a_0 is the semi-major axis of the induced orbit of the photocentre, and ω, Ω, i the orbital elements as defined in Section 1.2. X and Y are the orbital postition in elliptical rectangular coordinates.

$$X = \cos E - E, \tag{2.20}$$

$$Y = \sqrt{1-e^2}\sin E, \tag{2.21}$$

where E is the eccentric anomaly as discussed in Section 1.3.1 with $E - e\sin E = 2\pi(t - T_0)/P$.

These equations are for *Gaia* one-dimensional astrometric data. *Hipparcos* data is very similar and the analysis is almost identical, except that the scan angle definition is different (Sahlmann et al., 2011b; Holl et al., 2023).

These equations are implemented in `kima` within the GAIAmodel. There is the choice between sampling in the $(A - B - F - G)$ Thiele-Innes parameters or the $(a_0 - \omega - \Omega - i)$ Campbell parameters, this choice is made by selecting `thiele_innes = True/False` in the GAIAmodel setup. Either of these parameterisations works, but I favour using the Campbell parameters as these are more directly the observables, and one can define informed priors on them in a way which is not possible for the Thiele-Innes parameters.

2.4.2 Testing the GAIAmodel and RVGAIAmodel

Within `kima` I have developed a model for joint analysis of radial velocity data and *Gaia* epoch astrometry. The radial velocities give the motion along the line-of-sight complementing the

astrometry which gives the motion in the plane of the sky.

The two datasets are loaded separately and the analyses are as in each of the individual models (using Equation 2.14 for the *Gaia* data and Equation 1.16 for the radial velocities). The orbital paramters are all shared except for a reparameterisation of the amplitudes of signals. The masses of the star and companion can now be used as free parameters, and the radial velocity semi-amplitude (K) and the astrometric photocentre semi-major axis (a_0) can be calculated from the masses (along with other parameters).

The astrometric mass function is

$$f(M_2) = (M_1 + M_2)\left(\frac{M_2}{M_1 + M_2} - \frac{F_1}{F_0 + F_1}\right)^3 = \frac{(a_0/\varpi)^3}{(P/yr)^2}, \tag{2.22}$$

and therefore

$$a_0 = \left(\frac{P}{yr}\right)^{2/3} \varpi (M_1 + M_2)^{1/3} \left(\frac{M_2}{M_1 + M_2} - \frac{F_1}{F_0 + F_1}\right), \tag{2.23}$$

where F_0 and F_1 are the fluxes of the two bodies. If the flux-ratio F_1/F_0 is sufficiently small (i.e. for a planet around a star) then this simplifies to

$$a_0 = \left(\frac{P}{yr}\right)^{2/3} \varpi (M_1 + M_2)^{-2/3} M_2. \tag{2.24}$$

To get the radial velocity semi-amplitude from the masses and inclination Equation 2.6 is inverted,

$$K = \left(\frac{2\pi G}{P}\right)^{1/3} M_1 \sin i (M_1 + M_2)^{-2/3} (1 - e^2)^{-1/2}. \tag{2.25}$$

To show that the new models recover the parameters correctly, and to see the advantages that arise from fitting both radial velocities and astrometry together I test both GAIA and RVGAIA models with injection recovery. The injection is of a 1-planet system, generating the *Gaia* astrometry using Equation 2.14 and the radial velocities using Equation 1.16, both datasets are given extra white noise. The parameters of the injection are shown in Table 2.9. These injected parameters give a radial velocity semi-amplitude of $\approx$ 100 m/s, and a photocentre semi-major axis of $\approx$ 0.05 mas. The cadence of the simulated *Gaia* observations was calculated using the

Table 2.9: Table of parameters used in the injection of a planet into *Gaia* and radial velocity data.

Parameter	Injected value	Unit
Background astrometric parameters		
ϖ	14.32	mas
$\Delta\alpha^\star$	0.1	mas
$\Delta\delta$	-0.01	mas
$\mu_{\alpha^\star}$	46.3	mas/yr
μ_δ	10.8	mas/yr
Other parameters		
$M_\star$	1.2	$M_\odot$
$V_{\rm sys}$	0	m/s
$T_{\rm ref}$	57388.5	BJD - 2400000
Keplerian orbit parameters		
$P_{\rm pl}$	219.67	days
$M_{\rm pl}$	0.005	$M_\odot$
$e_{\rm pl}$	0.4	
$i_{\rm pl}$	0.6	rad
$\omega_{\rm pl}$	1.46	rad
$\Omega_{\rm pl}$	4.1	rad
$T_{\rm peri,pl}$	57028.288018	BJD - 2400000
Noise parameters		
$\sigma_{\rm Gaia}$	0.01	mas
$\sigma_{\rm rv}$	10	m/s

Gaia Observation Forecast Tool (GOST)[5], it was calculated for a star at the position of Kepler-16.

The results from using the new models on this synthetic data are shown in Figure 2.11 (GAIAmodel) and Figure 2.12 (RVGAIAmodel) with the injected values shown in blue. The datas and models are also shown in both cases. Both models recover the injected parameters, and this test shows the advantage of combining *Gaia* astrometry with ground-based radial velocities where possible. With *Gaia* data alone, there is a degeneracy whereby Ω and ω are not uniquely determined, this is because from the 2D projection of an orbit onto the plane of the sky it is not known which is the ascending node and which the descending node. Additionally, the two parameters are not so well constrained by the *Gaia* data alone. Including the radial velocities

[5] https://gaia.esac.esa.int/gost/

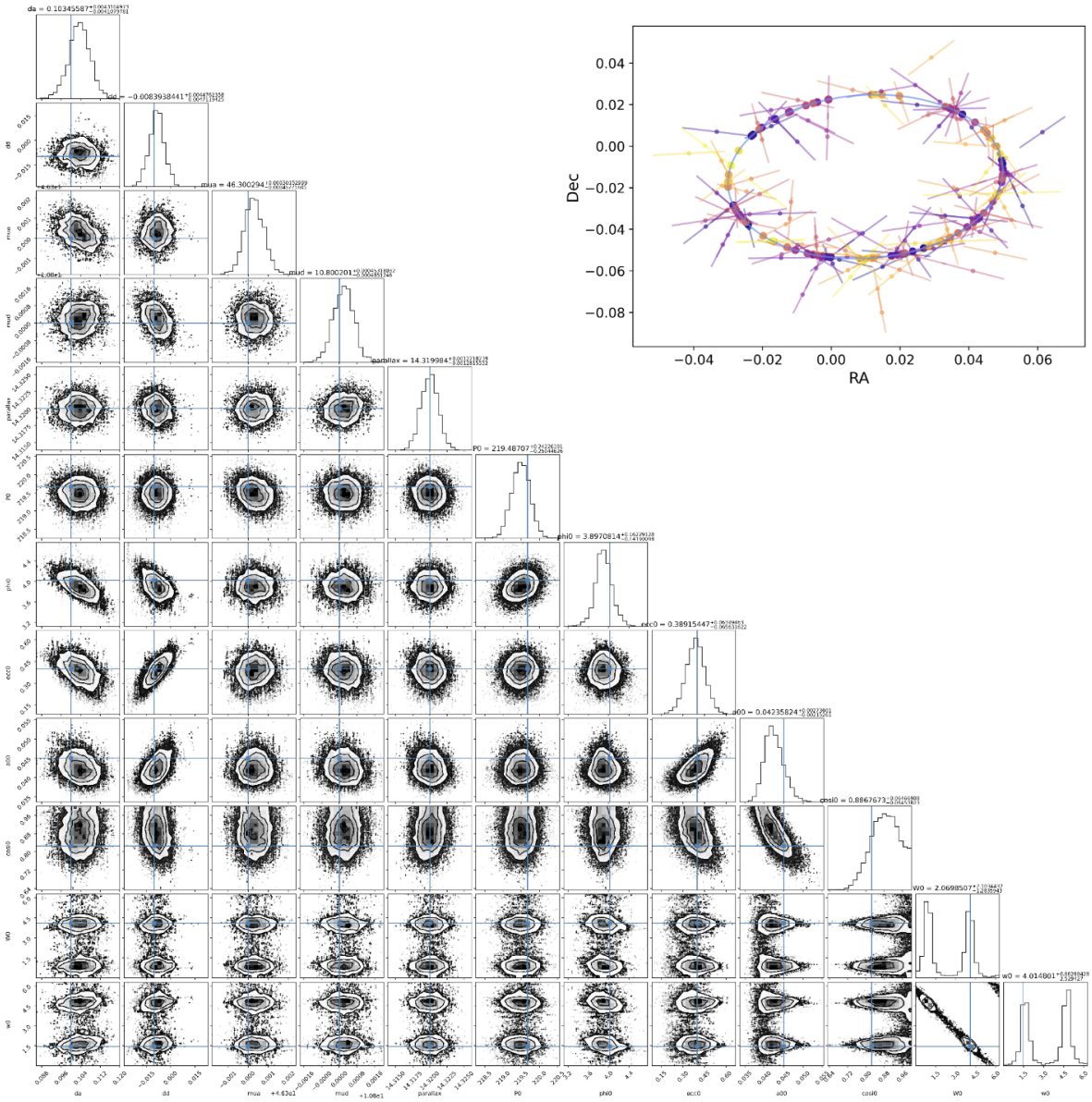


Figure 2.11: Corner plot showing the posteriors from the analysis of the synthetic *Gaia* data with the GAIAmodel of `kima`, the injected values are shown overtop. The paramters are $\Delta\alpha^\star$, $\Delta\delta$, $\mu_{\alpha^\star}$, μ_δ, ϖ, $P_{\rm pl}$, ϕ_0, $e_{\rm pl}$, $a_{0,\rm pl}$, $\cos i_{\rm pl}$, $\Omega_{\rm pl}$, $\omega_{\rm pl}$. The *Gaia* data and orbit model are shown in the top right, with the colours representing the time of the observations.

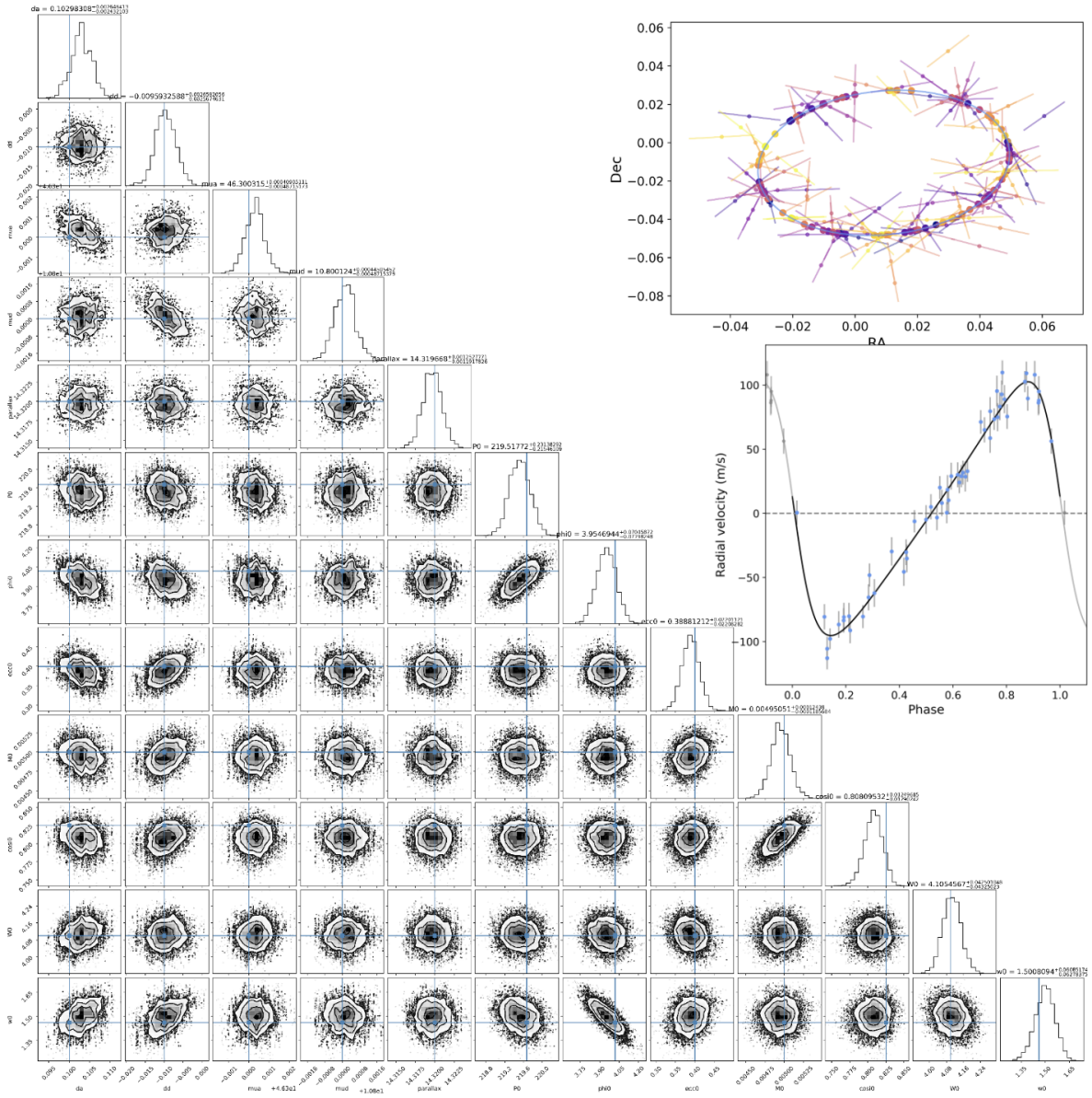


Figure 2.12: Corner plot showing the posteriors from the analysis of the synthetic *Gaia* and radial velocity data with the RVGAIAmodel of `kima`, the injected values are shown overtop. The paramters are $\Delta\alpha^\star$, $\Delta\delta$, $\mu_{\alpha\star}$, μ_δ, ϖ, $P_{\rm pl}$, ϕ_0, $e_{\rm pl}$, $M_{\rm pl}\sin i_{\rm pl}$, $\Omega_{\rm pl}$, $\omega_{\rm pl}$.The radial velocity and *Gaia* data and orbit models are shown in the top right, with the colours representing the time of the observations for the *Gaia* data.

removes the degenceracy, and improves the constraints on Ω and ω, consequently also improving the constraints on e and i.

Overall the GAIAmodel and RVGAIAmodel perform well and will allow for explotation of the *Gaia* data once the epoch astrometry is available. The ability to use `kima` for *Gaia* data analysis will mean that individual systems can be studied in depth with Bayesian model comparison for the number of planets (as is done for radial velocities, see Section 2.1.5) and allow for eccentric orbits to be studied. This will also allow for detection limits to be calculated for *Gaia* data in the same way as is done for radial velcoities (see Section 2.1.7). Ultimately these models will also be extended to best detect circumbinary planets by combining the GAIAmodel with the BINARIESmodel.

Chapter 3

Planets orbiting main-sequence binary stars: double-lined binaries

In this chapter, I include two published papers (Sairam et al., 2024a,b) that deal with double-lined binaries and a new method for the radial velocity extraction from double-lined binaries called DOLBY (DOuble Lined and BinarY). DOLBY has two implementations DOLBY-CCF and DOLBY-SD which were developed by Lalitha Sairam. These papers are first authored by her and part of their focus is on testing these methods of radial velocity determination. I was heavily involved in the projects, performing the orbital fit analysis of the radial velocity data that was produced by DOLBY and writing parts of the manuscripts. They can be found in Section 3.1 and Section 3.3.

This chapter also includes a discussion of the one-two punch and one-punch methods in Section 3.2, and an investigation of *Gaia*'s potential yield of astrometric circumbinary planet detections in Section 3.4.

3.1 New methods for radial-velocity measurements of double-lined binaries, and detection of a circumbinary planet orbiting TIC 172900988

The paper that follows presents DOLBY, and compares it to previous algorithms. The test system is TIC 172900988 which has a transiting circumbinary planet. The paper showcases a new radial velocity reduction method and applies it to the TIC 172900988 system, detecting the circumbinary planet but at a shorter period than was favoured by the published photodynamical fit. The DOLBY radial velocity reduction is shown to be an improvement relative to the TODCOR and TODMOR methods which are unable to give precise enough data to detect the planet. The main conclusion is that with adequate reduction techniques double-lined binaries can be suitable to circumbinary planet detection with radial velocities.

- Section 3.1.1 - Section 1 Introduction: written by Lalitha Sairam with some contribution from Amaury Triaud and from me.

- Section 3.1.2 - Section 2 GP-Based radial velocity extraction: written by Lalitha Sairam, she developed the DOLBY code.

- Section 3.1.3 - Section 3 Application to TIC 172900988: written by Lalitha Sairam, she analysed the spectra to produce the radial velocities bith with DOLBY and the other methods with which we compare DOLBY.

- Section 3.1.4 - Section 4 Results: written by me with some contribution from Lalitha Sairam. I analysed the radial velocity data to detect the circumbinary planet and perform the parameter estimation; investigated the one-two punch method (Kostov et al., 2020a), including it into the `kima` fit; performed the detection limit analysis; and investigated the apsidal precession of the binary and showed it to be consistent with the detected planet's mass and period.

- Section 3.1.5 - Section 5 Conclusions: written by Lalitha Sairam with some contribution from Amaury Triaud and from me.

- Section 3.1.6 - Appendix: Supporting figures and tables generated by Lalitha Sairam (Figures A1,A2,A3, and A5, Table A2) and by me (Figures A4 and A6, Table A1)

Monthly Notices of the ROYAL ASTRONOMICAL SOCIETY

MNRAS **527,** 2261–2278 (2024) https://doi.org/10.1093/mnras/stad3136
Advance Access publication 2023 November 14

New methods for radial-velocity measurements of double-lined binaries, and detection of a circumbinary planet orbiting TIC 172900988

Lalitha Sairam [1,2★] Amaury H. M. J. Triaud [1★] Thomas A. Baycroft [1★] Jerome Orosz,[3] Isabelle Boisse,[4] Neda Heidari,[5] Daniel Sebastian [1] Georgina Dransfield [1] David V. Martin [6] Alexandre Santerne [4] and Matthew R. Standing [7]

[1]*School of Physics and Astronomy, University of Birmingham, Edgbaston, Birmingham B15 2TT, UK*
[2]*Institute of Astronomy, University of Cambridge, Madingley Road, Cambridge CB3 0HA, UK*
[3]*Department of Astronomy, San Diego State University, 5500 Campanile Drive, San Diego, CA 92182, USA*
[4]*Aix Marseille Univ, CNRS, CNES, LAM, Aix Marseille Univ, F-13007 Marseille, France*
[5]*Institut d'astrophysique de Paris, UMR 7095 CNRS Université Pierre et Marie Curie, 98 bis, Boulevard Arago, F-75014 Paris, France*
[6]*Department of Physics and Astronomy, Tufts University, 574 Boston Avenue, Medford, MA 02155, USA*
[7]*School of Physical Sciences, The Open University, Milton Keynes, MK7 6AA, UK*

Accepted 2023 October 10. Received 2023 September 7; in original form 2023 May 31

ABSTRACT

Ongoing ground-based radial-velocity observations seeking to detect circumbinary planets focus on single-lined binaries even though over 9 in every 10 binary systems in the solar neighbourhood are double lined. Double-lined binaries are on average brighter, and should in principle yield more precise radial velocities. However, as the two stars orbit one another, they produce a time-varying blending of their weak spectral lines. This makes an accurate measure of radial velocities difficult, producing a typical scatter of 10–15 m s^{-1}. This extra noise prevents the detection of most orbiting circumbinary planets. We develop two new data-driven approaches to disentangle the two stellar components of a double-lined binary, and extract accurate and precise radial velocities. Both approaches use a Gaussian process regression, with the first one working in the spectral domain, whereas the second works on cross-correlated spectra. We apply our new methods to TIC 172900988, a proposed circumbinary system with a double-lined binary, and detect a circumbinary planet with an orbital period of 150 d, different than previously proposed. We also measure a significant residual scatter, which we speculate is caused by stellar activity. We show that our two data-driven methods outperform the traditionally used TODCOR and TODMOR, for that particular binary system.

Key words: techniques: radial velocities – planets and satellites: detection – planets and satellites: gaseous planets – planets and satellites: individual: TIC172900988 – binaries: eclipsing – binaries: spectroscopic.

1 INTRODUCTION

Planets orbiting around both stars of a binary star system are called *p-type* or *circumbinary* planets. The discovery of Kepler-16 (Doyle et al. 2011) marked the first confirmation of the existence of these long-theorized planets (Borucki & Summers 1984; Schneider 1994). Since then, the *Kepler* and *TESS* missions have identified an additional 13 transiting circumbinary planets in 11 binary star systems (e.g. Martin 2018; Kostov et al. 2020; Socia et al. 2020; Kostov et al. 2021). While the radial velocity method is a highly effective way to detect exoplanets since Mayor & Queloz (1995), only two circumbinary planets have been detected using this method: Kepler-16 b (Triaud et al. 2022) and TOI-1338/BEBOP-1 c (Standing et al. 2023).

Ground-based radial-velocity surveys of binary stars are more efficient, and less biased than transit surveys (Martin et al. 2019) and thus can construct a more insightful picture of the properties of the circumbinary planet population. The BEBOP survey (Binaries Escorted By Orbiting Planets; Martin et al. 2019) began in 2017 as a dedicated, blind, radial-velocity survey of single-lined eclipsing binary stars. The survey reaches a precision of a few metres per second (Triaud et al. 2022). However, the BEBOP survey currently remains confined to highly unequal stellar-mass pairs where the secondary's mass is usually less than 30 per cent of the primary star (Triaud et al. 2017; Martin et al. 2019). These single-lined binaries represents only around 8 per cent of all binaries; however, the remaining 92 per cent of binaries are double-line binaries (Kovaleva et al. 2016). Prior to the BEBOP survey, an extensive survey of double-line binaries was carried out by the TATOOINE survey (Konacki et al. 2009, 2010). However, TATOOINE did not yield any circumbinary planets and reported a 10–15 m s^{-1} scatter in the data, enough to hide most exoplanets. Konacki et al. (2009) had to first deconvolve their spectra to remove an iodine-cell absorption spectrum, then they use TODCOR (Zucker & Mazeh 1994) to obtain a guess radial velocity for each component of the

★ E-mail: lalitha.sairam@ast.cam.ac.uk (LS); a.triaud@bham.ac.uk (AHMJT); txb187@student.bham.ac.uk (TAB)

© 2023 The Author(s).
Published by Oxford University Press on behalf of Royal Astronomical Society. This is an Open Access article distributed under the terms of the Creative Commons Attribution License (http://creativecommons.org/licenses/by/4.0/), which permits unrestricted reuse, distribution, and reproduction in any medium, provided the original work is properly cited.

Downloaded from https://academic.oup.com/mnras/article/527/2/2261/7420283 by Health Services Management Centre Library user on 08 October 2024

binary. Then they perform their tomographic deconvolution method to accurately measure the radial velocity for each of the stellar components.

Radial velocities are also often extracted by cross-correlating the observed spectrum with a template spectrum, or with a line-list mask (the method we use; e.g. Baranne et al. 1996). When the template matches the observed spectrum a strong signal is recorded. The cross-correlation method is convenient to understand what might help address radial velocity scatter.

In addition to the large cross-correlation function (CCF) signal, weaker signals on either side of the main signal are also recorded. They are caused by coincidental correspondence between the template and the spectrum, which we call *wiggles*. The wiggles exhibit pseudo-static behaviour over time in relation to the main CCF signal. We refer to these wiggles as pseudo-static because their characteristics may vary depending on the observation conditions. As an example, Fig. 1 depicts a CCF time-series showing the strong stellar signal for HD 189733 but also its weaker, and stable wiggle signals.

In the context of double-line binary stars, the presence of two bright stars leads to two distinct, and strong CCF signals that vary in time based on the respective masses and orbital parameters of the binary system. Fig. 2 illustrates this time-varying signal, as well as the accompanying wiggles. Because there are two stars, there are two sets of wiggles. Each can interact with the strong CCF signal of the other star, and blending of a wiggle from star A with the CCF of star B, can lead to an error in estimating the radial velocity of star B (and vice versa). This effect also happens on the spectral side, where weak lines from star A can blend with strong lines of star B. If the template used for deconvolution is incomplete, this will cause a similar issue when estimating radial velocities. This phenomenon, which we refer to as the *double-lined binary problem*, is likely the issue that prevents the discovery of circumbinary planets.

With this effect in mind, it is obvious that a data-driven approach needs to be taken since no template can properly reproduce every spectral feature. Any error on the spectrum/template spectrum of one star can affect the radial-velocity measurement of the other star.

In this paper, we present two new methods to derive precise radial velocities of double-lined binaries. We treat the wiggles as a correlated signal. Such correlated signals are typically and accurately treated in a data-driven way using Gaussian processes (GP; Aigrain, Parviainen & Pope 2016). This method has had several successes (e.g. Czekala et al. 2017; Rajpaul, Aigrain & Buchhave 2020) within the exoplanet field.

The structure of the paper is as follow: Section 2 we introduce the GP framework. We then describe the two new techniques we developed for deriving radial velocities of double-lined binary stars. In Section 3, we choose to apply our two methods to the double-lined binary system TIC 172900988 because of the presence of a planet in the system that allows to test for the recovery of a Keplerian signal. In Section 4, we describe how we analyse the resulting radial velocities to model a binary's Keplerian motion, search for a circumbinary planet and infer its orbital parameters. Finally, we compare the radial velocities derived from our two new methods, and compare them to traditional and publicly available methods of measuring radial velocities (TODCOR and TODMOR; Mazeh & Zucker 1994; Zucker & Mazeh 1994; Zucker et al. 2004). We also discuss the implication of detecting a circumbinary planet in TIC 172900988 binary system. We conclude the paper with a summary of our key results in Section 5.

2 GP-BASED RADIAL VELOCITY EXTRACTION

In this section, we provide a brief overview of the GP framework, which is a non-parametric Bayesian modelling technique that we use to infer the spectra of double-lined binary star systems. A GP is a type of stochastic process that describes the distribution of a group of random variables. It can be thought of as an extension of kernel regression to probabilistic models. Using non-parametric GPs to model the unknown wiggle function of double-lined binaries is a powerful and flexible approach (Rasmussen & Williams 2006).

A normal distribution is often represented as $\mathcal{N}(\mu, \sigma^2)$. If a random variable x is normally distributed with mean and variance, it can be expressed as

$$x \sim \mathcal{N}(\mu_x, \Sigma_{xx}), \tag{1}$$

with μ_x represents mean vector and Σ_{xx} represents the covariance matrix. The covariance matrix describes the pairwise covariance between the different elements of the input data x.

The likelihood that a set of observations y is drawn from GP can be written as

$$\ln \mathcal{L} = \ln p(y|x, \phi, \theta), \tag{2}$$

$$= -\frac{1}{2}(y-\mu)^{\mathrm{T}} K^{-1}(y-\mu) - \frac{1}{2} \ln |K| - \frac{N}{2} \ln(2\pi), \tag{3}$$

where ϕ and θ are hyperparameters of the mean and covariance functions. In equation (3), K refers to the covariance matrix associated with the GP. The elements of the covariance matrix depend on the chosen covariance function and the values of the hyperparameters θ. N represents the number of elements in the vector y, which contains the observations. Evaluating this likelihood provides a posterior distribution of the hyperparameters.

2.1 Method 1: efficient spectral decomposition using GP (SD-GP)

The observed spectra of a double-line binary star system can be modelled as a GP (e.g. Czekala et al. 2017). The spectrum of a single star can be represented as a function $f(\lambda)$, where λ is the wavelength. If $\lambda > 0$, the observed spectrum of a single star can be modelled as a function $f(\lambda)$ with a mean function $\mu(\lambda)$ and a covariance kernel $k(\lambda, \lambda')$. If the observed spectrum has finite inputs $0 < \lambda_1 < \lambda_2 < \ldots\ldots < \lambda_w$, then the vector $[f(\lambda_1), f(\lambda_2), \ldots\ldots f(\lambda_w)]$ has a multivariate Gaussian distribution with a mean function $[\mu(\lambda_1), \mu(\lambda_2), \ldots\ldots \mu(\lambda_w)]$ and a covariance matrix with $k(\lambda_i, \lambda_j)$ as its elements, where k is the kernel function and $i, j = 1, 2, \ldots, w$. Therefore, the intrinsic continuous spectrum of a star can be assumed to be a function f generated from a GP:

$$f(\lambda) \sim \mathrm{GP}\left(\mu(\lambda), k(\lambda, \lambda')\right). \tag{4}$$

The observed spectra of a spectroscopic binary are composed of spectral lines from both stars as a composite. Due to the orbital motion of each stars in the binary, a Doppler shift is induced to the rest-frame stellar spectra that are observed in the composite spectra simultaneously. For a star moving with radial velocity v, the rest-frame wavelength of the observed spectra are shifted to

$$\lambda(v) = \left(\frac{c+v}{c-v}\right)^{\frac{1}{2}} \lambda_0, \tag{5}$$

where c is speed of light.

We describe the radial velocities of binary stars as a function of time using seven parameters: the semi-amplitude of the primary star

Downloaded from https://academic.oup.com/mnras/article/527/2/2261/7420283 by Health Services Management Centre Library user on 08 October 2024

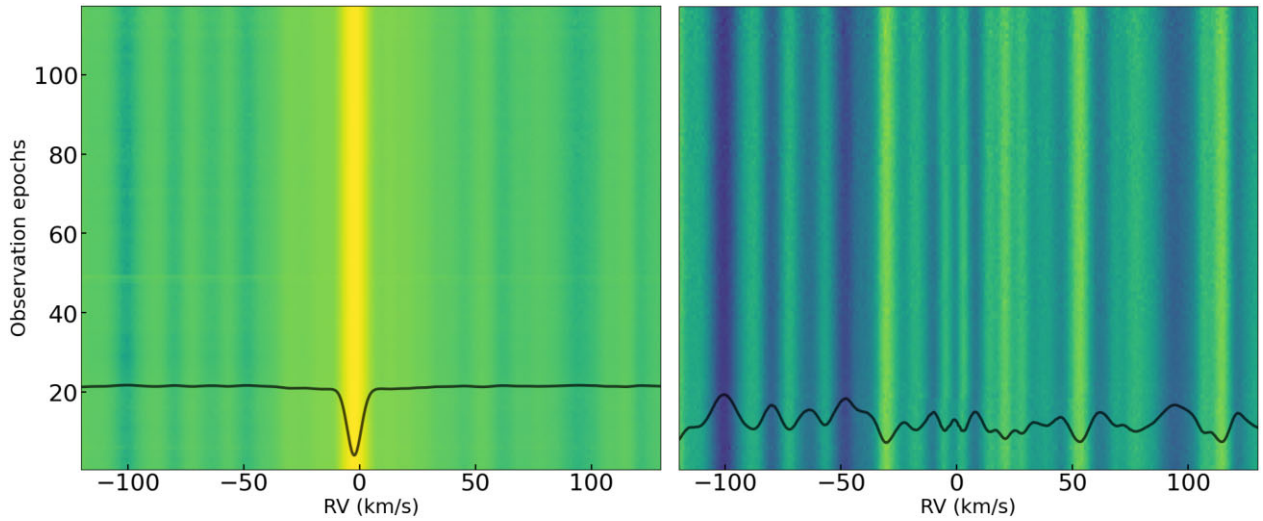


Figure 1. Left panel: A time-series of CCF for HD 189733. The bright profile shows the stellar profile. The wiggles appear on either side of bright profile. The black profile is the median CCF of all epochs. Right panel: Residual map of time-series on removal of stellar profile. Wiggles are seen as alternating static bands. Overlaid in black is the median wiggle of all epochs.

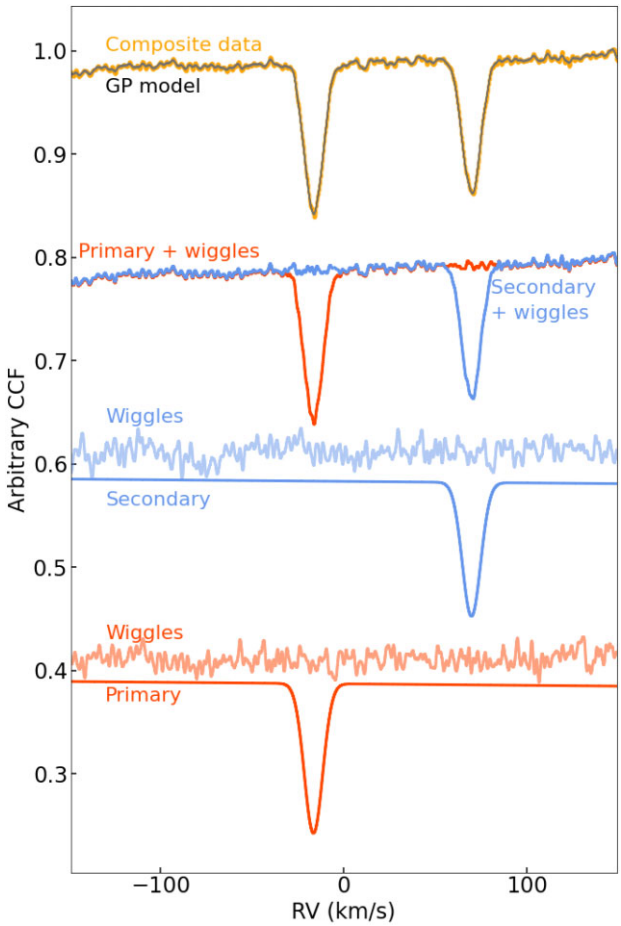


Figure 2. Schematic diagram showing the double-line binary problem and our solution to the problem using method 2 (CCF-GP).

(K_A), the binary stars mass ratio $\left(q = \frac{M_B}{M_A} = \frac{K_A}{K_B}\right)$, binary orbital period (P), the eccentricity (e), the argument of periastron (ω), the epoch of periastron (T_0), and systemic velocity (γ). The velocity of the primary and secondary stars as a function of time is

$$v_A = K_A[\cos(\omega + f(t)) + e\cos\omega] + \gamma \tag{6}$$

and

$$v_B = -\frac{K_A}{q}[\cos(\omega + f(t)) + e\cos\omega] + \gamma, \tag{7}$$

respectively.

For a single-epoch observation of a double-line binary star, we assume that the observed composite spectrum (s) is a sum of realization f for the primary star and g for the secondary star along with N, the noise process realization:

$$s = f + g + N, \tag{8}$$

$$\sim \mathcal{N}(\mu_f, \Sigma_f) + \mathcal{N}(\mu_g, \Sigma_g) + \mathcal{N}(0, \Sigma_N), \tag{9}$$

$$\sim \mathcal{N}(\mu_f + \mu_g, \Sigma_f + \Sigma_g + \Sigma_N), \tag{10}$$

where Σ_f and Σ_g are covariance matrices describing the primary and secondary star. We evaluate the covariance matrix Σ_f and Σ_g using the wavelengths corresponding to the primary and secondary components in their rest frame with the kernel function (equation 11). In Fig. 3, we show the realization f and g for both components of the binary star.

Similar to Rajpaul, Aigrain & Buchhave (2020), we choose the Matérn kernel to model our spectra. The Matérn kernel is often used when modelling spectra because it is a flexible and versatile covariance function that can capture a wide range of smoothness and correlation properties. The Matérn covariance kernel specifies the covariance between two pixels λ_i and λ_j as

$$k_{ij}(r_{ij}|\theta) = \sigma_f^2\left(1 + \frac{\sqrt{3}r}{\sigma_l}\right)\exp\left(-\frac{\sqrt{3}r}{\sigma_l}\right), \tag{11}$$

where r_{ij} has units of km s^{-1}

$$r_{ij} = r(\lambda_i, \lambda_j) = \frac{c}{2}\left|\frac{\lambda_i - \lambda_j}{\lambda_i + \lambda_j}\right|, \tag{12}$$

with c as the speed of light, σ_l is the characteristic length-scale, and σ_f is the signal standard deviation.

Downloaded from https://academic.oup.com/mnras/article/527/2/2261/7420283 by Health Services Management Centre Library user on 08 October 2024

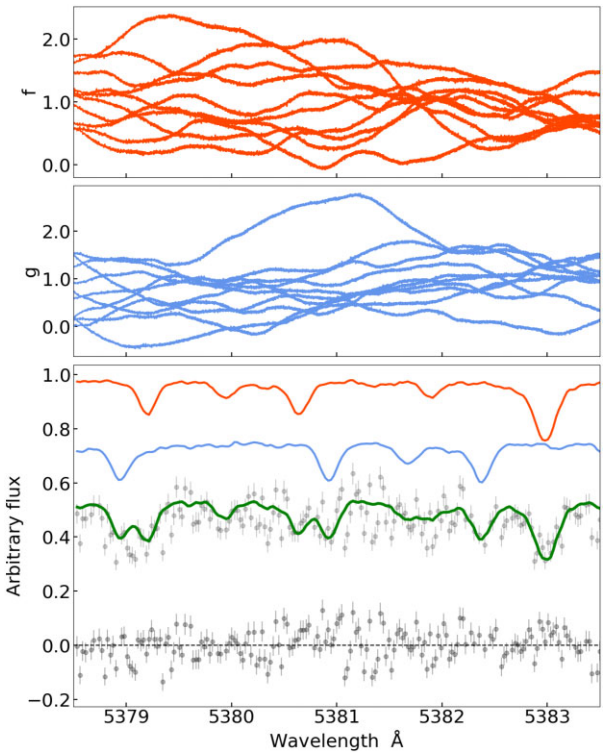


Figure 3. Depicted in the top two panels are the multivariate realization vector from prior distribution draw for GP hyperparameters of the primary and the secondary stars. The realizations are not constrained by the data. The bottom panel depicts the mean prediction (in green) from the posterior predictive distribution of GP drawn by conditioning on the observed data from a single-epoch observation. The orange and blue in the bottom panel represents the primary and the secondary star with an arbitrary offset. The bottom panel also includes the residuals.

In practice, we analyse our spectra with the following steps and assumptions:

(a) The observed composite spectra are divided into smaller wavelength subsets, which we call *chunks*. The radial velocity shift is computed separately for each chunk. In principle, this step is not necessary, but GPs are computationally intensive and without breaking each spectrum into smaller components, the calculation become intractable.

(b) We allow separate values for GP hyperparameters σ_f and σ_l (i.e. $\{\sigma_f, \sigma_l\}_f$, $\{\sigma_f, \sigma_l\}_g$) for each star of the binary system. This allows an optimal reconstruction of the spectrum taking into account the different spectral types of the stars. The mean function that is obtained by drawing samples from the GP distribution is shown in Fig. 3 (bottom panel).

(c) Rather than forcing a single set of hyperparameters to model a spectrum, we allow different sets of hyperparameters for different regions of a spectrum.

(d) To set reasonable initial values for the radial velocities of the primary and secondary stars, we first fit simple Gaussian functions to the CCFs of each component. We then use that result to define a flat/uniform prior distribution on the radial velocities of each component. A flat prior distribution assigns equal probability density to all values within a specified range. The bounds of the flat prior distribution can be defined as the minimum and maximum values of the range, which would depend on the expected range of radial velocities for each component. We chose the bounds carefully to avoid assigning unrealistic probabilities to certain values. We then use a χ^2 likelihood function to refine these estimates.

(e) We simultaneously explore the posterior distribution of the radial velocities and the GP hyperparameters using a Markov chain Monte Carlo (MCMC) sampler (the EMCEE PYTHON package; Goodman & Weare 2010; Foreman-Mackey et al. 2013).

(f) We reiterate these steps for each chunk, and then filter bad radial velocity estimates caused by telluric absorption, stellar activity contamination, or instrumental systematics.

(g) The radial velocities from individual chunks are combined by computing a weighted average. The weights used for computing the weighted average of the radial velocities from individual chunks are determined by the uncertainties associated with the radial velocity estimates obtained from each chunk.

(h) We normalize the observed spectra, and for the GP, we set the mean function to a constant value of 1.0 ($\mu = 1$).

2.2 Method 2: CCFs modelled using GP (CCF-GP)

Method 1 involves dividing the observed spectrum covering a large wavelength range into smaller chunks and applying a GP regression on each chunk. This process involves computing the kernel matrix, inverting it, and multiplying it by the training set data. The computational complexity of GP regression is $\mathcal{O}(N^3)$, where N is the number of data points in each chunk. Therefore, the overall complexity of method 1 would be $\mathcal{O}(MN^3)$, where M is the number of chunks in the spectrum. This can be computationally very expensive. Hence, we also develop an alternative method.

This alternative approach is similar to the previous one but instead of modelling the entire spectrum chunk by chunk, we instead model the cross-correlated spectra, which are a typical output of instruments such as HARPS, SOPHIE, and ESPRESSO (Baranne et al. 1996; Pepe et al. 2002; Perruchot et al. 2008). We assume that the CCFs are samples of GP. The mean function ($\mu(x)$) is constructed as the sum of two Gaussian functions. The covariance kernel function is used to model the correlated wiggle signal found within the CCF.

We employ a Gaussian fit jointly with a GP model for each of the components of binary. The baseline mean-function is a Gaussian function for each of the component of the binary

$$\mu(x) = 1 - \mathrm{A}_1 \exp\left(-\frac{(x-\mathrm{B}_1)^2}{2\mathrm{C}_1^2}\right) - \mathrm{A}_2 \exp\left(-\frac{(x-\mathrm{B}_2)^2}{2\mathrm{C}_2^2}\right), \tag{13}$$

where A_1, B_1, C_1, A_2, B_2, C_2 are free hyper-parameters. A_1 and A_2 correspond to the amplitude of the Gaussian, which represents the contrast of primary and secondary components. B_1 and B_2 represent the radial velocities of primary and secondary stars, while C_1 and C_2 correspond to the standard deviation of the Gaussian, which represents the full width at half-maximum (FWHM).

We create a custom model class that inherits from *celerite.modeling.Model*, which is used to define the mean function of the GP. We use a Matérn covariance kernel (equation 11), implemented in `celerite` (Foreman-Mackey et al. 2017) to model the correlated wiggle signal. We set bounds on the input parameters for the model and the hyperparameters of the Matérn kernel, and then creates two Matérn kernels, one for each Gaussian component, which are combined into a single kernel.

We optimize the GP model using the L-BFGS-B method (Byrd et al. 1995), which allows us to impose bounds on the parameters

Downloaded from https://academic.oup.com/mnras/article/527/2/2261/7420283 by Health Services Management Centre Library user on 08 October 2024

while minimizing the negative log-likelihood of the model. We use MCMC sampling to explore the posterior distribution of the hyperparameters. For this, we also use the EMCEE PYTHON package (Goodman & Weare 2010; Foreman-Mackey et al. 2013) with 50 walkers and a burn-in of 100 iterations. We set broad uniform priors for each hyperparameter, and run the final MCMC with 5000 iterations to converge on a solution. We take the median of the posterior distribution as the optimum solution for each hyperparameter. We then compute the 16th, 50th (median), and 84th percentiles of the posterior distribution. The uncertainties of the hyperparameters are taken as the difference between the 84th and 50th percentile (upper bound) and 50th and 16th percentile (lower bound).

The most intensive part of this method is the optimization of GP hyperparameters which is performed by L-BFGS-B method. However, for this method the main computational bottleneck could likely be the MCMC sampling step, which has a complexity that scales with the size of the CCF.

3 APPLICATION TO TIC 172900988

TIC 172 900 988 is an eclipsing double-lined binary system consisting of two stars with spectral types F9 and G0. The orbital period of the system is approximately ∼19.7 d. Kostov et al. (2021) reported the first discovery of a circumbinary planet via what is sometimes called the '1–2 punch technique,' where multiple transits occur during one conjunction event, the planet transits once over the primary and once over the secondary. Kostov et al. (2021) used a photodynamical analysis but did not find a single solution. The planetary radius is constrained at $R_p = 11.25 \pm 0.44$ R$_\oplus$. The planetary masses are proposed within a range of $823 < m_p < 981$ m$_\oplus$, and the orbital period within $188 < P_p < 204$ d.

We have collected radial-velocities with SOPHIE on 10 double-line binaries (including six from Konacki et al. 2009, 2010) in order to test our methods to different spectral types, orbital solutions, relative velocities, etc., and observe their limitations. Given the presence of a planet within the TIC 172 900 988 system, it serves as a good first testbed to demonstrate our ability to extract radial-velocities without removing a Keplerian signal. By focusing first on a known circumbinary planet host, we can evaluate the effectiveness and accuracy of our approaches. We plan to follow this paper with another paper analysing the rest of the sample that will show how precise our new methods are.

3.1 Observation

We collected 62 epochs of high-resolution spectra between 2020 October 16 and 2023 May 05 using the SOPHIE spectrograph mounted on the 1.93 m telescope at Observatoire de Haute Provence (OHP) in France (Perruchot et al. 2008). The spectra cover a wavelength range of 3872–6943 Å in 39 spectral orders, with a resolving power of $\delta\lambda/\lambda \approx 75\,000$. The exposure times ranged from 600 to 1800 s depending on the seeing conditions at OHP. They have an median signal-to-noise ratio (SNR) of 32 at 5500 Å. These are SNR for the composite spectra of the TIC 172 900 988 with an average flux fraction of 0.86. This corresponds to an SNR of ∼17 and ∼14 at 5500 Å for the primary and the secondary, respectively. SOPHIE was designed to detect exoplanets with a long-term stability of 2 m s^{-1}. The observations were taken in objAB mode, where one fibre is used to observe the starlight and another fibre is used to observe the sky brightness to estimate the background contamination such as that produced by moonlight. The wavelength calibration was performed before the night starts using a Thorium–Argon lamp and a Fabry–Pérot, fed into both fibres. Additional Fabry–Pérot calibrations are obtained roughly every 2 h within the night. The spectra are extracted using the SOPHIE automatic pipeline (Bouchy et al. 2009) and the resulting wavelength-calibrated spectra are correlated with a numerical binary mask to obtain the CCFs (Baranne et al. 1996; Pepe et al. 2002). We used a G2 mask for the correlation.

3.2 Method 1 – SD-GP

We first obtain the spectra and cross-correlate them using the SOPHIE Data Reduction Software. To effectively apply Method 1, we work with two-dimensional spectra (e2ds) at the instrument resolution instead of using 1D spectra (s1d), which operate at the pixel sampling level. We measure the radial velocities of both stellar components at the time of observation using a Gaussian fit to their cross-correlated spectra. Each SOPHIE spectrum covers from 3872 Å to 6943 Å. We divide each observed spectrum into chunks of 5Å each, totalling to 615 chunks. For each chunk, we apply the SD–GP method to measure the radial velocities of both stars at each epoch. Using the calculated velocities and the parameters of the GP, we deconvolve the composite spectra into the individual spectrum of both individual stars for each epoch, by optimizing the parameters of the model to fit the observed spectra. In Fig. A1 (left panels), we give examples of this step of our analysis, where we show median of posterior predictive distribution of the predicted composite spectrum and the reconstructed spectra of each component of the binary. For better visualization, we have arbitrarily included an offset to each spectrum. Note that the reconstructed spectrum matches the shape of the input composite spectrum. It is important to note that there may be chunks where the spectral lines are not present, possibly due to the continuum dominating the spectrum (Fig. A1, right panels), resulting in large uncertainties in the radial velocity (RV) measurements. After repeating this process for each chunk of spectra, we obtain the radial velocities for each star in the binary system at each epoch. We then apply outlier removal using a Student's-*t* distribution to remove any radial velocities that lie outside of the 95 per cent confidence interval. The remaining radial velocities are assigned weights considering the associated uncertainties to estimate the weighted average radial velocities for the binary system (see Section 2.1). We then estimate the uncertainty of the combined radial velocity by propagating the uncertainties of each individual chunk through the weighted average.

3.3 Method 2 – CCF-GP

All 62 epochs of spectroscopic data from SOPHIE were cross-correlated with a G2 mask. To determine the radial velocities of the primary and secondary star in the binary system TIC 172900988, we apply the CCF-GP to the resulting CCFs. To measure the radial velocities of the primary and secondary stars, we fit the CCF with a double Gaussian function, with the two Gaussians representing the primary and secondary stars, and two GPs to model each of *wiggles* caused by coincidental correspondence with the mask. In Fig. 4 (left panel), we show the CCF time-series along with the wiggles. We explore the posterior distribution of hyperparameters using MCMC sampling. We then calculate the 16th, 50th, and 84th percentiles of the samples of the radial velocity, FWHM, and contrast obtained from the MCMC simulation. These percentiles correspond to the lower uncertainty limit, the median value, and the upper uncertainty limit of the hyperparameters, respectively. The residuals following the subtraction of each component of the binary and the wiggles are shown in Fig. 4 (right panel).

Downloaded from https://academic.oup.com/mnras/article/527/2/2261/7420283 by Health Services Management Centre Library user on 08 October 2024

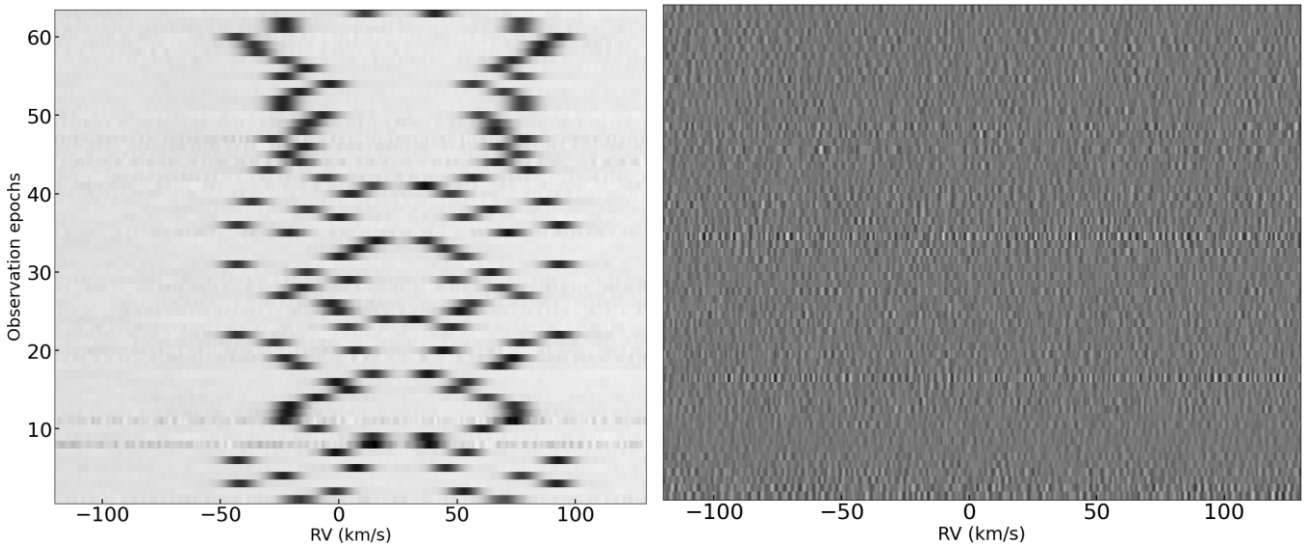


Figure 4. Left panel: A time-series of cross-correlation for double-line binary star showing the strong signals for each components. The wiggles appear as dark bands on either sides of the strong signal. Right panel: The wiggles as modelled by method 2 (CCF-GP).

3.4 TODCOR and TODMOR

We also compute radial velocities using traditional methods such as Two-Dimensional Correlation (TODCOR) and TODMOR (Two-Dimensional Modelling and Reconstruction). TODCOR is a method that uses a two-dimensional cross-correlation function (2D-CCF) to measure the radial velocities of the primary and secondary stars in a binary system (Mazeh & Zucker 1994; Zucker & Mazeh 1994). A modern implementation of TODCOR for multiorder spectra is TODMOR (Zucker et al. 2004). TODMOR also uses a two-dimensional model of the observed spectra. To measure the radial velocities of the primary and secondary stars TODMOR compares each stellar component with a template spectrum matching their spectral type.

In the next section, we compare our two new methods to results produced by TODCOR and TODMOR. As such we apply TODCOR and TODMOR to the same observed spectra that we used for our own approaches. To apply TODCOR and TODMOR, first we need to correct the SOPHIE spectra for the instrumental blaze function, and detrend the pseudo-continuum. We then use the PHOENIX stellar model (Husser et al. 2013) to determine the best-matching theoretical spectra for the primary and secondary stars, and use these to optimize the 2D-CCF for each order of the spectra. We apply TODMOR to each SOPHIE order and determine the radial velocities of both components, discarding orders strongly influenced by telluric lines.

TODCOR and TODMOR use template spectra for primary and secondary stars and cross-correlate them to the observed composite spectrum to determine the radial velocities. Neither TODCOR nor TODMOR treat the wiggles.

4 RESULTS

4.1 Binary model

Each of the measured radial velocities obtained from method 1 (Sections 2.1 and 3.2), method 2 (Sections 2.2 and 3.3), TODCOR, and TODMOR (Section 3.4) are independently modelled. We utilize KIMA, an open-source software package for fitting radial velocities, to determine the physical parameters of the binary (Faria et al. 2018). Specifically, an updated KIMA package is used, which now includes simultaneous fitting of both components of double-lined binaries, correction for General Relativity effects, and that can fit for apsidal precession of the binary (Baycroft et al. 2023). For sampling, KIMA employs a diffusive nested sampling algorithm (DNest4, Brewer & Foreman-Mackey 2018). To account for stellar variability effects, a radial velocity jitter term is incorporated. Outliers are included in the procedure, and are handled by fitting with a student's t distribution. The system's derived parameters using radial velocities from both of the new approaches are provided in Table 1 (columns 1 and 2).

The precision reached thanks to method 1 and 2 means we have to take the circumbinary planet into account in order to properly compare them between one another and to TODCOR/TODMOR. As a nested sampler KIMA can fit for the number of orbiting objects in a system (in our case binary and planet), and naturally marginalizes over all parameters, including the number of orbiting bodies and their possible orbits. We discuss the planet's parameters in Section 4.3.

4.2 Comparison of radial velocities

After removing all Keplerian signals, we find that the residuals' root mean square (RMS) scatter of method 1 (SD-GP) is 39.9 $\mathrm{m\,s^{-1}}$ for the primary star and 50.9 $\mathrm{m\,s^{-1}}$ for the secondary star, while the RMS scatter of method 2 (CCF-GP) is 48.8 $\mathrm{m\,s^{-1}}$ for the primary star, and 72.2 $\mathrm{m\,s^{-1}}$ for the secondary star.

It is worth mentioning the RMS values achieved by our new approaches are larger compared to the current state of the art, a scatter of 10–15 $\mathrm{m\,s^{-1}}$ reported by Konacki et al. (2009). However, it is crucial to recognise that this increased scatter is likely inherent to the characteristics of the star itself. We have tested our methods on other double-lined binary systems, where we find that the scatter can reach down to photon noise.

Individual measurement uncertainties for the primary and secondary stars, measured by each method, range between 5.8 and 7.5 $\mathrm{m\,s^{-1}}$ for method 1 and 4.7 and 13 $\mathrm{m\,s^{-1}}$ for method 2. In Fig. 5, we plot radial velocities measured using method 1 against radial velocities measured using method 2. We find the

Downloaded from https://academic.oup.com/mnras/article/527/2/2261/7420283 by Health Services Management Centre Library user on 08 October 2024

Table 1. Best-fitting parameters for each methods both including and not including the 1–2 punch into the fit. Solutions that cross the instability limit (Holman & Wiegert 1999) are excluded here (parameters from the full posteriors can be found in Table A1). The parameters are determined along with their corresponding 1σ uncertainties.

Parameters	**ADOPTED** Method 1 SD-GP	Method 2 CCF-GP	Method 1 (with 1–2 punch) SD-GP	Method 2 (with 1–2 punch) CCF-GP
Binary parameters				
P_B (d)	$19.657878^{+0.000029}_{-0.000034}$	19.657861 ± 0.000040	$19.657874^{+0.000030}_{-0.000037}$	$19.657869^{+0.000048}_{-0.000051}$
e_B	$0.448234^{+0.000090}_{-0.000071}$	0.44823 ± 0.00010	$0.448230^{+0.000081}_{-0.000083}$	0.44819 ± 0.00013
ω_B (rad)	$1.23147^{+0.00019}_{-0.00027}$	$1.23136^{+0.00035}_{-0.00038}$	$1.23142^{+0.00022}_{-0.00024}$	$1.23112^{+0.00049}_{-0.00036}$
K_B (km s^{-1})	$58.5494^{+0.0079}_{-0.0054}$	$58.5279^{+0.0076}_{-0.0074}$	58.580 ± 0.011	$58.5428^{+0.0104}_{-0.0092}$
q_B	$0.97196^{+0.00016}_{-0.00022}$	$0.97106^{+0.00025}_{-0.00023}$	0.97211 ± 0.00022	$0.97121^{+0.00029}_{-0.00027}$
$\dot{\omega}_B$(arcsec yr^{-1})	215^{+56}_{-59}	279^{+72}_{-70}	229^{+62}_{-71}	250^{+120}_{-110}
$T_{0,B}$ (BJD)	$2\,459\,566.00250^{+0.00044}_{-0.00061}$	$2\,459\,566.00210^{+0.00079}_{-0.00088}$	$2\,459\,566.00267^{+0.00053}_{-0.00062}$	$2\,459\,507.02830^{+0.00113}_{-0.00094}$
Planet parameters				
P_{pl} (d)	151.2 ± 1.8	149.3 ± 2.2	151.4 ± 1.7	$149.9^{+2.4}_{-2.2}$
e_{pl}	<0.11	<0.11	$0.1243^{+0.0183}_{-0.0090}$	$0.1251^{+0.0124}_{-0.0083}$
ω_{pl} (rad)	6.0 ± 1.8	4.9 ± 2.0	$5.00^{+0.31}_{-0.49}$	4.76 ± 0.41
K_{pl} (m s^{-1})	$40.1^{+5.1}_{-5.3}$	44.0 ± 6.8	$39.1^{+4.5}_{-4.3}$	$40.5^{+6.3}_{-6.6}$
$T_{0,pl}$ (BJD)	$2\,459\,442^{+40}_{-45}$	$2\,459\,425^{+45}_{-49}$	$2\,459\,419.7^{+7.8}_{-12.0}$	$2\,459\,421 \pm 10$
Derived parameters				
M_A ($M_\odot$)	$1.23681^{+0.00037}_{-0.00039}$	$1.23765^{+0.00051}_{-0.00046}$	1.23670 ± 0.00036	$1.23831^{+0.00060}_{-0.00063}$
M_B ($M_\odot$)	$1.20207^{+0.00033}_{-0.00026}$	$1.20184^{+0.00035}_{-0.00031}$	$1.20221^{+0.00032}_{-0.00028}$	$1.20264^{+0.00048}_{-0.00046}$
m_{pl} (M_{Jup})	1.90 ± 0.25	2.07 ± 0.32	1.84 ± 0.21	2.09 ± 0.27
a_{bin} (au)	$0.191879^{+0.000016}_{-0.000018}$	0.191894 ± 0.000021	0.191879 ± 0.000016	$0.191931^{+0.000026}_{-0.000028}$
a_{pl} (au)	$0.7474^{+0.0057}_{-0.0061}$	$0.7410^{+0.0069}_{-0.0075}$	$0.7479^{+0.0051}_{-0.0056}$	$0.7433^{+0.0079}_{-0.0072}$
Other parameters				
$V_{sys,A}$ (km s^{-1})	$25.9865^{+0.0045}_{-0.0047}$	26.0252 ± 0.0057	26.0144 ± 0.0045	26.0573 ± 0.0067
$V_{sys,B}$ (km s^{-1})	$26.0456^{+0.0062}_{-0.0060}$	$26.0969^{+0.0087}_{-0.0089}$	$26.0636^{+0.0059}_{-0.0061}$	26.116 ± 0.010

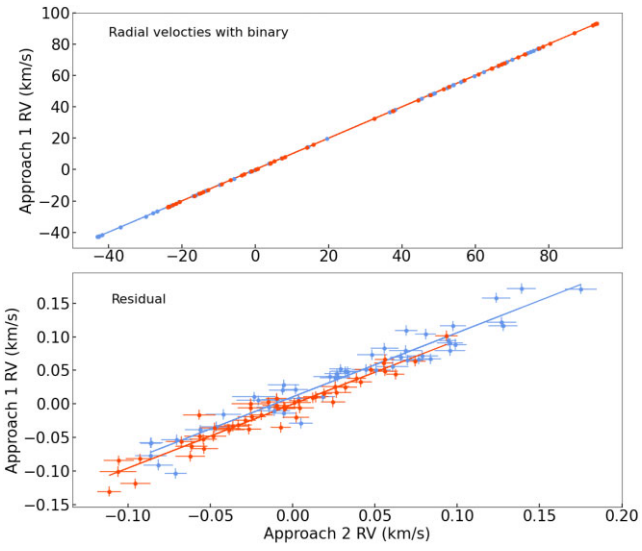


Figure 5. Top panel: Radial velocities extracted using method 1 versus the radial velocities from method 2, along with 1σ error bars. The red and blue colours represent the primary and the secondary stars along with their respective 1:1 identity lines. Bottom panel: The residual radial velocities after removing the binary signal for method 1 versus the residual radial velocities for method 2.

mean absolute difference between the two approaches to be 26.9 and 29.2 m s^{-1} for the primary and secondary stars, respectively. These mean differences are lower than the measured scatter, but exceed the uncertainties estimated by the GP fits, which suggests the presence of a systematic bias between them.[1] This bias could be due to various factors, such as the differences in the templates used for cross-correlation in method 2. In addition, method 1 might be more susceptible to the effects of stellar activity, which affect the accuracy of the radial velocities. Further analysis may be necessary to fully understand and quantify the sources of the observed differences.

In Fig. A2, we show the radial velocity time-series for each method, along with the binary + planet Keplerian models applied to them. We find radial velocities measured by our approaches are consistent with those measured by TODCOR and TODMOR within uncertainties. This suggests that our approaches are able to accurately measure the radial velocities of the primary and secondary stars. The distribution of residuals (Observed − Calculated; O–C) for TODCOR, TODMOR, method 1, and method 2 is presented in Fig. 6 using violin plots. Each violin plot represents the distribution of velocities clustered around mean O–C values in m s^{-1}, and the width of each plot functions like a histogram. Our proposed methods outperforms TODCOR and TODMOR in terms of root–mean–square (RMS) scatter (Fig. 6), producing an improvement of a factor of ∼4

[1]We tested method 1 and 2 on bright double-lined binaries from Konacki et al. (2009, 2010), observed with SOPHIE, and achieved accuracies of order 2–4 m s^{-1}, which will be the object of a follow-up paper.

Downloaded from https://academic.oup.com/mnras/article/527/2/2261/7420283 by Health Services Management Centre Library user on 08 October 2024

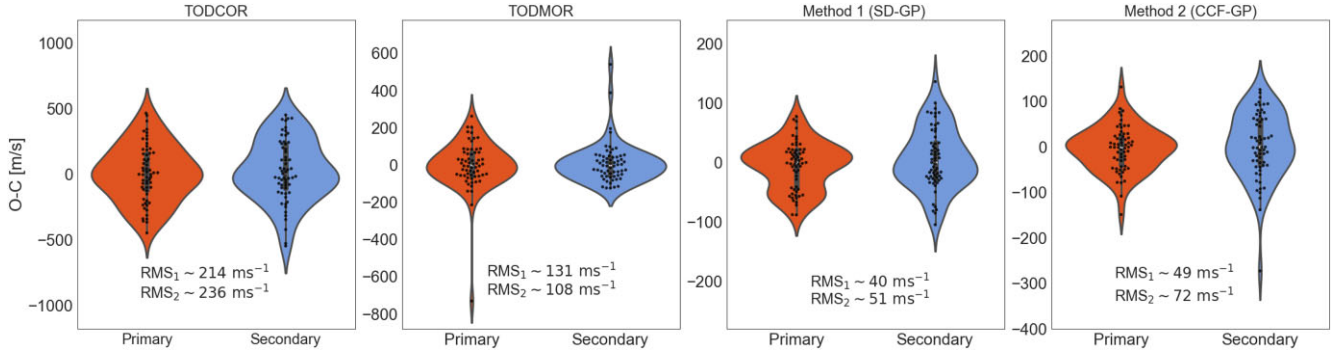


Figure 6. The distribution of O-C values for the primary (red) and secondary stars (blue) in TIC172900988, as determined by TODCOR, TODMOR, method 1 (SD-GP), and method 2 (CCF-GP), are displayed using violin plots. Note that the vertical scale is different on every panel.

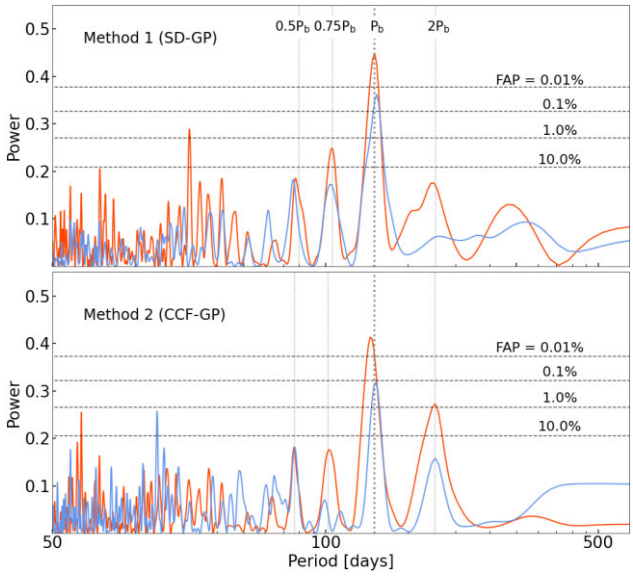


Figure 7. Lomb–Scargle periodogram of TIC172900988 radial velocities for method 1 (top) and method 2 (bottom). The radial velocities for the primary (red) and the secondary (blue) are plotted after removing the binary motion. The three horizontal dashed lines indicate 10 per cent, 1 per cent and 0.1 per cent false alarm probabilities. The vertical dotted lines indicates the highly significant peak around 150 d and its harmonics.

and ∼2, respectively. This indicates the effectiveness of our new approaches in measuring double-lined binary radial velocities more precisely than before. Since both our methods agree between one another, we are also confident our measurements gained in precision without compromising in accuracy.

4.3 The circumbinary planet within the TIC 172 900 988 system

The circumbinary planet is naturally detected and fitted by the Nested Sampler; however, we first describe a more frequentist approach as it might be closer to methods used in the binary star literature.

We initially compute a generalized Lomb–Scargle (GLS) periodogram (Zechmeister & Kürster 2009) for the radial velocities measured from the primary and the secondary stars, after having removed the best-fitting Keplerian motion for the binary star. In Fig. 7, we display the resulting periodogram for method 1 SD-GP (top panel) and method 2 CCF-GP (bottom panel). Using 10 000 bootstrap randomization of the input data, we compute the false alarm probability (FAP) levels of 10, 1, 0.1, and 0.01 per cent. This calculation can be done independently for the primary and secondary radial velocities. The periodogram for radial velocities using both method 1 and method 2 show excess power at $P_{\rm pl} \sim 151$ d with a FAP = 0.005 per cent. After subtracting the signal $P_{\rm pl}$, the periodogram has no significant peak (Fig. A3).

We perform a more thorough analysis of the data using the KIMA analysis package which uses diffusive nested sampling (Faria et al. 2018; Baycroft et al. 2023). KIMA allows for Bayesian model comparison by computing the Bayes factor between a model with a binary and one planet to one with a binary but no planet from posterior samples generated by the algorithm. Using the Jeffrey's scale (Kass & Raftery 1995), a Bayes factor (BF) over 150 is considered strong evidence in favour of the more complex model (here binary + planet). Therefore, we use this value as our confident detection threshold. In Fig. 8, we show the phased radial velocity data with the best-fitting Keplerian model for the circumbinary planet (the binary having been removed). This is done for the data from method 1 (top panel) and method 2 (bottom panel).

The version of KIMA we use fits for all the orbital elements of the binary, except Ω and i, but i is known from the eclipsing geometry (Kostov et al. 2021). A different systemic velocity parameter is fit for each of the two stars. Keplerian models of the planet also include all orbital parameters except Ω and i. Two jitter terms are also fit by KIMA, one for the primary and one for the secondary. To include outliers properly in our fit, we use Student's t statistics.

KIMA's fit of the SOPHIE data obtained on TIC 172 900 988 yields BF = 2300 000 using the SD-GP method (method 1) and BF = 16 000 using the CCF-GP method (method 2). Both approaches exceed the detection threshold and imply a confident detection of a circumbinary planet. The parameters for the planet (as well as the binary) are shown in Table 1. Since TIC 172 900 988 is a double-lined eclipsing binary, we obtain the absolute mass of each stellar component at high precision. Since the planet's orbital plane at the time of the observations is close to perpendicular to the line of sight (Kostov et al. 2021), we measure a mass that could be considered an absolute mass as well. However, it is likely the planetary orbital plane inclination has precessed, and might be out of transitability (e.g. Martin & Triaud 2014). We use the median of posteriors from KIMA and their 1σ confidence region to produce our fit's parameters and uncertainties. We find all binary parameters to be statistically consistent with the analysis of (Kostov et al. 2021), with a few caveats. The binary period ($P_{\rm B}$) we find is inconsistent with any

Downloaded from https://academic.oup.com/mnras/article/527/2/2261/7420283 by Health Services Management Centre Library user on 08 October 2024

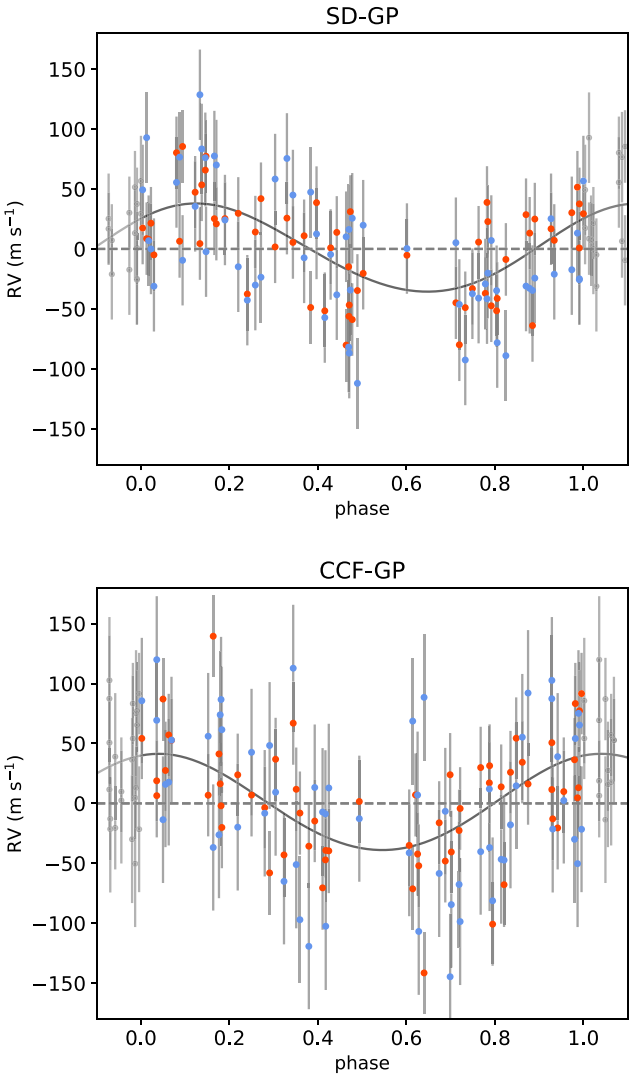


Figure 8. The residual RVs phase folded with corresponding best-fitting Keplerian circumbinary model (Table A1). The top and bottom panels correspond to our method 1 (SD-GP) and method 2 (CCF-GP), respectively.

of the six solutions proposed by Kostov et al. (2021), but it does lie within the range that these solutions cover.[2] The argument of periastron (ω_B) that we measure is not consistent, at first glance. However, our measurements were taken some time after the Kostov et al. (2021) paper. If we correct for the apsidal precession of the binary orbit, our value of ω_B is consistent with Kostov et al. (2021). The value we get for the apsidal precession rate ($\dot{\omega}_B$) is also consistent with the value quoted in Kostov et al. (2021). This precession rate exceeds that expected from General Relativity, and is attributed to the third-body perturbations produced by the planet. Fig. A4 shows the area of parameter-space a third body needs to have to produce and apsidal precession rate consistent with the observations. We overplot the location of the planetary parameters presented in this work and the solutions proposed by Kostov et al. (2021). All solutions can reproduce the detected precession rate well.

[2]These six solutions consist of osculating elements and the binary periods are internally inconsistent with each other.

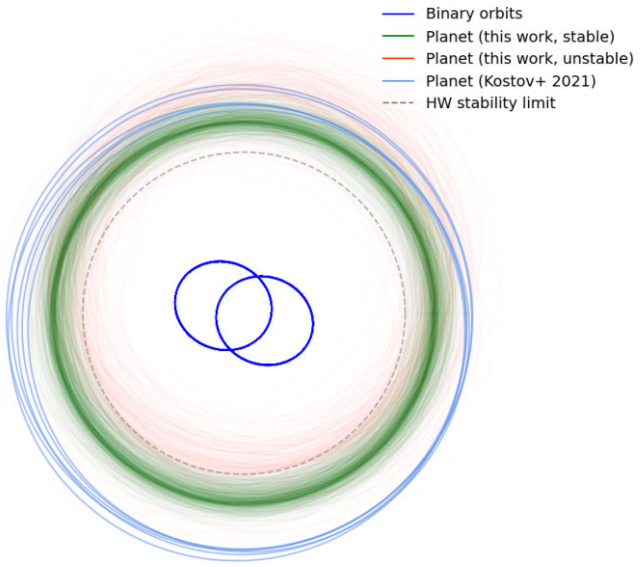


Figure 9. Orbital configuration of TIC 172 900 988 showing the orbits of the binary and the planet. The green orbits are a random sample of 1000 posteriors from `kima` fitting the radial velocities from SD-GP. The blue orbits are the six suggested solutions from Kostov et al. (2021), the dashed grey line is the stability limit as calculated by Holman & Wiegert (1999). The radial velocity data alone are fit (not including the 1–2 punch transit data).

For the planet, we find $P_{pl} \approx 150$ d and a mass $m_{pl} \approx 2$ M_{jup} (≈ 600 $M_\oplus$). While these are inconsistent with any of the six solutions proposed by Kostov et al. (2021), we fit the planet with a Keplerian model and report mean parameters, where Kostov et al. (2021) fit with a dynamical model and report osculating parameters. In such a dynamically complex orbit, it is difficult to compare these parameters properly. We note an additional important caveat here: We fit a static Keplerian to the planetary orbit and obtain a mean orbital period. Other parameters such as the semimajor axis and the mass are then calculated using Kepler's law. However, due to the proximity of this orbit to the binary it is expected that non-Keplerian effects (such as apsidal precession of the planetary orbit) are present and the orbit would not conform to Kepler's law. Hence, it is possible that the planet's true orbital distance and true mass are slightly larger than stated here.

Orbital parameters between both methods (SD-GP and CCF-GP) are internally consistent and are presented in Table 1 (columns 1 and 2). Any posterior samples where the proposed planet crosses into the instability region (calculated using the formula in Holman & Wiegert 1999) are excluded, as described in Standing et al. (2022). We adopt the parameters in column 1 of Table 1 as our preferred solution. We chose this solution as the SD-GP method results in a higher Bayes Factor than the CCF-GP. The method used for the parameters reported in columns 3 and 4 is described in Section 4.4. Table A1 shows the parameters obtained from the posterior sample with the 'unstable' solutions left in. These are therefore the parameters simply consistent with the data without dynamical stability being considered.

Fig. 9 shows the orbital configuration of TIC 172900988, displaying the orbits of the binary and the planet. A subsample of 1000 posterior samples are drawn: if a sample crosses into the instability zone it gets shown in red, otherwise in green. The parameters in Table 1 and the distributions shown in Fig. 11 correspond therefore

Downloaded from https://academic.oup.com/mnras/article/527/2/2261/7420283 by Health Services Management Centre Library user on 08 October 2024

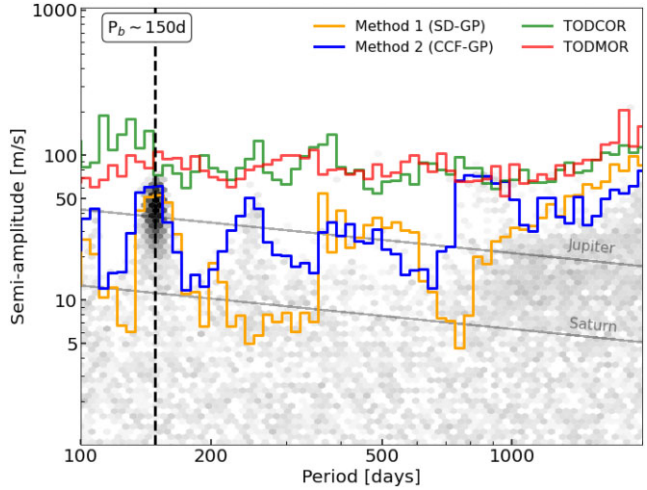


Figure 10. Detection sensitivity to planets plotted as semi-amplitude as a function of orbital period of planets. The density of posterior samples are depicted as grey hexagonal bins. The solid green, red, orange, and blue lines show the detection limit from posterior samples for TODCOR, TODMOR, method 1, and method 2, respectively. The diagonal lines are anticipated signals of Saturn and Jupiter mass planet.

to the orbits shown in green. The six solutions from Kostov et al. (2021) are also shown for comparison.[3]

The KIMA algorithm can generate detection limits for any further signals, following the method presented in Standing et al. (2022): first, all planetary detected signals are removed from the data (but the binary's orbital signature is kept), then KIMA is run once more and forced to fit a planetary signal (when presumably there are none left in the data). The resulting set of posterior samples corresponds to all signals that are compatible with the data, but have no statistically detectable signals. This method is an alternative to injection-recovery tests (e.g. Konacki et al. 2009, 2010; Martin et al. 2019) that allow to compute a detection limit efficiently over a large parameter space, while marginalizing over all orbital elements. The detection limits for TIC 172 900 988 are shown in Fig. A5 and reveal that the SOPHIE data analysed using our two new methods produce very similar results and that those are sensitive to planets with masses of order Jupiter's out to periods as large as 1000 d except for orbital periods around the 1 yr alias.

Finally, we run the same analysis on the TODCOR and TODMOR-produced radial velocities. These produced BF = 0.8 and 0.7, respectively, well below the accepted detection threshold, demonstrating that our new approaches out-performed TODCOR and TODMOR. We show a comparison of all the resulting detection limits in Fig. 10. The detection limits here are a little different than in Fig. A5, since the planet is not formally detected with all approaches. To allow for a proper comparison between the detection limits generated using the different methods we do not remove the planetary signal when calculating the detection limits on data from the SD-GP and CCF-GP methods. To ensure that the parameter space was well-covered in these cases we then force KIMA to fit two signals instead of the usual one signal.

[3]These may not be a full representation of the solutions from Kostov et al. (2021) since they quote osculating elements and we plot them as if they were mean elements.

4.4 Including the 1–2 punch technique

The detection of the planet, and the posteriors of its orbital and physical parameters can be improved by combining the radial velocity data with some aspects of the transit data. Ultimately, a full photodynamical analysis would need to be performed, but this is beyond the scope of our paper.

TIC 172 900 988 was discovered using the '1–2 punch' method (Kostov et al. 2021). Two transits within the same conjunction give an estimate of the planet's orbital period. The distance the planet has moved can be calculated from the position in its orbit of the transited star, at the time of each transit. The time between the transits and the distance travelled then allow us to calculate an estimate of the planet's orbital period (as in Kostov et al. 2020):

$$P_{\rm pl} = \frac{2\pi G M_{\rm bin}}{v^3}\left(\frac{e\sin\omega + \sin(\phi+\omega)}{\sqrt{1-e^2}}\right)^3, \tag{14}$$

where $M_{\rm bin}$ is the total mass of the binary, e and ω the eccentricity and argument of periastron of the planet, ϕ is the true anomaly at the point in the orbit that we are measuring and v the average velocity in the plane of the sky with which the planet moved between both transit mid-points. Since we know the planet is at conjunction, we can use $\sin(\phi+\omega) \approx 1$.[4]

We alter our version of KIMA and add an extra feature, to include the '1–2 punch' information as part of the the sampling process. When a solution is proposed by the sampler, the predicted period from the '1–2 punch' is calculated and compared to the proposed period. This is then included in the likelihood calculation of the sample in the same way as an extra data point would be, assuming a Gaussian distribution. Our new log-likelihood is therefore:

$$\log(\mathcal{L}) = \log(\mathcal{L}_{\rm RV}) - \frac{1}{2}\log(2\pi\sigma^2_{P_{12}}) - \frac{(P_{12}-P_{\rm pl})^2}{2\sigma^2_{P_{12}}}, \tag{15}$$

where $\log(\mathcal{L}_{\rm RV})$ is the log-likelihood from the radial velocity data, $P_{\rm pl}$ is the period for the planet proposed as part of the sampling process, P_{12} is the orbital period calculated using equation (14) using all other parameters proposed in the sample (e.g. $M_{\rm bin}$, e, etc.). Finally, $\sigma^2_{P_{12}}$ is the variance of P_{12}, which is derived from the uncertainty in the transit times propagated through equation (14).

We run the analysis on TIC 172 900 988 again, with the extra input of two transits with mid-times at 2 458 883.390879 ± 0.006188 and 2 458 888.309427 ± 0.003904.[5] We fix the number of planets searched for in KIMA to 1. The parameters for the planet and binary obtained are shown in Table 1 (columns 3 and 4). As with the previous analysis, any posterior samples where the proposed planet crosses into the instability are excluded.

A Keplerian fit of the radial velocity data probes the average parameters of the orbit over the time baseline, notably the average orbital period. A circumbinary planet, especially one like TIC 172900988 b which is quite close to the inner binary will see its orbital parameters vary throughout its orbital path meaning that when parameters of the orbit are measured over a short time frame,

[4]We note a difference from Kostov et al. (2020) where the value of this is quoted as −1, Kostov et al. (2016) use a value of 1, this may be down to the choice of reference frame.

[5]The transit mid-times were determined using the Eclipsing Light Curve (ELC) code. The segment of the data containing a single event was isolated, and a model was fitted to the transit (or eclipse) profile. Then we execute the DE-MCMC code, and the median along with 1σ uncertainties of the posterior sample was considered as the best-fitting transit time.

Downloaded from https://academic.oup.com/mnras/article/527/2/2261/7420283 by Health Services Management Centre Library user on 08 October 2024

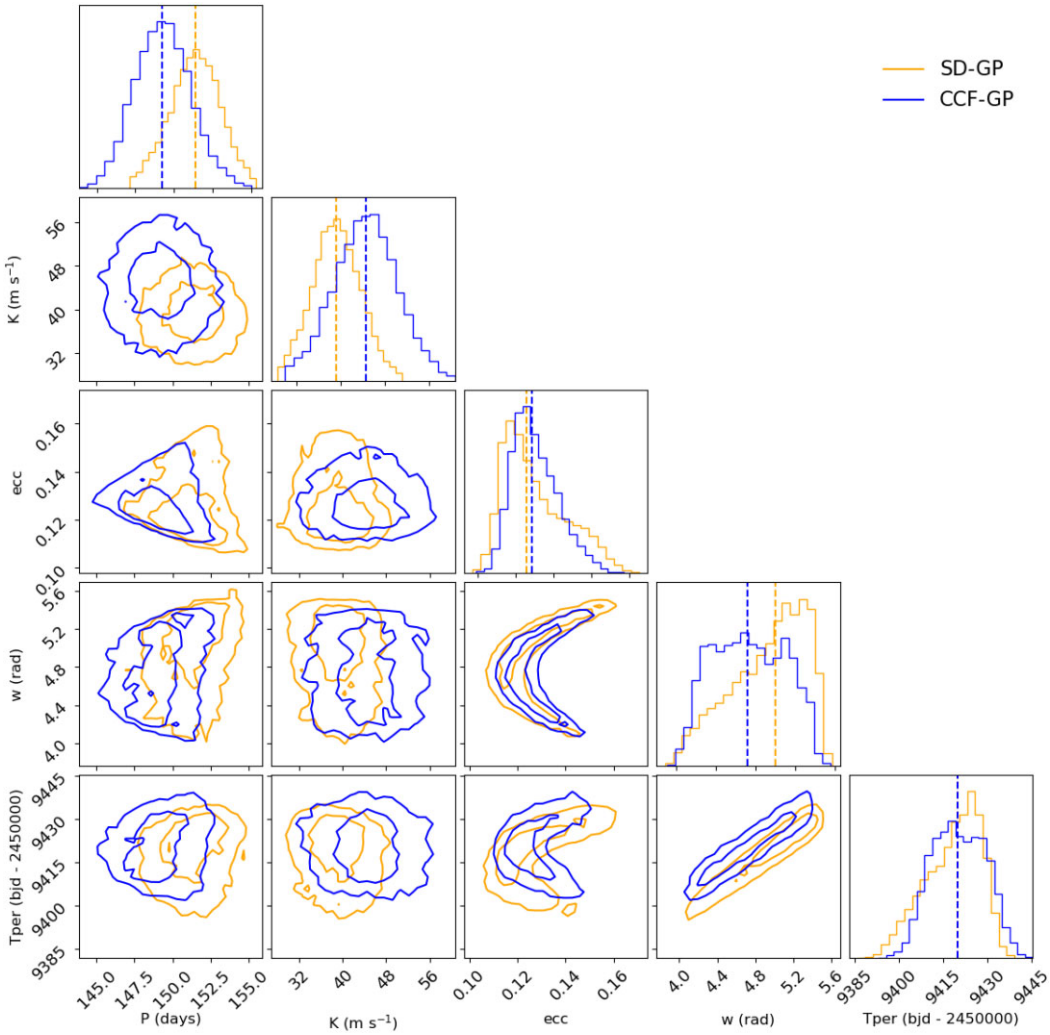


Figure 11. Corner plot showing the distributions and correlations of the planetary parameters from the simultaneous fit of the radial velocity data and the 1–2 punch transit times. The contours are the 50th and 90th percentiles. Orange shows the results using the radial velocity data using SD-GP, and blue from the CCF-GP.

they may not be representative of the average orbit. The 1–2 punch, method calculates the velocity and therefore the orbital period, over a short time frame. Using this method to constrain the average period might bring in a poorly understood bias. We therefore present the results from the combined radial velocity and 1–2 punch fit out of interest, but do not adopt these parameters as our preferred solution.

The posterior samples for the planet parameters are shown as a corner plot (Foreman-Mackey 2016) in Fig. 11 for both the CCF-GP method and the SD-GP method. We note that the crescent-shaped correlations involving the eccentricity are expected. We also note that while we report the median and 1σ in Table 1, some of the parameters have non-Gaussian distributions [in particular the eccentricity ($e_{\rm pl}$) and argument of periastron ($\omega_{\rm pl}$)].

We find these new solutions are consistent with solutions of fitting just the radial velocities or just the average orbital velocity at conjunction between the transits. The combined fit suggests the circumbinary planet's orbit must have an eccentricity $e_{\rm pl} > 0.1$ and an argument of periastron $4.35 \leq \omega_{\rm pl} \leq 5.31$ rad.

Fig. A6 shows the orbital configuration of TIC 172900988. This is the counterpart to Fig. 9 generated from posterior samples obtained from the KIMA analysis which included the 1–2 punch and using the SD-GP radial velocities.

5 CONCLUSIONS

In this work, we focus on the development of two new data-driven approaches to accurately measure radial velocities in double-lined binary systems. Despite being brighter and more precise in principle, the time-varying blending of the two stars' spectral lines makes accurate radial velocity measurement challenging. Previous methods (Konacki et al. 2009) been shown to have a typical scatter of 10–15 m s^{-1} that prevents the detection of most orbiting circumbinary planets.

In this paper, we introduce two new methods based on GP regression inspired by Czekala et al. (2017). The first method applies the GP in the spectral domain and the second is applied on cross-correlated spectra. We compare the precision and accuracy of our radial-velocity to two widely used methods: TODCOR and TODMOR (Mazeh & Zucker 1994; Zucker et al. 2004).

Downloaded from https://academic.oup.com/mnras/article/527/2/2261/7420283 by Health Services Management Centre Library user on 08 October 2024

To perform the comparison, we analyse 62 SOPHIE spectra of the binary TIC 172900988, a binary system which was also proposed to host a circumbinary planet (Kostov et al. 2021). We show that our two methods outperform both TODCOR and TODMOR, neither of which could recover the planet whereas both our GP approaches successfully detect a circumbinary planet. However, its parameters are found statistically different from previously published solutions (Kostov et al. 2021). TIC 172900988 b will now integrate the BEBOP catalogue for circumbinary exoplanets detected with radial-velocities as its second entry.

The RMS achieved by our new approaches are ≈50 and 70 m s^{-1} for the primary and secondary stars of TIC 172900988, respectively, are larger than our measurement uncertainties, and larger than the typical scatter reported for double-lined binaries in Konacki et al. (10 − 15 m s^{-1}; 2009, 2010). We speculate this increased scatter is most likely of stellar origin. Both stellar components are fairly high-mass stars. We note that TODCOR and TODMOR, both recognized methods of radial velocity extraction, also produce a high scatter. In those cases, TODCOR and TODMOR remain unable to detect the planetary signal which has a semi-amplitude $K_{\rm pl} \sim 42$ m s^{-1}. The fact our approaches both manage to overcome some of that scatter emphasizes the limitations of existing techniques when dealing with systems characterized by substantial scatter. The detection of a circumbinary planet in TIC 172 900 988 showcases the effectiveness of our data-driven methods in uncovering planetary signals even in challenging double-lined binary systems. We highlight here that should a circumbinary planet similar to the parameters of TIC 172900988 b have been present in a quieter binary star system, traditional methods such as TODCOR, TODMOR and the tomographic disentangling method have the nominal accuracy to detect it.

Our two new methods are a step forward, but there is always room for improvement. Further refinements and optimizations to these methods may lead to even more accurate and precise radial velocity measurements, particularly with the spectral decomposition.

Firstly, we recognize that our analysis does not account for possible contamination in the radial velocities obtained from each chunk of the spectra. Specifically, we do not consider the effects of stellar activity on our results. Also the chunking can be improved to avoid areas that are poor in absorption lines, and avoid areas that include band known to be highly variable such as Hα. In order to improve the accuracy and precision of our measurements, we plan to develop a more sophisticated approach that can identify regions of the spectra that are affected by these factors.

Secondly, we recognize that there is still much to be learned about the astrophysical properties of the binary stars themselves. In the case of TIC 172900988, both stars are of equal mass. The CCF and spectral decomposition methods might need to be adapted to non-equal mass binaries to account for the their differing spectral types.

In addition, we expect that the spectral deconvolution method will yield accurate spectra for both stars individually when all wavelength chunks are combined together. Such a spectrum could be used to constrain their properties such as their temperature, $v \sin i$ and metallicity, an important parameter to relate planet presence to planet formation (e.g. Santos, Israelian & Mayor 2004; Adibekyan et al. 2013).

Our methods open the door to extend the search for circumbinary planets using the radial-velocity method beyond single-lined binaries. With our two new approaches, it is highly probable that the discovery of circumbinary planets will be enhanced in the future. Finally, we highlight the success of our two new methods in being the first to detect a circumbinary planet using radial-velocities in a double-lined binary. Importantly, this detection is made independently of any other data. Interestingly our results produce planetary parameters different from those previously published demonstrating the need for radial-velocity follow-up of circumbinary planet candidates identified with the transit method.

ACKNOWLEDGEMENTS

We thank Tsevi Mazeh for suggesting we compare our methods to TODCOR and TODMOR, during the 2022 EAS conference in Valencia where preliminary results were presented.

This paper is based on observations collected the Observatoire de Haute Provence (OHP). Here, we would also like to acknowledge the staff, particularly the night assistants, at the OHP for their dedication and hard work, especially during the COVID pandemic.

This research received funding from the European Research Council (ERC) under the European Union's Horizon 2020 research and innovation programme (grant agreement no 803193/BEBOP) and from the Leverhulme Trust (research project grant no RPG-2018-418). The French group acknowledges financial support from the French Programme National de Planétologie (PNP, INSU). The acquisition of data was made possible by a series of allocations through the French PNP. The computations described in this paper were performed using the University of Birmingham's BlueBEAR high performance computing service (available at http://www.birmingham.ac.uk/bear).

DATA AVAILABILITY

The radial velocity data are included in the appendix of this paper. The reduced spectra are available at the SOPHIE archive: http://atlas.obs-hp.fr/sophie/ (Table A2).

REFERENCES

Adibekyan V. Z. et al., 2013, A&A, 560, A51
Aigrain S., Parviainen H., Pope B. J. S., 2016, MNRAS, 459, 2408
Baranne A. et al., 1996, A&AS, 119, 373
Baycroft T. A., Triaud A. H. M. J., Faria J., Correia A. C. M., Standing M. R., 2023, MNRAS, 521, 1871
Borucki W. J., Summers A. L., 1984, Icarus, 58, 121
Bouchy F. et al., 2009, A&A, 505, 853
Brewer B. J., Foreman-Mackey D., 2018, J. Stat. Softw., 86, 1
Byrd R. H., Lu P., Nocedal J., Zhu C., 1995, SIAM J. Sci. Comput., 16, 1190
Czekala I., Mandel K. S., Andrews S. M., Dittmann J. A., Ghosh S. K., Montet B. T., Newton E. R., 2017, ApJ, 840, 49
Doyle L. R. et al., 2011, Science, 333, 1602
Faria J. P., Santos N. C., Figueira P., Brewer B. J., 2018, J. Open Source Softw., 3, 487
Foreman-Mackey D., 2016, J. Open Source Softw., 1, 24
Foreman-Mackey D., Hogg D. W., Lang D., Goodman J., 2013, PASP, 125, 306
Foreman-Mackey D., Agol E., Ambikasaran S., Angus R., 2017, AJ, 154, 220
Goodman J., Weare J., 2010, Commun. Appl. Math. Comput. Sci., 5, 65
Holman M. J., Wiegert P. A., 1999, AJ, 117, 621
Husser T. O., Wende-von Berg S., Dreizler S., Homeier D., Reiners A., Barman T., Hauschildt P. H., 2013, A&A, 553, A6
Kass R. E., Raftery A. E., 1995, J. Am. Statist. Assoc., 90, 773
Konacki M., Muterspaugh M. W., Kulkarni S. R., Hełminiak K. G., 2009, ApJ, 704, 513
Konacki M., Muterspaugh M. W., Kulkarni S. R., Hełminiak K. G., 2010, ApJ, 719, 1293
Kostov V. B. et al., 2016, ApJ, 827, 86

Downloaded from https://academic.oup.com/mnras/article/527/2/2261/7420283 by Health Services Management Centre Library user on 08 October 2024

Kostov V. B. et al., 2020, AJ, 159, 253
Kostov V. B. et al., 2021, AJ, 162, 234
Kovaleva D., Malkov O., Yungelson L., Chulkov D., 2016, Baltic Astron., 25, 419
Martin D. V., 2018, Populations of Planets in Multiple Star Systems. Springer International Publishing, Cham
Martin D. V., Triaud A. H. M. J., 2014, A&A, 570, A91
Martin D. V. et al., 2019, A&A, 624, A68
Mayor M., Queloz D., 1995, Nature, 378, 355
Mazeh T., Zucker S., 1994, Ap&SS, 212, 349
Pepe F., Mayor M., Galland F., Naef D., Queloz D., Santos N. C., Udry S., Burnet M., 2002, A&A, 388, 632
Perruchot S. et al., 2008, in McLean I. S., Casali M. M., eds, Proc. SPIE Conf. Ser. Vol. 7014, Ground-based and Airborne Instrumentation for Astronomy II. SPIE, Bellingham, p. 70140J
Rajpaul V. M., Aigrain S., Buchhave L. A., 2020, MNRAS, 492, 3960
Rasmussen C. E., Williams C. K. I., 2006, Gaussian Processes for Machine Learning. MIT Press, Cambridge, Massachusetts
Santos N. C., Israelian G., Mayor M., 2004, A&A, 415, 1153
Schneider J., 1994, Planet. Space Sci., 42, 539
Socia Q. J. et al., 2020, AJ, 159, 94
Standing M. R. et al., 2022, MNRAS, 511, 3571
Standing M. R. et al., 2023, Nat. Astron., 7, 702
Triaud A. H. M. J. et al., 2017, A&A, 608, A129
Triaud A. H. M. J. et al., 2022, MNRAS, 511, 3561
Zechmeister M., Kürster M., 2009, A&A, 496, 577
Zucker S., Mazeh T., 1994, ApJ, 420, 806
Zucker S., Mazeh T., Santos N. C., Udry S., Mayor M., 2004, A&A, 426, 695

APPENDIX: SOME EXTRA MATERIAL

Downloaded from https://academic.oup.com/mnras/article/527/2/2261/7420283 by Health Services Management Centre Library user on 08 October 2024

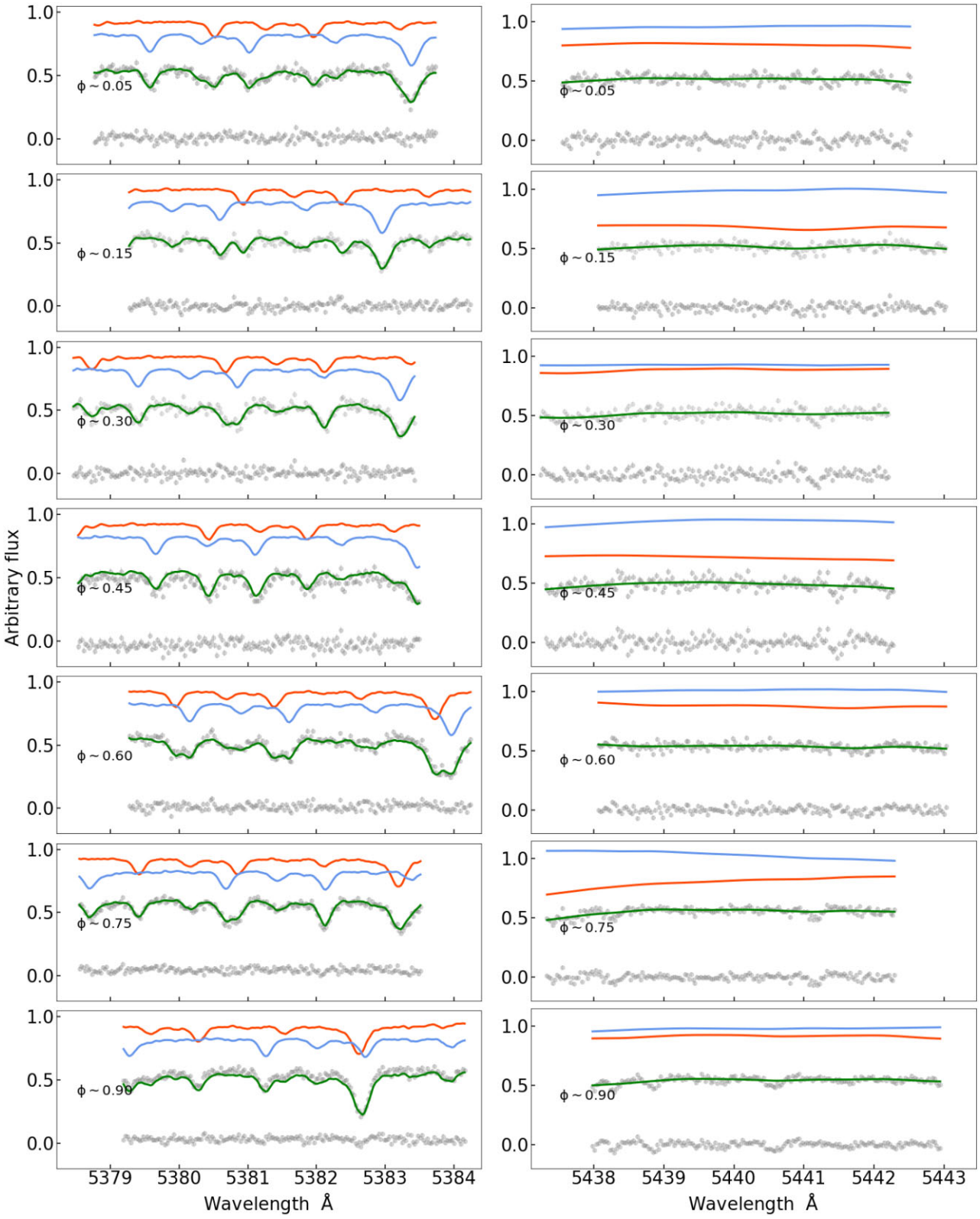


Figure A1. Seven epochs of composite spectra for two chunks between 5379–5384Å and 5437–5443 Å are shown in grey with composite model in green. The mean realization drawn from posterior predictive distribution are show in red and blue for the primary and secondary, respectively. The residuals are shown at the bottom of each panel. The first chunk shows several lines and the second chunk shows no lines in the composite spectra. The redial velocities from such chunks are weighted.

Downloaded from https://academic.oup.com/mnras/article/527/2/2261/7420283 by Health Services Management Centre Library user on 08 October 2024

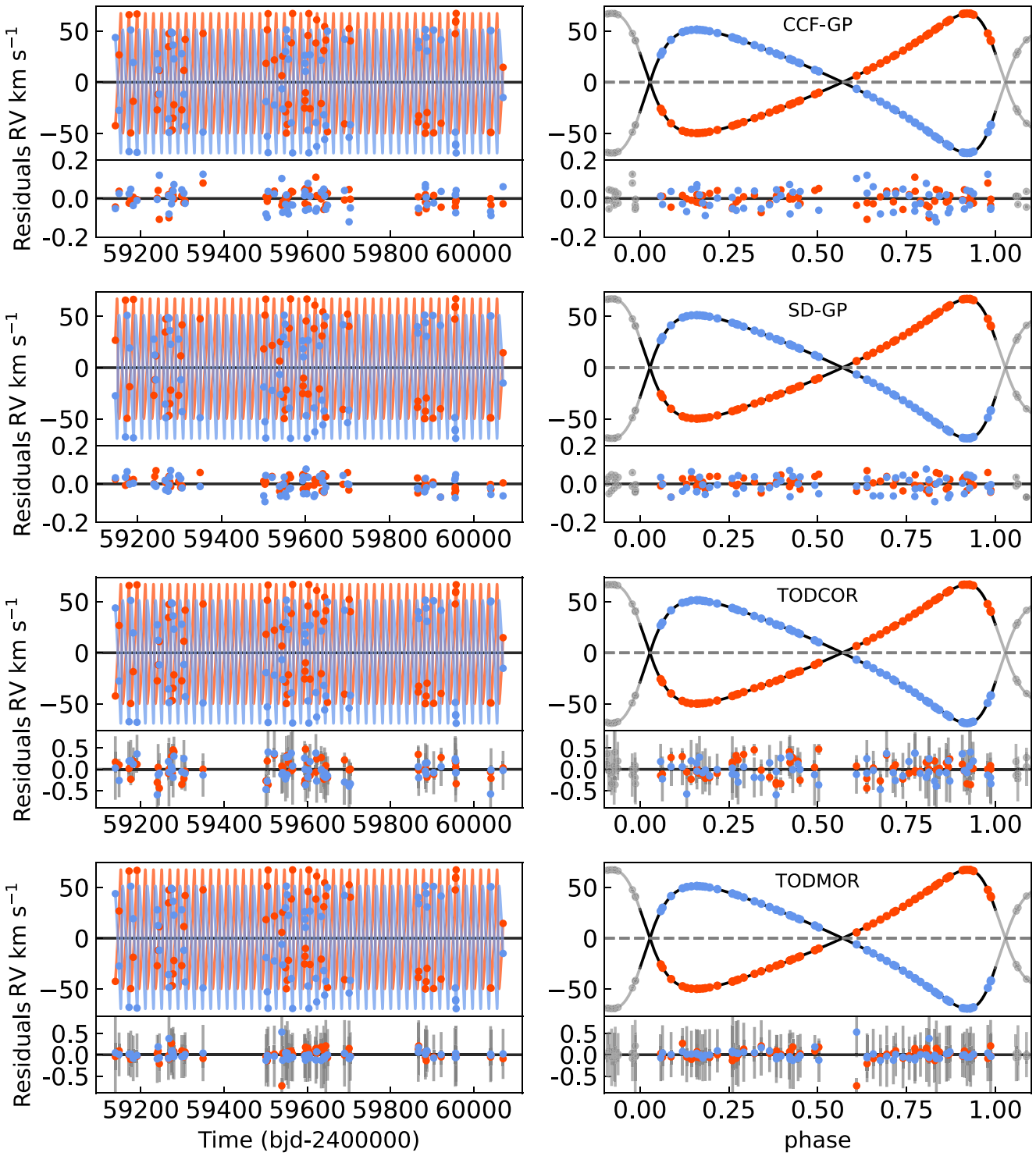


Figure A2. SOPHIE radial velocities as a function of time and the corresponding residuals for the method 1 (SD-GP), method 2 (CCF-GP), TODCOR, and TODMOR (top to bottom). The overplotted magenta and orange curves are the medial value of the posterior distribution models for the primary and the secondary stars corresponding to 2000 random MCMC steps.

Downloaded from https://academic.oup.com/mnras/article/527/2/2261/7420283 by Health Services Management Centre Library user on 08 October 2024

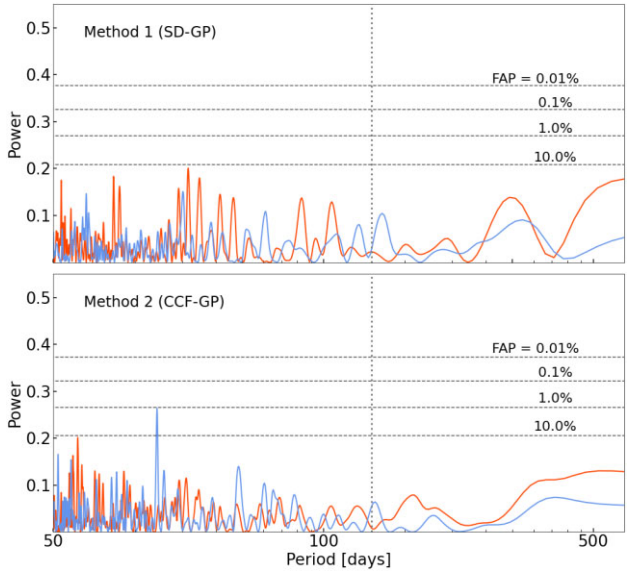


Figure A3. The residual periodgram after removing the signal P_b for both method 1 (top panel) and method 2 (bottom panel). The red and blue curves represent the primary and the secondary components of the binary. The grey vertical line indicates the period of P_b.

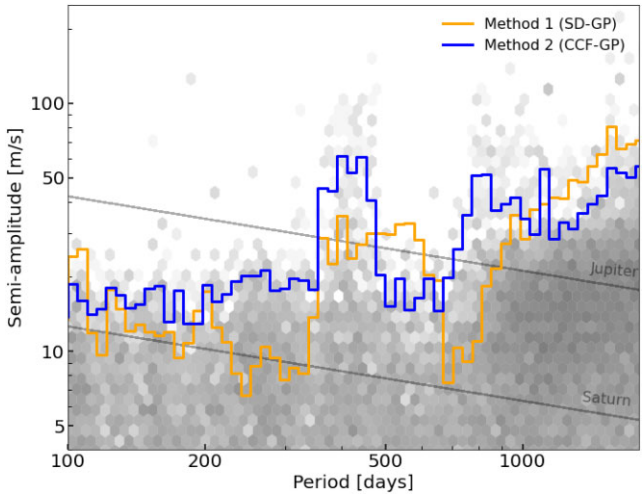


Figure A5. The density of posterior samples from `kima` run on TIC172900988 with N_p fixed to 1. The orange and blue lines indicate the detection limits for method 1 and method 2.

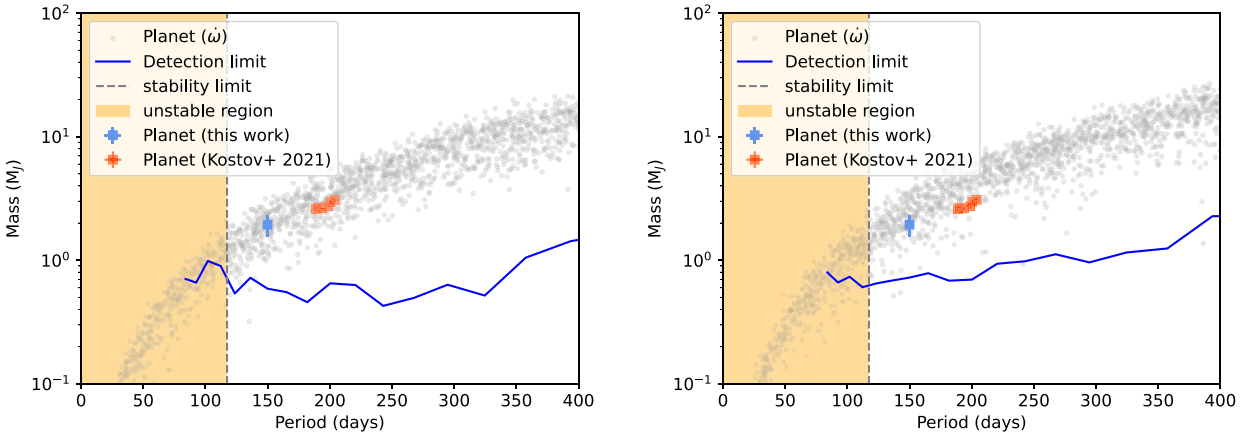


Figure A4. Left panel method 1 (SD-GP) and right panel method 2 (CCF-GP): Grey the scatter plot showing the planets consistent with the posterior distribution on the apsidal precession rate, the GR precession rate is accounted for both this and the third-body dynamical precession rate are calculated using the equations in Baycroft et al. (2023). Blue the locations of the solution presented in this work. Red the 6 suggested solutions from Kostov et al. (2021). Dashed line the HW-stability limit. Blue line the detection limit with planet b removed.

Downloaded from https://academic.oup.com/mnras/article/527/2/2261/7420283 by Health Services Management Centre Library user on 08 October 2024

Table A1. Best-fit parameters for each methods both including and not including the 1–2 punch into the fit. Solutions that cross the instability limit (Holman & Wiegert 1999) are not excluded here so these parameters are from the full posterior (parameters from the posteriors excluding unstable samples can be found in Table 1) The parameters are determined along with their corresponding 1σ uncertainties.

Parameters	Method 1 SD-GP	Method 2 CCF-GP	Method 1 (with 1–2 punch) SD-GP	Method 2 (with 1–2 punch) CCF-GP
Binary parameters				
P_B (d)	$19.657878^{+0.000030}_{-0.000035}$	19.657861 ± 0.000039	$19.657872^{+0.000033}_{-0.000038}$	$19.657865^{+0.000037}_{-0.000049}$
e_B	$0.448234^{+0.000090}_{-0.000071}$	0.44823 ± 0.00010	0.448232 ± 0.000083	0.44821 ± 0.00011
ω_B (rad)	$1.23146^{+0.00020}_{-0.00027}$	$1.23136^{+0.00034}_{-0.00038}$	$1.23142^{+0.00022}_{-0.00026}$	$1.23132^{+0.00042}_{-0.00038}$
K_B (km s^{-1})	$58.5494^{+0.0079}_{-0.0054}$	58.5278 ± 0.0076	$58.5557^{+0.0067}_{-0.0075}$	58.5320 ± 0.0085
q_B	$0.97196^{+0.00016}_{-0.00022}$	0.97106 ± 0.00025	$0.97211^{\pm}0.00022$	0.97118 ± 0.00026
$\dot{\omega}_B$(arcsec yr^{-1})	215 ± 59	279^{+73}_{-69}	230^{+62}_{-68}	279^{+87}_{-77}
$T_{0,B}$ (BJD)	$2\,459\,566.00248^{+0.00044}_{0.00060}$	$2\,459\,566.00209^{+0.00080}_{-0.00087}$	$2\,459\,566.00267^{+0.00053}_{-0.00067}$	$2\,459\,566.00236^{+0.00089}_{-0.00086}$
Planet parameters				
P_{pl} (d)	151.3 ± 1.8	$149.2^{+2.2}_{-2.5}$	$151.7^{+1.4}_{-1.7}$	$148.6^{+2.1}_{-2.4}$
e_{pl}	<0.21	<0.19	$0.153^{+0.095}_{-0.034}$	$0.141^{+0.059}_{-0.019}$
ω_{pl} (rad)	6.0 ± 1.5	$4.9^{+1.8}_{-2.0}$	$5.37^{+0.34}_{-0.69}$	$4.57^{+0.75}_{-0.61}$
K_{pl} (m s^{-1})	40.0 ± 5.2	43.8 ± 6.9	39.1 ± 4.4	44.6 ± 5.9
$T_{0,pl}$ (BJD)	$2\,459\,442 \pm 36$	$2\,459\,425^{+43}_{-45} \pm 36$	$2\,459\,428.6^{+8.2}_{-16.4}$	$2\,459\,417^{+17}_{-14}$
Derived parameters				
M_A ($M_\odot$)	$1.23681^{+0.00037}_{-0.00039}$	$1.23766^{+0.00051}_{-0.00047}$	$1.23670^{\pm}0.00036$	$1.23763^{+0.00056}_{-0.00052}$
M_B ($M_\odot$)	$1.20207^{+0.00032}_{-0.00027}$	$1.20184^{+0.00035}_{-0.00031}$	$1.20221^{+0.00032}_{-0.00029}$	$1.20196^{+0.00046}_{-0.00036}$
m_{pl} (M_{Jup})	1.88 ± 0.25	2.05 ± 0.33	1.82 ± 0.21	2.08 ± 0.28
a_{bin} (au)	$0.191879^{+0.000016}_{-0.000018}$	$0.191894^{+0.000021}_{-0.000019}$	0.191879 ± 0.000017	$0.191896^{+0.000026}_{-0.000020}$
a_{pl} (au)	$0.7478^{+0.0056}_{-0.0060}$	$0.7408^{+0.0073}_{-0.0082}$	$0.7488^{+0.0046}_{-0.0057}$	$0.7388^{+0.0070}_{-0.0080}$
Other parameters				
$V_{sys,A}$ (km s^{-1})	25.9867 ± 0.0047	$26.0254^{+0.0056}_{-0.0058}$	26.0146 ± 0.0045	26.0531 ± 0.0057
$V_{sys,B}$ (km s^{-1})	26.0459 ± 0.0060	$26.0970^{+0.0088}_{-0.0090}$	$26.0639^{+0.0058}_{-0.0060}$	$26.1144^{+0.0087}_{-0.0089}$

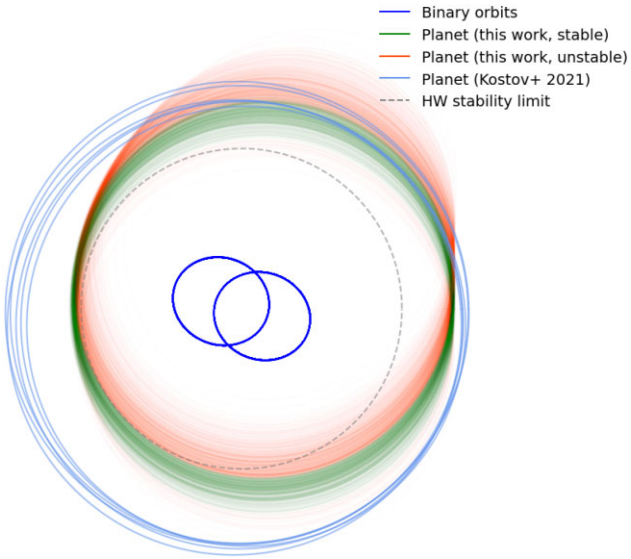


Figure A6. Orbital configuration of TIC 172900988 showing the orbits of the binary and the planet. The green orbits are a random sample of 1000 posteriors from `kima` fitting the radial velocities from SD-GP. The blue orbits are the 6 suggested solutions from Kostov et al. (2021), the dashed grey line is the stability limit as calculated by Holman & Wiegert (1999). The radial velocity data are fit along with the 1–2 punch transit times.

Downloaded from https://academic.oup.com/mnras/article/527/2/2261/7420283 by Health Services Management Centre Library user on 08 October 2024

Table A2. Radial velocities for TIC 172900988 from method 1 (SD-GP).

Time	Primary velocity (km s^{-1})	Secondary velocity (km s^{-1})
2459147.672	52.79199671 ± 0.006297356	− 1.341327759 ± 0.006306834
2459171.636	91.97097921 ± 0.005992599	− 41.7090222 ± 0.006286077
2459175.691	− 23.52844488 ± 0.00644886	77.15182984 ± 0.006474733
2459181.596	7.347251678 ± 0.006376945	45.27023063 ± 0.006680279
2459190.691	92.70303819 ± 0.006187038	− 42.5376363 ± 0.006332743
2459239.365	− 1.129883138 ± 0.006176608	53.91700289 ± 0.006657609
2459241.492	14.08887308 ± 0.005837241	38.29504511 ± 0.00627873
2459244.379	37.5613718 ± 0.006226358	14.18090136 ± 0.005747394
2459266.368	60.76693256 ± 0.005976897	− 9.64611818 ± 0.006047371
2459267.47	73.56029354 ± 0.006017367	− 22.86220394 ± 0.006961391
2459273.489	− 21.54275388 ± 0.005940911	75.02796022 ± 0.005957771
2459275.417	− 20.68023758 ± 0.006389657	74.17527381 ± 0.006500415
2459277.469	− 9.111063764 ± 0.006309079	62.28799085 ± 0.006159118
2459279.412	3.98339319 ± 0.006324967	48.82902088 ± 0.006526375
2459298.342	− 1.020137615 ± 0.006330255	54.01401655 ± 0.006227837
2459303.354	37.55683484 ± 0.0074648	14.27880206 ± 0.006027881
2459306.305	67.86532276 ± 0.006444953	− 16.94025943 ± 0.006238535
2459349.348	73.62773529 ± 0.006983177	− 22.86640098 ± 0.006296323
2459500.669	44.32693159 ± 0.006540338	7.125655004 ± 0.006049167
2459503.676	77.25865033 ± 0.006945358	− 26.80055497 ± 0.006602366
2459505.66	92.93966618 ± 0.005800538	− 42.7710604 ± 0.006673939
2459520.677	47.73082394 ± 0.006196444	3.716136893 ± 0.006353854
2459538.668	32.37888203 ± 0.006456517	19.38534042 ± 0.00619455
2459540.703	51.37790001 ± 0.005821974	− 0.173462113 ± 0.006350227
2459547.591	− 3.063614773 ± 0.006373649	55.9661014 ± 0.006367542
2459549.642	− 23.7319162 ± 0.006405175	77.21294787 ± 0.006348954
2459551.67	− 15.38293878 ± 0.00663949	68.53497782 ± 0.005787423
2459554.647	4.143067667 ± 0.006584258	48.46498983 ± 0.006984549
2459561.567	64.5010298 ± 0.006332341	− 13.53132504 ± 0.006124583
2459564.581	93.16248364 ± 0.006361619	− 42.99898808 ± 0.005963061
2459593.454	0.683072938 ± 0.006046486	52.26118897 ± 0.006787273
2459594.52	8.129553129 ± 0.007271555	44.54464934 ± 0.006443498

Table A2 – *continued*

Time	Primary velocity (km s^{-1})	Secondary velocity (km s^{-1})
2459595.551	15.80628424 ± 0.006564392	36.64180076 ± 0.00590492
2459601.498	71.67462121 ± 0.006331687	− 20.77559905 ± 0.006184636
2459603.604	93.11739363 ± 0.005906311	− 42.88178153 ± 0.005967396
2459606.465	0.153346735 ± 0.00681785	52.83101539 ± 0.006158358
2459620.521	64.26088258 ± 0.00619908	− 13.29834682 ± 0.006548925
2459622.461	87.01039359 ± 0.00627504	− 36.66314116 ± 0.006265194
2459633.431	5.236038169 ± 0.006660511	47.48907668 ± 0.006490337
2459639.522	56.92154995 ± 0.006093159	− 5.735897826 ± 0.006651901
2459641.539	80.41509092 ± 0.006584094	− 29.84720911 ± 0.006356079
2459644.369	67.1501422 ± 0.006394344	− 16.30315308 ± 0.006183854
2459648.487	− 22.40190367 ± 0.006323709	75.85843987 ± 0.005795921
2459689.378	− 14.79066973 ± 0.006230134	68.00513033 ± 0.00637691
2459700.34	78.32983042 ± 0.006419625	− 27.75129827 ± 0.006155616
2459703.361	66.33099669 ± 0.006216234	− 15.43700494 ± 0.005620311
2459866.605	− 12.90221977 ± 0.005845783	66.08328391 ± 0.006040523
2459867.575	− 6.810615935 ± 0.005947117	59.73342189 ± 0.005773165
2459883.659	− 23.8159665 ± 0.00648577	77.31777816 ± 0.006012319
2459883.678	− 23.774671 ± 0.006567066	77.31375696 ± 0.006051184
2459885.631	− 16.60526503 ± 0.006354589	69.98110091 ± 0.005834438
2459887.693	− 3.678472876 ± 0.006754954	56.62591044 ± 0.00647946
2459903.653	− 23.40576746 ± 0.006284945	77.00199673 ± 0.005950399
2459921.561	− 14.17031488 ± 0.006465102	67.36293503 ± 0.006204055
2459955.49	73.37103301 ± 0.006235832	− 22.72623035 ± 0.006626476
2459956.447	84.73111962 ± 0.006153014	− 34.38022166 ± 0.006084119
2459956.553	85.91070219 ± 0.006025253	− 35.6867799 ± 0.006509933
2459957.585	93.21325513 ± 0.00645166	− 43.09054178 ± 0.006232159
2460040.371	− 22.81230331 ± 0.006385354	76.3388599 ± 0.006613679
2460041.4	− 23.15597144 ± 0.00728653	76.62366086 ± 0.006686246
2460070.347	40.62749601 ± 0.006123952	11.0440643 ± 0.006351236

This paper has been typeset from a TEX/LATEX file prepared by the author.

Downloaded from https://academic.oup.com/mnras/article/527/2/2261/7420283 by Health Services Management Centre Library user on 08 October 2024

© 2023 The Author(s).
Published by Oxford University Press on behalf of Royal Astronomical Society. This is an Open Access article distributed under the terms of the Creative Commons Attribution License (http://creativecommons.org/licenses/by/4.0/), which permits unrestricted reuse, distribution, and reproduction in any medium, provided the original work is properly cited.

3.2 A geometric advantage for circumbinary planet transits

3.2.1 The one-two punch

Described in Section 1.6.2 and in Section 3.1.4 (section 4.4 of the paper), the one-two punch is a geometric peculiarity of circumbinary planets. It gives them a unique signature which is very hard to replicate and can allow for a confident detection of a long-period planet with a short timespan of photometric observations, which is not possible for a planet orbiting a single star (Kostov et al., 2020a). As mentioned in Section 3.1 the one-two punch was used to detect TIC 172900988b from a single sector of *TESS* data (Kostov et al., 2021).

3.2.2 Using the one-two punch in `kima`

In Section 3.1.4 (section 4.4 of the paper), the use of the one-two punch was included into `kima`. This involves calculating the one-two punch planet period and its uncertainty at each step of the sampler using Equation 1.35 where v, defined as

$$v = \frac{\Delta x}{T_1 - T_2}, \tag{3.1}$$

is the average velocity that the planet is travelling at during the one-two punch event. The uncertainty on the orbital period is calculated by error propagation through Equation 1.35

$$\begin{aligned} \sigma_P^2 &= \sigma_{(T_1-T_2)}^2 \left(\frac{\partial P}{\partial (T_1 - T_2)}\right)^2 + \sigma_{\Delta x}^2 \left(\frac{\partial P}{\partial \Delta x}\right)^2 \\ &= \sigma_{(T_1-T_2)}^2 \left(\frac{3P}{T_1 - T_2}\right)^2 + \sigma_{\Delta x}^2 \left(\frac{-3P}{\Delta x}\right)^2. \end{aligned} \tag{3.2}$$

Now

$$\sigma_{(T_1-T_2)}^2 = \sigma_{T_1}^2 + \sigma_{T_2}^2, \tag{3.3}$$

$$\sigma_{\Delta x}^2 = \sigma_{\Delta x_1}^2 + \sigma_{\Delta x_2}^2, \tag{3.4}$$

and

$$\Delta x_i = \frac{a_i(1-e_i^2)}{1+e_i\cos\nu_i}\cos\left(\omega_i+\nu_i\right), \tag{3.5}$$

so

$$\begin{aligned}\sigma^2_{\Delta x_i} &= \sigma^2_{\nu_i}\left(\frac{\partial \Delta x_i}{\partial \nu_i}\right)^2 \\ &= \sigma^2_{\nu_i} a_i^2(1-e_i^2)^2\left[\frac{-(1+e_i\cos\nu_i)\sin\left(\omega_i+\nu_i\right)+\cos\left(\omega_i+\nu_i\right)e_i\sin\nu_i}{(1+e_i\cos\nu_i)^2}\right]^2 \\ &= \sigma^2_{\nu_i} a_i^2(1-e_i^2)^2\left[\frac{e_i\sin\omega_i+\sin\left(\omega_i+\nu_i\right)}{(1+e_i\cos\nu_i)^2}\right]^2.\end{aligned} \tag{3.6}$$

The error can be propagated through Equations 1.18,1.19, and 1.20 to obtain $\sigma^2_{\nu_i}$ in terms of $\sigma^2_{T_i}$, producing the final expression:

$$\begin{aligned}\sigma_P^2 = &\left(\frac{3P}{T_1-T_2}\right)^2(\sigma^2_{T_1}+\sigma^2_{T_2})+ \\ &\left(\frac{3P}{\Delta x}\right)^2\sum_{i=1}^{2}\left[\frac{e_i\sin\omega_i+\sin\left(\omega_i+\nu_i\right)}{(1+e_i\cos\nu_i)^2}\right]^2\left(\frac{1-e_i^2}{1-e_i\cos E_i}\right)^2\frac{(1+e_i)\cos^4\left(\frac{\nu_i}{2}\right)}{(1-e_i)\cos^4\left(\frac{E_i}{2}\right)}\left(\frac{2\pi a_i}{P_{\rm bin}}\right)^2\sigma^2_{T_i}.\end{aligned} \tag{3.7}$$

Here $P_{\rm bin}$ is the orbital period of the binary and P that of the planet. All other orbital parameters (E, ϕ, ν, a, e, and ω) are that of the binary (index 1 or 2 referring to each star in turn).

Using `kima` with the one-two punch constraint gives the results presented in Section 3.1.4 (section 4.4 of the paper). Figure 3.18 shows how including the one-two punch constraint with the radial velocities constrains the solutions further but interior to the existing constraint from the radial velocities alone. The banana shaped joint distributions of e and ω seen here show the same degeneracies as in photodynamical models (e.g. Orosz et al., 2012a).

3.2.3 The one-punch

The one-two punch calculates the distance travelled by the planet during the time between the two transits and thus constrains the planet's orbital velocity. In principle, a similar calculation

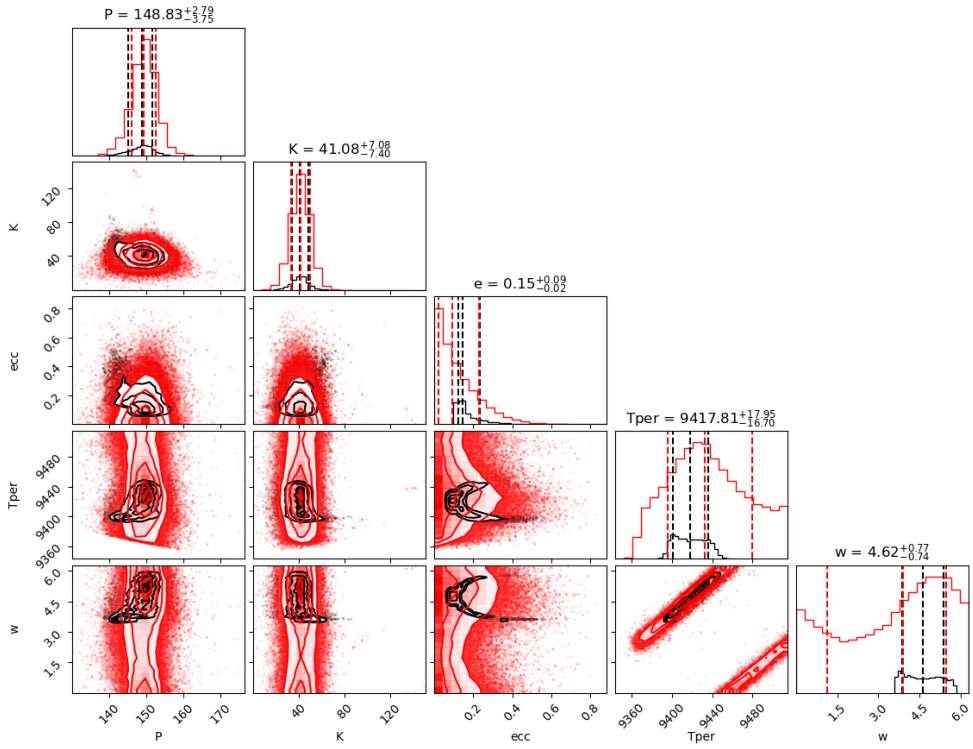


Figure 3.18: Corner plot for the orbital parameters of TIC 172900988b showing the radial velocity data alone being fit (red) and the one-two punch being included (black).

can be performed for a single transit by measuring the duration of the transit and the distance the planet would have travelled during that time. I dub this the *one-punch*. Combining this for each individual transit of a one-two punch can improve the constraints from the one-two punch. All this information gets incorporated into many photodynamical models, but this is still not infallible (e.g. TIC 172900988; Kostov et al., 2021).

The one-two punch and the one-punch share the issue that varying e and ω of the planet will have an effect on the measured orbital velocity and therefore the estimated orbital period. This degeneracy is hard to solve and was likely an issue with the initial solutions for TIC 172900988b. If another transit event is observed at a different epoch/conjunction, the period can be constrained from that, and the one-two punch can constrain the eccentricity. However in cases such as TIC 172900988, which was observed in a sector of TESS data, re-observing a transit at a future epoch is not easy.

The one-punch method is similar to the photoeccentric effect sometimes used for single stars (Dawson and Johnson, 2012). Circumbinary transits, however, have the advantage that the star

being transited is moving relative to the planet. Depending on where the star is in its orbit during the transit, the transit duration can be very long or very short (see Figure 1.15 and related discussion). This means that given a single circumbinary transit, the one-punch can be used as a check to test whether the duration of the transit is consistent with a stable planetary orbit. The orbital period can be calculated using Equation 1.35 as for the one-two punch, but with the velocity V calculated from the one-punch.

$$V = \frac{2R_\star - (r_2 \sin\theta_2 - r_1 \sin\theta_1)}{T_2 - T_1}, \tag{3.8}$$

where $R_\star$ is the radius of the star being transited, r_1 and θ_1 the radial distance and orbit angle of the star being transited at time T_1 and similarly for r_2, θ_2, and T_2. The angle $\theta_i = \nu_i - \nu_{\rm ecl}$ is shown in Figure 3.19, where ν_i is the true anomaly of the star's orbit at time T_i and $\nu_{\rm ecl}$ the true anomaly of the star at the time that it is eclipsed by the other star. T_1 and T_2 can be either the starts of ingress and egress, or the ends of ingress and egress.

In Equation 3.8, the distance used to calculate the velocity is the diameter of the star along with an added or subtracted distance based on the star's motion. Using the diameter of the star assumes a transit that has impact parameter $b = 0$ (i.e. crosses the equator of the star). $R_\star$ can be replaced by $R_\star\sqrt{1-b^2}$ if the impact parameter is known. Figure 3.20 shows a test of the one-punch method on a transit of TIC 172900988b. Each panel shows applying Equations 3.8 and 1.35 to 10000 realisations of the parameters. The vertical dashed green lines show the true planet period as calculated in Section 3.1. The first panel is as described and vastly underestimates the orbital period. Using only this information one would likely reject the transit as not real since this orbit would be unstable. The second panel is based on reducing the effective radius of the star since the transit does not have an impact parameter of 0, this is closer and compatible with the known value. The third panel incorporates $e = 0.12, \omega = 5$ into Equation 1.35 and shows good agreement with the known value. The one-punch method can therefore be used as a consistency test for a single circumbinary transit, however it is vital to know the impact parameter of the transit, and the degeneracy with e and ω is still present and an issue.

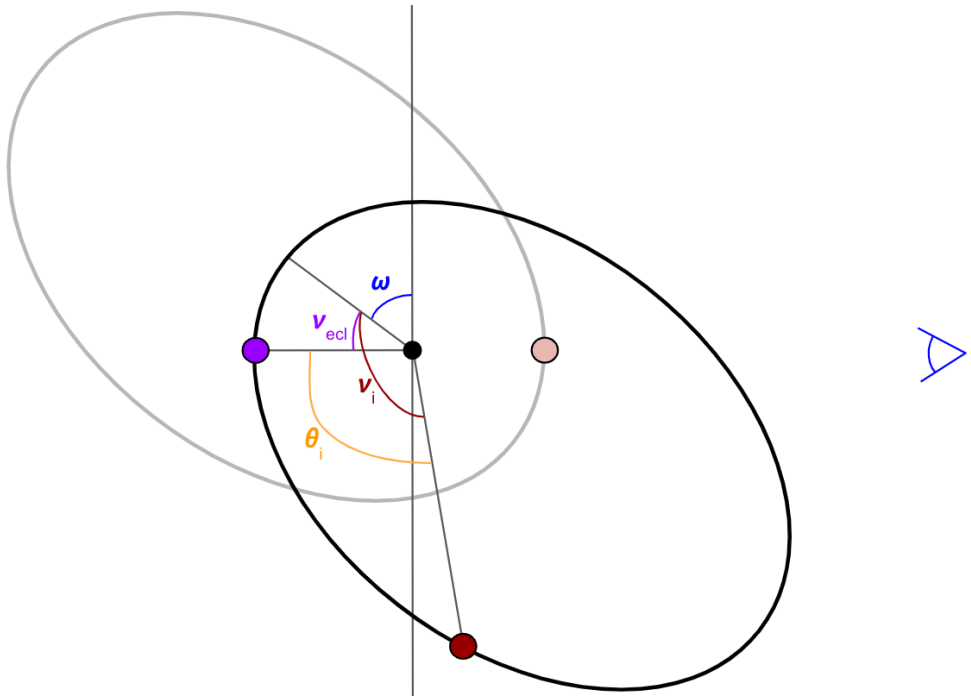


Figure 3.19: Configuration and angles used in the one-punch method. The black point is the centre-of-mass of the binary. The purple and salmon circles show the two stars at primary eclipse, the red is the primary star at time T_i. The observer is on the right. Angles shown are ω the argument of pericentre of the primary orbit, $\nu_{\rm ecl}$ the true anomaly of the primary when it is eclipsed, ν_i the true anomaly of the primary at time T_i, and $\theta_i = \nu_i - \nu_{\rm ecl}$.

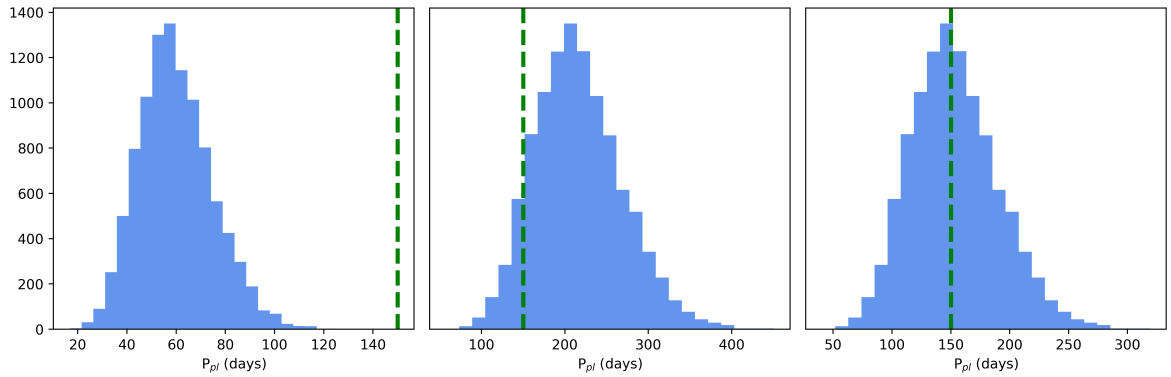


Figure 3.20: Three tests showing recovered orbital period using the one-punch on a transit of TIC 172900988b. Left: neither impact parameter not eccentricity of planet accounted for. Middle: impact parameter accounted for but not the planet's eccentricity. Right: both impact parameter and eccentricity of planet accounted for. In each case the dashed green line is the true value from the radial velocity detection.

3.3 BEBOP VI. Enabling the detection of circumbinary planets orbiting double-lined binaries with the DOLBY method of radial–velocity extraction

The following paper applies the DOLBY method to 6 known double-lined spectroscopic binaries to test the performance of the model. The work consists of an analysis of six double-lined binaries with data from SOPHIE. The analysis proceedure uses DOLBY-CCF to reduce the data and kima (BINARIESmodel) to analyse the RVs. These six systems had been studied in the past by the TATOOINE survey, a comparison is made and the results from this method are generally equal to or better than the previous results. The comparison is made both in the RMS of the residuals to the fit, and in the detection limits calculated from the data.

- Section 3.3.1 - Section 1 Introduction: Written by Lalitha Sairam with input from Amaury Triaud and me.
- Section 3.3.2 - Section 2 A summary of our double-lined binary observations: Written by Lalitha Sairam and Amaury Triaud.
- Section 3.3.3 - Section 3 A summary of the DOLBY method of radial velocity extraction: writen by Lalitha Sairam who analysed the spectra to produce the radial velocities.
- Section 3.3.4 - Section 4 Results from fitting the radial velocities: Written by me with input from Lalitha Sairam. I analysed the radial velocities and made the detection limits presented in this section.
- Section 3.3.5 - Section 5 Conclusions: written by Lalitha Sairam, Amaury Triaud and me.
- Section 3.3.6 - Appendix A Observed and modelled radial velocities: Plots generated by Lalitha Sairam.
- Section 3.3.7 - Appendix B Uncertainties and RMS values: written by Lalitha Sairam.

- Section 3.3.8 - Appendix C Detection Limits: written by me with input from Lalitha Sairam.

- Section 3.3.9 - Appendix D Radial velocity data: Compiled by Lalitha Sairam.

Monthly Notices of the ROYAL ASTRONOMICAL SOCIETY

MNRAS **534,** 3999–4017 (2024) https://doi.org/10.1093/mnras/stae2317
Advance Access publication 2024 October 10

BEBOP VI. Enabling the detection of circumbinary planets orbiting double-lined binaries with the DOLBY method of radial–velocity extraction

Lalitha Sairam [1,2★] Thomas A. Baycroft [2★] Isabelle Boisse,[3] Neda Heidari,[4] Alexandre Santerne [3] Amaury H. M. J. Triaud [2★] Gavin A. L. Coleman [5] Yasmin T. Davis [2] Magali Deleuil,[3] Guillaume Hébrard,[4] David V. Martin [6] Pierre F. L. Maxted [7] Richard P. Nelson,[5] Daniel Sebastian [2] Owen J. Scutt [2] and Matthew R. Standing [8]

[1]*Institute of Astronomy, University of Cambridge, Madingley road, Cambridge CB3 0HA, UK*
[2]*School of Physics and Astronomy, University of Birmingham, Edgbaston, Birmingham B15 2TT, UK*
[3]*Aix Marseille Univ, CNRS, CNES, LAM, 13007 Marseille, France*
[4]*Institut d'astrophysique de Paris, UMR 7095 CNRS université pierre et marie curie, 98 bis, boulevard Arago, F-75014 Paris, France*
[5]*Astronomy Unit, Queen Mary University of London, Mile End Road, London E1 4NS, UK*
[6]*Department of Physics and Astronomy, Tufts University, 574 Boston Avenue, Medford, MA 02155, USA*
[7]*Astrophysics Group, Keele University, Keele, Newcastle ST5 5BG, UK*
[8]*European Space Agency (ESA), European Space Astronomy Centre (ESAC), Madrid 28692, Spain*

Accepted 2024 October 3. Received 2024 October 3; in original form 2024 May 28

ABSTRACT

Circumbinary planets, orbiting both stars in a binary system, offer the opportunity to study planet formation and orbital migration in an environment different from that around single stars. However, despite the fact that > 90 % of binary systems in the solar neighbourhood are spectrally resolved double-lined binaries, there has been only one detection of a circumbinary planet orbiting a double-lined binary using the radial velocity method so far. Spectrally disentangling binary components is challenging due to blending of spectral lines and inaccuracies in spectral modelling. These inaccuracies add scatter to the measurements, which can hide the weak radial velocity signature of circumbinary exoplanets. We have obtained new high signal-to-noise, high-resolution spectra with the SOPHIE spectrograph, mounted on the 193 cm telescope at Observatoire de Haute-Provence (OHP), for six bright, double-lined binaries for which circumbinary exoplanet detection has been attempted in the past. To extract radial velocities, we use the DOLBY code, a recent method of spectral disentangling using Gaussian processes to model the time-varying components. We analyse the resulting radial velocities with a diffusive nested sampler to seek planets, and compute sensitivity limits. We do not detect any new circumbinary planet. However, we show that the combination of new data, new radial velocity extraction methods, and improved statistical methods to determine a data set's sensitivity to planets leads to an approximately one order of magnitude improvement compared to previous results. This improvement brings us into the range of known circumbinary exoplanets and paves the way for future observation campaigns targeting double-lined binaries.

Key words: techniques: radial velocities – techniques: spectroscopic - planets and satellites: detection – binaries: spectroscopic.

1 INTRODUCTION

One of the most remarkable discoveries from the *Kepler* mission is the identification of the first confirmed circumbinary planet, Kepler-16 b (Doyle et al. 2011). This planet orbits both stars of its binary host providing a novel environment to investigate the outcome of planet formation. The discovery of Kepler-16 b was surprising because theoretical work implies that circumbinary configurations prevent the formation of planets at such proximity to the binary (e.g. Meschiari 2012; Paardekooper et al. 2012; Lines et al. 2014; Pierens, McNally & Nelson 2020; Martin & Fitzmaurice 2022). In parallel, once planets have formed, disc-driven orbital migration parks the planets near the instability limit (e.g. Dvorak, Froeschle & Froeschle 1989; Holman & Wiegert 1999; Doolin & Blundell 2011; Coleman, Nelson & Triaud 2023a; Coleman et al. 2023b) in ways that encodes the conditions of their protoplanetary disc into their observable orbital properties (e.g. Penzlin, Kley & Nelson 2021). Thus, circumbinary planets offer new insights into planet formation mechanisms that will inform planet formation around single stars and that enhance our understanding of the exoplanet population at large, completing the tale behind the origins of the Solar System, and of our Earth.

Few circumbinary planets have been discovered so far, and most of them were found by analysing months-long space-based photometric time-series. This is expensive, and inefficient. A ground-based radial velocity survey of binaries is expected to be less biased towards planetary orbital plane perpendicular to the sky than the transit method, while finding as many planets in only a fraction of the telescope time, measuring more orbital parameters, and constructing

★ E-mail: lalitha.sairam@ast.cam.ac.uk (LS); txb187@student.bham.ac.uk (TB); a.triaud@bham.ac.uk (AT)

© 2024 The Author(s).
Published by Oxford University Press on behalf of Royal Astronomical Society. This is an Open Access article distributed under the terms of the Creative Commons Attribution License (https://creativecommons.org/licenses/by/4.0/), which permits unrestricted reuse, distribution, and reproduction in any medium, provided the original work is properly cited.

Downloaded from https://academic.oup.com/mnras/article/534/4/3999/7817980 by guest on 27 October 2024

a leaner, more intuitive picture of the circumbinary population. At the moment, single-lined binaries (SB1) are the only binaries for which a 1–2 m s^{-1} radial velocity accuracy has been demonstrated (Standing et al. 2022; Triaud et al. 2022), thus allowing for a more reliable planet detection success rate. The BEBOP survey (Binary Escorted by Orbiting Planets; Martin et al. 2019) has monitored a sample of single-lined binary systems in search of circumbinary planets leading to planet detections (e.g. TOI 1338c/ BEBOP-1c; Standing et al. 2023). Several other candidates have also been announced (Baycroft, Triaud & Lai 2024). However, in order to truly understand circumbinary systems and their formation, we need to expand the type of binaries around which circumbinary planets can be detected.

Around 90 per cent of binary systems in the solar neighbourhood are spectrally resolved as double-lined binaries (SB2; Kovaleva et al. 2016), possibly making them the most common circumbinary planet hosts. This is an opportunity to dramatically increase the sample available for circumbinary planet surveys, and perform better comparisons between the properties of exoplanets orbiting singles stars, and the properties of circumbinary planets. Double-lined binaries are on average brighter, further helping with the detection of small-mass exoplanets orbiting them. Furthermore, for each spectrum, two radial velocity measurements are obtained (for each of the components). Additionally, the vast majority of NASA's *TESS* mission (Ricker et al. 2014) might produce serendipitous circumbinary planet candidates as a '*1–2 punch*' transit event on double-lined binaries (Kostov et al. 2020). For most of the sky, only 27-d time series are available in *TESS*, and are themselves obtained once typically every other year. Because of circumbinary planet's intrinsically long orbital periods, this implies two transits of a circumbinary planet transits roughly one orbital period away from one another are challenging to obtain (except in *TESS*'s continuous viewing zone as in Kostov et al. 2021). However, within those short sectors, a circumbinary planet can still be identified when it first transits one star, and soon after transits the other star of the binary system, a *1–2 punch*. For both transit events to be detectable, both stars need to be of comparable brightness, hence, they will most likely be double-lined binaries. Without at least a 1–2 m s^{-1} accuracy on double-lined binaries, we might never know whether those events are truly produced by planets.

A dedicated search for circumbinary planets using the radial velocity method, TATOOINE, was attempted on ten double-lined binaries (SB2; Konacki et al. 2009, 2010). Despite being the state-of-the-art, their results showed a large scatter of 10–15 m s^{-1} in radial velocities (sometimes more), although photon noise reaches 1 m s^{-1} in some cases (they also had to deconvolve an iodine reference spectrum). This extra scatter would prevent the detection of most circumbinary gas giants (assuming similar planet population properties between single and binary stars). This 10–15 m s^{-1} problem is likely caused by an imperfect disentangling of the time-varying blending of weak spectral lines, as the two components orbit one another, translating across the spectrograph by $\sim$ 100 km s^{-1}. Konacki et al. (2009) disentangled their spectra to achieve a remarkable precision even at current standards, but it was not enough for identifying planets. Many lines have small signal-to-noise on each spectrum and are easy to miss. While individually they appear as noise, when hundreds of those are missed, they likely contribute to a spurious signal. Binary mask cross-correlation methods also handle line blends badly and those regions are usually avoided. They too produce extra-noise on double-lined binaries, even in 2D cross-correlations (Zucker et al. 2004).

As part of the BEBOP programme, we invested a small amount of telescope time to observing double-lined binaries, and in creating new ways of extracting radial velocities for SB2s. In Sairam et al. (2024), we produced two novel methods (now called `DOLBY`; DOuble-Lined BinarY) able to precisely measure the radial velocities of double-lined binaries. `DOLBY` uses a Gaussian process to help model both spectral components and disentangle them from one another. Applying the `DOLBY` methods to TIC 172900988, a proposed circumbinary planet transiting a double-lined binary (Kostov et al. 2021), we successfully detected a Doppler variation consistent with a circumbinary planet at an orbital period of $\sim$ 150 d (Sairam et al. 2024). However, the stars composing the TIC 172 900 988 system are both fairly hot, for the primary star, we obtained radial velocity scatters of approximately 40 and 49 m s^{-1} using both the `DOLBY`-SD and `DOLBY`-CCF methods, and for the secondary, we obtained scatters of approximately 50 and 72 m s^{-1}, respectively. This scatter did not fully demonstrate the potential of our new approach. In this paper, we report the `DOLBY` analysis of our observations of another six SB2 systems that were collected with the SOPHIE spectrograph (Perruchot et al. 2008). All six were specifically taken from the studies by Konacki et al. (2009, 2010) to enable a comparison with their results, and test how well the `DOLBY` methods perform.

This paper is structured as follows: Section 2 details the observations of SB2 systems used in our analysis. Section 3 describes the method employed to measure precise radial velocities for the binaries. In Section 4, we delve into the analysis of the radial velocities, including a comparison between those derived from the traditional TODMOR method. We also discuss the detection limit achieved for the circumbinary method using `kima` for each target system. We conclude the paper with a summary of our key results in Section 5.

2 A SUMMARY OF OUR DOUBLE-LINED BINARY OBSERVATIONS

In 2019, we initiated a sub-programme targeting 10 double-lined binaries with the SOPHIE spectrograph mounted on the 193 cm at Observatoire de Haute-Provence (Perruchot et al. 2008). Our primary objective was to collect a representative sample of double line binaries, bright and not so bright, across various spectral types and different binary orbital periods with the goal of developing and testing new methods of radial velocity extraction. Our secondary objective was to detect circumbinary planets in these systems. Our full list includes TIC 172900988, where we first presented the `DOLBY` methods and detected the circumbinary planet TIC 172900988 b (Sairam et al. 2024). We also survey another three double-lined binaries known to host circumbinary planets, from the *Kepler* field. These are typically faint. The remaining six systems, the subjects of this paper, are HD 195987, HD 210027, HD 9939, HD 78418, HD 13974, and HD 282975 (from the TATOOINE survey; Konacki et al. 2009, 2010). Their properties range 3.76 < Vmag < 10, F5 < type <G6 and 10 < P_{bin} < 57 d. Compared to the median Vmag $\sim$ 11.5 from BEBOP's main sample of single-lined eclipsing binaries (Martin et al. 2019), these six systems are much brighter and highlight well our motivation for observing them and improving radial velocity measurements for SB2s. The fundamental stellar properties of the targets are summarized in Table 1.

Between 2019 October 9 and 2023 May 6 we collected 244 spectra on the six binaries, with exposure times ranging from 200 to 1800 s. We obtained a median signal-to-noise ratio, SNR $\approx$ 85 at 5500 Å . Some of the observations were obtained in adverse weather conditions, since those systems are bright and could serve as back-up targets. Observations are summarized in Table 1, and spectra are publicly available in the SOPHIE archive.

Downloaded from https://academic.oup.com/mnras/article/534/4/3999/7817980 by guest on 27 October 2024

Table 1. Properties of SB2s.

Parameters	HD 210027	HD 13974	HD 78418	HD 9939	HD 195987	HD 282975
V (mag)	3.76	4.9	5.98	6.99	7.09	10.0
Spectral type	F5V/G8V	G0V	G5	K0IV	G3V/K2V	G6V
Effective temperatures (K)	6642/4991		6000/5900			
Number of epochs	56	35	37	43	52	21
i	95.83 ± 0.12	—	146.88 ± 0.25	61.56 ± 0.25	99.364 ± 0.080	—
Fit parameters						
P	10.2130447 ± 0.0000040	10.020195 ± 0.000020	$19.412378^{+0.000010}_{-0.000014}$	$25.208811^{+0.000015}_{-0.000018}$	$57.321927^{+0.000093}_{-0.000065}$	26.04626 ± 0.00035
e	$0.00183846^{+0.000043}_{-0.000046}$	0.0093 ± 0.00047	$0.194966^{+0.000050}_{-0.000054}$	$0.101283^{+0.000047}_{-0.000045}$	$0.305100^{+0.000034}_{-0.00031}$	$0.25051^{+0.00048}_{-0.00056}$
w	$4.730^{+0.024}_{-0.015}$	$6.188^{+0.042}_{-0.033}$	$4.94798^{+0.00045}_{-0.00042}$	$5.45092^{+0.00068}_{-0.00061}$	$6.23339^{+0.00011}_{-0.00018}$	$1.5652^{+0.0054}_{-0.0060}$
K	$48479.0^{+2.5}_{-2.2}$	10099.4 ± 4.5	$26488.66^{+0.97}_{-1.30}$	35116.0 ± 1.4	$28852.48^{+0.89}_{-0.99}$	$8169.5^{+4.7}_{-4.3}$
q	$0.623362^{+0.000083}_{-0.000065}$	$0.72090^{+0.00045}_{-0.00050}$	$0.86095^{+0.00017}_{-0.00013}$	$0.78692^{+0.00014}_{-0.00011}$	$0.786314^{+0.000119}_{-0.000098}$	$0.94962^{+0.00068}_{-0.00075}$
$\dot{\omega}$	0 ± 1000	0 ± 1000	158 ± 62	-60 ± 100	21^{+34}_{-27}	340 ± 700
T_{per}	$2459483.099^{+0.039}_{-0.024}$	$2459300.427^{+0.068}_{-0.051}$	2459409.0138 ± 0.0014	$2459374.6961^{+0.0026}_{-0.0023}$	$2459378.81855^{+0.00072}_{-0.00191}$	2459442.694 ± 0.022
$V_{sys,pri}$	-4800.8 ± 2.1	$-6558.4^{+3.9}_{-4.3}$	$9608.6^{+2.2}_{-2.0}$	-46047.8 ± 1.2	-5630.6 ± 1.0	6597.0 ± 4.5
$V_{sys,sec}$	-4240.2 ± 6.1	-6347.3 ± 6.2	$9961.6^{+4.1}_{-3.9}$	$-45670.7^{+6.0}_{-5.5}$	-5616.1 ± 4.0	$7659.2^{+5.1}_{-4.9}$
Derived parameters						
$M_{pri}\ \sin^3(i)$	1.31174 ± 0.00031	0.0084530 ± 0.0000095	0.191406 ± 0.000067	0.72977 ± 0.00026	0.80864 ± 0.00024	$0.0059273^{+0.0000098}_{-0.0000102}$
$M_{sec}\ \sin^3(i)$	0.81769 ± 0.00013	0.0060937 ± 0.0000060	$0.164793^{+0.000032}_{-0.000034}$	0.57427 ± 0.00011	0.63585 ± 0.00011	0.0056283 ± 0.0000077
M_{pri}	1.33233 ± 0.00092	—	1.173 ± 0.024	1.0733 ± 0.0076	$0.84184 \pm 6.4e{-}04$	—
M_{sec}	$0.83051 \pm 5.5e{-}04$	—	1.010 ± 0.021	0.8446 ± 0.0060	$0.66197 \pm 4.7e{-}04$	—
a_{bin}	$0.119137 \pm 2.7e{-}05$	—	0.1834 ± 0.0012	$0.20905 \pm 4.9e{-}0.4$	$0.333335 \pm 8.2e{-}05$	—
a_{pri}	0.045747 ± 0.000010	—	$0.08484^{+5.8e-04}_{-5.6e-04}$	$0.09206 \pm 2.2e{-}0.4$	$0.146733 \pm 3.4e{-}05$	—
a_{sec}	0.073390 ± 0.000018	—	$0.09854^{+6.7e-04}_{-6.5e-04}$	$0.11699 \pm 2.8e{-}0.4$	$0.186602 \pm 5.1e{-}05$	—
Bayes Factor $N_p = 1/N_p = 0$	1.6	6.6	2.1	0.4	1.2	40.6
mean $\sigma_{RV,pri}$	11.6	4.2	4.3	4.9	4.4	8.6
mean $\sigma_{RV,sec}$	44.3	29.0	14.8	29.1	9.3	9.5
rms_{pri}	12.5	18.1	6.2	5.8	4.8	10.6
rms_{sec}	40.3	24.9	21.0	63.4	27.3	20.6
$Jitter_{pri}$	< 4.0	14.9 ± 3.2	< 2.9	< 1.4	< 2.6	< 3.0
$Jitter_{sec}$	< 8.3	< 5.1	$12.3^{+5.1}_{-9.3}$	< 10.1	$25.6^{+3.4}_{-3.6}$	< 12.6

Note: Inclination values were obtained from previous literature sources: Boden, Torres & Latham (2006) for HD 9939, Konacki et al. (2009) for HD78418 and HD 210027, and Torres et al. (2002) for HD195987. No inclination measurements were found for HD 13974 and HD 282975.

Downloaded from https://academic.oup.com/mnras/article/534/4/3999/7817980 by guest on 27 October 2024

SOPHIE's high-resolution spectra cover a wide wavelength range from 3872 to 6943 Å divided into 39 spectral orders, with a resolving power of $\lambda/\delta\lambda \approx 75\,000$. The SOPHIE spectrograph was specifically designed to achieve long-term stability of $1 - 2\,\mathrm{m\,s^{-1}}$, enabling the detection of exoplanets. During the observations, we employed the `fpsimult` mode, utilizing one fibre to capture starlight and another fibre towards a Fabry–Pérot lamp, to measure the instrument drift. To ensure accurate wavelength calibration, we performed calibration procedures before the start of each night using a thorium–argon lamp and a Fabry–Pérot.

The data reduction process involved the SOPHIE automatic pipeline (Bouchy et al. 2009), which handled the extraction of the spectra and performed the necessary wavelength calibration. As described in Heidari et al. (2024), an additional colour correction was applied to account for instrumental effects. To ensure the accuracy of our spectroscopic data, we also applied a charge transfer inefficiency (CTI) correction to the SOPHIE spectra. The CTI correction[1] was performed using the method described in Bouchy et al. (2009). Subsequently, we cross-correlated the resulting wavelength-calibrated CTI corrected spectra with a numerical binary mask (Baranne et al. 1996; Pepe et al. 2002). This cross-correlation step allowed us to extract the cross-correlation functions (CCFs), which are essential for our subsequent analysis.

3 A SUMMARY OF THE DOLBY METHOD OF RADIAL VELOCITY EXTRACTION

In Sairam et al. (2024), we developed two data-driven approaches for accurately measuring radial velocities of double-lined binary systems (SB2s), that we now name DOLBY (DOuble-Lined BinarY). Both methods make use of Gaussian Processes (GP) to disentangle both stellar components. The first method works in wavelength space, and makes a spectral decomposition (DOLBY-SD), by modelling the observed spectra of a double-lined binary star as a sum of two GPsDoppler-shifted by their respective radial velocities (the quantity of interest). The second method works in velocity space, using the CCF produced by the SOPHIE pipeline (DOLBY-CCF). Here both components are each modelled as the sum of GPs and of a Gaussian function. The DOLBY-CCF approach is well suited for instruments such as HARPS, SOPHIE, and ESPRESSO that produce well characterized and stable CCFs.

In DOLBY-SD, we divide the observed spectra into smaller wavelength subsets or 'chunks' and applied GP regression separately to each chunk. This approach allows to account for different spectral types and optimizes the reconstruction of the observed spectrum. The method uses a Matérn kernel to model the covariance between the pixels. By exploring the posterior distribution of radial velocities of each chunk and the hyperparameters of the GP functions using a Markov Chain Monte Carlo sampler (MCMC), DOLBY-SD computes refined estimates of the radial velocities for each component.

In DOLBY-CCF, we instead employ a baseline mean function consisting of two Gaussian functions to capture each of the primary and secondary components of the double-lined binary star. In this method, the GPs are used to model the correlated wiggle signal of the CCF for each component using a Matérn covariance kernel. The GP models are optimized using L-BFGS-B method (Byrd et al. 1995) and the posterior distribution of hyperparameters are explored using MCMC sampling in the same way as is done for DOLBY-SD.

Both these methods are effective in accurately measuring the radial velocities of double-lined binary systems. More details on these methods and their implementation can be found in Sairam et al. (2024). For this paper we chose to use primarily the DOLBY-CCF method, which is by far the easiest to implement and more computationally efficient. This makes it the most likely to be used by other researchers. In the appendix, we provide Tables D1 through D6, which contain the radial velocities obtained using DOLBY-CCF method for the primary and secondary components of each of our targets.

4 RESULTS FROM FITTING THE RADIAL VELOCITIES

The radial velocities produced by DOLBY-CCF are fit using the *BINARIES* model of `kima` (Faria et al. 2018; Baycroft et al. 2023). `kima` is an orbital fitting algorithm utilizing the diffusive nested sampler DNEST4 (Brewer & Foreman-Mackey 2018). `kima` allows the number of Keplerian signals (N_p) applied to the data to be a free parameter. As such we can perform model comparison by computing a Bayes' factor (BF) comparing a system with $N_\mathrm{p} = 0$ (a simple binary system) to $N_\mathrm{p} = 1$ (or higher numbers of planets too) while keeping all binary and planetary orbital parameters free. `kima` fits for a systemic velocity, and also a radial-velocity jitter term which is added in quadrature to the uncertainties measured from DOLBY-CCF, and is used to account for scatter produced by any unmodelled effects such as stellar variability. The *BINARIES* model takes a different prior for the binary parameters as the planetary ones, using `kima`'s known-object mode. Apsidal precession of the binary orbit is included as an additional free parameter, and a correction to the radial velocities accounting for relativistic effects[2] is included (Baycroft et al. 2023). The *BINARIES* model fits SB1 and SB2 radial velocity data equally. In the SB2 case (used in this work), `kima` adjusts models to both the primary and secondary radial velocity time-series simultaneously. A separate systemic velocity and jitter are modelled for each of the primary star and secondary star. We use a Student's t distribution in the likelihood evaluation to account for any outliers in the radial velocities. In Figs A1 and A2, we present the radial velocity time-series for each target, along with the best-fitting binary Keplerian models.

After analysing all six double-lined binaries, we do not detect any planets that pass our detection threshold, BF $\geq$ 150 for a 1-planet model over a 0-planet model (Trotta 2008). We thus consider only the posterior samples where no planet is included to derive the orbital parameters of each of the binaries. We report the fit parameters and Bayes' factors in Table 1. A final advantage of a nested sampler is that it can be used to compute accurate sensitivity limits. We describe that procedure in Section 4.7.

Being conscious that nested samplers remain a fairly recent occurrence in the exoplanet scientific literature, we also produce a more classical test. We compute a series of generalized Lomb–Scargle (GLS) periodograms (Zechmeister & Kürster 2009). One periodogram is created for the radial velocities measured of each of the primaries, and for each of the secondary stars (see Fig. 1

[1]For HD9939 and HD195987 the CTI correction appears to induce a large residual scatter in the data for the secondary star, so for these two cases we do not apply the correction.

[2]These being the light travel-time, transverse Doppler, and gravitational redshift effects (Zucker & Alexander 2007; Sybilski et al. 2013).

Downloaded from https://academic.oup.com/mnras/article/534/4/3999/7817980 by guest on 27 October 2024

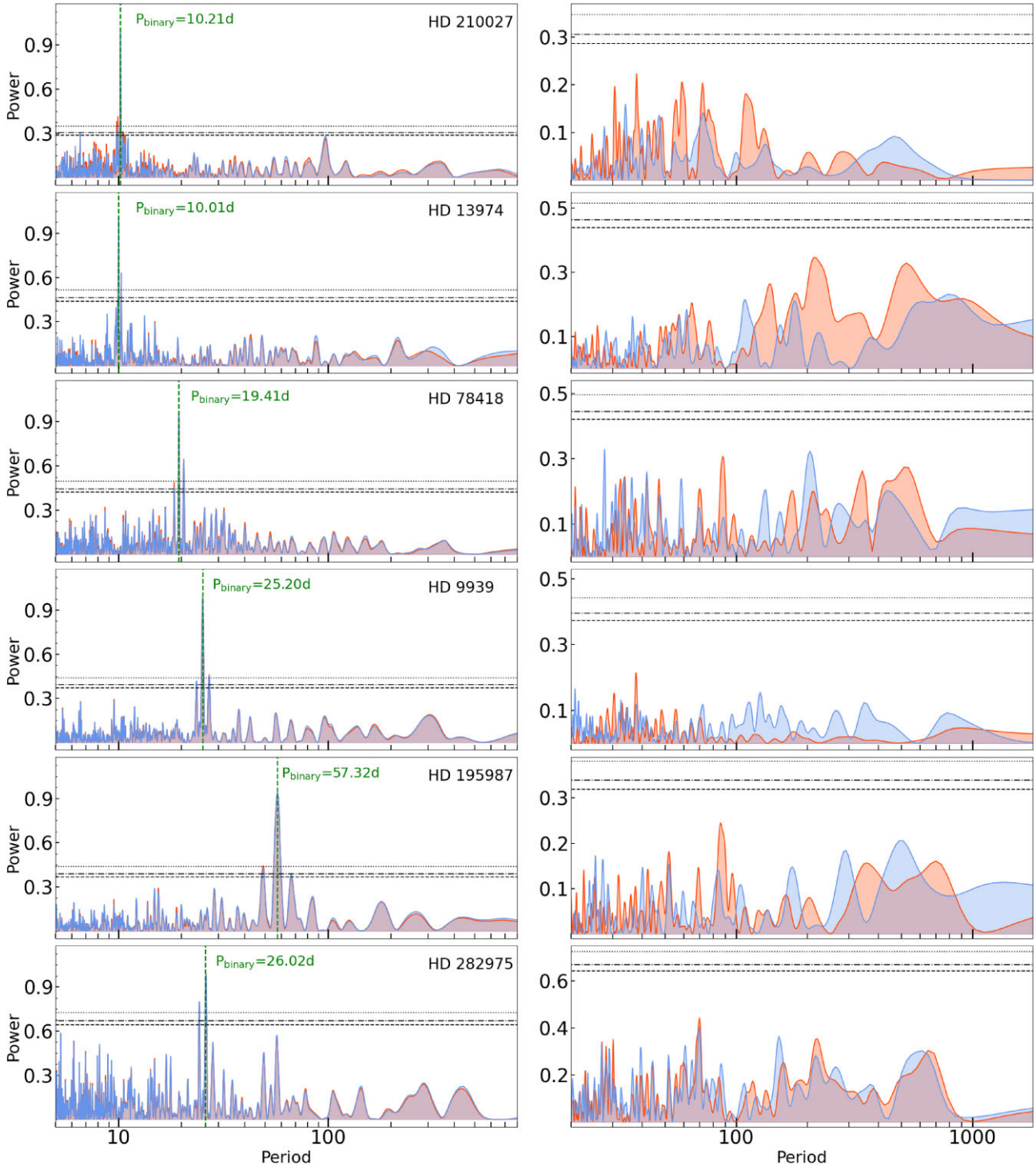


Figure 1. Left panels: Periodogram of radial velocities for the primary and the secondary stars with binary signal. Right panels: Periodograms after removing the binary motion. The three horizontal lines indicate 10 per cent (dashed line), 5 per cent (dotted dash line), and 1 per cent (dotted line) false alarm probabilities.

left panels). Any orbiting object should produce a similar signature in both the primary and secondary sets of radial velocities, whereas parasitic signals such as stellar variability are expected to only show in one of the two components. The primary and the secondary stars are depicted in red and blue colours, respectively. We use a 10 000 bootstrap randomization of each input data sets to compute false alarm probabilities (FAP) levels of 10 per cent, 5 per cent, and 1 per cent. The significant peaks shown in the left hand side columns of periodograms are associated with the binary star.

To test for the presence of circumbinary exoplanets we compute a second series of GLS, after having removed the binary's orbital motion. To do that we subtract the best-fitting Keplerian motion from the `kima` analysis for each of the binary stars (Fig. 1 right

Downloaded from https://academic.oup.com/mnras/article/534/4/3999/7817980 by guest on 27 October 2024

panels). There are no significant peaks in any of the radial-velocity residuals (right-hand column) that are consistent between the primary and secondary, and also consistent with the results obtained with `kima`.

We now describe the results for every system individually.

4.1 HD 210027

HD 210 027 is a bright F5V/G8V spectral type binary system with an orbital period of 10.2 d (Konacki et al. 2010). The SOPHIE observation period spans ∼800 d. The periodograms for HD 210 027 in Fig. 1 (left panel) shows excess at binary period at $P_{\rm bin} \sim 10.21$ d for both the primary and the secondary star with a FAP value significantly lower than $< 10^{-6}$. Subtracting this signal from the data and recalculating the periodogram (right panel) reveals a few moderate peaks at 5× and 8× the binary period for the primary star's radial velocities. These peaks have a FAP of less than 0.05. The Bayes' Factor for the $N_{\rm p} = 1$ model versus $N_{\rm p} = 0$ model is ∼1.6. We therefore do not associate this signal with a planetary signal, but possibly with stellar activity on the primary star instead. Our radial velocity solution has rms of 12.5 and 40.3 m s^{-1} for the primary and secondary stars, respectively. The $M \sin^3 i$ for the primary and secondary are $1.31174 \pm 0.00031\,{\rm M}_{\odot}$ and $0.81769 \pm 0.00013\,{\rm M}_{\odot}$, with a precision of 0.027 per cent and 0.015 per cent, respectively. Compared to the previous work, the mass estimates are ∼ 59 per cent and ∼ 77 per cent more precise for the primary and secondary stars.

4.2 HD 13974

HD 13 974 is a 10-d period binary with a spectral type of G0V Konacki et al. (2009). With an observation span extends over ∼ 1100-d, the periodograms for HD 13 974 (Fig. 1, left panel) reveal an evident excess at the binary period of approximately $P_{\rm bin} \sim 10.0177$ d for both the primary and secondary star with FAP $< 10^{-6}$. After removing the strong binary signal from the data, the periodogram is rerun on this binary-subtracted data (shown in the right panel of Fig. 1). This reveals that the primary star's radial velocity data still exhibits a peak, but the associated FAP is now less than 0.05(5 per cent). The BF for the $N_{\rm p} = 1$ model versus $N_{\rm p} = 0$ model is ∼6.6. Our radial velocity solution has an rms of 18.1 m s^{-1} for the primary star and 24.9 m s^{-1} for the secondary star.

4.3 HD 78418

HD 78 418 is a G5 spectral type binary system with 19.4 d orbital period (Konacki et al. 2010). The periodograms for HD 13 974 in Fig. 1 (left panel) reveal a notable signal at a binary period of approximately 19.3971 d for both the primary star and with an associated FAP $< 10^{-6}$. When we subtract this signal and re-run the periodogram, as shown in the right panel, we observe a peak at 87.88 d for the primary star and ∼205 d with FAP < 0.05(15 per cent) for the secondary star. However, due to the absence of significantly prominent peaks in both stars, we refrain from making definitive comments on the significance of these signals at this stage. The BF for the $N_{\rm p} = 1$ model versus $N_{\rm p} = 0$ model is ∼2.1. Nevertheless, we intend to continue monitoring this system. The duration of SOPHIE observations spans over 1135 d. The radial velocities derived by our method have an rms of 6.2 and 21 m s^{-1} for the primary and the secondary stars, respectively.

4.4 HD 9939

HD 9939 comprises a binary system characterized by a K0IV spectral type, with an orbital period of 25.2 d (Boden et al. 2006). The SOPHIE observation period spans over 1138 d. The periodograms for HD 9939 in Fig. 1 (left panel) shows excess at binary period at ∼25.2319 d for both the primary and the secondary stars with a FAP $< 10^{-6}$. The radial velocity determined using our methodology, exhibits rms of 5.8 m s^{-1} for the primary star and 63.4 m s^{-1} for the secondary star. We note that the scatter in radial velocity measurements is the largest among all the targets, and we speculate it might be caused by intrinsic variability of this particular star.

The BF for the $N_{\rm p} = 1$ model versus $N_{\rm p} = 0$ model is ∼0.4. When we subtract the Keplerian signal with a period of ∼25.2319 d, as depicted in the periodogram (right panel), we observe two peaks at around 38 and 48 d with a FAP exceeding ∼ 0.05(5 per cent) in the radial velocities of the primary star. Stellar variability could potentially be the source of this signal, which warrants further investigation.

4.5 HD 195987

HD 195 987 is a G3V/K2V binary system with an orbital period of 57 d (Torres et al. 2002), making it the system with the longest binary period within our set of targets. Our observational coverage with SOPHIE spans ∼766 d. In the periodogram analysis, a signal emerges at the binary period of ∼ 57.3129 d for both the primary and secondary stars with a FAP $< 10^{-6}$. Upon removing this signal from the data, we do not detect any other prominent peaks in the periodogram (Fig. 1, right panel). The BF for the $N_{\rm p} = 1$ model versus $N_{\rm p} = 0$ model is ∼1.2. In the case of HD 195987, our radial velocity solution produces a rms of 4.8 m s^{-1} for the primary star, effectively reaching the photon noise level, and 27.3 m s^{-1} for the secondary star.

4.6 HD 282975

HD 282 975 is a binary system featuring G6V stars with an orbital period of 26 d (Konacki et al. 2009). The duration of our survey extends to 1107 d. The periodogram analysis of the radial velocity data from HD 282 975 produces signal at a binary period of ∼26.1681 d for both the primary and the secondary stars with FAP $< 10^{-6}$. Following the removal of this prominent peak, no other significant peak emerges (Fig. 1, right panel). The BF for the $N_{\rm p} = 1$ model versus $N_{\rm p} = 0$ model is ∼40.6, a value below the detection threshold of 150. Furthermore, the results of our radial velocity analysis produces an rms of 10.6 m s^{-1} for the primary star and 20.6 m s^{-1} for the secondary star.

4.7 Detection limit

The use of `kima` (and nested sampling in general) lends itself to calculating detection limits in a single analysis. In cases where no planet is detected, as is the case for the systems in this work, we fix the number of Keplerian signals included in the model to one and perform another analysis. The posterior samples resulting from this analysis will then correspond to planetary signals that are consistent with the data but not formally detected. To obtain a detection limit the posterior samples are binned in period with bins of equal width in log-space, then within each bin the detection limit is the value of the semi-amplitude K below which 99 per cent of the posterior samples lie. A more detailed explanation of this method can be found

Downloaded from https://academic.oup.com/mnras/article/534/4/3999/7817980 by guest on 27 October 2024

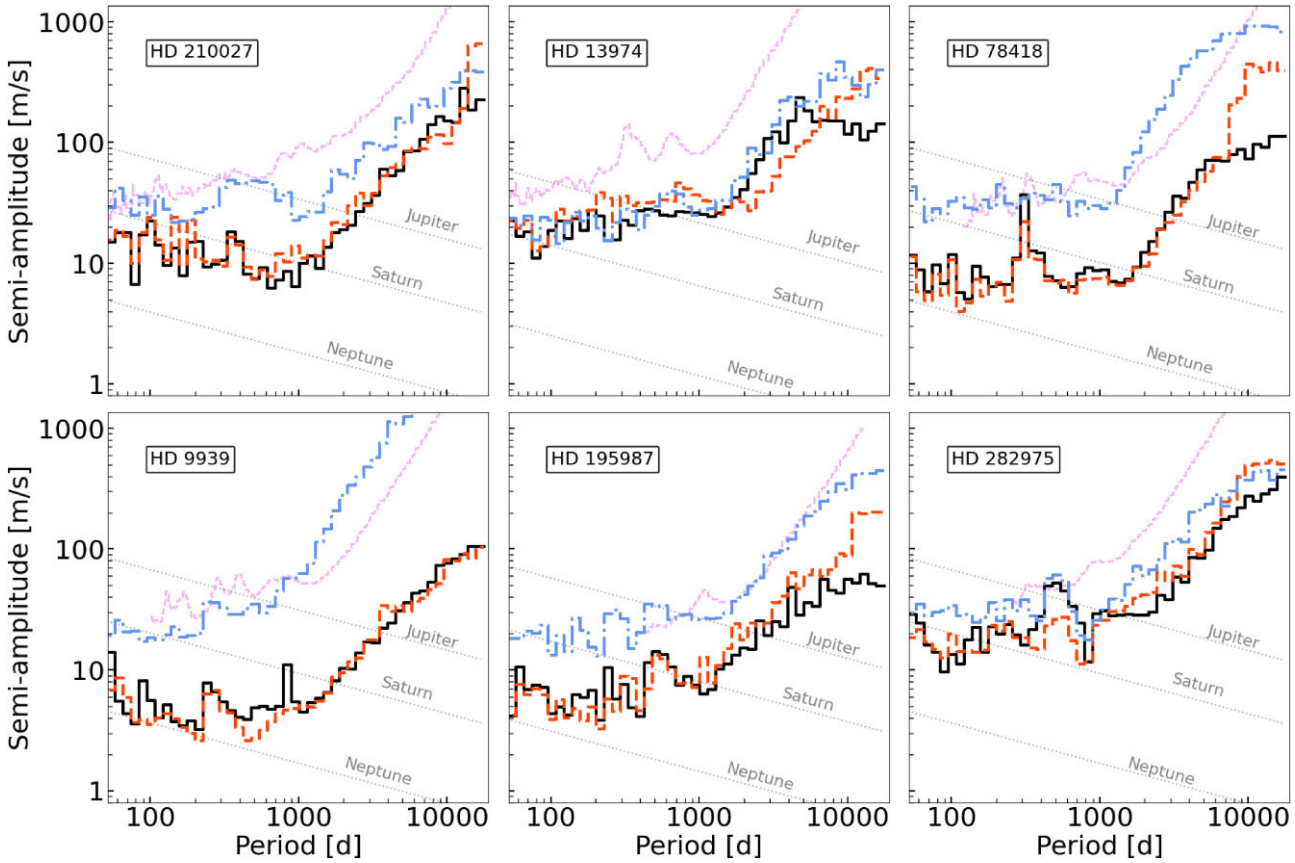


Figure 2. The sensitivity limits based on the density of posterior samples for each binary system from the `kima` run with N_P fixed to 1. Histograms lines show the amplitude at the 99th percentile within each period bin, giving us a 99 per cent confidence upper limit. The different lines represent analyses using data solely on the primary stars, secondary stars, and the combined data set, respectively. The detection limit curves from Konacki et al. (2009, 2010) are also shown. Diagonal lines represents the anticipated signals of Neptune, Saturn, and Jupiter mass planets orbiting stars with their respective binary masses.

in Standing et al. (2022). To ensure that the detection limit is robust we ensure that each period bin contains at least 1000 posterior samples.

For this work, we perform three detection limits for each binary, the first taking only the radial velocity data for the primary and fitting as a single-lined binary, the second taking only the data for the secondary, and the third taking both and fitting as a double-lined binary. These are shown in Fig. 2 alongside the detection limits from Konacki et al. (2009). The diagonal lines indicate the expected signal amplitudes of Neptune, Saturn, and Jupiter mass planets orbiting each binary. We see that our detection limits are consistently more sensitive, up to an order of magnitude better, in the best case. This could come from DOLBY being an improved method at extracting radial velocities, from an increase in data between Konacki et al. (2010) and our study, and/or from a difference in how the detection limits are estimated.

To further evaluate the performance of our radial-velocity extraction method, we check the influence of data amount and computation of the detection limit. To test the detection limit methods, we first focus on two specific systems, HD 210 027 and HD 78418. These systems were chosen because they are the only ones for which we have available radial velocity data from Konacki et al. (2010). We have applied the `kima` method to the radial velocity data from Konacki et al. (2010) for these systems to obtain detection limits. These results are compared with the detection limits derived from our `kima-DOLBY` analysis of the same data and with the original detection limits reported by Konacki et al. (2009). Fig. C1 shows the comparison of these detection limits for both systems. The solid black lines represent the detection limits obtained from our `kima-DOLBY` analysis, while the green lines correspond to the detection limits derived from the Konacki data using `kima`. The pink lines indicate the original detection limits reported by Konacki et al. (2009).

In our comparison of detection limits, we consistently observe that `DOLBY` performs better than previous approaches. Given that we have now employed `kima` on Konacki's radial velocity data and achieved consistent results, the improvement in detection limits is not attributable to the detection limit calculation method itself. Instead, the enhancement could likely be from either the superior accuracy of the `DOLBY` method or the increased number of measurements.

To quantify the impact of the number of observations, we systematically scaled the Konacki detection limits based on the square root of the relative number of measurements for each system, shown in Fig. C2. This scaling assumes that the detection limit improves proportionally with the square root of the number of observations. Our analysis reveals that even after accounting for this scaling, the `DOLBY` method still demonstrates an improved performance, suggesting that its inherent accuracy contributes significantly to the observed improvement in detection limits.

Downloaded from https://academic.oup.com/mnras/article/534/4/3999/7817980 by guest on 27 October 2024

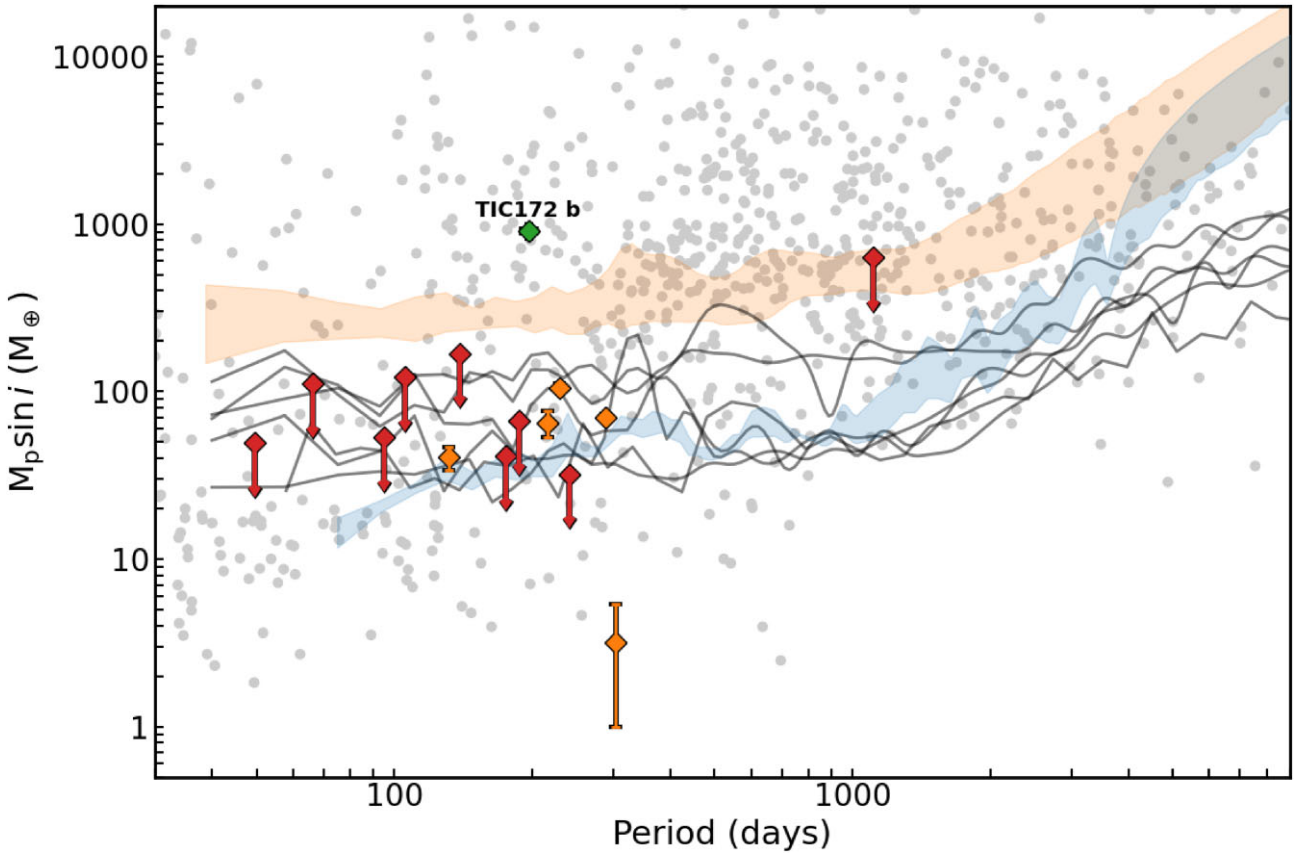


Figure 3. Minimum planet mass versus period plot showcasing the detection limits of DOLBY targets in this study, represented as black lines, alongside confirmed exoplanets as grey circles, and circumbinary planets as orange/red diamonds. Circumbinary planets with upper mass limits are marked with arrows signifying a 2σ upper limit. The band denotes the detection limits for SB1 systems (Standing et al. 2022), while the band represents the detection limits for SB2 systems (Konacki et al. 2009, 2010). The SB2 circumbinary planet TIC 172900988b (Sairam et al. 2024) is also shown.

4.8 Comparison between methods and data sets

Across the six systems analysed, the mean radial-velocity error for each system ranges between 4.2 and 11.6 m s^{-1} for the primaries and 9.3–44.3 m s^{-1} for the secondaries. In addition, we measure an RMS scatter after removing the most likely binary solution ranging from 4.8 to 18.1 and 20.6 to 63.4 m s^{-1} for primaries and secondaries, respectively. In all but 3 of the 12 cases the radial velocity jitter that is included in the fit is not constrained and is consistent with 0. This shows that we are reaching a regime where we are photon-noise limited in the best cases. It is also worth noting here that all of the six binaries have at least one of the primary and secondary radial velocities close to photon-noise, reinforcing the notion that observing double-lined binaries can be a favourable way to avoid stellar activity relative to single stars or single-lined binaries. When only one component is resolved, and if that component is active, then detecting exoplanets becomes challenging. In the case of double-lined systems, the activity cycle of both stars does not need to be related, and while one star is active, the other star might not be, providing a way to continue the radial-velocity monitoring.

The uncertainties and jitters are shown in Fig. B1, where the box plot showcases the distribution of uncertainties for each binary system and compares them to other results.

We note that DOLBY-CCF systematically outperforms TODMOR (Zucker et al. 2004), the only public code we could directly compare our results to, and analyse the same data with. In addition, the SOPHIE sample analysed with DOLBY produces uncertainties that are systematically smaller than results reported in Konacki et al. (2009, 2010) for the same systems. Also, the DOLBY results typically cover a narrower range of values (i.e. measurements are more consistent with one another). RMS values of the RV residuals are also depicted. Despite using a 2 m telescope and collecting on average twice as many measurements for each system, the detection sensitivity obtained with SOPHIE + DOLBY is better in all cases than those reported in Konacki et al. (2009, 2010), even though Konacki et al. used a combination of telescopes including the 10 m Keck/Hires, SHANE/CAT/Hamspec, and TNG/SARG. We take this as evidence that the DOLBY method is slightly more accurate than the disentangling method of Konacki et al. (2009, 2010).

5 CONCLUSIONS

This paper presents the application of a novel method, called DOLBY-CCF, to measure radial velocities of double-lined binary stars with high precision. We applied DOLBY-CCF to analyse newly collected SOPHIE observations of six double-lined systems previously observed by the TATOOINE survey (Konacki et al. 2009, 2010). Our goal was to assess the capability of DOLBY-CCF for accurate RV measurements of double-lined binary stars, and to assess its potential to detect circumbinary exoplanets.

Downloaded from https://academic.oup.com/mnras/article/534/4/3999/7817980 by guest on 27 October 2024

We achieved a significant improvement in RV precision compared to the traditional TODMOR method (Fig. B1). Our analysis did not reveal any significant detections of circumbinary planets within our sample. Fig. 3 depicts a plot of mass versus the orbital period of detection limits obtained from this work for double-lined binaries (black). It also includes detection limits for single-lined binaries (SB1; blue band) obtained by Standing et al. (2022) and confirmed exoplanets (grey filled circles; NASA Exoplanet Archive[3]). Known transiting circumbinary planets with mass measurements are represented as filled diamonds. We also show the range of detection limits reported by Konacki et al. (2009, 2010) as an orange band. While detection limits for single-lined binaries by Standing et al. (2022) are compatible to the DOLBY-CCF method for SB2s, our analysis offers up to one order-of-magnitude improvement in sensitivity compared to the previous results reported in Konacki et al. (2009, 2010). This improvement could come from various sources: (1) greater accuracy in the radial-velocity extraction, (2) more radial-velocity measurements, and (3) improved methods to compute sensitivity limits, however, by analysing publicly available data from Konacki et al. (2010), and rescaling detection limits to account of differences in the number of measurements, we show that the main improvement is most likely because DOLBY-CCF extracts more accurate radial velocities than previous methods. Fig. 3 also showcases it is now possible to detect circumbinary planets with masses below that of Saturn for orbital periods of up to 1000 d – mirroring the detection capacity observed in single-lined binaries (Standing et al. 2022). The high RV precision achieved by DOLBY-CCF paves the way for future, more sensitive searches for circumbinary planets around double-lined binary stars.

Future work will involve applying DOLBY-CCF to a larger sample of double-lined binary stars and incorporating additional observations to increase the sensitivity of our planet searches. In addition, we aim to test the DOLBY-SD method to compare it to the CCF approach. Our current results however demonstrate that DOLBY represents a valuable, public tool capable of advancing our understanding of circumbinary systems and their potential to harbour exoplanets.

ACKNOWLEDGEMENTS

This paper is based on observations collected at the Observatoire de Haute Provence (OHP). We are grateful to the entire staff at OHP, especially the night assistants, for their dedication and hard work in securing these observations, particularly during the challenging times of the COVID pandemic.

This research was funded by the European Research Council (ERC) under the European Union's Horizon 2020 research and innovation programme (grant agreement no. 803193/BEBOP) and by the Leverhulme Trust (research project grant no. RPG-2018-418). PM acknowledges support from STFC research grant number ST/S001301/1. MRS acknowledges support from the European Space Agency as an ESA Research Fellow. IB, GH, AS, MD acknowledge the Programme National de Planetologie (PNP) of the CNRS INSU co-funded by CNES for the funds received to support this work. The acquisition of data was facilitated by a series of allocations through the French PNP. The computations for this research were performed using the University of Birmingham's BlueBEAR HPC service http://www.birmingham.ac.uk/bear.

[3]https://exoplanetarchive.ipac.caltech.edu/index.html

DATA AVAILABILITY

The full radial velocity data for this study are provided in the appendix. Reduced spectra used in the analysis are publicly available through the SOPHIE archive http://atlas.obs-hp.fr/sophie/.

REFERENCES

Baranne A. et al., 1996, Astron. Astrophys. Suppl. Ser., 119, 373
Baycroft T. A., Triaud A. H. M. J., Faria J., Correia A. C. M., Standing M. R., 2023, MNRAS, 521, 1871
Baycroft T. A., Triaud A. H. M. J., Lai D., 2024, preprint (arXiv:2409.04191)
Boden A. F., Torres G., Latham D. W., 2006, ApJ, 644, 1193
Bouchy F., Isambert J., Lovis C., Boisse I., Figueira P., Hébrard G., Pepe F., 2009, in Kern P.,ed., EAS Publications Series, Vol. 37, EAS Publications Series. p. 247
Brewer B. J., Foreman-Mackey D., 2018, J. Stat. Softw., 86, 1
Byrd R. H., Lu P., Nocedal J., Zhu C., 1995, SIAM J. Sci. Comput., 16, 1190
Coleman G. A. L., Nelson R. P., Triaud A. H. M. J., 2023a, MNRAS, 522, 4352
Coleman G. A. L., Nelson R. P., Triaud A. H. M. J., Standing M. R., 2023b, MNRAS, 527, 414
Doolin S., Blundell K. M., 2011, MNRAS, 418, 2656
Doyle L. R. et al., 2011, Science, 333, 1602
Dvorak R., Froeschle C., Froeschle C., 1989, A&A, 226, 335
Faria J. P., Santos N. C., Figueira P., Brewer B. J., 2018, J. Open Source Softw., 3, 487
Heidari N. et al., 2024, A&A, 681, A55
Holman M. J., Wiegert P. A., 1999, AJ, 117, 621
Konacki M., Muterspaugh M. W., Kulkarni S. R., Hełminiak K. G., 2009, ApJ, 704, 513
Konacki M., Muterspaugh M. W., Kulkarni S. R., Hełminiak K. G., 2010, ApJ, 719, 1293
Kostov V. B. et al., 2020, AJ, 160, 174
Kostov V. B. et al., 2021, AJ, 162, 234
Kovaleva D., Malkov O., Yungelson L., Chulkov D., 2016, Balt. Astron., 25, 419
Lines S., Leinhardt Z. M., Paardekooper S., Baruteau C., Thebault P., 2014, ApJ, 782, L11
Martin D. V., Fitzmaurice E., 2022, MNRAS, 512, 602
Martin D. V. et al., 2019, A&A, 624, A68
Meschiari S., 2012, ApJ, 761, L7
Paardekooper S.-J., Leinhardt Z. M., Thébault P., Baruteau C., 2012, ApJ, 754, L16
Penzlin A. B. T., Kley W., Nelson R. P., 2021, A&A, 645, A68
Pepe F., Mayor M., Galland F., Naef D., Queloz D., Santos N. C., Udry S., Burnet M., 2002, A&A, 388, 632
Perruchot S. et al., 2008, in McLean I. S., Casali M. M., eds, Proc. SPIE Conf. Ser. Vol. 7014, Ground-based and Airborne Instrumentation for Astronomy II. SPIE, Bellingham, p. 235
Pierens A., McNally C. P., Nelson R. P., 2020, MNRAS, 496, 2849
Ricker G. R. et al., 2014, in Oschmann J. M. J., Clampin M., Fazio G. G., MacEwen H. A., eds, Proc. SPIE Conf. Ser. Vol. 9143, Space Telescopes and Instrumentation 2014: Optical, Infrared, and Millimeter Wave. SPIE, Bellingham, p. 914320
Sairam L. et al., 2024, MNRAS, 527, 2261
Standing M. R. et al., 2022, MNRAS, 511, 3571
Standing M. R. et al., 2023, Nat. Astron., 7, 702
Sybilski P., Konacki M., Kozłowski S. K., Hełminiak K. G., 2013, MNRAS, 431, 2024
Torres G., Boden A. F., Latham D. W., Pan M., Stefanik R. P., 2002, AJ, 124, 1716
Triaud A. H. M. J. et al., 2022, MNRAS, 511, 3561
Trotta R., 2008, Contemp. Phys., 49, 71
Zechmeister M., Kürster M., 2009, A&A, 496, 577
Zucker S., Alexander T., 2007, ApJ, 654, L83
Zucker S., Mazeh T., Santos N. C., Udry S., Mayor M., 2004, A&A, 426, 695

Downloaded from https://academic.oup.com/mnras/article/534/4/3999/7817980 by guest on 27 October 2024

APPENDIX A: OBSERVED AND MODELLED RADIAL VELOCITIES

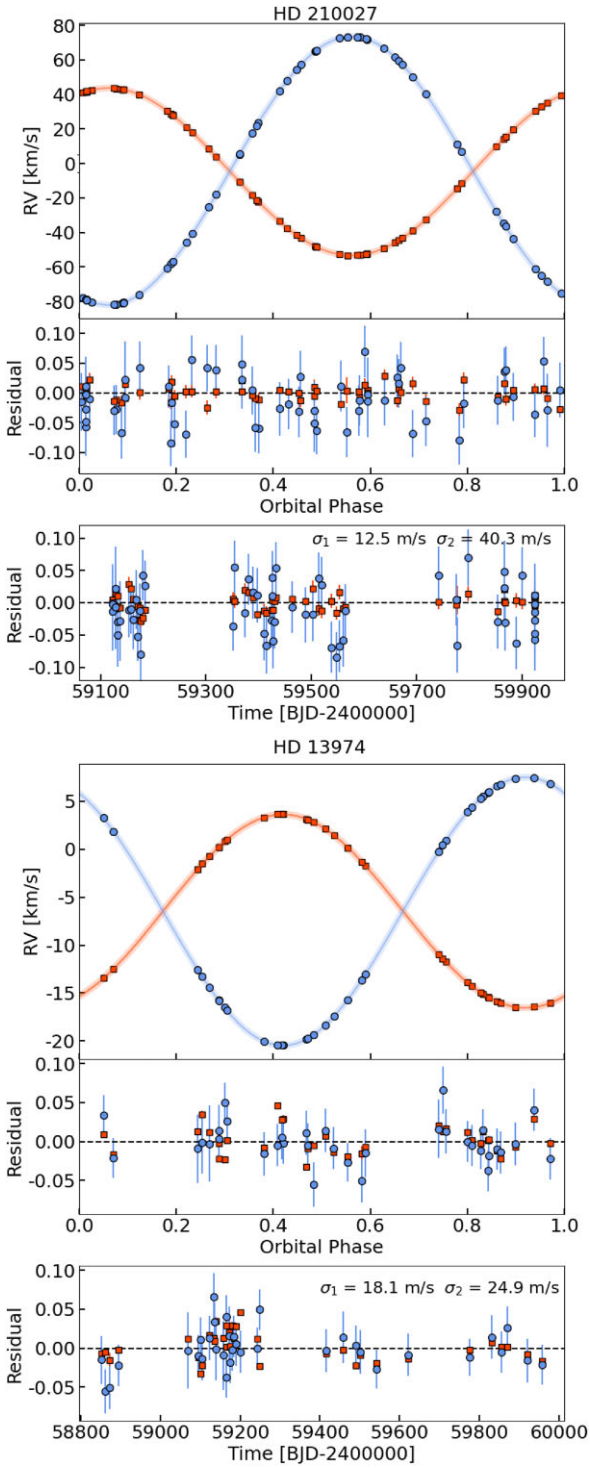


Figure A1. Observed and modelled radial velocities of HD 210027 and HD 13974 as a function of the orbital phase, their best-fitting residuals as a function of the orbital phase and time. The square symbols represent the primary star, and the circular symbols represent the secondary star.

Downloaded from https://academic.oup.com/mnras/article/534/4/3999/7817980 by guest on 27 October 2024

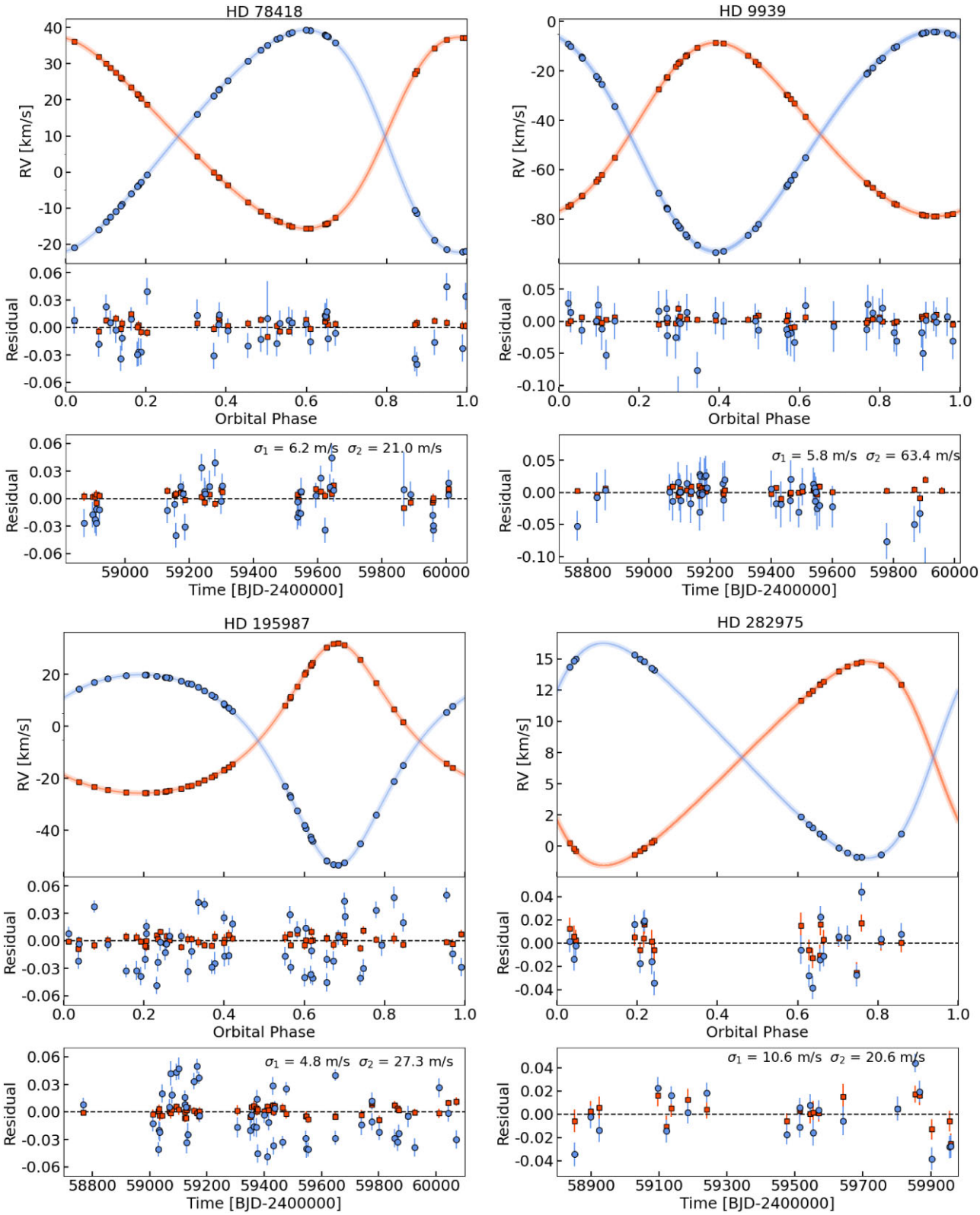


Figure A2. Observed and modelled radial velocities of HD 78418, HD 9939, HD 195987, and HD 282975 as a function of the orbital phase, their best-fitting residuals as a function of the orbital phase and time. The square symbols represent the primary star, and the circle symbols represent the secondary stars, respectively.

Downloaded from https://academic.oup.com/mnras/article/534/4/3999/7817980 by guest on 27 October 2024

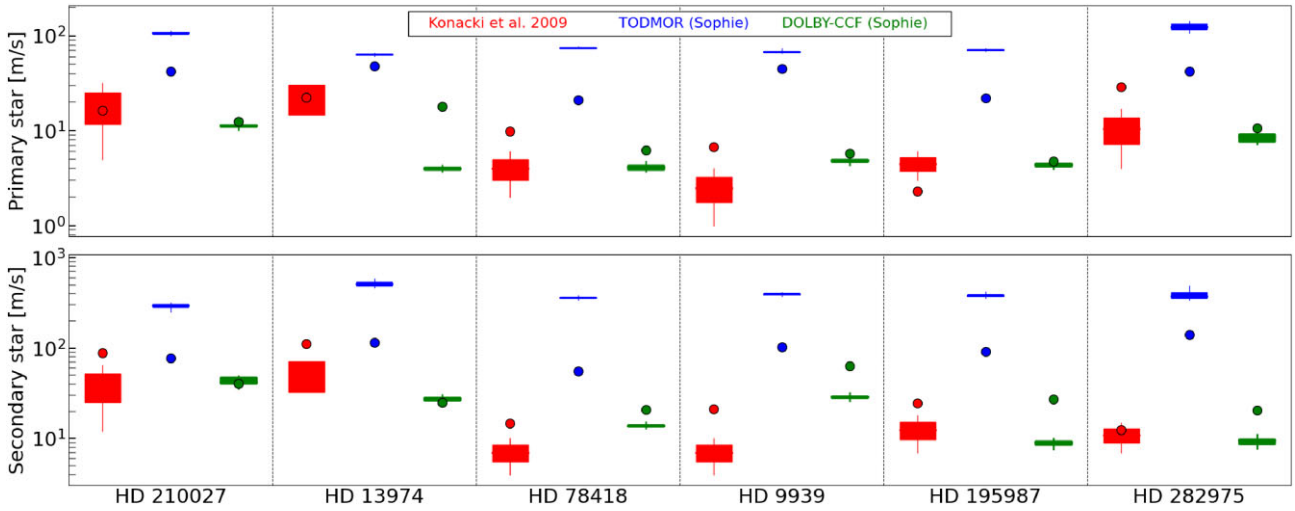


Figure B1. The uncertainties are presented for three measurement methods: Konacki et al. 2009 (Keck/HIRES), TODMOR (Sophie), and DOLBY-CCF (Sophie). Box plots represent the distribution of uncertainties associated with each method for both primary (top panel) and secondary (bottom panel) stars. Additionally, RMS values for each method are plotted as scattered points with the corresponding colours. Note: For HD 13974, data from the Shane/CAT/Hamspec instrument (as reported in Konacki et al. 2009) were used, as Keck/HIRES observations were not available for this system.

APPENDIX B: UNCERTAINTIES AND RMS VALUES

During our analysis, we attempted to compare the RMS values obtained from our kima-DOLBY analysis with those reported by Konacki et al. (2009) for all our target systems. In Fig. B1, the uncertainties are shown, where the box plot shows the distribution of uncertainties and the circles indicate the RMS for each binary system and compares them to other results. We focused on Keck/HIRES data for comparison, as this instrument provided the highest precision measurements used by Konacki et al. (2009). For the case of HD 13974, as it was not observed with Keck/HIRES, we used the numbers from the Shane/CAT/Hamspec data set (see table 1 in Konacki et al. 2009), which was the only available data.

Upon re-analysing the (Konacki et al. 2010) RVs with kima, we found that RMS values were consistently higher than those reported. This discrepancy prevented a meaningful comparison between the results and also questioning accuracy of the RMS values.

Although this re-analysis was carried out for just HD 78418 and HD 210027 in detail, the consistent overestimation of RMS values suggests that similar discrepancies might exist for other systems as well.

APPENDIX C: DETECTION LIMITS

When comparing the detection limits of the Konacki data with kima (we call kima-Konacki) and with their own analysis (we call Konacki et al. 2009), we find that while they are comparable in terms of their overall significance, they exhibit different shapes. In Fig. C1, we show the comparison of these detection limits for HD 78418 and HD 210027. Both sets of detection limits using Konacki et al. (2009) data are significantly above the detection limits obtained from our kima-DOLBY analysis, indicating that our kima-DOLBY method is more sensitive in detecting potential exoplanets.

In Fig. C2, we scale the planet detection limits from Konacki et al. (2009) to number of observations and compare with DOLBY detection limits. Our method consistently performs better than previous approaches in detecting exoplanets. This improvement is due to both our DOLBY method's accuracy and the increased number of measurements. Even when accounting for the number of measurements, DOLBY still demonstrates significantly better detection limits. This suggests that DOLBY's underlying methodology is a key factor in our improved performance.

Downloaded from https://academic.oup.com/mnras/article/534/4/3999/7817980 by guest on 27 October 2024

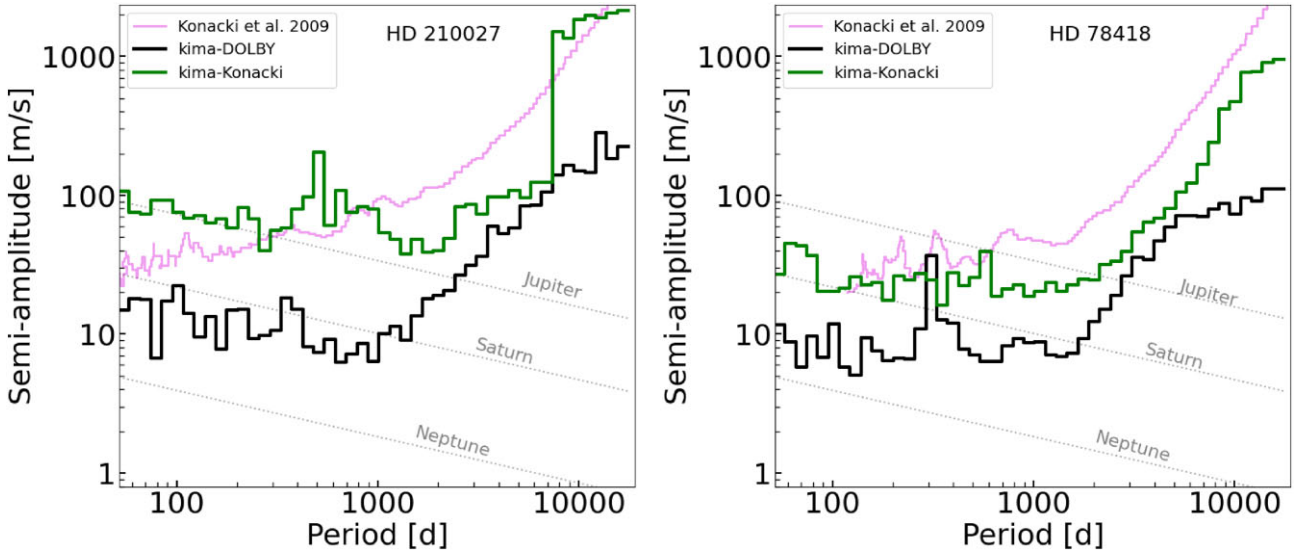


Figure C1. Detection limits based on the density of posterior samples for the HD 210027 and HD 78418 binary systems from the `kima` run with N_P fixed to 1. Solid lines represent the amplitude at the 99th percentile within each period bin, providing a 99 per cent confidence upper limit. The different lines correspond to the analysis of our combined data set (`kima-DOLBY`), the analysis using the `kima`-Konacki derived data and the planet detection limit from Konacki et al. (2009). Diagonal lines mark the expected signals for Neptune, Saturn, and Jupiter mass planets orbiting stars with their respective masses.

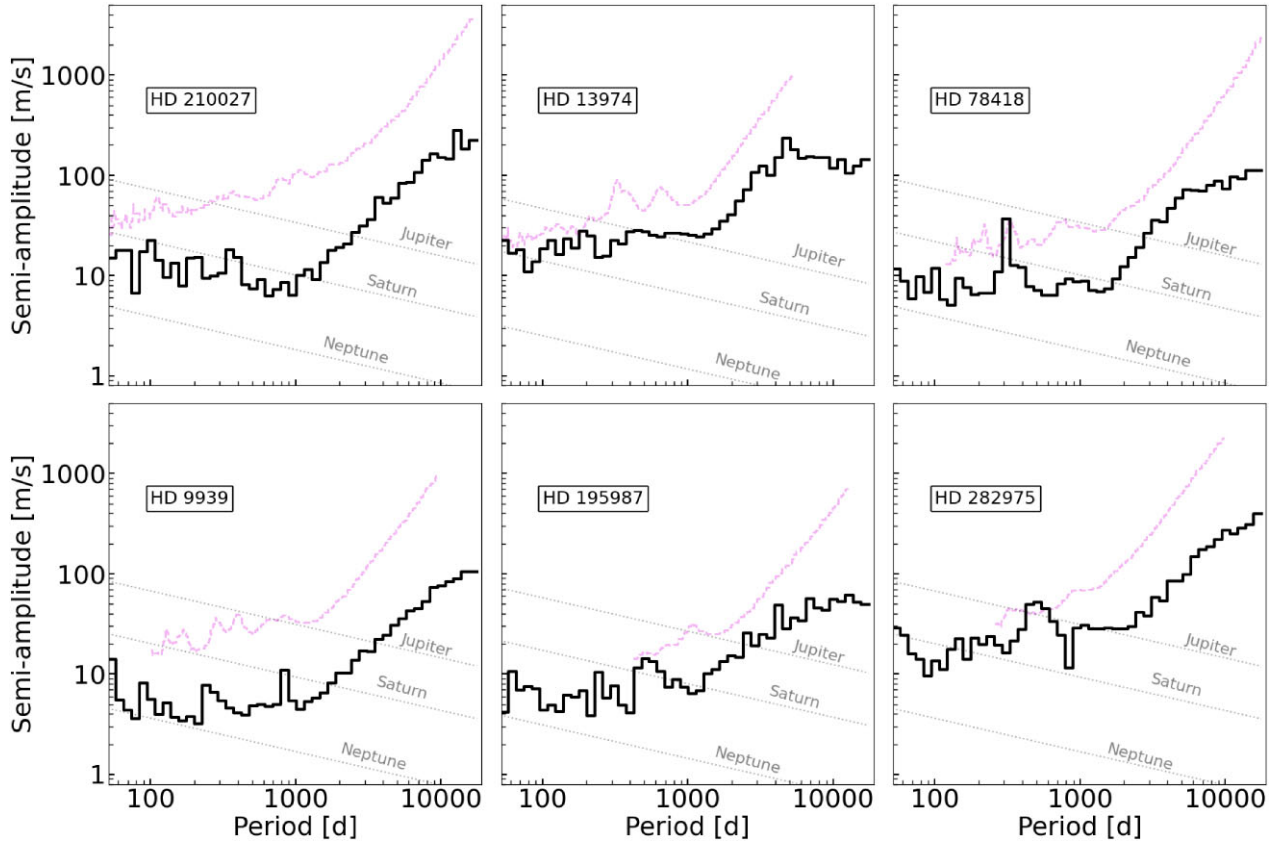


Figure C2. Detection limits for binary systems from the `kima` run with N_P fixed to 1. Histograms represent the distribution of semi-amplitudes within each period bin, with the vertical lines indicating the 99th percentile, corresponding to a 99 per cent confidence upper limit. Also represented are the planet detection limits from Konacki et al. (2009, 2010), scaled to the number of observations obtained for our paper, to enable as close to a like for like comparison as possible. The diagonal grey lines represent the expected signals of Neptune, Saturn, and Jupiter mass planets orbiting stars with their respective binary masses.

Downloaded from https://academic.oup.com/mnras/article/534/4/3999/7817980 by guest on 27 October 2024

APPENDIX D: RADIAL VELOCITY DATA

Table D1. RV data for HD 210027 using Dolby CCF method on Sophie spectrum.

BJD (d)	RV_1 (km s^{-1})	σ_{RV_1} (km s^{-1})	O-C_1 (km s^{-1})	RV_2 (km s^{-1})	σ_{RV_2} (km s^{-1})	O-C_2 (km s^{-1})
2459123.38091	−52.34232	0.01335	0.00938	72.11175	0.06193	−0.01038
2459123.38979	−52.29537	0.01307	0.00453	72.01824	0.06096	−0.02087
2459128.45234	42.93887	0.01271	0.01924	−80.69803	0.06467	0.01439
2459128.48099	42.75522	0.01251	−0.00456	−80.47051	0.06449	−0.01475
2459132.51401	−47.98416	0.01216	0.01493	65.10774	0.04950	−0.03731
2459132.51798	−48.05310	0.01206	−0.00057	65.17262	0.04864	−0.05809
2459137.39725	35.19619	0.01284	−0.00349	−68.35485	0.06139	−0.03636
2459154.37782	−49.12542	0.01119	0.03364	66.98514	0.04214	−0.01948
2459158.44617	42.58362	0.01174	0.02644	−80.14782	0.03846	−0.01739
2459162.39265	−33.48042	0.01064	0.01004	41.85057	0.04570	−0.03419
2459168.33550	39.52619	0.01138	−0.02196	−75.30244	0.04575	−0.00299
2459170.35326	28.16629	0.01078	−0.00049	−57.08909	0.03863	−0.05967
2459174.31727	−52.94527	0.01137	−0.00282	73.04889	0.04186	−0.02013
2459176.35188	−14.50687	0.01179	−0.02429	11.31581	0.04117	−0.08710
2459181.33461	8.41498	0.01145	−0.01973	−25.32817	0.03894	0.03443
2459185.26110	−45.73935	0.01163	−0.00722	61.52951	0.03888	0.01826
2459351.62279	30.55845	0.01095	0.01034	−60.89566	0.03765	−0.04413
2459354.61166	17.93299	0.01050	0.00754	−40.54485	0.04092	0.04753
2459374.58515	28.81861	0.01051	0.02387	−58.06133	0.03695	−0.02396
2459381.58875	14.16772	0.01027	0.02032	−34.50062	0.03904	0.02841
2459389.60043	−44.41779	0.01143	0.01247	59.43247	0.04067	0.00821
2459398.56787	−52.70122	0.01133	−0.01393	72.66380	0.04248	0.00383
2459410.59366	−32.47557	0.01028	−0.00835	40.18931	0.04127	−0.05512
2459414.44339	42.76507	0.01115	−0.01156	−80.55705	0.04341	−0.07423
2459424.49613	43.46540	0.01114	−0.00656	−81.63438	0.04170	−0.03518
2459425.57194	30.45091	0.01052	0.01262	−60.67250	0.03548	0.00302
2459426.60554	3.87457	0.01105	0.00766	−18.00283	0.04177	0.03073
2459427.49154	−22.03691	0.01100	−0.00689	23.44005	0.04240	−0.06716
2459429.57455	−53.12680	0.01122	0.00713	73.33900	0.04205	−0.03692
2459433.45656	33.09481	0.01060	0.01271	−64.87356	0.04046	0.04559
2459463.49870	19.65339	0.01058	0.01002	−43.36343	0.03972	−0.01442
2459489.37951	−37.38137	0.01114	0.00679	48.10777	0.04249	−0.02636
2459503.26544	−11.62182	0.01189	0.02698	6.83203	0.04118	−0.02556
2459514.40352	15.37954	0.01102	−0.00493	−36.48393	0.03982	0.03028
2459520.30192	−43.10972	0.01134	−0.00755	57.31461	0.04368	0.01968
2459538.32512	21.05451	0.01098	0.00717	−45.67957	0.03954	−0.07695
2459548.24825	27.88614	0.01079	−0.01125	−56.68909	0.03870	−0.09207
2459553.30195	−38.75507	0.01120	0.02067	50.28388	0.03966	−0.07523
2459560.22768	−21.10140	0.01147	−0.00414	21.94564	0.04147	−0.06566
2459565.27406	9.95154	0.01123	−0.00173	−27.81866	0.04056	−0.01984
2459741.57939	40.04336	0.01126	0.00540	−76.05172	0.04490	0.03423
2459774.60436	−18.34614	0.01109	0.00123	17.59785	0.04022	−0.00323
2459776.61296	−53.18037	0.02209	0.00901	73.39141	0.04257	−0.07335
2459797.43653	−52.36365	0.01130	0.01846	72.23316	0.04337	0.06229
2459853.40173	43.56933	0.01094	−0.00846	−81.80592	0.04184	−0.03683
2459866.25707	−10.62429	0.01320	0.02584	5.27034	0.04887	0.01512
2459866.26082	−10.75328	0.01319	0.00745	5.47359	0.04757	0.04095
2459867.45408	−41.37190	0.01131	0.00510	54.49047	0.04287	−0.03873
2459888.30601	−48.34365	0.01142	0.00867	65.64090	0.04064	−0.07038
2459900.31845	−43.26153	0.01145	0.00560	57.59416	0.04333	0.03451
2459924.23470	41.02977	0.01158	0.01571	−77.67567	0.04813	−0.02275
2459924.30571	41.67963	0.01133	0.01377	−78.76368	0.04836	−0.06429
2459924.30953	41.70923	0.01134	0.01082	−78.76205	0.04827	−0.01040
2459924.31335	41.73751	0.01140	0.00679	−78.83872	0.04868	−0.03522
2459924.31714	41.76263	0.01127	0.00013	−78.85060	0.04891	0.00394
2459924.32097	41.80818	0.01133	0.01381	−78.96153	0.04902	−0.05582

Downloaded from https://academic.oup.com/mnras/article/534/4/3999/7817980 by guest on 27 October 2024

Table D2. RV data for HD 13974 using Dolby CCF method on Sophie spectrum.

BJD (d)	RV_1 ($km\,s^{-1}$)	σ_{RV_1} ($km\,s^{-1}$)	O-C_1 ($km\,s^{-1}$)	RV_2 ($km\,s^{-1}$)	σ_{RV_2} ($km\,s^{-1}$)	O-C_2 ($km\,s^{-1}$)
2458851.36986	−1.73619	0.00467	−0.00665	−13.04684	0.03064	−0.01498
2458860.32662	2.80378	0.00399	−0.00540	−19.38319	0.02867	−0.05570
2458871.33474	−1.32472	0.00887	−0.01535	−13.66542	0.02769	−0.05077
2458895.26721	−16.07826	0.00392	−0.00223	6.84277	0.02696	−0.02227
2459068.59190	−0.72497	0.00391	0.01157	−14.41216	0.04891	−0.00296
2459094.56982	−15.89868	0.00386	−0.01229	6.59235	0.02681	−0.00972
2459100.65292	3.13285	0.00405	−0.03291	−19.81134	0.02858	0.01077
2459104.66467	−16.06569	0.00388	−0.02251	6.80556	0.02724	−0.01393
2459123.57672	−11.74338	0.00401	0.01705	0.89295	0.02872	0.01266
2459133.53153	−11.39425	0.00434	0.01315	0.45675	0.03071	0.06606
2459136.54978	−13.45844	0.00373	0.00943	3.28183	0.02582	0.03366
2459138.58370	−1.51518	0.00431	0.03473	−13.28270	0.03927	−0.00169
2459158.53279	−2.05556	0.00539	0.01251	−12.57175	0.04432	−0.00944
2459164.52865	−15.41809	0.00382	0.00156	5.91695	0.02634	−0.03787
2459165.48529	−16.47060	0.00399	0.02934	7.49353	0.02685	0.04064
2459173.53048	−10.93347	0.00542	0.02043	−0.22219	0.03723	0.01605
2459174.57244	−15.48454	0.00384	0.00199	6.02874	0.02634	−0.01881
2459180.33942	3.66827	0.00408	0.02940	−20.48049	0.02669	−0.00209
2459184.46913	−15.10267	0.00382	0.01293	5.54808	0.02630	0.01491
2459190.33616	3.66605	0.00410	0.02769	−20.47263	0.02809	0.00505
2459200.25548	3.65633	0.00411	0.04599	−20.44373	0.02720	−0.00491
2459244.27223	−13.92165	0.00373	0.01211	3.89420	0.02600	−0.00005
2459249.27867	0.81736	0.00393	−0.02331	−16.54747	0.02595	0.04944
2459415.60524	−16.48543	0.00400	−0.00738	7.41897	0.02737	−0.00356
2459459.57600	0.25367	0.00506	−0.00209	−15.77196	0.03292	0.01363
2459489.63908	0.24514	0.00387	−0.02267	−15.79874	0.02523	0.00356
2459501.49659	3.08327	0.00404	−0.00942	−19.72562	0.02812	−0.00485
2459542.39883	0.16392	0.00384	−0.01913	−15.71181	0.02459	−0.02705
2459622.27606	1.42672	0.00393	−0.01359	−17.43741	0.02701	−0.00872
2459775.60673	−14.94069	0.00399	−0.00263	5.27494	0.02393	−0.01203
2459832.51807	2.12060	0.00397	0.00688	−18.34861	0.02794	0.01418
2459855.59138	−14.28766	0.00379	0.00169	4.38260	0.02654	−0.00477
2459870.56860	1.00991	0.00412	0.00156	−16.80347	0.02777	0.02604
2459921.44118	3.32644	0.00407	−0.00759	−20.07147	0.02768	−0.01594
2459958.40976	−12.50915	0.00371	−0.01640	1.87455	0.02592	−0.02132

Downloaded from https://academic.oup.com/mnras/article/534/4/3999/7817980 by guest on 27 October 2024

Table D3. RV data for HD 78418 using Dolby CCF method on Sophie spectrum.

BJD (d)	RV_1 ($km\,s^{-1}$)	σ_{RV_1} ($km\,s^{-1}$)	O-C_1 ($km\,s^{-1}$)	RV_2 ($km\,s^{-1}$)	σ_{RV_2} ($km\,s^{-1}$)	O-C_2 ($km\,s^{-1}$)
2458872.37870	21.27676	0.00478	0.00243	−3.59807	0.01528	−0.02680
2458898.49292	−13.47233	0.00378	0.00228	36.76581	0.01414	−0.01753
2458907.47357	37.24499	0.00416	0.00233	−22.09402	0.01499	−0.02255
2458910.41886	25.84510	0.00446	0.00470	−8.88600	0.01388	−0.01146
2458911.33579	20.48118	0.00424	−0.00490	−2.68233	0.01424	−0.02657
2458920.37977	−14.04810	0.00372	0.00328	37.47144	0.01403	−0.01192
2459130.66567	−10.87384	0.00391	0.00873	33.76031	0.01343	−0.01297
2459153.68550	−12.63554	0.00369	0.00408	35.81088	0.01367	−0.00611
2459157.62496	28.01406	0.00432	0.00501	−11.42754	0.01325	−0.04023
2459172.58339	−14.51336	0.00372	0.00670	38.01254	0.01380	0.01307
2459181.62800	28.94156	0.00416	0.00581	−12.46418	0.01292	0.00555
2459186.60880	−0.01687	0.00412	−0.00104	21.14648	0.01415	−0.03093
2459237.62907	37.11821	0.00416	0.00216	−21.93676	0.01489	0.03397
2459248.49694	−14.84864	0.00402	−0.00381	38.38285	0.01461	0.00819
2459248.63740	−15.08212	0.00381	0.00540	38.66170	0.01424	0.00514
2459263.45847	4.40171	0.00510	0.00464	16.01318	0.01736	0.01311
2459280.45118	18.80057	0.00418	−0.00563	−0.66523	0.01464	0.03949
2459298.35123	27.60645	0.00439	0.00968	−10.91746	0.01347	−0.00294
2459303.36350	−1.53055	0.00416	0.00713	22.93540	0.01345	0.01393
2459536.71790	−3.63984	0.00433	0.00221	25.31719	0.01362	−0.00330
2459537.69503	−8.28468	0.00422	0.00437	30.72184	0.01352	−0.01972
2459540.71828	−15.61997	0.00388	−0.00113	39.25905	0.01431	−0.01525
2459546.72643	34.37384	0.00399	0.00767	−18.79004	0.01386	−0.01617
2459548.72050	36.20188	0.00411	0.00708	−20.89273	0.01468	0.00826
2459594.52691	−1.41021	0.00420	0.01081	22.78949	0.01379	0.00348
2459608.48351	30.07109	0.00402	0.00787	−13.75660	0.01311	0.02268
2459623.43923	27.20333	0.00442	0.00343	−10.48153	0.01340	−0.03430
2459638.50612	−14.43425	0.00382	0.01078	37.92500	0.01414	0.01261
2459644.38323	36.64494	0.00421	0.00544	−21.37130	0.01505	0.04458
2459648.51053	23.43053	0.00443	0.01470	−6.04911	0.01292	0.00938
2459868.64759	−12.01896	0.01200	−0.01003	35.03915	0.04037	0.01023
2459888.64574	−13.80355	0.00371	−0.00410	37.16529	0.01406	0.00471
2459957.53755	31.86693	0.00397	−0.00411	−15.93369	0.01387	−0.01783
2459958.61724	26.23676	0.00441	−0.00113	−9.37006	0.01354	−0.03385
2459959.41779	21.59474	0.00434	0.00075	−3.97159	0.01377	−0.02906
2460006.40723	−15.65450	0.00392	0.00856	39.29607	0.01421	0.00431
2460007.41061	−14.22850	0.00376	0.01059	37.69088	0.01387	0.01750

Downloaded from https://academic.oup.com/mnras/article/534/4/3999/7817980 by guest on 27 October 2024

Table D4. RV data for HD 9939 using Dolby CCF method on Sophie spectrum.

BJD (d)	RV_1 ($km\,s^{-1}$)	σ_{RV_1} ($km\,s^{-1}$)	O-C_1 ($km\,s^{-1}$)	RV_2 ($km\,s^{-1}$)	σ_{RV_2} ($km\,s^{-1}$)	O-C_2 ($km\,s^{-1}$)
2458858.37230	−69.59819	0.00515	0.00270	−15.63101	0.03004	−0.05248
2459068.58880	−55.01951	0.00495	−0.00328	−34.21645	0.02903	−0.00851
2459077.63446	−17.38670	0.00501	0.00615	−82.06566	0.03015	0.00370
2459096.55610	−27.41804	0.00492	0.00596	−69.30955	0.02952	0.00033
2459100.64992	−8.86494	0.00498	0.00891	−92.88379	0.02824	−0.01363
2459102.62882	−16.15512	0.00490	−0.00481	−83.63979	0.02759	0.01531
2459104.61855	−29.54584	0.00513	−0.00086	−66.60837	0.03219	0.00029
2459123.55891	−13.54038	0.00483	0.00498	−86.98169	0.02947	0.00025
2459136.58872	−73.58189	0.00507	0.00056	−10.64629	0.03260	−0.01308
2459138.58018	−78.44756	0.00496	0.00302	−4.48104	0.03072	0.01384
2459164.41903	−78.74896	0.00489	−0.00195	−4.10826	0.03023	−0.01774
2459165.48006	−77.71594	0.00511	0.00895	−5.40001	0.03057	0.00166
2459166.49085	−74.77060	0.00505	0.00970	−9.13958	0.03140	−0.00145
2459168.38319	−63.83368	0.00511	−0.00559	−23.05031	0.03003	−0.03120
2459173.47593	−16.64036	0.00493	−0.00323	−83.01520	0.02886	0.02846
2459173.52642	−16.29119	0.00499	0.00384	−83.46716	0.02892	0.02492
2459181.43455	−38.62125	0.00508	0.00235	−55.08504	0.02845	−0.00032
2459185.33203	−65.65455	0.00515	0.00756	−20.73494	0.03146	−0.00352
2459190.32281	−78.30099	0.00493	0.00660	−4.67014	0.03023	0.02450
2459242.29567	−74.04520	0.00514	0.00174	−10.09967	0.03274	0.02638
2459244.24760	−61.97739	0.00524	0.00606	−25.41548	0.03208	0.00685
2459248.33469	−22.62320	0.00504	0.00028	−75.38557	0.03036	0.01407
2459399.59509	−22.57071	0.00497	−0.00231	−75.47639	0.02970	−0.01187
2459415.60256	−78.12005	0.00502	0.00291	−4.88995	0.03065	0.01973
2459432.57414	−31.36037	0.00599	−0.00282	−64.31752	0.03795	0.00535
2459462.56743	−65.31155	0.00512	0.00724	−21.18090	0.03105	−0.01767
2459463.56289	−70.45211	0.00518	−0.01031	−14.63985	0.02922	−0.01885
2459489.64627	−74.07999	0.00512	−0.00204	−10.02058	0.03289	−0.01304
2459503.46598	−8.53155	0.00502	−0.00012	−93.33199	0.02811	0.02007
2459538.55434	−67.29364	0.00513	−0.00023	−18.64480	0.03261	−0.03109
2459542.39462	−78.74315	0.00494	0.00154	−4.10112	0.03110	0.00871
2459545.46940	−70.75187	0.00515	0.00295	−14.24031	0.02945	0.01263
2459546.41498	−64.59449	0.00514	0.00243	−22.06312	0.03049	0.00750
2459551.40013	−18.13658	0.00515	0.00577	−81.10746	0.03288	−0.01380
2459558.43304	−29.96531	0.00520	−0.00159	−66.06794	0.03387	0.00023
2459601.29306	−22.33338	0.00497	−0.00309	−75.75891	0.02978	−0.02485
2459779.61956	−10.65818	0.00492	0.00909	−90.54018	0.03178	−0.02012
2459797.62825	−70.34967	0.00519	0.00081	−14.64547	0.03007	−0.02225
2459854.52788	−14.02566	0.00486	0.00269	−86.19184	0.02820	−0.07637
2459869.42980	−78.21860	0.00496	0.00456	−4.61381	0.03050	−0.04957
2459886.56099	−33.09126	0.00509	−0.00906	−61.95479	0.02905	−0.03289
2459904.48732	−16.94018	0.00501	0.01999	−82.44737	0.02987	−0.11632
2459959.27294	−13.77033	0.00482	0.00285	−86.42047	0.02921	0.29986

Downloaded from https://academic.oup.com/mnras/article/534/4/3999/7817980 by guest on 27 October 2024

Table D5. RV data for HD 195987 using Dolby CCF method on Sophie spectrum.

BJD (d)	RV_1 ($km\,s^{-1}$)	σ_{RV_1} ($km\,s^{-1}$)	O-C_1 ($km\,s^{-1}$)	RV_2 ($km\,s^{-1}$)	σ_{RV_2} ($km\,s^{-1}$)	O-C_2 ($km\,s^{-1}$)
2458767.44980	−19.58729	0.00347	−0.00068	12.15788	0.00770	0.00767
2459010.57241	−24.99781	0.00519	−0.00263	19.01268	0.00888	−0.01264
2459031.58433	24.52511	0.00415	0.00087	−43.97312	0.00784	−0.04054
2459033.60485	30.51372	0.00442	0.00342	−51.56721	0.01024	−0.01998
2459034.55544	31.80618	0.00506	−0.00414	−53.22300	0.01027	−0.02187
2459044.54125	1.75428	0.00399	−0.00375	−14.96329	0.01010	0.02017
2459068.48549	−24.73894	0.00355	0.00059	18.70550	0.00891	0.00512
2459072.53538	−21.77383	0.00582	−0.00152	14.97086	0.01324	0.04196
2459077.47004	−14.56690	0.00376	0.00261	5.79191	0.00899	0.01842
2459093.48616	31.30272	0.00377	0.00578	−52.50469	0.00909	0.04346
2459100.50645	6.67546	0.00598	0.00272	−21.18494	0.01203	0.04708
2459122.46379	−25.65979	0.00465	−0.00675	19.86971	0.00706	0.00826
2459122.48541	−25.65150	0.00417	−0.00033	19.87494	0.00747	0.01586
2459127.40713	−23.83828	0.00342	−0.00694	17.55151	0.00698	0.00547
2459128.44366	−23.06215	0.00526	0.00214	16.53802	0.01249	−0.03307
2459132.26642	−18.82948	0.00611	0.00454	11.16976	0.01254	−0.02435
2459155.30948	16.79037	0.00418	0.00138	−34.06186	0.00883	0.03363
2459165.33216	−14.33204	0.00283	−0.00104	5.51959	0.00822	0.04999
2459172.35297	−23.24635	0.00510	−0.00492	16.83323	0.00677	0.03730
2459174.27477	−24.46398	0.00422	0.00084	18.34732	0.00755	−0.00367
2459305.64369	−16.61477	0.00566	0.00146	8.35839	0.01098	−0.01670
2459351.61913	−25.66858	0.00439	−0.00534	19.85431	0.01154	−0.02010
2459354.60816	−24.94729	0.00360	0.00534	18.96805	0.00897	−0.00318
2459363.54500	−15.57905	0.00500	0.00688	7.04920	0.01023	−0.01627
2459371.59079	8.05734	0.00568	0.00399	−23.00347	0.01043	−0.01700
2459374.60037	20.87997	0.00439	0.00052	−39.28299	0.01012	0.01382
2459377.52102	30.48196	0.00470	0.00299	−51.55269	0.00998	−0.04533
2459399.44040	−21.26427	0.00414	0.00068	14.28020	0.00838	−0.00339
2459410.58249	−25.39247	0.00386	0.00577	19.48908	0.00917	−0.04853
2459415.50033	−22.68478	0.00408	0.00184	16.07992	0.00904	−0.01112
2459429.57920	10.84287	0.00366	0.00714	−26.49598	0.00956	0.02835
2459432.56152	23.46212	0.00445	−0.00028	−42.61899	0.00980	−0.03699
2459436.49438	32.01894	0.00414	0.00667	−53.45443	0.00861	0.00369
2459463.48393	−25.43569	0.00453	0.00459	19.55807	0.00679	−0.03288
2459477.48547	−16.82898	0.00492	−0.00224	8.66785	0.00728	0.02519
2459544.32381	11.25872	0.00382	−0.00440	−27.09618	0.00771	−0.02841
2459546.35246	19.97966	0.00529	−0.00447	−38.19812	0.01023	−0.04000
2459554.28903	25.65379	0.00382	−0.00800	−45.42088	0.00755	−0.04084
2459646.69694	−20.74314	0.00373	−0.00458	13.65525	0.00663	0.04032
2459647.70492	−19.47515	0.00380	−0.00519	11.97384	0.00762	−0.02860
2459739.49580	−16.01978	0.00545	−0.00318	7.59803	0.01082	−0.01423
2459774.57537	15.41881	0.00458	0.00781	−32.33024	0.00907	0.01204
2459776.61934	23.95970	0.00447	0.00989	−43.21266	0.00908	−0.01070
2459800.63752	−21.21510	0.00434	−0.00839	14.18785	0.00926	−0.02171
2459855.36671	−17.94399	0.00422	0.00763	10.04320	0.01014	−0.02873
2459866.26356	−25.66229	0.00430	0.00409	19.84599	0.01060	−0.03239
2459869.34471	−25.34610	0.00370	0.00232	19.45066	0.00956	−0.02363
2459901.24851	13.68083	0.00463	−0.00370	−30.15247	0.01161	−0.00477
2459924.21804	−25.68638	0.00385	−0.00038	19.86468	0.01016	−0.03864
2460010.70041	31.20871	0.00500	−0.00157	−52.41145	0.01030	0.02645
2460041.66411	−25.23418	0.00358	0.00975	19.34025	0.00947	−0.00124
2460070.62334	24.11113	0.00473	0.01144	−43.42312	0.00977	−0.02995

Downloaded from https://academic.oup.com/mnras/article/534/4/3999/7817980 by guest on 27 October 2024

Table D6. RV data for HD 282975 using dolby CCF method on Sophie spectrum.

BJD (d)	RV_1 (km s^{-1})	σ_{RV_1} (km s^{-1})	O-C_1 (km s^{-1})	RV_2 (km s^{-1})	σ_{RV_2} (km s^{-1})	O-C_2 (km s^{-1})
2458851.38469	0.45294	0.00978	−0.00576	14.09135	0.01029	−0.03460
2458898.38654	−0.37863	0.00897	0.00240	15.00823	0.00983	−0.00228
2458924.31871	−0.20532	0.00965	0.00559	14.81763	0.01026	−0.01379
2459096.59172	12.95871	0.00923	0.01624	1.00437	0.00954	0.02252
2459122.61784	12.91231	0.00945	−0.01052	0.98820	0.00975	−0.01433
2459136.62423	−0.67026	0.00729	0.00498	15.33625	0.00768	0.01638
2459184.50882	0.26131	0.00932	0.01278	14.34905	0.00934	0.00129
2459241.40466	−0.17399	0.00768	0.00414	14.81492	0.00863	0.01846
2459475.58271	−0.39070	0.00717	−0.00602	14.99645	0.00822	−0.01749
2459513.54933	13.15543	0.00809	0.00320	0.74992	0.00929	−0.01107
2459514.55909	14.01542	0.00750	0.00432	−0.13764	0.00858	0.00567
2459544.64636	12.94248	0.00833	0.00038	0.99053	0.00936	0.00777
2459554.47041	0.30082	0.00970	0.00159	14.27782	0.01111	−0.01603
2459569.38751	14.52205	0.00735	0.00098	−0.67618	0.00821	0.00387
2459642.30919	11.64299	0.01070	0.01542	2.36058	0.01226	−0.00574
2459801.61970	14.38294	0.00916	0.00460	−0.52525	0.01032	0.00472
2459854.62748	14.76487	0.00732	0.01723	−0.87450	0.00808	0.04427
2459866.54498	−0.13297	0.00848	0.01645	14.78591	0.00906	0.01968
2459903.52873	12.42914	0.00872	−0.01281	1.47036	0.00980	−0.03849
2459955.38046	12.18273	0.00876	−0.00584	1.74739	0.00981	−0.02825
2459958.48351	14.63086	0.00886	−0.02523	−0.84999	0.00968	−0.02759

This paper has been typeset from a TEX/LATEX file prepared by the author.

Downloaded from https://academic.oup.com/mnras/article/534/4/3999/7817980 by guest on 27 October 2024

© 2024 The Author(s).
Published by Oxford University Press on behalf of Royal Astronomical Society. This is an Open Access article distributed under the terms of the Creative Commons Attribution License (https://creativecommons.org/licenses/by/4.0/), which permits unrestricted reuse, distribution, and reproduction in any medium, provided the original work is properly cited.

3.4 Predicting *Gaia*'s yield

With the aim of detecting planets around nearly equal mass main-sequence binaries, using astrometric observations is a potential path around the "double-line binary problem". This circumvents the problem rather than attempting to solve it by using the deconvolution of the double-lined spectra to obtain radial velocities as was described in Section 3.1. The *Gaia* telescope was a European Space Agency astrometric mission that operated from July 2014 to January 2025 (Gaia Collaboration et al., 2016), it scanned the sky for 10.5 years obtaining in that time 2.6 trillion individual astrometric measurements[1].

To detect an orbit with *Gaia* , the photocentre of the system must "orbit" the centre-of-mass on a wide enough orbit to be detected and a short enough orbit to be covered by the data (see Section 1.3.5). I will use a conservative signal-to-noise ratio (SNR) threshold for detection (as in Sahlmann et al., 2015), with $SNR > 100$ required to astrometrically detect a binary with sufficient precision on the orbital parameters, and $SNR > 20$ as the threshold for planet detection. The *Gaia* signal-to-noise ratio is defined as (Sahlmann et al., 2015)

$$SNR = \alpha \frac{\sqrt{N_{\rm obs}}}{\sigma}, \tag{3.9}$$

where $N_{\rm obs}$ is the number of *Gaia* observations, σ their average uncertainty, and α is the semi-major axis of the photocentre orbit. The average uncertainty was expected to be 30 μas[2] for stars brighter than Gmag of 12 (de-Bruijne et al., 2014). Since the most recent data release this has been revised, in particular, the precision is worse for bright stars (Gmag< 9; Holl et al., 2023). I use an approximation to the function in Holl et al. (2023) to calculate the precision of the *Gaia* astrometry for each star.

This signal-to-noise ratio cut is a simplified detection criterion, the true ability of *Gaia* to detect orbits has more aliases and caveats, such as dependence on eccentricity and sky position (El-Badry et al., 2024). In this case the simplified criterion is acceptable as the uncertainty in

[1] https://www.cosmos.esa.int/web/gaia/mission-numbers

[2] This is the uncertainty for one *Gaia* epoch which contains 9 individual CCD astrometric measurements.

the circumbinary planet population it is the limiting factor on a yield estimate. In analogy with Sahlmann et al. (2015), I will only consider the yield of circumbinary planets within 200pc. I aim for this work and that in Section 5.2 to be combined into a paper.

3.4.1 A synthetic population of binaries and circumbinary planets

I generate a synthetic population of binaries, using *Gaia* sources and the binary star population from Raghavan et al. (2010), and then inject a circumbinary planet population inspired by the detected population. The recovery rate is tested using the *Gaia* signal-to-noise ratio as a metric. The use of Raghavan et al. (2010) for the binary fractions and distributions is arbitrary to a certain extent, other similar studies exist (e.g. Duquennoy and Mayor, 1991; Duchêne and Kraus, 2013; Offner et al., 2023). These various studies are in broad agreement over the multiplicity rates, and Raghavan et al. (2010) gives the clearest distributions of binary mass ratios and eccentricities in a graphical format that we can then try to reproduce (see Figure 3.29). While the population of binary stars used will likely impact the exact numbers predicted below, the conclusions about how changing the planet distribution affects the yields will not be strongly affected.

The binary star population consists of the sample of *Gaia* sources within 200pc, restricted to the main sequence. Disregarding the fact that some of these are already known binaries, their parameters are assumed to be that of a single star and a population of binary stars is injected following Raghavan et al. (2010). The binary fraction based on spectral type is listed in Table 3.11, these values are the lower bounds on the *multiplicity fraction* from Raghavan et al. (2010).

Table 3.11: Fraction of stars in the synthetic sample to which a binary companion is assigned, divided by spectral type. Distribution based on Raghavan et al. (2010).

Spectral type	Multiplicity fraction
B	75%
A	70%
F	50%
G	45%
K	40%
M	20%

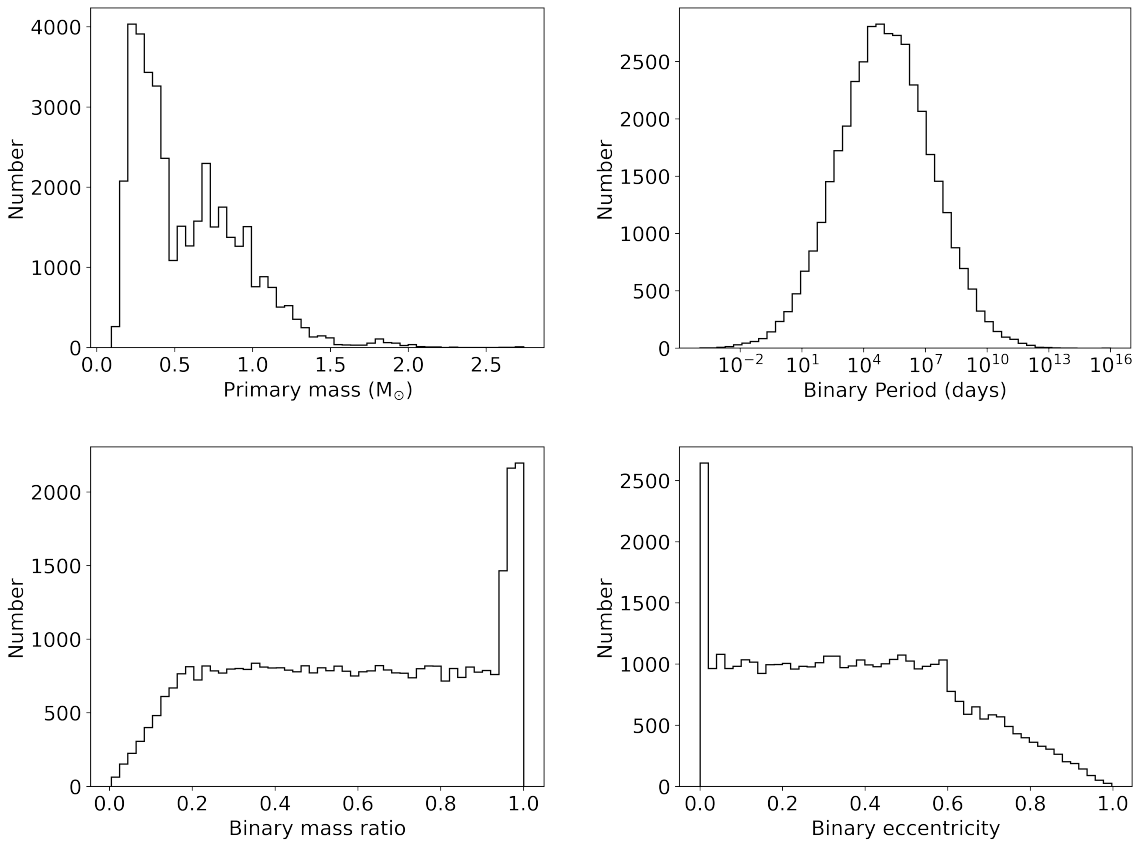


Figure 3.29: Distributions of parameters for the synthetic population of binary stars which will be used for simulation fo *Gaia* yield of circumbinary planets.

The injected binary parameter distributions are presented in Figure 3.29. The primary star masses are calculated from the *Gaia* bp-rp colour (Pecaut and Mamajek, 2013)[3]. The period, mass ratio, and eccentricity distributions are taken from Raghavan et al. (2010), where an approximation is made for the q and e distributions.

For q, the initially used distribution is uniform in the range $[0, 1]$. One change is performed to mimic the overabundance on equal mass binaries and the decreasing amount as q approches 0. Binaries with mass ratios closer to 0.2 should be preferentially retained, where as q approaches 0 more and more should be removed. To acheive this, for those binaries with $q < 0.182$, with probability $1 - 5.5q$ the mass ratio for those binaries is instead chosen uniformly between $[0.95, 1]$. This results in the linear slope seen in the bottom left hand panel of Figure 3.29.

For e I take an initially uniform distribution in the range $[0, 1]$, and perform two changes:

[3]Updated table taken from https://www.pas.rochester.edu/ẽmamajek/EEM_dwarf_UBVIJHK_colors_Teff.txt

1) all binaries with $P_{\rm bin} < 12$ days are made circular since they would likely have tidally circularised, and 2) in a similar way to what was done for the q distribution, in order to mimic the decrease in rate of extreme eccentricity, if a binary has $e > 0.6$ then with probability $2.5(e - 0.6)$ the eccentricity of that binary is instead chosen uniformly between $[0, 0.6]$. This results in the drop at $e = 0.6$ and then slow decrease up to $e = 1$ seen in the bottom right hand panel of Figure 3.29.

For the circumbinary planets, I only inject gas giants as these are the only planets that *Gaia* will realistically be sensitive to, and they are the circumbinary planet population for which we have at least some understanding. I inject a planet around 10% of the binaries (see Section 1.6.3). The mass and orbital period distributions of circumbinary planets are still not very well known. In the previous study on *Gaia*'s circumbinary planet yield (Sahlmann et al., 2015), the planet masses were drawn from the population around single-stars, and the orbital periods were all fixed at 6× the binary orbital period ($P_{\rm bin}$). The *Kepler* circumbinary planets had mostly been found clustered around $6 \times P_{\rm bin}$ so this was a good assumption at the time, but the results from the BEBOP survey are at odds with this (see Chapter 4).

In comparison with the injected population used by Sahlmann et al. (2015), fewer high-mass circumbinary objects have been found with most of the confirmed planets being between the mass of Saturn and the mass of Jupiter. However, there are still circumbinary super-Jupiters and low-mass brown dwarfs claimed. Some of these are less clearly confirmed (see Section 1.6.3) and one is yet-unpublished (see Section 4.3.1). The $5 M_{\rm Jup}$ planet orbiting Kepler-1660 is typically considered confirmed (Goldberg et al., 2023), as is the low-mass brown dwarf in VHS 1256 (Dupuy et al., 2023), hence massive circumbinary objects do exist.

I use 3 different mass distributions: combinations of a Gaussian $\mathcal{N}(0.3\,M_{\rm Jup}, 0.2\,M_{\rm Jup})$ and a LogUniform $\mathcal{LU}(0.2\,M_{\rm Jup}, 25\,M_{\rm Jup})$ with ratios 1:1, 4:1, and 1:4. These are cut to only include planets with mass $M > 0.2\,M_{\rm Jup}$[4]. These distributions are shown on the left hand side of Figure 3.30. I also test a fourth mass distribution, taking the 1:1 mixture, and scaling the mass of the planet linearly with the mass of the inner binary. The rationale for this test is that if the

[4]this cuts out a portion of the planets drawn from the Gaussian distribution, so the actual ratios of planets from each distribution included in the three populations are 1:1.4,2.8:1, and 1:5.8

protoplanetary disc mass is found to correlate with the mass of the central star (for single stars; Andrews et al., 2013) which implies more material available to form more massive planets.

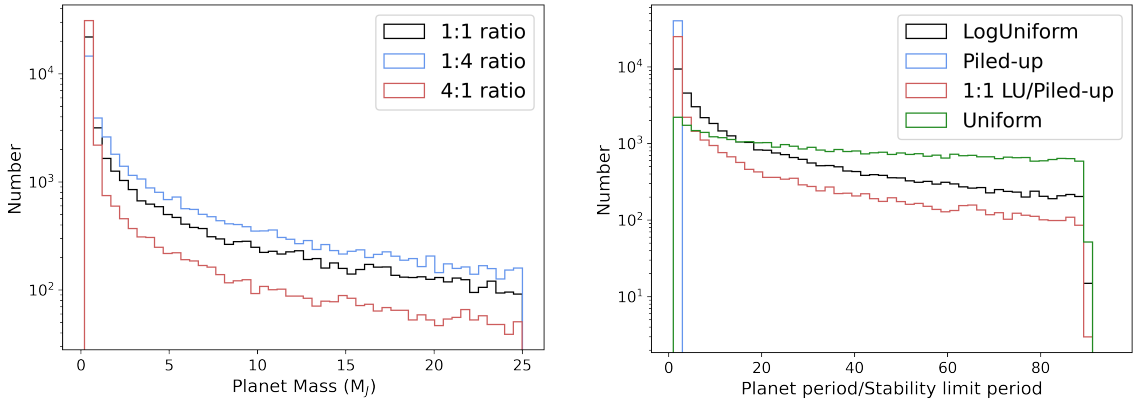


Figure 3.30: Planet mass and scaled orbital period distributions used in circumbinary planet injections to test *Gaia* yield. There are three different mass distributions used (left), and four different scaled period distributions used (right). The middle distribution (in black) in each case is our fiducial one, it is kept the same when varying the other parameter.

I use 4 different orbital period distributions, more specifically the distributions are generated in the space of $a_{sc} = a_{pl}/r_{stab}$, the semi-major axis of the circumbinary planet divided by the orbital radius of the stability limit (Holman and Wiegert, 1999). Unlike placing all the planets at $6 \times P_{bin}$ this takes into account the binary eccentricity and mass ratio to calculate the instability limit. The four distributions I use are: $a_{sc} \sim \mathcal{LU}(1, 20)$, $a_{sc} = 1.2$, $a_{sc} \sim \mathcal{U}(1, 20)$, and a hybrid half $a_{sc} \sim \mathcal{LU}(1, 20)$ and half $a_{sc} = 1.2$. These distributions are shown on the right hand side of Figure 3.30. $a_{sc} = 1.2$ is a population of planets piled-up outside the stability limit, analogous to $6 \times P_{bin}$. The 7 different setups are labelled and described in Table 3.12 along with the expected yield as described in the following section.

3.4.2 Testing *Gaia* sensitivity to circumbinary populations

Conditions for detection

To class as a detectable circumbinary planet in this analysis, two criteria are imposed here. First is that the planet is detectable in the *Gaia* astrometry, for which the constraints used are: $SNR > 20$ and $P_{pl} < T_{span}$. T_{span} is the coverage of the astrometric data, which is $\approx$ 1800 days

Table 3.12: The 6 setups and yields of circumbinary planets from *Gaia*. The input planet mass and scaled semi-major axis distributions are shown along with the planet yield from DR4 and DR5.

Setup number	$M_{\rm pl}$ distribution	$a_{\rm sc}$ distribution	DR4 planets	DR5 planets
1.1	1:1 $\mathcal{N}$ and $\mathcal{LU}$	$\mathcal{LU}$	51	175
1.2	1:4 $\mathcal{N}$ and $\mathcal{LU}$	$\mathcal{LU}$	77	253
1.3	4:1 $\mathcal{N}$ and $\mathcal{LU}$	$\mathcal{LU}$	24	81
2.1	1:1 $\mathcal{N}$ and $\mathcal{LU}$	= 1.2	125	398
2.2	1:1 $\mathcal{N}$ and $\mathcal{LU}$	1:1 $\mathcal{LU}$ and = 1.2	89	289
2.3	1:1 $\mathcal{N}$ and $\mathcal{LU}$	$\mathcal{U}$	34	105
3	1:1 $\mathcal{N}$ and $\mathcal{LU}$ scaled by $M_{\rm bin}$	$\mathcal{LU}$	47	160

for DR4 and $\approx$ 3800 days for DR5. Second is that the detected planet is orbiting a detectable binary. I allow three classes of detectable binaries:

- Astrometric binaries with *Gaia* $SNR > 100$.
- Spectroscopic binaries which have Gmag < 12, $q > 0.4$, and are not astrometric binaries, these would be detected by resolving two sets of spectral lines (likely noticed in the *Gaia* RVS spectra).
- Eclipsing binaries which are selected from those not astrometric or eclipsing based on the probability of eclipse (see Section 1.3.2).

For the calculated yields and figures presented in this section I perform the planet injections and obtain the number of detected planets 100 separate times, and take the average yields. This smooths out the effect of small number statistics.

Results

The orbital periods of the binaries around which planets are found in setup 1.1 are shown in Figure 3.31 comparing DR4 and DR5. Between DR4 and DR5 the total number of expected detections increases, aditionally detections extending to planets orbiting longer binary periods as they become detectable due to the timespan of *Gaia* increasing. This effect is most present in

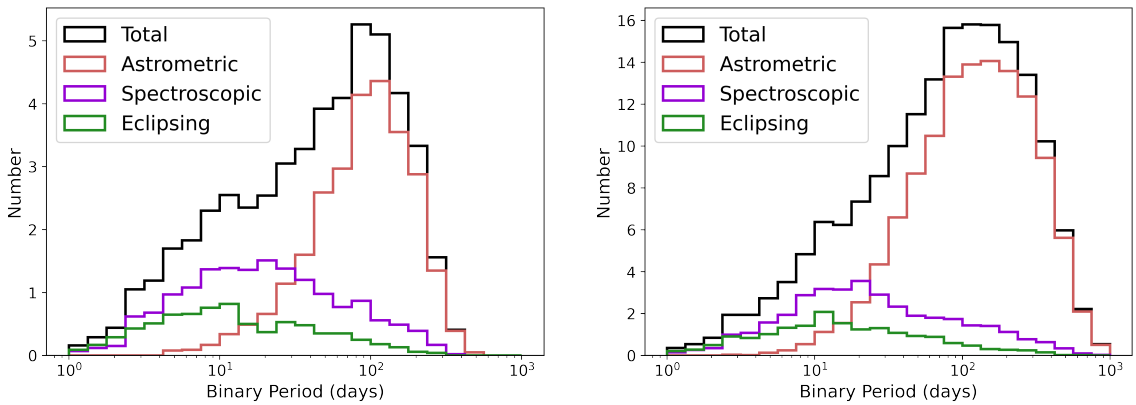


Figure 3.31: Distributions of the binary orbital periods around which circumbinary planets are expected to be detected in setup 1.1 (the default setup see Table 3.12). Left for DR4 and right for DR5, the coloured distributions are the sample divided into the different methods by which the binaries would be detected.

the planets orbiting astrometric binaries, with the distributions for spectroscopic and eclipsing remaining comparable, peaking between 10-20 days.

Table 3.13: Circumbinary planet yields in *Gaia* DR5 separated by the method by which the binary would be detected.

Setup number	Total	Astrometric binaries	Spectroscopic binaries	Eclipsing binaries
1.1	175	121	36	18
1.2	253	175	52	26
1.3	81	57	16	8
2.1	398	362	27	9
2.2	289	245	31	14
2.3	105	45	38	22
3	160	113	35	12

The circumbinary planet populations are labelled and the input mass and scaled semi-major axis distributions are shown in Table 3.12 along with the yields for *Gaia* DR4 and DR5. Table 3.13 shows the planet yield within each setup for *Gaia* DR5 seperated into planets around each type of binary detection.

As expected, increasing the amount of massive planets in the population leads to a clear increase in the yield, and this increase applies to all types of binary detection. The planet mass distributions for setups 1.1, 1.2, and 1.3 (the experiment in varying mass distribution) are shown in Figure 3.32. The shape of the distributions do not vary much across these three setups with

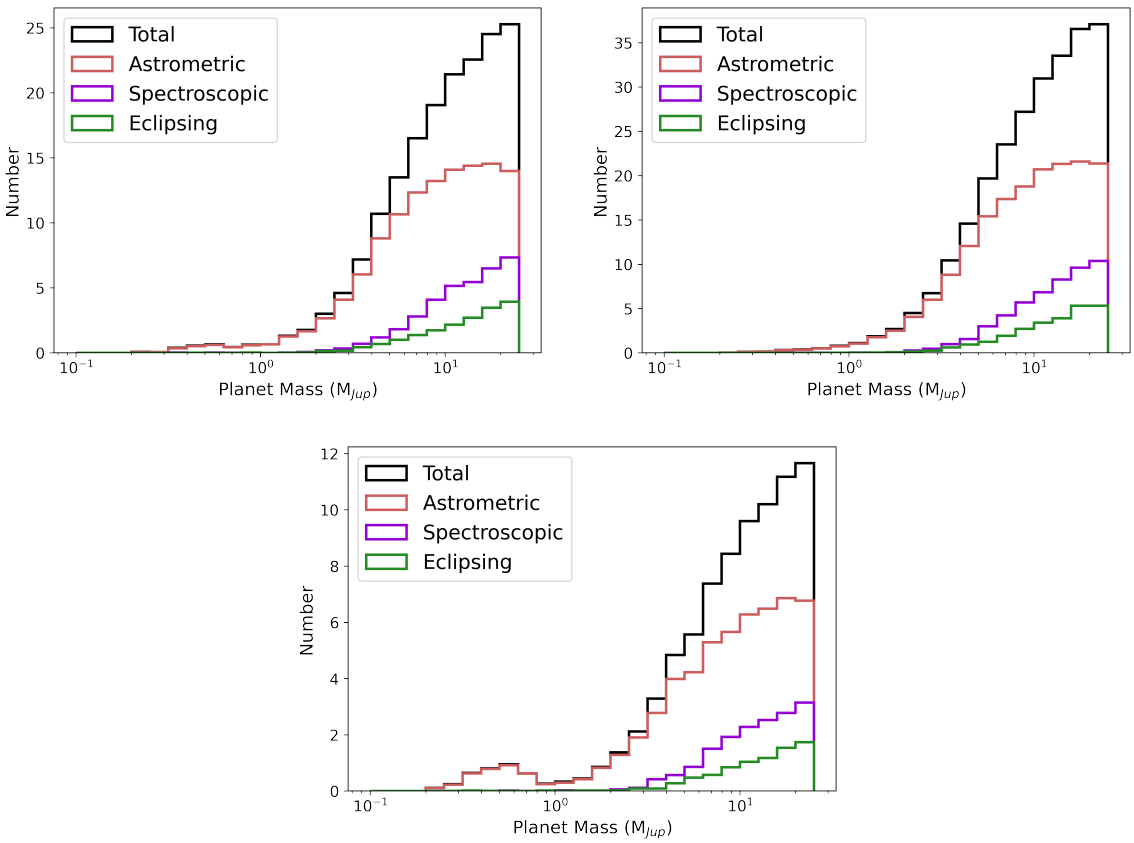


Figure 3.32: Distributions of detected planet masses of *Gaia* circumbinary planets in the setups 1.1, 1.2, and 1.3 (top-left,top-right,bottom). The coloured distributions are the sample divided into the different methods by which the binaries would be detected.

most planets found being high mass. One difference which does appear is that when more sub-Jupiter mass planets are injected (i.e. setup 1.3) there is a growing density of them being detected, however even in setup 1.3 this only gives an expected 4 detections. These low-mass detections are planets that were injected around the nearest binaries to earth.

Perhaps counter-intuitively, the more "short-period" planets[5] are injected, the higher the yield. The main reason for this is that there are more binaries with longer orbital periods (in the 10-1000 day range, see Figure 3.29). In setup 2.1 where all the planets are placed at the stability limit, this results in a higher rate of detectable planets around the longer period binaries, and since these are both more common and more easily detectable with *Gaia*, it results in a higher yield. *Gaia* therefore has an observing bias towards finding circumbinary planets nearer the

[5]Recall that the period distribution is actually a distribution in a_{sc}

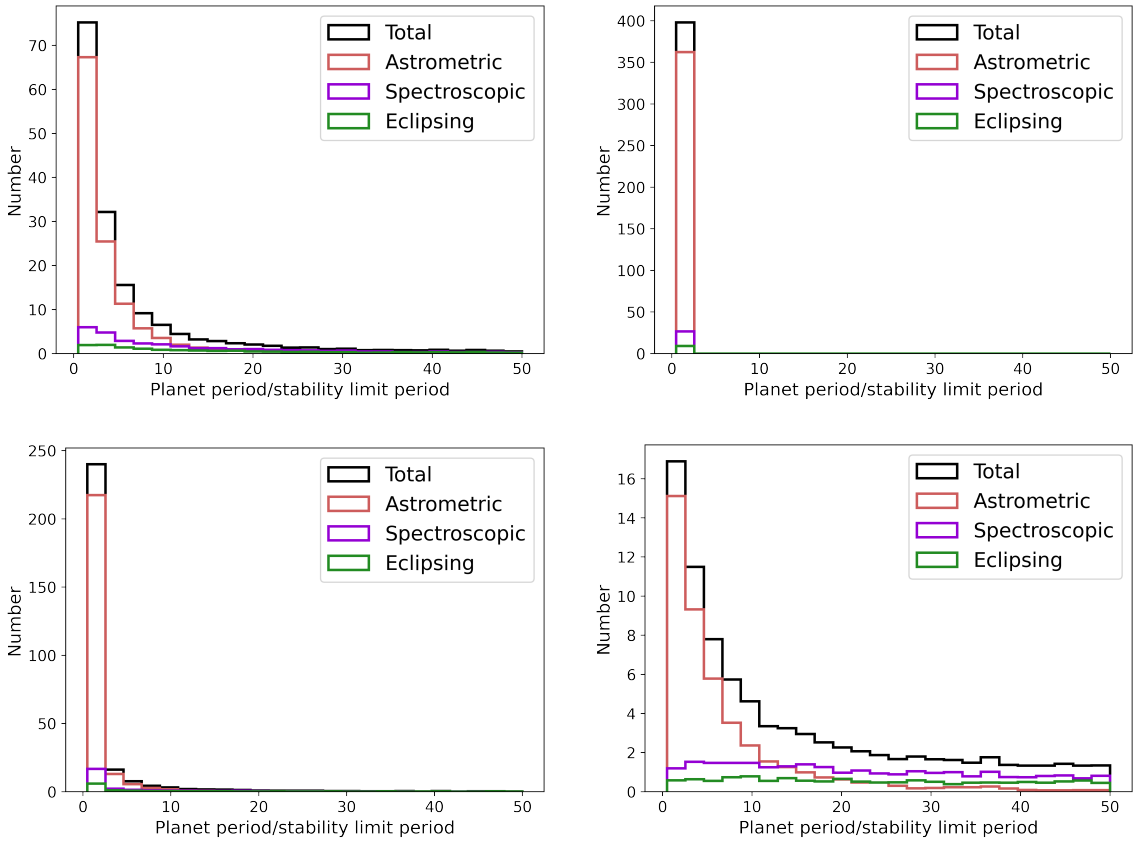


Figure 3.33: Distributions of planet's scaled orbital period for predicted *Gaia* circumbinary planet detections in the setups 1.1, 2.1, 2.2, and 2.3 (top-left,top-right,bottom-left,bottom-right). The coloured distributions are the sample divided into the different methods by which the binaries would be detected.

stability limit, but it is a bias inherent to which binaries are accessible astrometrically. Table 3.13 demonstrates that while shifting the planets period distribution nearer the binary drastically increases the yield orbiting astrometric binaries, it has a much lessened effect on the yield orbiting spectroscopic binaries and reduces the yield orbiting eclipsing binaries. This is also visible in Figure 3.33, which shows the distributions of scaled orbital period for setups 1.1, 2.1, 2.2 and 2.3. The bottom-right panel of Figure 3.33 displays the results from setup 2.3 where the period distribution is Uniform. The periods of the planets detected orbiting spectroscopic and eclipsing binaries is close to Uniform, whereas those around astrometric binaries is strongly biased towards the stability limit.

The final setup (not discussed so far) is that in which the masses of the inject planets are scaled linearly with the mass of the inner binary (those around $M_{\rm bin} = 1\,M_{\odot}$ are kept the same

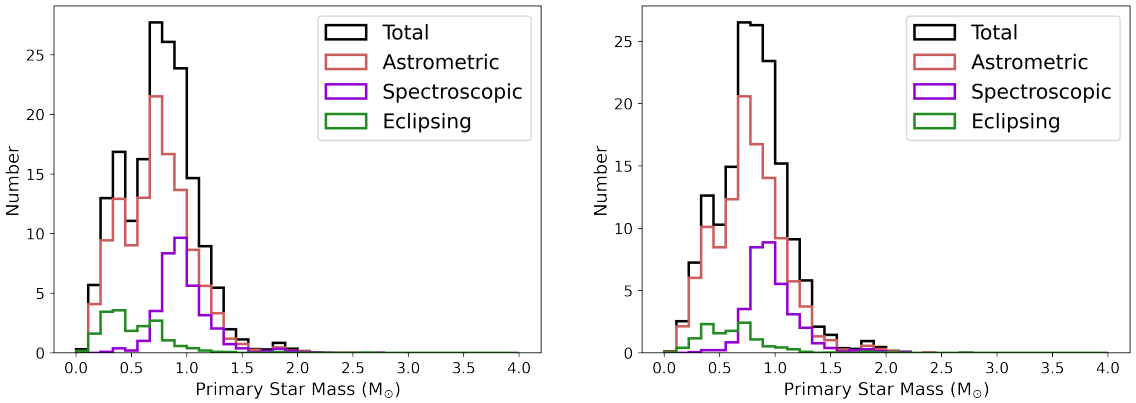


Figure 3.34: Distributions of the primary star mass for the systems in which circumbinary planets are detected in the normal setup 1.1 (left) and in the setup where the planet mass scales with mass of the binary star (right). The coloured distributions are the sample divided into the different methods by which the binaries would be detected.

mass). The main difference is displayed in Figure 3.34 which compares the masses of the primary stars in the detected systems. While there is still a small peak just below 0.5 $M_{\odot}$ in the distribution when the mass is scaled (right hand panel of Figure 3.34), the bimodality seen in setup 1.1 (left hand panel of Figure 3.34) is reduced with comparatively fewer planets detected around M-dwarf binaries than those with G-dwarf primaries.

While it is possible to claim the results from the fiducial setup 1.1 as the predicted yield of circumbinary planets from *Gaia*, I will not make a strong claim of this. The circumbinary planet population is not well enough known to say which of the various setups is most likely. The most important result from this set of tests is that the different setups led to such strong variations in the yield and in the way the yield manifests around the different binary types. This range of outcomes means that the results from *Gaia* will be able to constrain the population distributions of circumbinary planets, especially the massive planets and planets around longer-period binaries.

Chapter 4

Planets orbiting main-sequence binary stars: single-lined binaries/BEBOP

4.1 The BEBOP survey

Originally initiated in 2013 using the CORALIE spectrograph on the 1.2m Swiss Euler telescope in La Silla (Udry et al., 2000), BEBOP (Binaries Escorted By Orbiting Planets) is a radial velocity survey for circumbinary planets (Martin et al., 2019). In 2018 BEBOP was upgraded to using the HARPS spectrograph on the 3.6m telescope in la Silla (Mayor et al., 2003) to survey the southern sky, and in 2019 a northern survey was initiated using the SOPHIE specrograph on the T193 at OHP (Perruchot et al., 2008).

Some published milestone detections were discussed in Section 1.6.2. Six papers have been published in the BEBOP series so far. Martin et al. (2019) described the sample and the results from the CORALIE portion of the project. Standing et al. (2022) demonstrated the sensitivity of the HARPS survey on some of the best systems and presented a new detection limit method using `kima` (see Section 2.1.7). Triaud et al. (2022) presented the detection of Kepler-16b with radial velocities from SOPHIE. Standing et al. (2023)[1] published the first new discovery of a

[1] not officially numbered but given the implicit 4th number in the series of papers

circumbinary planet using radial velocities, the outer planet of the TOI-1338/BEBOP-1 system, and placed an upper limit on the mass of the inner planet. Freckelton et al. (2024) presented a homogeneous analysis of the stellar spectra of the BEBOP primary stars. Finally, Sairam et al. (2024a) demonstrated the sensitivity of combining SOPHIE data with the `DOLBY` method and is the paper shown in Section 3.3. Additionally, some yet-unpublished detections and candidates were included in a conference proceeding (Baycroft et al., 2024); these are investigated further in the rest of this chapter.

The next and seventh paper in the BEBOP series is shown in Section 4.2, presenting the detection of BEBOP3-b. A discussion of other detections and candidates, and a population-level comparison to the transiting planets is performed in Section 4.3.

4.2 BEBOP VII: Discovery of BEBOP-3b with SOPHIE, a circumbinary giant planet on an eccentric orbit

The following is a paper on which I am the first author, the 7th in the BEBOP paper series. It has been submitted to MNRAS and is currently under review.

The planet BEBOP-3b (known as J0723+79b during the day-to-day BEBOP analysis before becoming the third entry in the BEBOP catalogue) is the 2nd new planet discovery from BEBOP and the first from the northern sample. The planet passed the detection threshold in 2022, and the publication was delayed as in December 2023 we saw a sign that it might be an interesting 2 planet system with the planets in a 2:1 mean motion resonance (potentially with a crossing orbit). This required taking more data to investigate this model so the planet is only now being published[2].

In this paper, I performed the `kima` radial velocity analysis and wrote the majority of the manuscript. The data reduction was performed by Neda Heidari and Amaury Triaud, Neda Heidari writing the description of the reduction pipeline. Alix Freckelton performed the spectral analysis and wrote the section on that topic. Daniel Sebastian performed the HRCCS analysis

[2]Unsurprisingly the crossing orbit model was rejected by the subsequent data.

and wrote the section describing it. Yasmin Davis performed the joint photometric and radial velocity fit and wrote the relevant section. Lalitha Sairam investigated the stellar activity and wrote the corresponding section. Alexandre Correia wrote the section dealing with and performed the orbital stability computations. Many other authors were involved in the data collection for an observing program with Alexandre Santerne and Amaury Triaud as PIs.

MNRAS **000**, 1–15 (2023) Preprint 27 May 2025 Compiled using MNRAS LATEX style file v3.0

BEBOP VII. SOPHIE discovery of BEBOP-3b, a circumbinary giant planet on an eccentric orbit

Thomas A. Baycroft,[1]★ Alexandre Santerne,[2] Amaury H.M.J. Triaud,[1] Neda Heidari,[3] Daniel Sebastian,[1] Yasmin T. Davis,[1] Alexandre C.M. Correia,[4,5] Lalitha Sairam,[6] Alix V. Freckelton,[1] Aleyna Adamson,[1] Isabelle Boisse,[2] Gavin A.L. Coleman,[7] Georgina Dransfield,[8,9] João Faria,[10] Salomé Grouffal,[2] Nathan Hara,[2] Guillaume Hébrard,[3] Vedad Kunovac,[11,12] David V. Martin,[13] Pierre F.L. Maxted,[14] Richard P. Nelson,[7] Madison G. Scott,[1] Owen J. Scutt,[1] Matthew R. Standing,[15]

[1]*School of Physics and Astronomy, University of Birmingham, Edgbaston, Birmingham B15 2TT, UK*
[2]*Aix Marseille Univ, CNRS, CNES, LAM, Marseille, France*
[3]*Institut d'astrophysique de Paris, UMR 7095 CNRS université Pierre et Marie Curie, 98 bis, boulevard Arago, 75014 Paris, France*
[4]*CFisUC, Departamento de Fisica, Universidade de Coimbra, 3004-516 Coimbra, Portugal*
[5]*IMCCE, UMR8028 CNRS, Observatoire de Paris, PSL Université, 77avenue Denfert-Rochereau, 75014 , Paris, France*
[6]*Institute of Astronomy, University of Cambridge, Madingley road, Cambridge, CB3 0HA, UK*
[7]*Astronomy Unit, Department of Physics and Astronomy, Queen Mary University of London, Mile End Road, London, E1 4NS, UK*
[8]*Department of Astrophysics, University of Oxford, Denys Wilkinson Building, Keble Road, Oxford OX1 3RH, UK*
[9]*Magdalen College, University of Oxford, Oxford OX1 4AU, UK*
[10]*Observatoire Astronomique de l'Université de Genève, Chemin Pegasi 51, CH-1290 Versoix, Switzerland*
[11]*Department of Physics, University of Warwick, Coventry CV4 7AL, UK*
[12]*Centre for Exoplanets and Habitability, University of Warwick, Gibbet Hill Road, Coventry CV4 7AL, UK*
[13]*Department of Physics and Astronomy, Tufts University, 574 Boston Avenue, Medford, MA 02155, USA*
[14]*Astrophysics Group, Keele University, Keele, Staffordshire, ST5 5BG, UK*
[15]*European Space Agency (ESA), European Space Astronomy Centre (ESAC), Camino Bajo del Castillo s/n, E-28692 Villanueva de la Cañada, Madrid, Spain*

Accepted XXX. Received YYY; in original form ZZZ

ABSTRACT

Planetary systems orbiting close binaries are valuable testing grounds for planet formation and migration models. More detections with good mass measurements are needed. We present a new planet discovered during the BEBOP survey for circumbinary exoplanets using radial velocities. We use data taken with the SOPHIE spectrograph at the Observatoire de Haute-Provence, and perform a spectroscopic analysis to obtain high precision radial velocities. This planet is the first radial velocity detection of a previously unknown circumbinary system. The planet has a mass of $0.56\,M_{Jup}$ and orbits its host binary in 550 days with an eccentricity of 0.25. Compared to most of the previously known circumbinary planets, BEBOP-3b has a long period (relative to the binary) and a high eccentricity. There also is a candidate outer planet with a $\sim$ 1400 day orbital period. We test the stability of potential further candidate signals inside the orbit of BEBOP-3b, and demonstrate that there are stable orbital solutions for planets near the instability region which is where the *Kepler* circumbinary planets are located. We also use our data to obtain independent dynamical masses for the two stellar components of the eclipsing binary using High Resolution Cross-Correlation Spectroscopy (HRCCS), and compare those results to a more traditional approach, finding them compatible with one another.

Key words: binaries: eclipsing – planets and satellites: detection – stars: individual:BEBOP-3 – techniques: radial velocities.

1 INTRODUCTION

Circumbinary exoplanetary systems are a useful test of exoplanet formation and migration models, not only for binary stars but also applicable to single stars. Far from the binary the dynamical influence of the inner binary is negligible and planet formation is expected to be comparable to around single stars. In the inner region of the circumbinary disc, the influence of the binary causes drastically different conditions for nearby bodies compared to single stars. This has been shown to inhibit circumbinary planet formation in a region near the binary (Moriwaki & Nakagawa 2004; Paardekooper et al. 2012), however this region is precisely where almost all of the discovered circumbinary planets have been found to exist. These circumbinary exoplanets are therefore likely to have migrated to their current locations, meaning they are an excellent probe of migration theories in general (Pierens & Nelson 2008; Coleman et al. 2023, 2024).

There are currently 16 confirmed circumbinary exoplanets orbiting main-sequence binaries. Of these, 14 were discovered using the

★ E-mail: txb187@student.bham.ac.uk

© 2023 The Authors

transit method (e.g. Doyle et al. 2011), 1 using eclipse timing variations (Goldberg et al. 2023), and 1 using the radial velocity method (Standing et al. 2023). Of these, few are significantly eccentric (the most eccentric is Kepler-34 b with $e \approx 0.18$; Welsh et al. 2012)[1] and there are two multi-planet systems: TOI-1338/BEBOP-1 (Kostov et al. 2020; Standing et al. 2023) and Kepler-47 (Orosz et al. 2012, 2019).

Of the transiting circumbinary systems, all but one (Kepler-1647 b, Kostov et al. 2016) have their innermost planet orbiting very close to the boundary inside which orbits are unstable due to the dynamical influence of the binary (Holman & Wiegert 1999). This so called "pile-up" is thought to not be solely due to the observational bias of the transit method towards short-period planets (Martin & Triaud 2014; Li et al. 2016).

The BEBOP (Binaries Escorted By Orbiting Planets) survey is a radial velocity survey aiming to detect circumbinary planets (Martin et al. 2019). Its first phase had a focus on single-lined binaries - systems in which there are no obvious spectral lines observed from the secondary star. For a main-sequence binary this typically requires a mass ratio $q \lesssim 0.3$ (Triaud et al. 2017). So far BEBOP has made three circumbinary planet detections, with BEBOP-1c (Standing et al. 2023) being the first new planet. The other two detections were confirmations of Kepler-16b (Triaud et al. 2022) and of TIC 172900988b (Sairam et al. 2024). This paper, the seventh in the BEBOP series, presents our second circumbinary planet discovery using the radial velocity method, and the first such planet with a significant eccentricity measurement, BEBOP-3b. This newly detected circumbinary planet orbits the eclipsing binary star BD+79 230 (TIC 289949453).

There is a disadvantage to observing single-lined binaries instead of double-lined binaries. In double-lined binaries, the two sets of radial velocities mean that a model-independent dynamical mass can be derived. In single-lined systems, however, the stellar (and thus the planetary) physical parameters are ultimately dependent on the modeled parameters for the primary star. Recently, Sebastian et al. (2024b) demonstrated the use of High Resolution Cross-Correlation Spectroscopy (HRCCS) on single-lined binaries. This allows the signal of the secondary within the spectra to be retrieved, effectively converting the single-lined binary to a double-lined binary for the purposes of absolute mass determination. Sebastian et al. (2024b) apply the method to the TOI-1338/BEBOP-1 system using spectra from the HARPS and ESPRESSO spectrographs. They obtain a model-independent and more precise mass measurement for both stars in the binary. We repeat the same analysis to obtain dynamical masses for the two components of the BEBOP-3(AB) binary.

In Section 2 we describe the data collection and reduction pipeline. The various analyses performed are described in Section 3. We present the results of the radial velocity analysis and a stellar activity analysis in Section 4. We discuss the results and investigate the orbital stability of the system in Section 5, and conclude in Section 6.

2 RADIAL VELOCITY DATA

The sample selection for the southern component of the BEBOP survey is reported in Martin et al. (2019), but the northern sample has not been described much yet. The southern sample was built from a WASP (Wide Angle Search for Planets; Pollacco et al. 2006) false positives flag known as EBLM (Eclipsing Binary – Low Mass; Triaud et al. 2013; Maxted et al. 2023). Typically these are Sun-like stars with a stellar companion $< 0.3\ M_\odot$, producing transit-shaped primary eclipses. Whilst EBLM-flagged false positives exist for the Northern component of WASP, the record is not as thorough as it was for the south (Triaud 2011). This is why the northern BEBOP sample was selected not just from WASP, but also from the KELT survey's (Kilo-degree Extremely Little Telescope; Pepper et al. 2007) false positives (Collins et al. 2018). Systems selected are above the celestial equator, have orbital periods $P_{\rm bin} > 5$ days, and primary spectral types > F4. The restriction to relatively long period eclipsing binaries was driven by obtainable precision; tight binaries are tidally locked and stars in < 5 day binaries rotate quickly resulting in the spectral lines being so broadened that finding CBPs is very difficult. Coincidentally, the known transiting CBPs are all around similarly "long-period" binaries, potentially as a quirk of their formation process (Muñoz & Lai 2015; Martin et al. 2015). Only six systems were common between WASP-North and KELT. Following a short reconnaissance programme in 2018, we created a top priority sub-sample that became the BEBOP-North sample, where SOPHIE spectra typically produced radial velocity uncertainties $< 10\,{\rm m\,s^{-1}}$ in 1800s or under. The BEBOP-3 system was identified from the KELT false positive catalog (Collins et al. 2018).

Overall, 141 high resolution spectra were obtained between 2018-11-13 and 2024-11-18 with the high resolution échelle spectrograph SOPHIE, mounted on the T193 at the Observatoire de Haute-Provence (Perruchot et al. 2008). Data were acquired under programme ID 19A.PNP.SANT.

The data were acquired in ObjAB mode where fibre A is placed on the target and fibre B is placed on the sky to enable the removal of solar spectral lines reflected by the Moon. The observations were taken in high resolution (HR) mode with resolution $R = 75\,000$[2]. Standard calibrations were taken at the start of the night and at approximately 2 hr intervals throughout to track the instrumental zero-point error.

The SOPHIE radial velocities (RVs) are computed by the SOPHIE Data Reduction System (DRS, Bouchy et al. 2009b), which cross-correlates the spectra with a weighted numerical mask corresponding to a G2-type star and subsequently fits a Gaussian to the cross-correlation function (CCF) (Pepe et al. 2002; Baranne et al. 1996). To enhance the precision of the SOPHIE RV measurements, we applied the optimized procedures described in Heidari (2022) and Heidari et al. (2024), including: (1) corrections for charge transfer inefficiency in the CCD (Bouchy et al. 2009a); (2) correction of template (colour) effects (Heidari et al. 2024); (3) removal of moonlight contamination by utilising the simultaneous sky spectrum recorded via the second SOPHIE fiber (Pollacco et al. 2008); (4) correction for long-term instrumental drifts using the RV master constant time series, constructed from so-called 'constant' stars monitored each night by SOPHIE (Courcol et al. 2015; Heidari 2022; Heidari et al. 2024); and (5) correction for short-term instrumental drifts by interpolating drift measurements at the exact time of each observation, based on frequently measured drifts throughout the night. Radial velocity data are collated into Table A1.

The 141 spectra obtained have a median SNR[3] of 72.9 and me-

[1] The HD202206 system was discovered through radial-velocity (Correia et al. 2005; Benedict & Harrison 2017) but it is uncertain between a circumbinary brown dwarf and a planet orbiting a Star-Brown dwarf binary, the eccentricity of the "planet" is ≈ 0.22.

[2] At 5550 Å

[3] The signal-to-noise ratio quoted here is that achieved at the center of order 26 (out of orders 0-38), corresponding to 5550 Å (near the center of the V band)

dian radial velocity precision of 2.3 m s^{-1} Radial velocity outliers exist. These are dealt with in various ways for the different analyses. Outliers identified are flagged in Table A1.

3 ANALYSIS AND METHODS

3.1 Spectral analysis

In Freckelton et al. (2024), the 91 SOPHIE spectra available at the time were coadded and the combined spectrum analysed using the `PAWS` pipeline. This analysis achieved a signal-to-noise ratio of 555. Based on this signal-noise-ratio being already high enough that model uncertainty is dominant, we do not repeat the analysis from Freckelton et al. (2024) with extra spectra. Atmospheric parameters for the primary star were determined by applying the `PAWS` pipeline to this coadded spectrum. The pipeline implements the curve-of-growth equivalent widths (EW) and spectral synthesis methods via `iSpec` (Blanco-Cuaresma 2019). The advantage of combining the two methods sequentially is that the parameters $T_{\rm eff}$ (Effective temperature), log$g$ (Surface gravity), [Fe/H] (Iron abundance), and $v \sin i$ (projected rotational velocity), as presented in Table 1, are all allowed to freely vary to fit the observations in at least one stage of the pipeline. Using the `WIDTH` radiative transfer code (Sbordone et al. 2004), the EW method was used to determine an initial set of atmospheric parameters for the primary star. `PAWS` then applies the spectral synthesis method to allow a determination of $v \sin i$, using the initial atmospheric parameters as the start point for the first iteration. Synthetic spectra were generated using these parameters by the use of the `SPECTRUM` (Gray & Corbally 1994) radiative transfer code, with the parameters iterated until the synthetic spectrum sufficiently reproduced the observed one, which returned the final atmospheric parameters shown in Table 1. Homogeneity between the two methods was ensured by employing the `SPECTRUM` (Gray & Corbally 1994) line list and `ATLAS` (Kurucz 2005) model atmosphere set throughout the pipeline.

3.2 HRCCS measurement of the secondary component

The large number of SOPHIE observations allows us to detect the extremely small contribution (~ 0.1 % for the spectral range of SOPHIE) of the secondary star. Here we apply the High-Resolution Cross-Correlation Spectroscopy method (HRCCS; Snellen et al. 2010), which is commonly used to detect exoplanet atmospheres. This method turns the single-lined binary into a double-lined binary to derive model-independent dynamical masses for both stars. It has been successfully applied to optical high-resolution spectra of HARPS (Mayor et al. 2003) and ESPRESSO (Pepe et al. 2021) for the high-contrast binary TOI-1338/BEBOP-1 (Sebastian et al. 2024b). We follow closely the recipe outlined in that work.

We exclude 8 of the 141 SOPHIE spectra from our analysis. Three of which correspond to a wrong pointing and five with very low SNR (<23.5 @500 nm), which is 3 times lower than the average SNR (71) for the primary. SOPHIE spectra excluded from the HRCCS analysis are indicated in Table A1. The 133 remaining spectra have an average SNR of 73.9 per resolution element at 500 nm. This means for the faint secondary, the SNR is as low as 0.08 only.

First we split the one dimensional SOPHIE spectra (`s1d`) each into 70 chunks of 4387 pixels. We then shift the spectra into the rest frame of the primary, and perform continuum normalisation, sigma clipping, and singular-value decomposition (SVD) detrending (Kalman 1996). The latter will effectively remove the spectral lines of the primary star from the series of spectra. The number of excluded SVD components is determined automatically using the effective matrix rank (Roy & Vetterli 2007) for each chunk. We set the maximum number of components to 26 and find that the median is 5. This results in a reduced rank of 0.04 (the number of removed components divided by the number of spectra). According to Table 4 in Sebastian et al. (2024b), we expect that this detrending has removed ≤ 3 % of the secondary's spectral features. The secondary's signal in the data is therefore kept mainly intact.

We exclude a further 11 of the 133 spectra at orbital phases, where the velocity of the secondary's signal differs less than 10 km s^{-1} from the primary's absorption lines. In this way we make sure that possible residuals of the detrending do not interfere with our measurements. We also discharge the 20 bluest chunks (keeping data from 477 nm and redder) as those add significant noise to the secondary signal. We then use the k-focusing method (Sebastian et al. 2024a), which enhances the cross-correlation function (CCF) of the secondary star in the secondary's rest frame by scanning different semi-amplitudes (K_2). This method produces a $K_2 - V_{\rm rest}$ plane by combining all CCFs of the detrended data with an M2-dwarf line mask[4]. We sample the map for a velocity range between -5 km s^{-1} and 65 km s^{-1} and the unknown semi-amplitude of the secondary (K_2) from 55 – 105 km s^{-1}, each in steps of 1.5 km s^{-1}.

The resulting CCF map in the $K_2 - V_{\rm rest}$ - plane is shown in Figure 1. The CCF signal of the secondary is detected with a 5.5-σ significance at the expected semi-amplitude and systemic velocity. We measure this signal using the `Saltire` model (Sebastian et al. 2024a), which accurately reproduces the CCF signal by fitting a k-focused double-Gaussian function to the data. We estimate the best fitting parameters for K_2 and $V_{\rm rest}$ by sampling the data using Markov Chain Monte Carlo (MCMC) with a posterior distribution of 21,000 samples. In Table 2, we present the best parameters, given as the 50th percentile of the MCMC sampling. We then follow Sebastian et al. (Accepted) to estimate the systematic uncertainties and randomly draw 50 % of the data and measure the best fitting parameters. This is repeated 200 times and the systematic uncertainties are derived as the standard error of the 200 measurements. Results are presented in Section 4.1 and Tables 1 and 2.

Table 1. Stellar and binary parameters from three different analysis methods.

Parameter	HRCCS	RV+Photometry	Spectral
$i_{\rm bin}$ (°)		88.7488 ± 0.0092	
$M_{\rm pri}$ (M$_\odot$)	1.083 ± 0.026	1.163 ± 0.043	1.131±0.051*
$M_{\rm sec}$ (M$_\odot$)	0.2615 ± 0.0039	$0.2731^{+0.0065}_{-0.0064}$	
$R_{\rm pri}$ (R$_\odot$)		1.414 ± 0.017**	1.4107±0.0089*
$R_{\rm sec}$ (R$_\odot$)		0.2811 ± 0.0033	
$T_{\rm eff,pri}$ (K)			6033 ± 100
log $g_{\rm pri}$ (dex)		4.203 ± 0.017	4.27 ± 0.09
[Fe/H] (dex)			−0.02 ± 0.10
$v \sin i_{\rm pri}$ (km s^{-1})			2.00 ± 0.66

* from ISOCHRONE fitting
** from *GAIA*

[4] We use the line mask of the HARPS pipeline, which has been publicly released on https://www.eso.org

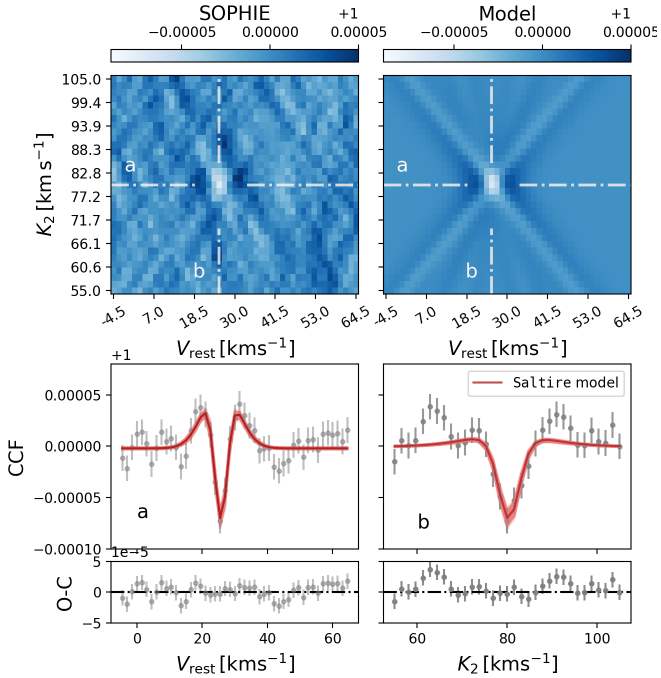


Figure 1. HRCCS 5.5-σ detection of the secondary. Upper panel: Cross-correlation map and `Saltire` model for SOPHIE data. White dotted lines show the positions of slices (a,b). Lower panel: Slices a & b through CCF map at maximum significance. Red line: best-fitting `Saltire` model, red shaded area: 1σ Uncertainties from the MCMC. Errorbars represent the MCMC jitter term (σ_{jit}) from the two dimensional fit.

3.3 Joint radial velocity and photometric analysis of the binary

The goal of the previous section is to obtain precise absolute, dynamical masses. Here we independently analyse the data, using the more standard method when dealing with single-lined eclipsing binaries (e.g. Triaud et al. 2013; Davis et al. 2024). Our goal in this section is firstly to obtain radii for the two stars and an inclination measurement for the binary, and secondly to be in a position to compare derived (model-dependent) stellar masses, to dynamical (model-independent) stellar masses.

Following Davis et al. (2024), we perform a simultaneous joint analysis of both the *TESS* (Transiting Exoplanet Survey Satellite; Ricker et al. 2015) photometric data (accessed using the Mikulski Archive for Space Telescopes (MAST) web service[5] and downloaded using the `lightkurve` software package (Lightkurve Collaboration et al. 2018)) and the SOPHIE spectroscopic data using the `allesfitter` package (Günther & Daylan 2019, 2021). `Allesfitter` uses the `dynesty` nested sampling package (Speagle 2020) and `ellc` (Maxted 2016) for binary system models. All currently available sectors (up to and including Sector 74) of *TESS* data are included from the *TESS* Science Processing Operations Center (SPOC) pipeline (with 120s cadence) (Jenkins et al. 2016).

The methods outlined in the remainder of this section are based on those presented in Davis et al. (in prep). The photometric data are chunked into individual datasets to be given to `allesfitter` as this allows for individual hybrid spline baselines to account for any out of eclipse variability. This is more computationally efficient as well as removing unnecessary complexity that comes from employing the use of a gaussian process. Upon visual inspection any events that were partial, showed larger fluctuations, or showed strong trends in the residuals were removed [6] (and the remaining data re-analysed). All radial velocity outliers identified in Section 3.4 are removed for this analysis.

Before completing the global modelling, the spectroscopic data is first analysed in isolation. This allows for appropriate prior values to be determined for radial velocity parameters related to both the binary and planetary companions. The simultaneous global fit is then completed for the photometric binary companion, and the binary and planetary companions in the spectroscopic timeseries. With the addition of photometric data in the analysis, additional parameters of the system can be determined, including the radius of the stellar companion and the inclination of the binary orbit. Furthermore, by following the parameter derivation method in Davis et al. (2024), the mass of the primary star (M_{pri}) can be determined alongside the mass and radius of the secondary star (M_{sec}, R_{sec}). These parameters are shown in Table 1. The phase-folded lightcurves are shown in Figure A1.

3.4 Search for planetary signals in the radial velocities

The radial velocity timeseries analysis is performed using the "BINARIESmodel" of `kima` (Faria et al. 2018; Baycroft et al. 2023a). `kima` utilises diffusive nested sampling (DNEST4; Brewer & Foreman-Mackey 2018) to explore the parameter space, and allows for the number of Keplerian signals to be a free parameter. The binary orbit is fit with a Keplerian, using separate priors to the planetary signals. The "BINARIESmodel" is tailored to fitting binary orbits by extending the binary's Keplerian fit with a linear apsidal precession term and by including the radial velocity contribution from general relativity (Baycroft et al. 2023a). The parameters used for the Keplerians are P, K, e, ω, M_0, where P is the orbital Period, K the radial velocity semi-amplitude, e the orbital eccentricity, and ω the argument of periastron. Here M_0 is the mean anomaly at the reference time; for the purpose of reporting the parameters this is converted into a time of pericentre passage T_{peri}. Priors used for the radial velocity analysis with `kima` are shown in Table A2.

Outliers are dealt with in a two-stage process. The likelihood calculation uses a Student's t distribution rather than a Gaussian distribution, the wide tails of which allow outliers to avoid skewing the fit while remaining accounted for. The Student's t distribution takes a shape parameter ν, a small value of which leads to a heavy tail, down-weighting outliers, and a large value results in a near-Gaussian likelihood. Some extreme outliers exist, likely due to incorrect pointings of the telescope. We identify and remove extreme outliers by performing a first analysis with `kima`, identifying any individual datapoints where the ratio of Student's t and Gaussian likelihoods $L_T/L_N \geq 10^{10}$. These points are removed and the final analysis is then performed, still using a Student's t likelihood to account for any remaining non-extreme outliers. The radial velocity data is made available in Table A1 with the points that we identify as outliers flagged: extreme outliers are flagged with an X; non-extreme outliers are flagged with a Y. Non-extreme outliers are those which have a likelihood ratio $L_T/L_N \geq 10$ in the final analysis.

[5] https://mast.stsci.edu

[6] Primary eclipse events At BJD 2459022.08, 2459035.13 and 2459405.39, and secondary eclipse events at BJD 2459755.74 and 2459768.92 are removed.

Table 2. Orbital parameters for the BEBOP-3 binary and general fit parameters. Parameters are taken from the `kima` analysis of RVs only unless otherwise specified. $^{(a)}$ Parameter from HRCCS. $^{(b)}$ Parameter from combining `kima` results with HRCCS results and using inclination from photometric analysis. $^{(c)}$ Parameter taken from joint analysis of RV and photometry. The reference time (BJD) used in the analysis is 2459766.975506

Parameter	Units	Value
P	[days]	13.2176657 ± 0.0000027
K	[km s^{-1}]	$19.36413^{+0.00091}_{-0.00102}$
K_2 $^{(a)}$	[km s^{-1}]	80.22 ± 0.74
e		0.063255 ± 0.000054
ω	[rad]	$4.90226^{+0.00097}_{-0.00090}$
$\dot{\omega}$	[arcsec yr^{-1}]	160 ± 100
$T_{\rm peri}$	[BJD-2450000]	$9756.1098^{+0.0021}_{-0.0019}$
$M_{\rm pri}$ $^{(b)}$	[M$_\odot$]	1.083 ± 0.026
$M_{\rm sec}$ $^{(b)}$	[M$_\odot$]	0.2615 ± 0.0039
i $^{(c)}$	[deg]	88.7488 ± 0.0092
$a_{\rm pri}$ $^{(b)}$	[AU]	$0.0234853^{+0.0000011}_{-0.0000013}$
$a_{\rm sec}$ $^{(b)}$	[AU]	0.09728 ± 0.00090
Jitter	[m s^{-1}]	$6.73^{+1.08}_{-0.93}$
ν	(Student's t shape)	$7.9^{+29.0}_{-3.6}$
$v_{\rm sys}$	[km s^{-1}]	$24.46146^{+0.00072}_{-0.00075}$
$v_{\rm rest,2}$ $^{(a)}$	[km s^{-1}]	25.77 ± 0.77

4 RESULTS

4.1 Absolute physical parameters for the binary

The radial velocity analysis is performed simultaneously for the binary and the potential planet signals searched for. The detection of a planet and criteria related to that are discussed in Section 4.2. The orbital parameters of the binary are presented in Table 2. We use the values of K_2 from Section 3.2 and $i_{\rm bin}$ from Section 3.3 to derive the masses of the two stars.

Table 1 shows parameters for the stars obtained from three different analyses, which each give an independent mass measurement. There is a slight tension between the different mass measurements. The measurements from HRCCS (Section 3.2) and joint radial velocity/photometry fit (Section 3.3) have a 1.7σ agreement. This difference is not so great, and a thorough study of potential systematic differences between the methods is beyond the scope of this work. We chose to use the mass from HRCCS as it is the least model-dependent, therefore we take $M_{\rm pri} = 1.083 \pm 0.026\,M_\odot$ and $M_{\rm sec} = 0.2615 \pm 0.0039\,M_\odot$.

The dynamical mass of each star is therefore obtained to a precision of 2.4% and 1.5%. The inclination of $88.7488 \pm 0.0092°$ is derived from the joint photometric and radial velocity analysis. We report orbital and fit parameters for the stars/binary in Table 2, this contains parameters from the radial velocity fit (A few of the parameters depend on results from the HRCCS or photometric fit and these are noted).

4.2 Detection of the planet BEBOP-3b

The trans-dimensional nature of `kima` makes comparing models with different numbers of signals possible from a single analysis. From a single `kima` analysis we can calculate the Bayes Factor for an (n)-planet model compared to a (n-1)-planet model, $BF_{n,n-1}$. A Bayes Factor over 150 is considered "very strong evidence" for one model over another (Trotta 2008). We find that $BF_{1,0} = 3.4 \times 10^{13}$ and $BF_{2,1} = 6.0$. This means there is overwhelming evidence for a 1-planet model over a 0-planet model, and weak-to-moderate evidence for a 2-planet model over a 1-planet model. For further discussion of the use of Bayesian model comparison with `kima` as a detection metric for planet signals see e.g. Standing et al. (2022); Triaud et al. (2022); Standing et al. (2023); Baycroft et al. (2023b).

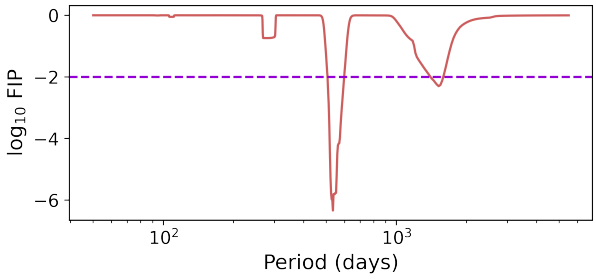


Figure 2. False Inclusion Probability (FIP) periodogram. The dashed purple line is at a 1% false inclusion probability.

Table 3. Orbital parameters of BEBOP-3 b, note that these are mean orbital elements rather osculating elements. $^{(a)}$ True mass of the planet under the assumption it is exactly coplanar with the binary.

Parameter	Units	Value
P	[days]	$547.0^{+6.2}_{-7.6}$
K	[m s^{-1}]	11.8 ± 1.1
e		$0.247^{+0.077}_{-0.089}$
ω	[rad]	$0.86^{+0.40}_{0.46}$
$T_{\rm peri}$	[BJD-2450000]	9633^{+31}_{-36}
$M^{(a)}$	[M$_{\rm Jup}$]	$0.558^{+0.051}_{-0.048}$
a	[AU]	1.444 ± 0.017

While the model comparison favours a 1-Keplerian model, this does not necessarily mean either that the signal is planetary in nature since some other signal could mimic a Keplerian (e.g. Baycroft et al. 2023b), or that the parameters of the planet are certain, with aliases and degeneracies being possible. Figure 2 shows the False Inclusion Probability (FIP) periodogram (Hara et al. 2022). The FIP is calculated from the proportion of weighted samples which contain a planet within each period bin. As seen in Figure 2 the main detected periodicity is the one between 500-600 days and a second periodicity is seen around 1400 days, just surpassing the 1% threshold recommended in Hara et al. (2022). The FIP has been mathematically shown to be optimal, in the sense that it is the exoplanet detection criterion which maximises true detections for a certain tolerance to false ones (Hara et al. 2024). The validation that these signals are not due to stellar activity is presented in Section 4.4.

A circumbinary planet with $P_{\rm pl} = 547^{+6.2}_{-7.6}$ days and $M_{\rm pl} = 0.558^{+0.051}_{-0.048}\,M_{\rm Jup}$ is therefore detected, BEBOP-3b. The model favours a moderate eccentricity of $e = 0.247^{+0.077}_{-0.089}$. The maximum-likelihood model for the planetary orbit is shown in Figure 3 with the individual data shown as well as the residuals below. The binned radial velocities are also shown to guide the eye. The median and 1σ uncertainties on the planet parameters are presented in Table 3. The distributions and correlations for the posterior samples with the number of planets $N_p = 1$ are shown in Figure A2.

The orbital configuration of the system is shown in Figure 4. The binary and planet orbits are shown as 600 posterior draws overlain. The region of potential transitability, discussed in Section 5.3, is highlighted in magenta for each planetary orbit shown. The direction

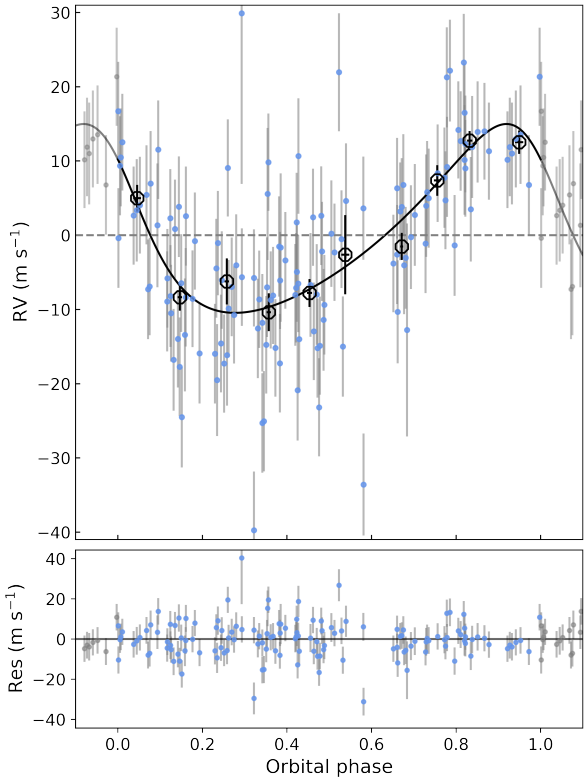


Figure 3. Phased RV plot of BEBOP-3 b, with the residuals below. The parameters for the planet shown are the maximum-likelihood solution. The binned RV data are shown to guide the eye.

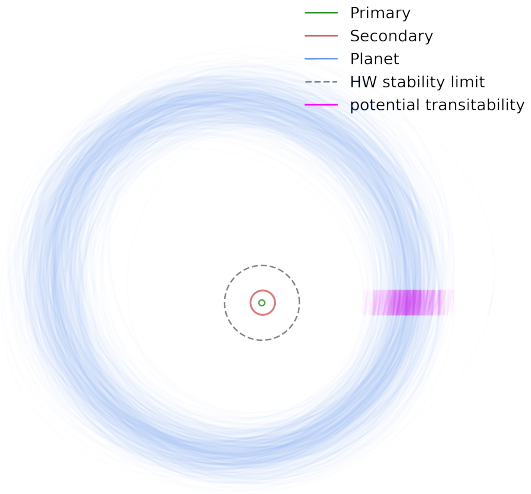


Figure 4. Orbital configuration of BEBOP-3 showing the orbits of each star and the planet for 600 posterior draws. The stability limit is shown as a dashed line, this was calculated given the binary orbital parameters from the maximum-likelihood solution.

to earth is off the right hand side of the diagram. Using the primary mass $M_{\rm pri} = 1.083\ M_\odot$ and the orbital parameters from the maximum likelihood posterior sample, we calculate the stability limit using the equation 3 from Holman & Wiegert (1999). This limit is shown on the diagram as a dashed grey line. Defining the scaled semi-major axis as $a_{\rm sc} = a_{\rm pl}/r_{\rm stab}$, where the semi-major axis of the planet divided by the radius of the stability limit (Holman & Wiegert 1999), the value for BEBOP-3b is $a_{\rm sc} = 4.845^{+0.073}_{-0.081}$. Of the known circumbinary planetary systems, all except for Kepler-1647b have their innermost known planet between $1 < a_{\rm sc} < 1.8$. This showcases how BEBOP-3b is distinct from the pile-up planets (see Section 5.2).

4.3 Further signals

As mentioned in Section 4.2, there is weak-to-moderate evidence for a second planet. The signal corresponds to a planet with $P \approx 1400$ days and $M \sin i \approx 0.2\,M_{\rm Jup}$. The posterior distributions and covariances for planet 1 and planet 2 within the $N_p = 2$ posteriors are shown in figures A3 and A4.

We compute a detection limit to constrain potential other planets in this system. These are computed as described in Standing et al. (2022, 2023). The maximum-likelihood signal of the detected planet is removed, and then the residual data is analysed with the number of planets that `kima` fits for being fixed to one. The binary signal is not removed, and is then fit in this second analysis in the same way as before. This analysis then returns a posterior distribution of orbits which are consistent with the data but were not detected. The resulting posterior density is shown in Figure 5 along with the 99% confidence detection limit. Sensitivity is reached down to Neptune-mass planets at short orbital periods and to Saturn-mass planets at long orbital periods.

In the detection limit in Figure 5, the posterior distributions for planet-b and this outer candidate signal are also displayed. The distribution for the outer signal is majoritarily below the detection limit because the signal is not large enough (or the data not precise/accurate enough) to be detected/refuted.

Further observations are ongoing to confirm/refute this candidate signal. In Section 4.4 the highest activity signal is found at $\sim$ 1000 days. Obtaining more data will also increase the significance and the precision of the activity peaks, and help to ascertain if the candidate signal is from activity or not.

4.4 Stellar activity analysis

To investigate the periodic variations in the chromospheric activity indicators, we performed a Generalised Lomb-Scargle periodogram analysis of the H-alpha and Na D indices (similar to Standing et al. 2023). These indices exhibit the highest signal-to-noise ratio in our dataset, making them the most reliable tracers of periodic signals. Other indicators, such as Ca I, He I, and Ca II, displayed significant noise and did not reveal clear periodicities. The analysis was conducted on all the observations spanning a time baseline of 2197 days except those deemed outliers. The same outliers were removed as in the `kima` radial velocity analysis with which the planet was identified, these are marked with an X in Table A1. The periodograms are shown in Figure 6 along with False Alarm Probability (FAP) levels. The FAP is calculated by determining the power levels corresponding to a given probability threshold, which quantifies the likelihood that a detected signal is due to random noise rather than a true periodic signal. In this analysis, the FAP levels are set at 10%, 1%, and 0.1%, and their corresponding power thresholds are computed from the periodogram to assess the significance of the detected peaks.

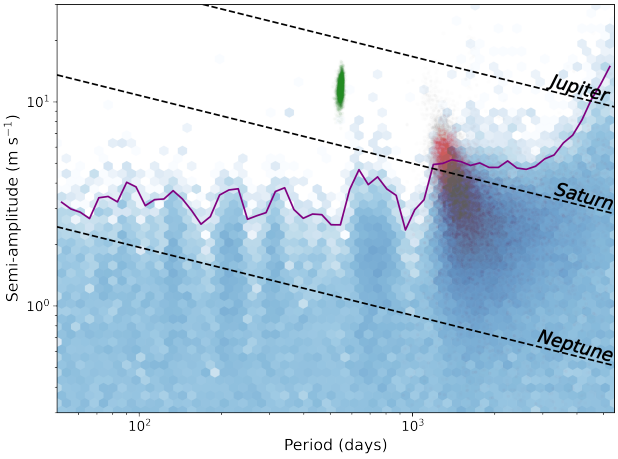


Figure 5. Detection limit for BEBOP-3. In blue, the posterior density of the `kima` run forced to fit a signal, with planet b removed. The posterior distribution for planet-b is shown in green and that for the candidate outer signal is shown in red. Dashed lines show expected signals of solar-system mass planets.

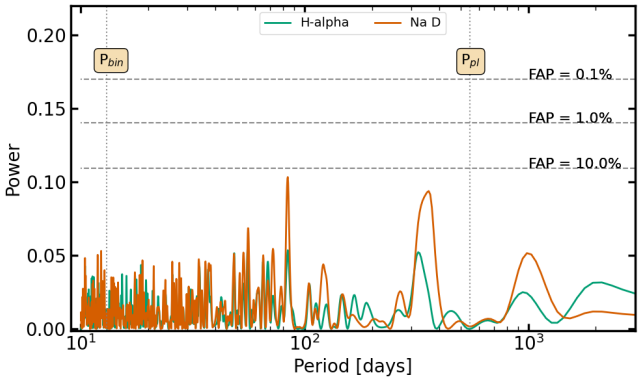


Figure 6. Periodograms of the activity indicators H-alpha and NaD are presented in orange and green, respectively. Grey dotted vertical lines denote the binary period and planetary period. Grey horizontal dashed lines represent FAP levels at 10%, 1%, and 0.1%

For the H-alpha index, the periodogram identifies a peak at a frequency of 0.0179 ± 0.0001 d^{-1}, corresponding to a period of 55.57 ± 0.35days. The maximum power of the detected signal is 0.05. However, when compared with the false alarm probability levels, this power remains below the 10% significance threshold, indicating that the detected periodicity is not statistically significant. The weighted mean of the H-alpha indices is 0.1868, with an RMS scatter of 0.006.

A similar analysis of the Na D index reveals a dominant period of 84.07 ± 0.72 days. The power of this signal is ∼0.1, which also remains below the 10% FAP significance threshold, suggesting that the observed periodicity is not robust. The weighted mean of the Na D indices is 0.4365, with an RMS scatter of 0.0195.

Although both indices exhibit periodic variations at similar timescales, the lack of statistical significance implies that these detections will require further observations and improved data sampling to confirm the nature of the signal. Neither H-alpha periodicity nor Na D periodicity are close to the strong signal seen around 550 days in the radial velocities. As such it is unlikely stellar photospheric processes are causing the observed radial-velocity modulation. We therefore interpret it as planetary.

5 DISCUSSION

5.1 Stability analysis

The BEBOP-3 system is hierarchical ($a_{\rm bin}/a_{\rm b} \ll 1$), and so the stability of BEBOP-3b should be assured (e.g. Correia et al. 2016). Motivated by the population of known circumbinary planets located near the stability limit, we investigate the stability of orbits interior to that of planet b. We simulate the BEBOP-3 system using two close-in stars in a nearly circular orbit ($a_{\rm bin}$ = 0.12 au, $e_{\rm bin}$ = 0.06, Table 2), together with an outer planet further away in an eccentric orbit ($a_{\rm b}$ = 1.44 au, $e_{\rm b}$ = 0.28[7], Table 3).

In order to get a reliable and comprehensive view of the stability of potential inner planets in the system, we performed a global frequency analysis (Laskar 1990, 1993) in the same way as achieved for other circumbinary planetary systems (eg. Correia et al. 2005; Standing et al. 2023). The system is integrated on a regular 2D mesh of initial conditions in the vicinity of the best fit (Tabs. 2 and 3). We used the symplectic integrator SABAC4 (Laskar & Robutel 2001), with a step size of 0.001 yr and general relativity corrections. Each initial condition is integrated for 5000 yr, and a stability indicator, $\Delta = |1 - n_{b'}/n_b|$, is computed. Here, n_b and n'_b are the main frequency of the mean longitude of the planet over 2500 yr and 5000 yr, respectively, calculated via the frequency analysis (Laskar 1993). The results are reported in color, where yellow represents strongly chaotic trajectories with $\Delta > 10^{-2}$, while extremely stable systems for which $\Delta < 10^{-8}$ are shown in purple/black. Orange indicates the transition between the two, with $\Delta \sim 10^{-4}$.

We test the possibility of an inner planet, between the binary stars and planet-b, with a radial-velocity signature of 1 m s^{-1}. Such a planet would correspond to a mass $m_{\rm inner} \sim 10$ M$_\oplus$. We assume the best fit solution for the already known bodies in the system (Tabs. 2 and 3), coplanar orbits, and vary the orbital period and the eccentricity of a putative inner planet (Figure 7). We observed that close to the binary ($50 \lesssim P_{\rm inner} \lesssim 200$ days), the system is mostly stable with small eccentricity ($e_{\rm inner} \lesssim 0.1 - 0.2$), except close to some mean-motion resonances between the putative inner planet and the binary. Interestingly, as we move further away ($P_{\rm inner} \gtrsim 200$ days), we observed the exact opposite behaviour: the system becomes globally unstable, but stability is still possible, even with moderate eccentricities, near some mean-motion resonances between the inner planet and planet-b.

In Figure 7, the location of the known innermost planets of all the known circumbinary systems (excluding Kepler-1647b) are shown. The orbital period has been scaled by the ratio of the orbital period of the respective binaries. All of these points lie in the region of stability, and 6 of these 12 planets have a mass measurement (or non-measurement) consistent with being below the mass of Neptune, which is the approximate sensitivity limit in this region for BEBOP-3. This suggests that an additional planet consistent with the current population would remain undetected in the data collected thus far.

[7] The maximum-likelihood parameters from the `kima` analysis are used for the stability analysis which while within the uncertainties presented in Tables 2 and 3, do not always correspond exactly to the mean values of the posterior reported.

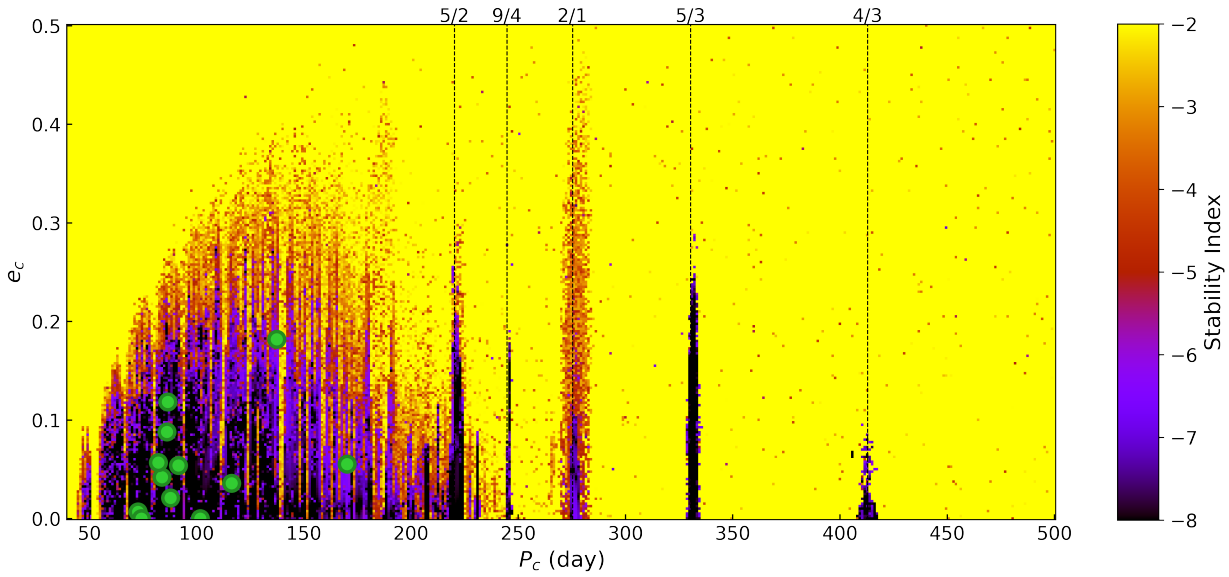


Figure 7. Stability analysis of an inner planet in the BEBOP-3 system assuming $m_{\rm inner} \sim 10\ {\rm M}_{\oplus}$ and coplanar orbits. For fixed initial conditions (Tabs. 2 and 3), the parameter space of the system is explored by varying the orbital period $P_{\rm inner}$ and the eccentricity $e_{\rm inner}$ of planet-c. The step size is 1.15 day in orbital period and 0.0025 in eccentricity. For each initial condition, the system is integrated over 5000 yr and a stability indicator is calculated which involved a frequency analysis of the mean longitude of the inner planet (see text). Chaotic diffusion is indicated when the main frequency of the mean longitude varies in time. Yellow points correspond to highly unstable orbits, while purple points correspond to orbits which are likely to be stable on a billion-years timescales. The dashed black lines indicate mean-motion resonances with the planet BEBOP-3b. The green circles represent the locations of the innermost circumbinary planet in the other known systems, scaled to the parameters of the BEBOP-3 binary.

5.2 An eccentric long-period circumbinary planet

Of the circumbinary planetary systems discovered so far, only Kepler-1647 (Kostov et al. 2016) does not contain a planet orbiting close to the instability limit (Martin & Triaud 2014). BEBOP-3 joins Kepler-1647 as the second circumbinary planetary system in this category. This has been interpreted as a result of migration through a circumbinary disc, and parking around the current location near where the disc gets truncated (Penzlin et al. 2021).

In the cases of Kepler-1647 and BEBOP-3 it is unclear whether there are additional, currently undetected, planets orbiting closer to the binary or whether these circumbinary systems followed a different formation and evolutionary pathway. The stability analysis in Section 5.1 shows that there is a significant stable region exactly where it would be expected for a planet comparable to the Kepler planets to exist. In addition, the inner planets of circumbinary systems regularly appear to have a low mass (e.g. Kepler-47b (Orosz et al. 2012), TOI-1338/BEBOP-1b (Standing et al. 2023)). In the case of TOI-1338/BEBOP-1b, despite 184 spectra, the planet remains undetected in the RVs alone (Standing et al. 2023). Based on these considerations it could be expected that either a planet below the radial velocity detection threshold is present there, or that a planet used to be present there but has since become destabilised.

BEBOP-3b has a marginal detection of eccentricity. It is the only circumbinary planet with a non-zero measured eccentricity from the radial velocity method so far. Figure 8 displays the location of BEBOP-3b compared to the other circumbinary planets in eccentricity and semi-major axis scaled by the radius of the stability limit (calculated from equation 3 in Holman & Wiegert 1999). The red curve shows an approximate stability envelope above which a planet's orbit would cross into the instability zone. The known circumbinary planets are mostly clustered in the bottom left corner of this plot, near the stability limit and at low eccentricities. The planets with higher eccentricities have a slightly larger semi-major axis to compensate for this, leading to a pattern of planets tracing just below the stability envelope. As is visible in Figure 8, BEBOP-3b is distinct from the other known circumbinary planets in being both eccentric and far from crossing into the instability region.

Despite appearing somewhat special among circumbinary planets, there are a few other considerations/caveats:

- Many gas giants orbiting single stars occupy eccentric orbits (e.g. Winn & Fabrycky 2015), and compared to them BEBOP-3b is not abnormal.
- This is only the second RV-discovered circumbinary planet, and the second longest orbital period; only more detections can tell whether its current parameters are unusual or not.
- Eccentricity measurements of planetary signals from radial velocities can sometimes be unreliable. This is made worse when there are undetected planets in the system (Hara et al. 2019), in particular when near orbital period commensurabilities (Anglada-Escudé et al. 2010). Comparing the eccentricity distributions in Figures A2 and A3 show that including the outer planet candidate slightly decreases the significance of the eccentricity measurement. More data is required to assess both the significance of the second planet and of the eccentricity measurement.
- The prior used for the eccentricity is that from Kipping (2013) which is tailored to planets around single-stars and may not be suitable for circumbinary planets.

More circumbinary planet detections and better characterisation of the existing planets are needed to determine whether there is a

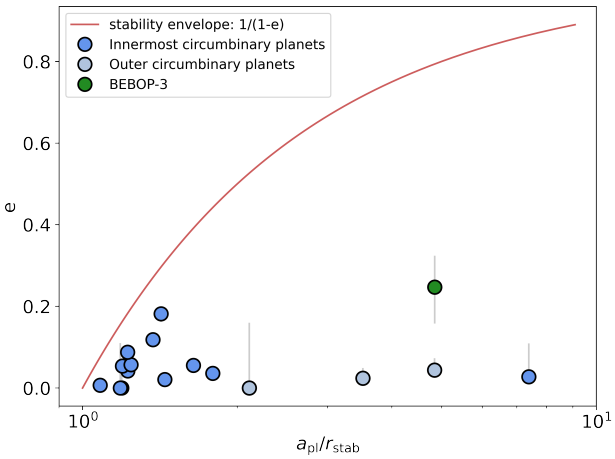


Figure 8. Eccentricity distribution of the population of currently known Circumbinary exoplanets. The x-axis is the semi-major axis of the planets scaled by the Holman-Wiegert stability radius for each binary. The green point represents BEBOP-3 b. The red curve is an indicative stability envelope above which orbits are expected to be unstable.

population of lone long-period circumbinary planets, and also to better constrain the eccentricity distribution.

Coleman et al. (2024) investigated the formation history of circumbinary planets in the TOI-1338/BEBOP-1 system, which has similar stellar masses and binary orbital period to BEBOP-3 (see Table A3. The parameters of BEBOP-3b presented here appear consistent with the population of planets formed in their model.

5.3 Transitability prospects

Circumbinary planets, if misaligned with the inner binary, will undergo nodal precession of their orbit. This means that most ($\approx 95\%$) of circumbinary planets orbiting eclipsing binaries are expected to eventually come into a transitable configuration (Martin & Triaud 2015). Transitability means that the planet crosses in front of the path of the binary orbit and might therefore transit in front of one or both of the stars, however in a given conjunction the planet still might happen to not transit. More thorough discussions can be found in Martin & Triaud (2015) and Martin (2017).

From our radial velocity solution for BEBOP-3b, we cannot assess the mutual inclination between the orbits of the planet and binary, or the position of the planet in its nodal precession cycle. We therefore consider times of "possible transitability", when the planet is near inferior conjunction. If the planet is the correct orientation to be able to transit, it would have to do so during these times.

We take 1000 posterior samples for the binary and planet parameters and calculate the times of possible transitability for each sample. We then plot a histogram of these times, giving a posterior probability distribution of times of possible transitability for each conjunction of the planet. These are compared with the times that the system has been observed with *TESS* (TIC 289949453) (Ricker et al. 2015). Based on this, even if the planet did transit at any of these conjunctions, it is highly unlikely to be present in any *TESS* data. We do note that the orbital configuration of the planet, as shown in Figure 4 is optimal for a planetary transit as the transit would occur very near pericentre where the distance between planet and star is smallest.

5.4 The BEBOP catalogue of circumbinary planets with radial velocity measurements

BEBOP-3b is now the fourth published circumbinary planet detected using radial velocities. We introduce here the BEBOP catalogue of circumbinary planets with radial velocity measurements and the rationale for the numbering. The catalogue is shown in table A3. This catalogue is intended to collect all of the circumbinary planetary systems with parameters measured using radial velocities in one place. The catalogue does include circumbinary planets that were detected first in transit and might include planets detected by other teams using radial velocities. For each system we give a BEBOP catalogue entry number without presuming to replace the names.

Kepler-16b and TIC 172900988b were first detected in transit (Doyle et al. 2011; Kostov et al. 2021) and subsequently detected in radial velocities (Triaud et al. 2022; Sairam et al. 2024). Based on the timing of their detections relative to BEBOP-1c (Standing et al. 2023) we number them 0 and 2 in the BEBOP catalogue leaving the new planet presented here as number 3. Note that TOI-1338b which was detected in transit (Kostov et al. 2020) has not yet been detected in radial velocities[8] so the inner planet is only given an upper mass-limit in the BEBOP catalogue.

6 CONCLUSION

In this work we present the radial velocity detection of a circumbinary planet BEBOP-3b. This planet holds a distinct position relative to the known population of circumbinary planets orbiting main-sequence binaries. BEBOP-3b orbits with a long period relative to the binary and is on a moderately eccentric orbit. A dynamical analysis reveals that there is ample space for another undetected planet near the stability limit, so BEBOP-3 may not be so outlying relative to the known population. There is an additional longer-period candidate signal with insufficient evidence to claim as a detection. We extracted stellar activity indices, and none show variability on the radial-velocity modulation we observed. We consequently interpret this modulation as being produced by Doppler reflex motion of a circumbinary planet. The absolute dynamical mass of the stars are calculated using high resolution cross-correlation spectroscopy. The planet's minimum mass as derived from the radial velocities is likely close to its true mass, assuming coplanarity. Should the inclination of its orbit become known, BEBOP-3b would also have an absolute mass.

ACKNOWLEDGEMENTS

These scientific results would not have been possible without a generous allocation of telescope time by France Programme National de Planétologie, and by the dedicated staff working at the Observatoire de Haute-Provence, particularly during the COVID pandemic. We also would like to thank the help of other observers part of the timeshare agreement between groups using the SOPHIE instruments. This research leading to these results is supported by a grant from the European Research Council (ERC) under the European Union's Horizon 2020 research and innovation programme

[8] There is a photodynamical mass measurement presented in Wang & Liu (2024) but it is unclear to what extent the measurement is influenced by the radial velocities.

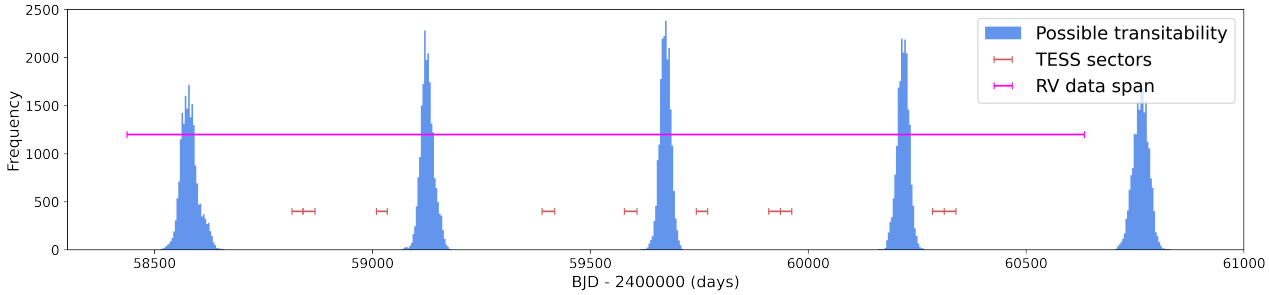


Figure 9. Distributions of potential transitability of BEBOP-3 b from the radial velocity fit. The TESS sectors in which BEBOP-3 was observed are shown, along with the range of time over which the radial velocities were taken.

(grant agreement n° 803193/BEBOP) and by the ERC/UKRI Frontier Research Guarantee programme (EP/Z000327/1/CandY). This work was supported by the "Programme National de Planétologie" (PNP) of CNRS/INSU co-funded by CNES and the "Action Thématique de Physique Stellaire" (ATPS) of CNRS/INSU PN Astro co-funded by CEA and CNES. ACMC acknowledges support from FCT - Fundação para a Ciência e a Tecnologia, I.P., Portugal, through the projects 2024.01252.BD, CFisUC (UIDB/04564/2020 and UIDP/04564/2020, with DOI identifiers 10.54499/UIDB/04564/2020 and 10.54499/UIDP/04564/2020, respectively). AVF acknowledges the support of the IOP through the Bell Burnell Graduate Scholarship Fund. Computations for this research were performed using the University of Birmingham's BlueBEAR HPC service http://www.birmingham.ac.uk/bear. The stability maps were performed at the Oblivion Supercomputer at the University of Évora (https://oblivion.hpc.uevora.pt).

DATA AVAILABILITY

The *TESS* data is available to download via the MAST portal (https://mast.stsci.edu). Spectroscopic data are available on the SOPHIE archive (http://atlas.obs-hp.fr/sophie/), and were obtained under Prog.ID 19A.PNP.SANT. Reduced radial velocities are found in Table A1, a full version of which can be found online.

REFERENCES

Anglada-Escudé G., López-Morales M., Chambers J. E., 2010, The Astrophysical Journal, 709, 168
Baranne A., et al., 1996, Astronomy and Astrophysics Supplement, v.119, p.373-390, 119, 373
Baycroft T. A., Triaud A. H. M. J., Faria J., Correia A. C. M., Standing M. R., 2023a, Monthly Notices of the Royal Astronomical Society, 521, 1871
Baycroft T. A., Triaud A. H. M. J., Kervella P., 2023b, Monthly Notices of the Royal Astronomical Society, 526, 2241
Benedict G. F., Harrison T. E., 2017, The Astronomical Journal, 153, 258
Blanco-Cuaresma S., 2019, Monthly Notices of the Royal Astronomical Society, 486, 2075
Bouchy F., Isambert J., Lovis C., Boisse I., Figueira P., Hébrard G., Pepe F., 2009a, EAS Publications Series, 37, 247
Bouchy F., et al., 2009b, Astronomy and Astrophysics, 505, 853
Brewer B. J., Foreman-Mackey D., 2018, Journal of Statistical Software, 86, 1
Coleman G. A. L., Nelson R. P., Triaud A. H. M. J., 2023, Monthly Notices of the Royal Astronomical Society, 522, 4352
Coleman G. A. L., Nelson R. P., Triaud A. H. M. J., Standing M. R., 2024, Monthly Notices of the Royal Astronomical Society, 527, 414
Collins K. A., et al., 2018, The Astronomical Journal, 156, 234
Correia A. C. M., Udry S., Mayor M., Laskar J., Naef D., Pepe F., Queloz D., Santos N. C., 2005, Astronomy and Astrophysics, 440, 751
Correia A. C. M., Boué G., Laskar J., 2016, Celestial Mechanics and Dynamical Astronomy, 126, 189
Courcol B., et al., 2015, Astronomy and Astrophysics, 581, A38
Davis Y. T., et al., 2024, Monthly Notices of the Royal Astronomical Society, 530, 2565
Doyle L. R., et al., 2011, Science, 333, 1602
Faria J. P., Santos N. C., Figueira P., Brewer B. J., 2018, The Journal of Open Source Software, 3, 487
Freckelton A. V., et al., 2024, Monthly Notices of the Royal Astronomical Society, 531, 4085
Goldberg M., Fabrycky D., Martin D. V., Albrecht S., Deeg H. J., Nowak G., 2023, Monthly Notices of the Royal Astronomical Society, 525, 4628
Gray R. O., Corbally C. J., 1994, The Astronomical Journal, 107, 742
Günther M. N., Daylan T., 2019, Astrophysics Source Code Library, p. ascl:1903.003
Günther M. N., Daylan T., 2021, The Astrophysical Journal Supplement Series, 254, 13
Hara N. C., Boué G., Laskar J., Delisle J.-B., Unger N., 2019, Monthly Notices of the Royal Astronomical Society, Volume 489, Issue 1, p.738-762, 489, 738
Hara N. C., Unger N., Delisle J.-B., Díaz R. F., Ségransan D., 2022, Astronomy and Astrophysics, 663, A14
Hara N. C., de Poyferré T., Delisle J.-B., Hoffmann M., 2024, Annals of Applied Statistics, 18, 749
Heidari N., 2022, PhD Thesis, Universit\'e C\^ote d'Azur; Shahid Beheshti University (Tehran)
Heidari N., et al., 2024, Astronomy and Astrophysics, 681, A55
Holman M. J., Wiegert P. A., 1999, The Astronomical Journal, 117, 621
Jenkins J. M., et al., 2016, Proceedings of the SPIE, 9913, 99133E
Kalman D., 1996, The College Mathematics Journal, 27, 2
Kipping D. M., 2013, Monthly Notices of the Royal Astronomical Society, 434, L51
Kostov V. B., et al., 2016, The Astrophysical Journal, 827, 86
Kostov V. B., et al., 2020, The Astronomical Journal, 159, 253
Kostov V. B., et al., 2021, The Astronomical Journal, 162, 234
Kurucz R. L., 2005, Memorie della Societa Astronomica Italiana Supplementi, 8, 14
Laskar J., 1990, Icarus, 88, 266
Laskar J., 1993, Physica D Nonlinear Phenomena, 67, 257
Laskar J., Robutel P., 2001, Celestial Mechanics and Dynamical Astronomy, 80, 39
Li G., Holman M. J., Tao M., 2016, The Astrophysical Journal, 831, 96
Lightkurve Collaboration et al., 2018, Astrophysics Source Code Library, p. ascl:1812.013
Martin D. V., 2017, Monthly Notices of the Royal Astronomical Society, 465, 3235
Martin D. V., Triaud A. H. M. J., 2014, Astronomy & Astrophysics, 570, A91
Martin D. V., Triaud A. H. M. J., 2015, Monthly Notices of the Royal Astro-

nomical Society, 449, 781
Martin D. V., Mazeh T., Fabrycky D. C., 2015, Monthly Notices of the Royal Astronomical Society, 453, 3554
Martin D. V., et al., 2019, Astronomy and Astrophysics, 624, A68
Maxted P. F. L., 2016, Astronomy and Astrophysics, 591, A111
Maxted P. F. L., Triaud A. H. M. J., Martin D. V., 2023, Universe, 9, 498
Mayor M., et al., 2003, The Messenger, 114, 20
Moriwaki K., Nakagawa Y., 2004, The Astrophysical Journal, 609, 1065
Muñoz D. J., Lai D., 2015, Proceedings of the National Academy of Science, 112, 9264
Orosz J. A., et al., 2012, Science, 337, 1511
Orosz J. A., et al., 2019, The Astronomical Journal, 157, 174
Paardekooper S.-J., Leinhardt Z. M., Thébault P., Baruteau C., 2012, The Astrophysical Journal, 754, L16
Penzlin A. B. T., Kley W., Nelson R. P., 2021, Astronomy and Astrophysics, 645, A68
Pepe F., Mayor M., Galland F., Naef D., Queloz D., Santos N. C., Udry S., Burnet M., 2002, Astronomy and Astrophysics, 388, 632
Pepe F., et al., 2021, Astronomy and Astrophysics, 645, A96
Pepper J., et al., 2007, Publications of the Astronomical Society of the Pacific, 119, 923
Perruchot S., et al., 2008, Proceedings of the SPIE, 7014, 70140J
Pierens A., Nelson R. P., 2008, Astronomy and Astrophysics, 483, 633
Pollacco D. L., et al., 2006, Publications of the Astronomical Society of the Pacific, 118, 1407
Pollacco D., et al., 2008, Monthly Notices of the Royal Astronomical Society, 385, 1576
Ricker G. R., et al., 2015, Journal of Astronomical Telescopes, Instruments, and Systems, 1, 014003
Roy O., Vetterli M., 2007, 15th European Signal Processing Conference, pp 606–610
Sairam L., et al., 2024, Monthly Notices of the Royal Astronomical Society, 527, 2261
Sbordone L., Bonifacio P., Castelli F., Kurucz R. L., 2004, Memorie della Societa Astronomica Italiana Supplementi, 5, 93
Sebastian D., Triaud A. H. M. J., Brogi M., 2024a, Monthly Notices of the Royal Astronomical Society, 527, 10921
Sebastian D., et al., 2024b, Monthly Notices of the Royal Astronomical Society, 530, 2572
Snellen I. A. G., de Kok R. J., de Mooij E. J. W., Albrecht S., 2010, Nature, 465, 1049
Speagle J. S., 2020, Monthly Notices of the Royal Astronomical Society, 493, 3132
Standing M. R., et al., 2022, Monthly Notices of the Royal Astronomical Society, 511, 3571
Standing M. R., et al., 2023, Nature Astronomy, 7, 702
Triaud A. H. M. J., 2011, Ph.D. thesis, `https://ui.adsabs.harvard.edu/abs/2011PhDT.....22T`
Triaud A. H. M. J., et al., 2013, Astronomy and Astrophysics, 549, A18
Triaud A. H. M. J., et al., 2017, Astronomy and Astrophysics, 608, A129
Triaud A. H. M. J., et al., 2022, Monthly Notices of the Royal Astronomical Society, 511, 3561
Trotta R., 2008, Contemporary Physics, 49, 71
Wang M.-T., Liu H.-G., 2024, The Astronomical Journal, 168, 31
Welsh W. F., et al., 2012, Nature, 481, 475
Winn J. N., Fabrycky D. C., 2015, Annual Review of Astronomy and Astrophysics, vol. 53, p.409-447, 53, 409

APPENDIX A: APPENDIX

Table A1. Radial velocity observations taken with SOPHIE between 2018-11-13 and 2024-11-18. Radial velocity outliers are indicated with one of two flags X: those that are vast outliers found in the preliminary run and removed, these are likely wrong pointings of the telescope, and Y: those that are not excluded from the fit but accounted for with the Student's t and have a ratio of $L_T/L_N >= 10$ in the second analysis. Spectra excluded from the HRCCS analysis are given the flag A (wrong pointing), B (low SNR), or C (blended phases).

Flag	Time [BJD - 2 400 000]	$V_{\rm rad}$ [$km\,s^{-1}$]	$\sigma_{V_{\rm rad}}$ [$km\,s^{-1}$]
	58436.63359	43.7735	0.0039
	58437.68801	42.9949	0.0018
	58536.46316	5.4022	0.0024
	58539.46867	21.9657	0.0021
	58541.46505	40.2170	0.0018
	58556.34359	43.7120	0.0021
	58560.44450	16.9170	0.0029
	58564.34291	8.8614	0.0018
	58794.64166	42.7380	0.0026
	58804.69818	30.9787	0.0024
	58828.65843	8.6339	0.0025
Y	58855.59869	11.8996	0.0028
	58894.46828	7.3007	0.0020
	58899.35178	43.9156	0.0026
C	58903.33834	22.9174	0.0020
	58907.45466	6.4592	0.0027
B	58912.32987	43.4670	0.0129
	58917.38073	16.4726	0.0031
	58922.32180	17.3861	0.0028
X,A	59130.68250	-3.6578	0.0361
	59155.65324	13.9372	0.0018
...			

Table A2. Prior distributions used in the `kima` analysis. $\mathcal{N}$ is a Normal/Gaussian distribution, $\mathcal{U}$ is a Uniform distribution, $\mathcal{LU}$ is a LogUniform distribution, $\mathcal{MLU}$ is a ModifiedLogUniform distribution (LogUniform between the two values and Uniform between 0 and the lower value), $\mathcal{K}$ is a Kumaraswamy distribution (a computationally efficient approximation to a β distribution).

Parameter	Units	Prior distribution
$P_{\rm bin}$	[days]	$\mathcal{N}(13.2177, 0.001)$
$K_{\rm bin}$	[km s^{-1}]	$\mathcal{N}(19.366, 0.05)$
$e_{\rm bin}$		$\mathcal{N}(0.063, 0.01)$
$\omega_{\rm bin}$	[rad]	$\mathcal{N}(4.9, 0.1)$
$M_{0,\rm bin}$	[rad]	$\mathcal{U}(0, 2\pi)$
$\dot{\omega}_{\rm bin}$	[arcsec yr^{-1}]	$\mathcal{N}(0, 1000)$
$P_{\rm pl}$	[days]	$\mathcal{LU}(50, 5490)$
$K_{\rm pl}$	[m s^{-1}]	$\mathcal{MLU}(0.1, 1000)$
$e_{\rm pl}$		$\mathcal{K}(0.867, 3.03)$
$\omega_{\rm pl}$	[rad]	$\mathcal{U}(0, 2\pi)$
$M_{0,\rm pl}$	[rad]	$\mathcal{U}(0, 2\pi)$
$V_{\rm sys}$	[km s^{-1}]	$\mathcal{U}(23.968, 24.968)$
Jitter	[m s^{-1}]	$\mathcal{MLU}(0.1, 100)$
ν		$\mathcal{LU}(2, 1000)$

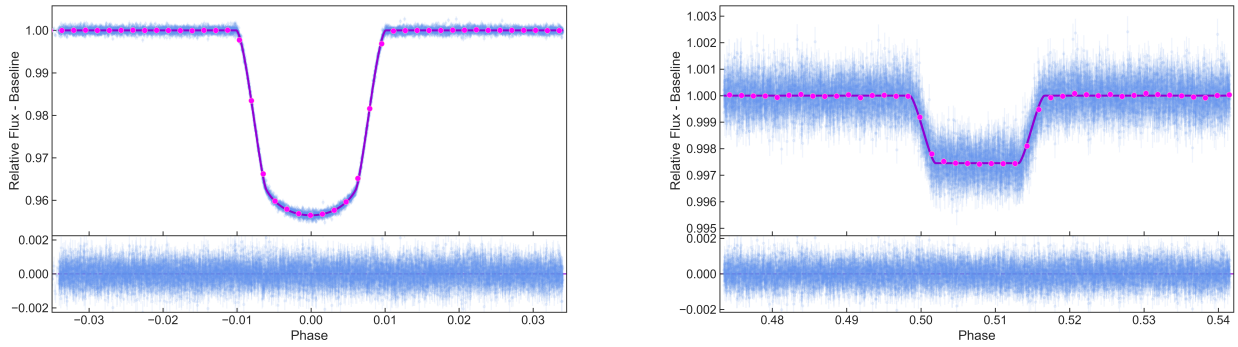


Figure A1. Left panels: Phase folded primary eclipses for the binary and the residuals for the best fit model. Right panels: Phase folded secondary eclipses for the binary and the residuals for the best fit model. In both plots, 50 random posterior samples are displayed.

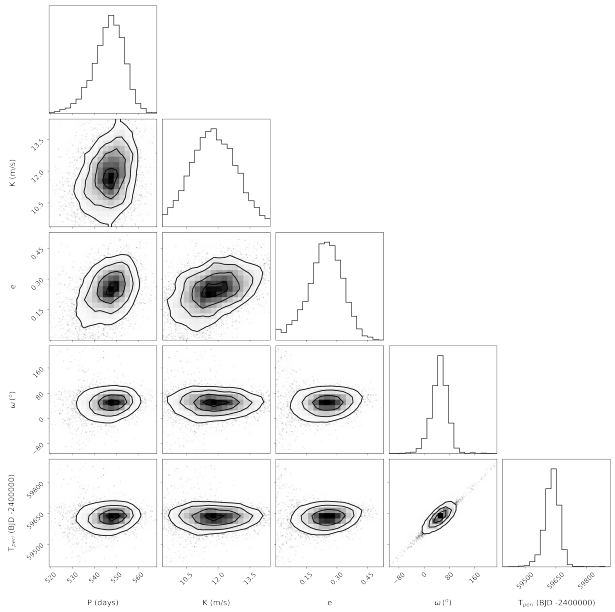


Figure A2. Corner plot showing posterior distributions and correlations for the 1-planet model.

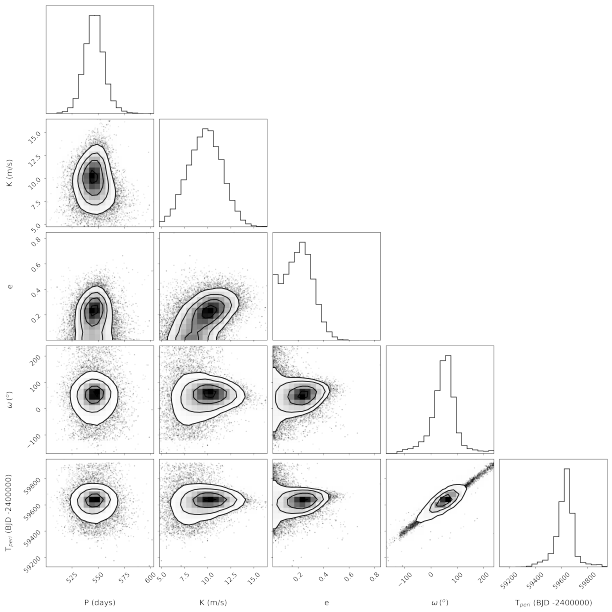


Figure A3. Corner plot showing posterior distributions and correlations for planet 1 in the 2-planet model.

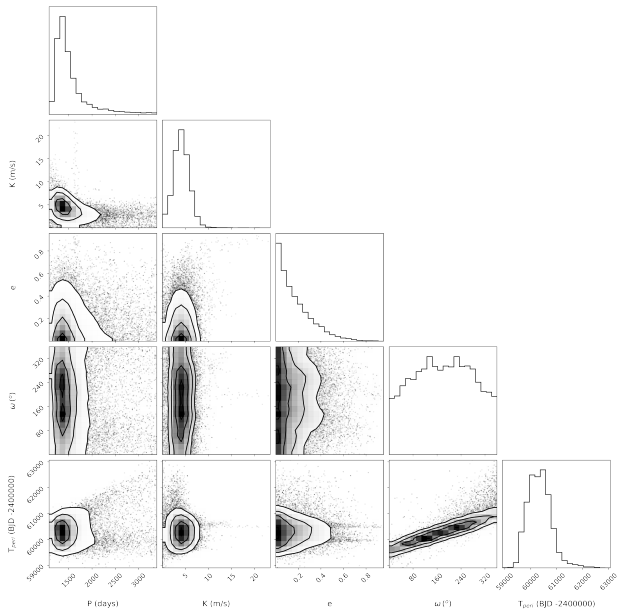


Figure A4. Corner plot showing posterior distributions and correlations for planet 2 in the 2-planet model.

Table A3. The BEBOP catalogue of circumbinary planets with radial velocity measurements. 1σ uncertainties on parameters are provided at the level of the last two significant digits. [x] Transit detection from Doyle et al. (2011) .[y] Transit detection and parameters from Kostov et al. (2020) .[z] Transit detection from Kostov et al. (2021).

Catalogue entry	Other names	$P_{\rm bin}$ [days]	$M_{\rm pri}$ [$M_\odot$]	$M_{\rm sec}$ [$M_\odot$]	$e_{\rm bin}$	$P_{\rm pl}$ [days]	$M_{\rm pl}$ $M_{\rm Jup}$	$e_{\rm pl}$	Source of RVs	TIC ID
BEBOP-0 b	Kepler-16 b[x]	41.077772(51)	0.654(17)	0.1964(31)	0.15994(10)	226.0(1.7)	0.313(39)	≤ 0.21	Triaud et al. (2022)	299096355
BEBOP-1 b	TOI-1338 b[y]	14.6085579(57)	1.098(17)	0.307(3)	0.155522(29)	95.174(35)[y]	$< 0.0685(29)$	0.0880(43)[y]	Standing et al. (2023)	260128333
BEBOP-1 c	TOI-1338 c	14.6085579(57)	1.098(17)	0.307(3)	0.155522(29)	215.5(3.3)	0.205(37)	≤ 0.16	Standing et al. (2023)	260128333
BEBOP-2 b	TIC 172900988 b[z]	19.657878(34)	1.23681(39)	1.20207(33)	0.448234(90)	151.2(1.8)	1.90(25)	≤ 0.11	Sairam et al. (2024)	172900988
BEBOP-3 b		13.2176657(27)	1.083(26)	0.3615(39)	0.063255(54)	$547.0^{(+6.2)}_{(-7.6)}$	$0.558^{(+51)}_{(-48)}$	$0.247^{(+77)}_{(-89)}$	This work	289949453

4.3 Detections and candidates from BEBOP

Other individual results from the BEBOP survey are now presented, divided into four categories:

- Clear detections with a Bayes Factor > 150.
- Tentative detections which while also having a Bayes Factor > 150, the orbit of the planet has only been covered ≈ 1 time.
- Candidates which have a Bayes Factor < 150.
- Long-period planetary-mass signals which typically have a significant Bayes Factor, but where less than half an orbit has been covered, the planetary nature of these are uncertain but at the moment they are consistent with a planetary-mass object.

The scaled semi-major axis $a_{\rm sc}$ (introduced in Section 1.6.3) is used to compare planets in this section. Two versions are used, the first is as defined before $a_{\rm sc} = a_{\rm pl}/r_{\rm stab}$, with uncertainities being those on the parameters. The second takes eccentricity of the planet into account, the value of $a_{\rm sc}$ is the same as before but the uncertainties quoted (and errorbars shown) also include the varying orbital distance of an eccentric orbit such that $a_{\rm sc,\,max} = a_{\rm pl,\,max}(1 + e_{\rm max})/r_{\rm stab}$ and $a_{\rm sc,\,min} = a_{\rm pl,\,min}(1 - e_{\rm max})/r_{\rm stab}$. The first is an assessment of how close to the stability limit the planet is measured to be, the second is a measure of how close the planet could possibly get to the stability limit during its orbit.

In this section I will refer to "planets", e.g. a 1-planet model. Strictly speaking this refers to Keplerians rather than planets and validation involving activity analysis as in Section 4.2.4 (Section 4.4 in the paper) is required.

4.3.1 BEBOP detections

On top of BEBOP-1c and BEBOP-3b there are five additional BEBOP systems which fall into the class of having a clear detection. These are J0110-44, J0503-25, J1250+26, J1525-36, and J1540-09.

J0110-44

This system (currently with a paper in prep - Santerne, Baycroft et al.) will end up being named BEBOP-5. Due to an unfortunate typo, it is named J0110-40 in the HARPS data archive.

The binary is composed of two stars of mass 1.4 and 0.2 $M_\odot$, in a 28.8 day orbit of eccentricity 0.09. A total of 39 radial velocity data have been collected with HARPS covering a span of 1349 days. The Bayes Factor for the 1-planet vs 0-planet model is $\sim$ 150 000. The phased radial velocity curve, N_p histogram, corner plot of planet parameters, and orbital configuration are all shown in Figure 4.14.

J0110-44b is a detected planet with $M \sin i = 0.573^{+0.076}_{-0.074}\ M_{\rm Jup}$, $P = 247.1^{+2.6}_{-2.4}$ days, and $e \leq 0.18$. Its scaled semi-major axis $a_{\rm sc} = 4.8 \pm 1.7$ if including eccentricity and $a_{\rm sc} = 4.845^{+0.087}_{-0.093}$ if not.

J0503-25

The binary is composed of two stars of mass 1.7 and 0.14 $M_\odot$, in a 15.3 day orbit of eccentricity 0.09. A total of 32 radial velocity data have been collected with HARPS covering a span of 1396 days.

J0503-25 has 2 signals, one that extends beyond the timespan of data and one with a shorter orbital period. The first `kima` analysis shown uses a cubic to fit the outer signal as well as a free planet search. The phased radial velocity curve, N_p histogram, corner plot of planet parameters, and orbital configuration are all shown in Figure 4.15. This gives a Bayes Factor of $\sim$ 1600 for a 1-planet vs 0-planet model.

If instead, the fit does not include the cubic function but only free Keplerians, the favoured model is 2-planets with a Bayes Factor of $\sim$ 400[3] over the 1-planet model. The phased radial velocity curve, FIP periodogram, corner plot of planet parameters, and orbital configuration are all shown in Figure 4.16. From the FIP periodogram, both signals pass the detection threshold of FIP = 0.01 that is recomended in Hara et al. (2022). The inner planet is classed as a detection,

[3]The Bayes factor plot is not shown for this, but there is an interesting effect, where the Bayes Factor for 1-planet vs 0-planet model is only 12, the interpretation is that both planets are needed to fit the data well, and only one alone is not enough. This is likely because the two signals both have a very similar amplitude $\sim$ 30 m/s.

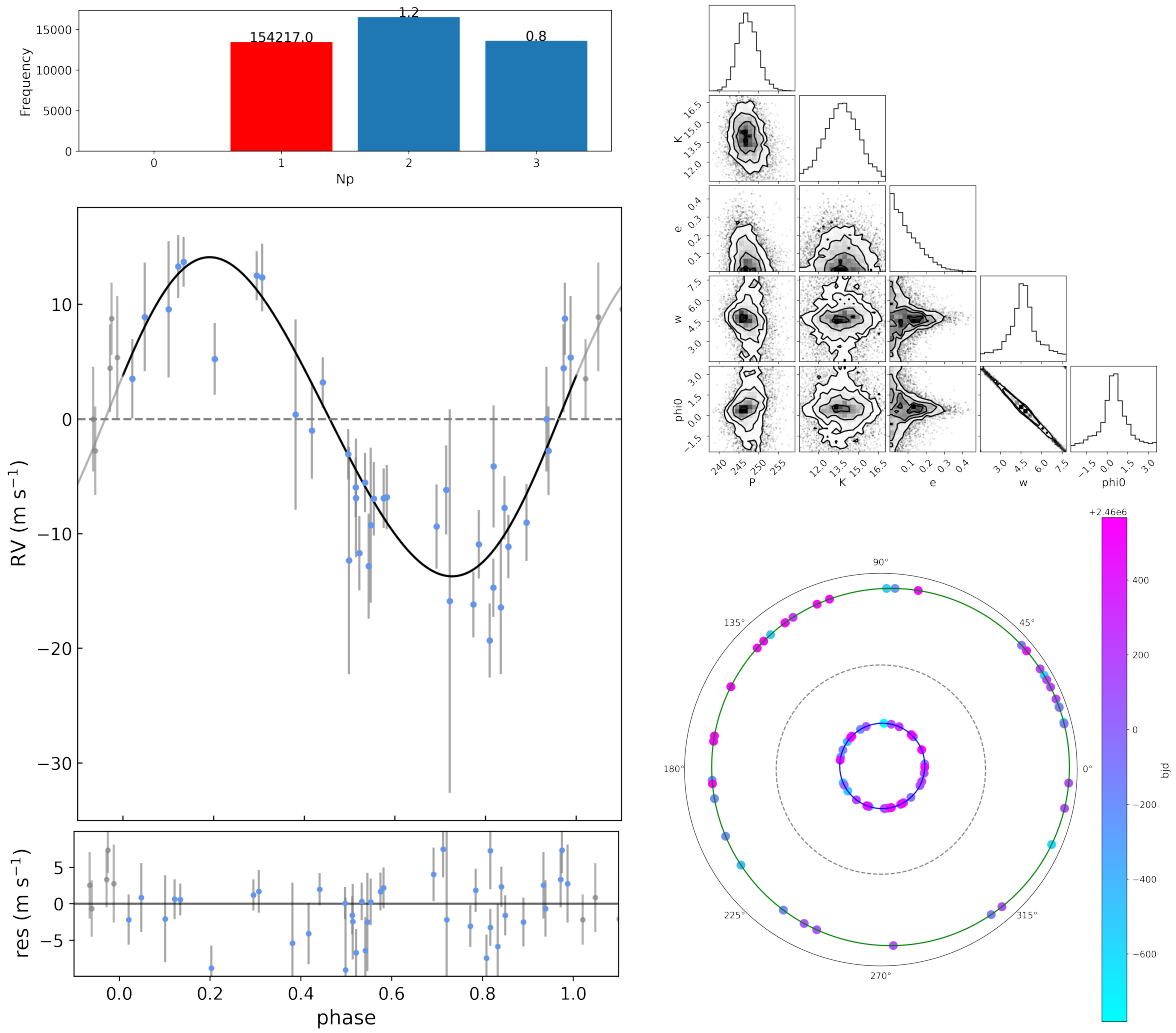


Figure 4.14: J0110-44b. Top-left: N_p histogram showing Bayes Factors comparing models $N_p = n$ to $N_p = n - 1$. Bottom-left: phased radial velocity curve and residuals for planet model. Top-right: corner plot of planet parameters P, K, e, ω, ϕ_0. Bottom-right: Orbital configuration of binary (secondary orbiting primary) and planet, points show the radial velocity measurements coloured by time, the dashed grey line is the stability limit.

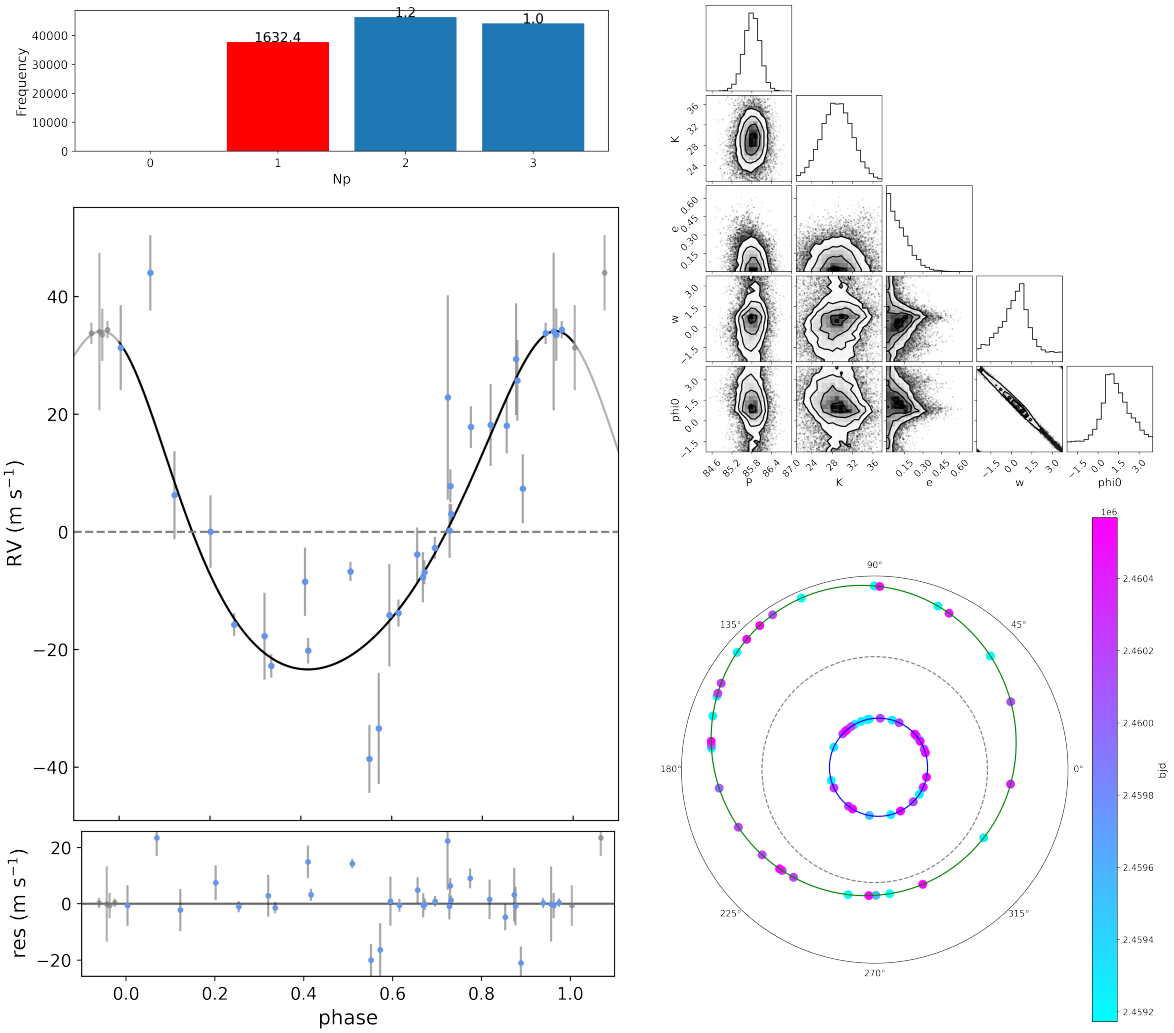


Figure 4.15: J0503-25b. Top-left: N_p histogram showing Bayes Factors comparing models $N_p = n$ to $N_p = n - 1$. Bottom-left: phased radial velocity curve and residuals for planet model. Top-right: corner plot of planet parameters P, K, e, ω, ϕ_0. Bottom-right: Orbital configuration of binary (secondary orbiting primary) and planet, points show the radial velocity measurements coloured by time, the dashed grey line is the stability limit.

and the outer signal as a tentative detection because of its incomplete orbit.

J0503-25b is a detected planet with $M \sin i = 0.94 \pm 0.11\, M_{\rm Jup}$, $P = 85.81 \pm 0.24$ days, and $e \leq 0.2$. Its scaled semi-major axis $a_{\rm sc} = 1.38 \pm 0.31$ if including eccentricity and $a_{\rm sc} = 1.380 \pm 0.027$ if not.

J0503-25c is a tentative detection with $M \sin i = 1.63^{+0.33}_{-0.30}\, M_{\rm Jup}$, $P = 1820^{+550}_{-220}$ days, and $e \leq 0.31$. Its scaled semi-major axis $a_{\rm sc} = 10.6^{+6.2}_{-4.0}$ if including eccentricity and $a_{\rm sc} = 10.6^{+2.2}_{-1.0}$ if not.

J1250+26

This system (currently with a paper in prep- Triaud, Baycroft et al.) will end up being named BEBOP-4. While the mass of the planet, at$\approx 17\, M_{\rm Jup}$, puts it slightly above the typical delimiter between planets and brown dwarfs, it will still be included in the BEBOP catalogue of circumbinary planets.

The binary is composed of two stars of mass 1.584 and $0.473\, M_{\odot}$, in a 72 day orbit of eccentricity 0.27. This is the longest period binary in the BEBOP sample. A total of 84 radial velocity data have been collected with SOPHIE covering a span of 2243 days. The phased radial velocity curve, N_p histogram, corner plot of planet parameters, and orbital configuration are all shown in Figure 4.17. While the orbit of the planetary-mass companion has only been covered a single time with a small amount of overlap, the amplitude of the signal makes it a clear detection with Bayes Factor $\sim 10^{64}$. The pericentre is poorly covered as it happened during the COVID pandemic. Observations being collected this year and next will cover most of the next pericentre passage, albeit with a small gap exactly at (and for $\sim$ 2 months either side of) the pericentre passage due to observability constraints.

J1250+26b is a detected planet(/brown dwarf) with $M \sin i = 21.56 \pm 0.83\, M_{\rm Jup}$, $P = 1823.5 \pm 5.0$ days, and $e = 0.418 \pm 0.016$. Its scaled semi-major axis $a_{\rm sc} = 2.7 \pm 1.3$ if including eccentricity and $a_{\rm sc} = 2.684 \pm 0.049$ if not.

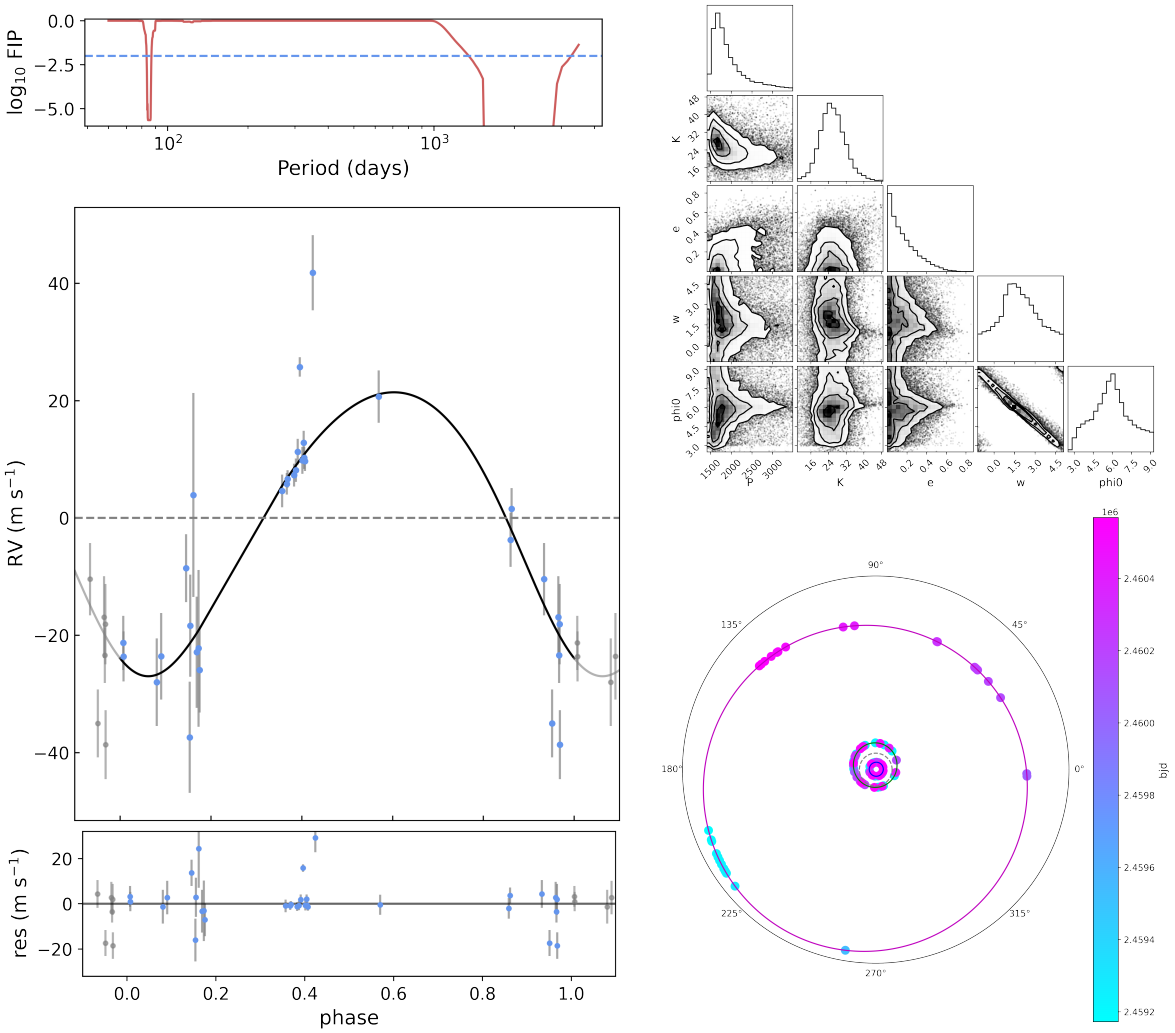


Figure 4.16: J0503-25b/c. Top-left: FIP periodogram. Bottom-left: phased radial velocity curve of the outer planet and residuals for the 2-planet model. Top-right: corner plot of planet parameters P, K, e, ω, ϕ_0 of the outer planet. Bottom-right: Orbital configuration of binary (secondary orbiting primary) and the two planets, points show the radial velocity measurements coloured by time, the dashed grey line is the stability limit.

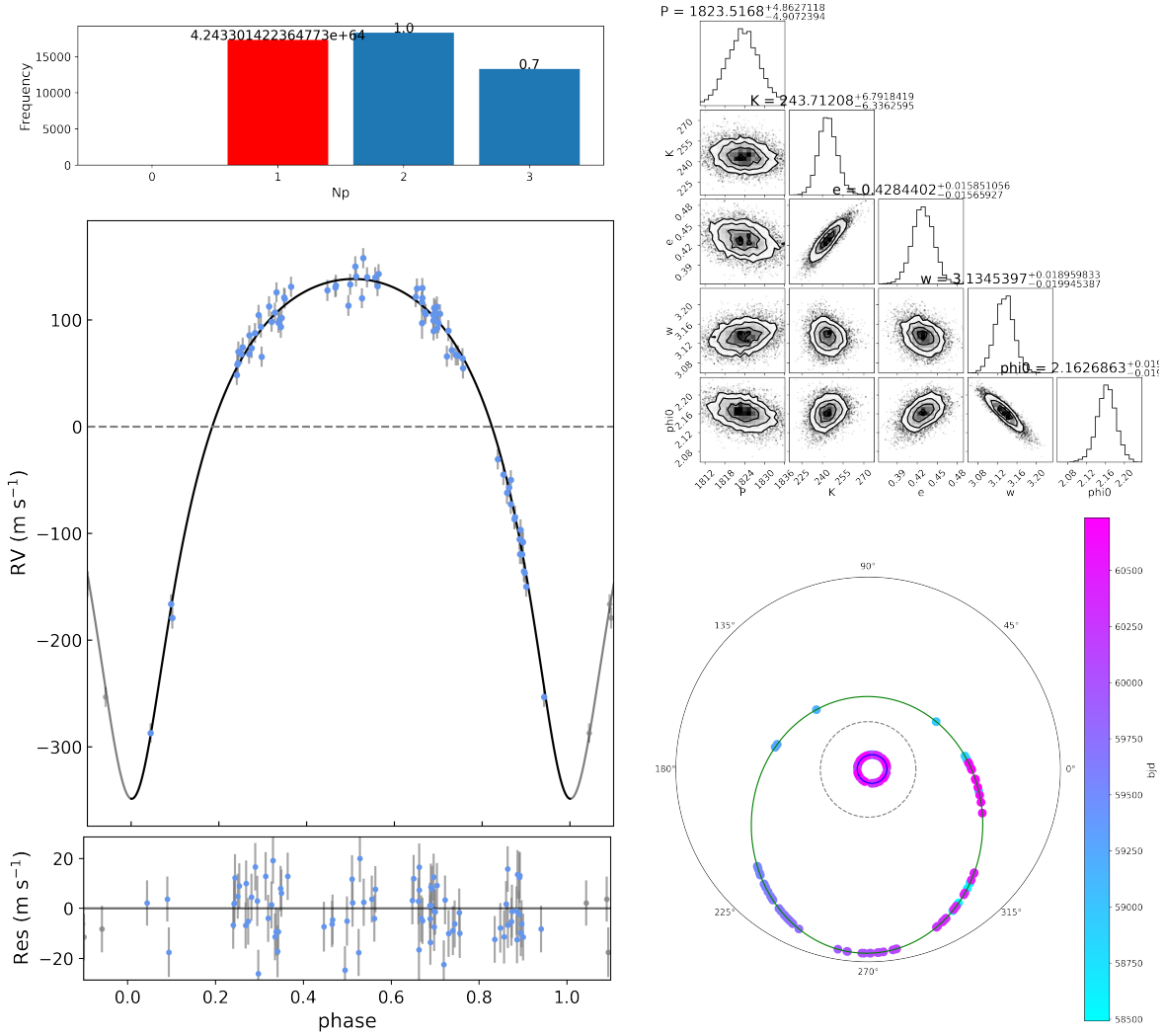


Figure 4.17: J1250+26b. Top-left: N_p histogram showing Bayes Factors comparing models $N_p = n$ to $N_p = n - 1$. Bottom-left: phased radial velocity curve and residuals for planet model. Top-right: corner plot of planet parameters P, K, e, ω, ϕ_0. Bottom-right: Orbital configuration of binary (secondary orbiting primary) and planet, points show the radial velocity measurements coloured by time, the dashed grey line is the stability limit.

J1525-36

The binary is composed of two stars of mass 1.3 and 0.22 $M_\odot$, in a 9 day close-to-circular orbit. A total of 45 radial velocity data have been collected with HARPS covering a span of 2291 days. The phased radial velocity curve, N_p histogram, corner plot of planet parameters, and orbital configuration are all shown in Figure 4.18. The Bayes Factor for the detection is ~ 650. While still consistent with a circular orbit, an eccentric solution is favoured, the pericentre passage is well sampled across multiple orbits so the eccentricity is credible.

J1525-36b is a detected planet with $M \sin i = 2.71^{+0.50}_{-0.46}\, M_{\rm Jup}$, $P = 725^{+11}_{-16}$ days, and $e = 0.47^{+0.11}_{-0.23}$. Its scaled semi-major axis $a_{\rm sc} = 8.9^{+6.0}_{-5.4}$ if including eccentricity and $a_{\rm sc} = 8.90^{+0.53}_{-0.60}$ if not.

J1540-09

The binary is composed of two stars of mass 1.05 and 0.41 $M_\odot$, in a 26.3 day orbit of eccentricity 0.12. A total of 87 radial velocity data have been collected with HARPS covering a span of 2685 days.

The Bayes Factor for a 1-planet model vs a 0-planet model is $\sim$ 1000, however there is uncertainty as to the planet's orbital period. As was discussed in Section 2.1.5, the Bayes Factor can strongly support a 1-planet model, but due to aliases in the sampling, there could be multiple options for the orbital period. In this case the favoured orbital period is $\approx$ 1000 days and is shown in Figure 4.19.

The favoured solution is favoured for two reasons, it is the best fitting solution when restricting to orbits with $e < 0.1$, and the FIP periodogram, shown in Figure 4.20 favours this period. Note that no peak passes the FIP detection threshold of 0.01. The eccentric solution that has a shorter orbital period of $\sim$ 550 days is also shown in Figure 4.20. This is at half the orbital period of the preferred signal which is an indication that the dichotomy here is likely an alias.

The two models are compared in Figure 4.21. The radial velocity curves of 100 random draws from the relevant posterior distributions are shown along with the times at which the data was taken. The 2:1 alias is evident in this plot, and the fact that most data was taken at

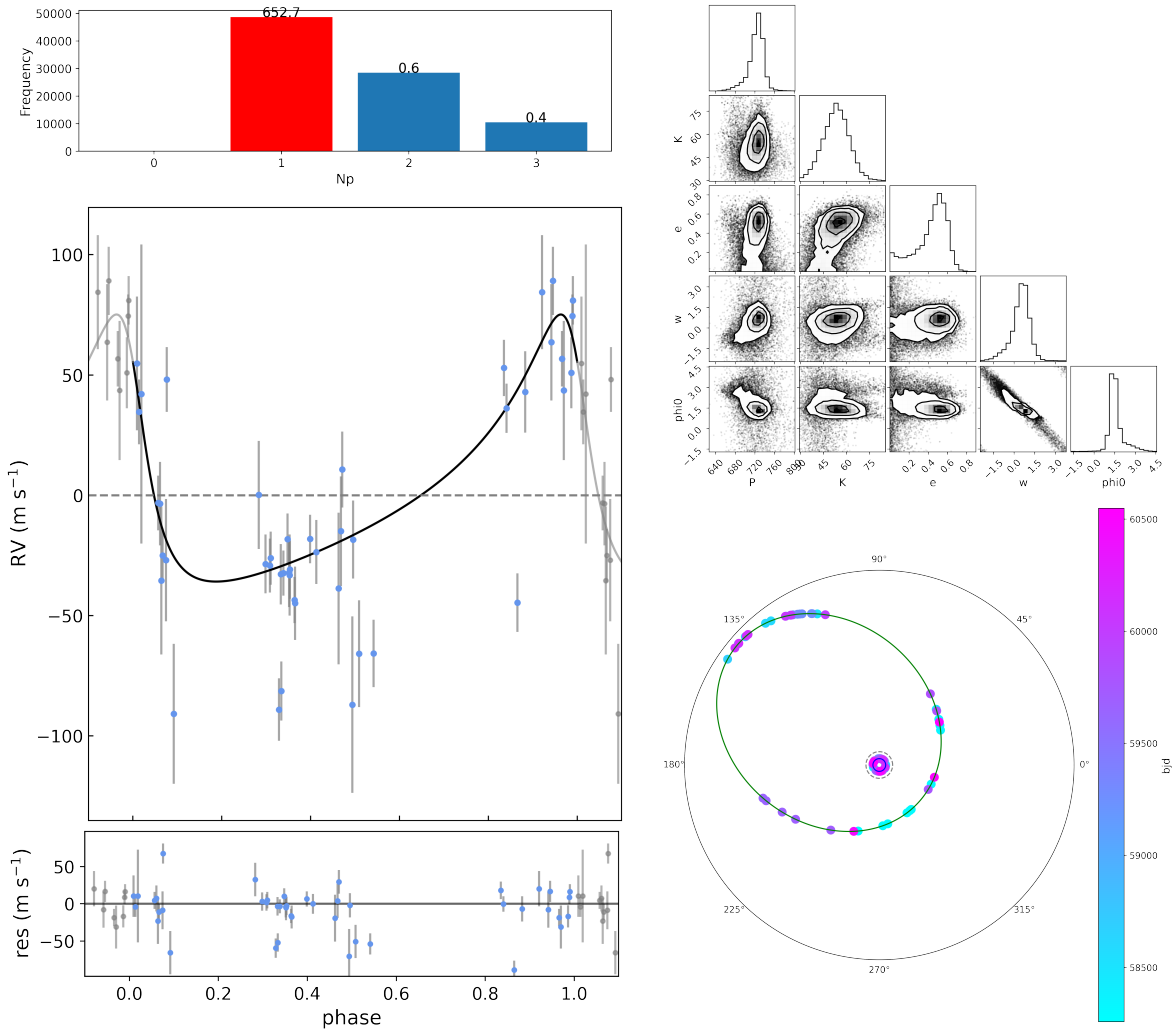


Figure 4.18: J1525-36b. Top-left: N_p histogram showing Bayes Factors comparing models $N_p = n$ to $N_p = n - 1$. Bottom-left: phased radial velocity curve and residuals for planet model. Top-right: corner plot of planet parameters P, K, e, ω, ϕ_0. Bottom-right: Orbital configuration of binary (secondary orbiting primary) and planet, points show the radial velocity measurements coloured by time, the dashed grey line is the stability limit.

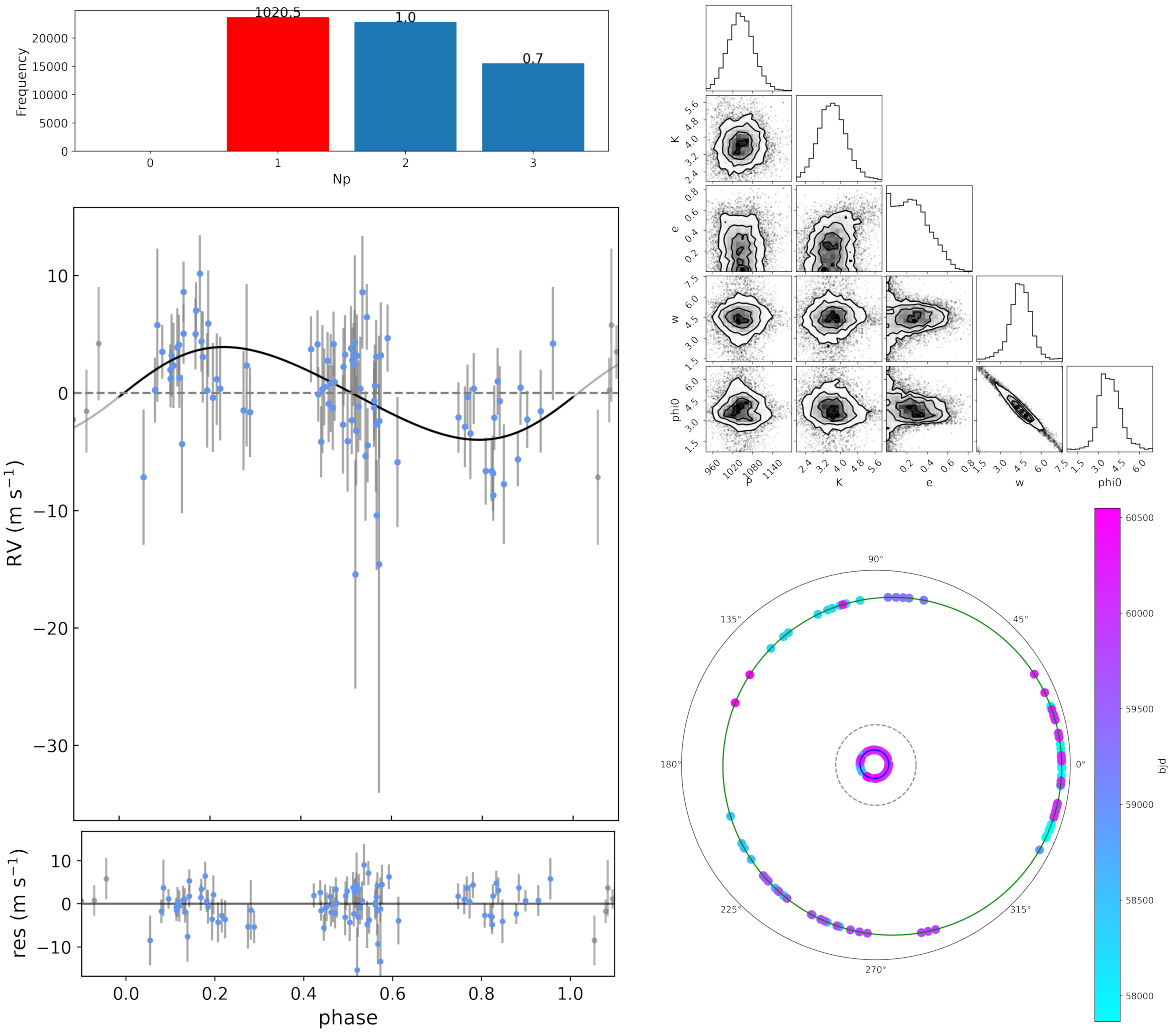


Figure 4.19: J1540-09 longer period circular model. Top-left: N_p histogram showing Bayes Factors comparing models $N_p = n$ to $N_p = n - 1$. Bottom-left: phased radial velocity curve and residuals for planet model. Top-right: corner plot of planet parameters P, K, e, ω, ϕ_0. Bottom-right: Orbital configuration of binary (secondary orbiting primary) and planet, points show the radial velocity measurements coloured by time, the dashed grey line is the stability limit.

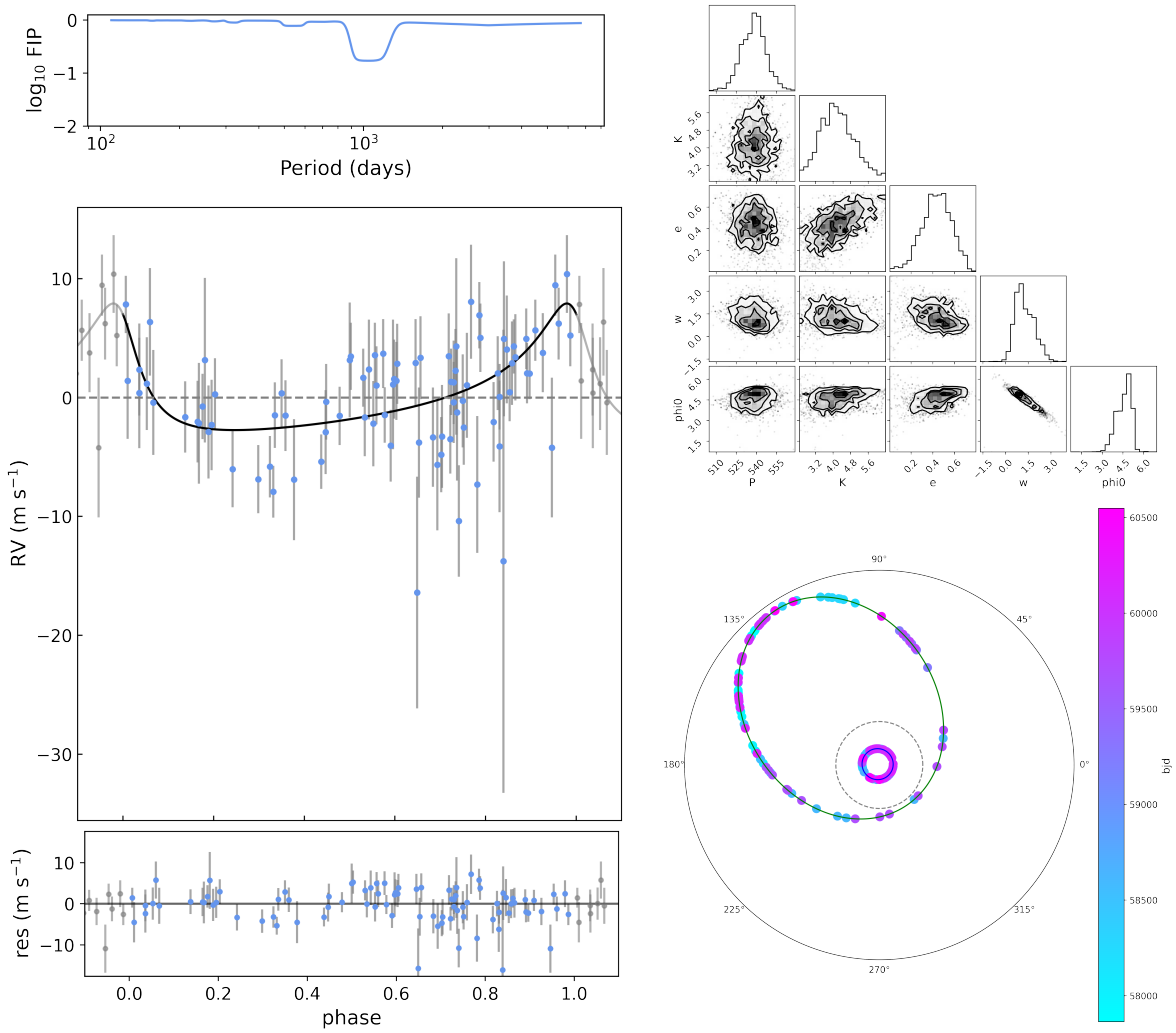


Figure 4.20: J1540-09b shorter period eccentric model. Top-left: False Inclusion Probability periodogram. Bottom-left: phased radial velocity curve and residuals for planet model. Top-right: corner plot of planet parameters P, K, e, ω, ϕ_0. Bottom-right: Orbital configuration of binary (secondary orbiting primary) and planet, points show the radial velocity measurements coloured by time, the dashed grey line is the stability limit.

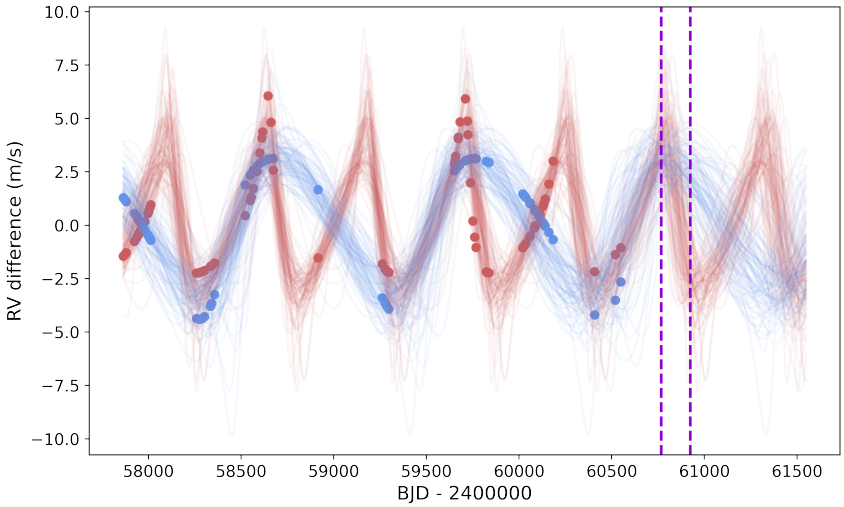


Figure 4.21: Radial velocity curves for 100 random draws from the competing models for J1540-09b. The points where the data has been taken is shown by the points. The vertical dashed lines show the range of time over which more data is going to be taken.

points where the models are close shows why the confusion exists. This system is included in a observing campaign that is ongoing (observability bounded by the dashed vertical purple lines). This data will be taken at a point where the models diverge, if the observations are pushed as late as they can be taken, the power of that data to distinguish the two models will increase. The range of time when observations will be taken is also the point where the shorter period eccentric planet model is passing pericentre, a high cadence of observations in this range will help constrain whether the eccentricity is favoured and therefore if the model is viable.

J1540-09b is a detected planet with preferred parameters $M \sin i = 0.220^{+0.042}_{-0.039}\, M_{\rm Jup}$, $P = 1044 \pm 38$ days, and $e \leq 0.46$. Its scaled semi-major axis $a_{\rm sc} = 4.2^{+2.3}_{-2.1}$ if including eccentricity and $a_{\rm sc} = 4.16 \pm 0.26$ if not.

4.3.2 BEBOP tentative detections

On top of the outer signal in J0503-25 discussed above, four systems fall into the tentative detection category. These are J0310-31, J0418-53, J0708-68, J1305-31. These have not had enough orbital coverage to be classed as a detection.

J0310-31

The binary is composed of two stars of mass 1.19 and 0.39 $M_\odot$, in a 12.6 day orbit with eccentricity 0.31. A total of 108 radial velocity data have been collected with HARPS covering a span of 2625 days. The phased radial velocity curve, N_p histogram, corner plot of planet parameters, and orbital configuration are all shown in Figure 4.22. The Bayes Factor for the detection is $\sim 150\,000$.

A highly eccentric planet model is favoured, $e \approx 0.6$, the orbit has been covered a little over once, but the pericentre passage is the part that has been covered twice and it has a good amount of coverage lending confidence in the eccentric model.

J0310-31b is a tentative detection with $M \sin i = 0.303^{+0.050}_{-0.046}\,M_{\rm Jup}$, $P = 2013^{+45}_{-40}$ days, and $e = 0.640^{+0.078}_{-0.088}$. Its scaled semi-major axis $a_{\rm sc} = 8.8^{+7.2}_{-6.4}$ if including eccentricity and $a_{\rm sc} = 8.78 \pm 0.51$ if not.

J0418-53

The binary is composed of two stars of mass 1.03 and 0.13 $M_\odot$, in a 13.7 day circular orbit. A total of 61 radial velocity data have been collected with HARPS covering a span of 2347 days. The phased radial velocity curve, N_p histogram, corner plot of planet parameters, and orbital configuration are all shown in Figure 4.23. The Bayes Factor for the detection is $\sim 5\,000\,000$. This long-period signal has not yet closed, it is favoured to have a high eccentricity $e \approx 0.4$.

J0418-53b is a tentative detection with $M \sin i = 0.75 \pm 0.12\,M_{\rm Jup}$, $P = 3000^{+620}_{-440}$ days, and $e = 0.42 \pm 0.12$. Its scaled semi-major axis $a_{\rm sc} = 18^{+15}_{-11}$ if including eccentricity and $a_{\rm sc} = 18.2^{+3.2}_{-2.5}$ if not.

J0708-68

The binary is composed of two stars of mass 0.95 and 0.15 $M_\odot$, in a 54.7 day orbit with eccentricity 0.69. A total of 31 radial velocity data have been collected with HARPS covering a span of 1377 days. The phased radial velocity curve, N_p histogram, corner plot of planet parameters, and orbital configuration are all shown in Figure 4.24. The Bayes Factor for the

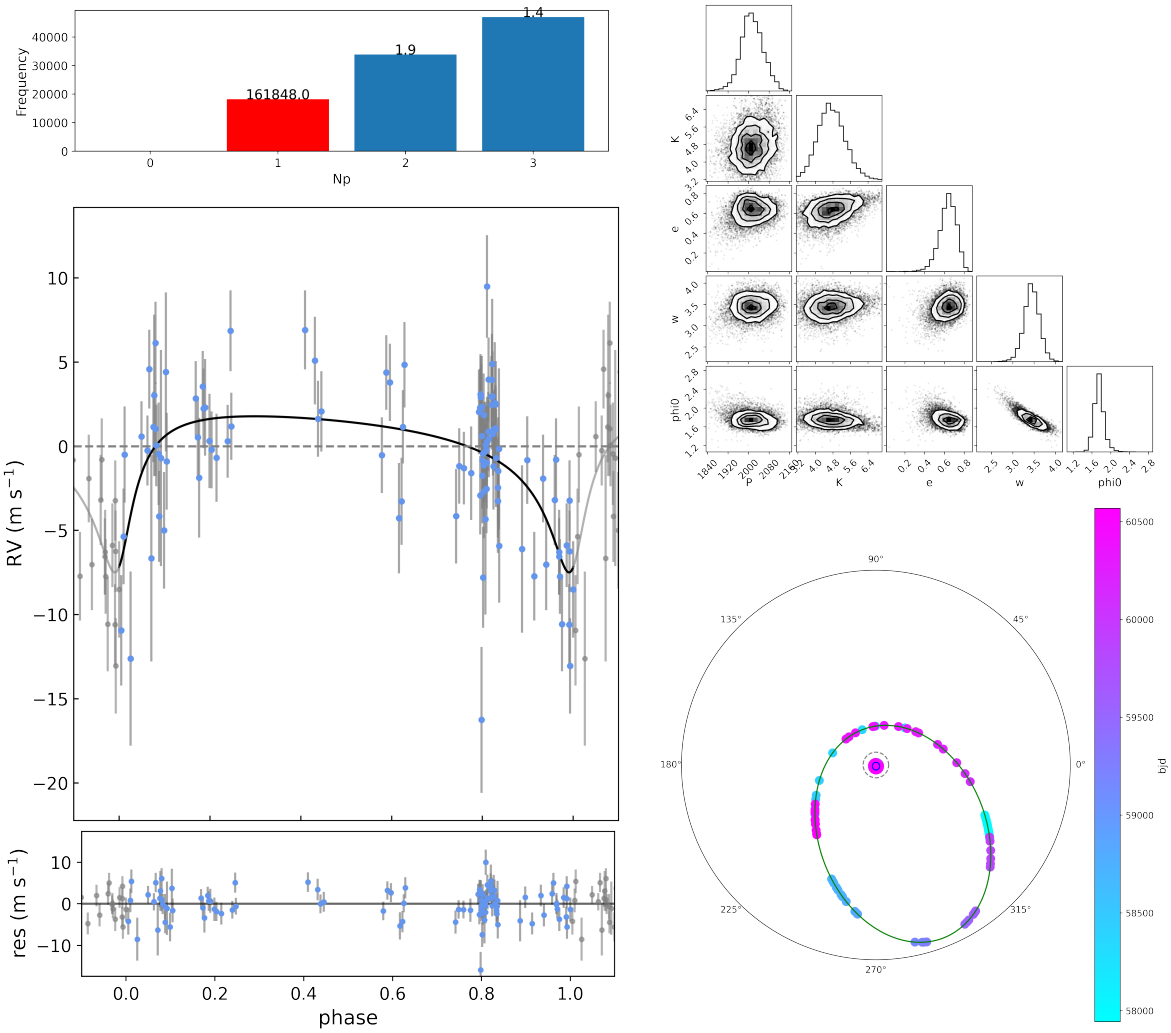


Figure 4.22: J0310-31b. Top-left: N_p histogram showing Bayes Factors comparing models $N_p = n$ to $N_p = n - 1$. Bottom-left: phased radial velocity curve and residuals for planet model. Top-right: corner plot of planet parameters P, K, e, ω, ϕ_0. Bottom-right: Orbital configuration of binary (secondary orbiting primary) and planet, points show the radial velocity measurements coloured by time, the dashed grey line is the stability limit.

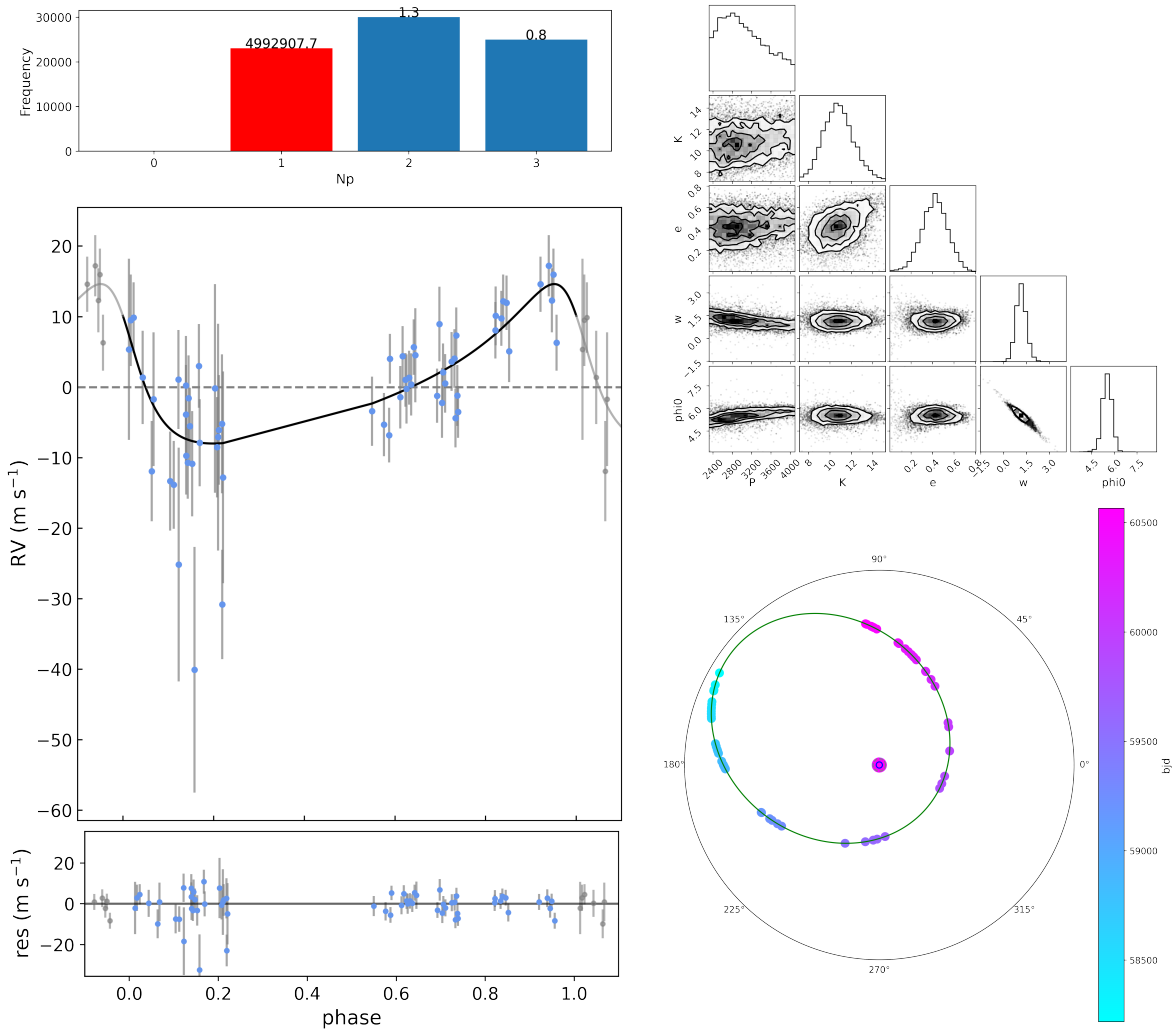


Figure 4.23: J0418-53b. Top-left: N_p histogram showing Bayes Factors comparing models $N_p = n$ to $N_p = n - 1$. Bottom-left: phased radial velocity curve and residuals for planet model. Top-right: corner plot of planet parameters P, K, e, ω, ϕ_0. Bottom-right: Orbital configuration of binary (secondary orbiting primary) and planet, points show the radial velocity measurements coloured by time, the dashed grey line is the stability limit.

detection is $\sim 1\,000\,000$.

This orbit has not yet closed, in fact without the most recent measurement it would have fallen into Section 4.3.4 instead. More data is planned to be acquired to close the orbit and confirm this tentative signal. While the orbit is long-period, it is not so far outside the stability limit (see bottom-right panel of Figure 4.24), especially compared to, say, J0418-53. This proximity to the stability limit is due the binary orbital period being quite long, and the binary eccentricity being high, so the stability limit is equivalent to a ≈ 450 day orbit.

J0708-68b is a tentative detection with $M \sin i = 1.18^{+0.23}_{-0.17}\,M_{\rm Jup}$, $P = 1900^{+530}_{-240}$ days, and $e \leq 0.32$. Its scaled semi-major axis $a_{\rm sc} = 2.6^{+1.6}_{-1.0}$ if including eccentricity and $a_{\rm sc} = 2.58^{+0.58}_{-0.32}$ if not.

J1305-31

The binary is composed of two stars of mass 1.07 and $0.28\,M_\odot$, in a 10.6 day orbit with eccentricity 0.04. A total of 47 radial velocity data have been collected with HARPS covering a span of 2273 days. The phased radial velocity curve, N_p histogram, corner plot of planet parameters, and orbital configuration are all shown in Figure 4.25. The Bayes Factor for the detection is ~ 600.

The orbit here is covered twice, so the system could be instead classified in Section 4.3.1, however without the final three measurements it would only have been covered 1.5 times. These last three measurements have a large uncertainty so for now this classification stands. The planet is consistent with a circular orbit though there is weighting towards higher eccentricities as well.

J1305-31b is a tentative detection with $M \sin i = 2.35^{+0.49}_{-0.42}\,M_{\rm Jup}$, $P = 1134^{+54}_{-58}$ days, and $e \leq 0.5$. Its scaled semi-major axis $a_{\rm sc} = 9.4^{+5.7}_{-5.0}$ if including eccentricity and $a_{\rm sc} = 9.39^{+0.64}_{-0.68}$ if not.

4.3.3 BEBOP candidates

In addition to the outer candidate in the BEBOP-3 system (see Section 4.2), the candidates which do not pass the detection threshold in Bayes Factor are: J0353-16, J1200+42, J1204-47,

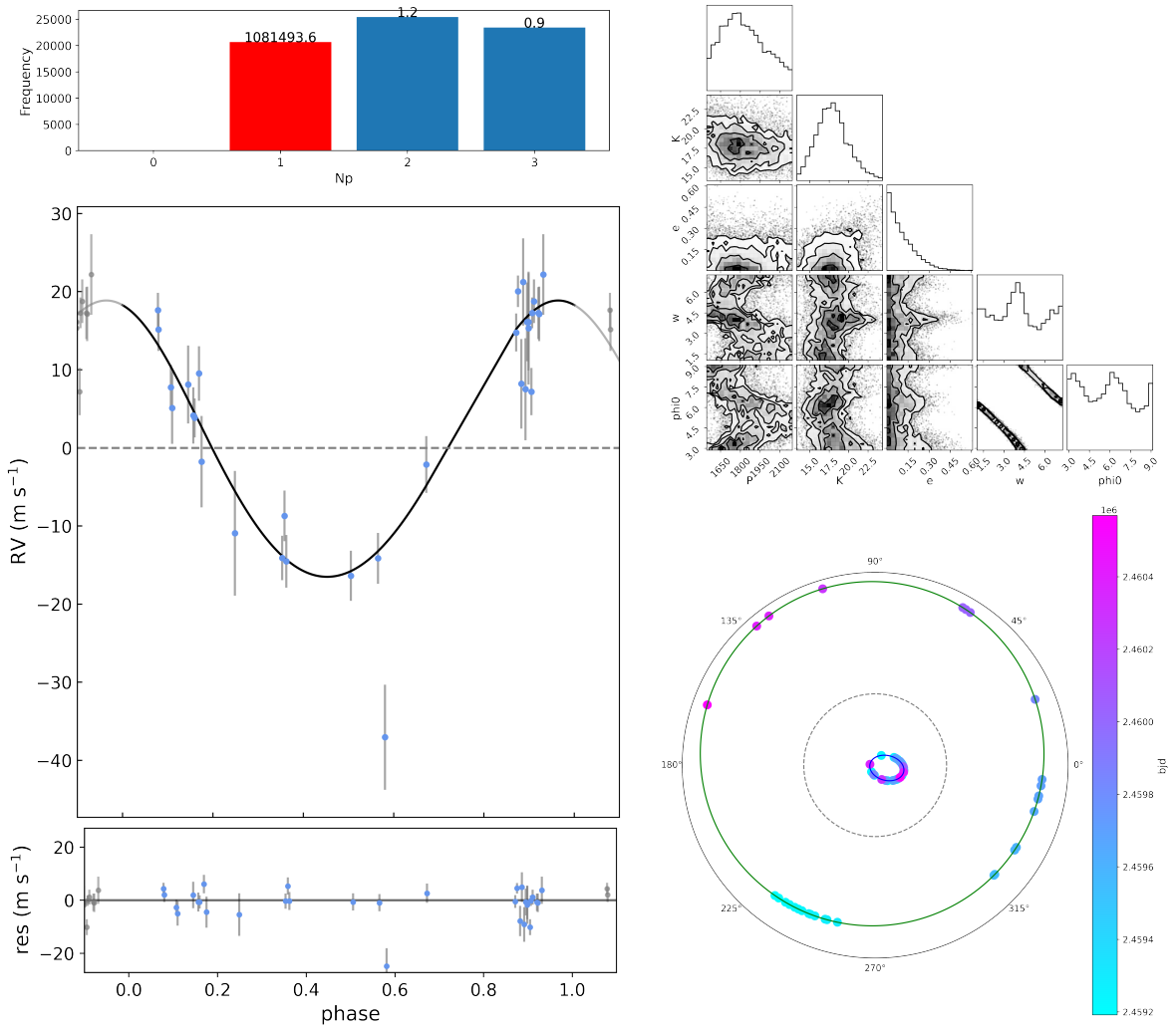


Figure 4.24: J0708-68b. Top-left: N_p histogram showing Bayes Factors comparing models $N_p = n$ to $N_p = n - 1$. Bottom-left: phased radial velocity curve and residuals for planet model. Top-right: corner plot of planet parameters P, K, e, ω, ϕ_0. Bottom-right: Orbital configuration of binary (secondary orbiting primary) and planet, points show the radial velocity measurements coloured by time, the dashed grey line is the stability limit.

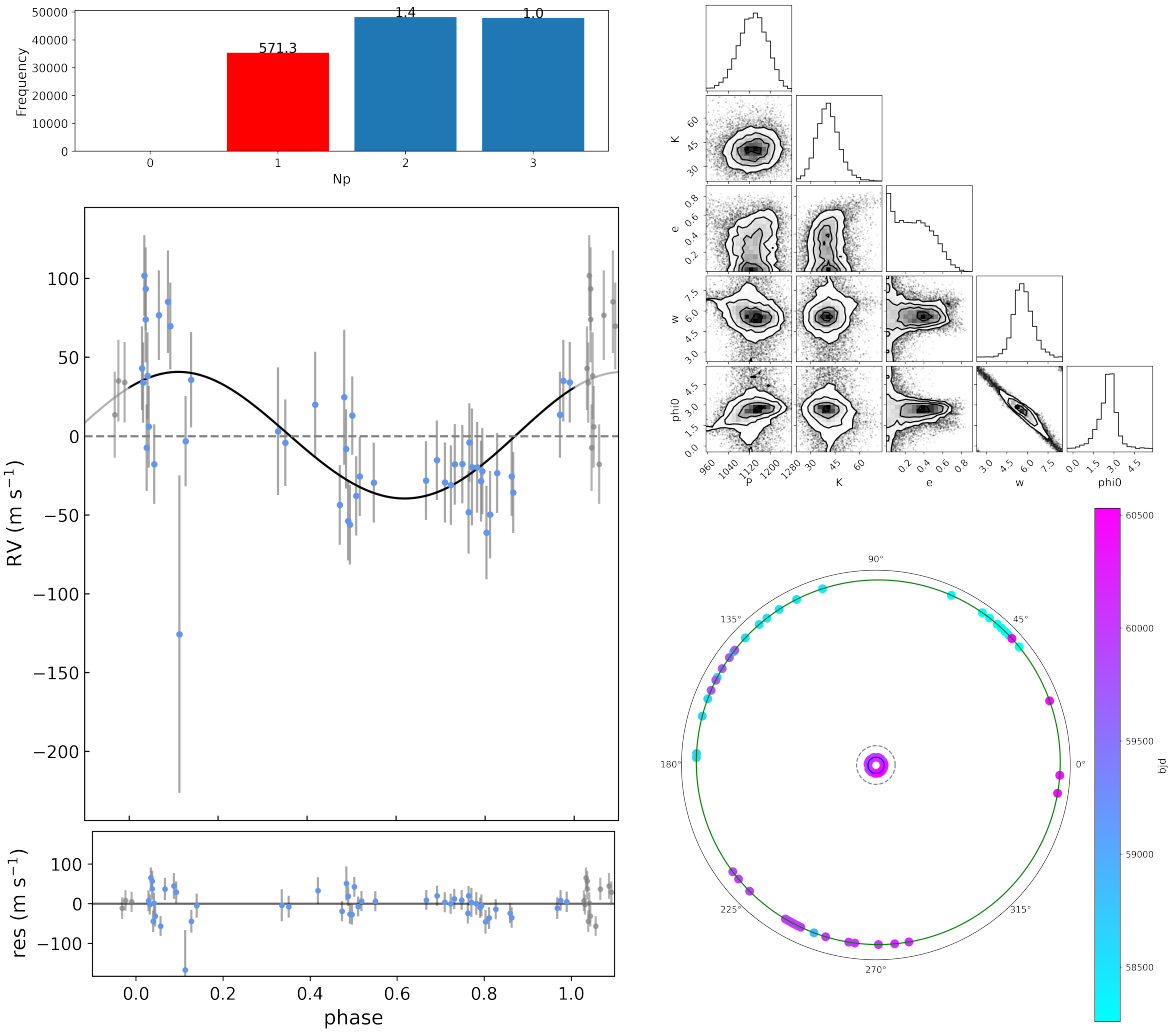


Figure 4.25: J1305-31b. Top-left: N_p histogram showing Bayes Factors comparing models $N_p = n$ to $N_p = n - 1$. Bottom-left: phased radial velocity curve and residuals for planet model. Top-right: corner plot of planet parameters P, K, e, ω, ϕ_0. Bottom-right: Orbital configuration of binary (secondary orbiting primary) and planet, points show the radial velocity measurements coloured by time, the dashed grey line is the stability limit.

J1329+48, J1403-32, J2046+06, and J2233+43.

J0353-16

The binary is composed of two stars of mass 1.09 and 0.21 $M_\odot$, in a 11.8 day orbit with eccentricity 0.006. A total of 97 radial velocity data have been collected with HARPS covering a span of 3960 days. The phased radial velocity curve, N_p histogram, corner plot of planet parameters, and orbital configuration are all shown in Figure 4.26. The Bayes Factor for the candidate is ~ 50. While the most likely signal is around 800 days, there are also other various periods possible (likely aliases of the true period).

J0353-16b is a candidate planet with $M \sin i = 0.331^{+0.070}_{-0.068}\, M_{\rm Jup}$, $P = 800 \pm 17$ days, and $e \leq 0.42$. Its scaled semi-major axis $a_{\rm sc} = 7.7^{+3.8}_{-3.4}$ if including eccentricity and $a_{\rm sc} = 7.71 \pm 0.42$ if not.

J1200+42

The binary is composed of two stars of mass 1.37 and 0.23 $M_\odot$, in a 21.9 day orbit with eccentricity 0.45. A total of 20 radial velocity data have been collected with SOPHIE covering a span of 2193 days.

There are two competing solutions for this, one near the stability limit, and one long period which is not yet closed. The phased radial velocity curves and orbital configuration for both models are shown in Figure 4.27. The Bayes Factor for the candidate is ~ 10. In both cases here, the companion would be an object on the planet-brown dwarf boundary ($\sim 14\, M_{\rm Jup}$). A potentially discriminating factor is the induced apsidal precession rate, or lack thereof. The measured apsidal precession rate for the binary is approximately 0 ± 500 "/yr. The short-period signal should induce 1200 ± 500 "/yr whereas the long-period signal should induce 5 ± 3 "/yr. Thus the long-period signal is favoured. This candidate is similar to J1250+26 with an eccentric circumbinary low-mass brown dwarf, suggesting similar formation pathways for both systems.

J1200+42b is a candidate planet(/brown dwarf) with $M \sin i = 13.8^{+6.5}_{-4.3}\, M_{\rm Jup}$, $P = 4000 \pm 1000$ days, and $e \leq 0.37$. Its scaled semi-major axis $a_{\rm sc} = 8.8^{+5.9}_{-4.5}$ if including eccentricity and

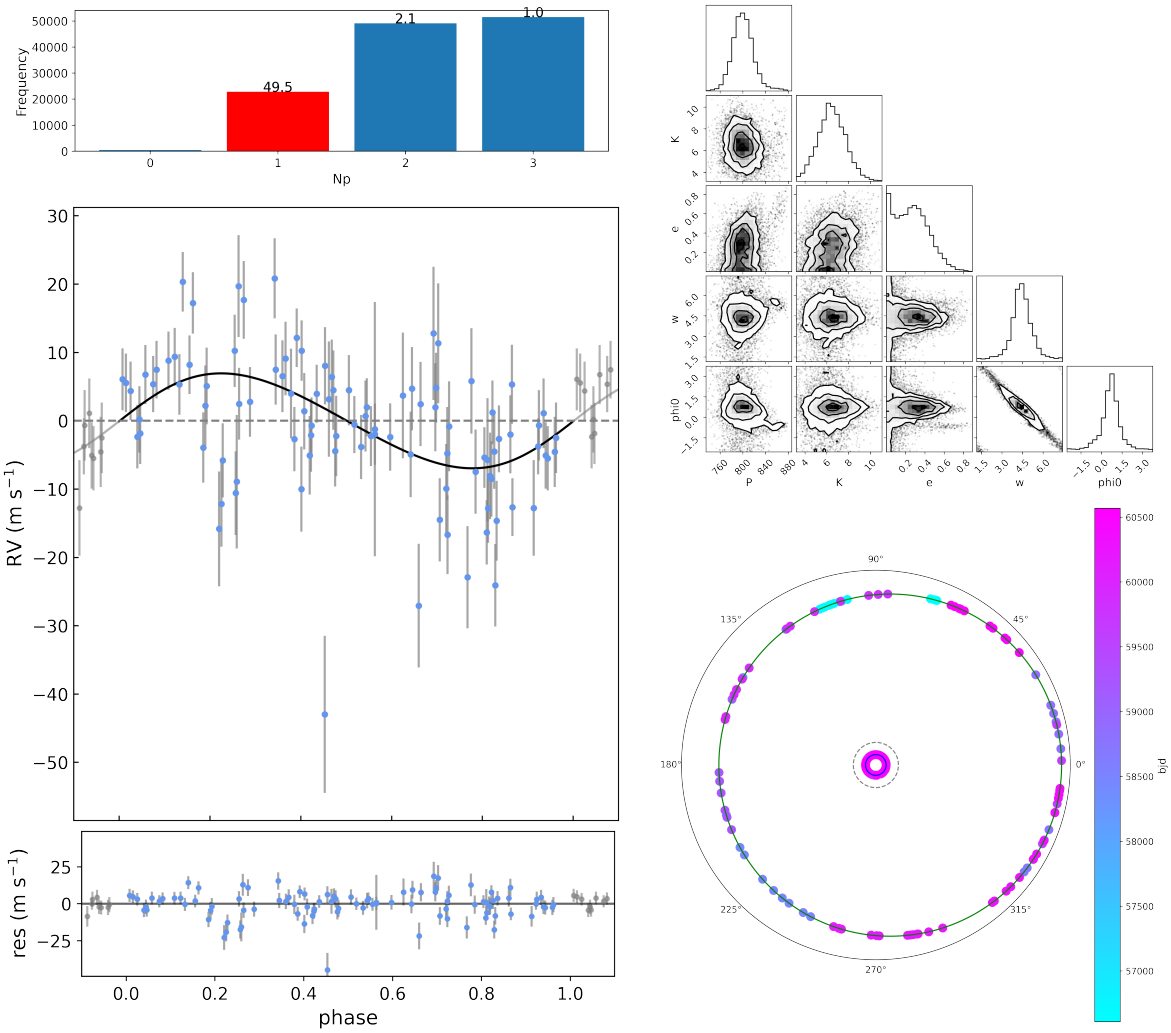


Figure 4.26: J0353-16b. Top-left: N_p histogram showing Bayes Factors comparing models $N_p = n$ to $N_p = n - 1$. Bottom-left: phased radial velocity curve and residuals for planet model. Top-right: corner plot of planet parameters P, K, e, ω, ϕ_0. Bottom-right: Orbital configuration of binary (secondary orbiting primary) and planet, points show the radial velocity measurements coloured by time, the dashed grey line is the stability limit.

$a_{sc} = 8.8 \pm 2.0$ if not.

J1204-47

The binary is composed of two stars of mass 1.22 and 0.33 $M_\odot$, in a 13.7 day orbit with eccentricity 0.18. A total of 79 radial velocity data have been collected with HARPS covering a span of 2242 days. The phased radial velocity curve, N_p histogram, corner plot of planet parameters, and orbital configuration are all shown in Figure 4.28. The Bayes Factor for the candidate is ~ 30. The favoured solution is around a period of 400 days, but there is also the possibility of confusion with a long-period signal similar to those shown in Section 4.3.4. More data is being collected on this system which will likely distinguish the two models.

J1204-47 is a candidate planet with $M \sin i = 0.345^{+0.090}_{-0.083} M_{\rm Jup}$, $P = 396.2^{+6.7}_{-7.2}$ days, and $e \leq 0.3$. Its scaled semi-major axis $a_{sc} = 3.2 \pm 1.2$ if including eccentricity and $a_{sc} = 3.23 \pm 0.19$ if not.

J1329+48

The binary is composed of two stars of mass 0.94 and 0.5 $M_\odot$, in a 18.95 day orbit of eccentricity 0.43. A total of 59 radial velocity data have been collected with SOPHIE covering a span of 2015 days.

J1329+48 has 2 signals, one that is longer than the timespan of data and one with a shorter orbital period. The first `kima` analysis shown uses a quadratic to fit the outer signal and a free planet search on top of this. The phased radial velocity curve, N_p histogram, corner plot of planet parameters, and orbital configuration are all shown in Figure 4.29. This gives a Bayes Factor of ~ 85 for a 1-planet vs 0-planet model.

If instead, the fit does not include the quadratic function but only free Keplerians, the favoured model is 2-planets with a Bayes Factor of ~ 600. The outer signal is included in Section 4.3.4 and would correspond to a $\sim 10\, M_{\rm Jup}$ body. Note that the results here are enforcing models that have $e < 0.1$, allowing to chose more eccentric results gives two signals at ≈ 2000 days rather than one at ≈ 1000 and one at ≈ 4000. This is attributed to the proximity of the orbital periods

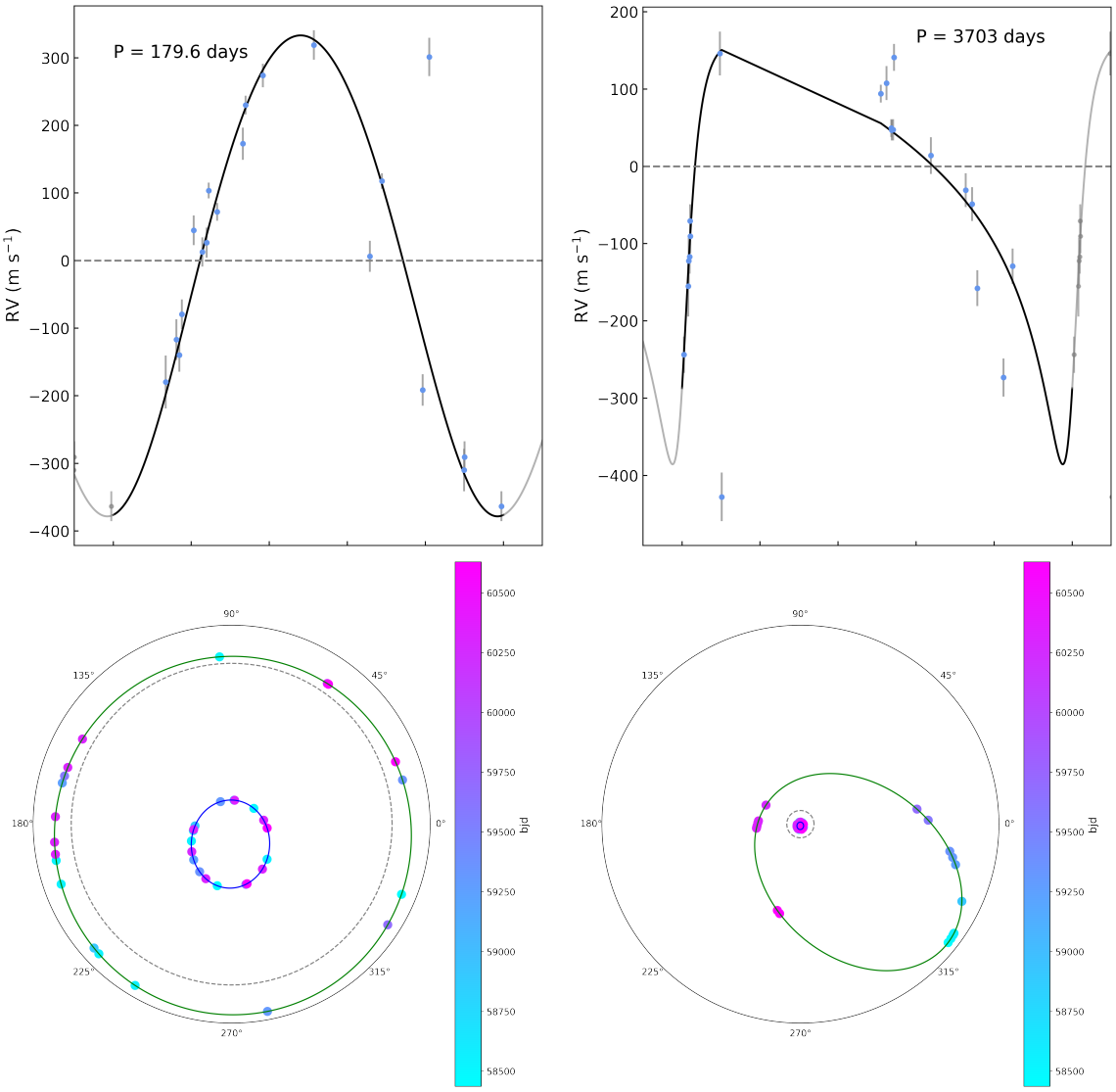


Figure 4.27: J1200+42b. Left: circular short-period solution, top is phased radial velocity curve, and bottom is the orbital configuration of binary (secondary orbiting primary) and planet, points show the radial velocity measurements coloured by time, the dashed grey line is the stability limit. Right: same as left but for long-period eccentric model, this is the favoured model.

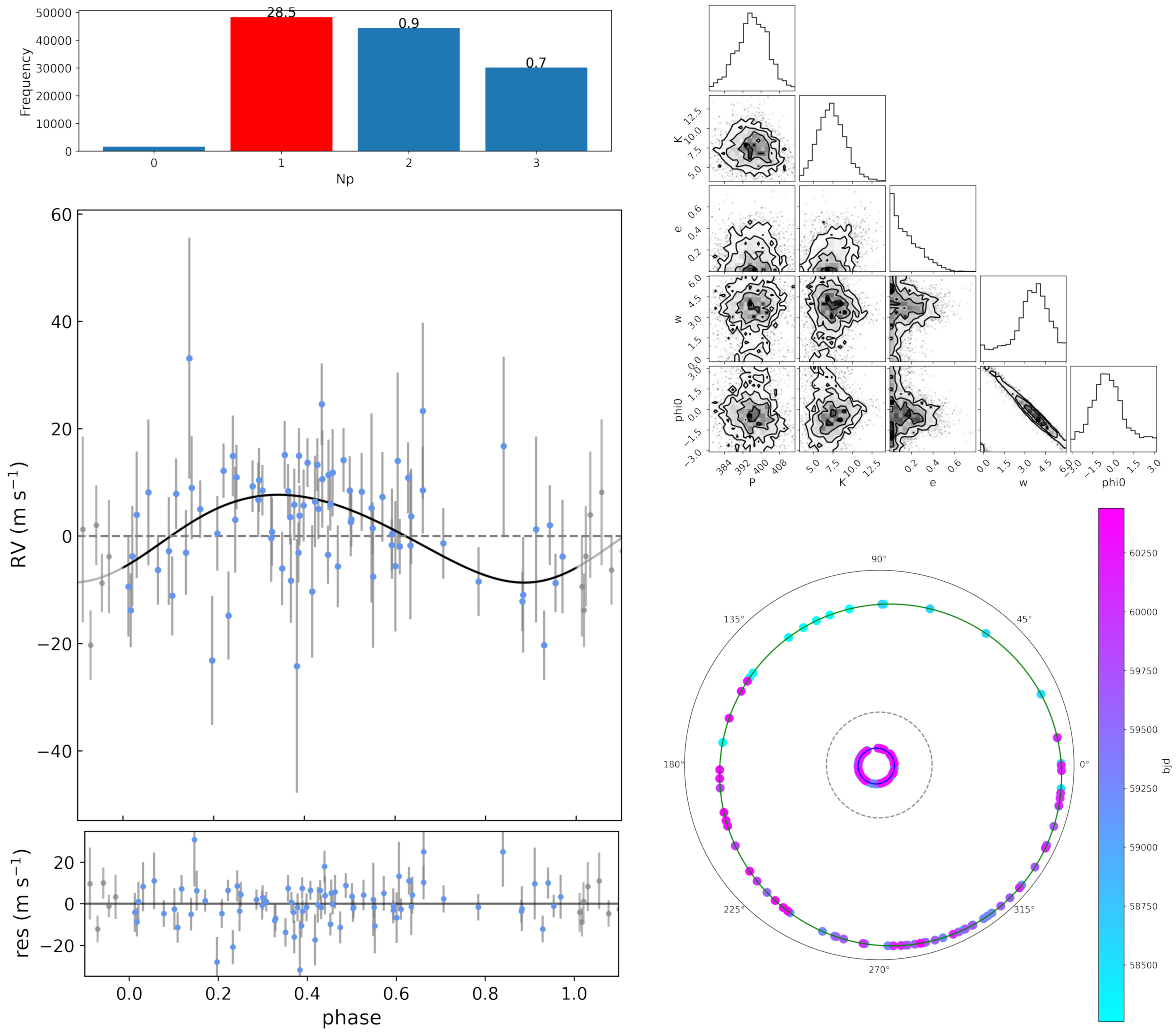


Figure 4.28: J1204-47b. Top-left: N_p histogram showing Bayes Factors comparing models $N_p = n$ to $N_p = n - 1$. Bottom-left: phased radial velocity curve and residuals for planet model. Top-right: corner plot of planet parameters P, K, e, ω, ϕ_0. Bottom-right: Orbital configuration of binary (secondary orbiting primary) and planet, points show the radial velocity measurements coloured by time, the dashed grey line is the stability limit.

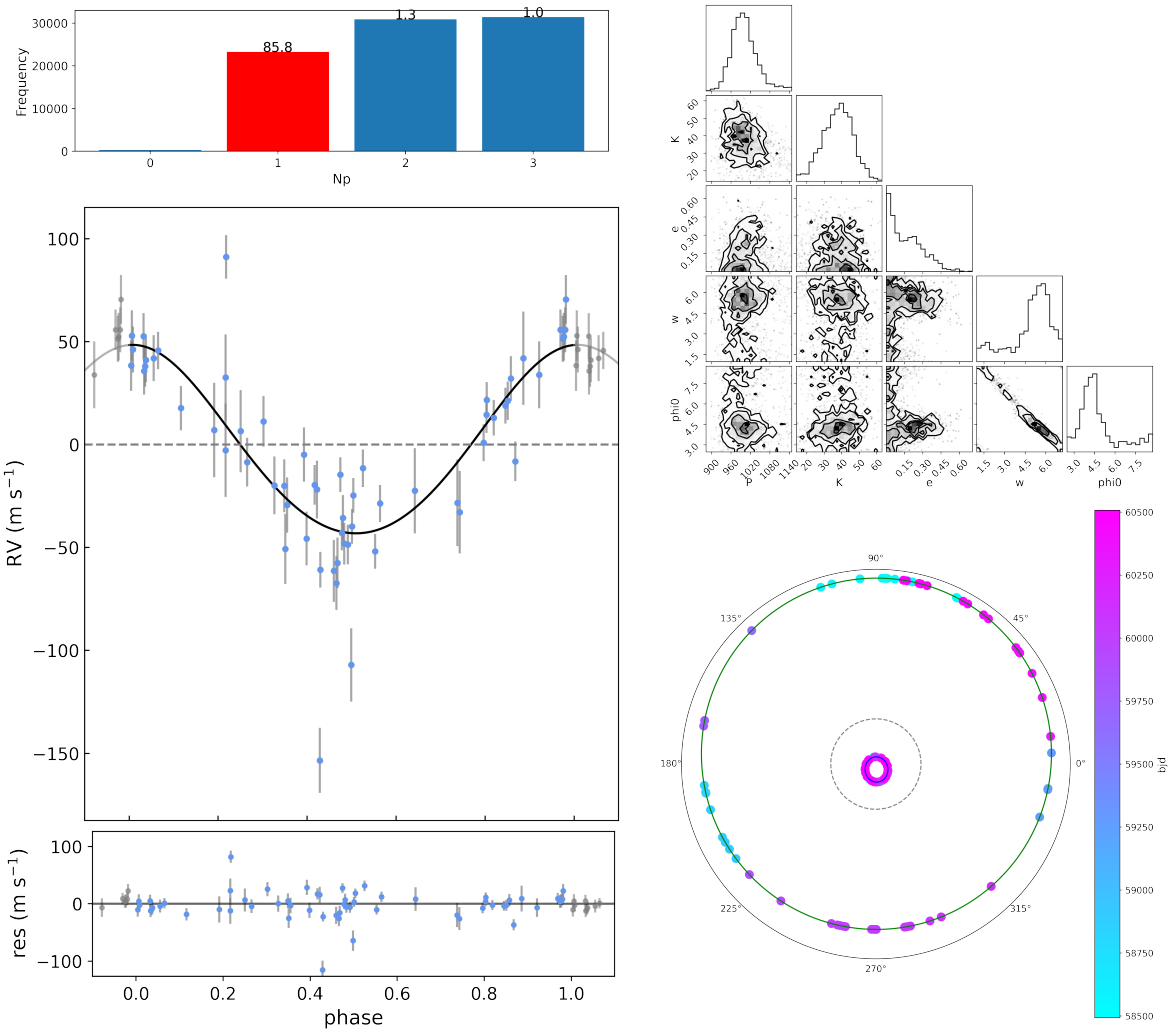


Figure 4.29: J1329+48b. Top-left: N_p histogram showing Bayes Factors comparing models $N_p = n$ to $N_p = n - 1$. Bottom-left: phased radial velocity curve and residuals for planet model. Top-right: corner plot of planet parameters P, K, e, ω, ϕ_0. Bottom-right: Orbital configuration of binary (secondary orbiting primary) and planet, points show the radial velocity measurements coloured by time, the dashed grey line is the stability limit.

to an integer ratio and the fact the outer signal has not been fully covered.

J1329+48b is a candidate planet with $M \sin i = 2.12 \pm 0.49\, M_{\rm Jup}$, $P = 920^{+21}_{-30}$ days, and $e \leq 0.4$. Its scaled semi-major axis $a_{\rm sc} = 3.7^{+1.8}_{-1.6}$ if including eccentricity and $a_{\rm sc} = 3.74^{+0.19}_{-0.22}$ if not.

J1403-32

The binary is composed of two stars of mass 0.98 and $0.26\, M_{\odot}$, in a 11.9 day orbit with eccentricity 0.11. A total of 63 radial velocity data have been collected with HARPS covering a span of 2272 days. The phased radial velocity curve, N_p histogram, corner plot of planet parameters, and orbital configuration are all shown in Figure 4.30. The Bayes Factor for the candidate is ~ 60. The orbital period posterior distribution straddles the 2272 mark, the best fitting circular orbit being one where the whole orbit has been covered once (this is the one shown in Figure 4.30).

J1403-32b is a candidate planet with $M \sin i = 0.82^{+0.37}_{0.22}\, M_{\rm Jup}$, $P = 2200^{+1100}_{-460}$ days, and $e \leq 0.34$. Its scaled semi-major axis $a_{\rm sc} = 12.2^{+10.0}_{-5.6}$ if including eccentricity and $a_{\rm sc} = 12.2^{+4.4}_{-2.2}$ if not.

J2046+06

The binary is composed of two stars of mass 1.22 and $0.19\, M_{\odot}$, in a 10.1 day orbit with eccentricity 0.34. A total of 61 radial velocity data have been collected with HARPS and 29 with SOPHIE covering a span of 2319 days. The phased radial velocity curve, N_p histogram, corner plot of planet parameters, and orbital configuration are all shown in Figure 4.31. The Bayes Factor for the candidate is ~ 60.

J2046+06b is a candidate planet with $M \sin i = 0.350^{+0.080}_{-0.075}\, M_{\rm Jup}$, $P = 608 \pm 13$ days, and $e \leq 0.28$. Its scaled semi-major axis $a_{\rm sc} = 4.6 \pm 1.6$ if including eccentricity and $a_{\rm sc} = 4.58 \pm 0.28$ if not.

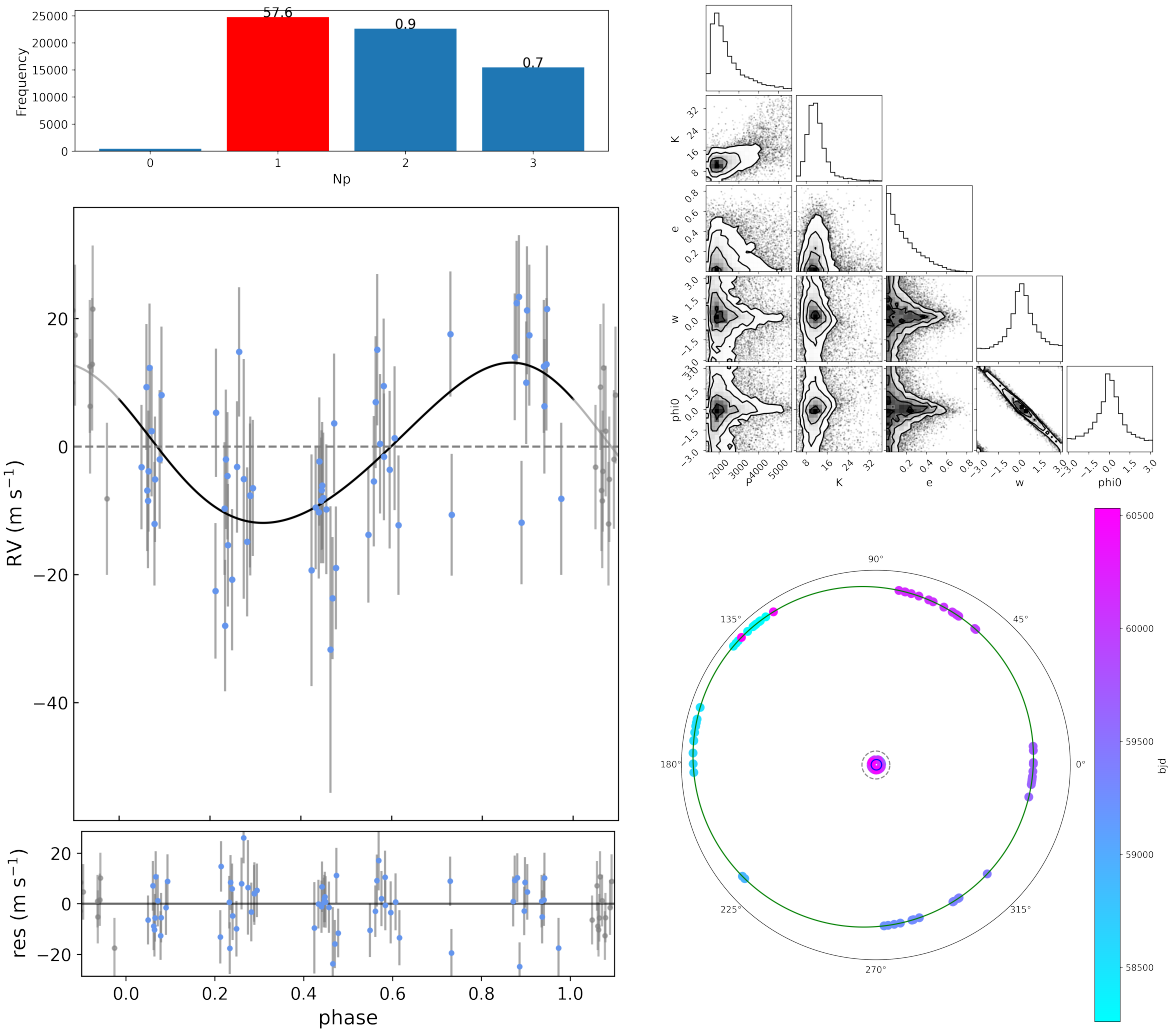


Figure 4.30: J1403-32b. Top-left: N_p histogram showing Bayes Factors comparing models $N_p = n$ to $N_p = n - 1$. Bottom-left: phased radial velocity curve and residuals for planet model. Top-right: corner plot of planet parameters P, K, e, ω, ϕ_0. Bottom-right: Orbital configuration of binary (secondary orbiting primary) and planet, points show the radial velocity measurements coloured by time, the dashed grey line is the stability limit.

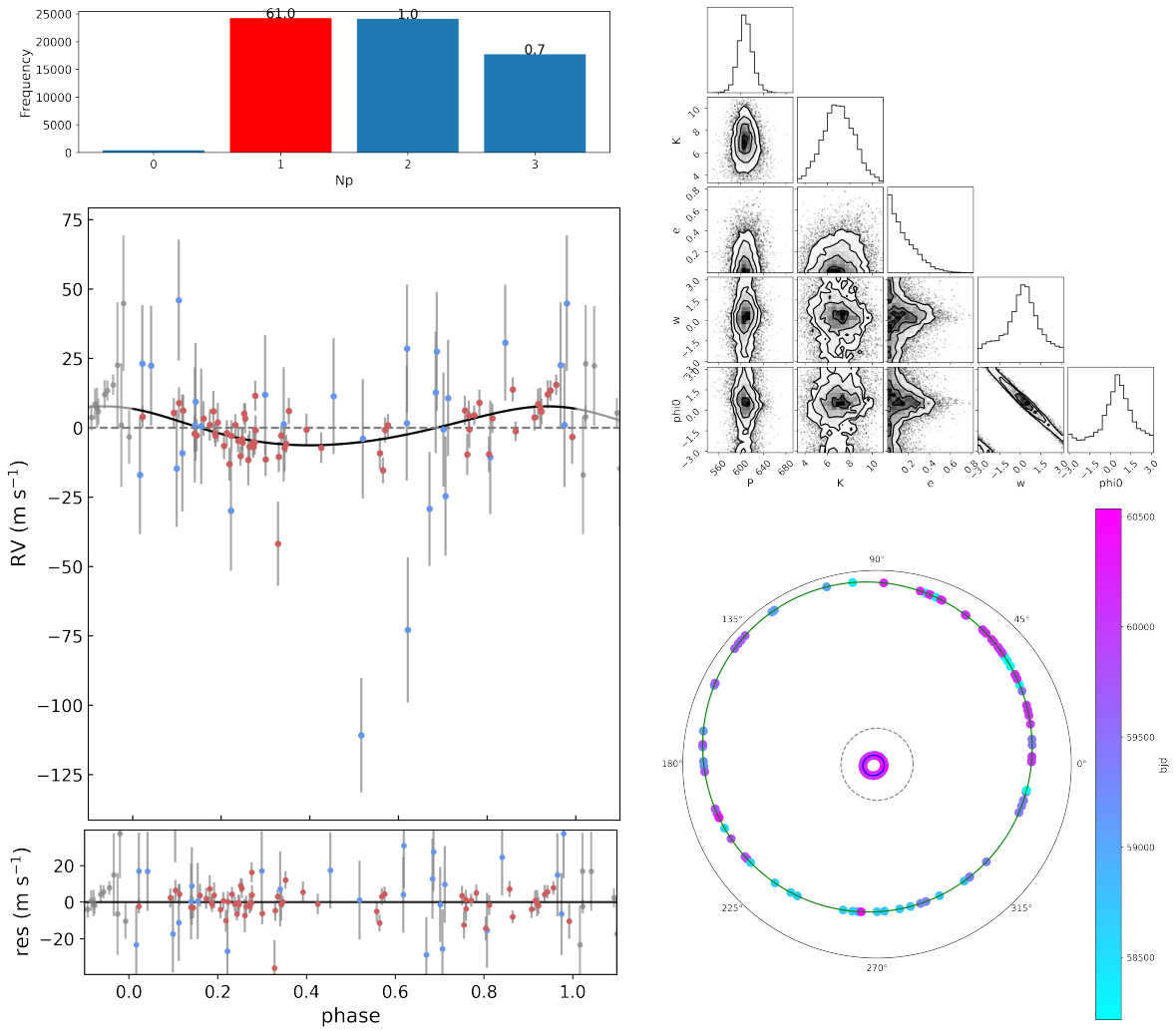


Figure 4.31: J2046+06b. Top-left: N_p histogram showing Bayes Factors comparing models $N_p = n$ to $N_p = n - 1$. Bottom-left: phased radial velocity curve and residuals for planet model. Red is the HARPS data and blue the SOPHIE data. Top-right: corner plot of planet parameters P, K, e, ω, ϕ_0. Bottom-right: Orbital configuration of binary (secondary orbiting primary) and planet, points show the radial velocity measurements coloured by time, the dashed grey line is the stability limit.

J2233+43

The binary is composed of two stars of mass 1.05 and 0.18 $M_{\odot}$, in a 8.1 day orbit with eccentricity 0.0016. A total of 81 radial velocity data have been collected with SOPHIE covering a span of 2200 days. The phased radial velocity curve, N_p histogram, corner plot of planet parameters, and orbital configuration are all shown in Figure 4.32. The Bayes Factor for the candidate is ~ 10.

J2233+43b is a candidate planet with $M \sin i = 1.50^{+0.49}_{-0.43}\ M_{\rm Jup}$, $P = 965^{+66}_{-47}$ days, and $e = 0.31^{+0.27}_{-0.24}$. Its scaled semi-major axis $a_{\rm sc} = 11.6^{+8.2}_{-7.1}$ if including eccentricity and $a_{\rm sc} = 11.55^{+0.98}_{-0.83}$ if not.

4.3.4 BEBOP long-period planetary-mass signals

There are 11 systems which have a long-period unclosed signal or drift which is consistent with a planetary-mass object. The names of the systems follow along with an approximate mass and orbital period which are that of the maximum-likelihood solution with $e < 0.1$ and rounded to the nearest 500 days or 0.5 $M_{\rm Jup}$: J0055-00 (3000 days - 2 $M_{\rm Jup}$); J0415-16 (2000 days - 0.5 $M_{\rm Jup}$); J0759-69 (2500 days - 1.5 $M_{\rm Jup}$); J0946-29 (2000 days - 6.5 $M_{\rm Jup}$); J1201-36 (5500 days - 0.5 $M_{\rm Jup}$); J1329+48 (4500 days - 12 $M_{\rm Jup}$); J1613-76 (2500 days - 2.5 $M_{\rm Jup}$); J1630+10 (4000 days - 14.5 $M_{\rm Jup}$); J1928-38 (3000 days - 1 $M_{\rm Jup}$); J2207-41 (5500 days - 1 $M_{\rm Jup}$); J2215+02 (2500 days - 2 $M_{\rm Jup}$); and J2343+29 (5000 days - 2.5 $M_{\rm Jup}$). The radial velocity curves for each of these is shown in Figure 4.33.

There are also 20 systems with long-period signals/drifts that are consistent with orbits of stellar mass or non-planetary sub-stellar mass objects. These are not discussed further.

4.3.5 Overview of BEBOP results

The parameters (Masses, Orbital periods, and eccentricities) for the binaries and planets presented above are shown in Table 4.7. This includes the BEBOP-3 system from Section 4.2, the candidates from Section 4.3.3, the tentative detections from Section 4.3.2 and detections

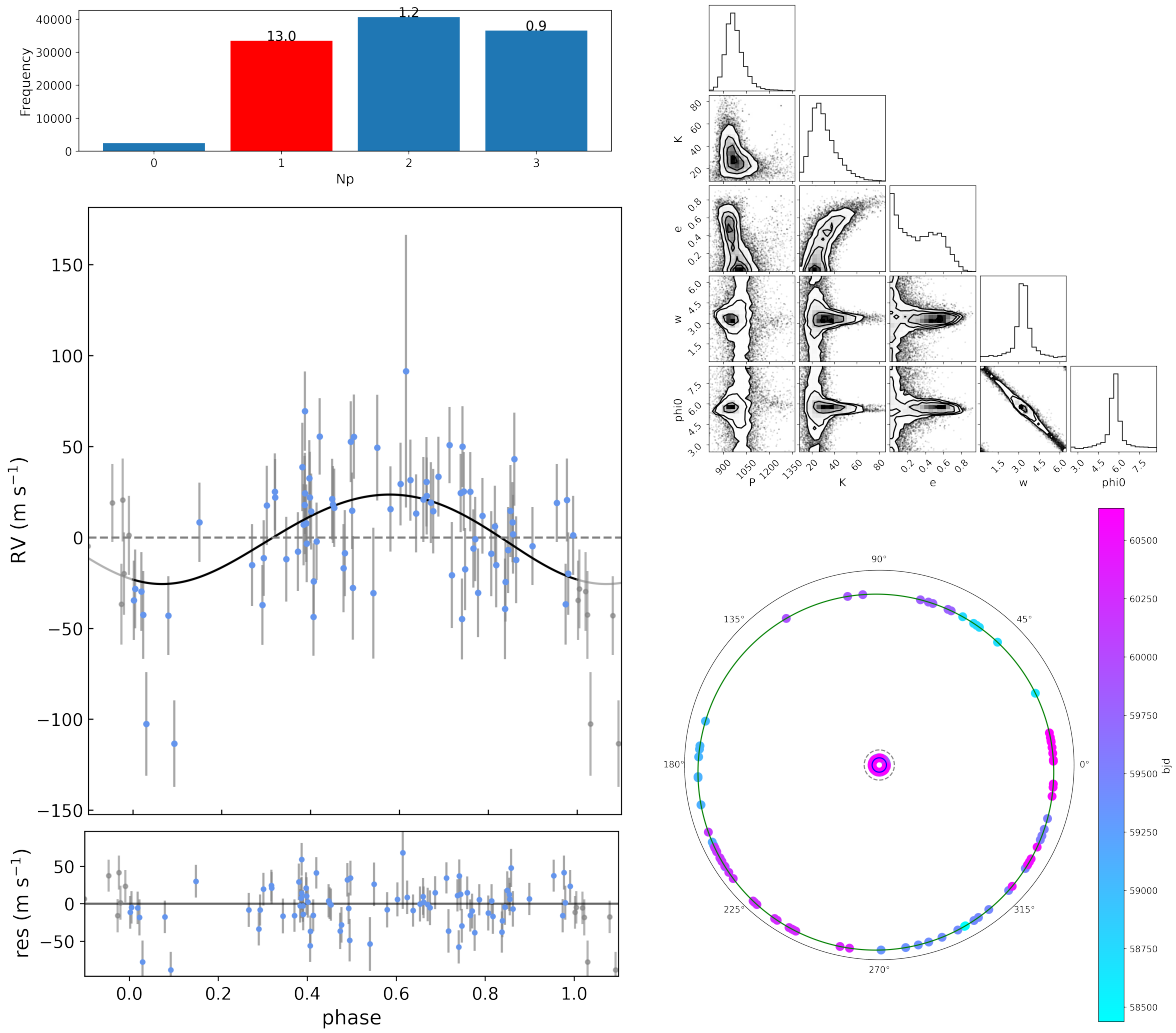


Figure 4.32: J2233+43b. Top-left: N_p histogram showing Bayes Factors comparing models $N_p = n$ to $N_p = n - 1$. Bottom-left: phased radial velocity curve and residuals for planet model. Top-right: corner plot of planet parameters P, K, e, ω, ϕ_0. Bottom-right: Orbital configuration of binary (secondary orbiting primary) and planet, points show the radial velocity measurements coloured by time, the dashed grey line is the stability limit.

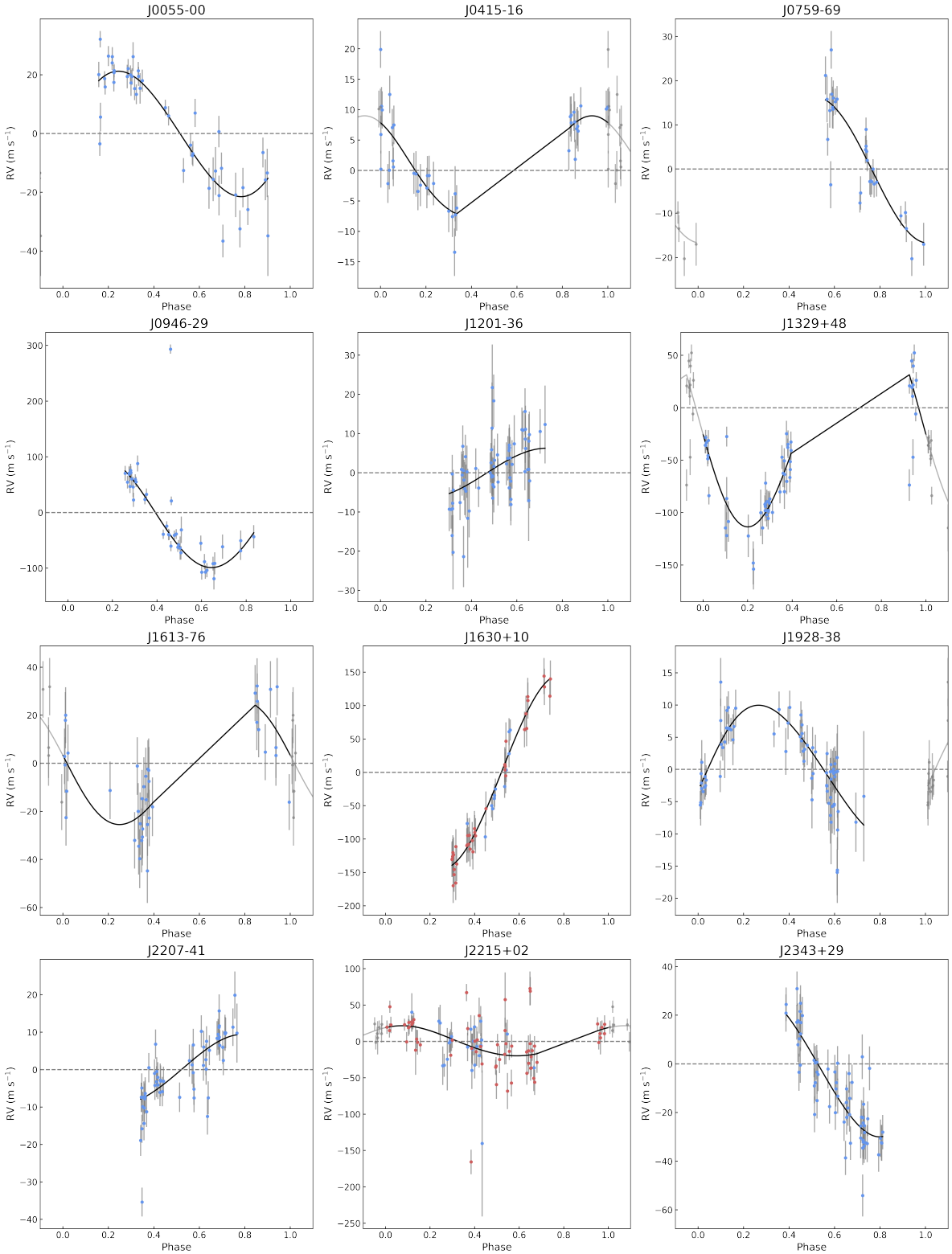


Figure 4.33: Long-period signals consistent with a planetary-mass companion orbiting BEBOP targets. When two sources of data are present they are shown in different colours.

from Section 4.3.1. The masses quoted for the planets in Table 4.7 are strictly speaking $M \sin i$ however the expectation is that the circumbinary planets will be coplanar with the binary (which are all eclipsing). I report the values as M but note that if any of the planets are misaligned (which some may in fact be) then this is instead a lower limit.

Table 4.7: Binary and planet parameters for BEBOP detections, tentative detections and candidates presented in this thesis. 1σ uncertainties are shown at the significance of last digits of the value. The uncertainty values in a_{sc} are the closest and furthest that the orbit moves relative to stability limit based on both the 84% confidence upper limit on eccentricity and the uncertainty in orbital parmaters.

Name	M_{pri} [$M_\odot$]	M_{sec} [$M_\odot$]	P_{bin} [days]	e_{bin}	P_{pl} [days]	M_{pl} [M_{Jup}]	e_{pl}	a_{sc}
				Detections				
BEBOP-3b	1.083(26)	0.2614(39)	13.217663(35)	0.063244(57)	$547.0^{(+6.2)}_{(-7.6)}$	0.560(49)	$0.247^{(+77)}_{(-89)}$	4.8(1.7)
J0110-44b	1.40(20)	0.200(18)	$28.781550^{(+57)}_{(-55)}$	$0.091883^{(+99)}_{(-97)}$	$247.1^{(+2.6)}_{(-2.4)}$	$0.573^{(+76)}_{(-74)}$	≤ 0.18	$1.72^{(+41)}_{(-39)}$
J0503-25b	1.71(09)	0.1366(47)	15.265148(26)	0.09040(40)	85.81(24)	0.94(11)	≤ 0.2	1.38(31)
J1250+26b	1.584(86)	0.473(16)	$71.96858^{(+13)}_{(-15)}$	0.26887(11)	1823.5(5.0)	21.56(83)	0.428(16)	2.7(1.3)
J1525-36b	1.30(21)	0.221(23)	$9.0089179^{(+88)}_{(-93)}$	$0.00081^{(+52)}_{(-48)}$	$725^{(+11)}_{(-16)}$	$2.71^{(+50)}_{(-46)}$	$0.47^{(+11)}_{(-23)}$	$8.9^{(+6.0)}_{(-5.4)}$
J1540-09b	1.05(13)	0.414(30)	26.3382848(34)	0.120471(26)	1044(38)	$0.220^{(+42)}_{(-39)}$	≤ 0.46	$4.2^{(+2.3)}_{(-2.1)}$
				Tentative Detections				
J0310-31b	1.19(17)	0.394(34)	12.6427923(43)	$0.308706^{(16)}_{(14)}$	$2013^{(+45)}_{(-40)}$	$0.303^{(+50)}_{(-46)}$	$0.640^{(+78)}_{(-88)}$	$8.8^{(+7.2)}_{(-6.4)}$
J0418-53b	1.03(13)	0.129(11)	$13.6993184^{(+40)}_{(-42)}$	$0.000123^{(+110)}_{(-87)}$	$3000^{(+620)}_{(-440)}$	0.75(12)	0.42(12)	$18^{(+15)}_{(-11)}$
J0503-25c	1.71(09)	0.1366(47)	15.265148(26)	0.09040(40)	$1820^{(+550)}_{(-220)}$	$1.63^{(+33)}_{-30}$	≤ 0.31	$10.6^{(+6.2)}_{(-4.0)}$
J0708-68b	0.95(12)	0.148(12)	$54.66192^{(+37)}_{(-57)}$	$0.69273^{(+50)}_{(-53)}$	$1900^{(+530)}_{(-240)}$	$1.18^{(+23)}_{(-17)}$	≤ 0.32	$2.6^{(+1.6)}_{(-1.0)}$
J1305-31b	1.07(13)	0.283(22)	10.6191497(79)	0.03845(30)	$1134^{(+54)}_{(-58)}$	$2.35^{(+49)}_{(-42)}$	≤ 0.5	$9.4^{(+5.7)}_{(-5.0)}$
				Candidates				
BEBOP-3c	1.083(26)	0.2614(39)	13.217663(35)	0.063244(57)	$1500^{(+500)}_{(-200)}$	$0.253^{(+88)}_{(-80)}$	≤ 0.32	$9.1^{(+5.1)}_{(-3.4)}$
J0353-16b	1.09(14)	0.212(18)	11.7611970(12)	$0.005661^{(+69)}_{(-67)}$	800(17)	$0.331^{(+70)}_{(-68)}$	≤ 0.42	$7.7^{(+3.8)}_{(-3.5)}$
J1200+42b	1.37(24)	$0.226^{(+24)}_{(-26)}$	21.89158(20)	0.4543(19)	4000(1000)	$13.8^{(+6.5)}_{(-4.3)}$	≤ 0.37	$8.8^{(+5.9)}_{(-4.5)}$
J1204-47b	1.22(18)	0.333(29)	13.7146055(26)	$0.175310^{(+62)}_{(-56)}$	$396.2^{(+6.7)}_{(-7.2)}$	$0.345^{(+90)}_{(-83)}$	≤ 0.3	3.2(1.2)
J1329+48b	0.94(12)	$0.503^{(+35)}_{(-37)}$	18.9510188(88)	$0.431120^{(+84)}_{(-89)}$	$920^{(+21)}_{(-30)}$	2.12(49)	≤ 0.4	$3.7^{(+1.8)}_{(-1.6)}$
J1403-32b	1.02(13)	0.260(20)	$11.9087108^{(+38)}_{(-33)}$	0.10917(10)	$2200^{(+1100)}_{(-460)}$	$0.82^{(+37)}_{(-22)}$	≤ 0.34	$12.2^{(+10.0)}_{(-5.6)}$
J2046+06b	1.22(18)	0.186(18)	10.10778897(18)	$0.343436^{(+71)}_{(-75)}$	608(13)	$0.350^{(+80)}_{(-75)}$	≤ 0.28	4.6(1.6)
J2233+43b	1.05(13)	0.180(14)	8.0738719(43)	0.00156(28)	$965^{(+66)}_{(-47)}$	$1.50^{(+49)}_{(-43)}$	$0.31^{(+27)}_{(-24)}$	$11.6^{(+8.2)}_{(-7.1)}$

4.4 Circumbinary planet population results

Based on the results from BEBOP, a preliminary look at population level results is possible. A full occurence rate calculation is foregone as the BEBOP survey is not completed, this will be done once all data has been acquired and the candidates have been confirmed or refuted. The results that follow are an updated version of those presented in Baycroft et al. (2024). Figure 4.34 is a repeat of Figure 1.17 with the planets from BEBOP as well as TOI-1338b and TIC 172900988b included. All of the planets in Table 4.7 are included, with *Tentative detections* and *Candidates* both included in the plots as *BEBOP Candidates*.

The bottom-left hand panel of Figure 4.34 shows that while only a handful of the BEBOP systems are measurably eccentric, since the radial velocity solutions have a wide uncertainty on eccentricity, there is the potential for a sub-population of planets on wide eccentric orbits. The middle panels of Figure 4.34 afford few conclusions, the restricted stellar-mass range of the BEBOP survey makes any correlations between planet and binary mass difficult to spot. There also appears to be no correlation (or very slight positive correlation) between planet mass and $a_{\rm sc}$. The relationship between mass and $a_{\rm sc}$ has implications for models of planet migration in circumbinary discs (see the discussion below).

In Section 1.6.3 the claimed *pile-up* of circumbinary planets near the stability limit was discussed. If real, it would be expected that the majority of circumbinary planets discovered with the radial velocity method would also be located in the piled-up population, since the radial velocity method also has a bias towards shorter period planets. Seeking planets at the stability limit was an early goal of BEBOP. Unexpectedly, only two of the detected or candidate planets from BEBOP are compatible with the pile-up population[4]. This lack of piled-up planets delayed the BEBOP results by many years since the early programme had banked on quick detections, but instead the planets and candidates are mostly found at long orbital period. While most of them are found orbiting binaries with periods between 10-20 days, none (except for the outer planet in the TOI 1338/BEBOP-1 system) are located in the arbitrarily chosen blue area that had

[4]Note that both TOI-1338b and TIC 172900988b detected with *TESS* are located in the pile-up

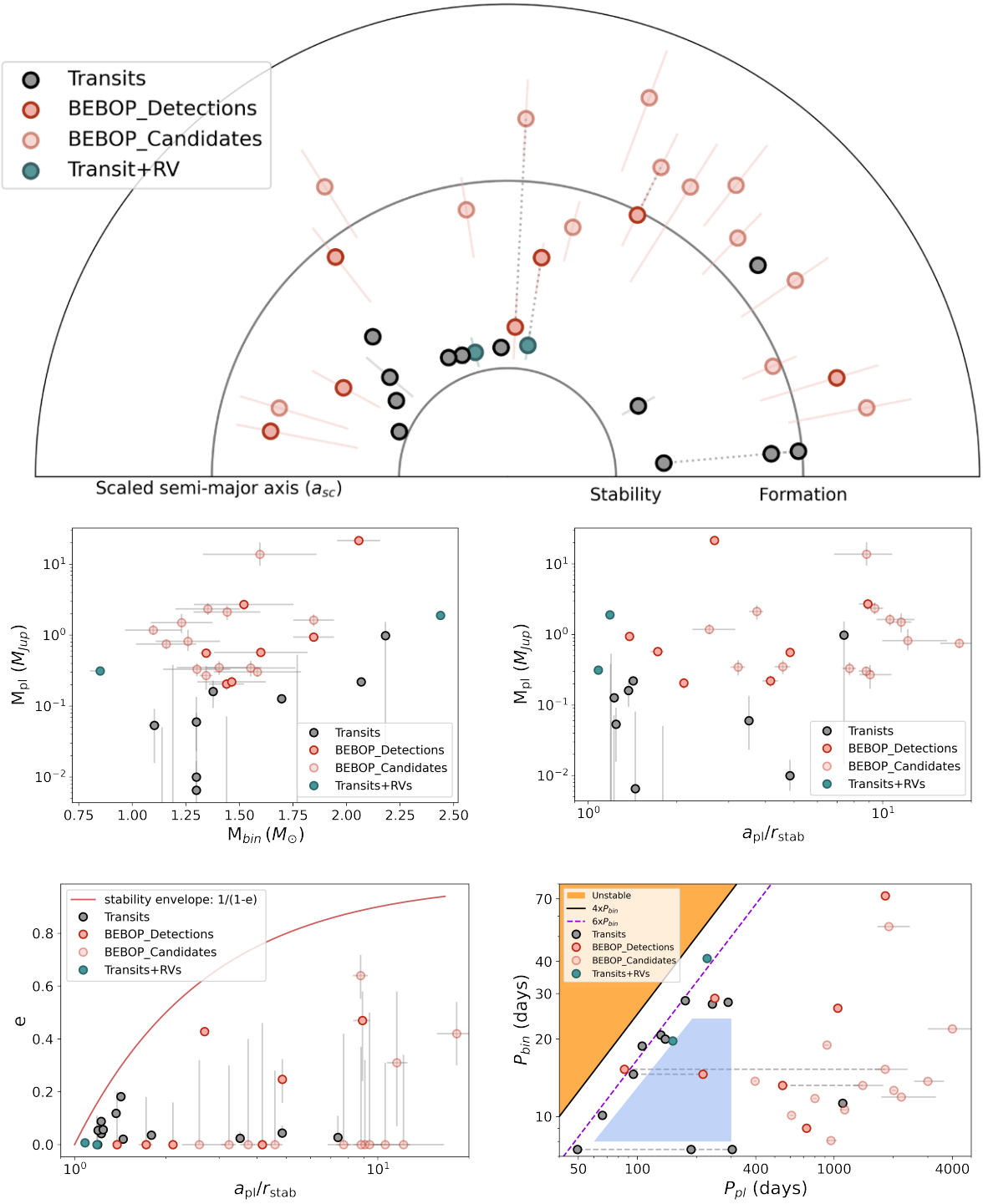


Figure 4.34: The circumbinary planets (Transiting, Transiting+RVs, BEBOP detections, and BEBOP Candidates) in various parameter configurations. Top: Proximity to stability limit with increasing binary orbital period anti-clockwise, radially is a_{sc} where the uncertainties include the potential eccentricity of the planet. The radial direction is log-scaled. Middle left: planet mass vs total binary mass. Middle right: planet mass vs proximity to stability limit. Bottom left: eccentricity vs proximity to stability limit, stable orbits should be below the red envelope. Bottom right: binary orbital period vs planet orbital period, blue region shows unexpected dearth of planets from *Kepler* implying pile-up.

been shaded based on the *Kepler* planets.

The low rate of detections of planets near the stability limit from radial velocities is a puzzle. A potential solution (already suggested in Baycroft et al., 2024) is that the planets in the pile-up are predominantly inflated, with large radii and low masses. This cannot be the case for all of them as some have good mass measurements (e.g. Kepler-16b) but others have very imprecise mass measurements or even only an upper limit. It is already known that TOI-1338b is inflated falling almost into the super-puff category (Standing et al., 2023). Inflated planets would explain the pile-up, as planets in the blue region from the bottom right hand panels of Figure 1.17 and Figure 4.34 would have smaller radii than those nearer the stability limit and thus be harder to detect. Planets near the stability limit being predominantly low-mass also explains the limited number of radial velocity detections of planets located there.

Other than inflated planets, if the BEBOP sample is biased in some way (e.g. systems with planets in the pile-up being removed from the sample for having a high residual scatter) this could explain the low rate of BEBOP detections in the pile-up. This does not fully resolve the tension as based on the BEBOP results, *Kepler* might be expected to have found more long-period planets such as Kepler-1647b. This could be resolved if the circumbinary planets far from the stability limit have a wider spread of mutual inclinations meaning they might be less likely to transit. I expect that it is likely a combination of both inflation and poorly understood survey biases as well as perhaps other explanations that have not yet been proposed.

To be able to solve this pile-up tension, more circumbinary planet detections are needed. An independant radial velocity survey run in a different (and as unbiased as possible) way, could help confirm or contradict the BEBOP results. Revisiting the *Kepler* field with a similarly precise space-based photometric mission would allow for a different population of transiting circumbinary planets to be probed. This could confirming the effect of nodal precession, improving the statistics on the frequency of circumbinary planets and also the significance of the pile-up. Improving the mass measurements of the known *Kepler* circumbinary planets (such as obtaining follow-up eclipse to improve the measured apsidal precession rate, see Chapter 6) would allow the inflation theory to be tested. A study of circumbinary planets with *Gaia* as

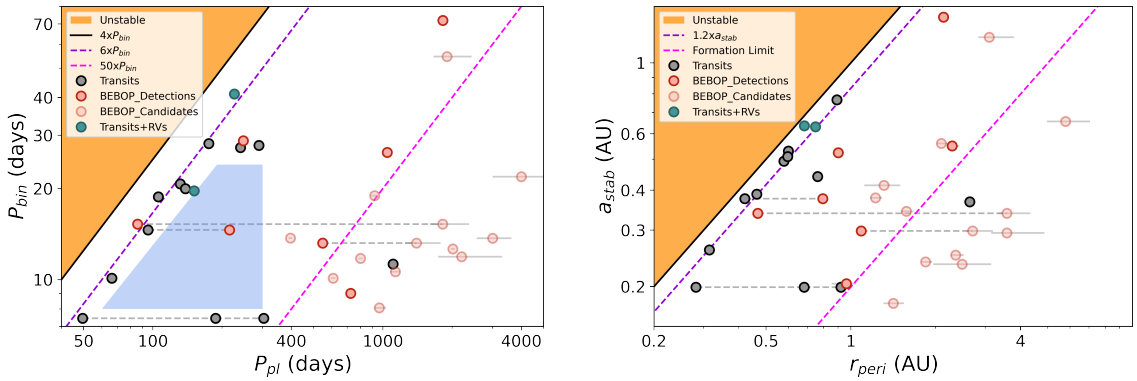


Figure 4.35: Left: same as bottom right of Figure 4.34 binary period against planet period. Right: Semi-major axis of the stability limit against pericentre distance of planet orbit. Purple and magenta lines here are $1.2 \times a_{\rm stab}$ and the approximate location of the formation limit. Coloured points represent the various circumbinary planets(Transiting, Transiting+RVs, BEBOP detections, and BEBOP Candidates).

described in Section 3.4, could give an independent probe of circumbinary planet statistics and shed more light on this problem.

The bottom right hand panel of Figure 4.34 suggests that the BEBOP planets are drawn from a population different from most of the *Kepler* circumbinary planets. They are seemingly akin to Kepler-1647b, the outlier of the *Kepler* distribution. Kepler-1647b is one of the more massive of the *Kepler* circumbinary systems[5]. Similarly the BEBOP circumbinary planets shown here are typically more massive than the *Kepler* circumbinary planet sample, with masses approximately ranging $1\ M_{\rm Sat} - 2\ M_{\rm Jup}$. This is as expected since the radial velocity method is most sensitive to the large-mass planets.

The similarity with Kepler-1647b is also seen in the top panel of Figure 4.34, where it appears that most of these planets are beyond the approximate threshold where planet formation is thought to be possible. This raises the question of whether these planets simply formed where they are now found and did not migrate. Larger planets are expected to undergo Type II migration which is slower than Type I migration which smaller planets undergo (see Section 1.5) which could explain this. Around single stars, the occurence of gas giants (thought to have unbergone Type II migration) peaks around 400 days (Santerne et al., 2016). However, early

[5]Its mass is only detected at 2 sigma, so it is actually more of a "big" planet than a "massive" planet at the moment.

studies in circumbinary planet formation and migration still find that Jovian planets migrate to the stability limit and are likely to then be ejected either totally or to a larger separation. It would be unlikely for this scattering to place all these planets neatly just beyond the formation limit.

Figure 4.35 shows the bottom right panel of Figure 4.34 with an extra line at $50 \times P_{\rm bin}$ as well as an alternate version, this has the radius of the stability limit on the y-axis, and the pericentre distance on the x-axis. In contrast with the previous version this takes into account the binary mass ratio and eccentricity, as well as the planetary eccentricity. In Figure 4.35 the dashed magenta line is the approximate formation boundary. In transitioning from the left to right hand configurations, the trend that most of the BEBOP planets lie just beyond the formation limit gets smeared out. This showcases how the parameters used to represent the circumbinary population and compare the different planets are important, and that more circumbinary planet detections are needed to allow trends to become clearer accross this high-dimensional parameter space.

Chapter 5

Planets orbiting evolved binaries

In this Chapter, I present results on post common-envelope binaries and potential circumbinary planets orbiting these. Such planets could be the end stage of the evolution of planets known to exist around main-sequence binaries (Columba et al., 2023) such as those discovered in the BEBOP survey, or a different class of planet born from a second generation of planet formation (e.g. Ledda et al., 2023). Section 5.1 is a case study of the system HW Virginis, and Section 5.2 investigates how *Gaia* astrometry will help resolve the question of whether such planets do exist.

5.1 New evidence about HW Vir's circumbinary planets from *Hipparcos-Gaia* astrometry and a reanalysis of the eclipse timing variations using nested sampling

The following is a published paper (Baycroft et al., 2023a) that I first authored on the system HW Virginis (HW Vir) applying the astrometric proper-motion anomaly, and reanalysing existing eclipse timing data using the ETVmodel of `kima` described in Section 2.3.

This project was inspired by the prediction of Sahlmann et al. (2015) that *Gaia* would have the astrometric sensitivity to constrain the claimed planets around HW Vir (among other systems).

At a summer school on statistics in exoplanet data analysis held in Geneva in September 2022, Pierre Kervella presented the proper-motion anomaly method and made available some code to access the catalogue (Kervella et al., 2022) and generate sensitivity plots. The result of a 2σ measurement led me to investigating HW Vir in more detail, revisiting the eclipse timing variations with `kima`, and to writing this paper.

Pierre Kervella assisted in the proper motion anomaly method analysis and description in Section 5.1.2. I performed the analyses presented, and wrote the manuscript.

Monthly Notices of the ROYAL ASTRONOMICAL SOCIETY

MNRAS **526,** 2241–2250 (2023) https://doi.org/10.1093/mnras/stad2794
Advance Access publication 2023 September 13

New evidence about HW Vir's circumbinary planets from *Hipparcos-Gaia* astrometry and a reanalysis of the eclipse timing variations using nested sampling

Thomas A. Baycroft [1]★ Amaury H.M.J. Triaud [1] and Pierre Kervella [2]

[1]*School of Physics and Astronomy, University of Birmingham, Edgbaston, Birmingham B15 2TT, UK*
[2]*LESIA, Observatoire de Paris, Université PSL, CNRS, Sorbonne Université, Université Paris Cité, 5 place Jules Janssen, F-92195 Meudon, France*

Accepted 2023 September 11. Received 2023 September 7; in original form 2023 August 3

ABSTRACT

The post common-envelope eclipsing binary HW Virginis (HW Vir) has had many circumbinary companions proposed based on eclipse timing variations. Each proposed solution has lacked in predictability and orbital stability, leaving the origin of the eclipse timing variations an active area of research. Leveraging the catalogue of *Hipparcos* and *Gaia* proper motion anomalies, we show there is slight evidence for a circumbinary companion orbiting HW Vir. We place an upper limit in mass for such a companion which excludes some previously claimed companions. We also apply this method to V471 Tauri and confirm the non-detection of a previously claimed brown dwarf. We adapt the KIMA nested sampling code to analyse eclipse timing variations and re-analyse archival data on HW Vir, varying the order of the ephemeris that we fit for and the amount of the data that we use. Although signals are clearly present, we find two signals around 2500 and 4000-d periods that are not coherent between different *chunks* of the data, so are likely to not be of planetary origin. We analyse the whole data set and find the best solution to contain four signals. Of these four we argue the outermost is the most compatible with astrometry and thus the most likely to be of planetary nature. We posit the other three pseudo-periodic signals are caused by physical processes on the white dwarf. The eventual release of the full *Gaia* epoch astrometry is a promising way to confirm whether circumbinary planets exist around HW Vir (and other similar systems), and explore white dwarf physics.

Key words: astrometry – planets and satellites: detection – binaries: close – binaries: eclipsing – stars: individual: HW Vir – stars:subdwarfs.

1 INTRODUCTION

Although the majority of known exoplanets have been detected around single stars on the main sequence, planetary systems around post-main sequence stars and in binary star systems are known to exist. The first detected exoplanetary system was around a pulsar (Wolszczan & Frail 1992) and planets orbiting single white dwarfs are known to exist (e.g. Bachelet et al. 2012; Vanderburg et al. 2015, 2020). Many single white dwarf stars have been found to exhibit irregular transit-like and dimming events as well as having atmospheres polluted with heavy elements, both pointing to debris being accreted onto the star which could potentially have been scattered inwards by an invisible companion (Koester, Gänsicke & Farihi 2014; Farihi et al. 2022). Planetary systems around main sequence binaries have been detected in transit by Kepler (e.g. Doyle et al. 2011) and *TESS* (e.g. Kostov et al. 2020) and also in radial velocity (e.g. Standing et al. 2023).

Planets are therefore known to orbit main-sequence binaries and are able to survive the evolution of a single star. There have been many claims of planets[1] orbiting evolved binaries, but they are yet to be fully confirmed as planets. These candidate planets, orbiting post-common envelope binaries, are currently claimed based on periodic variations of the binary's mid-eclipse times. These variations can arise due to the light travel-time effect (LTTE) from the eclipsing binary orbiting the common centre-of-mass between itself and the companion. These putative planets could be the counterparts of the detected main-sequence circumbinary planets that have lived through the evolution of their host binary (e.g. Columba et al. 2023).

The existence of these planets has been debated (Mustill et al. 2013). In many cases the claimed planetary solutions fail to predict future eclipses (e.g. Pulley et al. 2022). One candidate, orbiting V471 Tauri (Beavers, Herczeg & Lui 1986) was later followed up with direct imaging and was not detected with a high confidence (Hardy et al. 2015).

HW Virginis (HW Vir) is one of the most famous examples of post-common envelope binaries with claimed companions, first proposed by Lee et al. (2009). The system consists of a sdB pri-

[1]Many of these have masses that would put them above the Deuterium burning limit and should be referred to as brown dwarfs; however, for simplicity we refer to call them all 'planets'.

★ E-mail: txb187@bham.ac.uk

© 2023 The Author(s).
Published by Oxford University Press on behalf of Royal Astronomical Society. This is an Open Access article distributed under the terms of the Creative Commons Attribution License (http://creativecommons.org/licenses/by/4.0/), which permits unrestricted reuse, distribution, and reproduction in any medium, provided the original work is properly cited.

Downloaded from https://academic.oup.com/mnras/article/526/2/2241/7273133 by Health Services Management Centre Library user on 08 October 2024

mary of mass $M_A = 0.418 \pm 0.008\,M_\odot$ and an M-dwarf secondary of mass $M_B = 0.128 \pm 0.004\,M_\odot$ in a binary with orbital period $P_{bin} = 0.116719556 \pm 7.4 \times 10^{-9}$ d.[2] Eclipses have been precisely measured for over 30 yr, with many conflicting solutions proposed (e.g. Beuermann et al. 2012; Esmer et al. 2021) with either one or two planets proposed as the cause of the eclipsing timing variations. One major issue is that none of the single-planet solutions fit the data satisfactorily, but none of the better-fitting two-planet solutions appear to be dynamically stable (Brown-Sevilla et al. 2021; Mai & Mutel 2022). Another issue, as mentioned above, is that all of the proposed solutions very quickly diverge from the data subsequently collected.

Non-planetary explanations have been suggested which can produce eclipse timing variations in short-period binaries such as HW Vir. The period (or apparent period) of the binary could be affected by apsidal precession if it is eccentric, and magnetic braking (Rappaport, Verbunt & Joss 1983) or emission of gravitational waves (Paczyński 1967) could cause the orbit to shrink due to angular momentum loss. Other magnetic effects have also been proposed, such as the Applegate mechanism (Applegate 1992), or a more recent mechanism, requiring less energy suggested by Lanza (2020). However in most cases these are insufficient to fully explain the shape or the amplitude of the observed modulations in eclipse time.

Many of these candidate planets will need to be confirmed/rejected through other methods. One example of this happening is with V471 Tau. This system consists of a WD primary of mass $M_A = 0.797 \pm 0.016\,M_\odot$ and a K-Dwarf secondary of mass $M_B = 0.864 \pm 0.029\,M_\odot$ in a binary with orbital period $P_{bin} = 0.5211834194 \pm 7.2 \times 10^{-9}$ d (Muirhead, Nordhaus & Drout 2022). This system shows periodic variations of the mid-eclipse times, which have been used to suggest an orbiting brown dwarf (Beavers et al. 1986; Guinan & Ribas 2001). The system has since been directly imaged with SPHERE, and these observations resulted in a non-detection (Hardy et al. 2015), thus rejecting the claimed brown dwarf.

Planets around ultra-short period evolved binaries such as these may also eventually be detectable in gravitational waves, for example, by the Laser Interferometer Space Antenna (LISA; Danielski et al. 2019). LISA will however only be sensitive to binaries of shorter orbital period than HW Vir.

Another possibility for confirming or rejecting post-common envelope circumbinary planets is precise astrometry. The space telescope *Gaia* (Gaia Collaboration2021) is performing a precise astrometric survey of the whole sky which will have a baseline of about 10 yr. *Gaia*'s astrometric solution will be able to investigate some of these systems without relying on any eclipse timing data (Sahlmann, Triaud & Martin 2015). However, individual astrometric measurements are expected to released around late 2025. In the meantime, we can only rely on the proper motion anomaly method (Kervella et al. 2019). Before *Gaia*, *Hipparcos* (ESA 1997) also performed an astrometric survey, but of a much smaller sample of stars, at a lower precision. HW Vir is within that sample, as is V471 Tau. The proper motion anomaly method combines positions and proper motions of a star from *Hipparcos* and one of *Gaia*'s recent data releases to estimate the effect of an orbiting of an orbiting companion on the proper motion of the star. This method has been applied to single stars, and combined with other techniques such as radial velocity, has led to the detection and characterization of several planetary companions (e.g. Mesa et al. 2022; Rickman et al. 2022).

[2]Parameters are taken from Esmer et al. (2021), these values are used for the rest of the analysis when the mass of the central binary is needed

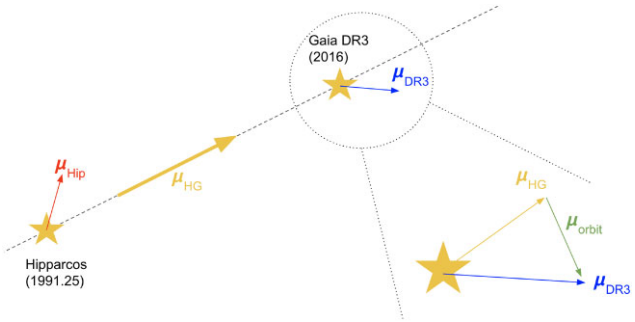


Figure 1. Diagram of the proper motion anomaly method.

In this paper we present a new piece of astrometric information, in the form of the proper motion anomaly, to the puzzle that is HW Vir, and we perform a new fit of the eclipse timing data utilizing nested sampling and analysing different *chunks* of data separately. We report on the lack of consistency of signals in the eclipse times and present the model that we find to fit best to the whole data set, providing a suggestion of which signal is favoured to be planetary since not all the detected signals can be.

The paper is set out as follows. We describe the proper motion anomaly method, and apply it to both V471 Tau and HW Vir in Section 2. In Section 3, the use of KIMA to fit eclipse times is described. Section 4 details the eclipse timing data used, and the results from the analysis of the data. We discuss the results and implications and conclude in Section 5.

2 ASTROMETRY: USING THE PROPER MOTION ANOMALY METHOD

We first explain the method of the astrometric proper motion anomaly, and secondly apply this to both V471 Tau and HW Vir. We compare the results from the astrometric proper motion anomaly to some of the previously proposed planetary solutions.

2.1 How does the proper motion anomaly work?

The proper motion anomaly analysis method is described in detail in Kervella et al. (2019). Using positional measurements from *Gaia* and *Hipparcos*, we determine the long-term, mean proper motion vector of the system μ_{HG} by dividing the observed change in position by the time baseline δt_{HG} between the two measurements (that is, 24.75 yr between *Hipparcos* and *Gaia* DR3). For the nearest stars, second order effects must be taken into account in this computation, but they are negligible for the systems discussed in the present paper.

Thanks to the long time baseline, and assuming that the orbital period of the companion is significantly shorter than δt_{HG}, μ_{HG} essentially traces the proper motion of the centre of mass of the system. Separately, the short-term proper motion measurements μ_{Hip} and μ_{DR3} (obtained respectively by *Hipparcos* and *Gaia*) trace the vector sum of (1) the linear proper motion of the centre of mass and (2) the orbital motion μ_{orbit} of the photocentre of the system around the centre of mass. Fig. 1 visually presents the different vector quantities considered in these computations.

When considering a planetary companion, the photocentre is located very close to the geometrical centre of the star. In this configuration, subtracting the long-term proper motion μ_{HG} from the *Gaia* DR3 short-term proper motion μ_{DR3} gives access to the proper motion anomaly of the star $\Delta\mu$ that traces the orbital motion of the star around the centre of mass of the system. The quantity

Downloaded from https://academic.oup.com/mnras/article/526/2/2241/7273133 by Health Services Management Centre Library user on 08 October 2024

$\Delta\mu$ can be scaled to a linear tangential velocity anomaly $v_{\rm tan}$ using the parallax. This is the two-dimensional counterpart of the radial velocity that is traditionally employed to detect exoplanets.

Corrective terms must be considered to interpret the measured proper motion anomaly in terms of companion properties. First, the $\mu_{\rm orbit}$ quantity is an average quantity over the *Gaia* integration window, that has a duration of $\delta t_{\rm DR3} = 34$ months. This averaging implies that the measured proper motion anomaly will be smeared, reducing the sensitivity in terms of companion mass. This loss of sensitivity is particularly strong for orbital periods shorter than $\delta t_{\rm DR3}$ Secondly, the time baseline $\delta t_{\rm HG}$ between *Hipparcos* and *Gaia* DR3 results in the subtraction of part of the proper motion signature of very long period companions ($P > 3 \times \delta t_{\rm HG}$) during the computation of the $\mu_{\rm HG}$ quantity. This effect induces a loss of sensitivity to such very long period companions. These two effects determine the companion mass sensitivity function of the proper motion anomaly method.

We now derive the equation for the tangential velocity caused by a companion if measured instantaneously. This equation can then be combined with the sensitivity function calculated numerically. The proper motion is usually divided into its components in right ascension (RA) and declination (Dec).

$$\mu = \mu_{\rm RA}\mathbf{e}_{\rm RA} + \mu_{\rm Dec}\mathbf{e}_{\rm Dec}, \tag{1}$$

with $\mathbf{e}_{\rm RA}$ and $\mathbf{e}_{\rm Dec}$ the basis vectors in RA and Dec. We then subtract the long-term HG proper motion from the *Gaia* DR3 proper motion and take the magnitude of this vector to get the tangential velocity anomaly.

$$\Delta\mu = (\mu_{\rm DR3,RA} - \mu_{\rm HG,RA})\mathbf{e}_{\rm RA} + (\mu_{\rm DR3,Dec} - \mu_{\rm HG,Dec})\mathbf{e}_{\rm Dec}, \tag{2}$$

$$v_{\rm tan} = \frac{1}{\varpi}\sqrt{(\mu_{\rm DR3,RA} - \mu_{\rm HG,RA})^2 + (\mu_{\rm DR3,Dec} - \mu_{\rm HG,Dec})^2}, \tag{3}$$

where ϖ is the parallax. Now given an inner mass M and an outer mass m the relative orbital velocity is

$$V = \sqrt{G(M+m)}\left(\frac{2}{r} - \frac{1}{a}\right)^{1/2}, \tag{4}$$

where G is the gravitational constant, a the semi-major axis of the relative orbit, and r the relative orbital distance at the measured time. The distance is given by

$$r = \frac{a(1-e^2)}{1 + e\cos f}, \tag{5}$$

with e and f the eccentricity and true anomaly of the orbit at the measured time (they are the same for the relative orbit or the orbit of one of the components). Combining these two equations and using that the velocity of the inner body (i.e. the luminous one) relates to the outer velocity by

$$v_0 = \frac{m}{M+m}V, \tag{6}$$

gives us

$$v_{\rm tan} = \sqrt{\frac{Gm^2}{a(M+m)}}\left(\frac{2(1+e\cos f)}{(1-e^2)} - 1\right)^{1/2} \tag{7}$$

$$v_{\rm tan} = \sqrt{\frac{Gm^3}{a_1(M+m)^2}}\left(\frac{2(1+e_1\cos f_1)}{(1-e_1^2)} - 1\right)^{1/2}, \tag{8}$$

where a_1 is the semi-major axis of the outer orbit which relates to that of the relative orbit by $a_1 = \frac{m}{M+m}a$.

This derivation is valid for an instantaneous measurement of $v_{\rm tan}$, which would correspond to an instantaneous measurement of $\mu_{\rm DR3}$ and an infinitely long baseline for $\mu_{\rm HG}$. This is, of course, not the case.

Table 1. Tangential velocities from the proper motion anomaly between *Gaia* DR3 and the *Hipparcos*−*Gaia* long-term vector, for HW Vir and V471 Tau.

	HW Vir	V471 Tau	
Kervella et al. (2022)	214 ± 111	38 ± 13	m s^{-1}
Brandt (2021)	226 ± 111	28 ± 13	m s^{-1}

Values are reported using both the Kervella et al. (2022) and Brandt (2021) catalogues of accelerations.

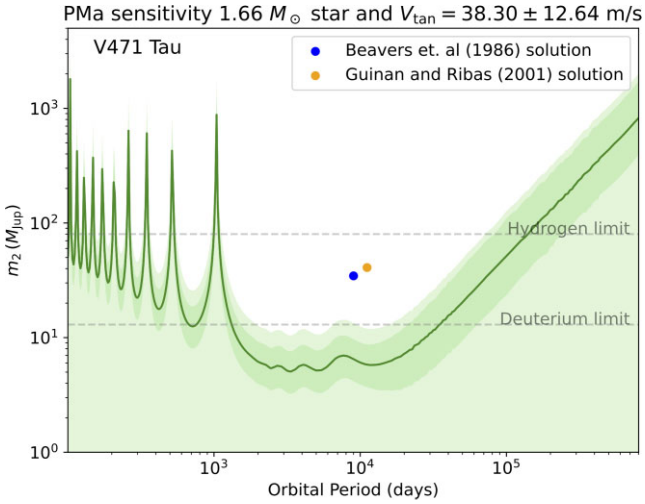


Figure 2. Sensitivity curve for proper motion anomaly applied to V471 Tau. Green shows the mean, 1σ region, and 3σ region of parameter space that could correspond to an orbiting body giving rise to the proper motion anomaly. The coloured dots show locations of claimed solutions by two previous papers. The dashed lines show the locations of the hydrogen and deuterium fusing limits.

As described above we must also include a sensitivity function. This function has been numerically calculated by Kervella et al. (2019). This leads to the sensitivity curve for the proper motion anomaly at different periods which is used in the following section. These curves give the areas of Period-Mass space that are consistent with a measured proper motion anomaly, under the assumption of a circular orbit.

2.2 Applying the proper motion anomaly to V471 Tau and HW Vir

Calculating the long-term proper motion between *Hipparcos* and *Gaia* DR3 has been done and combined into a catalogue by both Kervella, Arenou & Thévenin (2022) and Brandt (2021), using different combinations of the main *Hipparcos* reductions. The values for the tangential velocity for HW Vir and V471 Tau are shown in Table 1. We note that the values are in good agreement between both catalogues and choose arbitrarily to use the Kervella et al. (2022) value from now on.

2.2.1 V471 Tau

For V471 Tau, we have a proper motion anomaly between 2σ and 3σ. Fig. 2 shows the sensitivity curve of the proper motion anomaly method associated with the value for V471 Tau from Kervella et al. (2022). The dark green line shows the curve on which a body needs to lie to produce the observed tangential velocity value, the darker

Downloaded from https://academic.oup.com/mnras/article/526/2/2241/7273133 by Health Services Management Centre Library user on 08 October 2024

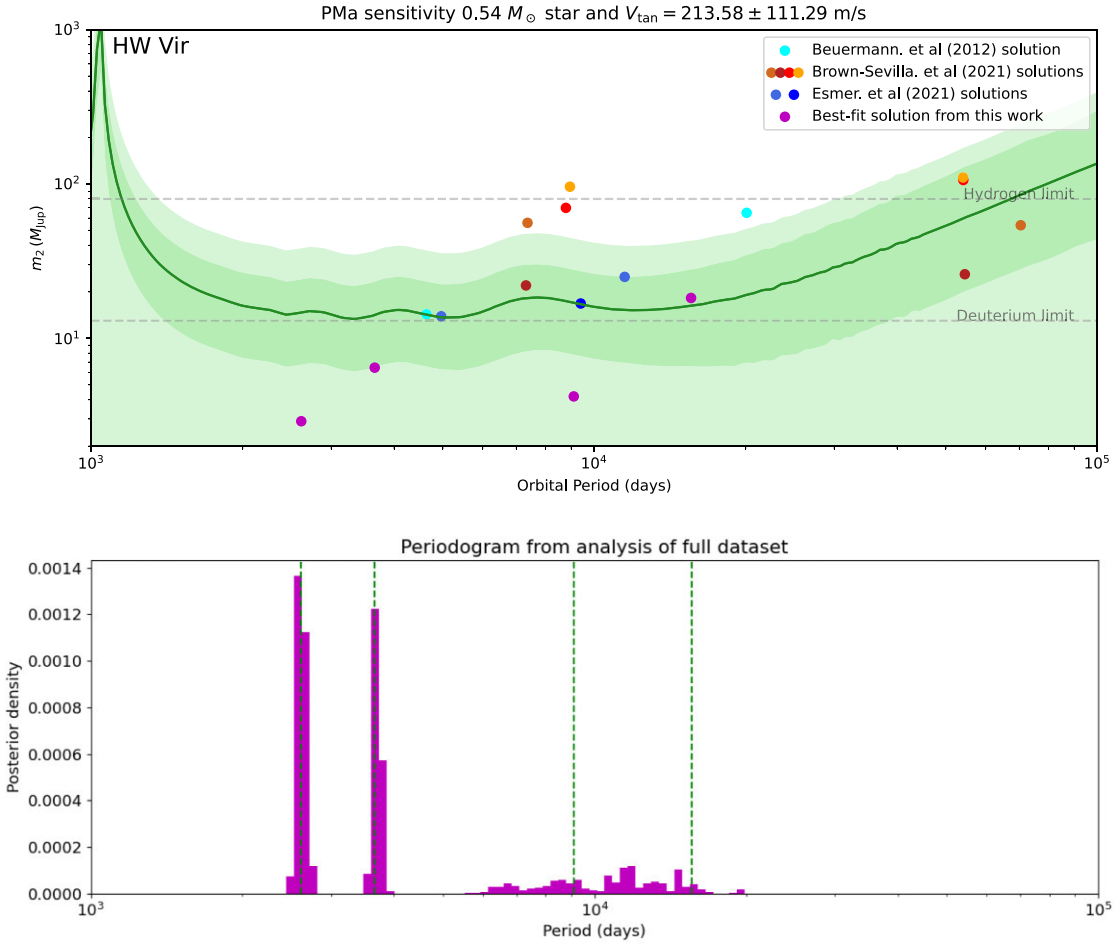


Figure 3. Top: Sensitivity curve for proper motion anomaly applied to HW Vir. Green shows the mean, 1σ region, and 3σ region of parameter space that could correspond to an orbiting body giving rise to the proper motion anomaly. The coloured dots show locations of claimed solutions by three previous analyses as well as the best-fitting solution from this work. The dashed lines show the locations of the hydrogen and deuterium fusing limits. Middle: Posterior density histogram of the periods of planets suggested in all Np = 4 posterior samples from the analysis of the full data set. Dashed lines show the locations of the best-fitting four-planet solution.

and lighter shaded regions show the 1σ and 3σ regions around that line. The spikes towards shorter orbital periods are the result of the sensitivity function as described above. The slope at longer orbital periods is produced when only small fraction of an orbital arc is covered and hence the efficiency function is small. In between is a region of highest sensitivity. This provides an upper bound that is far below the mass of the proposed solutions by Beavers et al. (1986) and Guinan & Ribas (2001). This re-affirms the conclusion of Hardy et al. (2015) which did not find evidence of the proposed brown dwarf, and confirms that the variations in the mid-eclipse times must be coming from some other source.

We numerically estimate the proper motion anomaly that would be caused by the binary. For a given set of parameters (M_0, M_1, P) we perform a bisection algorithm suggesting values for v_{tan}, and comparing the value of M_1 obtained (given M_0 and P) to the given value, until the masses agree to 0.001 M_{jup}. We repeat this for 1000 realizations of the binary parameters to then obtain the median and 1σ values of 32^{+13}_{-21} m s^{-1}. This is entirely consistent with the tentative signal that is seen. The proper motion anomaly is sensing the smeared binary motion and so does not suggest an orbiting companion.

2.2.2 *HW Vir*

For HW Vir, the tangential velocity is distinct from zero at around 2σ confidence in both catalogues. We cannot therefore conclude from the proper motion anomaly that there is definitely an orbiting body, but this *Gaia-Hipparcos* combined measurement brings new evidence that suggests such a body is more likely to exist than not.

First, we validate that this tentative proper motion anomaly is not caused by the smeared orbital motion of binary. In the same way as for V471 Tau, we numerically estimate the proper motion anomaly that would be induced by the binary and obtain the median and 1σ values of $2.52^{+0.80}_{-1.60}$ m s^{-1}. The excess tangential velocity is therefore not caused by the HW Vir binary.

The top panel of Fig. 3 shows the sensitivity curve of the proper motion anomaly method associated with HW Vir. The curve has the same shape as in Fig. 2 (since all the spikes are primarily related with the *Gaia* 34-month observing window) but is zoomed in on the area of best sensitivity. We overplot the locations of the orbiting bodies proposed by three previous studies (Beuermann et al. 2012; Brown-Sevilla et al. 2021; Esmer et al. 2021). We note that four of the proposed solutions include one orbiting body above the 3σ

Downloaded from https://academic.oup.com/mnras/article/526/2/2241/7273133 by Health Services Management Centre Library user on 08 October 2024

line. These solutions are disfavoured[3] by the observed proper motion anomaly which is too weak to have been produced by these putative objects. This plot also shows the locations of the four components from our best-fitting model,[4] which we describe in Section 4.2.2.

This tentative proper motion anomaly is an extra piece of information about the HW Vir system which provides astrometric evidence that there may be an orbiting circumbinary companion.

The catalogues of accelerations mentioned above rely on *Gaia* EDR3 (Gaia Collaboration 2021). The same analysis was done earlier using *Gaia* DR2 (Gaia Collaboration 2018), and the value from Kervella et al. (2019) for HW Vir is 309 ± 200. From this we infer that the astrometric signal is getting more confident as more *Gaia* data becomes available. This implies that if there is indeed a signal there, it should be detectable from future *Gaia* data releases.

3 FITTING ECLIPSE TIMING VARIATIONS WITH KIMA

Whilst verifying whether proposed solutions for the HW Vir systems were compatible with the proper motion anomaly, we also decided to re-analyse the eclipse times of HW Vir with a nested sampler, which we believe has not been attempted yet. Most of the literature uses χ^2 maps or reduced χ^2_ν to make inferences about the number of signals present in the data, but none have conducted a Bayesian model comparison in this way yet.

Amongst Bayesian methods, nested sampling has the advantage to let some key parameters free that are usually fixed in other types of analyses. In our case, the number of orbiting planets, N_p, is a free parameter which allows for a robust model comparison, based on a ratio of Bayesian evidence. All planetary signals are adjusted at once and models with 0, 1, 2... planets are constantly compared to one another.

KIMA is an orbital fitting algorithm originally designed for application to radial velocities (Faria et al. 2018). We adapt it to fit mid-eclipse times instead, to then apply it to HW Vir. KIMA leverages nested sampling using DNEST4 (Brewer & Foreman-Mackey 2018) to explore parameter space and calculate the likelihood of proposed samples. Using the trans-dimensional sampling in KIMA the number of Keplerian signals, N_p, being fit is a free parameter as described above. This allows a comparison of the different numbers of signals present in the data with a Bayes Factor. The Bayes Factor for a $N_\mathrm{p} = n$ model[5] compared to a $N_\mathrm{p} = n - 1$ model is the ratio of the evidence Z for each model.

The evidence is the primary output of nested sampling and is the integral of the likelihood over the prior mass. In nested sampling this integral is calculated as a weighted sum, with the weights being associated to the change in prior mass between consecutive samples (Skilling 2006). In this case the evidence for an $N_\mathrm{p} = n$ model is the sum of the *weights* of all the samples with n planets, and then the Bayes Factor is $BF = \frac{Z_n}{Z_{n-1}}$.

We use a detection threshold of 150 as recommended by Kass & Raftery (1995). A Bayes Factor larger than 150 is taken as very strong evidence for the more complex model over the less complex model (and roughly equivalent to a p-value of 0.001). It is common that a nested sampler finds the sum of the *weights* of all the samples is highest for the highest N_p explored by the sampler (Faria et al. 2018; Standing et al. 2022). However, so long as the ratio is not >150 those most complex solutions, whilst providing a better fit to the data, do not contain enough statistical evidence to warrant the extra number of parameters.

As a by-product of the nested sampling to calculate the evidences, we can obtain posterior samples for the various parameters from KIMA. These allow us to perform parameter estimation on any detected signals, assuming a LTTE model with a companion on a Keplerian orbit. KIMA has already been used to detect and test the detectability of circumbinary planets with radial-velocities (Standing et al. 2022, 2023; Triaud et al. 2022). We redirect the reader to these publications for more thorough explanations of how the model comparison works.

We fit the eclipse times in KIMA with a number of Keplerian signals as well as an ephemeris function. We allow the ability to fit for one of a linear, quadratic or cubic ephemeris. These are shown in equation (9) below:

$$T(E) = T_0 + P_0 E + \frac{1}{2}\dot{P}_0 P_0 E^2 + \frac{1}{6}\ddot{P}_0 P_0^2 E^3 + \sum_i \tau_i(E), \tag{9}$$

where E is the epoch of an eclipse (i.e. the number of the eclipse with the first eclipse being 0), $T(E)$ is the time of that eclipse in our model, T_0 is the reference time (time at epoch 0 here), P_0 is the period of the eclipsing binary at the reference time, $\dot{P}_0$ and $\ddot{P}_0$ are the first and second time-derivatives of the binary period (at the reference time), and τ_i is the time-delay due to the LTTE of an orbiting body. The middle three terms are a Taylor series and if we ignore the terms of order $\geq E^2$ we are using a linear ephemeris, if we ignore terms of order $\geq E^3$ we are using a quadratic ephemeris, and using all the terms above is a cubic ephemeris. The functional form for the LTTE due to an orbiting body is as in Irwin (1952),

$$\tau(t) = \frac{K}{\sqrt{1 - e^2\cos^2\omega}}\left(\frac{1 - e^2}{1 + e\cos\nu(t)}\sin(\nu(t) + \omega) + e\sin\omega\right), \tag{10}$$

where e and ω are the eccentricity and argument of periastron of the orbiting body, $\nu(t)$ its true anomaly at time t and K the semi-amplitude of the signal,

$$K = \frac{m\sin i}{c(M + m)}\left(\frac{G(M + m)}{4\pi^2}\right)^{1/3} P^{2/3}, \tag{11}$$

where m and P are the mass and orbital period of the orbiting body, M the total mass of the eclipsing binary, i the inclination to the line of sight of the planetary orbit, and c and G the speed of light and gravitational constant.

In equation (10), τ and ν are functions of t (time). The orbital period of an orbiting body is much greater than the difference in time from all other terms, so we use $t \approx P_0 E$ as a first order approximation.

4 FITTING ECLIPSE TIMES

In this section we first detail from where the eclipse timing data is obtained, and then present the results from the analysis using KIMA.

4.1 Data for HW Vir

We use archival data for HW Vir eclipse times (considering only the primary eclipse). We use the data from Brown-Sevilla et al. (2021), which collated data from Kilkenny, Marang & Menzies (1994), Lee et al. (2009), and Beuermann et al. (2012), as well as their own data. To this we add the data from Baran et al. (2018), Esmer et al. (2021),

[3]They may still be possible in reality, if we have a very eccentric orbit for the companion, and we observe it close to apastron (where the motion is slower)
[4]We do not claim that all four of the signals are indeed planets
[5]N_p meaning number of planets in the model

Downloaded from https://academic.oup.com/mnras/article/526/2/2241/7273133 by Health Services Management Centre Library user on 08 October 2024

Table 2. Division of the eclipse time data into *chunks*, the names of the *chunks* are specified as well as the corresponding epoch ranges included in each one.

Chunk	Epoch range
tier1	$0 \leq E < 40\,000$
tier2	$40\,000 \leq E < 80\,000$
tier3	$70\,000 \leq E$
tier1-2	$0 \leq E < 80\,000$
tier2-3	$40\,000 \leq E$
tier1–3	$E \leq 40\,000$ or $80\,000 \leq E$
full	$0 \leq E$

The data is effectively partitioned into thirds.

and Mai & Mutel (2022). Of the data reported in Baran et al. (2018), we find that the data taken with *SAAO* have a small offset of ∼80 s from the rest of the data sets (including the other data reported in the same publication). Since there is still good coverage without this, we exclude these data from our analysis.

We perform the analysis on the whole data set, but also divide it into smaller *chunks* to assess how consistent any signals that appear are. This way we can assess if, although the overall model does not have good predictive power, a subset of the signals might be predictably and consistently present. We divide the data set into *chunks* of approximately 1/3 and 2/3 the length of the whole data set, with epochs as shown in Table 2. The *chunk* 'tier3', is extended back an extra 10 000 epochs and overlaps with 'tier2'. The different *chunks* are also visualized alongside the data in the top panel of Fig. 4.

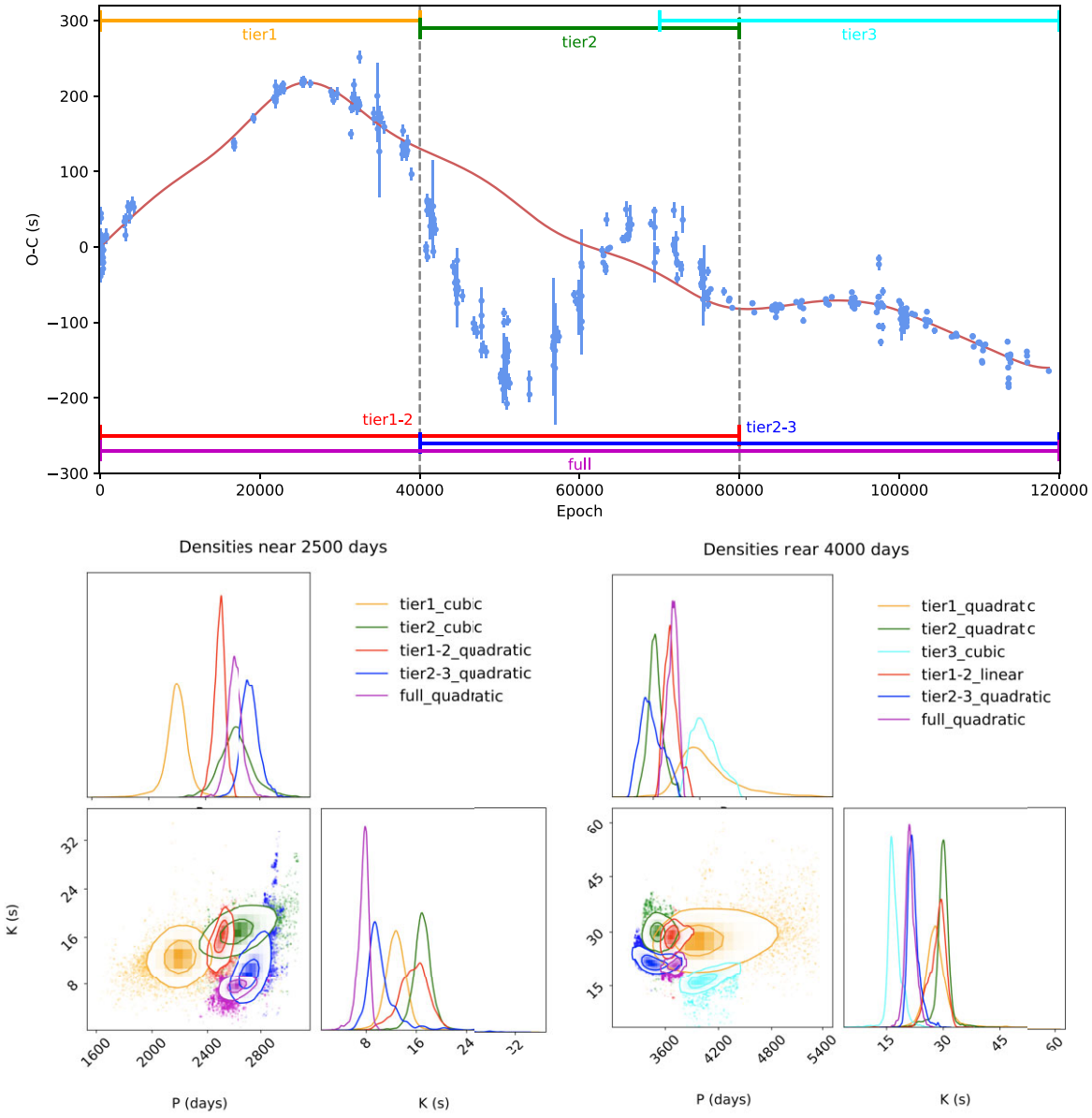


Figure 4. Top: Best-fitting solution from the analysis of *chunk* tier1-3, which is all the data except that which is between the dashed grey lines. The best-fitting model is shown in red, the full data set (including the middle *chunk* that was not included in the fit) is shown in blue. Highlighted in colour are the names and spans of data covered by the other *chunks*. The x-axis is the Epoch E as in equation (9). Bottom: Posterior density smoothed corner plots showing the period and semi-amplitude of signals found around 2500 d (left) and 4000 d (right). The different colours correspond to analysis of different *chunks* of the data being analysed.

Downloaded from https://academic.oup.com/mnras/article/526/2/2241/7273133 by Health Services Management Centre Library user on 08 October 2024

Table 3. Prior distributions for the nested sampling analysis.

Parameter	Unit	Prior distribution
Ephemeris parameters		
P_0	d	$\mathcal{N}(0.11672, 0.00001)$
$P_{t,0}$		$\mathcal{N}(0, 0.00001)$
$P_{tt,0}$	d^{-1}	$\mathcal{N}(0, 0.0000001)$
Planet parameters		
P	d	$\mathcal{LU}(500, 20000)$
K	s	$\mathcal{MLU}(0.1, 10000$
e		$\mathcal{K}(0.867, 3.03)$
ω	rad	$\mathcal{U}(0, 2\pi)$
ϕ_0	rad	$\mathcal{U}(0, 2\pi)$
Other parameters		
N_P		$\mathcal{U}(0, 3)*$
σ_{jit}	s	$\mathcal{MLU}(0.01, 1000)$

$\mathcal{N}$, $\mathcal{LU}$, $\mathcal{MLU}$, $\mathcal{K}$ refer to Normal, log-Uniform, Modified log-Uniform (with a knee and an upper limit), and Kumaraswamy distributions, each taking two parameters. ∗This prior for Np is used in all cases except the analysis of the full data set where instead the prior used is $\mathcal{U}(0, 6)$.

4.2 Results from eclipse timing variation fits

In this section we present the results from a reanalysis of the mid-eclipse time data, analysed using KIMA. The nested sampling implemented requires a prior distribution for each parameter, these are detailed in Table 3. The Kumaraswamy distribution (Kumaraswamy 1980) approximates the beta distribution, and the shape parameters as shown in Table 3 are those that Kipping (2013) argues best represent the distribution of exoplanetary eccentricities, based on exoplanets detected with the radial velocity method. The analysis is performed with each of a linear, quadratic, and cubic ephemeris for each *chunk* as well as for the whole data set.

4.2.1 Results from analysing different chunks

A LTTE signal due to an orbiting companion should to be coherent in time. The analysis of different *chunks*, using a Keplerian prescription, would therefore be expected to lead to posteriors that are consistent across *chunks*. Our analysis of the different *chunks* shows a lack of consistency and therefore casts doubts on the ETV signals being solely due to an orbiting companion (or more).

Throughout the analysis of the different *chunks* of data, recurring signals are seen around two periods: 4000 and 2500 d. Longer period (and higher amplitude) signals do exist in many of the *chunks*, however they are far from consistent.

To assess the consistency of the signals at the recurring periods, the clustering algorithm HDBSCAN (McInnes, Healy & Astels 2017) is used to identify clusters in the P–K plane from the KIMA posterior samples. The clusters are then visually associated with one of the two recurring periods or not. The lower panels of Fig. 4 show the clusters of posterior density around 2500 and around 4000 d from runs of KIMA on different *chunks* of data.[6] These are shown as corner plots (Foreman-Mackey 2016) between the period P and semi-amplitude K. While there is a cluster of posterior density around this period in each[7] of these runs, the periods and amplitudes of the signals vary between the runs.

[6]tier3 did not show signature of a detectable signal around 2500 d so only five *chunks* are shown

[7]tier3 notwithstanding

Table 4. Bayes Factors produced by KIMA when analysing the entire eclipsing timing data set.

Number of planets compared	Bayes Factor
1 : 0	$>1.8 \times 10^{308}$
2 : 1	1.8×10^{80}
3 : 2	4.0×10^{44}
4 : 3	1.1×10^{5}
5 : 4	2.1
6 : 5	1.5

The lack of consistency of these signals points to them not being due to a Keplerian LTTE orbit. These signals may then have a non-periodic or quasi-periodic source. If this is the case, then attempting to fit them with strictly periodic Keplerian signals is unideal. This is exemplified in the upper panel of Fig. 4, where we show the best-fitting model from the run where tier1–3 is analysed using a linear ephemeris. The best model, a sum of three Keplerian orbits, is woefully incorrect for the middle section. This shows how not only are Keplerian LTTE models not successful at predicting future eclipse times, but they are unsuccessful at interpolating.

In the future, a better approach might be to use Gaussian Processes (Rasmussen & Williams 2006) to model the shorter eclipse timing variation signals. These tools are particularly good at modelling quasi-periodic functions to stellar activity for instance (in photometry and spectroscopy; Faria et al. 2016; Barros et al. 2020) and would seem appropriate in the case of HW Vir.

4.2.2 Results from analysing the full data set

We now show the results from an analysis of the full data set. We allow KIMA to fit freely up to $N_p = 6$ signals along with a quadratic ephemeris. One advantage of using KIMA is its ability to assess the number of signals present using Bayesian model comparison. In this case a four-signal solution is favoured as it is the highest number of planets with a significant Bayes Factor over a model with one fewer planet. The respective Bayes Factors can be seen in Table 4.

Four signals is more than most other analyses which only find up to two signals. The two signals already discussed (around 2500 and 4000 d) are both present in the best-fitting solution. We know this because a large fraction of the posterior sample congregate at these two orbital periods (as shown in the upper panel of Fig. 3). The other two signals are not nearly as well constrained and do not correspond to any clear over-density in the posterior, likely because these are longer signals that have not had the chance to repeat yet, making their parameters uncertain.

Past analyses have regularly identified a signal corresponding to the one we find around 4000 d (e.g. Beuermann et al. 2012; Esmer et al. 2021); however, none have identified a signal near 2500 d.

We do not consider any formal stability arguments. Many previous studies have found that multiple-planet solutions are unstable, and since we have a strong reason to doubt that the detected signals within the eclipsing times are produced by an orbiting planet, we feel a stability analysis is meaningless. The upper-left diagram of Fig. 5 shows the orbital configuration of planets corresponding to all four signals. The inner two of them are reasonably circular, the outer two are more eccentric, and the outermost crosses the other orbits. Clearly not all four signals can be from orbiting bodies. Ignoring the outermost, eccentric orbit, the lower-left diagram in Fig. 5 shows the orbital configuration of planets corresponding to the inner three signals. While these three signals do not cross into each others orbits,

Downloaded from https://academic.oup.com/mnras/article/526/2/2241/7273133 by Health Services Management Centre Library user on 08 October 2024

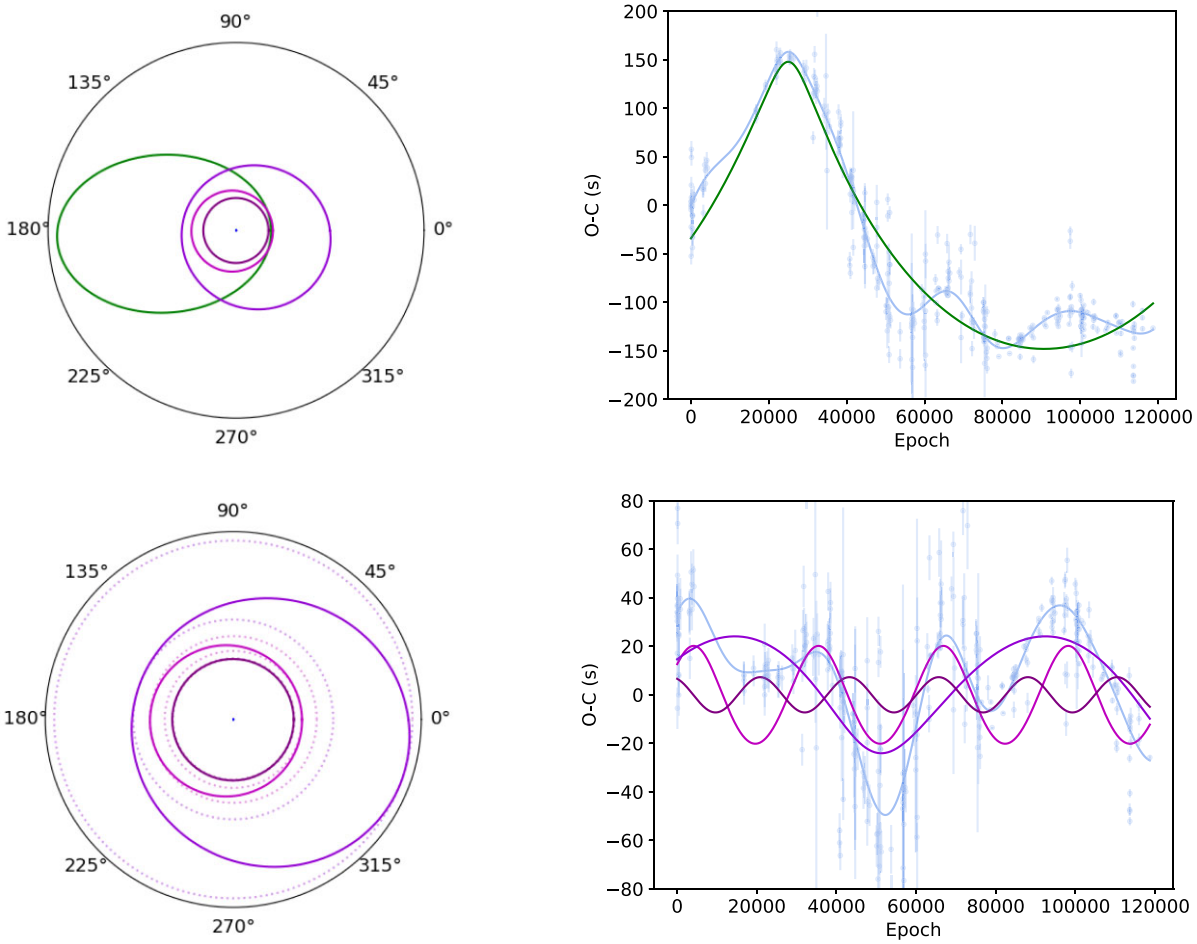


Figure 5. Orbital configurations shown on the left. Top left: All four signals from the best-fitting model obtained from the analysis of the whole eclipse timing data set. Bottom left: The eccentric outer orbit is removed and the remain three signals are shown along with the dashed lines showing circular orbits at apo- and peri-centre. Best-fitting model obtained from the analysis of the whole eclipse timing data set as well as the data itself is shown on the right (ephemeris removed). Top right: A four signals included, the most massive is shown in green and the sum of all four in blue, this signal in green is the one we claim as the most likely candidate for being a planet. The x-axis is the Epoch E as in equation (9). Bottom right: The inner three Keplerian functions are shown with the sum of these three in blue. The data is represented with the fourth large-amplitude signal removed. These three signals are most likely not of planetary nature.

they present a very compact configuration, that would likely not be stable either.

The astrometric tangential velocity implies it is more likely than not there is one orbiting companion to the HW Vir binary. Of the four signals, if one is of planetary nature, we favour the fourth and outermost signal. The analysis reported in Section 4.2.1 casts strong doubts on the inner two signals since they appear only quasi-periodic. The third signal has too long a period to assess the consistency with the chunking method, but its 'orbital parameters' are similar to the inner two signals with a small amplitude and mild eccentricity. Compared to all others, the outermost signal lies closest to where the median value of the proper motion anomaly predicts (the dark line on Fig. 3). We note that this candidate planet signal is of a similar mass and period to components of the solutions by Esmer et al. (2021) and Brown-Sevilla et al. (2021). These all likely correspond to the same signal but vary in orbital period due to the data having not covered multiple cycles yet.

The plots on the right-hand side of Fig. 5 show the model curves for each of the signals along with the combined model and data. The upper right panel shows the full model in the background and the outer orbit Keplerian signal in green, the lower right panel shows the other three individual signals in shades of purple as well as their sum in the background. The three signals shown together in the lower right panel are those we claim to be most likely not produced by a planet (especially the two at shorter periods), these might be better modelled together as a Gaussian Process.

While we know that this four-component solution cannot correspond to four orbiting companions, to allow future comparison with our work, we still report the parameters of the orbits as if they were real. The parameters are detailed in Table 5. The uncertainties associated with the parameters of the inner two orbits are well-defined as they are associated with clear clusters of posterior density (clustering using HDBSCAN is also used here). The outer two orbits do not belong to large clusters, so while they can be associated with clusters found by HDBSCAN the uncertainty on the parameters extracted from these are likely underestimated. This is because there has not been enough data for the signal to repeat. In the case of the outer signal the data has not even covered a whole phase yet. This also causes a degeneracy between the orbital parameters of

Downloaded from https://academic.oup.com/mnras/article/526/2/2241/7273133 by Health Services Management Centre Library user on 08 October 2024

Table 5. Parameters from the analysis of the full data set, with a quadratic ephemeris.

Parameter	Value	Units
Assumed parameters		
$M_0 + M_1$	0.54 ± 0.0089	$M_\odot$
Binary parameters		
P_0	$0.116719590^{+1.0e-8}_{-1.8e-8}$	d
$\dot{P}_0$	$-1.03e-11^{+4.4e-12}_{-2.0e-12}$	d/d
Keplerian parameters		
P_1	$2\,612^{+43}_{-41}$	d
K_1	$7.66^{+0.60}_{-0.81}$	s
e_1	<0.1	
$\omega_1 + \phi_{0,1}$ [a]	1.97 ± 0.38	rad
$M_1(\sin i_1)$	$2.88^{+0.22}_{-0.29}$	M_{Jup}
P_2	$3\,710^{+58}_{-76}$	d
K_2	$21.2^{+1.5}_{-1.2}$	s
e_2	$0.089^{+0.035}_{-0.038}$	
ω_2	$1.74^{+0.54}_{-0.44}$	rad
$T_{per,\,2}$	$2\,442\,500^{+380}_{-350}$	BJD
$M_2(\sin i_2)$	$6.34^{+0.45}_{-0.36}$	M_{Jup}
P_3 [c]	$8\,400 \pm 1600$	days
K_3 [c]	23 ± 10	s
e_3 [b]	<0.45	
ω_3 [b]	4.5 ± 1.3	rad
$T_{per,3}$ [b]	$2\,443\,600 \pm 2000$	BJD
$M_3(\sin i_3)$ [c]	4.0 ± 1.9	M_{Jup}
P_4 [c]	$15\,600 \pm 3500$	d
K_4 [c]	148 ± 45	s
e_4 [b]	0.6867 ± 0.013	
ω_4 [b]	$1.77^{+0.06}_{-1.4}$	rad
$T_{per,4}$ [b]	$2\,433\,100^{+140}_{-120}$	BJD
$M_4(\sin i_4)$ [c]	$17.4^{+6.5}_{-5.7}$	M_{Jup}
Other fit parameters		
Jitter	0.92 ± 0.23	s
T_0	2 445 730.556669	BJD

The keplerian parameters for each signal is shown as if it was keplerian LTTE orbit. [a]For the circular orbit we combine the ω and ϕ parameters together since otherwise they are extremely correlated and no information can be gained. [b]For the two outer signals, the posterior density is not well constrained so clusters around the best-fitting solutions are used for some of the parameters. We note the uncertainties are likely too small to represent the true uncertainty in the model. [c]For these periods and amplitudes, the uncertainty is reported as the difference between the value of the parameter when a linear ephemeris is fit and when a quadratic ephemeris is fit. The median of the posterior density cluster from the quadratic ephemeris fit is retained as the quoted value. The mass distribution is the propagated in a Monte-Carlo way.

the outer signals and the ephemeris terms. To partly address the underestimation, we take two analysis runs with KIMA, one using a linear ephemeris and one using a quadratic. The uncertainty on the amplitude, period are then taken as the difference between the values from the two models, with the quoted value remaining the value from the analysis with a quadratic ephemeris. This is to keep the whole table representing a coherent solution. Corresponding planetary masses for the outer two signals are then produced in a monte-carlo way. It should be noted this is therefore not a statistically derived uncertainty, but is a rough representation of the uncertainty from the fitting procedure.

5 DISCUSSION AND CONCLUSION

Our analysis of the eclipse times of HW Vir does not find a single conclusive solution. This is in agreement with past work since every published solution has subsequently diverged from new data acquired afterwards (e.g. Pulley et al. 2022). We have shown that there are two strong periodicities in the full data set which are also seen independently in some of the smaller *chunks*. However, though signals can be found near these periods in most of the *chunks*, their posterior distributions in P and K are not completely coherent in time, nor statistically consistent with one another. While past analyses have identified the periodicity around 4000 d, none have identified the signal around 2500 d.

We have presented our solution from the analysis of the whole eclipse timing data set performed in a fully Bayesian way using nested sampling within KIMA. This four-component model includes signals at both of the strong periodicities. It is abundantly clear that not all four of the signals in this model are due to orbiting companions; in fact it is possible that none of them are. There likely must be some other mechanism involved for the variation in eclipse times, one possibility being a magnetic effect which is not yet fully understood (e.g. Lanza 2020). We suggest that using a Keplerian prescription for non-planetary, quasi-periodic signals like what these appear to be is insufficient and that using a Gaussian Process method may work better (as in Faria et al. 2016). We propose that of the four signals, if one is produced by a planet, it is most likely to be the outermost one. This signal also best fits the astrometric evidence and has a signature that looks most different to the other three.

We have applied the proper motion anomaly method to V471 Tau and confirmed the non-detection of a previously proposed orbiting brown dwarf. We have also applied it to HW Vir and shown that there is a tentative 2σ signal of an acceleration due to an orbiting body. From the upper limit this poses, we can discount some previously proposed companions which are too massive to be consistent with the proper motion anomaly. Comparing the astrometric signal with the four signals we extract from the eclipse timings in Fig. 3, we find that the outermost signal is the most consistent. If correct this corresponds to a 17 M_{jup}, 16 000 d, highly eccentric companion. Thanks to additional data, a longer baseline, and an improved astrometric solution, the full epoch astrometry from *Gaia* will (circa 2025) likely be able to help resolve whether the HW Vir binary is indeed host to an orbiting circumbinary companion. The *Gaia* baseline will still be much shorter than the most likely planet's orbital period, so while the whole period would not be covered, astrometry may still tell us whether or not such a planet exists, independently of the ETVs. This will help identify which (if any) of the varying eclipse timing signals is actually caused by that orbiting body. In turn, this will help isolate the functional form of the potential new physics causing the other signals (for instance the 2500 and 4000 d signals). As described in Sahlmann et al. (2015), thanks to *Gaia*'s final solution, other post-common envelope circumbinary systems will be solved astrometrically with our paper being the first attempt at doing so.

ACKNOWLEDGEMENTS

This paper is dedicated to the memory of Tom Marsh whose kindness, curiosity and many discussions inspired much interest in circumbinary planets, and more specifically to those in post-common envelope systems.

We thank Annelies Mortier and Lalitha Sairam for productive discussions and insightful comments on this work.

Downloaded from https://academic.oup.com/mnras/article/526/2/2241/7273133 by Health Services Management Centre Library user on 08 October 2024

This research leading to these results is supported by two grants from the European Research Council (ERC) under the European Union's Horizon 2020 research and innovation programme (grant agreements no. 803193/BEBOP and 951549/UniverScale).

The computations described in this paper were performed using the University of Birmingham's BlueBEAR HPC service.

DATA AVAILABILITY

Proper motion anomaly and eclipse timing data are available from the original publications cited in this work and described in Sections 2 and 4.1. The version of KIMA used to analyse the eclipse timing data is available at https://github.com/TomAB99/kima/tree/etvs

REFERENCES

Applegate J. H., 1992, ApJ, 385, 621
Bachelet E. et al., 2012, ApJ, 754, 73
Baran A. S. et al., 2018, MNRAS, 481, 2721
Barros S. C. C., Demangeon O., Díaz R. F., Cabrera J., Santos N. C., Faria J. P., Pereira F., 2020, A&A, 634, A75
Beavers W. I., Herczeg T. J., Lui A., 1986, ApJ, 300, 785
Beuermann K., Dreizler S., Hessman F. V., Deller J., 2012, A&A, 543, A138
Brandt T. D., 2021, ApJS, 254, 42
Brewer B. J., Foreman-Mackey D., 2018, J. Stat. Softw., 86, 1
Brown-Sevilla S. B. et al., 2021, MNRAS, 506, 2122
Columba G., Danielski C., Dorozsmai A., Toonen S., Lopez Puertas M., 2023, A&A, 675, A156
Danielski C., Korol V., Tamanini N., Rossi E. M., 2019, A&A, 632, A113
Doyle L. R. et al., 2011, Science, 333, 1602
ESA, 1997, ESA Special Publication, 1200 Noordwijk, Netherlands: ESA Publications Division
Esmer E. M., Baştürk Ö., Hinse T. C., Selam S. O., Correia A. C. M., 2021, A&A, 648, A85
Faria J. P., Haywood R. D., Brewer B. J., Figueira P., Oshagh M., Santerne A., Santos N. C., 2016, A&A, 588, A31
Faria J. P., Santos N. C., Figueira P., Brewer B. J., 2018, J. Open Source Softw., 3, 487
Farihi J. et al., 2022, MNRAS, 511, 1647
Foreman-Mackey D., 2016, J. Open Source Softw., 1, 24
Gaia Collaboration, 2018, A&A, 616, A1
Gaia Collaboration, 2021, A&A, 649, A1
Guinan E. F., Ribas I., 2001, ApJ, 546, L43
Hardy A. et al., 2015, ApJ, 800, L24
Irwin J. B., 1952, ApJ, 116, 211
Kass R. E., Raftery A. E., 1995, J. Am. Statist. Assoc., 90, 773
Kervella P., Arenou F., Mignard F., Thévenin F., 2019, A&A, 623, A72
Kervella P., Arenou F., Thévenin F., 2022, A&A, 657, A7
Kilkenny D., Marang F., Menzies J. W., 1994, MNRAS, 267, 535
Kipping D. M., 2013, MNRAS, 434, L51
Koester D., Gänsicke B. T., Farihi J., 2014, A&A, 566, A34
Kostov V. B. et al., 2020, AJ, 159, 253
Kumaraswamy P., 1980, J. Hydrol., 46, 79
Lanza A. F., 2020, MNRAS, 491, 1820
Lee J. W., Kim S.-L., Kim C.-H., Koch R. H., Lee C.-U., Kim H.-I., Park J.-H., 2009, AJ, 137, 3181
McInnes L., Healy J., Astels S., 2017, J. Open Source Software, 2, 205
Mai X., Mutel R. L., 2022, MNRAS, 513, 2478
Mesa D. et al., 2022, A&A, 665, A73
Muirhead P. S., Nordhaus J., Drout M. R., 2022, AJ, 163, 34
Mustill A. J., Marshall J. P., Villaver E., Veras D., Davis P. J., Horner J., Wittenmyer R. A., 2013, MNRAS, 436, 2515
Paczyński B., 1967, Acta Astron., 17, 287
Pulley D., Sharp I. D., Mallett J., von Harrach S., 2022, MNRAS, 514, 5725
Rappaport S., Verbunt F., Joss P. C., 1983, ApJ, 275, 713
Rasmussen C. E., Williams C. K. I. , 2006, Gaussian Processes for Machine Learning. MIT Press
Rickman E. L. et al., 2022, A&A, 668, A140
Sahlmann J., Triaud A. H. M. J., Martin D. V., 2015, MNRAS, 447, 287
Skilling J., 2006, Bayesian Analysis, 1, 833
Standing M. R. et al., 2022, MNRAS, 511, 3571
Standing M. R. et al., 2023, Nature Astron., 7, 702
Triaud A. H. M. J. et al., 2022, MNRAS, 511, 3561
Vanderburg A. et al., 2015, Nature, 526, 546
Vanderburg A. et al., 2020, Nature, 585, 363
Wolszczan A., Frail D. A., 1992, Nature, 355, 145

This paper has been typeset from a TEX/LATEX file prepared by the author.

Downloaded from https://academic.oup.com/mnras/article/526/2/2241/7273133 by Health Services Management Centre Library user on 08 October 2024

© 2023 The Author(s).
Published by Oxford University Press on behalf of Royal Astronomical Society. This is an Open Access article distributed under the terms of the Creative Commons Attribution License (http://creativecommons.org/licenses/by/4.0/), which permits unrestricted reuse, distribution, and reproduction in any medium, provided the original work is properly cited.

5.2 Post common-envelope binaries with *Gaia*

5.2.1 Previously claimed planets

Circumbinary planets and planetary-mass objects have been claimed orbiting post common-envelope binaries using eclipse timing variations. These are for the most part controversial, their existence being called into question. The planetary solutions do not predict future data well and are often in unstable configurations (Pulley et al., 2022). Various magnetic field-based mechanisms have been posited as potential other explanations for the eclipse timing variations (e.g. Applegate, 1992; Lanza, 2020). See Sections 1.6.2 and 5.1 for more details. As stated in Section 5.1.5 (Section 5 in the paper), *Gaia* astrometry should have the ability to help resolve the question of their existence for HW Vir and some of the other claimed systems.

I have collated and tabulated all such claimed planets that I was able to locate in the literature. This is shown in Table 5.6. A large portion of this is based on the table in Baştürk et al. (2023), supplemented by other systems not included in that table[1]. Only systems where the third body is possibly below stellar mass are included, but others exist with a more massive tertiary object. Table 5.6 shows the parameters for each system required to calculate the *Gaia* signal-to-noise ratio of each planet. Uncertainties are not provided as in many cases the mass or period of the planet is uncertain, varying, or an estimate.

The *Gaia* signal-to-noise ratio is calculated as in Section 3.4 for both *Gaia* DR4 and DR5 for each claimed planet. The fraction of the orbit that will be covered by the dataspan of DR4 and DR5 is also calculated. The signal-to-noise ratio and coverage are shown in Table 5.6 for *Gaia* DR5. This information is also displayed for DR4 and DR5 in Figure 5.6 along with the distance to each system. Figure 5.6 reveals the expected trend for *Gaia* data that the systems with the high signals are those that are nearby, with sensitivity decreasing as distance increases. It is also clear that a significant number of these claimed planets will have a large *Gaia* signal-to-noise ratio, but not many of these will have a full orbit covered.

[1] I expect that this list is not exhaustive

Table 5.6: Table of post common-envelope binaries with planetary-mass companions claimed from eclipse timing variations. Those in bold are the 12 that meet the relaxed criteria for detection with *Gaia*. [(1)] There is evidence against its existence from Hardy et al. (2015) and Section 5.1.

System name	Publication	M_{bin} [$M_\odot$]	Distance [pc]	M_{pl} [M_{Jup}]	P_{pl} [days]	*Gaia* DR5 SNR	*Gaia* DR5 Coverage
HW Vir	Section 5.1	0.54	173	17.8	15000	531.7	0.26
DE CVn	Han et al., 2018	0.92	31	11.5	4100	584.	0.93
NN Ser	Özdönmez et al., 2023	0.65	521	2.6	3000	2.0	1.28
NN Ser	Özdönmez et al., 2023	0.65	521	10.5	7300	14.6	0.52
RR Cae	Rattanamala et al., 2023	0.62	21	3.1	6000	336.2	0.64
2M1938+4603/Kepler-451	Esmer et al., 2022	0.6	400	1.9	43	0.5	89.13
2M1938+4603/Kepler-451	Esmer et al., 2022	0.6	400	2.0	410	2.2	9.35
2M1938+4603/Kepler-451	Esmer et al., 2022	0.6	400	1.7	1460	4.4	2.62
NSVS 14256825/V1828 Aql	Wolf et al., 2021	0.53	753	3.0	1280	4.0	2.99
NSVS 14256825/V1828 Aql	Wolf et al., 2021	0.53	753	8.4	2500	17.0	1.53
NY Vir	Esmer et al., 2023	0.6	595	2.1	3200	5.7	1.2
NY Vir	Esmer et al., 2023	0.6	595	4.2	8400	21.5	0.46
DP Leo	Baştürk et al., 2023	0.7	305	6.3	10500	5.4	0.36
HU Aqr	Qian et al., 2011	1.08	191	6.3	2370	8.6	1.62
HU Aqr	Qian et al., 2011	1.08	191	4.7	4360	9.7	0.88
QS Vir	Baştürk et al., 2023	1.28	50	6.7	2870	114.1	1.34
V808 Aur	Leichty et al., 2024	0.95	214	7.1	4100	7.8	0.93
HT Cas	Han et al., 2023	0.7	142	13.6	11000	97.3	0.35
CM Dra	Deeg et al., 2008	0.44	15	1.0	6760	250.4	0.57
V470 Cam	Sale et al., 2020	0.61	1267	28.3	2870	22.6	1.34
V470 Cam	Sale et al., 2020	0.61	1267	12.4	4840	14.2	0.79
KIC 10544976	Baştürk et al., 2023	1.0	517	13.6	6000	3.3	0.64
OY Car	Baştürk et al., 2023	0.75	91	8.9	5110	83.2	0.75
V2051 Oph	Baştürk et al., 2023	0.93	109	7.6	7880	77.2	0.49
V893 Sco	Baştürk et al., 2023	0.88	124	10.	3720	78.6	1.03
DV Uma	Baştürk et al., 2023	1.3	387	27.2	6420	8.5	0.6
FBS 1531+381	Baştürk et al., 2023	0.49	525	1.5	3830	6.3	1.0
SDSS J143547.87+373338.5	Wolf et al., 2021	0.71	184	17.8	4770	38.9	0.8
GK Vir	Baştürk et al., 2023	0.62	493	1.0	8760	1.4	0.44
UZ For	Baştürk et al., 2023	0.84	239	3.6	2120	3.8	1.81
UZ For	Baştürk et al., 2023	0.84	239	10.5	5400	20.7	0.71
KIC 3853259	Borkovits et al., 2016	2.0	455	10.5	330	3.2	11.61
V471 Tau	Guinan and Ribas, 2001 [(1)]	1.61	48	41.9	11130	1809.2	0.34

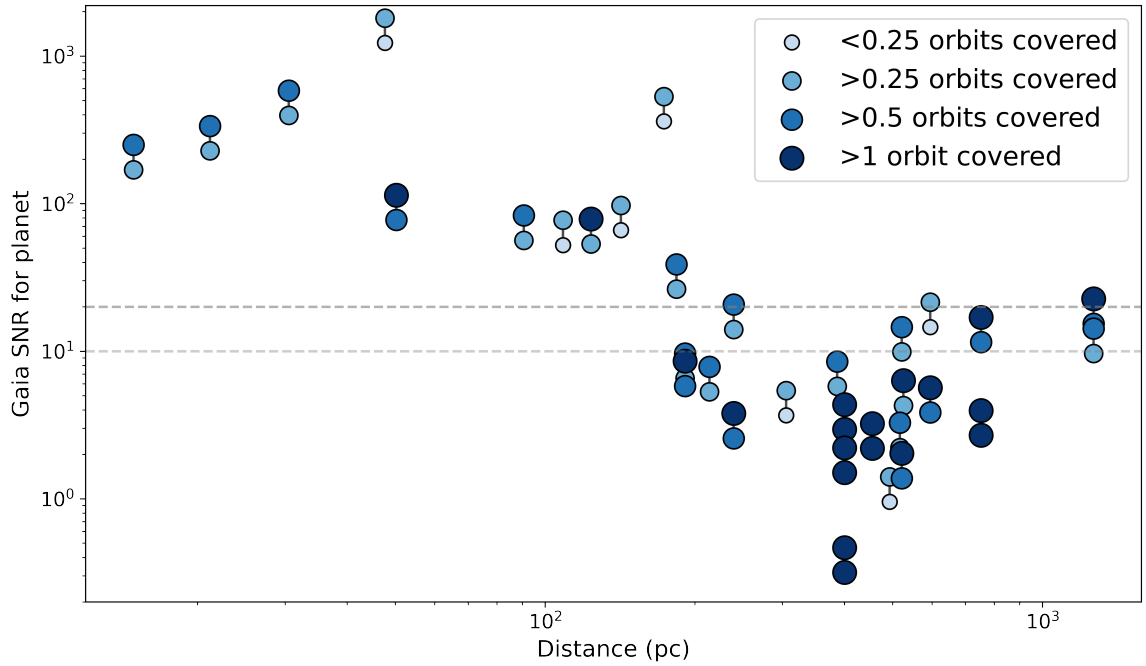


Figure 5.6: *Gaia* signal-to-noise ratio vs distance for the claimed planets orbiting post common-envelope binaries shown in Table 5.6. Each has two markers showing the signal-to-noise ratio for *Gaia* DR4 and DR5, with the size and darkness of the marker showing how much of the orbit of the claimed planet would have been covered. Dashed lines show the strong and weak detection thresholds of 20 and 10.

The restriction that the signal-to-noise ratio cut should be 20 and that one whole orbit is covered (as used in Section 3.4) can be relaxed since, these have known orbits which can be tested against. While only three claimed planets would meet the strict criteria in *Gaia* DR5, 12 claimed planets would meet the relaxed criteria of SNR $>$ 10 and an orbital coverage above 0.5. These 12 planets are highlighted in bold in Table 5.6. The most strongly constrained system will be QS Vir (Qian et al., 2010). It is uncertain exactly how well the *Gaia* astrometry will constrain partial orbits, it should be investigated before or during the application of *Gaia* data to these systems.

5.2.2 Sensitivity to a population

These claimed planets are orbiting post common-envelope binaries that have had eclipses measured over long timespan (typically in the 10s of years). More post common-envelope binaries

exist where planets have not been claimed, or that do not eclipse. I now analyse the sensitivity of *Gaia* to planet around a sample of post common-envelope binaries. The catalogue of potential post common-envelope binaries is taken from Kruckow et al. (2021). The original 848 from the catalogue are filtered to only conserve those with Gmag values in *Simbad*[2] and with measured masses for primary and secondary[3]. The filtering leaves 432 systems.

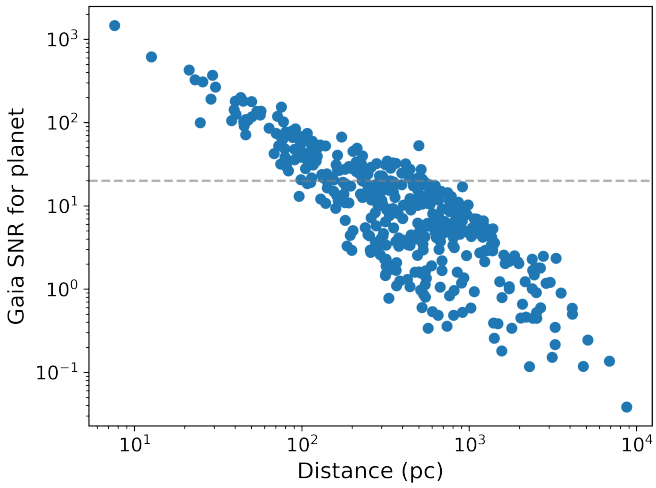


Figure 5.7: The *Gaia* signal-to-noise ratio that would be acheived by a 6.5 $M_{\rm Jup}$ planet on a 3000 day orbit for each system in the post common-envelope binary catalogue. Horizontal dashed line shows the detection sensitivity threshold of SNR = 20.

Figure 5.7 shows the *Gaia* signal-to-noise ratio that would be achieved by a 6.5 $M_{\rm Jup}$ planet on a 3000 day orbit for each system in the catalogue. These are the approximate parameters of the claimed planet orbiting QS Vir (see Table 5.6). In this case there would be sensitivity to such a planet in 127 out of the 432 systems (29%). Sensitivity here is calculated strictly as in Section 3.4 with a signal-to-noise ratio cut of 20. Repeating this calculation for a series of different masses and orbital periods produces Figure 5.8. Only periods less than the timespan of *Gaia* DR5 are considered.

The results in Figure 5.8 reveals that a large population of planetary-mass circumbinary objects existing orbiting post common-envelope binaries would be detectable in this sample. Therefore *Gaia* and in particular *Gaia* DR5 will be able to constrain the population of high-mass

[2] https://simbad.u-strasbg.fr/simbad/sim-fid
[3] only a value is needed, even if there are no uncertainties

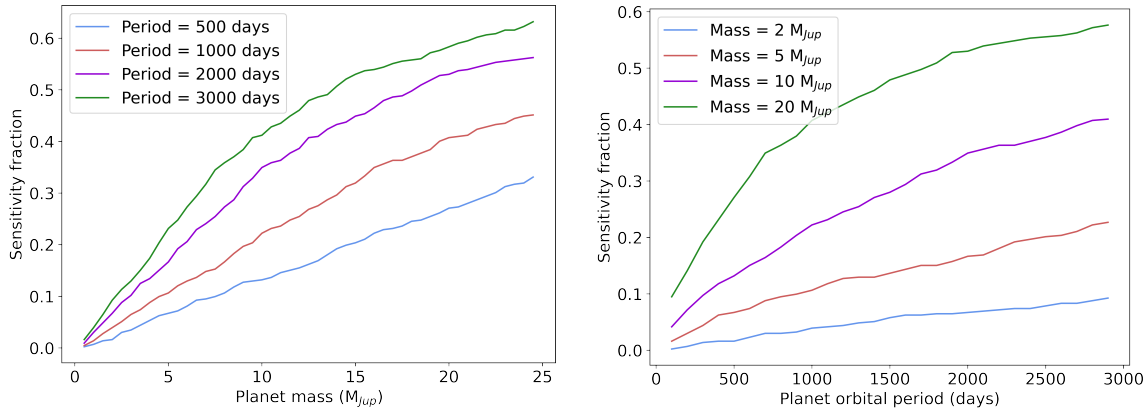


Figure 5.8: *Gaia* DR5 sensitivity to planets of varying mass and orbital period for the catalogue of post common-envelop binaries. Left: range of masses for 4 different periods. Right: range of periods for 4 different masses.

planets orbiting post common-envelope binaries, and assess how common systems such as many of those claimed planets in Table 5.6 actually are.

If planets are found to truly exist orbiting post common-envelope binaries, there is then the question of whether these are planets that survived the evolution of the binary star, or planets that formed in a second generation disc. The masses of the claimed companions seen in Table 5.6 are very large, mostly in the brown dwarf regime. Based on the BEBOP results (see Section 4.3.1) circumbinary brown dwarf companions do exist, but it is hard to say yet whether in high enough numbers to produce the full population claimed orbiting post common-envelope binaries. *Gaia* will likely constrain the occurrence of circumbinary brown dwarfs well and enable this comparison to be made. As seen in Section 5.2.1, *Gaia* will be sensitive to around 1/3 of the claimed planets (in DR5) which is enough to test how reliable the eclipse timing variations are for detecting planets, as if all 12 are confirmed or all 12 refuted these would give strong conclusions on their reliability.

Chapter 6

Apsidal precession: a powerful predictive tool

In this Chapter, I investigate the use of measuring the apsidal precession of a binary as a diagnostic tool for circumbinary planets. In Section 6.1, I present its use to constrain the mutual inclination of a circumbinary system by inferring a planet candidate on a polar circumbinary orbit. Section 6.2 provides a disucssion of how apsidal precession measurements can be made, what detections and constraints on apsidal precession from the BEBOP sample can tell us, and how apsidal precession can be used to compile a catalogue of candidate circumbinary planets based only on existing archival data.

6.1 Evidence for a polar circumbinary exoplanet orbiting a pair of eclipsing brown dwarfs

The following is a paper I first authored on the system 2MASS J15104786-2818174 (2M1510) analysing the radial velocity data, detecting a retrograde apsidal precession. Ruling out other causes, the retrograde apsidal precession is attributed to a perturbing planet on a polar orbit. This paper was published in Science Advances (Baycroft et al., 2025).

This was a serendipitous discovery. 2M1510 is a binary brown dwarf which was discovered based on a single eclipse in 2017 (which itself was serendipitous) from SPECULOOS (Triaud et al., 2020). Radial velocities were obtained at the time using UVES spectra. More UVES spectra were obtained recently in order to refine the characterisation of the binary, and to deploy `DOLBY-SD` (see Chapter 3) on an ultracool binary. In analysing the radial velocities obtained from `DOLBY-SD` with the BINARIESmodel of `kima`, I noticed that a negative apsidal precession was favoured. This led to an investigation of what could cause such a result and eventually to this paper.

Lalitha Sairam performed the radial velocity reduction using `DOLBY-SD`, Alexandre Correia and I performed the derivation of the spin-induced precession formulae. Amaury Triaud and Lalitha Sairam led the observing proposals to obtain UVES data. I developed the N-body fitting code, performed the radial velocity analyses presented, and wrote the manuscript.

Since the acceptance of the paper, I have come across some pieces of information that are relevant to this system and that had been missed. First is that there is another similar system with a polar companion. VHS 1256 (Dupuy et al., 2023) is a binary consisting of two likely brown dwarfs with total mass $M_{\rm bin} = 0.141 \pm 0.008\,M_{\odot}$ and a polar orbiting companion of mass either $12 \pm 0.1\,M_{\rm Jup}$ or $16 \pm 0.1\,M_{\rm Jup}$. This other example could imply that the polar planet candidate in 2M1510 is similarly a massive object at or near the planet brown dwarf boundary. In fact, in (Calissendorff et al., 2019) a companion is detected at 4 AU from the central object in 2M1510 with a predicted mass of $17.68^{+4.2}_{-2.1}\,M_{\rm Jup}$. This is a larger separation and/or lower mass that is expected from the work in the paper below, which assumes a circular orbit. Figure 6.1 shows the precession rate induced by a strictly polar planet of the mass found by Calissendorff et al. (2019) for a range of eccentricities and apocentre distances. This is calculated using Equation A5 from Section 2.2.7. To bring consistency between the two measurements, an eccentricity of $e > 0.5$ is required.

If systems consisting of a stellar binary with a polar circumbinary companion are typical across the stellar mass domain, it would be surprising that the best examples so far are in systems where the binary consists of two brown dwarfs. If 2M1510 follows the example of VHS 1256,

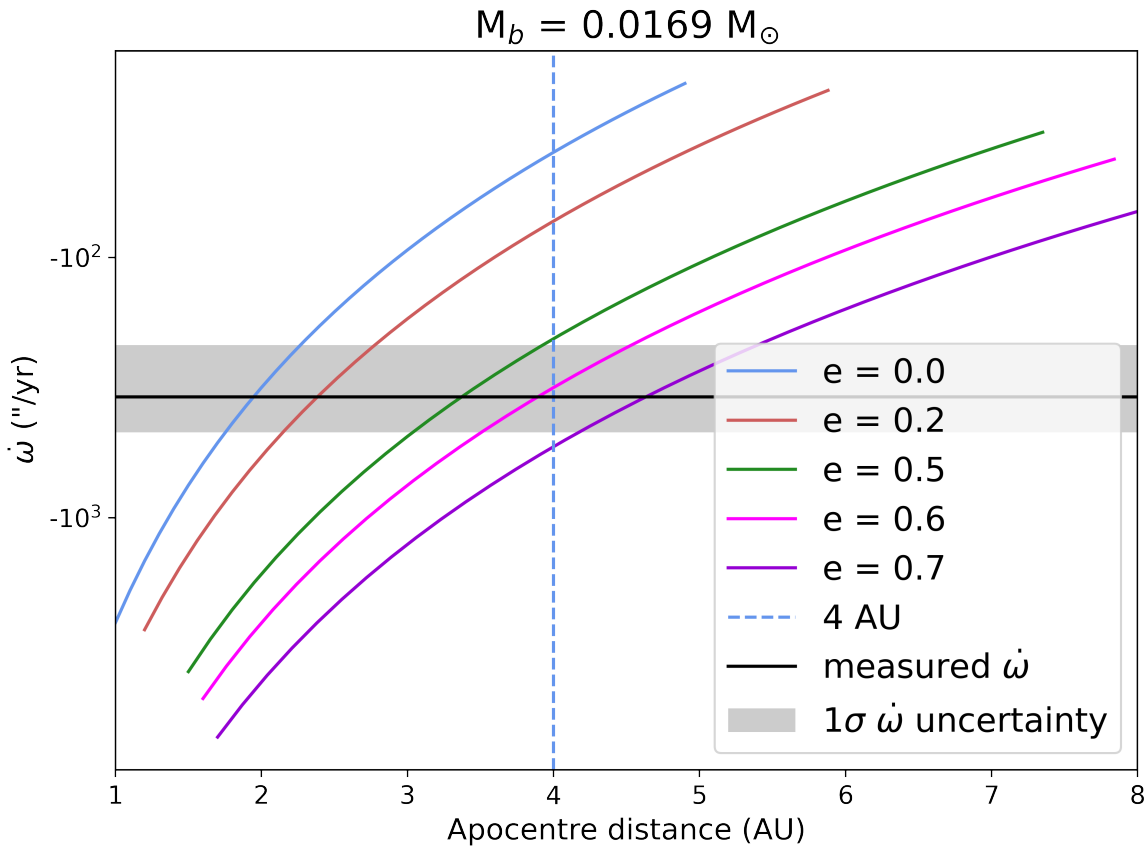


Figure 6.1: Apsidal precession rate induced by a polar companion with $m = 17.7\,M_{\rm Jup}$ for a range of eccentricities and apocentre distances. Line at 4 AU is the separation at which the companion was observed by Calissendorff et al. (2019).

such massive polar companions might therefore be a relatively common output of binary brown dwarf formation. Another fact missed in the paper is that it had been predicted that the best type of binary for planets to be able to form in a polar configuration, and therefore the type of binary most suited to the discovery of polar circumbinary planets is an equal-mass binary with moderate ($e \sim 0.4$) eccentricity (Cuello and Giuppone, 2019). Very few of the BEBOP systems fall into this category whereas 2M1510 does.

The paper discusses the difference between librating and circulating circumbinary orbits, this is introduced in Section 1.6.1. Circulating orbits are those where the angular momentum vector of the planet precesses around the angular momentum vector of the binary, and librating orbits are those where the angular momentum vector of the planet precesses around the eccentricity vector of the binary. The two states are seen in phase space in Figure 6.5 (Figure 4 in the

paper). These dynamical states and the potential alignment of initially misaligned circumbinary discs to polar or coplanar states are seen in simulations of both protoplanetary discs around stellar binaries (Zanazzi and Lai, 2018) and discs around black hole binaries (Aly et al., 2015). Mechanisms exist for circumbinary discs to be initially misaligned or made to misalign very early on in their lifetime. Simulations of dense star forming regions contain discs being destroyed and reformed or altered strongly (e.g. Bate, 2018). Additionally a stellar flyby could result in a misaligned disc, which does not necessitate a very dense star-forming environment.

Evidence for a polar circumbinary exoplanet orbiting a pair of eclipsing brown dwarfs

Evidence for a polar circumbinary exoplanet

Thomas A. Baycroft[1*], Lalitha Sairam[1,2], Amaury H.M.J. Triaud[1]

Alexandre C.M. Correia[3,4]

[1]School of Physics and Astronomy, University of Birmingham, Edgbaston, Birmingham, B15 2TT, United Kingdom.

[2]Institute of Astronomy, University of Cambridge, Madingley road, Cambridge, CB3 0HA, United Kingdom.

[3]CFisUC, Departamento de Fisica, Universidade de Coimbra, 3004-516 Coimbra, Portugal.

[4]IMCCE, UMR8028 CNRS, Observatoire de Paris, PSL Universite, 77 avenue Denfert-Rochereau, 75014 , Paris, France.

[*]Corresponding author. Email: txb187@bham.ac.uk

One notable example of exoplanet diversity is the population of *circumbinary planets*, which orbit around both stars of a binary star system. There are so far only 16 known circumbinary exoplanets, all of which lie in the same orbital plane as the host binary. Suggestions exist that circumbinary planets could also exist on orbits highly inclined to the binary, close to 90°, *polar* orbits. No such planets have been found yet but polar circumbinary gas and debris discs have been observed and if these were to form planets then those would be left on a polar orbit. We report strong evidence for a polar circumbinary exoplanet, which orbits a close pair of brown dwarfs which are on an eccentric orbit. We use radial-velocities to measure a retrograde apsidal precession for the binary, and show that this can only be attributed to the presence of a polar planet.

Using the dynamics of the 3-body problem, a planet orbiting at an angle close to 90 degrees

from a binary orbit is inferred.

1 Introduction

Sixteen circumbinary exoplanets have been detected to-date. The majority were identified using the transit method with *Kepler* (*1*) and *TESS* (*2*). Given the sample of 12 transiting circumbinary planets found by *Kepler*, it is argued that the main population of circumbinary planets must be close to coplanar with the binary (with mutual inclinations $\Delta i < 5°$) (*3*), otherwise the occurrence rate of circumbinary planets would be greater than that of similar-sized planets orbiting single stars. (Preliminary results from the BEBOP (Binaries Escorted By Orbiting Planets) search for circumbinary planets using radial velocities are broadly consistent with those results (*4*)).

Despite this observational evidence, there may still exist a comparatively small and yet-undetected population of circumbinary planets occupying misaligned (*5, 6*) or polar (*7*) orbits. Polar circumbinary orbits are stable, even very close to the binary, if the binary is eccentric enough and the third body's orbital plane lies perpendicular to the inner binary's line of apsides (*8–10*). A circumbinary orbit can exist in one of two possible states. With sufficient inclination to an eccentric binary the orbit will *librate* about the binary's eccentricity vector. The critical inclination above which this happens depends on the binary eccentricity (*8*), if the inclination is below this limit then the orbit will instead *circulate* about the binary's angular momentum vector.

The existence of circumbinary planets on polar orbits, while exotic and seemingly unlikely, has a theoretical and observational basis, and has been postulated before (*5, 11*). Circumbinary protoplanetary and debris discs in a polar orientation have been observed in a few systems (*12, 13*), and various mechanisms exist to form misaligned discs (*14–17*) as well as to form planets from these discs that would therefore be misaligned or polar (*6, 7*). One of the polar discs also displays evidence for dust growth, indicating planet formation within polar discs is feasible (*13*). While no polar circumbinary planets have been found so far, it has been suggested that AC Her a post-asymptotic giant branch binary star, which has a polar circumbinary disc (*18*), may also host a third body. The disc in that case is truncated and could be explained by a companion orbiting the binary

interior to the disc (*19*) in an assumed polar orbit. Polar orbits are also fairly frequently encountered for hot Jupiters orbiting single stars (*20, 21*). It has been suggested that polar circumbinary planets where the inner binary has subsequently merged could be a possible origin of polar planets around single stars (*22*).

The radial velocity method has now detected three circumbinary planets: detecting Kepler-16b (*23*), confirming the detection of and improving the physical and orbital parameters of TIC 172900988 b (*24*), and the first stand-alone radial velocity discovery of BEBOP-1c (*25*) (the inner planet TOI-1338b having been found in transit (*2*)). These are all detections made by measuring the reflex orbital motion of the centre-of-mass of the system caused by a planet. A third body such as a circumbinary planet also has a dynamical influence on the orbit of the binary, most notably on its apsidal precession rate. Measurements of the apsidal precession rate have been used to constrain the masses of some of the *Kepler* transiting circumbinary planets (*26*) and can in principle be used on their own to infer the presence of a planet within radial-velocity data.

2MASS J15104786-2818174 (hearafter 2M1510) is a double-lined eclipsing binary composed of two equal-mass brown dwarfs (*27*) of mass 0.0331 and 0.0332 $M_{\odot}$ respectively. The orbital geometry of the binary results in a single eclipse. This is due to the combination of a high eccentricity, a very slight inclination with respect to the line-of-sight, and the line-of-apsides being along the line-of-sight. The system has been found to be a kinematic member of the 45 ± 5 Myr old Argus moving group, making it the second of only two known young eclipsing double-lined brown dwarf binaries, important objects for calibrating brown dwarf evolutionary models (*27–29*). The binary has an orbital period of 20.9 days, an eccentricity of 0.36, and there is also a visual brown dwarf tertiary companion, at a projected separation of $\sim$ 250 AU from the central, eclipsing pair (*27*).

Archival and newly obtained radial velocities of 2M1510 exist, observed with the UVES (Ultraviolet and Visual Echelle Spectrograph) instrument on the European Southern Observatory (ESO)'s Very Large Telescope (VLT). In this work we analyse the radial velosities and detect strong evidence for a retrograde apsidal precession. We interpret this as a sign of a polar orbiting circumbinary planet, one of the few possible causes for a retrograde precession (*30*).

2 Results

Retrograde apsidal precession

We perform a first fit to the radial velocities using `kima` (*31*), an exoplanetary tool that utilises nested sampling to search for an arbitrary number of Keplerian signals, and explore their parameter space. We use `kima` to fit the radial velocities of both brown dwarfs simultaneously assuming a Keplerian model, but also adding an apsidal precession rate $\dot{\omega}$ (*32*), the most important Newtonian perturbation. This analysis leads to improved constraints on the parameters of the binary, which we present in the first column of Table 1, and importantly, to a measure of $\dot{\omega} = -343 \pm 126$ "/yr, corresponding to a negative apsidal precession rate, which is detected with 99.7% confidence. The radial velocity residuals and the posterior distribution on the precession rate are shown in Fig 1 and Fig 2. No Doppler reflex signal consistent with a circumbinary planet signal is detected in the radial velocities.

A negative (i.e. retrograde) apsidal precision is a rare and immediately noticeable result. Typical effects inducing an apsidal precession (General relativity, tidal distortion) would *always* result in a prograde (i.e. positive) apsidal precession rate (*32*). For 2M1510, these effects combined result in a precession $\dot{\omega}_{\rm bin} \lesssim 4$ " yr^{-1} much smaller in magnitude than what is measured. Apsidal precession induced by a third body is also only prograde if the companion is coplanar with the binary. However, a companion on a highly misaligned/polar orbit could cause a retrograde apsidal motion (*30*). The most stable circumbinary polar orbit is perpendicular to the eclipsing binary's apsides (*8, 9*), and because of the binary's orbital parameters ($i_{\rm bin} \sim 90°, \omega_{\rm bin} \sim 270°$) mean that its apsides are along the line-of-sight, the polar planet would therefore appear face-on from our point of view, which is consistent with the absence of Doppler reflex motion observed in the radial-velocity timeseries. Alternative explanations are explored in section 3 but none can explain the measurement or retrograde precession. In the absence of any other viable mechanism to cause it, the precession must therefore be due to a perturbing third body on a polar orbit.

The companion responsible for the retrograde apsidal precession is most likely planetary. There are only two sets of absorption lines in the UVES spectra and the extracted radial velocities based on a 2-spectrum model have a small scatter (< 60 m/s), so the third body must be much less luminous

than the inner brown dwarf pair. Since their individual masses are around $35 M_{\rm Jup}$, a fainter, inclined companion is very likely be planetary in nature.

N-body analysis

To assess what planet configurations could cause this precession rate we fit the radial velocity data using an N-body fit (more details in section 4. The binary parameters from this fit are shown in Table 1.

Fig 3 shows the constraints on the mass and orbital period of the third body from the N-body fit. Since the radial velocities are not directly sensitive to that third object, neither the mass nor the orbital period is individually constrained (testing with different priors shows that we remain prior-dominated). However, the relationship between mass and period is constrained through the the apsidal precession rate. This leads to a "wedge" of masses and periods where the N-body integrator reproduces the observed radial-velocities. Most circumbinary planets are detected right outside the unstable region surrounding the inner binary (*5, 8*). Should this be the case for 2M1510 b, the polar planet, then its parameters would be of order $P \approx 100$ days and $M \approx 10\, M_\oplus$. If instead $P \approx 400$ days, then $M \approx 100\, M_\oplus$.

The planet is indeed a polar planet in the librating regime. Fig 4 shows the energy levels of the Hamiltonian with the posteriors from the N-body fit plotted on top. We show the islands of libration and circulation of a test particle within the 2M1510 binary, with red showing circulation and orange depicting libration. We take a random sample of 600 posteriors from the run restricted to periods < 300 days. 16 of these are unstable (the orbital period of the planet changes by a factor of 1.5 within 400,000 days) and of the remaining 584 posterior samples, 96% are in the librating regime.

3 Discussion

We discuss alternative explanations for the retrograde apsidal precession measurement, ultimately finding no suitable explanation other than a polar planet. We then discuss methods to follow-up and confirm the planet and highlight a point on the nomenclature.

Alternative explanations

In this section we explore alternative explanations for the measured $\dot{\omega}$. Each of the following subsections is given one alternative hypothesis as a title, this hypothesis is then discussed. Overall we find that there is no suitable explanation other than a polar-orbiting planet.

The precession is a false-positive

The evidence for this candidate planet is predicated on the measurement of a retrograde apsidal precession. This measurement is over the detection thresholds and we now perform some checks of the reliability by re-analysing with `kima`, using different portions of the data.

First, we separate the data into the radial velocities from each of the primary and secondary brown dwarfs, and analyse each separately. The analysis produces independent measurements of $\dot{\omega}_{\rm bin} = -410 \pm 200$ " yr^{-1} for the primary and $\dot{\omega}_{\rm bin} = -250 \pm 180$ " yr^{-1} for the secondary. The posterior distributions for these are shown in the right hand panel of Fig 2. Both results are consistent with one another. The left hand panel of Fig 2 shows the relationship between the residuals of the primary and the residuals of the secondary when fit with a static (non-precessing) Keplerian. The lack of correlation shows that the two datasets are indeed independent measures of the apsidal precession rate, so the detection is not due to a spurious structure in the residuals of one of the two components.

Second, we separate the data in time. The data was taken in 3 different groups (see Fig 1). We analyse the first two groups (covering a baseline of 650 days) and the second two groups (covering a baseline of 1600 days). The apsidal precession measurements are $+860 \pm 650$ and -460 ± 350 " yr^{-1} respectively. While the first measurement is prograde, it is $< 2\sigma$ from the retrograde value based on analysing the full dataset, and it is taken over a very small time baseline from which conclusions

about the long-term precession rate are hard to extract. This shows that the measurement is most strongly reliant on the final group of data, but this is expected as this group extends the baseline the most and a long baseline is vital to a good measurement of the apsidal precession rate of a binary. The fact that the measurement refines in precision and becomes more negative when more data is included gives us confidence the signal is real. However, further radial velocity measurements extending the baseline would be very helpful in constraining the negative $\dot{\omega}$, refining its precision. This is also important to better constrain the possible mass and period combinations for the polar planet, the current constraint being shown in Fig 3.

The companion is non-planetary

The companion causing this precession must be planetary mass. Unfortunately, we cannot put an upper limit on the companion's mass based on an N-body fit as there will always be perfectly face-on orbits of very massive bodies on long-period orbits that can induce the apsidal precession but create no radial velocity signature. However, it is unlikely that the third body is itself a brown dwarf, as it would have already been noticed. Prior to 2M1510 being known to be eclipsing, (*33*) had speculated decades ahead this system was an equal brightness binary, based on its overall luminosity. To avoid photometric and spectroscopic detection, any companion to the binary would have to be much weaker. Since both components of the binary are themselves low-mass brown dwarfs ($\sim 30\,\mathrm{M_{jup}}$), this only leaves the planetary realm as a reasonable solution.

The distant tertiary is producing the precession

2M1510 AB, the eclipsing binary brown dwarf in question here, has a visual companion of the same magnitude (2M1510 C). It was shown that with the projected separation of 250 AU and an orbital period of $\sim 11,000$ years, the tertiary is unable to have caused the binary to reach its current state through high-eccentricity migration (*27*). We use equation A5. from (*32*) to calculate the precession rate due to the tertiary and find that the effect is six orders of magnitude too small. The distant tertiary cannot be the cause of the apsidal precession.

Proper-motion changing the viewing angle

An apparent apsidal precession can occur for a high proper-motion system due to the viewing angle changing (*34*). This is only important for very high proper-motion systems, for 2M1510 we calculate an upper limit of $|\dot{\omega}| < 0.13$ ”/yr, so this effect is negligible here.

A spin–orbit misalignment

Retrograde precession can also be induced if the binary has a spin–orbit misalignment, as is the case in DI Her (*35*) where the retrograde precession induced in this system made its measured precession, while still prograde, much smaller than is predicted by GR alone. However, this effect is negligible here too.

We utilise eq. (7) derived below. The eccentricity (e), semi-major-axis (a), and the masses are observables that we have measured or derivable from them. (*27*) measured the inclination (I), and constrained the rotational periods of the stars to be between 20-30 hours. We assume 20 hours rotation period for both brown dwarfs to be conservative. We use Love numbers ($k_{2,i}$) of 0.4, corresponding to apsidal constants of 0.2 slightly more conservative that the value of 0.143 used for a similar brown dwarf system (*36*). We draw $1,000,000$ randomisations of the binary longitude of ascending node (Ω), and the angles ε_i and φ_i. From these we calculate that $\dot{\omega} > -2.15$ ”/yr so the spin-induced apsidal precession is two orders of magnitude too small to cause the measured effect.

A polar disc

Apsidal precession induced by a third body is a secular effect. This could equally be produced by a highly inclined circumbinary disc. However, while the binary is relatively young at ~ 45 Myr (*27*) it is old enough for the protoplanetary disc to have dissipated (*37*), and no infrared excess is noticed (*27*). Any remaining and undetected disc would presumably be a debris disc. Distinguishing a massive close-in debris disc from a single planet, or from multiple planets is not possible. All contribute to apsidal precession, and we chose to favour the simplest version of a single perturbing body.

Follow-up

Next steps should extend the baseline that is covered with more radial velocities to improve the precision on the apsidal precession rate. We estimate that if 20 radial velocity measurements are taken in the next observing period (ESO P115) with UVES this would lead to a precision on $\dot{\omega}$ of ~ 90 " yr^{-1} and another 20 measurements the next observing period (ESO P117) to a precision of ~ 75 " yr^{-1}. However even with more data, we expect the mass-period degeneracy will remain very difficult to break. A few additional ways of confirming the planet and its polar nature and constraining the planet parameters are possible.

Firstly, measuring the binary's eclipse times (and depths) precisely could in principle detect the planet's perturbation on the binary and constrain their mutual inclination as in (*38*). The eclipse obtained with one of the SPECULOOS (Search for Planetary transits EClipsing ULtra cOOl Stars) telescopes in (*27*) has a precision just under 1 minute. Using random draws from the posterior sample of the N-body fit, we calculate the eclipse times over 2 years and measure the amplitude of the O-C residuals. 65% of the draws had an amplitude > 5 mins, and 88% an amplitude > 1 min. These are the dynamical Eclipse Timing Variations (ETVs). We also test whether the Light Travel Time Effect (LTTE) ETVs would be detectable using equation 26 from (*39*), however even in the best case with the planet as inclined to the line-of-sight as it can possibly be, this would produce an ETV amplitude of ~ 20 s. The dynamical ETVs are a particularly promising way to confirm this planet, and two years of eclipses at 1 minute precision would be sufficient to confirm or rule-out most of the parameter space consistent with the planet. This does however, assume that most of the eclipses over the two years are actually observed and does not take into account difficulties with observations due to daytime or bad weather.

Secondly, a detailed astrometric study, such as those done using FORS2 on the VLT by (*40*) could reveal the signature of such a planet, which is expected on a face-on orbit. (*41*) find a typical sensitivity of around 50 μas, this would be equivalent to a Saturn mass planet on a 400 day orbit around our binary brown dwarf, and is therefore a promising follow-up technique which will be sensitive to gas giants on orbits of intermediate separation. At a Gmag of 17.5, Gaia astrometry

will not be sensitive enough to constrain a planet as well as ground-based astrometry.

A third option is the direct-imaging method where a planet can be detected from its formation's residual heat, using an adaptive optics system to distinguish it from the glare of its host. At its best, the method can detect an object with a flux ratio Δ F$\sim$ 10^{-5} at an angular separation of 0.2" (*42*). At the distance of 2M1510, this corresponds to a projected orbital separations > 7.3AU (which is $\sim$ 27 000 days). At this separation a companion would have to have a mass of $\sim$ 0.7 $M_{\odot}$ to induce the required apsidal precession. Direct imaging will therefore not be sensitive to the planet causing the precession, but it could be sensitive to other planets on more distant orbits. Assuming a system age of 50 Myr (*27*), and using the Baraffe models (COND03) (*43,44*) we estimate a 3.4 M_{Jup} planet could be detectable in this system if at 7.3 AU. At further orbital distances, sensitivity improves to 1.7 M_{Jup}.

The regions of sensitivity of a 3 year campaign of precise ground-based astrometry, and of a 2 year complete set of eclipse measurements are highlighted in Fig 3.

Nomenclature

We clarify the naming convention that we are using. While the discovery paper for the eclipsing binary (*27*) referred to the eclipsing binary as 2M1510 A and the distant companion as 2M1510 B. Instead we refer the the two components of the eclipsing binary as 2M1510 A and 2M1510 B; the visual companion is 2M1510 C; the eclipsing binary as a pair of stars is 2M1510 AB; and the planet is 2M1510 (AB)b though we simplify and refer to it as 2M1510 b. Fig 5 shows the configuration of the system and shows the naming convention we have just described.

4 Materials and Methods

Observations and radial velocities

35 spectra were obtained with the UVES instrument (*45*) on the VLT between 2017-08-16 and 2023-08-25 (Prog.ID 299.C-5046, 2100.C-5024 and 0103.C-0042, PI Triaud). All observations used the UVES instrument on UT2-Kueyen. Of these, 13 are recent UVES observations obtained

under Prog.ID 111.24ZA.001 (PI Sairam), greatly extending the timespan of observation. The spectra were reduced with the standard ESO pipelines for UVES.

We extracted the radial velocities from the spectra using the `DOLBY`-SD method (previously known as SD-GP) presented in (*24*), and inspired by (*46*). `DOLBY`-SD uses Gaussian Processes to disentangle both spectral components from one another, and calculate precise and accurate radial velocity measurements. This method treats the intrinsic stellar spectra as realisation of Gaussian process with a Matérn kernel. By modelling the radial velocity shift of each star in the binary system due to their orbital motion, the Gaussian process allows us to deconvolve the composite spectrum of the binary system into the individual spectra of each star. We divided the observed spectrum into smaller wavelength chunks to make the Gaussian process calculations tractable. We used the independent sets of hyperparameters to model the spectra of each star within each chunk, accounting for potential differences in the spectral characteristics of each star. We employed Markov Chain Monte-Carlo (MCMC) methods to explore the posterior distribution of both the radial velocities and the Gaussian process hyperparameters. Finally, we combined the radial velocities from each chunk using a weighted average, with weights determined by the uncertainties from each chunk.

We reanalyse all old and newly obtained UVES data. We reach a median radial velocity precision of 47 $\mathrm{m\,s^{-1}}$. Thanks to `DOLBY`-SD we improve the radial-velocity precision on the already published UVES data from $\sim$ 1600 $\mathrm{m\,s^{-1}}$. We compare our newly obtained radial velocities to values obtained on the old UVES data, reported in (*27*). As shown in Fig 6, the performance of DOLBY-SD is evident, achieving a remarkable precision for brown dwarfs. For comparison, (*47*) report a typical precision of 200 $\mathrm{m\,s^{-1}}$ for L dwarfs. The radial velocities can be found in Table 2-3.

Radial velocity analysis

We perform the initial radial velocity analysis using `kima` (*31*), a nested sampling powered analysis package allowing to fit for the number of orbiting objects in a system as a free parameter. Within `kima`, we employ the BINARIESmodel , which includes the apsidal precession of the binary as a free parameter, $\dot{\omega}$, a time derivative of the argument of periastron (*32*). Parameters are shown in

Table 1. We achieve a precision of 0.2% on the components' masses (a factor of 30 better than the precision of 6.8% from (*27*)). No planet or additional third body is detected in the radial velocities.

We find apsidal precession rate of the binary to be significantly negative, with a value of $\dot{\omega}_{\rm bin} = -343 \pm 126$ "/yr. The posterior distribution of $\dot{\omega}$ is shown in Fig 2. Comparing the posterior density with a positive precession rate to that with a negative precession rate reveals a evidence for the negative solution with a confidence of 99.7%. Alternatively framed in terms of Bayesian model comparison, this is a Bayes' Factor of 340. A typical value of 150 is used as a confidence threshold for Bayes' Factors corresponding to "strong evidence" (*48*). Hence our detection of retrograde apsidal precession is above the standard confidence threshold.

We perform a N-body fit with the N-body package `rebound` (*49*) using an Integrator with Adaptive Step-size (IAS15) (*50*) to simulate a radial velocity time-series that is compared to the observed data, and the MCMC algorithm *emcee* (*51*) to explore parameter space. We fit a 3-body model with the third body initialised to a circular orbit, but with a range of initial inclinations. There is thus no prior weight given to polar vs coplanar orbits. The algorithm explores the parameter space, sampling from the posterior distribution, from which physical and orbital parameters are extracted.

Derivation of spin-induced precession equations

In this section we derive the spin-induced precession rate in the observer's frame. This is an extension of the derivation in the appendix of (*32*) where spin alignment had been assumed. We relax that assumption such that the Hamiltonian from the rotational effect is (*52*)

$$\mathcal{H} = -\frac{C_{r,0}P_2(\cos(\theta_0)) + C_{r,1}P_2(\cos(\theta_1))}{(1-e^2)^{3/2}}, \tag{1}$$

where

$$C_{r,i} = \frac{\mathcal{G}m_0 m_1 J_{2,i} R_i^2}{2a^3}. \tag{2}$$

Here, $\mathcal{G}$ is the gravitational constant, m_i and R_i the mass and radius of the two components of the binary, a the total semi-major axis of the binary orbit, P_2 is the second order Legendre

polynomial $P_2(x) = \dfrac{3x^2 - 1}{2}$, and

$$J_{2,i} = k_{2,i} \frac{\Omega_i^2 R_i^3}{3\mathcal{G} m_i}, \tag{3}$$

where Ω_i and $k_{2,i}$ are the rotation rate and second Love number for body i respectively. The angle θ_i is the obliquity, i.e. the angle between the spin axis of star i and the normal to the orbit. It can be expressed in the observer's frame as (*53*)

$$\cos\theta_i = \cos I \cos\varepsilon_i + \sin I \sin\varepsilon_i \cos(\Omega - \varphi_i), \tag{4}$$

where I and Ω are the orbital inclination and longitude of ascending node of the binary orbit, ε_i is the angle between the equator of star i and the plane of the sky, and φ_i, the spin precession angle, is the angle between the the x reference axis in the plane of the sky and the line of nodes between this plane and the equator of star i.

We use the Lagrange Planetary Equations (*54*)

$$\frac{d\omega}{dt} = -\frac{(1-e^2)}{eG_1}\frac{\partial \mathcal{H}}{\partial e} + \frac{\cot I}{G_1}\frac{\partial \mathcal{H}}{\partial I}, \tag{5}$$

where G_1 is the norm of the orbital angular momentum

$$G_1 = \frac{m_0 m_1}{m_0 + m_1}\sqrt{\mathcal{G}(m_0 + m_1)a(1-e^2)}. \tag{6}$$

Substituting in the Hamiltonian from eq. (1), we get that the spin-induced apsidal precession rate is

$$\begin{aligned}\frac{d\omega}{dt} =& 3\frac{(C_{r,0}P_2(\cos(\theta_0)) + C_{r,1}P_2(\cos(\theta_1)))}{G_1(1-e^2)^{3/2}} \\ &- \frac{\cot I}{G_1(1-e^2)^{3/2}}\left(C_{r,0}\frac{\partial P_2(\cos\theta_0)}{\partial I} + C_{r,1}\frac{\partial P_2(\cos\theta_1)}{\partial I}\right),\end{aligned} \tag{7}$$

and

$$\frac{\partial P_2(\cos\theta_i)}{\partial I} = 3\cos\theta_i \left[\cos I \sin\varepsilon_i \cos(\Omega - \varphi_i) - \sin I \cos\varepsilon_i\right]. \tag{8}$$

References and Notes

1. L. R. Doyle, J. A. Carter, D. C. Fabrycky, R. W. Slawson, S. B. Howell, J. N. Winn, J. A. Orosz, A. Přsa, W. F. Welsh, S. N. Quinn, D. Latham, G. Torres, L. A. Buchhave, G. W. Marcy, J. J. Fortney, A. Shporer, E. B. Ford, J. J. Lissauer, D. Ragozzine, M. Rucker, N. Batalha, J. M. Jenkins, W. J. Borucki, D. Koch, C. K. Middour, J. R. Hall, S. McCauliff, M. N. Fanelli, E. V. Quintana, M. J. Holman, D. A. Caldwell, M. Still, R. P. Stefanik, W. R. Brown, G. A. Esquerdo, S. Tang, G. Furesz, J. C. Geary, P. Berlind, M. L. Calkins, D. R. Short, J. H. Steffen, D. Sasselov, E. W. Dunham, W. D. Cochran, A. Boss, M. R. Haas, D. Buzasi, D. Fischer, Kepler-16: A Transiting Circumbinary Planet. *Science* **333**, 1602 (2011), aDS Bibcode: 2011Sci...333.1602D, doi:10.1126/science.1210923, https://ui.adsabs.harvard.edu/abs/2011Sci...333.1602D.

2. V. B. Kostov, J. A. Orosz, A. D. Feinstein, W. F. Welsh, W. Cukier, N. Haghighipour, B. Quarles, D. V. Martin, B. T. Montet, G. Torres, A. H. M. J. Triaud, T. Barclay, P. Boyd, C. Briceno, A. C. Cameron, A. C. M. Correia, E. A. Gilbert, S. Gill, M. Gillon, J. Haqq-Misra, C. Hellier, C. Dressing, D. C. Fabrycky, G. Furesz, J. M. Jenkins, S. R. Kane, R. Kopparapu, V. K. Hodžić, D. W. Latham, N. Law, A. M. Levine, G. Li, C. Lintott, J. J. Lissauer, A. W. Mann, T. Mazeh, R. Mardling, P. F. L. Maxted, N. Eisner, F. Pepe, J. Pepper, D. Pollacco, S. N. Quinn, E. V. Quintana, J. F. Rowe, G. Ricker, M. E. Rose, S. Seager, A. Santerne, D. Ségransan, D. R. Short, J. C. Smith, M. R. Standing, A. Tokovinin, T. Trifonov, O. Turner, J. D. Twicken, S. Udry, R. Vanderspek, J. N. Winn, E. T. Wolf, C. Ziegler, P. Ansorge, F. Barnet, J. Bergeron, M. Huten, G. Pappa, T. van der Straeten, TOI-1338: TESS' First Transiting Circumbinary Planet. *The Astronomical Journal* **159**, 253 (2020), aDS Bibcode: 2020AJ....159..253K, doi:10.3847/1538-3881/ab8a48, https://ui.adsabs.harvard.edu/abs/2020AJ....159..253K.

3. D. J. Armstrong, H. P. Osborn, D. J. A. Brown, F. Faedi, Y. Gómez Maqueo Chew, D. V. Martin, D. Pollacco, S. Udry, On the abundance of circumbinary planets. *Monthly Notices of the Royal Astronomical Society* **444**, 1873–1883 (2014), aDS Bibcode: 2014MNRAS.444.1873A, doi:10.1093/mnras/stu1570, https://ui.adsabs.harvard.edu/abs/2014MNRAS.444.1873A.

4. T. A. Baycroft, A. H. M. J. Triaud, D. Lai, Progress report on the BEBOP search for circumbinary planets with radial velocities **382**, 51–58 (2024), conference Name: IAU Symposium ADS Bibcode: 2024IAUS..382...51B, doi:10.1017/S1743921323004180, https://ui.adsabs.harvard.edu/abs/2024IAUS..382...51B.

5. D. V. Martin, A. H. M. J. Triaud, Planets transiting non-eclipsing binaries. *Astronomy & Astrophysics* **570**, A91 (2014), doi:10.1051/0004-6361/201323112, https://ui.adsabs.harvard.edu/abs/2014A%26A...570A..91M/abstract.

6. A. C. Childs, R. G. Martin, Misalignment of Terrestrial Circumbinary Planets as an Indicator of Their Formation Mechanism. *The Astrophysical Journal* **927**, L7 (2022), publisher: IOP ADS Bibcode: 2022ApJ...927L...7C, doi:10.3847/2041-8213/ac574f, https://ui.adsabs.harvard.edu/abs/2022ApJ...927L...7C.

7. A. C. Childs, R. G. Martin, Formation of Polar Terrestrial Circumbinary Planets. *The Astrophysical Journal* **920**, L8 (2021), publisher: IOP ADS Bibcode: 2021ApJ...920L...8C, doi:10.3847/2041-8213/ac2957, https://ui.adsabs.harvard.edu/abs/2021ApJ...920L...8C.

8. S. Doolin, K. M. Blundell, The dynamics and stability of circumbinary orbits. *Monthly Notices of the Royal Astronomical Society* **418**, 2656–2668 (2011), aDS Bibcode: 2011MNRAS.418.2656D, doi:10.1111/j.1365-2966.2011.19657.x, https://ui.adsabs.harvard.edu/abs/2011MNRAS.418.2656D.

9. C. Chen, A. Franchini, S. H. Lubow, R. G. Martin, Orbital dynamics of circumbinary planets. *Monthly Notices of the Royal Astronomical Society* **490** (4), 5634–5646 (2019), doi:10.1093/mnras/stz2948, https://academic.oup.com/mnras/article/490/4/5634/5602605.

10. C. Chen, S. H. Lubow, R. G. Martin, Polar planets around highly eccentric binaries are the most stable. *Monthly Notices of the Royal Astronomical Society* **494** (4), 4645–4655 (2020), arXiv: 2004.07230, doi:10.1093/mnras/staa1037, http://arxiv.org/abs/2004.07230.

11. J. Schneider, On the occultations of a binary star by a circum-orbiting dark companion. *Planetary and Space Science* **42**, 539–544 (1994), aDS Bibcode: 1994P&SS...42..539S, doi:10.

1016/0032-0633(94)90075-2, https://ui.adsabs.harvard.edu/abs/1994P&SS...42..539S.

12. G. M. Kennedy, M. C. Wyatt, B. Sibthorpe, G. Duchêne, P. Kalas, B. C. Matthews, J. S. Greaves, K. Y. L. Su, M. P. Fitzgerald, 99 Herculis: host to a circumbinary polar-ring debris disc. *Monthly Notices of the Royal Astronomical Society* **421**, 2264–2276 (2012), publisher: OUP ADS Bibcode: 2012MNRAS.421.2264K, doi:10.1111/j.1365-2966.2012.20448.x, https://ui.adsabs.harvard.edu/abs/2012MNRAS.421.2264K.

13. G. M. Kennedy, L. Matrà, S. Facchini, J. Milli, O. Panić, D. Price, D. J. Wilner, M. C. Wyatt, B. M. Yelverton, A circumbinary protoplanetary disk in a polar configuration. *Nature Astronomy* **3**, 230–235 (2019), aDS Bibcode: 2019NatAs...3..230K, doi:10.1038/s41550-018-0667-x, https://ui.adsabs.harvard.edu/abs/2019NatAs...3..230K.

14. I. Bonnell, P. Bastien, Fragmentation of Elongated Cylindrical Clouds. V. Dependence of Mass Ratios on Initial Conditions. *The Astrophysical Journal* **401**, 654 (1992), publisher: IOP ADS Bibcode: 1992ApJ...401..654B, doi:10.1086/172093, https://ui.adsabs.harvard.edu/abs/1992ApJ...401..654B.

15. S. S. R. Offner, K. M. Kratter, C. D. Matzner, M. R. Krumholz, R. I. Klein, The Formation of Low-mass Binary Star Systems Via Turbulent Fragmentation. *The Astrophysical Journal* **725**, 1485–1494 (2010), publisher: IOP ADS Bibcode: 2010ApJ...725.1485O, doi:10.1088/0004-637X/725/2/1485, https://ui.adsabs.harvard.edu/abs/2010ApJ...725.1485O.

16. M. R. Bate, On the diversity and statistical properties of protostellar discs. *Monthly Notices of the Royal Astronomical Society* **475**, 5618–5658 (2018), publisher: OUP ADS Bibcode: 2018MNRAS.475.5618B, doi:10.1093/mnras/sty169, https://ui.adsabs.harvard.edu/abs/2018MNRAS.475.5618B.

17. R. Nealon, N. Cuello, R. Alexander, Flyby-induced misalignments in planet-hosting discs. *Monthly Notices of the Royal Astronomical Society* **491**, 4108–4115 (2020), publisher: OUP ADS Bibcode: 2020MNRAS.491.4108N, doi:10.1093/mnras/stz3186, https://ui.adsabs.harvard.edu/abs/2020MNRAS.491.4108N.

18. R. G. Martin, S. H. Lubow, D. Vallet, N. Anugu, D. R. Gies, AC Her: Evidence of the First Polar Circumbinary Planet. *The Astrophysical Journal* **957**, L28 (2023), publisher: IOP ADS Bibcode: 2023ApJ...957L..28M, doi:10.3847/2041-8213/ad0730, https://ui.adsabs.harvard.edu/abs/2023ApJ...957L..28M.

19. J. Kluska, H. Van Winckel, Q. Coppée, G. M. Oomen, K. Dsilva, D. Kamath, V. Bujarrabal, M. Min, A population of transition disks around evolved stars: Fingerprints of planets. Catalog of disks surrounding Galactic post-AGB binaries. *Astronomy and Astrophysics* **658**, A36 (2022), aDS Bibcode: 2022A&A...658A..36K, doi:10.1051/0004-6361/202141690, https://ui.adsabs.harvard.edu/abs/2022A&A...658A..36K.

20. A. H. M. J. Triaud, *The Rossiter-McLaughlin Effect in Exoplanet Research* (Springer) (2018), doi:10.1007/978-3-319-55333-7_2, https://ui.adsabs.harvard.edu/abs/2018haex.bookE...2T, pages: 2 Publication Title: Handbook of Exoplanets ADS Bibcode: 2018haex.bookE...2T.

21. S. H. Albrecht, M. L. Marcussen, J. N. Winn, R. I. Dawson, E. Knudstrup, A Preponderance of Perpendicular Planets. *The Astrophysical Journal* **916**, L1 (2021), publisher: IOP ADS Bibcode: 2021ApJ...916L...1A, doi:10.3847/2041-8213/ac0f03, https://ui.adsabs.harvard.edu/abs/2021ApJ...916L...1A.

22. C. Chen, S. A. Baronett, C. J. Nixon, R. G. Martin, On the origin of polar planets around single stars. *Monthly Notices of the Royal Astronomical Society* **533**, L37–L42 (2024), publisher: OUP ADS Bibcode: 2024MNRAS.533L..37C, doi:10.1093/mnrasl/slae058, https://ui.adsabs.harvard.edu/abs/2024MNRAS.533L..37C.

23. A. H. M. J. Triaud, M. R. Standing, N. Heidari, D. V. Martin, I. Boisse, A. Santerne, A. C. M. Correia, L. Acuña, M. Battley, X. Bonfils, A. Carmona, A. Collier Cameron, P. Cortés-Zuleta, G. Dransfield, S. Dalal, M. Deleuil, X. Delfosse, J. Faria, T. Forveille, N. C. Hara, G. Hébrard, S. Hoyer, F. Kiefer, V. Kunovac, P. F. L. Maxted, E. Martioli, N. J. Miller, R. P. Nelson, M. Poveda, H. Rein, L. Sairam, S. Udry, E. Willett, BEBOP III. Observations and an independent mass measurement of Kepler-16 (AB) b - the first circumbinary planet detected with radial velocities. *Monthly Notices of the Royal Astronomical Society* **511**,

3561–3570 (2022), aDS Bibcode: 2022MNRAS.511.3561T, doi:10.1093/mnras/stab3712, https://ui.adsabs.harvard.edu/abs/2022MNRAS.511.3561T.

24. L. Sairam, A. H. M. J. Triaud, T. A. Baycroft, J. Orosz, I. Boisse, N. Heidari, D. Sebastian, G. Dransfield, D. V. Martin, A. Santerne, M. R. Standing, New methods for radial-velocity measurements of double-lined binaries, and detection of a circumbinary planet orbiting TIC 172900988. *Monthly Notices of the Royal Astronomical Society* **527**, 2261–2278 (2024), aDS Bibcode: 2024MNRAS.527.2261S, doi:10.1093/mnras/stad3136, https://ui.adsabs.harvard.edu/abs/2024MNRAS.527.2261S.

25. M. R. Standing, L. Sairam, D. V. Martin, A. H. M. J. Triaud, A. C. M. Correia, G. A. L. Coleman, T. A. Baycroft, V. Kunovac, I. Boisse, A. C. Cameron, G. Dransfield, J. P. Faria, M. Gillon, N. C. Hara, C. Hellier, J. Howard, E. Lane, R. Mardling, P. F. L. Maxted, N. J. Miller, R. P. Nelson, J. A. Orosz, F. Pepe, A. Santerne, D. Sebastian, S. Udry, W. F. Welsh, Radial-velocity discovery of a second planet in the TOI-1338/BEBOP-1 circumbinary system. *Nature Astronomy* **7**, 702–714 (2023), aDS Bibcode: 2023NatAs...7..702S, doi:10.1038/s41550-023-01948-4, https://ui.adsabs.harvard.edu/abs/2023NatAs...7..702S.

26. V. B. Kostov, J. A. Orosz, W. F. Welsh, L. R. Doyle, D. C. Fabrycky, N. Haghighipour, B. Quarles, D. R. Short, W. D. Cochran, M. Endl, E. B. Ford, J. Gregorio, T. C. Hinse, H. Isaacson, J. M. Jenkins, E. L. N. Jensen, S. Kane, I. Kull, D. W. Latham, J. J. Lissauer, G. W. Marcy, T. Mazeh, T. W. A. Müller, J. Pepper, S. N. Quinn, D. Ragozzine, A. Shporer, J. H. Steffen, G. Torres, G. Windmiller, W. J. Borucki, KEPLER-1647B: THE LARGEST AND LONGEST-PERIOD *KEPLER* TRANSITING CIRCUMBINARY PLANET. *The Astrophysical Journal* **827** (1), 86 (2016), doi:10.3847/0004-637X/827/1/86, https://iopscience.iop.org/article/10.3847/0004-637X/827/1/86.

27. A. H. M. J. Triaud, A. J. Burgasser, A. Burdanov, V. Kunovac Hodžić, R. Alonso, D. Bardalez Gagliuffi, L. Delrez, B.-O. Demory, J. de Wit, E. Ducrot, F. V. Hessman, T.-O. Husser, E. Jehin, P. P. Pedersen, D. Queloz, J. McCormac, C. Murray, D. Sebastian, S. Thompson, V. Van Grootel, M. Gillon, An eclipsing substellar binary in a young triple system discovered by SPECULOOS. *Nature Astronomy* **4**, 650–657 (2020),

aDS Bibcode: 2020NatAs...4..650T, doi:10.1038/s41550-020-1018-2, https://ui.adsabs.harvard.edu/abs/2020NatAs...4..650T.

28. A. Burrows, W. B. Hubbard, J. I. Lunine, J. Liebert, The theory of brown dwarfs and extrasolar giant planets. *Reviews of Modern Physics* **73**, 719–765 (2001), publisher: APS ADS Bibcode: 2001RvMP...73..719B, doi:10.1103/RevModPhys.73.719, https://ui.adsabs.harvard.edu/abs/2001RvMP...73..719B.

29. K. G. Stassun, R. D. Mathieu, J. A. Valenti, Discovery of two young brown dwarfs in an eclipsing binary system. *Nature* **440** (7082), 311–314 (2006), publisher: Nature Publishing Group, doi:10.1038/nature04570, https://www.nature.com/articles/nature04570.

30. Z. Zhang, D. C. Fabrycky, Distinguishing Polar and Coplanar Circumbinary Exoplanets by Eclipse Timing Variations. *The Astrophysical Journal* **879** (2), 92 (2019), publisher: The American Astronomical Society, doi:10.3847/1538-4357/ab24d5, https://dx.doi.org/10.3847/1538-4357/ab24d5.

31. J. P. Faria, N. C. Santos, P. Figueira, B. J. Brewer, kima: Exoplanet detection in radial velocities. *The Journal of Open Source Software* **3**, 487 (2018), aDS Bibcode: 2018JOSS....3..487F, doi:10.21105/joss.00487, https://ui.adsabs.harvard.edu/abs/2018JOSS....3..487F.

32. T. A. Baycroft, A. H. M. J. Triaud, J. Faria, A. C. M. Correia, M. R. Standing, Improving circumbinary planet detections by fitting their binary's apsidal precession. *Monthly Notices of the Royal Astronomical Society* **521**, 1871–1879 (2023), aDS Bibcode: 2023MNRAS.521.1871B, doi:10.1093/mnras/stad607, https://ui.adsabs.harvard.edu/abs/2023MNRAS.521.1871B.

33. J. E. Gizis, Brown Dwarfs and the TW Hydrae Association. *The Astrophysical Journal* **575**, 484–492 (2002), publisher: IOP ADS Bibcode: 2002ApJ...575..484G, doi:10.1086/341259, https://ui.adsabs.harvard.edu/abs/2002ApJ...575..484G.

34. R. R. Rafikov, Stellar Proper Motion and the Timing of Planetary Transits. *The Astrophysical Journal* **700**, 965–970 (2009), publisher: IOP ADS Bibcode: 2009ApJ...700..965R, doi:10.

1088/0004-637X/700/2/965, https://ui.adsabs.harvard.edu/abs/2009ApJ...700..965R.

35. S. Albrecht, S. Reffert, I. A. G. Snellen, J. N. Winn, Misaligned spin and orbital axes cause the anomalous precession of DI Herculis. *Nature* **461**, 373–376 (2009), aDS Bibcode: 2009Natur.461..373A, doi:10.1038/nature08408, https://ui.adsabs.harvard.edu/abs/2009Natur.461..373A.

36. R. Heller, B. Jackson, R. Barnes, R. Greenberg, D. Homeier, Tidal effects on brown dwarfs: application to the eclipsing binary 2MASS J05352184-0546085 - The anomalous temperature reversal in the context of tidal heating. *Astronomy & Astrophysics* **514**, A22 (2010), publisher: EDP Sciences, doi:10.1051/0004-6361/200912826, https://www.aanda.org/articles/aa/abs/2010/06/aa12826-09/aa12826-09.html.

37. E. E. Mamajek, Initial Conditions of Planet Formation: Lifetimes of Primordial Disks **1158**, 3–10 (2009), conference Name: Exoplanets and Disks: Their Formation and Diversity Place: eprint: arXiv:0906.5011 Publisher: AIP ADS Bibcode: 2009AIPC.1158....3M, doi:10.1063/1.3215910, https://ui.adsabs.harvard.edu/abs/2009AIPC.1158....3M.

38. M. Goldberg, D. Fabrycky, D. V. Martin, S. Albrecht, H. J. Deeg, G. Nowak, A 5MJup non-transiting coplanar circumbinary planet around Kepler-1660AB. *Monthly Notices of the Royal Astronomical Society* **525**, 4628–4641 (2023), aDS Bibcode: 2023MNRAS.525.4628G, doi:10.1093/mnras/stad2568, https://ui.adsabs.harvard.edu/abs/2023MNRAS.525.4628G.

39. T. Borkovits, S. Csizmadia, E. Forgács-Dajka, T. Hegedüs, Transit timing variations in eccentric hierarchical triple exoplanetary systems. I. Perturbations on the time scale of the orbital period of the perturber. *Astronomy and Astrophysics* **528**, A53 (2011), aDS Bibcode: 2011A&A...528A..53B, doi:10.1051/0004-6361/201015867, https://ui.adsabs.harvard.edu/abs/2011A&A...528A..53B.

40. J. Sahlmann, P. F. Lazorenko, D. Ségransan, E. L. Martín, M. Mayor, D. Queloz, S. Udry, Astrometric planet search around southern ultracool dwarfs. I. First results, including parallaxes of 20 M8-L2 dwarfs. *Astronomy and Astrophysics* **565**, A20 (2014), aDS Bib-

code: 2014A&A...565A..20S, doi:10.1051/0004-6361/201323208, https://ui.adsabs.harvard.edu/abs/2014A&A...565A..20S.

41. P. F. Lazorenko, M. Mayor, M. Dominik, F. Pepe, D. Segransan, S. Udry, Precision multi-epoch astrometry with VLT cameras FORS1/2. *Astronomy and Astrophysics* **505**, 903–918 (2009), aDS Bibcode: 2009A&A...505..903L, doi:10.1051/0004-6361/200912026, https://ui.adsabs.harvard.edu/abs/2009A&A...505..903L.

42. A. Chomez, A. M. Lagrange, P. Delorme, M. Langlois, G. Chauvin, O. Flasseur, J. Dallant, F. Philipot, S. Bergeon, D. Albert, N. Meunier, P. Rubini, Preparation for an unsupervised massive analysis of SPHERE high-contrast data with PACO. Optimization and benchmarking on 24 solar-type stars. *Astronomy and Astrophysics* **675**, A205 (2023), aDS Bibcode: 2023A&A...675A.205C, doi:10.1051/0004-6361/202245723, https://ui.adsabs.harvard.edu/abs/2023A&A...675A.205C.

43. I. Baraffe, G. Chabrier, T. S. Barman, F. Allard, P. H. Hauschildt, Evolutionary models for cool brown dwarfs and extrasolar giant planets. The case of HD 209458. *Astronomy and Astrophysics* **402**, 701–712 (2003), aDS Bibcode: 2003A&A...402..701B, doi:10.1051/0004-6361:20030252, https://ui.adsabs.harvard.edu/abs/2003A&A...402..701B.

44. I. Baraffe, D. Homeier, F. Allard, G. Chabrier, New evolutionary models for pre-main sequence and main sequence low-mass stars down to the hydrogen-burning limit. *Astronomy and Astrophysics* **577**, A42 (2015), aDS Bibcode: 2015A&A...577A..42B, doi:10.1051/0004-6361/201425481, https://ui.adsabs.harvard.edu/abs/2015A&A...577A..42B.

45. H. Dekker, S. D'Odorico, A. Kaufer, B. Delabre, H. Kotzlowski, Design, construction, and performance of UVES, the echelle spectrograph for the UT2 Kueyen Telescope at the ESO Paranal Observatory **4008**, 534–545 (2000), conference Name: Optical and IR Telescope Instrumentation and Detectors ADS Bibcode: 2000SPIE.4008..534D, doi:10.1117/12.395512, https://ui.adsabs.harvard.edu/abs/2000SPIE.4008..534D.

46. I. Czekala, K. S. Mandel, S. M. Andrews, J. A. Dittmann, S. K. Ghosh, B. T. Montet, E. R. Newton, Disentangling Time-series Spectra with Gaussian Processes: Applications to Radial

Velocity Analysis. *The Astrophysical Journal* **840**, 49 (2017), publisher: IOP ADS Bibcode: 2017ApJ...840...49C, doi:10.3847/1538-4357/aa6aab, https://ui.adsabs.harvard.edu/abs/2017ApJ...840...49C.

47. C. H. Blake, D. Charbonneau, R. J. White, The NIRSPEC Ultracool Dwarf Radial Velocity Survey. *The Astrophysical Journal* **723**, 684–706 (2010), publisher: IOP ADS Bibcode: 2010ApJ...723..684B, doi:10.1088/0004-637X/723/1/684, https://ui.adsabs.harvard.edu/abs/2010ApJ...723..684B.

48. R. Trotta, Bayes in the sky: Bayesian inference and model selection in cosmology. *Contemporary Physics* **49**, 71–104 (2008), aDS Bibcode: 2008ConPh..49...71T, doi:10.1080/00107510802066753, https://ui.adsabs.harvard.edu/abs/2008ConPh..49...71T.

49. H. Rein, S.-F. Liu, REBOUND: an open-source multi-purpose N-body code for collisional dynamics. *Astronomy and Astrophysics* **537**, A128 (2012), doi:10.1051/0004-6361/201118085, https://ui.adsabs.harvard.edu/abs/2012A&A...537A.128R/abstract.

50. H. Rein, D. S. Spiegel, IAS15: a fast, adaptive, high-order integrator for gravitational dynamics, accurate to machine precision over a billion orbits. *Monthly Notices of the Royal Astronomical Society* **446**, 1424–1437 (2015), publisher: OUP ADS Bibcode: 2015MNRAS.446.1424R, doi:10.1093/mnras/stu2164, https://ui.adsabs.harvard.edu/abs/2015MNRAS.446.1424R.

51. D. Foreman-Mackey, D. W. Hogg, D. Lang, J. Goodman, emcee: The MCMC Hammer. *Publications of the Astronomical Society of the Pacific* **125**, 306 (2013), publisher: IOP ADS Bibcode: 2013PASP..125..306F, doi:10.1086/670067, https://ui.adsabs.harvard.edu/abs/2013PASP..125..306F.

52. P. Goldreich, History of the Lunar Orbit. *Reviews of Geophysics and Space Physics* **4**, 411–439 (1966), aDS Bibcode: 1966RvGSP...4..411G, doi:10.1029/RG004i004p00411, https://ui.adsabs.harvard.edu/abs/1966RvGSP...4..411G.

53. A. C. M. Correia, G. Boué, J. Laskar, Secular and tidal evolution of circumbinary systems. *Celestial Mechanics and Dynamical Astronomy* **126**, 189–225 (2016), publisher: Springer ADS

Bibcode: 2016CeMDA.126..189C, doi:10.1007/s10569-016-9709-9, https://ui.adsabs.harvard.edu/abs/2016CeMDA.126..189C.

54. C. D. Murray, S. F. Dermott, *Solar System Dynamics* (Cambridge University Press) (1999), doi:10.1017/CBO9781139174817, https://ui.adsabs.harvard.edu/abs/1999ssd..book.....M, publication Title: Solar System Dynamics ADS Bibcode: 1999ssd..book.....M.

Acknowledgments

We thank the anonymous referees for their helpful comments. We acknowledge receiving observations from the European Southern Observatory (ESO), under Prog.ID 299.C-5046, 2100.C-5024, 0103.C-0042 and 111.24ZA.001. We thank the kind staff at ESO for collecting our observations.

Funding: AHMJT acknowledges funding from the European Research Council (ERC) under the European Union's Horizon 2020 research and innovation programme (grant agreement 803193/BEBOP), by the Leverhulme Trust (research project grant RPG-2018-418), and from the ERC/UKRI Frontier Research Guarantee programme (EP/Z000327/1/CandY). ACMC acknowledges support from the FCT, Portugal, through the CFisUC projects UIDB/04564/2020 and UIDP/04564/2020, with DOI identifiers 10.54499/UIDB/04564/2020 and 10.54499/UIDP/04564/2020, respectively.

Author contributions: TAB developed methods and software used and perfomed the data analysis. AHMJT and LS led the observing proposals that obtained the UVES data. LS developed software, and curated the data reducing the spectra and calculating the radial velocities. TAB, LS and AHMT were involved in the inital investigation. ACMC and TAB derived the spin-induced precession equations, and studied the orbital dynamics of the system. AHMJT and ACMC acquired funding and performed validation. AHMJT supervised the work done. All authors contributed to conceptualising the experiment and to the methodology used and the vizualisation of data and results. The project administration was preformed by TAB and AHMJT. TAB wrote the majority of the manuscript with all authors contributing.

Competing interests: There are no competing interests to declare.

Data and materials availability: All data needed to evaluate the conclusions in the paper are present in the paper and/or the Supplementary Materials. The radial velocity data are included in the manuscript in Tab. 2-3. The spectra are available on the ESO archive. The codes utilised in this work are all publicly available.

`kima`: https://www.kima.science/

`rebound`: https://rebound.readthedocs.io/en/latest/

`emcee`: https://emcee.readthedocs.io/en/stable/

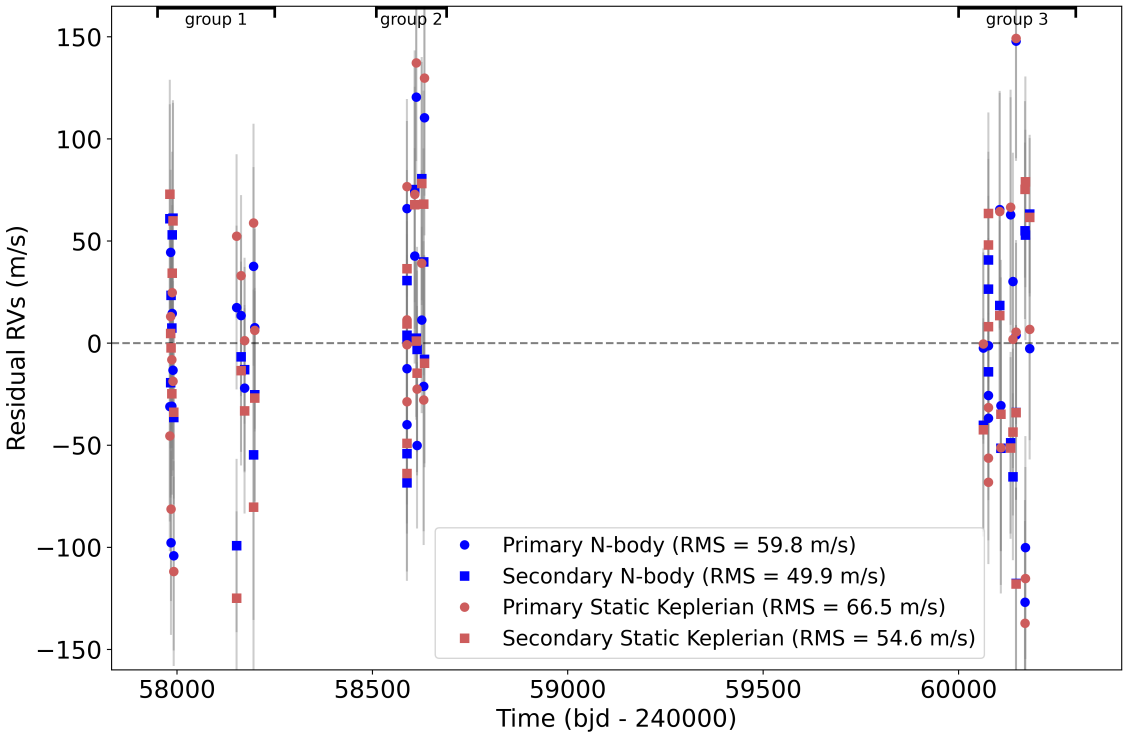


Figure 1: **Comparison of N-body residuals and static-Keplerian residuals.** The division into different groups used to see the evolution of $\dot{\omega}$ is shown. The RMS of the residuals for each dataset is also listed.

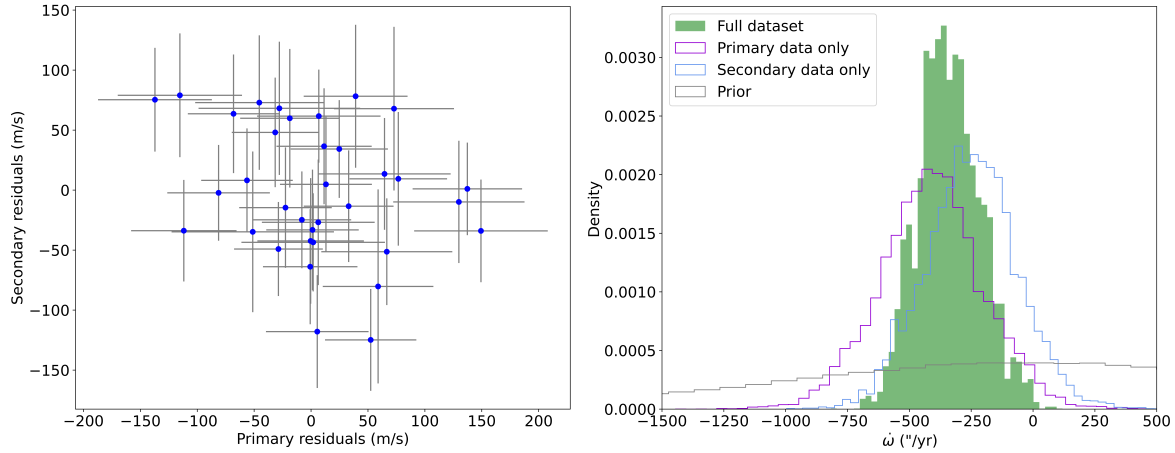


Figure 2: **Independent analysis of primary and secondary radial velocity data.** Panel A (left) shows the lack of correlation between the residuals of the primary and secondary. Panel B (right) shows the posterior distribution of $\dot{\omega}$ for the analyses of the primary, the secondary, and the full dataset compared to the prior distribution.

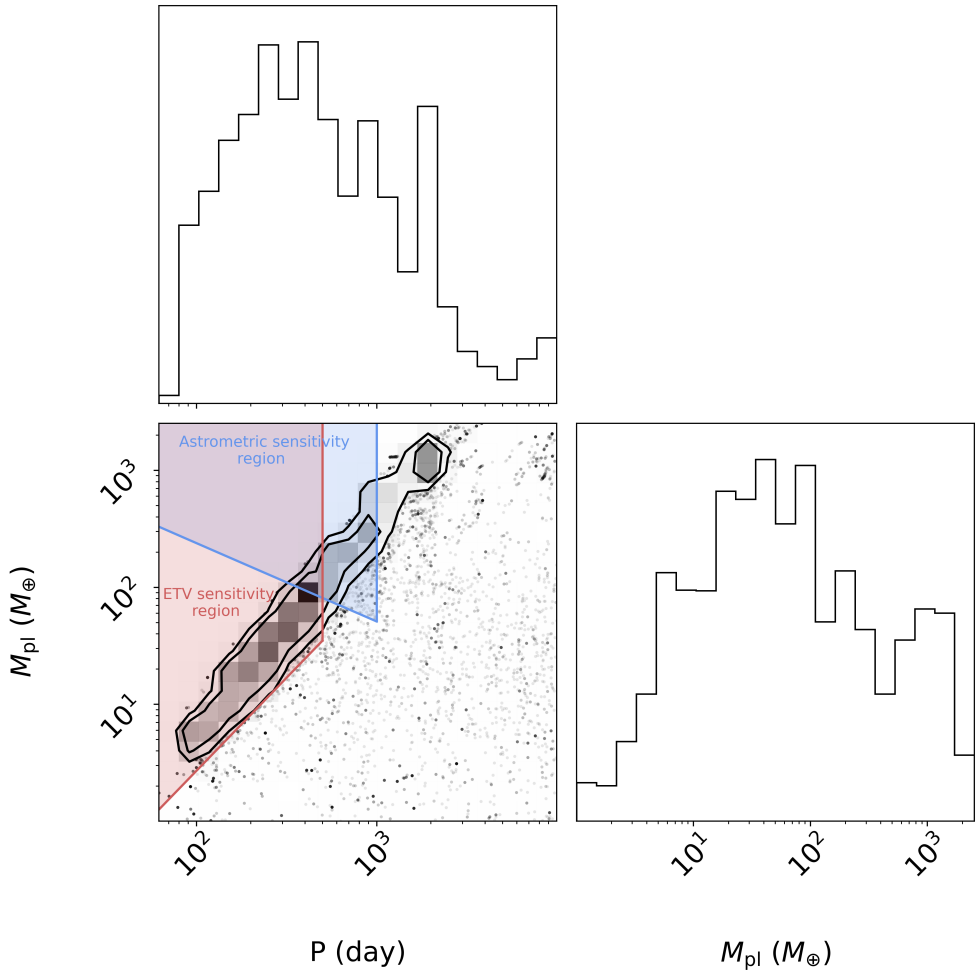


Figure 3: **Planet masses and periods** Corner plot of Periods and masses consistent with the induced precession rate from an N-body fit. Regions of sensitivity are shown for: 1) a three year astrometric campaign with the VLT in blue and 2) two years of eclipse timing monitoring with 1 minute timing precision (as was achieved with SPECULOOS) in red.

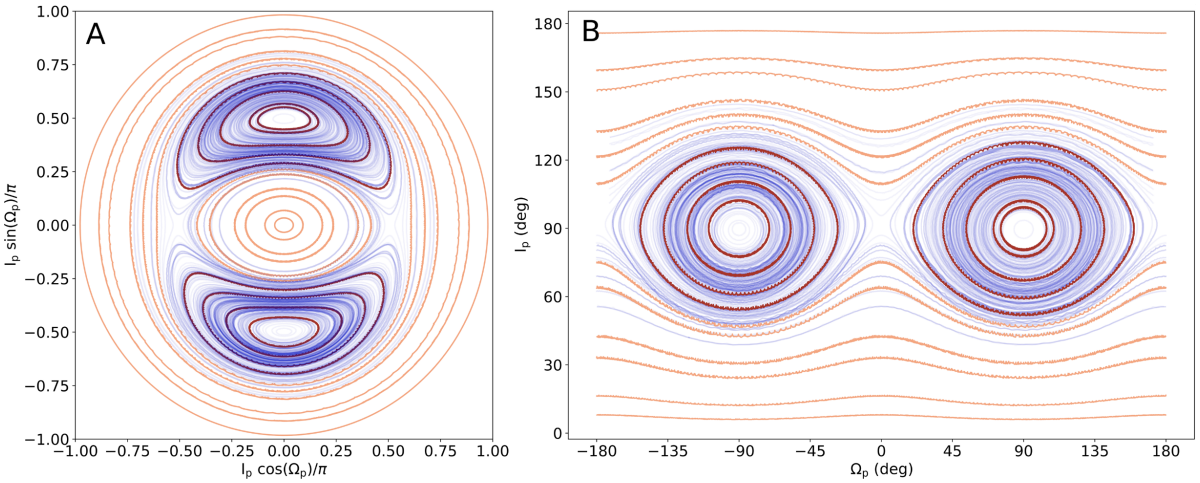


Figure 4: **Level curves of the Hamiltonian for 2M1510 with the colours denoting the regions of libration and circulation.** These are trajectories of test particles orbiting the binary. The red trajectories show the regions of libration and the orange trajectories the regions of circulation. The 584 stable orbits of 600 randomly drawn simulations from the posterior of the N- body fit are integrated and the trajectories overplotted in blue. Note that since the simulations shown in blue are drawn from the N-body fit they are for massive objects not test particles. Two different projections are shown.

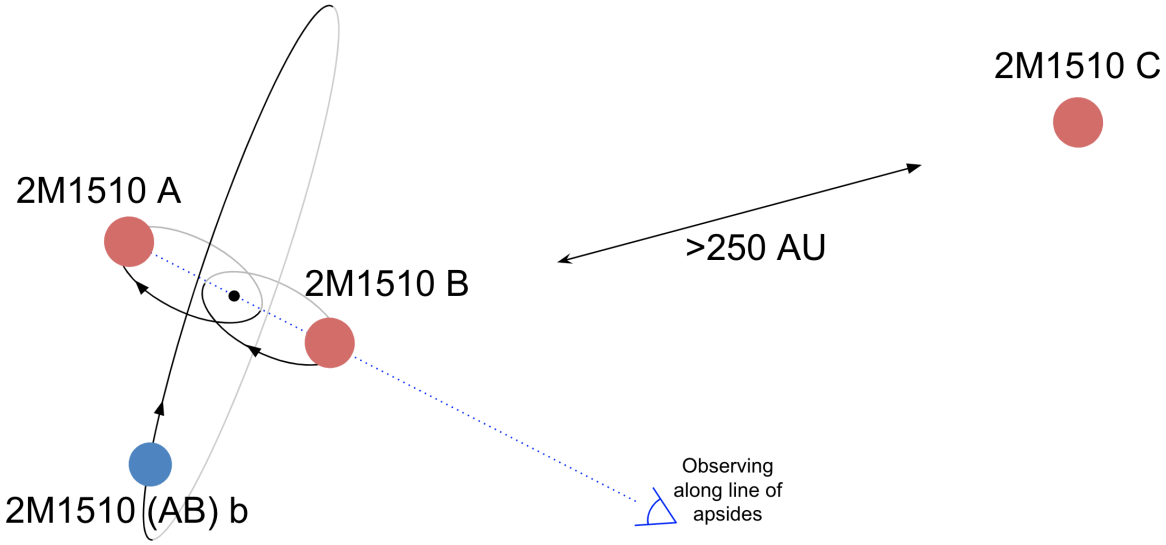


Figure 5: **Configuration of 2M1510 and naming convention for the various bodies.** Brown dwarfs are in red and the planet is in blue. Direction to earth relative to the binary is shown.

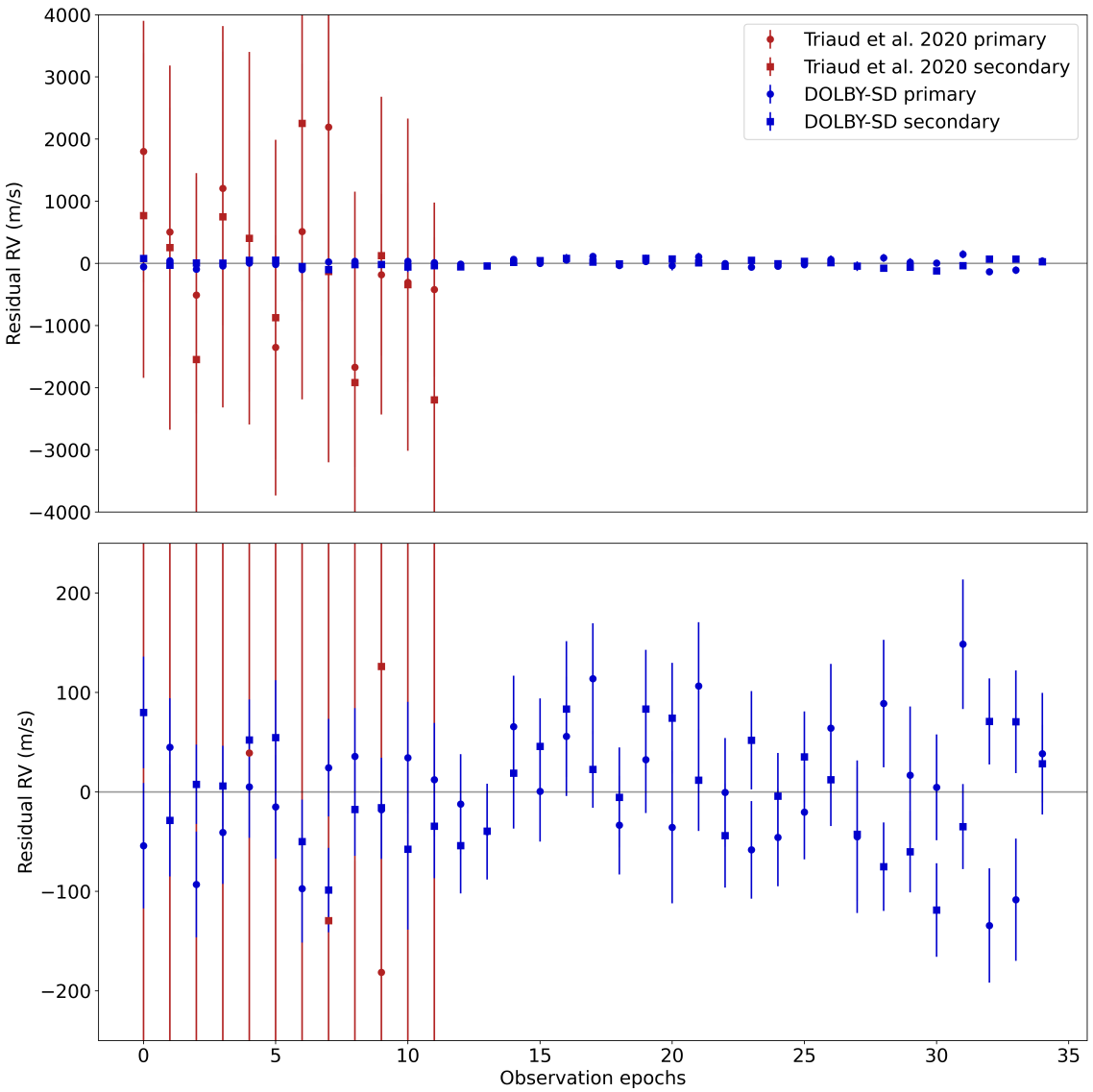


Figure 6: **Comparison of radial velocity reduction methods.** Figure showing residuals relative to the first epoch in m/s for the two stars, primary (circles) and secondary (squares). The blue points represent the RVs measured using the DOLBY-SD method (this work) and the red circles represent literature values from (*27*). Panel B (bottom) is a zoom-in of panel A (top) so that the uncertainties on the DOLBY-SD data can be seen.

Table 1: **Table of parameters for the binary brown dwarf.** Parameters from both the Keplerian (+precession) fit and from the n-body fit. 1σ uncertainties are reported in brackets precise to the last two significant digits. [1]N-body fit parameters are osculating parameters at reference time bjd 2 458 984.600486. [2] Inclination value taken from (*27*). [3] Masses for keplerian fit are derived from P, K, e, and i.

Parameter & units	Keplerian fit	N-body fit[1]
$P_{\rm bin}$ (days)	20.907495(88)	20.90769(28)
$e_{\rm bin}$	0.36035(51)	0.35957(67)
$\omega_{\rm bin}$ (deg)	284.33(13)	284.36(11)
$T_{\rm peri}$ (BJD)	2 459 070.5568(73)	2 459 070.5601(70)
$\dot{\omega}_{\rm bin}$ (" yr^{-1})	−343(126)	—
$i_{\rm bin}$ (deg)	88.5(0.1)[2]	88.5(0.1)[2]
$K_{\rm A}$ (km s^{-1})	16.792(13)	—
$q_{\rm bin}$	1.0034(10)	—
$M_{\rm A}$ ($M_\odot$)	0.033104(68)[3]	0.033101(73)
$M_{\rm B}$ ($M_\odot$)	0.033219(67)[3]	0.033212(69)

Table 2: **Radial velocity data.** Radial velocity observations taken with UVES between August 2017 - April 2019. RV extraction performed with DOLBY-SD.

Times	RV_1	$RVerr_1$	RV_2	$RVerr_2$
(BJD)	m s^{-1}	m s^{-1}	m s^{-1}	m s^{-1}
2457981.558	-23.106923	0.056350	-0.613241	0.056057
2457983.531	-4.406202	0.040391	-19.255910	0.056296
2457984.532	3.761294	0.045071	-27.494813	0.039901
2457986.559	5.374921	0.043314	-29.052112	0.040323
2457987.537	2.988056	0.042744	-26.582181	0.040730
2457989.558	-2.997553	0.043627	-20.635972	0.057756
2457991.534	-8.681811	0.046340	-15.158845	0.042329
2458152.334	5.912090	0.040125	-29.627186	0.042429
2458163.834	-20.875167	0.039464	-2.845042	0.046541
2458172.846	4.554757	0.040630	-28.234090	0.050263
2458195.825	5.034781	0.048589	-28.702016	0.080853
2458198.845	-3.593771	0.049554	-20.103728	0.052319
2458588.224	-20.862209	0.041492	-2.942019	0.047969
2458588.243	-20.753037	0.039004	-3.063875	0.039198
2458588.265	-20.486708	0.042863	-3.165794	0.055679
2458588.284	-20.410925	0.041825	-3.279154	0.048291

Table 3: **Radial velocity data continued.** Radial velocity observations taken with UVES between May 2019 - August 2023. RV extraction performed with DOLBY-SD.

Times	RV_1	$RVerr_1$	RV_2	$RVerr_2$
(BJD)	m s^{-1}	m s^{-1}	m s^{-1}	m s^{-1}
2458608.228	-25.351097	0.052723	1.735621	0.068176
2458612.145	5.589511	0.048110	-29.095287	0.038565
2458614.158	4.526084	0.040668	-28.210611	0.050178
2458626.097	-25.371938	0.045630	1.733123	0.059567
2458631.143	-10.272900	0.070999	-13.387907	0.055523
2458633.165	5.892015	0.057684	-29.415012	0.050951
2460063.308	-13.600389	0.046803	-10.155635	0.052327
2460076.259	6.356078	0.040115	-30.001234	0.049416
2460076.280	6.375967	0.040250	-30.064740	0.043314
2460076.295	6.405569	0.038149	-30.029529	0.045650
2460105.150	-13.603015	0.058107	-10.032466	0.046587
2460108.154	-20.791822	0.071329	-3.033409	0.066947
2460132.984	-27.027480	0.057553	3.280402	0.044459
2460139.089	6.451245	0.063070	-30.133414	0.040886
2460146.995	-13.737078	0.045084	-10.089194	0.047018
2460147.010	-13.630654	0.058699	-9.967987	0.042765
2460170.042	-19.002846	0.050005	-4.791411	0.043216
2460171.022	-21.174264	0.054583	-2.602333	0.051557
2460181.984	5.098614	0.054269	-28.675622	0.038783

6.2 Detecting circumbinary planets using apsidal precession

Three ingredients are important for a measurement of apsidal precession: a large signal amplitude of apsidal precession, a long baseline of data, and precise measurements. Admittedly, for most signals one could want to measure, a large amplitude and precise data are always important, however the long baseline is a particularity of this kind of linear long-term signal. What follows are some examples of how different combinations of these three can lead to and have led to insights on binary systems and circumbinary planets based on both radial velocity data and eclipse timing variations.

6.2.1 Apsidal precession from radial velocities

Apsidal precession of an eccentric orbit causes the shape of the radial velocity curve to change, this is shown in Figure 6.8. Many studies have observed apsidal precession of massive binaries as a means to study the internal structure and spin-alignment of massive stars (e.g. Rauw et al., 2016; Schmitt et al., 2016; Rosu et al., 2020, 2022). Many of these studies make use of radial velocities covering an extended time baseline (e.g. Schmitt et al., 2016 use data dating back to 1908). In the cases of very massive stars and evolved stars, tidal interactions are strong and can dominate the apsidal precession rate, this can also be true for hot Jupiter systems (Ragozzine and Wolf, 2009). For lower-mass main-sequence binaries, such as those studied in BEBOP, the orbital separations are wide enough that tidally/rotationally induced apsidal precession is typically lower than the precession from general relativistic effects (see Section 2.2) and these can both be small compared to that induced by a circumbinary companion.

Another system which has a long-baseline of radial velocity data is AI Hya (Kahraman Aliçavuş et al., 2023). Taking the radial velocities and applying the BINARIESmodel gives $\dot{\omega} = 600 \pm 190$ "/yr. The left hand panel of Figure 6.9 shows the distribution of masses and orbital periods that is consistent with this precession rate. On the right is shown the similar figure for TIC 172900988 which has a detected planet consistent with the measured apsidal precession rate of $\dot{\omega} = 215^{+56}_{-59}$ "/yr (see Section 3.1). The detection limit from the radial velocities is also shown

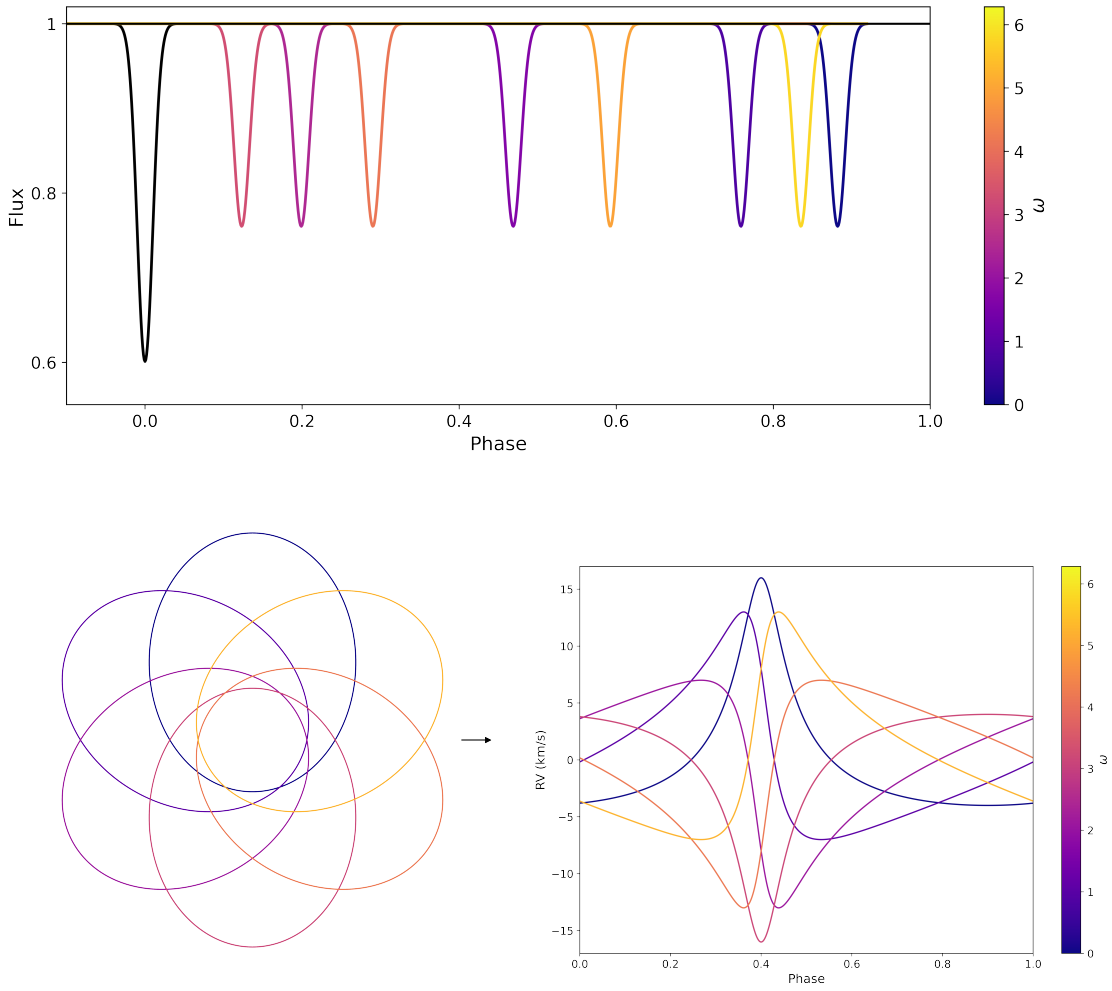


Figure 6.8: Top: apsidal precession's effect on the offset between primary and secondary eclipse. Bottom left: apsidal precession's effect on the orbit, the arrow points to the observer. Bottom right: apsidal precession's effect on the shape of the radial velocity curve. Colours in all panels correspond to the value of ω.

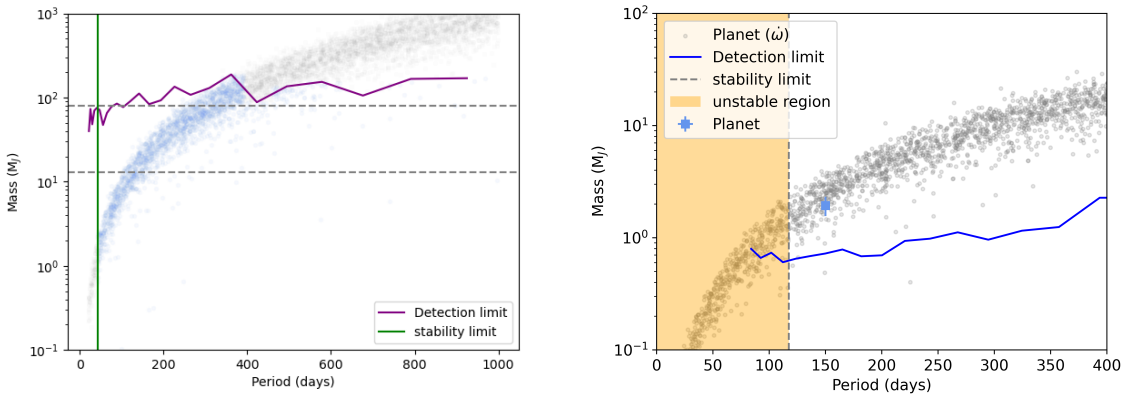


Figure 6.9: Planet masses and orbital periods consistent with apsidal precession rate relative to instability limit and radial velocity sensitivity threshold. Left: AI Hya. Right: TIC 172900988 (figure similar to Figure 3.15).

in Figure 6.9. AI Hya does not have high precision radial velocities due to the stellar types, so the precession rate is consistent with being produced by a third object with mass ranging from planetary up to a low-mass star. AI Hya has a large apsidal precession signal and a long baseline (51 years) but imprecise data ($\approx$ 2 km/s); TIC 172900988 has a moderate signal and short baseline (923 days), but precise data ($\approx$ 30 m/s).

A few BEBOP systems have a notable apsidal precession measurement. The first is J1250+26 (see Section 4.3.1 Figure 4.17), which has a measured value of $\dot{\omega} = 174 \pm 63$ "/yr. The same figure as above is produced for this system and shown on the left hand side of Figure 6.10[1]. The posterior distribution in mass and period for the planet/brown dwarf companion is also plotted and can be seen to be consistent with producing the apsidal precession. This is also shown on the right hand side of Figure 6.10 where the posterior distribution in $\dot{\omega}$ is compared to the calculated values for the induced $\dot{\omega}$ by the third body (calculated using equations from the appendix of the paper in Section 2.2).

J0310-31 (see Section 4.3.1 Figure 4.22) also has a significant measurement of apsidal precession at $\dot{\omega} = 21.3^{+4.5}_{-4.2}$ "/yr. This is not (fully) due to a circumbinary planet, but is instead probing the apsidal precession from general relativity. Shown on the left in Figure 6.11 is the posterior distribution on $\dot{\omega}$ as measured compared to that from the general relativity contribution.

[1]The apsidal precession contribution from general relativity is accounted for but not that which is tidally/rotationally induced.

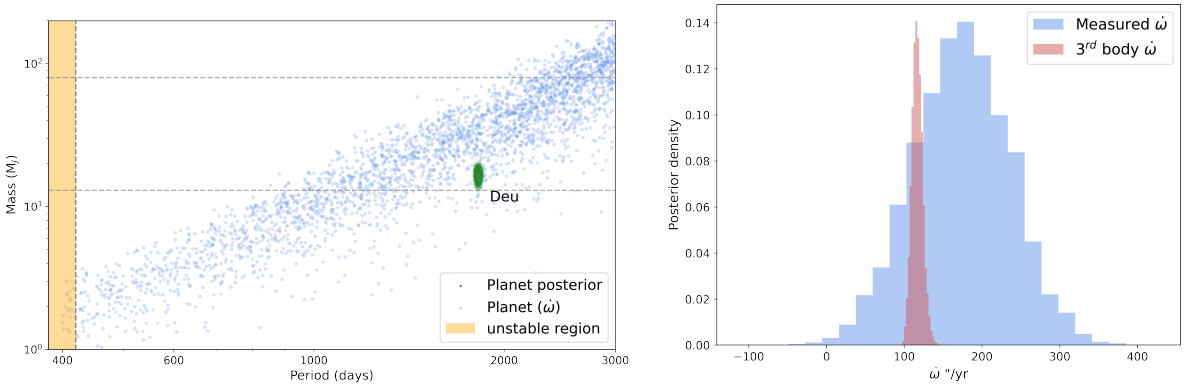


Figure 6.10: J1250+26. Left: planet masses and periods consistent with $\dot{\omega}$ measurement, posterior distribution from the planet detection is also shown as well as the instability zone. Right: Histograms of measured $\dot{\omega}$ and the calculated 3rd body induced $\dot{\omega}$.

With enough precision to rule out all other causes of apsidal precession (circumbinary planets, tides, etc) this kind of measurement could be a test of general relativity. In this case the measurement is consistent with general relativity. This is one of the first extrasolar constraints on relativistic apsidal precession, one previous example is DI Her (Martynov and Khaliullin, 1980; Guinan and Maloney, 1985; Albrecht et al., 2009)[2]

On the right hand side of Figure 6.11 is the posterior masses and period for all possible planets in the `kima` analysis alongside the distribution of planets that could cause the precession once the general relativity contribution has been removed. Note that the posteriors from $\dot{\omega}$ look clustered at high masses even though the residual measurement is consistent with 0. This is because the half-Gaussian from which the points are drawn is being represented on a log-distributed scale. Any planet posteriors above the points based on precession can, however, be rejected as they would cause a precession rate higher than has been detected (assuming coplanarity). The planet candidate and many other periodicities in this system are therefore still credible. Some posterior densities are inconsistent with the apsidal precession, these mostly correspond to orbits that would be inside the unstable region.

J0759-69 is one of the BEBOP systems with a long-period signal. It has a measurement of $\dot{\omega} = 323 \pm 96$ "/yr. This is higher than that which could be caused by the long-period planet (< 7 "/yr), or by GR alone (9.7 ± 0.9 "/yr). Figure 6.12 presents similar information to the

[2]I was unable to find any other published measurements of GR $\dot{\omega}$ on exoplanets or binaries.

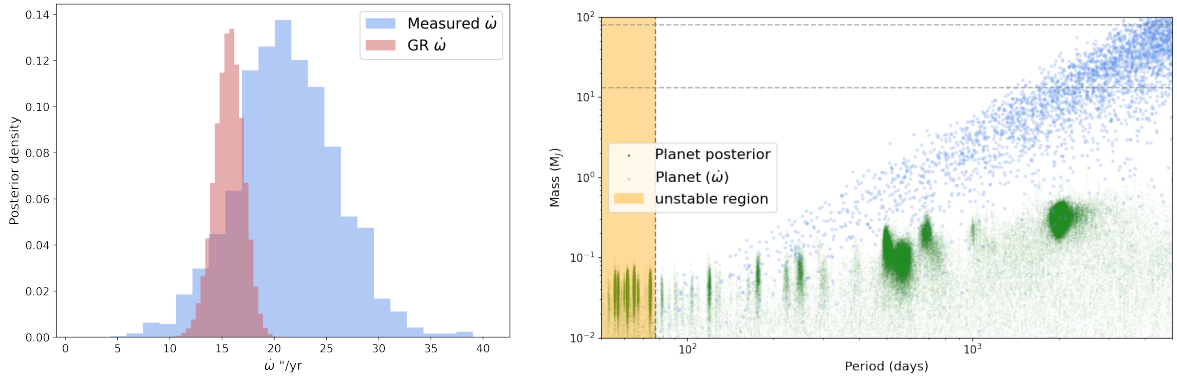


Figure 6.11: J0310-31. Left: Histograms of measured $\dot{\omega}$ and the calculated general relativity induced $\dot{\omega}$. Right: planet masses and periods consistent with residual $\dot{\omega}$ values, posterior distribution of all planets up to Np=3 are shown as well as the instability zone.

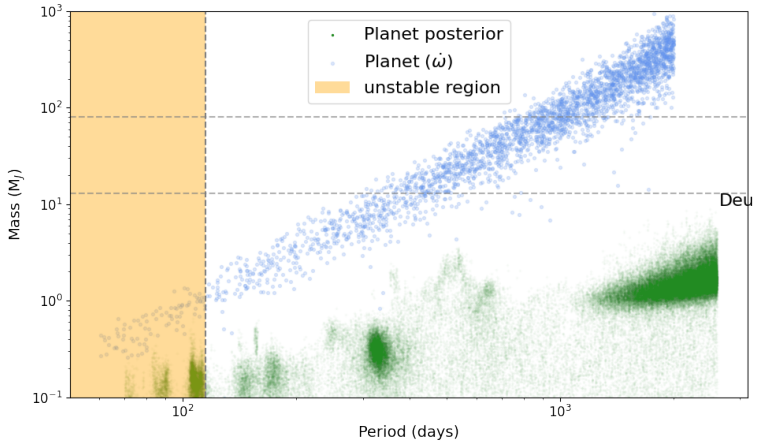


Figure 6.12: J0759-69. Planet masses and periods consistent with $\dot{\omega}$ values, posterior distribution of all planets up to Np=3 are shown as well as the instability zone.

figures described above, but for J0759-69. Possible explanations for the high precession rate are: multiple planets and GR are all combining to cause a high precession rate; the outer planet is not coplanar with the binary and the increased mass counters the lessened precession rate due to misalignment; the measurement is anomalous.

In Figure 6.13 two histograms of the distribution of the significance of the $\dot{\omega}$ measurements across the BEBOP sample can be seen. In the panel on the left, the overdensity around zero is attributed to the prior distribution used in the general BEBOP analysis of $\mathcal{N}(0, 1000)$. Binaries on circular orbits return the prior (or close-to it) as a posterior since varying ω has little effect of the radial velocities. Therefore these will give a result biased towards 0σ. The panel on the right

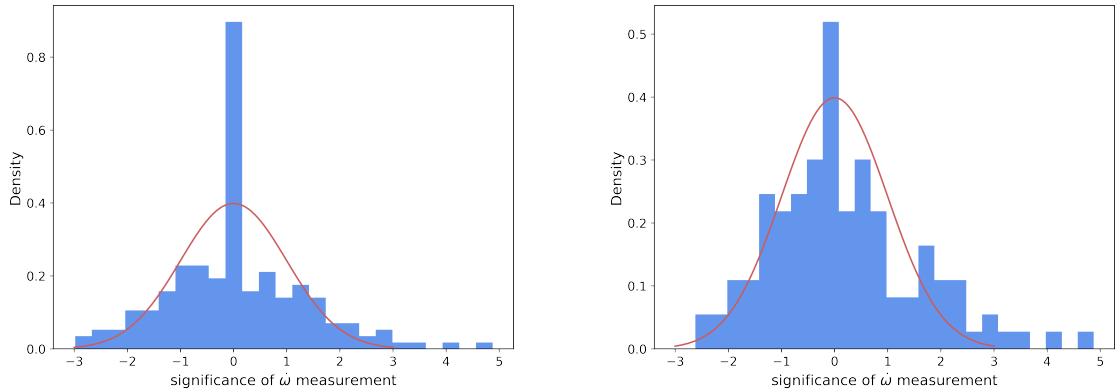


Figure 6.13: Distribution of the significance of the $\dot{\omega}$ measurements from the BEBOP sample shown alongside a Gaussian with $\mu = 0$, $\sigma = 1$. Left: all binaries. Right: restricted to binaries with $e > 0.05$.

displays the same information including only those binaries with $e > 0.05$. The overdensity at positive sigma is expected to be real and from planets or general relativity causing precession. A much smaller excess is seen on the negative side implying that polar planets are likely rare within BEBOP sample. The lack of evidence for polar planets is not surprising based on the expectation that they should form preferentially around equal mass binaries (Cuello and Giuppone, 2019), and the BEBOP binaries typically have mass ratio $q < 0.3$. The BEBOP apsidal precession measurements rely on a moderate-long baseline (≈1000-2000 days) and precise measurements (≈3-30 m/s).

6.2.2 Apsidal precession from eclipse timing variations

Apsidal precession also causes a variation in the offset between primary and secondary mid-eclipse time, as shown in Figure 6.8 (see Section 1.3.2 to recall why e and ω affect the offset between eclipses). Measuring the binary's apsidal precession based on the offset changing has been used to measure/constrain the masses of the *Kepler* circumbinary planets where possible (e.g. Doyle et al., 2011; Kostov et al., 2016). This has been the main source of planet mass estimates for the *Kepler* circumbinary systems. These measurements used the precise mid-eclipse times from *Kepler* and the moderate time-baseline of four years.

Apsidal precession was also measured in the TIC 172900988 system (Kostov et al., 2021). In

this case archival eclipses from various ground-based photometric surveys were combined along with *TESS* data to obtain a measurement of the precession rate used to measure the planet's mass (Kostov et al., 2021) (Both the mass and period were overestimated here, see Section 3.1). This measurement used less precise eclipse measurements than those used for the *Kepler* systems, but covered a long baseline of $\approx$ 14 years, compared to the four years from *Kepler*. The radial velocity follow-up also measured the apsidal precession rate measurement (see the discussion in Section 6.2.1).

TIC 172900988b was discovered from a one-two punch event (Kostov et al., 2021). However, the archival eclipses dating back many years already existed, and in principle, a planetary mass companion could have been inferred in the absence of transits (and possibly even in absence of any TESS data). It is therefore expected that other systems have a similar significant apsidal precession that is detectable in archival data but the responsible planet hasn't happened to transit during a *TESS* sector.

An efficient way to detect more circumbinary planet candidates is therefore to search archival photometry for TIC 172900988-like systems (or archival radial velocities for AI Hya-like systems). Such measurements would not guarantee a companion to be planetary due to the degeneracy in mass and orbital period (as seen in Figure 6.9), but can be used to compile a list of likely circumbinary planet candidates. Various methods of confirmation/validation can be deployed on this sample. To assess the yield that might be expected from such a study, I generate a synthetic population of circumbinary planets, and assess what fraction would lead to a detectable apsidal precession measurement.

The synthetic population of binaries uses the distributions from Duquennoy and Mayor (1991). Two separate circumbinary planet populations are injected, gas giants and sub-neptunes. The various parameters used are shown in Table 6.4. I will consider two predicted sensitivities to apsidal precession rates from eclispe timing variations, one optimistic and one conservative. With a 10 year time baseline, a timing precision of 17 minutes leads to an $\dot{\omega}$ threshold of 100 "/yr and a precision of 3.5 minutes to a threshold of 20 "/yr.

To 10% of the synthetic binaries a planet drawn randomly from the existing population of

Table 6.4: Parameters used in yield estimate of detectable apsidal precession rates. Binaries are generated based on the distributions shown, planets are drawn from the NASA exoplanet archive based on the constraints shown, with caveats for those that would be inside the unstable region. Unstable gas giants are replaced with a random other planet until stable. *Sub-neptunes that are unstable are with 50% chance either placed at 1.2× the stability limit or removed, this assumes that in their migration, half of the sub-neptunes are ejected and half park outside the disc cavity (Martin and Triaud, 2014). This leads to a true injected occurrence of sub-neptunes of ~ 26%

Binary parameter distributions		Restricted to
$log(P_{\rm bin}) \sim \mathcal{N}(4.8, 2.3)$		$10 \leq P_{\rm bin} \leq 60$ days
$e_{\rm bin} \sim \mathcal{N}(0.3, 0.2)$		$e \geq 0.3$
$q_{\rm bin} \sim \mathcal{N}(0.23, 0.42)$		$0 \leq q_{\rm bin} \leq 1$
$M_1 \sim \mathcal{N}(1, 0.1)\, M_\odot$		—
Planet params:	Gas Giants	Sub-Neptunes
$P_{\rm pl}$	40 days $\leq P \leq$ 10 yrs	$P \leq$ 1000 days
$M_{\rm pl}$	$0.1\, M_{\rm Jup} \leq M \leq 2\, M_{\rm Jup}$	$1\, M_\oplus \leq M \leq 0.1\, M_{\rm Jup}$
Injected occurrence rate	10%	50%*

gas giants is assigned. In this setup, 50% of the planets are in a polar orientation under the assumption that polar circumbinary discs are as common as coplanar discs (Kennedy et al., 2019) and that polar discs form planets at a similar rate to coplanar discs (Childs and Martin, 2021). These assumptions are optimistic. Ceppi et al. (2024) find that 17 ± 8% of circumbinary discs are polar, based on a sample size of 15 discs. However the relative distribution is expected to depend on binary eccentricity (Kennedy et al., 2019), and in this prediction only binaries with $e > 0.3$ are considered. While no polar circumbinary planet has been confirmed, the sensitivity to polar circumbinary planets of various circumbinary planet surveys is not clear, so there are no strong observational constraints of the planet-formation ability of polar circumbinary discs.

The resulting $\dot{\omega}$'s are presented in the left-hand panel of Figure 6.14. From the two expected $\dot{\omega}$ sensitivities, such a study would expect to detect significant apsidal precession on 1.7%-4.5% of binaries (the *Kepler* and *TESS* EB catalogues have 2878 and 4580 entries each). Separating into polar and coplanar (retrograde and prograde apsidal precession) give 0.4%-1.7% of binaries with a coplanar gas-giant companion and 1.3%-2.8% with a polar gas-giant companion.

A similar yield calculation to above can be done for the sub-neptunes. Their occurrence is ~ 50% around single stars (Petigura et al., 2013), so I inject a sub-neptune around half of

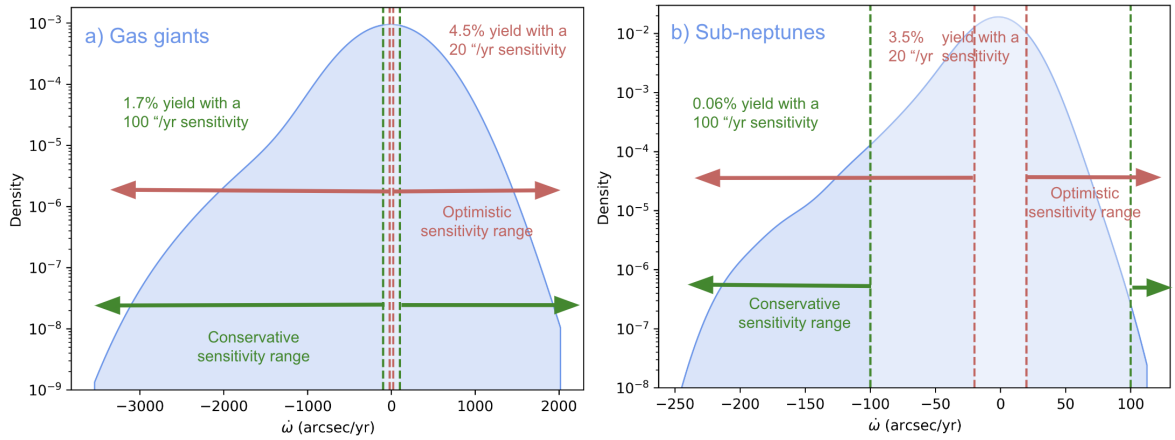


Figure 6.14: Estimated yields of circumbinary planets inducing a significant apsidal precession, for a potential study of a eclipse timing variations. Vertical dashed lines show the cutoffs in sensitivity to $\dot{\omega}$. Left: Gas giant planets $0.1M_{\rm Jup} \leq M \leq 2M_{\rm Jup}$. Right: sub-neptune planets $1M_{\oplus} \leq M \leq 0.1M_{\rm Jup}$. For visual clarity, all binaries with no planets (and hence $\dot{\omega} = 0$) have been removed.

the binaries in the population, again placing half of the planets on polar orbits. After stability considerations (Table 6.4) 25.4% of the synthetic binaries have a sub-neptune. From the expected $\dot{\omega}$ sensitivity thresholds, the expected yield of significant apsidal precession measurements is 0.06%-3.5%. This is also shown in Figure 6.14. As above separating this yield gives 0%-0.4% of binaries with a coplanar sub-neptune and 0.06%-3.1% with a polar sub-neptune.

The yields calculated are higher for polar planets than coplanar planets despite the number of each injected being the same. This discrepancy is because the apsidal precession rate induced by a polar planet has a larger magnitude than that from a coplanar planet of otherwise identical parameters (Zhang and Fabrycky, 2019). A search based on apsidal precession will therefore be more sensitive to polar planets than coplanar ones and can be expected to constrain their relative occurrence rate. With this bias towards detecting polar planets in mind if fewer binaries are found to have retrograde precession than prograde, a lower comparative rate of either polar discs or polar planet formation, or a differnce in the mass and orbital periods of these planets can be inferred. This can be done by comapring the true distributions of $\dot{\omega}$ to those shown in Figure 6.14.

The apsidal precession of a binary is a useful parameter for the study of circumbinary systems. It can constrain the mutual inclination of the system, distinguishing between polar

and coplanar orbits. Measuring apsidal precession can confirm the presence of and provide a mass constraint for a circumbinary planet, or even predict the presence of a previously-unknown circumbinary planet.

Building a population of polar circumbinary planets, as well as constraining the relative occurence rates between them and coplanar planets can help better understand the initial condidtions and early evolution of circumbinary discs. This has studied based on known polar circumbinary discs (Czekala et al., 2019; Ceppi et al., 2024). A sample of planets on top of this would be greatly beneficial. The wider the understanding of planetary systems at different stages of their evolution and in different stellar and planetary configurations is pushed, the closer a universal picture of planet formation and evolution becomes.

Chapter 7

Concluding remarks

This thesis has explored the topic of circumbinary planets, placed within the context of exoplanet science in general. The impetus for this work is that compared to both planets around single stars and S-type planets in wide binaries, there are much fewer known (and reliable) circumbinary planet detections.

I have attempted to deal with this lack of reliable detections by: improving the current ability to detect circumbinary planets; preparing for ways to detect circumbinary planets more easily and using data that will be available in the future; and by working on a test of the reliability of the controversial detections. I have made use of available analysis tools and developed them, as well as developing new tools designed to detect and characterise circumbinary exoplanets. The binary-specifc model development (along with a large amount of work from many other people) has led to new detections of circumbinary planets using the radial velocity method (Chapter 3 and Chapter 4). I have investigated how the use of apsidal precession and *Gaia* astrometry will lead to more circumbinary planet detections in the future, initiating the development of tools for these works as well as making predictions of yields (Section 3.4, Section 5.2, and Section 6.2). I have made use of an apsidal precession measurement leading to an exciting serendipitous discovery of a candidate planet on a polar orbit (Section 6.1). I have developed a tool to analyse the eclipse timing variations and implemented a test to validate the uncertain signals claimed as circumbinary planets in the HW Vir system (Section 5.1).

Future applications and extensions of this work abound. The radial velocity tools I developed will continue to be used within BEBOP and other circumbinary radial velocity studies that may arise. The BEBOP analysis and observations will continue, and occurence rates will be calculated. The survey will also be extended the to new binaries, pushing sensitivity down to lower-mass planets. The eclipse timing variation method can be applied to the wider set of eclipse timing variation signals from post common-envelope binaries giving them another test to pass and help distinguish the real planets. The astrometric tool will be applied to many systems after the next data release from *Gaia* (scheduled to be released "no earlier than mid-2026"). The use of apsidal precession to detect circumbinary planets is exciting and the project laid out at the end of Chapter 6 will be undertaken in the coming years. I expect this to detect circumbinary gas giants similar to ones known, increasing the sample size. This project is a promising way to detect polar circumbinary planets and measure their occurence relative to coplanar circumbinary planets (even with no detections of polar planets this will be possible).

Overall, my past and future work involves: detecting more circumbinary planets, refining the parameters of the known circumbinary planets, confirming/refuting the uncertain planet candidates, and extending to detect more different morphologies of circumbinary planets. These will, combined, give rise to a better understanding of circumbinary planet formation and evolution, and allow comparisons to other planet populations.

References

Agol, E. et al. (May 2005). "On detecting terrestrial planets with timing of giant planet transits". en. In: *Monthly Notices of the Royal Astronomical Society* 359.2, pp. 567–579. ISSN: 0035-8711, 1365-2966. DOI: 10.1111/j.1365-2966.2005.08922.x.

Aigrain, S., F. Pont, and S. Zucker (Feb. 2012). "A simple method to estimate radial velocity variations due to stellar activity using photometry". In: *Monthly Notices of the Royal Astronomical Society* 419. Publisher: OUP ADS Bibcode: 2012MNRAS.419.3147A, pp. 3147–3158. ISSN: 0035-8711. DOI: 10.1111/j.1365-2966.2011.19960.x.

Alaguero, Antoine et al. (July 2024). "V892 Tau: A tidally perturbed circumbinary disc in a triple stellar system". In: *Astronomy and Astrophysics* 687. Publisher: EDP ADS Bibcode: 2024A&A...687A.311A, A311. ISSN: 0004-6361. DOI: 10.1051/0004-6361/202449683.

Albrecht, Simon et al. (Sept. 2009). "Misaligned spin and orbital axes cause the anomalous precession of DI Herculis". In: *Nature* 461. ADS Bibcode: 2009Natur.461..373A, pp. 373–376. ISSN: 0028-0836. DOI: 10.1038/nature08408.

Albrecht, Simon H., Rebekah I. Dawson, and Joshua N. Winn (Aug. 2022). "Stellar Obliquities in Exoplanetary Systems". In: *Publications of the Astronomical Society of the Pacific* 134. Publisher: IOP ADS Bibcode: 2022PASP..134h2001A, p. 082001. ISSN: 0004-6280. DOI: 10.1088/1538-3873/ac6c09.

Albrecht, Simon H. et al. (July 2021). "A Preponderance of Perpendicular Planets". In: *The Astrophysical Journal* 916. Publisher: IOP ADS Bibcode: 2021ApJ...916L...1A, p. L1. ISSN: 0004-637X. DOI: 10.3847/2041-8213/ac0f03.

Aly, Hossam et al. (May 2015). "Misaligned gas discs around eccentric black hole binaries and implications for the final-parsec problem". In: *Monthly Notices of the Royal Astronomical Society* 449. Publisher: OUP ADS Bibcode: 2015MNRAS.449...65A, pp. 65–76. ISSN: 0035-8711. DOI: 10.1093/mnras/stv128.

Andrews, Sean M. et al. (July 2013). "The Mass Dependence between Protoplanetary Disks and their Stellar Hosts". In: *The Astrophysical Journal* 771. Publisher: IOP ADS Bibcode: 2013ApJ...771..129A, p. 129. ISSN: 0004-637X. DOI: 10.1088/0004-637X/771/2/129.

Applegate, James H. (Feb. 1992). "A Mechanism for Orbital Period Modulation in Close Binaries". In: *The Astrophysical Journal* 385. ADS Bibcode: 1992ApJ...385..621A, p. 621. ISSN: 0004-637X. DOI: 10.1086/170967.

Armitage, Philip J. (Dec. 2024). *Planet formation theory: an overview*. arXiv:2412.11064 [astro-ph]. DOI: 10.48550/arXiv.2412.11064.

Armstrong, D. J. et al. (Oct. 2014). "On the abundance of circumbinary planets". In: *Monthly Notices of the Royal Astronomical Society* 444. ADS Bibcode: 2014MNRAS.444.1873A, pp. 1873–1883. ISSN: 0035-8711. DOI: 10.1093/mnras/stu1570.

El-Badry, Kareem et al. (Nov. 2024). "A generative model for Gaia astrometric orbit catalogs: selection functions for binary stars, giant planets, and compact object companions". In: *The Open Journal of Astrophysics* 7. ADS Bibcode: 2024OJAp....7E.100E, p. 100. ISSN: 2565-6120. DOI: 10.33232/001c.125461.

Bakos, G. Á. et al. (Dec. 2009). "HAT-P-13b,c: A Transiting Hot Jupiter with a Massive Outer Companion on an Eccentric Orbit". In: *The Astrophysical Journal* 707. Publisher: IOP ADS Bibcode: 2009ApJ...707..446B, pp. 446–456. ISSN: 0004-637X. DOI: 10.1088/0004-637X/707/1/446.

Ballard, Sarah et al. (Dec. 2011). "The Kepler-19 System: A Transiting 2.2 R_earth Planet and a Second Planet Detected via Transit Timing Variations". In: *The Astrophysical Journal* 743. Publisher: IOP ADS Bibcode: 2011ApJ...743..200B, p. 200. ISSN: 0004-637X. DOI: 10.1088/0004-637X/743/2/200.

Baranne, A. et al. (Oct. 1996). "ELODIE: A spectrograph for accurate radial velocity measurements." In: *Astronomy and Astrophysics Supplement Series* 119. ADS Bibcode: 1996A&AS..119..373B, pp. 373–390. ISSN: 0365-0138.

Barragán, Oscar et al. (Jan. 2022). "PYANETI - II. A multidimensional Gaussian process approach to analysing spectroscopic time-series". In: *Monthly Notices of the Royal Astronomical Society* 509. Publisher: OUP ADS Bibcode: 2022MNRAS.509..866B, pp. 866–883. ISSN: 0035-8711. DOI: 10.1093/mnras/stab2889.

Baştürk, Özgür et al. (Jan. 2023). "Eclipse Timing Variations Observed in PCEB Systems". In: *Bulletin de la Societe Royale des Sciences de Liege* 92. ADS Bibcode: 2023BSRSL..9211197B, p. 11197. DOI: 10.25518/0037-9565.11197.

Bate, Matthew R. (Apr. 2018). "On the diversity and statistical properties of protostellar discs". In: *Monthly Notices of the Royal Astronomical Society* 475. Publisher: OUP ADS Bibcode: 2018MNRAS.475.5618B, pp. 5618–5658. ISSN: 0035-8711. DOI: 10.1093/mnras/sty169.

Baycroft, Thomas A., Amaury H. M. J. Triaud, and Pierre Kervella (Dec. 2023a). "New evidence about HW Vir's circumbinary planets from Hipparcos-Gaia astrometry and a reanalysis of the eclipse timing variations using nested sampling". In: *Monthly Notices of the Royal Astronomical Society* 526. ADS Bibcode: 2023MNRAS.526.2241B, pp. 2241–2250. ISSN: 0035-8711. DOI: 10.1093/mnras/stad2794.

Baycroft, Thomas A., Amaury H. M. J. Triaud, and Dong Lai (Jan. 2024). "Progress report on the BEBOP search for circumbinary planets with radial velocities". In: 382. Conference Name: IAU Symposium ADS Bibcode: 2024IAUS..382...51B, pp. 51–58. DOI: 10.1017/S1743921323004180.

Baycroft, Thomas A. et al. (Aug. 2023b). "GJ 9404 b: A Confirmed Eccentric Planet, and not a Candidate". In: *Research Notes of the American Astronomical Society* 7. Publisher: IOP ADS Bibcode: 2023RNAAS...7..175B, p. 175. ISSN: 2515-5172. DOI: 10.3847/2515-5172/acefc5.

Baycroft, Thomas A. et al. (May 2023c). "Improving circumbinary planet detections by fitting their binary's apsidal precession". In: *Monthly Notices of the Royal Astronomical Society* 521. ADS Bibcode: 2023MNRAS.521.1871B, pp. 1871–1879. ISSN: 0035-8711. DOI: 10.1093/mnras/stad607.

Baycroft, Thomas A. et al. (Apr. 2025). "Evidence for a polar circumbinary exoplanet orbiting a pair of eclipsing brown dwarfs". In: *Science Advances* 11. ADS Bibcode: 2025SciA...11..627B, eadu0627. DOI: 10.1126/sciadv.adu0627.

Bayeri, Ioannis (1603). *Ioannis Bayeri Uranometria omnium asterismorum continens schemata, nova methodo delineata aereis laminis expressa / tabulae in aes incidit Alexander Mair*. en.

Benedict, G. Fritz and Thomas E. Harrison (June 2017). "HD 202206: A Circumbinary Brown Dwarf System". In: *The Astronomical Journal* 153. Publisher: IOP ADS Bibcode: 2017AJ....153..258B, p. 258. ISSN: 0004-6256. DOI: 10.3847/1538-3881/aa6d59.

Bennett, D. P. et al. (Nov. 2016). "The First Circumbinary Planet Found by Microlensing: OGLE-2007-BLG-349L(AB)c". In: *The Astronomical Journal* 152. Publisher: IOP ADS Bibcode: 2016AJ....152..125B, p. 125. ISSN: 0004-6256. DOI: 10.3847/0004-6256/152/5/125.

Berger, James O. and Donald A. Berry (1988). "Statistical Analysis and the Illusion of Objectivity". In: *American Scientist* 76.2. Publisher: Sigma Xi, The Scientific Research Society, pp. 159–165. ISSN: 0003-0996.

de-Beurs, Zoe. L. et al. (Aug. 2022). "Identifying Exoplanets with Deep Learning. IV. Removing Stellar Activity Signals from Radial Velocity Measurements Using Neural Networks". In: *The Astronomical Journal* 164. Publisher: IOP ADS Bibcode: 2022AJ....164...49D, p. 49. ISSN: 0004-6256. DOI: 10.3847/1538-3881/ac738e.

Bitsch, Bertram et al. (Mar. 2015). "The structure of protoplanetary discs around evolving young stars". In: *Astronomy and Astrophysics* 575. ADS Bibcode: 2015A&A...575A..28B, A28. ISSN: 0004-6361. DOI: 10.1051/0004-6361/201424964.

Boley, Kiersten M. et al. (Sept. 2021). "Searching For Transiting Planets Around Halo Stars. II. Constraining the Occurrence Rate of Hot Jupiters". In: *The Astronomical Journal* 162. Publisher: IOP ADS Bibcode: 2021AJ....162...85B, p. 85. ISSN: 0004-6256. DOI: 10.3847/1538-3881/ac0e2d.

Bonfils, X. et al. (Jan. 2013). "The HARPS search for southern extra-solar planets. XXXI. The M-dwarf sample". en. In: *Astronomy & Astrophysics* 549, A109. ISSN: 0004-6361. DOI: 10.1051/0004-6361/201014704.

Borkovits, T. et al. (Feb. 2016). "A comprehensive study of the Kepler triples via eclipse timing". In: *Monthly Notices of the Royal Astronomical Society* 455. Publisher: OUP ADS Bibcode: 2016MNRAS.455.4136B, pp. 4136–4165. ISSN: 0035-8711. DOI: 10.1093/mnras/stv2530.

Borucki, W. J. and A. L. Summers (Apr. 1984). "The photometric method of detecting other planetary systems". In: *Icarus* 58. ADS Bibcode: 1984Icar...58..121B, pp. 121–134. ISSN: 0019-1035. DOI: 10.1016/0019-1035(84)90102-7.

Borucki, William J. et al. (Feb. 2003). "The Kepler mission: a wide-field-of-view photometer designed to determine the frequency of Earth-size planets around solar-like stars". In: 4854. Conference Name: Future EUV/UV and Visible Space Astrophysics Missions and Instrumentation. ADS Bibcode: 2003SPIE.4854..129B, pp. 129–140. DOI: 10.1117/12.460266.

Bouchy, F., F. Pepe, and D. Queloz (Aug. 2001). "Fundamental photon noise limit to radial velocity measurements". In: *Astronomy and Astrophysics* 374. ADS Bibcode: 2001A&A...374..733B, pp. 733–739. ISSN: 0004-6361. DOI: 10.1051/0004-6361:20010730.

Brewer, Brendon J. (Jan. 2015). *Inference for Trans-dimensional Bayesian Models with Diffusive Nested Sampling*. arXiv:1411.3921 [stat]. DOI: 10.48550/arXiv.1411.3921.

Brewer, Brendon J. and Courtney P. Donovan (Apr. 2015). "Fast Bayesian Inference for Exoplanet Discovery in Radial Velocity Data". In: *Monthly Notices of the Royal Astronomical Society* 448.4. arXiv:1501.06952 [astro-ph], pp. 3206–3214. ISSN: 1365-2966, 0035-8711. DOI: 10.1093/mnras/stv199.

Brewer, Brendon J. and Daniel Foreman-Mackey (Sept. 2018). "DNest4: Diffusive Nested Sampling in C++ and Python". en. In: *Journal of Statistical Software* 86, pp. 1–33. ISSN: 1548-7660. DOI: 10.18637/jss.v086.i07.

Brewer, Brendon J., Livia B. Pártay, and Gábor Csányi (2011). "Diffusive nested sampling". en. In: *Statistics and Computing* 21.4. ISSN: 0960-3174. DOI: 10.1007/s11222-010-9198-8.

de-Bruijne, J. H. J., K. L. J. Rygl, and T. Antoja (July 2014). "Gaia Astrometric Science Performance - Post-Launch Predictions". In: 67-68. Conference Name: EAS Publications Series Place: eprint: arXiv:1502.00791 ADS Bibcode: 2014EAS....67...23D, pp. 23–29. DOI: 10.1051/eas/1567004.

Bryan, Marta L. et al. (Apr. 2016). "Statistics of Long Period Gas Giant Planets in Known Planetary Systems". In: *The Astrophysical Journal* 821. Publisher: IOP ADS Bibcode: 2016ApJ...821...89B, p. 89. ISSN: 0004-637X. DOI: 10.3847/0004-637X/821/2/89.

Bryson, Steve et al. (Jan. 2021). "The Occurrence of Rocky Habitable-zone Planets around Solar-like Stars from Kepler Data". In: *The Astronomical Journal* 161. Publisher: IOP ADS Bibcode: 2021AJ....161...36B, p. 36. ISSN: 0004-6256. DOI: 10.3847/1538-3881/abc418.

Calissendorff, Per et al. (July 2019). "Spectral characterization of newly detected young substellar binaries with SINFONI". en. In: *Astronomy & Astrophysics* 627, A167. ISSN: 0004-6361, 1432-0746. DOI: 10.1051/0004-6361/201935319.

Canup, Robin M. (Apr. 2004). "Simulations of a late lunar-forming impact". In: *Icarus* 168. ADS Bibcode: 2004Icar..168..433C, pp. 433–456. ISSN: 0019-1035. DOI: 10.1016/j.icarus.2003.09.028.

Carter, Joshua A. et al. (Aug. 2012). "Kepler-36: A Pair of Planets with Neighboring Orbits and Dissimilar Densities". In: *Science* 337.6094. arXiv:1206.4718 [astro-ph], pp. 556–559. ISSN: 0036-8075, 1095-9203. DOI: 10.1126/science.1223269.

Ceppi, Simone et al. (Feb. 2024). "Probing initial distributions of orbital eccentricity and disc misalignment via polar discs". en. In: *Astronomy & Astrophysics* 682, A104. ISSN: 0004-6361, 1432-0746. DOI: 10.1051/0004-6361/202348375.

Chen, Cheng, Stephen H. Lubow, and Rebecca G. Martin (June 2020). "Polar planets around highly eccentric binaries are the most stable". In: *Monthly Notices of the Royal Astronomical Society* 494.4. arXiv: 2004.07230, pp. 4645–4655. ISSN: 0035-8711, 1365-2966. DOI: 10.1093/mnras/staa1037.

Chen, Cheng et al. (Dec. 2019). "Orbital dynamics of circumbinary planets". en. In: *Monthly Notices of the Royal Astronomical Society* 490.4, pp. 5634–5646. ISSN: 0035-8711, 1365-2966. DOI: 10.1093/mnras/stz2948.

Childs, Anna C. and Rebecca G. Martin (Oct. 2021). "Formation of Polar Terrestrial Circumbinary Planets". In: *The Astrophysical Journal* 920. Publisher: IOP ADS Bibcode: 2021ApJ...920L...8C, p. L8. ISSN: 0004-637X. DOI: 10.3847/2041-8213/ac2957.

Clement, Matthew S. et al. (Nov. 2024). *Formation of Terrestrial Planets*. arXiv:2411.03453.

Collier Cameron, A. et al. (Aug. 2021). "Separating planetary reflex Doppler shifts from stellar variability in the wavelength domain". In: *Monthly Notices of the Royal Astronomical Society* 505. Publisher: OUP ADS Bibcode: 2021MNRAS.505.1699C, pp. 1699–1717. ISSN: 0035-8711. DOI: 10.1093/mnras/stab1323.

Columba, G. et al. (July 2023). "Statistics of Magrathea exoplanets beyond the main sequence. Simulating the long-term evolution of circumbinary giant planets with TRES". In: *Astronomy and Astrophysics* 675. ADS Bibcode: 2023A&A...675A.156C, A156. ISSN: 0004-6361. DOI: 10.1051/0004-6361/202345843.

Correia, A. C. M. et al. (Sept. 2005). "The CORALIE survey for southern extra-solar planets. XIII. A pair of planets around HD 202206 or a circumbinary planet?" In: *Astronomy and Astrophysics* 440. ADS Bibcode: 2005A&A...440..751C, pp. 751–758. ISSN: 0004-6361. DOI: 10.1051/0004-6361:20042376.

Correia, Alexandre C. M., Gwenaël Boué, and Jacques Laskar (Nov. 2016). "Secular and tidal evolution of circumbinary systems". In: *Celestial Mechanics and Dynamical Astronomy* 126. Publisher: Springer ADS Bibcode: 2016CeMDA.126..189C, pp. 189–225. ISSN: 0923-2958. DOI: 10.1007/s10569-016-9709-9.

Couetdic, J. et al. (Sept. 2010). "Dynamical stability analysis of the HD 202206 system and constraints to the planetary orbits". In: *Astronomy and Astrophysics* 519. ADS Bibcode: 2010A&A...519A..10C, A10. ISSN: 0004-6361. DOI: 10.1051/0004-6361/200913635.

Cretignier, M., X. Dumusque, and F. Pepe (Mar. 2022). "Stellar activity correction using PCA decomposition of shells". In: *Astronomy and Astrophysics* 659. ADS Bibcode: 2022A&A...659A..68C, A68. ISSN: 0004-6361. DOI: 10.1051/0004-6361/202142435.

Cuello, Nicolás and Cristian A. Giuppone (Aug. 2019). "Planet formation and stability in polar circumbinary discs". In: *Astronomy and Astrophysics* 628. ADS Bibcode: 2019A&A...628A.119C, A119. ISSN: 0004-6361. DOI: 10.1051/0004-6361/201833976.

Cumming, Andrew et al. (May 2008). "The Keck Planet Search: Detectability and the Minimum Mass and Orbital Period Distribution of Extrasolar Planets". In: *Publications of the Astronomical Society of the Pacific* 120. Publisher: IOP ADS Bibcode: 2008PASP..120..531C, p. 531. ISSN: 0004-6280. DOI: 10.1086/588487.

Czekala, Ian et al. (Sept. 2019). "The Degree of Alignment between Circumbinary Disks and Their Binary Hosts". In: *The Astrophysical Journal* 883. Publisher: IOP ADS Bibcode: 2019ApJ...883...22C, p. 22. ISSN: 0004-637X. DOI: 10.3847/1538-4357/ab287b.

Dawson, Rebekah I. and Daniel C. Fabrycky (Oct. 2010). "Radial Velocity Planets De-aliased: A New, Short Period for Super-Earth 55 Cnc e". In: *The Astrophysical Journal* 722. Publisher: IOP ADS Bibcode: 2010ApJ...722..937D, pp. 937–953. ISSN: 0004-637X. DOI: 10.1088/0004-637X/722/1/937.

Dawson, Rebekah I. and John Asher Johnson (Aug. 2012). "THE PHOTOECCENTRIC EFFECT AND PROTO-HOT JUPITERS. I. MEASURING PHOTOMETRIC ECCENTRICITIES OF INDIVIDUAL TRANSITING PLANETS". en. In: *The Astrophysical Journal* 756.2. Publisher: The American Astronomical Society, p. 122. ISSN: 0004-637X. DOI: 10.1088/0004-637X/756/2/122.

Deck, Katherine M. and Eric Agol (Apr. 2015). "Measurement of Planet Masses with Transit Timing Variations Due to Synodic "Chopping" Effects". In: *The Astrophysical Journal* 802. Publisher: IOP ADS Bibcode: 2015ApJ...802..116D, p. 116. ISSN: 0004-637X. DOI: 10.1088/0004-637X/802/2/116.

Deeg, H. J. et al. (Mar. 2008). "Extrasolar planet detection by binary stellar eclipse timing: evidence for a third body around CM Draconis". In: *Astronomy and Astrophysics* 480. ADS Bibcode: 2008A&A...480..563D, pp. 563–571. ISSN: 0004-6361. DOI: 10.1051/0004-6361:20079000.

Delisle, J.-B., A. C. M. Correia, and J. Laskar (July 2015). "Stability of resonant configurations during the migration of planets and constraints on disk-planet interactions". en. In: *Astronomy & Astrophysics* 579. Publisher: EDP Sciences, A128. ISSN: 0004-6361, 1432-0746. DOI: 10.1051/0004-6361/201526285.

Delorme, P. et al. (May 2013). "Direct-imaging discovery of a 12-14 Jupiter-mass object orbiting a young binary system of very low-mass stars". In: *Astronomy and Astrophysics* 553. ADS Bibcode: 2013A&A...553L...5D, p. L5. ISSN: 0004-6361. DOI: 10.1051/0004-6361/201321169.

Doolin, Samuel and Katherine M. Blundell (Dec. 2011). "The dynamics and stability of circumbinary orbits". In: *Monthly Notices of the Royal Astronomical Society* 418. ADS Bibcode: 2011MNRAS.418.2656D, pp. 2656–2668. ISSN: 0035-8711. DOI: 10.1111/j.1365-2966.2011.19657.x.

Doyle, Laurance R. (May 2019). "The discovery of "Tatooine": Kepler-16b". In: *New Astronomy Reviews* 84. ADS Bibcode: 2019NewAR..8401515D, p. 101515. ISSN: 1387-6473. DOI: 10.1016/j.newar.2019.05.001.

Doyle, Laurance R. et al. (Sept. 2011). "Kepler-16: A Transiting Circumbinary Planet". In: *Science* 333. ADS Bibcode: 2011Sci...333.1602D, p. 1602. ISSN: 0036-8075. DOI: 10.1126/science.1210923.

Duchêne, Gaspard and Adam Kraus (Aug. 2013). "Stellar Multiplicity". In: *Annual Review of Astronomy and Astrophysics* 51. ADS Bibcode: 2013ARA&A..51..269D, pp. 269–310. ISSN: 0066-4146. DOI: 10.1146/annurev-astro-081710-102602.

Dupuy, Trent J. et al. (Feb. 2023). "On the masses, age, and architecture of the VHS J1256-1257AB b system". In: *Monthly Notices of the Royal Astronomical Society* 519. Publisher: OUP ADS Bibcode: 2023MNRAS.519.1688D, pp. 1688–1694. ISSN: 0035-8711. DOI: 10.1093/mnras/stac3557.

Duquennoy, A. and M. Mayor (Aug. 1991). "Multiplicity among Solar Type Stars in the Solar Neighbourhood - Part Two - Distribution of the Orbital Elements in an Unbiased Sample". en. In: *Astronomy and Astrophysics* 248, p. 485. ISSN: 0004-6361.

Dvorak, R. (Jan. 1982). "Planetenbahnen in Doppelsternsystemen." In: *Oesterreichische Akademie Wissenschaften Mathematisch naturwissenschaftliche Klasse Sitzungsberichte Abteilung* 191. ADS Bibcode: 1982OAWMN.191..423D, pp. 423–437. ISSN: 0723-9319.

Dvorak, R., C. Froeschle, and Ch Froeschle (Dec. 1989). "Stability of outer planetary orbits (P-types) in binaries." en. In: *Astronomy and Astrophysics* 226, pp. 335–342. ISSN: 0004-6361.

Dyson, F. W., A. S. Eddington, and C. Davidson (Jan. 1920). "A Determination of the Deflection of Light by the Sun's Gravitational Field, from Observations Made at the Total Eclipse of May 29, 1919". In: *Philosophical Transactions of the Royal Society of London Series A* 220. ADS Bibcode: 1920RSPTA.220..291D, pp. 291–333. ISSN: 1364-503X0080-46140962-8436. DOI: 10.1098/rsta.1920.0009.

Einstein, A. (1911). "Über den Einfluß der Schwerkraft auf die Ausbreitung des Lichtes". en. In: *Annalen der Physik* 340.10. _eprint: https://onlinelibrary.wiley.com/doi/pdf/10.1002/andp.19113401005, pp. 898–908. ISSN: 1521-3889. DOI: 10.1002/andp.19113401005.

Esmer, Ekrem Murat, Özgür Baştürk, and Selim Osman Selam (Nov. 2023). "Testing the planetary hypothesis of NY Virginis: anticipated change in the eclipse timing trend within the next five years". In: *Monthly Notices of the Royal Astronomical Society* 525. Publisher: OUP ADS Bibcode: 2023MNRAS.525.6050E, pp. 6050–6063. ISSN: 0035-8711. DOI: 10.1093/mnras/stad2648.

Esmer, Ekrem Murat et al. (Apr. 2022). "Detection of two additional circumbinary planets around Kepler-451". In: *Monthly Notices of the Royal Astronomical Society* 511. Publisher: OUP ADS Bibcode: 2022MNRAS.511.5207E, pp. 5207–5216. ISSN: 0035-8711. DOI: 10.1093/mnras/stac357.

Fabrycky, Daniel C. et al. (May 2012). "Transit Timing Observations from Kepler. IV. Confirmation of Four Multiple-planet Systems by Simple Physical Models". In: *The Astrophysical Journal* 750. Publisher: IOP ADS Bibcode: 2012ApJ...750..114F, p. 114. ISSN: 0004-637X. DOI: 10.1088/0004-637X/750/2/114.

Farago, F. and J. Laskar (Jan. 2010). "High-inclination orbits in the secular quadrupolar three-body problem". In: *Monthly Notices of the Royal Astronomical Society* 401. Publisher: OUP ADS Bibcode: 2010MNRAS.401.1189F, pp. 1189–1198. ISSN: 0035-8711. DOI: 10.1111/j.1365-2966.2009.15711.x.

Faria, J. P. et al. (June 2018). "kima: Exoplanet detection in radial velocities". In: *The Journal of Open Source Software* 3. ADS Bibcode: 2018JOSS....3..487F, p. 487. DOI: 10.21105/joss.00487.

Fitzmaurice, Evan, David V. Martin, and Daniel C. Fabrycky (June 2022). "Sculpting the circumbinary planet size distribution through resonant interactions with companion planets". In: *Monthly Notices of the Royal Astronomical Society* 512. Publisher: OUP ADS Bibcode: 2022MNRAS.512.5023F, pp. 5023–5036. ISSN: 0035-8711. DOI: 10.1093/mnras/stac741.

Flamsteed, John (1725). *Historia Coelestis Britannica: Complectens Praefationem spatiosam (sive in Stellarum Fixarum Catalogum Prolegomena) quae brevem Astronomiae Historiam praebet, atque Descriptionem Observationum peractarum, & Organorum adhibitorum tum a pristinis Astronomis, tum In Observatorio Regio Grenovicensi ; Deinceps Fixarum Catalogum a Ptolemaeo, Uleg Beig, Tychone Brahaeo, Gulielmo Hessiae Landtgravio, ac Hevelio constructum ... : Quibus adnexus est Fixarum quarundam Australium Catalogus,*

in nostro Hemisphaerio non adspectabilium, Denique Tabulae .... 3. la. Google-Books-ID: 4K9FAAAAcAAJ. Meere.

Freckelton, Alix V. et al. (July 2024). "BEBOP V. Homogeneous stellar analysis of potential circumbinary planet hosts". In: *Monthly Notices of the Royal Astronomical Society* 531. Publisher: OUP ADS Bibcode: 2024MNRAS.531.4085F, pp. 4085–4098. ISSN: 0035-8711. DOI: 10.1093/mnras/stae1405.

Fulton, Benjamin J. et al. (Sept. 2017). "The California-Kepler Survey. III. A Gap in the Radius Distribution of Small Planets". In: *The Astronomical Journal* 154. Publisher: IOP ADS Bibcode: 2017AJ....154..109F, p. 109. ISSN: 0004-6256. DOI: 10.3847/1538-3881/aa80eb.

Fulton, Benjamin J. et al. (July 2021). "California Legacy Survey. II. Occurrence of Giant Planets beyond the Ice Line". In: *The Astrophysical Journal Supplement Series* 255. Publisher: IOP ADS Bibcode: 2021ApJS..255...14F, p. 14. ISSN: 0067-0049. DOI: 10.3847/1538-4365/abfcc1.

Gaia Collaboration et al. (Nov. 2016). "The Gaia mission". In: *Astronomy and Astrophysics* 595. ADS Bibcode: 2016A&A...595A...1G, A1. ISSN: 0004-6361. DOI: 10.1051/0004-6361/201629272.

Gamerman, Dani and Hedibert F. Lopes (May 2006). *Markov Chain Monte Carlo: Stochastic Simulation for Bayesian Inference, Second Edition*. 2nd ed. New York: Chapman and Hall/CRC. ISBN: 978-0-429-18334-8. DOI: 10.1201/9781482296426.

Gaudi, B. S. (Dec. 2010). *Microlensing by Exoplanets*. Pages: 79-110 Publication Title: Exoplanets ADS Bibcode: 2010exop.book...79G.

Georgakarakos, Nikolaos et al. (Nov. 2024). "Empirical Stability Criteria for 3D Hierarchical Triple Systems. I. Circumbinary Planets". In: *The Astronomical Journal* 168. Publisher: IOP ADS Bibcode: 2024AJ....168..224G, p. 224. ISSN: 0004-6256. DOI: 10.3847/1538-3881/ad7a78.

Gillon, Michaël et al. (Feb. 2017). "Seven temperate terrestrial planets around the nearby ultracool dwarf star TRAPPIST-1". In: *Nature* 542. ADS Bibcode: 2017Natur.542..456G, pp. 456–460. ISSN: 0028-0836. DOI: 10.1038/nature21360.

Ginzburg, Sivan, Hilke E Schlichting, and Re'em Sari (May 2018). "Core-powered mass-loss and the radius distribution of small exoplanets". In: *Monthly Notices of the Royal Astronomical Society* 476.1, pp. 759–765. ISSN: 0035-8711. DOI: 10.1093/mnras/sty290.

Gold, T. (May 1968). "Rotating Neutron Stars as the Origin of the Pulsating Radio Sources". en. In: *Nature* 218.5143. Publisher: Nature Publishing Group, pp. 731–732. ISSN: 1476-4687. DOI: 10.1038/218731a0.

Goldberg, Max et al. (Nov. 2023). "A 5MJup non-transiting coplanar circumbinary planet around Kepler-1660AB". In: *Monthly Notices of the Royal Astronomical Society* 525. ADS Bibcode: 2023MNRAS.525.4628G, pp. 4628–4641. ISSN: 0035-8711. DOI: 10.1093/mnras/stad2568.

Gratton, Raffaele et al. (Oct. 2023). "Jupiter-like planets might be common in a low-density environment". In: *Nature Communications* 14. ADS Bibcode: 2023NatCo..14.6232G, p. 6232. ISSN: 2041-1723. DOI: 10.1038/s41467-023-41665-0.

Gray, David F. (June 2009). "The Third Signature of Stellar Granulation". In: *The Astrophysical Journal* 697. Publisher: IOP ADS Bibcode: 2009ApJ...697.1032G, pp. 1032–1043. ISSN: 0004-637X. DOI: 10.1088/0004-637X/697/2/1032.

Green, Peter. J (Dec. 1995). "Reversible jump Markov chain Monte Carlo computation and Bayesian model determination". In: *Biometrika* 82.4, pp. 711–732. ISSN: 0006-3444. DOI: 10.1093/biomet/82.4.711.

Gregory, Phil (2005). *Bayesian Logical Data Analysis for the Physical Sciences: A Comparative Approach with Mathematica® Support*. Cambridge: Cambridge University Press. ISBN: 978-0-521-84150-4. DOI: 10.1017/CBO9780511791277.

Grether, Daniel and Charles H. Lineweaver (Apr. 2006). "How Dry is the Brown Dwarf Desert? Quantifying the Relative Number of Planets, Brown Dwarfs, and Stellar Companions around Nearby Sun-like Stars". In: *The Astrophysical Journal* 640. Publisher: IOP ADS Bibcode: 2006ApJ...640.1051G, pp. 1051–1062. ISSN: 0004-637X. DOI: 10.1086/500161.

Guinan, E. F. and F. P. Maloney (Aug. 1985). "The apsidal motion of the eccentric eclipsing binary DI Herculis - an apparent discrepancy with general relativity." In: *The Astronomical Journal* 90. Publisher: IOP ADS Bibcode: 1985AJ.....90.1519G, pp. 1519–1528. ISSN: 0004-6256. DOI: 10.1086/113865.

Guinan, Edward F. and Ignasi Ribas (Jan. 2001). "The Best Brown Dwarf Yet? A Companion to the Hyades Eclipsing Binary V471 Tauri". In: *The Astrophysical Journal* 546. ADS Bibcode: 2001ApJ...546L..43G, pp. L43–L47. ISSN: 0004-637X. DOI: 10.1086/318065.

Hadden, Sam and Yoram Lithwick (July 2017). "Kepler Planet Masses and Eccentricities from TTV Analysis". In: *The Astronomical Journal* 154. Publisher: IOP ADS Bibcode: 2017AJ....154....5H, p. 5. ISSN: 0004-6256. DOI: 10.3847/1538-3881/aa71ef.

Han, Z. -T. et al. (Aug. 2023). "Orbital Period Variations in HT Cas: Evidence for Additional Angular Momentum Loss and a High-eccentricity Giant Planet". In: *The Astrophysical Journal* 953. Publisher: IOP ADS Bibcode: 2023ApJ...953...63H, p. 63. ISSN: 0004-637X. DOI: 10.3847/1538-4357/acdd6e.

Han, Z.-T. et al. (Nov. 2018). "DE CVn: An Eclipsing Post-common Envelope Binary with a Circumbinary Disk and a Giant Planet". en. In: *The Astrophysical Journal* 868.1. Publisher: The American Astronomical Society, p. 53. ISSN: 0004-637X. DOI: 10.3847/1538-4357/aae64d.

Hara, Nathan C. et al. (July 2022). "Detecting exoplanets with the false inclusion probability. Comparison with other detection criteria in the context of radial velocities". In: *Astronomy and Astrophysics* 663. ADS Bibcode: 2022A&A...663A..14H, A14. ISSN: 0004-6361. DOI: 10.1051/0004-6361/202140543.

Hardy, A. et al. (Feb. 2015). "The First Science Results from Sphere: Disproving the Predicted Brown Dwarf Around V471 Tau". In: *The Astrophysical Journal* 800. ADS Bibcode: 2015ApJ...800L..24H, p. L24. ISSN: 0004-637X. DOI: 10.1088/2041-8205/800/2/L24.

Haywood, R. D. et al. (Sept. 2014). "Planets and stellar activity: hide and seek in the CoRoT-7 system". In: *Monthly Notices of the Royal Astronomical Society* 443. Publisher: OUP ADS Bibcode: 2014MNRAS.443.2517H, pp. 2517–2531. ISSN: 0035-8711. DOI: 10.1093/mnras/stu1320.

Ho, Cynthia S. K. et al. (July 2024). "Shallower radius valley around low-mass hosts: evidence for icy planets, collisions, or high-energy radiation scatter". In: *Monthly Notices of the Royal Astronomical Society* 531. Publisher: OUP ADS Bibcode: 2024MNRAS.531.3698H, pp. 3698–3714. ISSN: 0035-8711. DOI: 10.1093/mnras/stae1376.

Holl, B. et al. (June 2023). "Gaia Data Release 3. Astrometric orbit determination with Markov chain Monte Carlo and genetic algorithms: Systems with stellar, sub-stellar, and planetary mass companions". In: *Astronomy and Astrophysics* 674. ADS Bibcode: 2023A&A...674A..10H, A10. ISSN: 0004-6361. DOI: 10.1051/0004-6361/202244161.

Holman, Matthew J. and Paul A. Wiegert (Jan. 1999). "Long-Term Stability of Planets in Binary Systems". In: *The Astronomical Journal* 117. ADS Bibcode: 1999AJ....117..621H, pp. 621–628. ISSN: 0004-6256. DOI: 10.1086/300695.

Holman, Matthew J. et al. (Oct. 2010). "Kepler-9: A System of Multiple Planets Transiting a Sun-Like Star, Confirmed by Timing Variations". In: *Science* 330. ADS Bibcode: 2010Sci...330...51H, p. 51. ISSN: 0036-8075. DOI: 10.1126/science.1195778.

Howard, Andrew W. et al. (Oct. 2010). "The Occurrence and Mass Distribution of Close-in Super-Earths, Neptunes, and Jupiters". In: *Science* 330. ADS Bibcode: 2010Sci...330..653H, p. 653. ISSN: 0036-8075. DOI: 10.1126/science.1194854.

Irwin, John B. (May 1959). "Standard light-time curves". In: *The Astronomical Journal* 64. ADS Bibcode: 1959AJ.....64..149I, p. 149. ISSN: 0004-6256. DOI: 10.1086/107913.

Ivanova, N. et al. (Feb. 2013). "Common envelope evolution: where we stand and how we can move forward". In: *Astronomy and Astrophysics Review* 21. Publisher: Springer ADS Bibcode: 2013A&ARv..21...59I, p. 59. ISSN: 0935-4956. DOI: 10.1007/s00159-013-0059-2.

Izidoro, Andre et al. (Sept. 2017). "Breaking the chains: hot super-Earth systems from migration and disruption of compact resonant chains". In: *Monthly Notices of the Royal Astronomical Society* 470. Publisher: OUP ADS Bibcode: 2017MNRAS.470.1750I, pp. 1750–1770. ISSN: 0035-8711. DOI: 10.1093/mnras/stx1232.

Janson, Markus et al. (Dec. 2021). "A wide-orbit giant planet in the high-mass b Centauri binary system". In: *Nature* 600. ADS Bibcode: 2021Natur.600..231J, pp. 231–234. ISSN: 0028-0836. DOI: 10.1038/s41586-021-04124-8.

Jefferys, William H. and James O. Berger (1992). "Ockham's Razor and Bayesian Analysis". In: *American Scientist* 80.1. Publisher: Sigma Xi, The Scientific Research Society, pp. 64–72. ISSN: 0003-0996.

Jeffreys, Harold (1961). *Theory of Probability*. en. Google-Books-ID: AavQAAAAMAAJ. Clarendon Press.

Johnson, John Asher et al. (Aug. 2010). "Giant Planet Occurrence in the Stellar Mass-Metallicity Plane". In: *Publications of the Astronomical Society of the Pacific* 122. Publisher: IOP ADS Bibcode: 2010PASP..122..905J, p. 905. ISSN: 0004-6280. DOI: 10.1086/655775.

Kahraman Aliçavuş, F. et al. (Apr. 2023). "Comprehensive spectroscopic and photometric study of pulsating eclipsing binary star AI Hya". In: *Monthly Notices of the Royal Astronomical Society* 520. Publisher: OUP ADS Bibcode: 2023MNRAS.520.1601K, pp. 1601–1612. ISSN: 0035-8711. DOI: 10.1093/mnras/stad137.

Kant, Immanuel (Jan. 1755). *Allgemeine Naturgeschichte und Theorie des Himmels*. Publication Title: Zeitz ADS Bibcode: 1755anth.book.....K.

Kass, Robert E. and Adrian E. Raftery (June 1995). "Bayes Factors". In: *Journal of the American Statistical Association* 90.430. Publisher: Taylor & Francis _eprint: https://www.tandfonline.com/doi/pdf/10.10 pp. 773–795. ISSN: 0162-1459. DOI: 10.1080/01621459.1995.10476572.

Kennedy, Grant M. et al. (Jan. 2019). "A circumbinary protoplanetary disk in a polar configuration". In: *Nature Astronomy* 3. ADS Bibcode: 2019NatAs...3..230K, pp. 230–235. ISSN: 2397-3366. DOI: 10.1038/s41550-018-0667-x.

Kepler, Johannes (Jan. 1609). *Astronomia nova ..., seu physica coelestis, tradita commentariis de motibus stellae martis*. Publication Title: Astronomia nova ADS Bibcode: 1609asno.book.....K. DOI: 10.3931/e-rara-558.

Kervella, Pierre, Frédéric Arenou, and Frédéric Thévenin (Jan. 2022). "Stellar and substellar companions from Gaia EDR3. Proper-motion anomaly and resolved common proper-motion pairs". In: *Astronomy and Astrophysics* 657. ADS Bibcode: 2022A&A...657A...7K, A7. ISSN: 0004-6361. DOI: 10.1051/0004-6361/202142146.

Kipping, D. M. (July 2013). "Parametrizing the exoplanet eccentricity distribution with the beta distribution." In: *Monthly Notices of the Royal Astronomical Society* 434. ADS Bibcode: 2013MNRAS.434L..51K, pp. L51–L55. ISSN: 0035-8711. DOI: 10.1093/mnrasl/slt075.

Kley, W. and R. P. Nelson (Sept. 2012). "Planet-Disk Interaction and Orbital Evolution". In: *Annual Review of Astronomy and Astrophysics* 50. ADS Bibcode: 2012ARA&A..50..211K, pp. 211–249. ISSN: 0066-4146. DOI: 10.1146/annurev-astro-081811-125523.

Kley, Wilhelm and Nader Haghighipour (Apr. 2014). "Modeling circumbinary planets: The case of Kepler-38". In: *Astronomy and Astrophysics* 564. ADS Bibcode: 2014A&A...564A..72K, A72. ISSN: 0004-6361. DOI: 10.1051/0004-6361/201323235.

Konacki, Maciej and Alex Wolszczan (July 2003). "Masses and Orbital Inclinations of Planets in the PSR B1257+12 System". In: *The Astrophysical Journal* 591. Publisher: IOP ADS Bibcode: 2003ApJ...591L.147K, pp. L147–L150. ISSN: 0004-637X. DOI: 10.1086/377093.

Konacki, Maciej et al. (Oct. 2009). "The Radial Velocity Tatooine Search for Circumbinary Planets: Planet Detection Limits for a Sample of Double-Lined Binary Stars—Initial Results from Keck I/Hires, Shane/CAT/Hamspec, and TNG/Sarg Observations". In: *The Astrophysical Journal* 704. ADS Bibcode: 2009ApJ...704..513K, pp. 513–521. ISSN: 0004-637X. DOI: 10.1088/0004-637X/704/1/513.

— (Aug. 2010). "High-precision Orbital and Physical Parameters of Double-lined Spectroscopic Binary Stars—HD78418, HD123999, HD160922, HD200077, and HD210027". In: *The Astrophysical Journal* 719. ADS Bibcode: 2010ApJ...719.1293K, pp. 1293–1314. ISSN: 0004-637X. DOI: 10.1088/0004-637X/719/2/1293.

Kostov, V. B. et al. (Mar. 2014). "Kepler-413b: A Slightly Misaligned, Neptune-size Transiting Circumbinary Planet". In: *The Astrophysical Journal* 784. Publisher: IOP ADS Bibcode: 2014ApJ...784...14K, p. 14. ISSN: 0004-637X. DOI: 10.1088/0004-637X/784/1/14.

Kostov, Veselin B. et al. (Aug. 2016). "KEPLER-1647B: THE LARGEST AND LONGEST-PERIOD *KEPLER* TRANSITING CIRCUMBINARY PLANET". en. In: *The Astrophysical Journal* 827.1, p. 86. ISSN: 1538-4357. DOI: 10.3847/0004-637X/827/1/86.

Kostov, Veselin B. et al. (Sept. 2020a). "Multiple Transits during a Single Conjunction: Identifying Transiting Circumbinary Planetary Candidates from TESS". In: *The Astronomical Journal* 160.4. arXiv:2008.02756 [astro-ph], p. 174. ISSN: 1538-3881. DOI: 10.3847/1538-3881/abad40.

Kostov, Veselin B. et al. (June 2020b). "TOI-1338: TESS' First Transiting Circumbinary Planet". In: *The Astronomical Journal* 159. ADS Bibcode: 2020AJ....159..253K, p. 253. ISSN: 0004-6256. DOI: 10.3847/1538-3881/ab8a48.

Kostov, Veselin B. et al. (Dec. 2021). "TIC 172900988: A Transiting Circumbinary Planet Detected in One Sector of TESS Data". In: *The Astronomical Journal* 162.6. arXiv: 2105.08614, p. 234. ISSN: 0004-6256, 1538-3881. DOI: 10.3847/1538-3881/ac223a.

Kovács, G., S. Zucker, and T. Mazeh (Aug. 2002). "A box-fitting algorithm in the search for periodic transits". In: *Astronomy and Astrophysics* 391. ADS Bibcode: 2002A&A...391..369K, pp. 369–377. ISSN: 0004-6361. DOI: 10.1051/0004-6361:20020802.

Kramer, Michael et al. (July 1998). "The Characteristics of Millisecond Pulsar Emission. I. Spectra, Pulse Shapes, and the Beaming Fraction". In: *The Astrophysical Journal* 501. Publisher: IOP ADS Bibcode: 1998ApJ...501..270K, pp. 270–285. ISSN: 0004-637X. DOI: 10.1086/305790.

Kratter, Kaitlin and Giuseppe Lodato (Sept. 2016). "Gravitational Instabilities in Circumstellar Disks". In: *Annual Review of Astronomy and Astrophysics* 54. ADS Bibcode: 2016ARA&A..54..271K, pp. 271–311. ISSN: 0066-4146. DOI: 10.1146/annurev-astro-081915-023307.

Kruckow, Matthias U. et al. (Oct. 2021). "A Catalog of Potential Post-Common Envelope Binaries". In: *The Astrophysical Journal* 920. Publisher: IOP ADS Bibcode: 2021ApJ...920...86K, p. 86. ISSN: 0004-637X. DOI: 10.3847/1538-4357/ac13ac.

Kuang, Renkun et al. (Oct. 2022). "OGLE-2019-BLG-1470LABc: Another microlensing giant planet in a binary system?" In: *Monthly Notices of the Royal Astronomical Society* 516.2, pp. 1704–1720. ISSN: 0035-8711. DOI: 10.1093/mnras/stac2315.

Lagrange, Anne-Marie (Apr. 2014). "Direct imaging of exoplanets". In: *Philosophical Transactions of the Royal Society A: Mathematical, Physical and Engineering Sciences* 372.2014. Publisher: Royal Society, p. 20130090. DOI: 10.1098/rsta.2013.0090.

Laibe, G., J. -F. Gonzalez, and S. T. Maddison (Jan. 2012). "Revisiting the "radial-drift barrier" of planet formation and its relevance in observed protoplanetary discs". In: *Astronomy and Astrophysics* 537. ADS Bibcode: 2012A&A...537A..61L, A61. ISSN: 0004-6361. DOI: 10.1051/0004-6361/201015349.

Lanza, A. F. (Jan. 2020). "Internal magnetic fields, spin-orbit coupling, and orbital period modulation in close binary systems". In: *Monthly Notices of the Royal Astronomical Society* 491. ADS Bibcode: 2020MNRAS.491.1820L, pp. 1820–1831. ISSN: 0035-8711. DOI: 10.1093/mnras/stz3135.

Ledda, Sebastiano, Camilla Danielski, and Diego Turrini (July 2023). "The quest for Magrathea planets. I. Formation of second-generation exoplanets around double white dwarfs". In: *Astronomy and Astrophysics* 675. ADS Bibcode: 2023A&A...675A.184L, A184. ISSN: 0004-6361. DOI: 10.1051/0004-6361/202245827.

Leichty, McKenna et al. (June 2024). "An Eccentric Planet Orbiting the Polar V808 Aurigae". In: *The Astrophysical Journal* 967. Publisher: IOP ADS Bibcode: 2024ApJ...967...81L, p. 81. ISSN: 0004-637X. DOI: 10.3847/1538-4357/ad3bac.

Leleu, A. et al. (Nov. 2021a). "Alleviating the transit timing variation bias in transit surveys. I. RIVERS: Method and detection of a pair of resonant super-Earths around Kepler-1705". In: *Astronomy and Astrophysics* 655. Publisher: EDP ADS Bibcode: 2021A&A...655A..66L, A66. ISSN: 0004-6361. DOI: 10.1051/0004-6361/202141471.

Leleu, A. et al. (May 2021b). "Six transiting planets and a chain of Laplace resonances in TOI-178". In: *Astronomy and Astrophysics* 649. Publisher: EDP ADS Bibcode: 2021A&A...649A..26L, A26. ISSN: 0004-6361. DOI: 10.1051/0004-6361/202039767.

Leleu, A. et al. (Jan. 2023). "Removing biases on the density of sub-Neptunes characterised via transit timing variations. Update on the mass-radius relationship of 34 Kepler planets". In: *Astronomy and Astrophysics* 669. Publisher: EDP ADS Bibcode: 2023A&A...669A.117L, A117. ISSN: 0004-6361. DOI: 10.1051/0004-6361/202244132.

Leleu, Adrien et al. (July 2024). "Resonant sub-Neptunes are puffier". en. In: *Astronomy & Astrophysics* 687. arXiv:2406.18991 [astro-ph], p. L1. ISSN: 0004-6361, 1432-0746. DOI: 10.1051/0004-6361/202450587.

Li, Gongjie, Matthew J. Holman, and Molei Tao (Nov. 2016). "Uncovering Circumbinary Planetary Architectural Properties from Selection Biases". In: *The Astrophysical Journal* 831. Publisher: IOP ADS Bibcode: 2016ApJ...831...96L, p. 96. ISSN: 0004-637X. DOI: 10.3847/0004-637X/831/1/96.

Lin, D. N. C. and John Papaloizou (Oct. 1986). "On the Tidal Interaction between Protoplanets and the Protoplanetary Disk. III. Orbital Migration of Protoplanets". In: *The Astrophysical Journal* 309. Publisher: IOP ADS Bibcode: 1986ApJ...309..846L, p. 846. ISSN: 0004-637X. DOI: 10.1086/164653.

Lithwick, Yoram, Jiwei Xie, and Yanqin Wu (Dec. 2012). "Extracting Planet Mass and Eccentricity from TTV Data". In: *The Astrophysical Journal* 761. Publisher: IOP ADS Bibcode: 2012ApJ...761..122L, p. 122. ISSN: 0004-637X. DOI: 10.1088/0004-637X/761/2/122.

Lomb, N. R. (Feb. 1976). "Least-Squares Frequency Analysis of Unequally Spaced Data". In: *Astrophysics and Space Science* 39. Publisher: Springer ADS Bibcode: 1976Ap&SS..39..447L, pp. 447–462. ISSN: 0004-640X. DOI: 10.1007/BF00648343.

Lopez, Eric D. and Jonathan J. Fortney (Sept. 2013). "THE ROLE OF CORE MASS IN CONTROLLING EVAPORATION: THE KEPLER RADIUS DISTRIBUTION AND THE KEPLER-36 DENSITY DICHOTOMY". en. In: *The Astrophysical Journal* 776.1. Publisher: The American Astronomical Society, p. 2. ISSN: 0004-637X. DOI: 10.1088/0004-637X/776/1/2.

— (Sept. 2014). "Understanding the Mass-Radius Relation for Sub-neptunes: Radius as a Proxy for Composition". In: *The Astrophysical Journal* 792. Publisher: IOP ADS Bibcode: 2014ApJ...792....1L, p. 1. ISSN: 0004-637X. DOI: 10.1088/0004-637X/792/1/1.

Lovis, C. and D. Fischer (Dec. 2010). *Radial Velocity Techniques for Exoplanets*. Pages: 27-53 Publication Title: Exoplanets ADS Bibcode: 2010exop.book...27L.

Lubow, S. H. and S. Ida (Dec. 2010). *Planet Migration*. Pages: 347-371 Publication Title: Exoplanets ADS Bibcode: 2010exop.book..347L.

Luque, Rafael and Enric Pallé (Sept. 2022). "Density, not radius, separates rocky and water-rich small planets orbiting M dwarf stars". In: *Science* 377. ADS Bibcode: 2022Sci...377.1211L, pp. 1211–1214. ISSN: 0036-8075. DOI: 10.1126/science.abl7164.

Ma, Bo and Jian Ge (Apr. 2014). "Statistical properties of brown dwarf companions: implications for different formation mechanisms". In: *Monthly Notices of the Royal Astronomical Society* 439.3, pp. 2781–2789. ISSN: 0035-8711. DOI: 10.1093/mnras/stu134.

MacDougall, Mason G., Gregory J. Gilbert, and Erik A. Petigura (Aug. 2023). "Accurate and Efficient Photoeccentric Transit Modeling". In: *The Astronomical Journal* 166. Publisher: IOP ADS Bibcode: 2023AJ....166...61M, p. 61. ISSN: 0004-6256. DOI: 10.3847/1538-3881/ace16d.

Mandel, Kaisey and Eric Agol (Dec. 2002). "Analytic Light Curves for Planetary Transit Searches". In: *The Astrophysical Journal* 580. Publisher: IOP ADS Bibcode: 2002ApJ...580L.171M, pp. L171–L175. ISSN: 0004-637X. DOI: 10.1086/345520.

Mao, Shude and Bohdan Paczynski (June 1991). "Gravitational Microlensing by Double Stars and Planetary Systems". In: *The Astrophysical Journal* 374. ADS Bibcode: 1991ApJ...374L..37M, p. L37. ISSN: 0004-637X. DOI: 10.1086/186066.

Marley, Mark S. et al. (Jan. 2007). "On the Luminosity of Young Jupiters". In: *The Astrophysical Journal* 655. Publisher: IOP ADS Bibcode: 2007ApJ...655..541M, pp. 541–549. ISSN: 0004-637X. DOI: 10.1086/509759.

Marois, Christian et al. (Dec. 2010). "Images of a fourth planet orbiting HR 8799". en. In: *Nature* 468.7327. Publisher: Nature Publishing Group, pp. 1080–1083. ISSN: 1476-4687. DOI: 10.1038/nature09684.

Martin, David V. (Jan. 2018). *Populations of Planets in Multiple Star Systems*. Pages: 156 Publication Title: Handbook of Exoplanets ADS Bibcode: 2018haex.bookE.156M. DOI: 10.1007/978-3-319-55333-7_156.

Martin, David V. and Daniel C. Fabrycky (Sept. 2021). "Searching for Small Circumbinary Planets. I. The STANLEY Automated Algorithm and No New Planets in Existing Systems". In: *The Astronomical Journal* 162. Publisher: IOP ADS Bibcode: 2021AJ....162...84M, p. 84. ISSN: 0004-6256. DOI: 10.3847/1538-3881/abeab1.

Martin, David V., Tsevi Mazeh, and Daniel C. Fabrycky (Nov. 2015). "No circumbinary planets transiting the tightest Kepler binaries - a possible fingerprint of a third star". In: *Monthly Notices of the Royal Astronomical Society* 453. Publisher: OUP ADS Bibcode: 2015MNRAS.453.3554M, pp. 3554–3567. ISSN: 0035-8711. DOI: 10.1093/mnras/stv1870.

Martin, David V. and Amaury H. M. J. Triaud (Oct. 2014). "Planets transiting non-eclipsing binaries". en. In: *Astronomy & Astrophysics* 570, A91. ISSN: 0004-6361. DOI: 10.1051/0004-6361/201323112.

— (May 2015). "Circumbinary planets - why they are so likely to transit". In: *Monthly Notices of the Royal Astronomical Society* 449. ADS Bibcode: 2015MNRAS.449..781M, pp. 781–793. ISSN: 0035-8711. DOI: 10.1093/mnras/stv121.

Martin, David V. et al. (Apr. 2019). "The BEBOP radial-velocity survey for circumbinary planets. I. Eight years of CORALIE observations of 47 single-line eclipsing binaries and abundance constraints on the masses of circumbinary planets". en. In: *Astronomy and Astrophysics* 624, A68. ISSN: 0004-6361. DOI: 10.1051/0004-6361/201833669.

Martin, Rebecca G., Mario Livio, and Divya Palaniswamy (Dec. 2016). "Why are Pulsar Planets Rare?" en. In: *The Astrophysical Journal, Volume 832, Issue 2, article id. 122, <NUMPAGES>9</NUMPAGES> pp. (2016).* 832.2, p. 122. ISSN: 0004-637X. DOI: 10.3847/0004-637X/832/2/122.

Martynov, D. Ia. and Kh. F. Khaliullin (Aug. 1980). "On the Relativistic Motion of the Periastron in the Eclipsing Binary System Di-Herculis". In: *Astrophysics and Space Science* 71. Publisher: Springer ADS Bibcode: 1980Ap&SS..71..147M, pp. 147–170. ISSN: 0004-640X. DOI: 10.1007/BF00646915.

Mayor, M. et al. (Dec. 2003). "Setting New Standards with HARPS". In: *The Messenger* 114. ADS Bibcode: 2003Msngr.114...20M, pp. 20–24. ISSN: 0722-6691.

Mayor, M. et al. (Sept. 2011). *The HARPS search for southern extra-solar planets XXXIV. Occurrence, mass distribution and orbital properties of super-Earths and Neptune-mass planets*. Tech. rep. Publication Title: arXiv e-prints ADS Bibcode: 2011arXiv1109.2497M Type: article.

Mayor, Michel and Didier Queloz (Nov. 1995). "A Jupiter-mass companion to a solar-type star". In: *Nature* 378. ADS Bibcode: 1995Natur.378..355M, pp. 355–359. ISSN: 0028-0836. DOI: 10.1038/378355a0.

Mazeh, T., T. Holczer, and S. Faigler (May 2016). "Dearth of short-period Neptunian exoplanets: A desert in period-mass and period-radius planes". In: *Astronomy and Astrophysics* 589. Publisher: EDP ADS Bibcode: 2016A&A...589A..75M, A75. ISSN: 0004-6361. DOI: 10.1051/0004-6361/201528065.

Meschiari, Stefano (Dec. 2012). "Planet Formation in Circumbinary Configurations: Turbulence Inhibits Planetesimal Accretion". In: *The Astrophysical Journal* 761. Publisher: IOP ADS Bibcode: 2012ApJ...761L...7M, p. L7. ISSN: 0004-637X. DOI: 10.1088/2041-8205/761/1/L7.

Meunier, N., M. Desort, and A. -M. Lagrange (Mar. 2010). "Using the Sun to estimate Earth-like planets detection capabilities . II. Impact of plages". In: *Astronomy and Astrophysics* 512. ADS Bibcode: 2010A&A...512A..39M, A39. ISSN: 0004-6361. DOI: 10.1051/0004-6361/200913551.

Mignon, L. et al. (Feb. 2025). *Radial velocity homogeneous analysis of M dwarfs observed with HARPS. II. Detection limits and planetary occurrence statistics*. Publication Title: arXiv e-prints ADS Bibcode: 2025arXiv250206553M. DOI: 10.48550/arXiv.2502.06553.

Moriwaki, Kazumasa and Yoshitsugu Nakagawa (July 2004). "A Planetesimal Accretion Zone in a Circumbinary Disk". In: *The Astrophysical Journal* 609. ADS Bibcode: 2004ApJ...609.1065M, pp. 1065–1070. ISSN: 0004-637X. DOI: 10.1086/421342.

Mortier, A. et al. (Mar. 2013). "On the functional form of the metallicity-giant planet correlation". In: *Astronomy and Astrophysics* 551. ADS Bibcode: 2013A&A...551A.112M, A112. ISSN: 0004-6361. DOI: 10.1051/0004-6361/201220707.

Mróz, Przemek et al. (Feb. 2019). "Two new free-floating or wide-orbit planets from microlensing". In: *Astronomy and Astrophysics* 622. ADS Bibcode: 2019A&A...622A.201M, A201. ISSN: 0004-6361. DOI: 10.1051/0004-6361/201834557.

Murray, C. D. and A. C. M. Correia (Dec. 2010). *Keplerian Orbits and Dynamics of Exoplanets*. Pages: 15-23 Publication Title: Exoplanets ADS Bibcode: 2010exop.book...15M.

Murray, Carl D. and Stanley F. Dermott (Feb. 1999). *Solar System Dynamics*. Publication Title: Solar System Dynamics ADS Bibcode: 1999ssd..book.....M. DOI: 10.1017/CBO9781139174817.

Nelson, Richard P. (Oct. 2003). "On the evolution of giant protoplanets forming in circumbinary discs". In: *Monthly Notices of the Royal Astronomical Society* 345. Publisher: OUP ADS Bibcode: 2003MNRAS.345..233N, pp. 233–242. ISSN: 0035-8711. DOI: 10.1046/j.1365-8711.2003.06929.x.

Nesvorný, David et al. (June 2012). "The Detection and Characterization of a Nontransiting Planet by Transit Timing Variations". In: *Science* 336. ADS Bibcode: 2012Sci...336.1133N, p. 1133. ISSN: 0036-8075. DOI: 10.1126/science.1221141.

Nesvorný, David et al. (Nov. 2013). "KOI-142, The King of Transit Variations, is a Pair of Planets near the 2:1 Resonance". In: *The Astrophysical Journal* 777. Publisher: IOP ADS Bibcode: 2013ApJ...777....3N, p. 3. ISSN: 0004-637X. DOI: 10.1088/0004-637X/777/1/3.

Niţu, Iuliana C. et al. (May 2022). "A search for planetary companions around 800 pulsars from the Jodrell Bank pulsar timing programme". In: *Monthly Notices of the Royal Astronomical Society* 512. Publisher: OUP ADS Bibcode: 2022MNRAS.512.2446N, pp. 2446–2459. ISSN: 0035-8711. DOI: 10.1093/mnras/stac593.

Offner, S. S. R. et al. (July 2023). *The Origin and Evolution of Multiple Star Systems*. Conference Name: Protostars and Planets VII Volume: 534 ADS Bibcode: 2023ASPC..534..275O. eprint: arXiv:2203.10066. DOI: 10.48550/arXiv.2203.10066.

Ogihara, Masahiro and Shigeru Ida (July 2009). "N-Body Simulations of Planetary Accretion Around M Dwarf Stars". In: *The Astrophysical Journal* 699. Publisher: IOP ADS Bibcode: 2009ApJ...699..824O, pp. 824–838. ISSN: 0004-637X. DOI: 10.1088/0004-637X/699/1/824.

Ormel, C. W., S. Ida, and H. Tanaka (Oct. 2012). "Migration Rates of Planets due to Scattering of Planetesimals". In: *The Astrophysical Journal* 758. Publisher: IOP ADS Bibcode: 2012ApJ...758...80O, p. 80. ISSN: 0004-637X. DOI: 10.1088/0004-637X/758/2/80.

Ormel, Chris (Oct. 2024). *Planet Formation Mechanisms*. arXiv:2410.14430.

Orosz, Jerome A. et al. (Sept. 2012a). "Kepler-47: A Transiting Circumbinary Multiplanet System". In: *Science* 337. ADS Bibcode: 2012Sci...337.1511O, p. 1511. ISSN: 0036-8075. DOI: 10.1126/science.1228380.

Orosz, Jerome A. et al. (Oct. 2012b). "The Neptune-sized Circumbinary Planet Kepler-38b". In: *The Astrophysical Journal* 758. ADS Bibcode: 2012ApJ...758...87O, p. 87. ISSN: 0004-637X. DOI: 10.1088/0004-637X/758/2/87.

Orosz, Jerome A. et al. (May 2019). "Discovery of a Third Transiting Planet in the Kepler-47 Circumbinary System". In: *The Astronomical Journal* 157. ADS Bibcode: 2019AJ....157..174O, p. 174. ISSN: 0004-6256. DOI: 10.3847/1538-3881/ab0ca0.

Owen, James E. and Yanqin Wu (Oct. 2013). "Kepler Planets: A Tale of Evaporation". In: *The Astrophysical Journal* 775. Publisher: IOP ADS Bibcode: 2013ApJ...775..105O, p. 105. ISSN: 0004-637X. DOI: 10.1088/0004-637X/775/2/105.

Özdönmez, Aykut, Huseyin Er, and Ilham Nasiroglu (Dec. 2023). "Investigation on the orbital period variations of NN Ser: implications for the hypothetical planets, the Applegate mechanism, and the orbital stability". In: *Monthly Notices of the Royal Astronomical Society* 526. Publisher: OUP ADS Bibcode: 2023MNRAS.526.4725O, pp. 4725–4734. ISSN: 0035-8711. DOI: 10.1093/mnras/stad3086.

Paardekooper, Sijme-Jan et al. (July 2012). "How Not to Build Tatooine: The Difficulty of In Situ Formation of Circumbinary Planets Kepler 16b, Kepler 34b, and Kepler 35b". In: *The Astrophysical Journal* 754. ADS Bibcode: 2012ApJ...754L..16P, p. L16. ISSN: 0004-637X. DOI: 10.1088/2041-8205/754/1/L16.

Palme, Herbert (May 2004). "The Giant Impact Formation of the Moon". In: *Science* 304.5673. Publisher: American Association for the Advancement of Science, pp. 977–979. DOI: 10.1126/science.1097059.

Pecaut, Mark J. and Eric E. Mamajek (Sept. 2013). "Intrinsic Colors, Temperatures, and Bolometric Corrections of Pre-main-sequence Stars". In: *The Astrophysical Journal Supplement Series* 208. Publisher: IOP ADS Bibcode: 2013ApJS..208....9P, p. 9. ISSN: 0067-0049. DOI: 10.1088/0067-0049/208/1/9.

Penzlin, Anna B. T., Wilhelm Kley, and Richard P. Nelson (Jan. 2021). "Parking planets in circumbinary discs". In: *Astronomy and Astrophysics* 645. ADS Bibcode: 2021A&A...645A..68P, A68. ISSN: 0004-6361. DOI: 10.1051/0004-6361/202039319.

Pepe, F. et al. (Jan. 2021). "ESPRESSO at VLT. On-sky performance and first results". In: *Astronomy and Astrophysics* 645. ADS Bibcode: 2021A&A...645A..96P, A96. ISSN: 0004-6361. DOI: 10.1051/0004-6361/202038306.

Perruchot, S. et al. (July 2008). "The SOPHIE spectrograph: design and technical key-points for high throughput and high stability". In: *Proceedings of the SPIE* 7014. Conference Name: Ground-based and Airborne Instrumentation for Astronomy II ADS Bibcode: 2008SPIE.7014E..0JP, 70140J. DOI: 10.1117/12.787379.

"Astrometry" (2018). In: *The Exoplanet Handbook*. Ed. by Michael Perryman. 2nd ed. Cambridge: Cambridge University Press, pp. 81–102. ISBN: 978-1-108-41977-2. DOI: 10.1017/9781108304160.004.

Perryman, Michael et al. (Dec. 2014). "Astrometric Exoplanet Detection with Gaia". In: *The Astrophysical Journal* 797. Publisher: IOP ADS Bibcode: 2014ApJ...797...14P, p. 14. ISSN: 0004-637X. DOI: 10.1088/0004-637X/797/1/14.

Petigura, Erik A., Geoffrey W. Marcy, and Andrew W. Howard (June 2013). "A Plateau in the Planet Population below Twice the Size of Earth". In: *The Astrophysical Journal* 770. Publisher: IOP ADS Bibcode: 2013ApJ...770...69P, p. 69. ISSN: 0004-637X. DOI: 10.1088/0004-637X/770/1/69.

Pierens, A. and R. P. Nelson (May 2008). "On the formation and migration of giant planets in circumbinary discs". en. In: *Astronomy and Astrophysics* 483.2, pp. 633–642. ISSN: 0004-6361. DOI: 10.1051/0004-6361:200809453.

Pinamonti, M. et al. (Aug. 2022). "HADES RV Programme with HARPS-N at TNG. XV. Planetary occurrence rates around early-M dwarfs". In: *Astronomy and Astrophysics* 664. Publisher: EDP ADS Bibcode: 2022A&A...664A..65P, A65. ISSN: 0004-6361. DOI: 10.1051/0004-6361/202142828.

Pollacco, D. L. et al. (Oct. 2006). "The WASP Project and the SuperWASP Cameras". In: *Publications of the Astronomical Society of the Pacific* 118. Publisher: IOP ADS Bibcode: 2006PASP..118.1407P, pp. 1407–1418. ISSN: 0004-6280. DOI: 10.1086/508556.

Pulley, D. et al. (Aug. 2022). "Eclipse timing variations in post-common envelope binaries: Are they a reliable indicator of circumbinary companions?" In: *Monthly Notices of the Royal Astronomical Society* 514. ADS Bibcode: 2022MNRAS.514.5725P, pp. 5725–5738. ISSN: 0035-8711. DOI: 10.1093/mnras/stac1676.

Qian, S. -B. et al. (Jan. 2010). "A giant planet in orbit around a magnetic-braking hibernating cataclysmic variable". In: *Monthly Notices of the Royal Astronomical Society* 401. Publisher: OUP ADS Bibcode: 2010MNRAS.401L..34Q, pp. L34–L38. ISSN: 0035-8711. DOI: 10.1111/j.1745-3933.2009.00780.x.

Qian, S. -B. et al. (June 2011). "Detection of a planetary system orbiting the eclipsing polar HU Aqr". In: *Monthly Notices of the Royal Astronomical Society* 414. Publisher: OUP ADS Bibcode: 2011MNRAS.414L..16Q, pp. L16–L20. ISSN: 0035-8711. DOI: 10.1111/j.1745-3933.2011.01045.x.

Quarles, B. et al. (Apr. 2018). "Stability Limits of Circumbinary Planets: Is There a Pile-up in the Kepler CBPs?" In: *The Astrophysical Journal* 856. ADS Bibcode: 2018ApJ...856..150Q, p. 150. ISSN: 0004-637X. DOI: 10.3847/1538-4357/aab264.

Raghavan, Deepak et al. (Sept. 2010). "A Survey of Stellar Families: Multiplicity of Solar-type Stars". In: *The Astrophysical Journal Supplement Series* 190. Publisher: IOP ADS Bibcode: 2010ApJS..190....1R, pp. 1–42. ISSN: 0067-0049. DOI: 10.1088/0067-0049/190/1/1.

Ragozzine, Darin and Aaron S. Wolf (June 2009). "Probing the Interiors of very Hot Jupiters Using Transit Light Curves". In: *The Astrophysical Journal* 698. ADS Bibcode: 2009ApJ...698.1778R, pp. 1778–1794. ISSN: 0004-637X. DOI: 10.1088/0004-637X/698/2/1778.

Rattanamala, R. et al. (Aug. 2023). "Eclipse timing variations in the WD + dM eclipsing binary RR Cae". In: *Monthly Notices of the Royal Astronomical Society* 523. Publisher: OUP ADS Bibcode: 2023MNRAS.523.5086R, pp. 5086–5108. ISSN: 0035-8711. DOI: 10.1093/mnras/stad1733.

Rauw, G. et al. (Oct. 2016). "Apsidal motion in the massive binary HD 152218". en. In: *Astronomy & Astrophysics* 594, A33. ISSN: 0004-6361, 1432-0746. DOI: 10.1051/0004-6361/201628766.

Reffert, Sabine et al. (Feb. 2015). "Precise radial velocities of giant stars. VII. Occurrence rate of giant extrasolar planets as a function of mass and metallicity". In: *Astronomy and Astrophysics* 574. Publisher: EDP ADS Bibcode: 2015A&A...574A.116R, A116. ISSN: 0004-6361. DOI: 10.1051/0004-6361/201322360.

Ricker, George R. et al. (Jan. 2015). "Transiting Exoplanet Survey Satellite (TESS)". In: *Journal of Astronomical Telescopes, Instruments, and Systems* 1. ADS Bibcode: 2015JATIS...1a4003R, p. 014003. DOI: 10.1117/1.JATIS.1.1.014003.

Roberts, S. et al. (Feb. 2013). "Gaussian processes for time-series modelling". In: *Philosophical Transactions of the Royal Society A: Mathematical, Physical and Engineering Sciences* 371.1984. Publisher: Royal Society, p. 20110550. DOI: 10.1098/rsta.2011.0550.

Rosenthal, Lee J. et al. (July 2021). "The California Legacy Survey. I. A Catalog of 178 Planets from Precision Radial Velocity Monitoring of 719 Nearby Stars over Three Decades". In: *The Astrophysical Journal Supplement Series* 255. ADS Bibcode: 2021ApJS..255....8R, p. 8. ISSN: 0067-0049. DOI: 10.3847/1538-4365/abe23c.

Rosu, S. et al. (Mar. 2020). "Apsidal motion in the massive binary HD152248". In: *Astronomy & Astrophysics* 635. arXiv: 2002.01271, A145. ISSN: 0004-6361, 1432-0746. DOI: 10.1051/0004-6361/201937285.

Rosu, S. et al. (Feb. 2022). "Apsidal motion in massive eccentric binaries in NGC 6231: The case of HD 152219". In: *arXiv:2202.02012 [astro-ph]*. arXiv: 2202.02012.

Sabotta, S. et al. (Sept. 2021). "The CARMENES search for exoplanets around M dwarfs. Planet occurrence rates from a subsample of 71 stars". In: *Astronomy and Astrophysics* 653. ADS Bibcode: 2021A&A...653A.114S, A114. ISSN: 0004-6361. DOI: 10.1051/0004-6361/202140968.

Sahlmann, J., A. H. M. J. Triaud, and D. V. Martin (Feb. 2015). "Gaia's potential for the discovery of circumbinary planets". In: *Monthly Notices of the Royal Astronomical Society* 447. ADS Bibcode: 2015MNRAS.447..287S, pp. 287–297. ISSN: 0035-8711. DOI: 10.1093/mnras/stu2428.

Sahlmann, J. et al. (Apr. 2011a). "HD 5388 b is a 69 MJup companion instead of a planet". In: *Astronomy and Astrophysics* 528. ADS Bibcode: 2011A&A...528L...8S, p. L8. ISSN: 0004-6361. DOI: 10.1051/0004-6361/201116533.

Sahlmann, J. et al. (Jan. 2011b). "Search for brown-dwarf companions of stars". In: *Astronomy and Astrophysics* 525. Publisher: EDP ADS Bibcode: 2011A&A...525A..95S, A95. ISSN: 0004-6361. DOI: 10.1051/0004-6361/201015427.

Sahlmann, J. et al. (Aug. 2013). "Astrometric orbit of a low-mass companion to an ultracool dwarf". In: *Astronomy and Astrophysics* 556. ADS Bibcode: 2013A&A...556A.133S, A133. ISSN: 0004-6361. DOI: 10.1051/0004-6361/201321871.

Sairam, Lalitha et al. (Nov. 2024a). "BEBOP VI. Enabling the detection of circumbinary planets orbiting double-lined binaries with the DOLBY method of radial-velocity extraction". In: *Monthly Notices of the Royal Astronomical Society* 534. Publisher: OUP ADS Bibcode: 2024MNRAS.534.3999S, pp. 3999–4017. ISSN: 0035-8711. DOI: 10.1093/mnras/stae2317.

Sairam, Lalitha et al. (Jan. 2024b). "New methods for radial-velocity measurements of double-lined binaries, and detection of a circumbinary planet orbiting TIC 172900988". In: *Monthly Notices of the Royal Astronomical Society* 527. ADS Bibcode: 2024MNRAS.527.2261S, pp. 2261–2278. ISSN: 0035-8711. DOI: 10.1093/mnras/stad3136.

Sale, O. et al. (Dec. 2020). "Eclipse time variations in the post-common envelope binary V470 Cam". In: *Monthly Notices of the Royal Astronomical Society* 499. Publisher: OUP ADS Bibcode: 2020MNRAS.499.3071S, pp. 3071–3084. ISSN: 0035-8711. DOI: 10.1093/mnras/staa3013.

Santerne, A. et al. (Mar. 2016). "SOPHIE velocimetry of Kepler transit candidates. XVII. The physical properties of giant exoplanets within 400 days of period". In: *Astronomy and Astrophysics* 587. Publisher: EDP ADS Bibcode: 2016A&A...587A..64S, A64. ISSN: 0004-6361. DOI: 10.1051/0004-6361/201527329.

Scargle, J. D. (Dec. 1982). "Studies in astronomical time series analysis. II. Statistical aspects of spectral analysis of unevenly spaced data." In: *The Astrophysical Journal* 263. Publisher: IOP ADS Bibcode: 1982ApJ...263..835S, pp. 835–853. ISSN: 0004-637X. DOI: 10.1086/160554.

Schmitt, J. H. M. M. et al. (Feb. 2016). "The alpha CrB binary system: A new radial velocity curve, apsidal motion, and the alignment of rotation and orbit axes". en. In: *Astronomy & Astrophysics* 586, A104. ISSN: 0004-6361, 1432-0746. DOI: 10.1051/0004-6361/201526662.

Schneider, J. (July 1994). "On the occultations of a binary star by a circum-orbiting dark companion". en. In: *Planetary and Space Science* 42.7, pp. 539–544. ISSN: 0032-0633. DOI: 10.1016/0032-0633(94)90075-2.

Schneider, J. et al. (Aug. 2011). "Defining and cataloging exoplanets: the exoplanet.eu database". In: *Astronomy and Astrophysics* 532. ADS Bibcode: 2011A&A...532A..79S, A79. ISSN: 0004-6361. DOI: 10.1051/0004-6361/201116713.

Schwamb, Megan E. et al. (May 2013). "Planet Hunters: A Transiting Circumbinary Planet in a Quadruple Star System". In: *The Astrophysical Journal* 768. ADS Bibcode: 2013ApJ...768..127S, p. 127. ISSN: 0004-637X. DOI: 10.1088/0004-637X/768/2/127.

Sigurdsson, Steinn et al. (July 2003). "A Young White Dwarf Companion to Pulsar B1620-26: Evidence for Early Planet Formation". In: *Science* 301.5630. Publisher: American Association for the Advancement of Science, pp. 193–196. DOI: 10.1126/science.1086326.

Silva Aguirre, Víctor et al. (Feb. 2017). "Standing on the Shoulders of Dwarfs: the Kepler Asteroseismic LEGACY Sample. II.Radii, Masses, and Ages". In: *The Astrophysical Journal* 835. Publisher: IOP ADS Bibcode: 2017ApJ...835..173S, p. 173. ISSN: 0004-637X. DOI: 10.3847/1538-4357/835/2/173.

Skilling, John (Dec. 2006). "Nested sampling for general Bayesian computation". In: *Bayesian Analysis* 1.4. Publisher: International Society for Bayesian Analysis, pp. 833–859. ISSN: 1936-0975, 1931-6690. DOI: 10.1214/06-BA127.

Socia, Quentin J. et al. (Mar. 2020). "Kepler-1661 b: A Neptune-sized Kepler Transiting Circumbinary Planet around a Grazing Eclipsing Binary". In: *The Astronomical Journal* 159. Publisher: IOP ADS Bibcode: 2020AJ....159...94S, p. 94. ISSN: 0004-6256. DOI: 10.3847/1538-3881/ab665b.

Soderblom, David R. (Sept. 2010). "The Ages of Stars". In: *Annual Review of Astronomy and Astrophysics* 48. ADS Bibcode: 2010ARA&A..48..581S, pp. 581–629. ISSN: 0066-4146. DOI: 10.1146/annurev-astro-081309-130806.

Spiegel, David S. and Adam Burrows (Jan. 2012). "SPECTRAL AND PHOTOMETRIC DIAGNOSTICS OF GIANT PLANET FORMATION SCENARIOS". en. In: *The Astrophysical Journal* 745.2. Publisher: The American Astronomical Society, p. 174. ISSN: 0004-637X. DOI: 10.1088/0004-637X/745/2/174.

Standing, Matthew R. et al. (Apr. 2022). "BEBOP II: sensitivity to sub-Saturn circumbinary planets using radial-velocities". In: *Monthly Notices of the Royal Astronomical Society* 511. ADS Bibcode: 2022MNRAS.511.3571S, pp. 3571–3583. ISSN: 0035-8711. DOI: 10.1093/mnras/stac113.

Standing, Matthew R. et al. (June 2023). "Radial-velocity discovery of a second planet in the TOI-1338/BEBOP-1 circumbinary system". In: *Nature Astronomy* 7. ADS Bibcode: 2023NatAs...7..702S, pp. 702–714. ISSN: 2397-3366. DOI: 10.1038/s41550-023-01948-4.

Stevenson, A. T. et al. (Mar. 2025). "RV-exoplanet eccentricities: Good, Beta, and Best". In: *Monthly Notices of the Royal Astronomical Society*. Publisher: OUP ADS Bibcode: 2025MNRAS.tmp..487S. ISSN: 0035-8711. DOI: 10.1093/mnras/staf502.

Szabó, Gy. M. and L. L. Kiss (Feb. 2011). "A Short-period Censor of Sub-Jupiter Mass Exoplanets with Low Density". In: *The Astrophysical Journal* 727. Publisher: IOP ADS Bibcode: 2011ApJ...727L..44S, p. L44. ISSN: 0004-637X. DOI: 10.1088/2041-8205/727/2/L44.

Tamayo, Daniel et al. (May 2017). "Convergent Migration Renders TRAPPIST-1 Long-lived". In: *The Astrophysical Journal* 840. Publisher: IOP ADS Bibcode: 2017ApJ...840L..19T, p. L19. ISSN: 0004-637X. DOI: 10.3847/2041-8213/aa70ea.

Tokovinin, Andrei (Mar. 2018). "The Updated Multiple Star Catalog". In: *The Astrophysical Journal Supplement Series* 235. Publisher: IOP ADS Bibcode: 2018ApJS..235....6T, p. 6. ISSN: 0067-0049. DOI: 10.3847/1538-4365/aaa1a5.

Traub, W. A. and B. R. Oppenheimer (Dec. 2010). *Direct Imaging of Exoplanets*. Pages: 111-156 Publication Title: Exoplanets ADS Bibcode: 2010exop.book..111T.

Triaud, A. H. M. J. et al. (Dec. 2010). "Spin-orbit angle measurements for six southern transiting planets. New insights into the dynamical origins of hot Jupiters". In: *Astronomy and Astrophysics* 524. Publisher: EDP ADS Bibcode: 2010A&A...524A..25T, A25. ISSN: 0004-6361. DOI: 10.1051/0004-6361/201014525.

Triaud, Amaury H. M. J. (Jan. 2018). *The Rossiter-McLaughlin Effect in Exoplanet Research*. Pages: 2 Publication Title: Handbook of Exoplanets ADS Bibcode: 2018haex.bookE...2T. Springer. DOI: 10.1007/978-3-319-55333-7_2.

Triaud, Amaury H. M. J. et al. (Dec. 2017). "The EBLM Project. IV. Spectroscopic orbits of over 100 eclipsing M dwarfs masquerading as transiting hot Jupiters". In: *Astronomy and Astrophysics* 608. ADS Bibcode: 2017A&A...608A.129T, A129. ISSN: 0004-6361. DOI: 10.1051/0004-6361/201730993.

Triaud, Amaury H. M. J. et al. (Mar. 2020). "An eclipsing substellar binary in a young triple system discovered by SPECULOOS". In: *Nature Astronomy* 4. ADS Bibcode: 2020NatAs...4..650T, pp. 650–657. ISSN: 2397-3366. DOI: 10.1038/s41550-020-1018-2.

Triaud, Amaury H. M. J. et al. (Apr. 2022). "BEBOP III. Observations and an independent mass measurement of Kepler-16 (AB) b - the first circumbinary planet detected with radial velocities". In: *Monthly Notices of the Royal Astronomical Society* 511. ADS Bibcode: 2022MNRAS.511.3561T, pp. 3561–3570. ISSN: 0035-8711. DOI: 10.1093/mnras/stab3712.

Trotta, Roberto (Mar. 2008). "Bayes in the sky: Bayesian inference and model selection in cosmology". In: *Contemporary Physics* 49. ADS Bibcode: 2008ConPh..49...71T, pp. 71–104. ISSN: 0010-7514. DOI: 10.1080/00107510802066753.

Udalski, A. et al. (Mar. 2002). "The Optical Gravitational Lensing Experiment. Search for Planetary and Low-Luminosity Object Transits in the Galactic Disk. Results of 2001 Campaign". In: *Acta Astronomica* 52. ADS Bibcode: 2002AcA....52....1U, pp. 1–37. ISSN: 0001-5237. DOI: 10.48550/arXiv.astro-ph/0202320.

Udry, S. et al. (Jan. 2000). *The CORALIE Planet-Search Sample*. Conference Name: From Extrasolar Planets to Cosmology: The VLT Opening Symposium Pages: 571 ADS Bibcode: 2000fepc.conf..571U. DOI: 10.1007/10720961_83.

Van Eylen, Vincent et al. (Feb. 2019). "The Orbital Eccentricity of Small Planet Systems". In: *The Astronomical Journal* 157. Publisher: IOP ADS Bibcode: 2019AJ....157...61V, p. 61. ISSN: 0004-6256. DOI: 10.3847/1538-3881/aaf22f.

Venturini, J. et al. (June 2024). "A fading radius valley towards M dwarfs, a persistent density valley across stellar types". In: *Astronomy and Astrophysics* 686. ADS Bibcode: 2024A&A...686L...9V, p. L9. ISSN: 0004-6361. DOI: 10.1051/0004-6361/202349088.

Venturini, Julia et al. (Nov. 2020). "The nature of the radius valley. Hints from formation and evolution models". In: *Astronomy and Astrophysics* 643. ADS Bibcode: 2020A&A...643L...1V, p. L1. ISSN: 0004-6361. DOI: 10.1051/0004-6361/202039141.

Weidenschilling, S. J. (July 1977). "Aerodynamics of solid bodies in the solar nebula." In: *Monthly Notices of the Royal Astronomical Society* 180. Publisher: OUP ADS Bibcode: 1977MNRAS.180...57W, pp. 57–70. ISSN: 0035-8711. DOI: 10.1093/mnras/180.2.57.

Welsh, William F. et al. (Jan. 2012). "Transiting circumbinary planets Kepler-34 b and Kepler-35 b". In: *Nature* 481. ADS Bibcode: 2012Natur.481..475W, pp. 475–479. ISSN: 0028-0836. DOI: 10.1038/nature10768.

Welsh, William F. et al. (Apr. 2014). "Recent Kepler Results On Circumbinary Planets". In: 293. Conference Name: Formation, Detection, and Characterization of Extrasolar Habitable Planets Place: eprint: arXiv:1308.6328 ADS Bibcode: 2014IAUS..293..125W, pp. 125–132. DOI: 10.1017/S1743921313012684.

Welsh, William F. et al. (Aug. 2015). "Kepler 453 b - The 10th Kepler Transiting Circumbinary Planet". In: *The Astrophysical Journal* 809. Publisher: IOP ADS Bibcode: 2015ApJ...809...26W, p. 26. ISSN: 0004-637X. DOI: 10.1088/0004-637X/809/1/26.

Winn, J. N. (Dec. 2010). *Exoplanet Transits and Occultations*. Pages: 55-77 Publication Title: Exoplanets ADS Bibcode: 2010exop.book...55W. DOI: 10.48550/arXiv.1001.2010.

Wittenmyer, Robert A. et al. (Feb. 2020). "Cool Jupiters greatly outnumber their toasty siblings: occurrence rates from the Anglo-Australian Planet Search". In: *Monthly Notices of the Royal Astronomical Society* 492. Publisher: OUP ADS Bibcode: 2020MNRAS.492..377W, pp. 377–383. ISSN: 0035-8711. DOI: 10.1093/mnras/stz3436.

Wolf, M. et al. (Mar. 2021). "Possible substellar companions in dwarf eclipsing binaries. SDSS J143547.87+373338.5, NSVS 7826147, and NSVS 14256825". In: *Astronomy and Astrophysics* 647. ADS Bibcode: 2021A&A...647A..65W, A65. ISSN: 0004-6361. DOI: 10.1051/0004-6361/202039851.

Wolszczan, A. and D. A. Frail (Jan. 1992). "A planetary system around the millisecond pulsar PSR1257 + 12". In: *Nature* 355. ADS Bibcode: 1992Natur.355..145W, pp. 145–147. ISSN: 0028-0836. DOI: 10.1038/355145a0.

Wolszczan, Alexander (Apr. 1994). "Confirmation of Earth-Mass Planets Orbiting the Millisecond Pulsar PSR B1257+12". In: *Science* 264. ADS Bibcode: 1994Sci...264..538W, pp. 538–542. ISSN: 0036-8075. DOI: 10.1126/science.264.5158.538.

Youdin, Andrew N. and Jeremy Goodman (Feb. 2005). "Streaming Instabilities in Protoplanetary Disks". In: *The Astrophysical Journal* 620. Publisher: IOP ADS Bibcode: 2005ApJ...620..459Y, pp. 459–469. ISSN: 0004-637X. DOI: 10.1086/426895.

Zanazzi, J. J. and Dong Lai (Jan. 2018). "Inclination evolution of protoplanetary discs around eccentric binaries". In: *Monthly Notices of the Royal Astronomical Society* 473. Publisher: OUP ADS Bibcode: 2018MNRAS.473..603Z, pp. 603–615. ISSN: 0035-8711. DOI: 10.1093/mnras/stx2375.

Zhang, Zhanbo and Daniel C. Fabrycky (July 2019). "Distinguishing Polar and Coplanar Circumbinary Exoplanets by Eclipse Timing Variations". en. In: *The Astrophysical Journal* 879.2. Publisher: The American Astronomical Society, p. 92. ISSN: 0004-637X. DOI: 10.3847/1538-4357/ab24d5.

Zucker, Shay and Tal Alexander (Jan. 2007). "Spectroscopic Binary Mass Determination using Relativity". In: *The Astrophysical Journal* 654.1. arXiv: astro-ph/0609753, pp. L83–L86. ISSN: 0004-637X, 1538-4357. DOI: 10.1086/510799.